UNIVERSITY OF GLASGOW

DEPARTMENT OF CIVIL ENGINEERING

"" EFFECTS OF CUT-OFF (FLOOD RELIEF) CHANNEL INTERSECTION ON BEND FLOW CHARACTERISTICS ""

A THESIS SUBMITTED IN FULFILMENT OF THE REQUIREMENTS FOR THE DEGREE OF DOCTOR OF PHILOSOPHY IN CIVIL ENGINEERING

BY

YOUSSEF RAMSIS FARES B.Sc. , M.Sc.

1989

†

to my daughter .....

" MARY ANN "

ACKNOWLEDGEMENTS

The writer wishes to express his respect, gratitude and appreciation to Mr *A.F. ABDELNOUR* for providing the necessary funds for this study and for his continuous encouragement. This also applies to *VINA* , writer's wife, for her moral support, cooperation, patience and understanding throughout the course of study. The writer's parents also gave substantial encouragement.

In the Department of Civil Engineering, the writer would like to acknowledge the following:

- Dr J.G. HERBERTSON , advisor of studies, for his helpful suggestions during the experimental part of the work and for his valuable review of the early draft of this manuscript.

- Dr D.A. ERVINE for stimulating some relevant discussions.

- Mr A. BURNETT and Mr A. GRAY for respectively, providing the necessary materials and for building the experimental apparatus.

- Mr G. IRVING and Miss J. SUTHERLAND , previous and current computer manager, for their suggestions during the development of the computer program.

- Last but not least, Mr W. WITHERS , writer's colleague, for his fruitful cooperation during the course of experiments.

ABSTRACT

The characteristics of flow in a gentle wide channel bend at the intersection with a cut–off (flood relief) channel are studied. The studies are restricted to subcritical flows in bends with rigid boundaries and uniform rectangular cross sections. The object is to demonstrate how the intersection affects the water surface and velocities profiles in the channel bend.

Two approaches are employed in the study namely;

+ **Mathemetical Approach**
+ **Experimental Approach**

The mathematical approach is divided into two stages. The first stage is concerned with the formulation of the flow in a gentle wide channel bend and the second stage with the formulation of the flow at the intersection with the flood channel. The flow entering the flood channel is treated as the flow spilling over a side weir with a broad crest. The conventional equations of motion are used to establish the model equations which are then solved numerically using a finite difference technique.

For the experimental approach, a laboratory model was constructed in order to obtain physical data principally for the verification of the mathematical model.

The analysis of the results follows two distinct lines:

+ **Quantitative Analysis:** where comparisons between the theoretical and experimental profiles are made for the bend flow with and without the introduction of the flood channel intersection. Principally for verification of the mathematical model results.

+ **Qualitative Analysis:** where qualitative comparisons between the flow profiles in both cases are made in order to show the influence of the intersection on the bend flow characteristics.

The analysis shows that the suggested mathematical model can be used satisfactorily for high to medium flood channel bed levels. It is further shown that the bend characteristics continue to dominate the flow again for high to medium (weir) flood channel bed levels but that at medium to low (weir) channel bed levels, the local effects produced by the intersection predominate.

CONTENTS

CHAPTER III

MATHEMATICAL FORMULATION OF FLOW IN A GENTLE WIDE CHANNEL BEND

CHAPTER V

EXPERIMENTAL INVESTIGATION OF THE PROBLEM

CHAPTER VI

FLOW BEHAVIOUR IN A GENTLE WIDE CHANNEL BEND

CHAPTER VII

FLOW AT BEND/FLOOD RELIEF CHANNEL INTERSECTION

LIST OF FIGURES

CHAPTER I

CHAPTER II

CHAPTER III

CHAPTER V

CHAPTER VI

CHAPTER VII

APPENDIX (D)

LIST OF PLATES

CHAPTER V

CHAPTER VII

LIST OF TABLES

NOMENCLATURE

A = cross–sectional area of the main channel

A_c = side weir coefficient which includes the velocity and the discharge coefficients for flow across the flood relief channel (in equation (4.23))

A_λ, A_χ = power expansions for the variables λ and χ respectively (in Appendix (B))

B = width of the channel bend

B_λ, B_χ = power expansions for the variables λ and χ respectively (in Appendix (B))

c , c_1 = integration constants defined in equations (3.84) and (3.89) respectively

C = Chezy coefficient for the channel bed roughness

C' = non–dimensional Chezy coefficient (= $C/\sqrt{g}$)

C_d = coefficient of weir discharge

C_e = bend loss coefficient

C_f = side weir coefficient (in equation 4.14))

C_h = weir crest height

C_p = circulation strength of the potential vortex

C_{op} = discharge coefficient for flow passing through the orifice plate

C_v = velocity coefficient allows for the effect of the approach flow

C_{vn} = discharge coefficient for flow over the "V–notch"

C_w = weir crest width

d = diameter of the orifice plate

$\overline{dA}$ = flow area vector

D = internal diameter of upstream pipe of the orifice plate

D_t = time total derivative

$\tilde{e}$ = time rate of strain tensor

$\underline{e}_r, \underline{e}_s, \underline{k}$ = unit vectors in r,s,z directions respectively

E_i = power expansion defined in equation (B– 23), Appendix (B)

E_v = velocity approach factor (defined in equation (5.4), Chapter V)

f = drowned flow reduction factor

f_d = Darcy– Weisbach friction factor

$\underline{F}$ = external body forces vector

$F_1(\lambda)$ = mathematical integration function (in equation (3.75))

$F_2(\lambda)$ = mathematical integration function (in equation (3.76))

$F_4(\lambda)$ = mathematical integration function (in equation (3.77))

F_i = power expansion defined in equation (B– 25), Appendix (B)

F_r = Froude number of the flow

F_g = force due to gravity (in equation (4.1))

F_τ = force due to bed friction (in equation (4.1))

$\sum F$ = sum of all forces acting upon the control volume (in equation (4.1))

g = gravitational acceleration

$\underline{G}$ = gravitational acceleration vector

h = water depth along and beyond the channel bend

h_a = sum of water depths at the sides of each strip of the bend

h_b = mean water depth at the entrance of the channel bend

h_e = effective flow head over the "V– notch"

h_f = total head loss in the flow

h_L = head loss in the flow due to bend resistance

h_s = mean water depth in the upstream section of the channel bend

h_w = water head above the crest level of the side weir

Δh = superelevation of the water surface

Δh_{op} = pressure head difference between upstream and downstream side of the orifice plate

h_v = measured flow head over the V– notch

$\hbar_1, \hbar_2, \hbar_3$ = integration constants (in Appendix (B))

H_r = hydraulic radius for each strip of the channel bend

[i,j,k] = local grid point in the finite difference scheme

$\underline{i},\underline{j},\underline{k}$ = unit vectors in x,y,z directions respectively

I_i, J_i = index of the power expansions defined in equations (B– 22) and (B– 24), Appendix (B)

k_r = coefficient for bend geometry [= $B/(2\ r_m)$]

K = Von–Karman universal constant (= 0.40)

K_h = an experimentally determined quantity (in equation (5.9))

n = Manning coefficient of bed roughness

$\bar{n}$ = value of the power law (in equation (3.73))

N,M,L = total number of sections considered for the grid points in the numerical in r,s,z directions respectively

N_t = is a coefficient which included in estimating the length of the flow affected by the secondary circulation beyond the bend

P = flow pressure field

ΔP = difference in the hydraustatic pressure force (in equation (4.1))

Q = flow discharge in the main channel at the side weir intersection

Q_0 = initial flow discharge in the main channel upstream of the side weir

Q_1, Q_2 = flow discharges upstream and downstream of the element Δx (in equation (4.15))

Q_{fR} = folw discharge spilling across the flood relief channel

Q_F = total side overflow discharge taken from each bend strip

Q_o = discharge in upstream pipe of the orifice plate

Q_{op} = flow discharge through the orifice plate

Q_s = flow discharge in the upstream reach of the bend

Q_r = net flow discharge in the radial direction

Q_v = flow discharge over the V– notch

Q_w = flow discharge over the side weir crest

r = local radius of bend curvature at any flow depth

r,s,z = cylindrical polar coordinates

r_f = mid radius of each curved strip of the channel bend

r_i,r_o = inner and outer bend radii

r_m = central (mean) radius of curvature

r_{mt} = radius of curvature at which the depth–averaged velocity of the flow is equal to its mean value

$\bar{R}$ = bend radius vector

R_b = parameter for the superelevation of the water surface (expressed in equation (3.94))

R_e = Reynolds number of the flow

R_{eo} = Reynolds number of the flow in the upstream pipe of the orifice plate

S = total energy gradient of the flow

S',S'' = longitudinal and transverse components of the total energy gradient

S_f = total energy (friction) slope

S_0 = longitudinal bed slope of the channel flume

S_r = transverse (radial) water surface slope

S_s = longitudinal water surface slope

$\%S_{xy}$ = strength of the spiral flow

$\%S_{rs}$ = local strength of the secondary circulation in the flow

u = mean velocity component of the flow

u_c = depth–averaged velocity at the central radius of curvature

u_m = depth–averaged velocity of the flow in the bend

u_{mb} = depth–averaged velocity of flow at the bend entrance

u_{mi}, u_{mo} = depth–averaged velocities at the inner and outer radii at the bend entrance respectively

u_{ms} = depth–averaged velocity upstream of the bend

u_{mt} = mean flow velocity in the cross section of the channel bend

u_o = mean flow velocity in upstream pipe of the orifice plate

u_{ro} = radial velocity component at the location Θ_{lim}

u_r, u_s, u_z = radial, longitudinal and vertical velocity components of the flow in r,s,z directions respectively

u_r', u_s', u_z' = fluctuation velocity components in r,s,z directions respectively

u_{sm} = maximum longitudinal velocity component at the water surface

u_x = longitudinal velocity component of the flow beyond the bend

u_* = shear (friction) velocity

u_{*i}, u_{*o} = friction velocities at the inner and outer radii at the bend entrance respectively

$\bar{U}$ = point velocity vector of the flow

$\underline{U}$ = Velocity field of the flow

V = voltage reading of the angle probe (equation (5.11))

x = distance along the crest length of the side weir ($\equiv$ weir width)

x_d = distance downstream of the bend where the decaying process of the secondary currents takes place

x_{dt} = distance downstream of the bend at which the residual secondary currents reduce to 10% of their initial value

x_{fd} = length of the channel at which the flow reached its fully developed state

x, y, z = cartesian rectangular coordinates

X_t = total distance of flow affected by secondary currents

α = kinetic energy coefficient

α_v = central angle of the "V– notch" ($\alpha_v = 90^\circ$)

β = momentum flux correction factor

γ = secondary flow convection factor

δ = verical distance measured from the channel bed to the point " T " at which $\partial_\lambda u_r = 0$ (see Fig.(3.))

$\eta_1(\lambda), \eta_2(\lambda)$ = mathematical integration functions expressed in equations (3.80) and (3.81) respectively

ζ = coefficient for bed roughness [= 1/(KC')]

ξ = coefficient for bed roughness (= 1 + ζ)

Θ_b = local angle of the bend

$\underline{\Theta}_b$ = central (total) angle of the channel bend

Θ_d = deviation angle of the horizontal resultant velocity from the tangential direction of the bend curved path

Θ_{lim} = bend angle at which the growth of the secondary circulation is effectively completed

λ = non– dimensional water depth (= z/h)

λ = non– dimensional water depth (= 1 – λ)

ϵ = expansibility factor defined in equation (5.3), Chapter V

$\Phi_1(\lambda)$ = mathematical integration function (section (3.5), Chapter III)

$\Phi_2(\lambda)$ = ,, ,, ,, ,, ,, ,, ,, ,, ,, ,,

$\Phi_{11}, \Phi_{12}, \Phi_{21}$ = sub– integrals of the functions $\Phi_1(\lambda)$ and $\Phi_2(\lambda)$

$\Phi_{51}, \Phi_{52}, \Phi_{53}$ = sub– integrals of the mathematical integral Φ_5, Appendix (C)

$\Phi_3, \Phi_4 .... \Phi_6$ = mathematical integrals (see section (3.7), Chapter III)

$\Phi_{61} .... \Phi_{64}$ = sub– integrals of the mathematical integral Φ_6, Appendix (C)

Ψ_1 , Ψ_2 = mathematical integrals

μ = diameter ratio (d/D) of the orifice plate design

ν = turbulent kinematic eddy viscosity of the flow

ν_o = mean kinematic eddy viscosity of the flow

ν' = non– dimensional kinematic eddy viscosity of the flow

ρ = density field of the flow

$\tilde{\tau}$ = shear stress tensor

τ_i, τ_o = longitudinal components of the bed shear stress at the inner and outer radii at the bend entrance respectively

τ_{or}, τ_{os} = radial and longitudinal components of the bed shear stress

τ_{rz} , τ_{sz} = vertical shear stresses in r and z directions respectively

ℓ = Prandtl mixing length

∂_t = time gradient operator

$\partial_r, \partial_s, \partial_z$ = gradient operators in r,s,z directions respectively

$\partial_x, \partial_y, \partial_z$ = gradient operators in x,y,z directions respectively

∇ = $\partial_x \underline{i} + \partial_y \underline{j} + \partial_z \underline{k}$ for cartesian coordinates

= $\partial_r \underline{e}_r + \partial_s \underline{e}_s + \partial_z \underline{k}$ for polar coordinates

CHAPTER I

DEFINITION AND OBJECT OF STUDY

CHAPTER I

DEFINITION AND OBJECT OF STUDY

(1.1) INTRODUCTION

Under natural conditions rivers rarely take straight courses but instead take winding courses. This is known as **"meandering"**. Investigation of the flow motion in a meandering stream is one of the most important problems of open channel hydraulics. One of the most significant features of flow around channel bends is the **"spiral motion"** produced by action of the centrifugal forces on the variable flow depth resulting from boundary friction. The spiral motion produces an essentially three–dimensional flow. The transverse components of the flow in the plane of the channel cross section (i.e. the **"secondary currents"**) cause successive scour and deposition processes along the outer and the inner banks of the bend. If systematic variations in the erosional and depositional activities take place, the channel bend becomes **active** and consequently forms a highly irregular plan pattern. However, depending upon the strength of the spiral motion of the flow and the sediment properties of the channel structure, a limiting condition occurs. Thereafter the meander becomes **overgrown** and **cut–off** occurs (see Fig.(1.1)). The time taken for the meander to reach the limiting condition is many years e.g. Gagliano et al (1983) state that the process may take from 2 → 10 years. After the **"cut–off"** channel has developed, the flow will divide into two components. One component continues to flow along the channel bend and the other spills

across the cut–off channel. The order of magnitude of the latter flow component depends on the magnitude of the total discharge and on the relative bed levels of the two channels.

According to Fisk (1944), there are two kinds of **"cut–off"**: (see Fig.(1.2))

- **Chute cut–off.**
- **Neck cut–off.**

- <u>Chute cut–off</u>

Chute cut–off occurs where the flow in a meander loop shortens its course by gradually reducing the length of the curved path. Flow during flood periods usually initiates this flow shortcut. In the process of developing a chute cut–off, low water flow continues across the chute and the new channel gradually deepens. As a consequence, the old bendway experiences a continual reduction of flow as the chute cut–off becomes dominant. The accompanying erosion and deposition processes result in the plugging of the original bend path. This process, however, takes place at a slow rate as the angle of the flow diversion down the chute is relatively small.

- <u>Neck cut–off</u>

Neck cut–off is a more important and a more frequent form of cut–off and it occurs late in the development of the meander loop. Neck cut–off can be initiated by one of the following causes:

(1) by the river bend becoming overgrown (i.e. bend sinuosity increases substantially) as a result of the continual scour and deposition processes going on within the active channel bend.

(2) by one arm of the meander loop migrating to the other. This one arm migration is generally caused by differences in boundary roughness and hence, by the resistance to migration experienced by the two arms of the loop.

(3) by artificial means (i.e. by man–made cut–off). This type of cut–off is constructed by trenching across the neck of the meander loop in order to allow excess flood flow to spill across the neck (either partially or fully). Such a neck cut–off is usually known as a **"flood relief channel"**.

In all cases of full neck cut–off, the meander loop is gradually blocked up by the deposition of sediment and eventually the so–called **"oxbow lake"** is formed (refer also to Fig.(1.2)).

Regardless of how neck cut–off is developed, opinion is divided on its benefits (Thorn (1966) and Winkley (1971)). One group states that flood relief channels reduce surface levels during flood periods, improve navigation in the main channel and do not cause any adverse changes to the river regime. The other group indicates that flood relief channels intensify channel stabilisation problems by causing increases in water surface slopes and velocities which, in turn, cause bank failures and, in general, upset the equilibruim condition of the river. Essentially, the difference of opinion centres on **" whether the local effects, often assumed determinal, at the intersection of the channels outweigh the benefits of the more stable regime produced in the main part of the meander loop "**. Regardless of which opinion is accepted as to the practical value of flood relief channels, there still remains considerable interest from a hydraulics point of view in the behaviour

of the flow at the upstream and downstream intersections of the flood relief channels and meander loops. This leads to a number of questions. These questions are:

- **What is the ratio of the discharge between that in the bend and that in the cut off (flood relief) channel ?**
- **What are the characteristics of the flow in the channel bend at the upstream and downstream intersections ?**
- **What is the effect of the flood relief channel dimensions on the bend flow behaviour ?**
- **What is the effect of different relative bed levels on the flow behaviour at the intersections ?**
- **What is the influence of placing a flow control device at the downstream end of the flood relief channel ?**
- **What effect does the intersection have on the approach flow in the bend ?**

i.e. the general question is:

- **What is the influence of the flood relief channel intersection on the flow regime in the channel bend ?**

Clearly it is outwith the scope of any one study to look at all the questions, particularly as very little data on the flood relief channel/bend channel problem is available in the literature. Hence, the present study will concentrate on the behaviour of the flow at the upstream intersection of the flood relief channel and the channel bend. A further study will be required to investigate the effects of the downstream intersection.

(1.2) OBJECT AND APPROACHES

As stated in the foregoing section, the main object of the present investigation is to determine the flow characteristics in a channel bend at the upstream intersection with the flood relief channel (see Fig.(1.3)). In order to accomplish this, the characteristic features of flow around a channel bend will be considered first in order to establish the initial flow conditions upstream of the intersection. The formulation of the flow at the intersection itself will then follow. The study will concentrate on the following bend flow characteristics (with and without the introduction of the flood relief channel):

- **Water surface profiles.**
- **Distribution of depth–averaged velocities.**
- **Vertical distribution of longitudinal velocities.**
- **Secondary currents (in case of a bend without a flood relief channel).**
- **Deviation angles of horizontal resultant velocities (in case of a bend with a flood relief channel).**

Two approaches will be employed in the investigation:

- **The Mathematical Approach.**
- **The Experimental Approach.**

In the mathematical approach described in Chapters III and IV, the problems associated with the flow in a gentle wide channel bend will be formulated. The

development of the superelevation phenomenon at the water surface and the secondary circulation along the curved path of the bend will be simulated by applying appropriate assumptions and boundary conditions to the conventional dynamic equations of motion. In the second stage of the formulation, the effect of the flood relief channel on the bend flow features will be simulated by superimposing a side weir on to the channel bend. In most of the mathematical formulation, solutions will be obtained numerically by using a suitable finite difference technique.

For the experimental approach, a physical model described in Chapter V was constructed especially for this study. This was necessary to provide data suitable for quantitative comparisons with the theoretical predictions obtained from the mathematical approach.

For the purposes of this initial investigation of the flood relief channel/bend channel problem, it was decided to restrict the study to the case of a gentle wide* channel bend with rigid boundaries and a uniform rectangular cross section.

* width / depth ratio $\geq$ 10

* width / depth ratio $\geq$ 10 and mid bend radius / width ratio $\geq$ 3

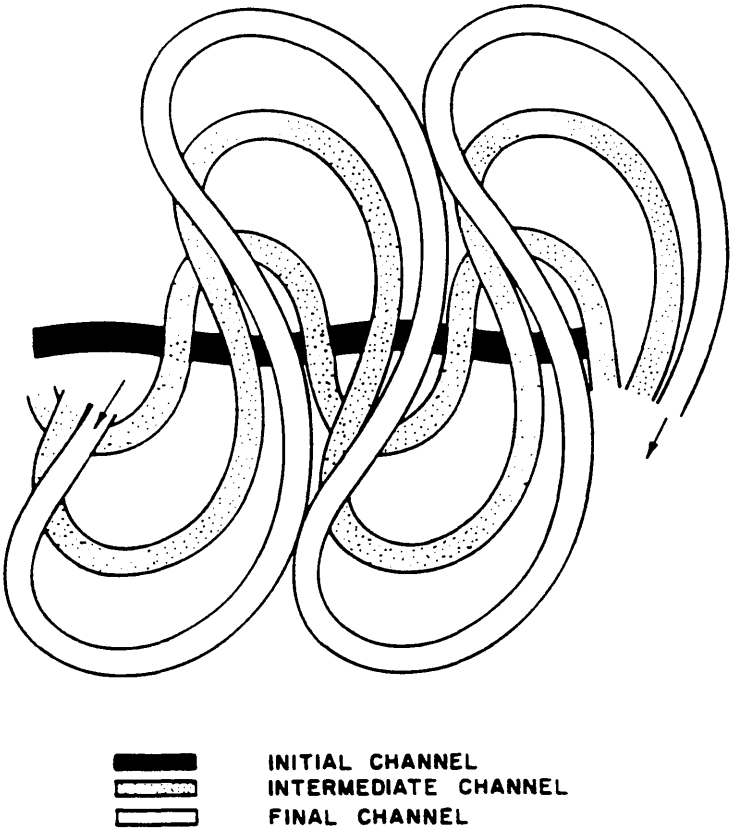

FIG. (1.1) – Development of Cut–offs
(after Beck (1983))

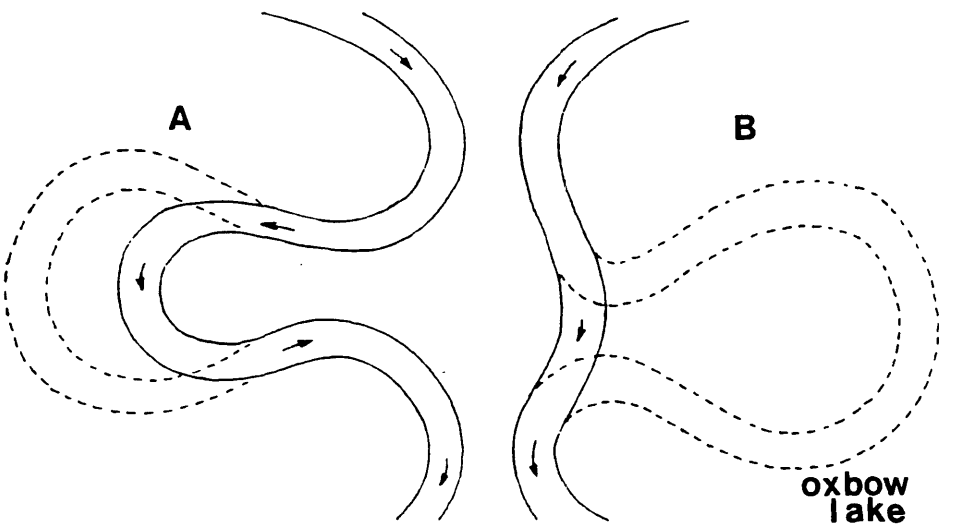

FIG.(1.2) – Types of Cut–offs (after Fisk (1944))
(A) Chute Cut–off
(B) Neck Cut–off

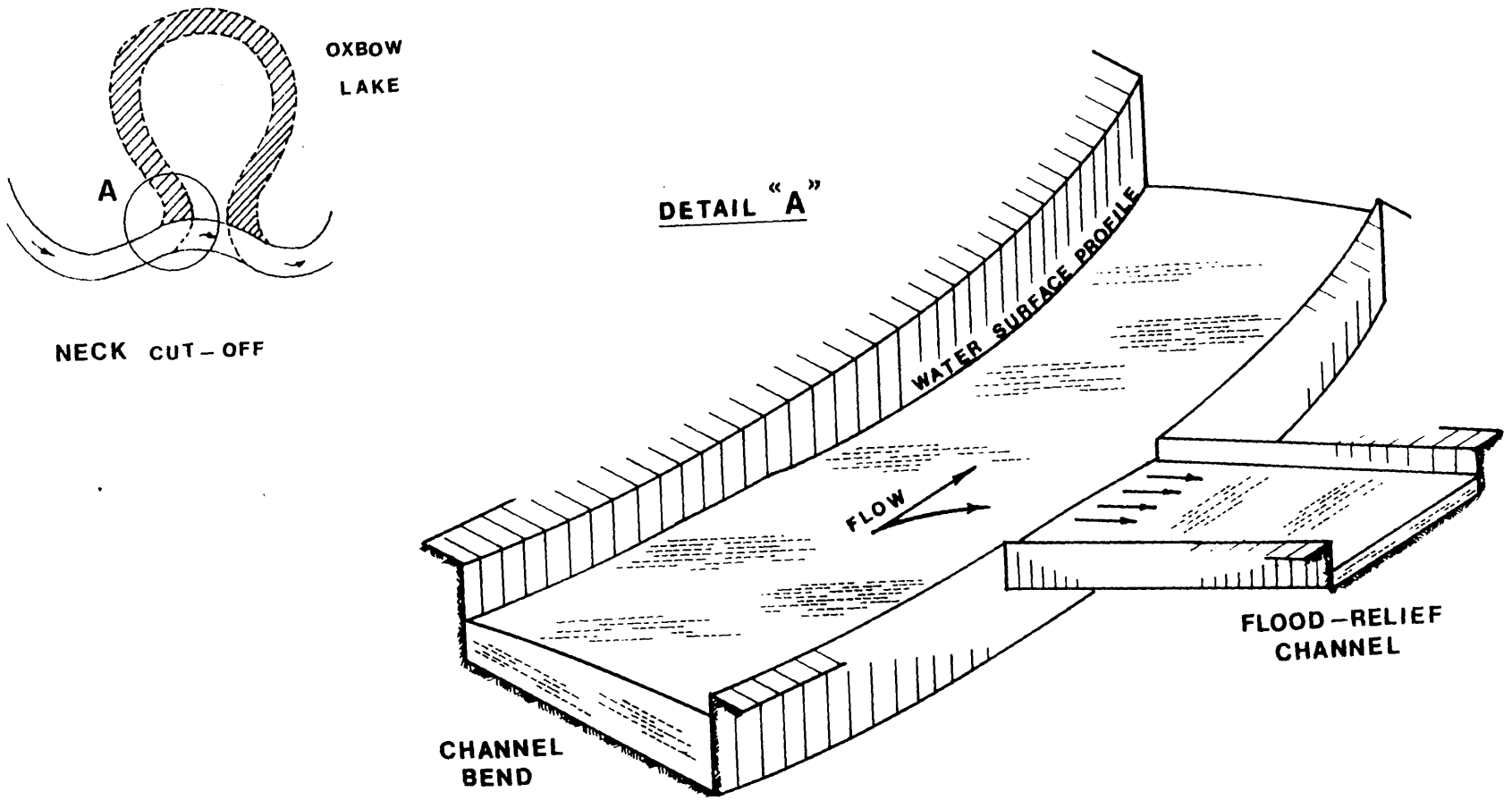

FIG. (1.3) – Definition Sketch

CHAPTER II

PRINCIPAL FEATURES OF FLOW IN CHANNEL BENDS

CHAPTER II

PRINCIPAL FEATURES OF FLOW IN CHANNEL BENDS

(2.1) INTRODUCTION

Investigation of the movement of water in bends is one of the most important problems of the hydraulics of open channels. The centrifugal force generated due to the curved flow path produces complex features within the flow. These features have a long term effect on the processes of flow resistance, sediment transport, bed and bank erosion, and in general on the development of channel morphology.

Flow in curved open channels has been studied for more than a century. Thomson (1876) published one of the first reports dealing with the flow behaviour in a channel bend. He described vividly the most significant feature of such a flow, i.e. the development of a spiral flow pattern. Thomson also explained the existence of the spiral flow as being the result of the variation in the centrifugal force acting upon the fluid particles over the water depth. Since then, numerous studies have considerably advanced the understanding of the flow mechanism in channel bends. These studies lie, in general, within three categories:

- Theoretical Studies (mathematical models)

- Experimental Studies (laboratory flumes)

- Field Studies (river meanders)

The development of the theoretical studies has only taken place within about the last 30 years, whereas extensive experimental and field stuides have been undertaken ever since Thomson's (1876) report. In recent years, a number of scientific theses have been published (e.g. see Khalid (1964), Abdulla (1976), Sarmah (1977), Damaskinidou– Georgiadou (1980), Spyratos (1981), Hussein (1984) and Salleh (1985)). These theses all contain very full literature reviews for flow around channel bends. Thus, it is not the writer's intention to re– describe the work published in the previous theses, but to give a global picture on the main characteristic features of the mechanism of such flows.

The main features of the flow in channel bends will be addressed under the following headings:

- Nature of flow
- Secondary currents
- Superelevation
- Separation zones
- Boundary shear stresses
- Energy losses

(2.2) NATURE OF FLOW

The characteristics of flow in a channel bend are complex. Not only is the flow turbulent and strongly three–dimensional, but the streamlines of the flow are curvilinear and interwoven as well. As a consequence, the flow in the channel bend possesses a rotation or circulation around an axis parallel to the main flow direction transferring it into a **"helical"** or **"spiral"** flow (see Fig.(2.1)). That is, in addition to the main (longitudinal) velocity component, there are transverse (secondary) components in the plane of the channel cross section, which are defined as the **"secondary currents"**. The importance of the secondary currents in the channel bend flow is their influence on the distortion of the main velocity and hence, the boundary shear stresses. This distortion is responsible mainly for the erosion and deposition processes along the outer and inner banks respectively in river bends. Fig.(2.2) demonstrates the effect of the secondary circulation on the bottom topagraphy in a river bend.

Early investigations of flow in channel bends (e.g. Mockmore (1943), Shukry (1949) and Chow (1959)) indicated that the main causes of the spiral flow are:

(1) The friction of the channel walls, which results in higher velocities near the central region of the channel bend than near the banks.

(2) The centrifugal force, which deflects the fluid particles from following the uniform curvature of the flow streamlines. This force is also responsible for the generation of the **superelevation** effect on the water surface.

(3) The non–uniform vertical distribution of the longitudinal velocity component, which exists in the approach channel to the bend and thus, initiates the spiral motion in the flow.

In order to evaluate the order of magnitude of the secondary currents within the channel cross section, Shukry (1949) developed a term called the "strength of the spiral flow" $\%S_{xy}$ which is defined as:

$\%S_{xy}$ = (kinetic energy of the secondary flow / total kinetic energy) x 100

From Shukry's experimental results on flow in a 180° channel bend with rectangular cross section, the strength of the spiral flow is found to be affected by :

(1) Reynolds number of the flow R_e . At low values of R_e the strength of spiral flow $\%S_{xy}$ is high, but decreases considerably as R_e increases.

(2) Reciprocal of aspect ratio h/B (i.e. water depth/channel width ratio). It is found that $\%S_{xy}$ decreases as h/B ratio increases.

(3) Bend tightness (i.e. mid radius of curvature/channel width) ratio r_m/B . It is found that $\%S_{xy}$ decreases gradually with increasing r_m/B ratio.

(4) Central angle of bend curvature θ_b . At large values of $\theta_b/180^\circ$ ratio, $\%S_{xy}$ increases.

Fig.(2.3) illustrates the influence of the four parametric functions R_e , h/B , r_m/B and $\theta_b/180^\circ$ on the strength of the spiral flow. It can be seen that $\%S_{xy}$ attained its minimum value at $r_m/B = 3.0$, which indicates that the excess energy losses in the flow due to the bend resistance can be considered as a minor effect. This will be discussed in more detail in section (2.7).

(2.3) SECONDARY CURRENTS

Secondary currents are the main feature of the flow in a channel bend. They are defined as the currents that occur in the plane of the bend cross section normal to the axis of the main flow. They are brought about by the interaction of the main flow with gross channel features.

Secondary currents are important because they distort the distributions of the longitudinal velocities of the flow and the boundary shear stresses from a symmetric behaviour about the channel centreline. Therefore, they affect the processes of the flow resistance, sediment transport and, in general, the flow regime in channel bends.

Below, types and characteristics of secondary currents found in open channel flows will be described.

(2.3.1) Types of Secondary Currents

Secondary currents can be developed in flows along straight channels as well as in channel bends. The spiral flow, which is produced by the combination of the main flow and the secondary currents, can be visualised as a streamwise vorticity (or rotation) about the main axis of the flow (see Prandtl (1952) and Einstein et al (1954)). The secondary currents can be classified according to the method by which the streamwise vorticity is produced.

Prandtl (1952) identified three major types of the secondary currents, namely :

(2.3.1.1) Type 1 – Skew Induced Currents

They appear where pre–existing cross stream (or spanwise) vorticity is twisted to present a component about the main axis of the channel. In open channel flows, the shear stress field necessary for the generation of the cross–stream vorticity is created by the boundary friction at the channel bed. But the production of the streamwise vorticity is otherwise independent of friction. Therefore, skew induced currents can appear in inviscid, laminar and turbulent flow, provided that cross–stream vorticity is present. The skewing itself is generally caused by the non–uniformity in the channel plan form (e.g. a channel bend). This type of secondary current is the type found in channel bends.

(2.3.1.2) Type 2 – Stress Induced Currents

They appear where streamwise vorticity is generated directly from the flow. This is possible only in turbulent flows where there is anisotropic turbulence and a non–uniform distribution of boundary shear stress. Stress induced currents occur generally in straight channels. Fig.(2.4) shows the stress induced currents in a closed triangle conduit and a rectangular open channel (after Prandtl (1952)). The main distinguishing feature is the peculiarities in the distribution of currents which is explained by a transverse flow reaching the corners of the channel cross section and then returning to its centre. Prandtl described the patterns of these currents in channels with sharp corners as a direct result of the interfering of two boundary layers generated at the bed and the walls of the channel. These currents are directed along the bisector of the angle towards the corner. Whereas along the sides, the secondary current movement is away from the corner.

(2.3.1.3) Type 3

This kind of secondary current is caused by solid bodies oscillating in a fluid or by a fluid oscillating next to a solid boundary. These currents are observed near a boundary in the case of standing waves in a fluid.

Prandtl (1952) classified these secondary currents as **"weak"** or **"strong"** according to the strength of the streamwise vorticity generated in the flow field. **Type 2** secondary currents, the stress induced currents are classified as **"weak"**, whereas **Type 1** secondary currents, the skew induced currents are **"strong"** and found much more frequently in channel flows. Since the secondary currents at channel bends are of the skew induced type, further consideration will be given to their development, behaviour and patterns in the following sections.

(2.3.2) Secondary Currents in Channel Bends

Development of the skew induced currents occurs almost immediately after entry to the channel bend, but their decay at exit from the bend takes place along a distance of up to 50 times the flow depth (see e.g. Rozovskii (1961), Bradshaw (1971), Bathurst et al (1979) and Nouh et al (1979)). The growth and decay of the secondary currents depend mainly on the flow discharge, Reynolds number, aspect ratio and bend tightness.

The various forms of secondary circulation that occur at various sections and bend angles along a 180° channel bend for different values of Reynolds number R_e , aspect ratio B/h and flow discharge Q are shown in Fig.(2.5) (after Francis et al (1970)). From their experimental results, Francis et al concluded

that for relatively small values of aspect ratio and Reynolds number, a two cell type of secondary current is likely to develop. As aspect ratio values increase, the two cell pattern is replaced by a multiple cell pattern. At high values of aspect ratio, the effect of the turbulent fluctuations gives the secondary currents a random structure and no cell pattern appears.

Along the course of a channel bend, the centrifugal force acting on the flow has different effects at different depths because of variation of the longitudinal velocity component with depth. As a consequence, the shear stress field becomes skewed. The resulting secondary currents drive the surface water particles towards the outer bank and the bed water particles towards the inner bank. This pattern of circulation is of the **single cell type** and is observed in both bends with rigid boundaries and natural river bends (see Fig.(2.6)a).

Both experimental results and field measurements indicate the existence of an additional **small cell of reverse circulation** to the main cell (Fig.(2.6)b). This reverse cell exists locally close to or at the outer bank of the bend. Many investigators (e.g. Rozovskii (1961), Hey et al (1975), (1976), Bathurst et al (1979), De Vriend et al (1981), (1983), Thorne et al (1983) and others) concluded that this cell is due to the bank roughness effect and extends over a region of one to two water depths from the outer bank. It is negligible in wide channel bends (i.e. of high aspect ratios). The existence of the reverse cell depends on the slope of the outer bank. When the bank is steep the cell is more likely to develop than in case of a shelving bank, where cell development is hindered by bank roughness and the small depth of water at the bank. Figures (2.7) and (2.8) show the structure of the secondary currents and the flow isovels (i.e. the lines of equal longitudinal velocity component) in river bends, in the case of steep and shelving banks.

(2.3.3) Effect of the Flow Discharge on the Strength of the Secondary Currents

In channel bends with rigid boundaries, the strength of the secondary circulation increases as the flow discharge increases. This is because the centrifugal force which drives the secondary currents in the flow increases due to its dependence on flow velocity and radius of curvature. In contrast, field measurements of the flow in river bends indicate that the secondary circulation is weak at low and high discharges but strong at medium discharges. Bhowmik et al (1978) and Bathurst et al (1979) explain this feature as a result of the non– uniform distribution of bed topography along the bend. The existence of riffles (i.e. sediment deposits) along the inner bank and pools (i.e. scour holes) along the outer bank causes a substantial change in the effective radius of curvature and hence a change in the centrifugal force acting on the flow.

At low and high flow discharges, the relative magnitude of the main flow velocity and the radius of bend curvature is small. Thus, the centrifugal force and hence the strength of the secondary currents becomes weak. At medium discharges, the main flow velocity is higher than the radius of curvature and as a result, the strength of the secondary circulation becomes strong.

(2.4) SUPERELEVATION

The centrifugal force, which develops in the flow due to the bend curvature, produces a unique feature known as **"superelevation"**. It is defined as a rise in the water surface at the outer bank with an accompanying depression at the inner bank. In general, superelevation of the water surface will lead to two occurrences

of radial increase in depth. First, at the bend entry where the water surface rises at the outer bank, and second at the bend exit along the inner bank where the water surface reverts to the horizontal level. While the above is true in the general case, under certain conditions, such as bends with high bend tightness and low Froude number, superelevation is negligible.

The measured water surface configuration in the form of contours of equal levels in a 90° gently curved channel bend, (a) with a trapezoidal cross section and (b) with a mobile bed , is shown in Fig.(2.9) (after Yen et al (1971)). It can be seen that the superelevation effect is greater in the bend with a mobile bed than in the bend with the rigid trapezoidal section. The reason for this is that the bed topography influences the strength of the spiral motion in the flow. In contrast, Fig.(2.10) gives the water surface contourlines for a 180° strongly curved channel bend with a rectangular cross section (after Rozovskii (1961)). In this case, there is a continuous build up and subsequent decrease of the superelevation within the bend so that no distinct region exists in which a state of axial symmetry prevails. This lack of axial symmetry in the superelevation represents the main difference between the flow in strongly curved and gently curved channel bends.

Numerous investigators (e.g. Mockmore (1943), Shukry (1949), Chow (1959), Ippen et al (1962), Yen et al (1971) and Steffler et al (1985)) have indicated that for a fully developed flow in channel bends, the frictional effects (i.e. boundary shear stresses) on the superelevation are small. This finding suggests that potential vortex theory should be suitable for describing the flow in channel bends. By use of this theory, the distribution of the radial velocity component is given by the constant product of the longitudinal velocity component and the associated radius of curvature. The resulting radial profile of the water surface is hyperbolic with convex upwards. Shukry (1949) found that the superelevation of the water surface, by application of the potential vortex theory, is

$$\Delta h = (C_p^2 / 2\ g)\ [(1/r_i^2) - (1/r_o^2)] \qquad (2.1)$$

where

Δh is the superelevation of the water surface

C_p is the circulation constant of the potential vortex

r_i & r_o are the inner and the outer bend radii respectively

g is the acceleration of gravity

By assuming the flow depth upstream of the bend is equal to the average depth in the bend, Ippen et al (1962) developed the formula

$$\Delta h = (u^2/2\ g)\ (2\ B/r_m) / [1 - (B/2r_m)^2] \qquad (2.2)$$

where

u is the mean flow velocity

B is the channel width

r_m is the mid radius of bend curvature

Ippen et al also considered the situations where high velocities occur near the outer bank of the bend (especially near the bend exit). By employing the forced vortex theory, with the assumption of constant average specific energy head to approximate the flow pattern, Ippen et al developed the following expression for the superelevation:

$$\Delta h = (u^2/2\ g)\ (2\ B/r_m) / [1 + (B^2/12\ r_m)] \qquad (2.3)$$

Field measurements have shown that the radial water surface profile may have a central trough. Based upon this observation, Simons (1971) combined potential

and the forced vortex theory to simulating the flow pattern inward and outward from the centreline using the expression:

$$\Delta h = (u_c^2/2\ g)\ [2 - (r_i/r_m)^2 - (r_m/r_o)^2] \qquad (2.4)$$

where u_c is the flow velocity at the mid radius of curvature.

It should be noted that the foregoing formulae for superelevation are based upon the following assumptions:

(a) The vertical distribution of the pressure field is hydrostatic.

(b) The radial and the vertical velocity components are much smaller than the longitudinal velocity component.

(2.5) SEPARATION ZONES

The separation phenomenon may occur in the flow when the static pressure near the channel wall increases. The fluid particles near the channel wall have insufficient kinetic energy to overcome the pressure gradient (simulated by the local slope of the water surface in the upstream direction). As a result, separation of the boundary layer from the channel banks may occur (Shukry (1949), Rozovskii (1961), Ippen et al (1962)).

Separation of the flow streamlines from the channel bend walls may develop in two regions:

- Along the outer channel wall as the water surface rises on entering the bend.
- Along the inner bank within the channel bend and for some distance downstream of the bend exit.

In most circumstances, the potential separation zone at the outer bank is overcome by the turbulent exchange of momentum from the main body of the channel. In contrast, the separation zone at the inner bank is more persistent. The persistence and extent of this latter zone is caused by the abrupt rise in water surface on the opposite bank and the spiral motion of the flow which encourages the faster moving fluid to go towards the outer bank (Soliman et al (1968)).

Leeder et al (1975) indicated that flow separation in channel bends is best expressed as a function of:

- Bend tightness r_m/B , where r_m is the mid radius and B is the channel width.
- Froude number of the flow $F_r = u/\sqrt{(g\ h)}$, where u is the mean flow velocity and h is the mean flow depth.

The use of these non-dimensional factors allow data from a wide range of channel bends to be compared. Leeder et al (1975) also stated that the effect of flow separation is a reduction in the effective width of the channel downstream of and opposite to the separation zone (this reduction can be as great as 50% in some cases). As a result, the local longitudinal velocity component of the flow increases greatly enhancing the erosion rate at the outer bank. Fig.(2.11) shows the characteristic features of separation at the inner bank of a channel bend and Fig.(2.12) shows how the separation may be related to Froude number and bend tightness ratio (after Leeder et al (1975)).

As will be discussed later in section (2.7), separation zones have a considerable influence on the energy losses in a channel bend.

(2.6) BOUNDARY SHEAR STRESSES

In the bend, the secondary circulation affects the distribution of the main velocity and leads to a redistribution of the shear stresses. In a channel bend with a mobile bed, the redistribution of the boundary shear stresses causes bed deformation usually resulting in serious erosion at the outer bank and deposition along the inner bank. Protection of the outer bank, in particular at exit from the bend, poses a difficult problem for engineers engaged in the task of river training.

Experimental studies of flow in channel bends (see e.g. Ippen et al (1962), Shukry (1963), Khalid (1964), Yen (1970), Varshney et al (1975), Choudhary (1977), Nouh et al (1979), Chen et al (1983) and Pacheco– Ceballos (1983)) indicate that the main factors affecting the distribution of the boundary shear stress in channel bends are:

- The bend tightness ratio r_m / B
- The flow distribution at the entrance to the bend
- The total angle of the bend θ_b
- The flow aspect ratio B / h
- The Froude number F_r and the Reynolds number R_e of the flow
- The surface roughness of the channel bed.

Of these factors, the first i.e. "the bend tightness" appreared to have the most dominant effect. Figures (2.13), (2.14), (2.15) and (2.16) show contour-lines of measured shear stress in channel bends with different values of r_m/B , θ_b , F_r and R_e . It is difficult to compare, quantitatively, the experimental results from the different investigations because of the different experimental conditions. Nevertheless, these Figures allow the characteristics of the boundary shear stresses in channel bends to be summarised as follows:

(1) For a channel bend with $r_m/B \geq 3.5$, the distribution of shear stress (expressed non-dimensionally $\tau_0 / \bar{\tau}_0$, where τ_0 and $\bar{\tau}_0$ are the local and the averaged shear stress respectively) is nearly uniform at the entrance to the bend. While at the exit, a zone of high shear stress is observed near the outer bank.

(2) As the value of r_m/B decreases below 3.5 , two zones of high shear stress occur. The first zone occurs at the inner bank at the bend entrance and the second zone occur at the outer bank at the bend exit.

(3) As bend tightness r_m/B decreases to 1.25 , a very high shear stress region lies along the entire inner bank of the bend.

Previous authors have also indicated that the potential vortex behaviour in the flow at the bend entrance is weak for $r_m/B \geq 4.0$. While, for $r_m/B \leq 3.5$, the potential vortex motion becomes more noticable with the maximum shear stress occurring in the vicinity of the inner bank. At the bend exit, forced vortex motion appeared to be significant even for values of $r_m/B \geq 4.0$, where the maximum shear stress occurred at the outer bank. The exception to these

indications were the experimental results obtained by Yen (1970) (see Fig.(2.16)), where the potential vortex pattern in the flow appeared to be strong both at the bend entrance and along its curved path. This peculiarity in Yen's results can be attributed to the observed non– uniformity of the velocity distributions across the channel width before the bend entrance.

From field measurements of flow in river meanders (see e.g. Bathurst et al (1977), (1979) and Thorne et al (1983)), it may be concluded that the distribution of the boundary shear stress is affected by the structure of the secondary circulation near the outer bank. At the outer bank, the reverse cell of secondary currents is affected the boundary shear stress and hence, by whether the bank is steep or shelving. In the case of a steep bank, the peak shear stress is below the water surface especially at high discharges. This is mainly because the outer bank cell pushes the isovels of the main flow at the water surface away from the bank, reducing the the velocity gradient and hence, the bottom shear stress. In the case of a shelving bank, the outer bank cell is inhibited and the shear stress is reduced to a minimum. This minimum shear stress is always found near the junction between the bed and the bank of the channel. Fig.(2.17) shows the distribution of the boundary shear stress and the corresponding isovels for different discharges (after Bathurst et al (1979)).

In general, the location of the peak values of the boundary shear stress depends on the velocity gradient close to the channel bed. These peak values occur in :

(1) regions of converging secondary currents, where the isovels are compressed towards the channel bed. In contrast to that, low shear stresses are found in regions where the secondary currents diverge (see Fig.(2.18)).

(2) regions where the main velocity of the flow is high.

The relative magnitudes and the positions of the peaks depend on the strength of the secondary circulation and hence, on the flow discharge. At low discharges, both main and secondary flows are weak thus, it is possible for either to produce the peak shear stress. As discharge continues to increase, the peak of the boundary shear stress associated with the converging of the secondary cuurents is higher than the peak generated by the main velocity. At high discharges, the maximum shear stress is associated with the main velocity rather than with the converging of the secondary currents.

(2.7) ENERGY LOSSES

The mechanisms causing energy dissipation in the flow around curved open channels are much more complex than those in straight channels. The effect of curvature is similar to that produced in a straight channel by increasing the roughness. Investigations of flow resistance in curved channels (e.g. Mockmore (1944), Shukry (1949), Chow (1959), Leopold et al (1960), Rozovskii (1961), Ippen et al (1962), Yen (1965) and Soliman et al (1968)) led to the conclusions that the increase in energy losses may be attributed to the following:

- Internal fluid friction (i.e. momentum exchange between the flow layers) due to the secondary circulation in the flow.
- Boundary resistance associated with radial component of the boundary shear stress.
- Eddy losses resulting from the separation zones generated along the channel banks.

- **Eddy losses due to jumps and cross waves occurring in supercritical flows.**

Early investigations of energy losses in bends by Shukry (1949), Chow (1959) and Ippen et al (1962) were limited to one-dimensional analyses, in which the bend effect was simulated by a bend loss coefficient C_e as

$$h_L = C_e \ (u^2/2\ g) \qquad (2.5)$$

where

h_L is the head loss due to bend resistance.

$u^2/2\ g$ is the mean kinetic energy head of the flow.

C_e is the bend loss coefficient.

Shukry (1949) found experimentally that C_e was dependent on Reynolds number R_e, aspect ratio h/B, bend tightness r_m/B and $\theta_b/180^\circ$ (where θ_b is the total angle of the bend). Fig.(2.19) shows the relationship between these parameters and C_e. Shukry also found that the additional energy losses due to the bend effect could be neglected for $R_e \geq 3 \times 10^4$ and $r_m/B \geq 3$.

Soliman et al (1968) found that the energy losses depend not only on the bend geometry but also on the Froude number. It was concluded that losses due to bends approach those of straight channels at $F_r \leq 0.6$ and $k_r \leq 0.15$ (where F_r is the Froude number and k_r is a coefficient represents the bend geometry ($k_r = B/(2\ r_m)$). Soliman et al also found that energy losses due to bends reach a minimum value at $r_m/B = 3.3$. Thus confirming Shukry's previous findings. Fig.(2.20) gives the relation between the bend geometry coefficient k_r and the Froude number F_r necessary to attain minimum energy losses. The theoretical and the experimental curves agree well for values of $F_r \leq 0.6$, but for $F_r > 0.6$ the theoretical curve deviates noticably from the

experimental values. Soliman et al attributed this to the instability of the water surface and the generation of the surface waves which cause an increase in the head loss.

Recently, Chang (1983) and (1984a) has developed an analytical model to compute the rate of energy dissipation of a subcritical and fully developed flow in a channel bend. He divided the total energy gradient S into two components S' and S" (where S' and S" are the longitudinal and the transverse energy gradients respectively). Equating the rate of work done by an elementary control volume of the flow to the rate of energy expenditure, Chang developed simplified formulae for the transverse energy gradient S" and for the ratio S"/ S in a wide channel bend as:

$$S'' = F_r^2 (h/r_m)^2 [2.86 \sqrt{f_d} + 2.07 f_d] / [0.565 + \sqrt{f_d}] \quad (2.6)$$

and

$$S''/ S = (h/r_m)^2 [22.84 + 16.6 \sqrt{f_d}] / [0.565 \sqrt{f_d} + f_d] \quad (2.7)$$

where

S is the total energy gradient of the flow.

S' is the longitudinal component of the energy gradient

S" is the transverse component of the energy gradient

h is the averaged water depth in the bend

r_m is the mid radius of curvature

f_d is the Darcy– Weisbach friction factor

F_r is the Froude number of the flow

Chang (1983) found that, for a wide channel bend with a rectangular cross section, the energy dissipation due to the transverse circulation S" is directly

proportional to F_r , h/r_m and f_d . He concluded that while the secondary currents are generally lower in order of magnitude than the longitudinal velocity component, this is not the case for the energy expenditure. The energy losses due to the transverse circulation may be the same order of of magnitude as that due to the longitudinal velocities. Fig.(2.21) shows the energy gradients of the flow S , S' and S'' as functions of F_r^2 and h . It may be seen that these energy gradients and hence the rates of energy losses vary linearly with the Froude number. Fig.(2.22) gives comparisons between the analytical and the experimental values of S''/S as a function of $(h/r_m)^2$. Despite the scattering of the data points about the theoretical curves, there is general agreement between the analytical and experimental results. The scattering is explained by Chang as a result of the sensitivity of the energy gradient to inaccuracies in the measurement of the water surface elevation.

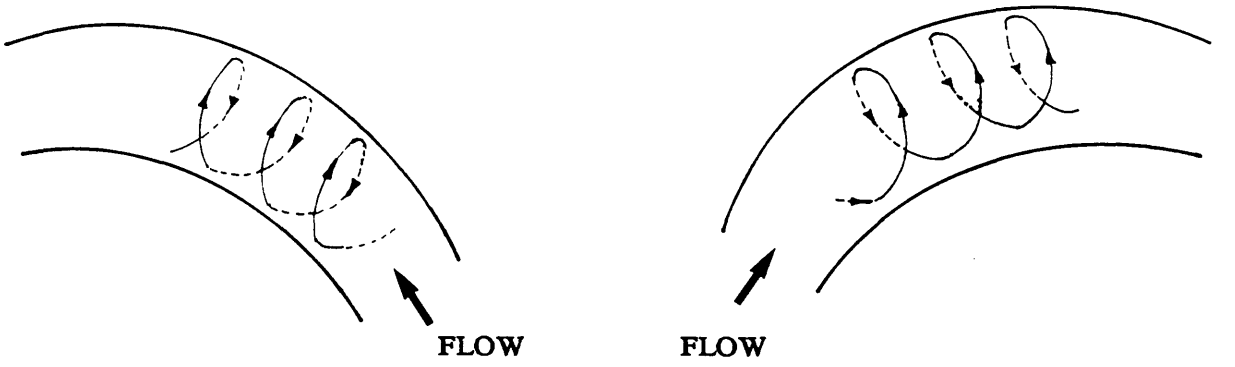

FIG.(2.1) – Spiral Flow in a Channel Bend

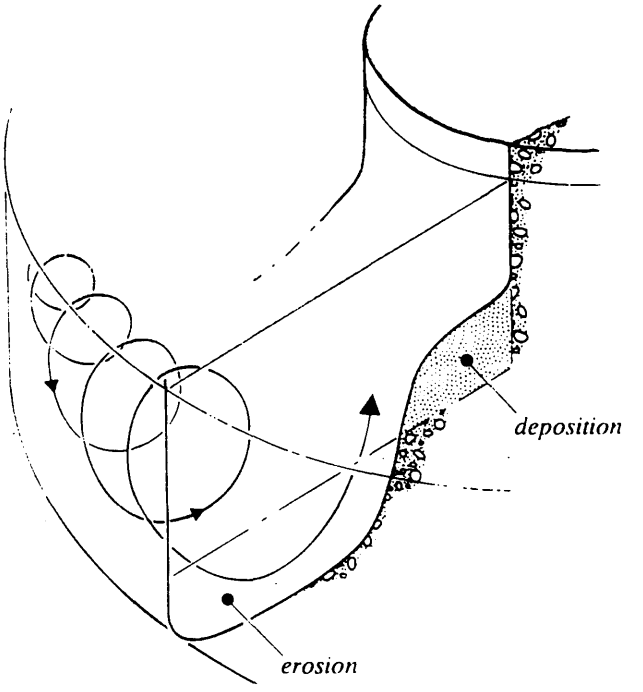

FIG.(2.2) – Effect of the Spiral Flow on the Bed Topography in a Channel Bend (after Chadwick et al (1986))

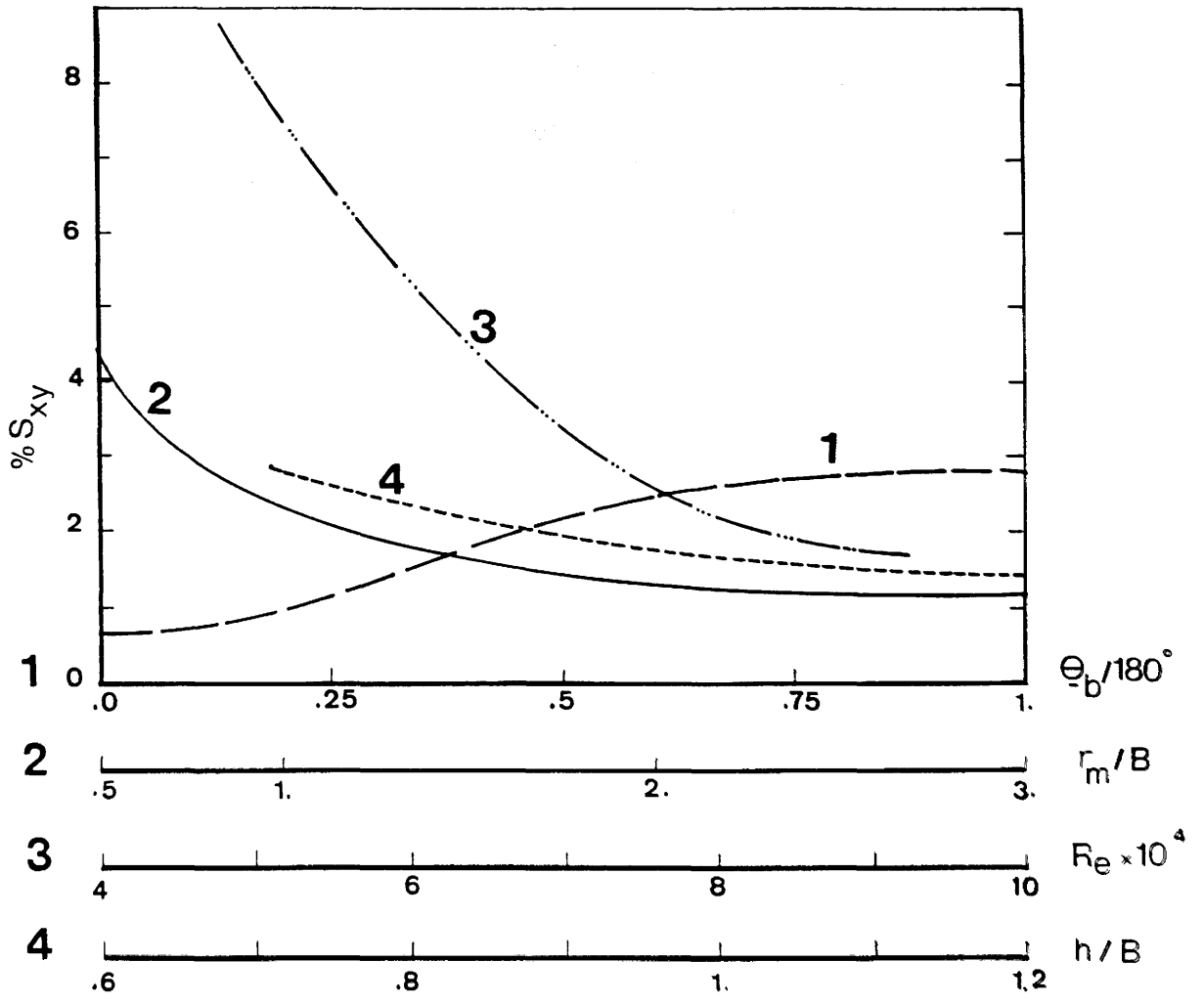

FIG.(2.3) – Effect of the Parametric Functions $\Theta_b/180^\circ$, r_m/B, R_e and h/B on the Strength of the Spiral Flow (after Shukry (1949))

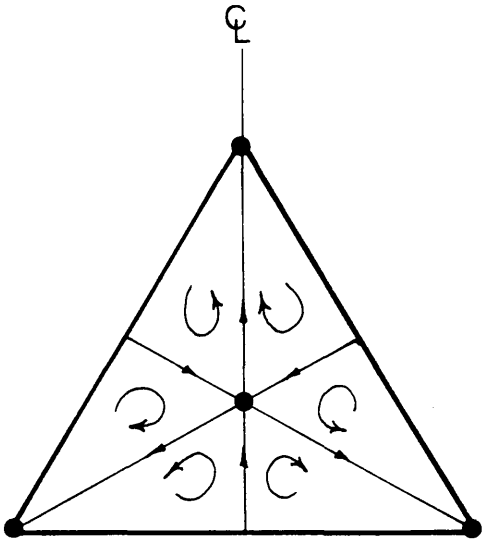

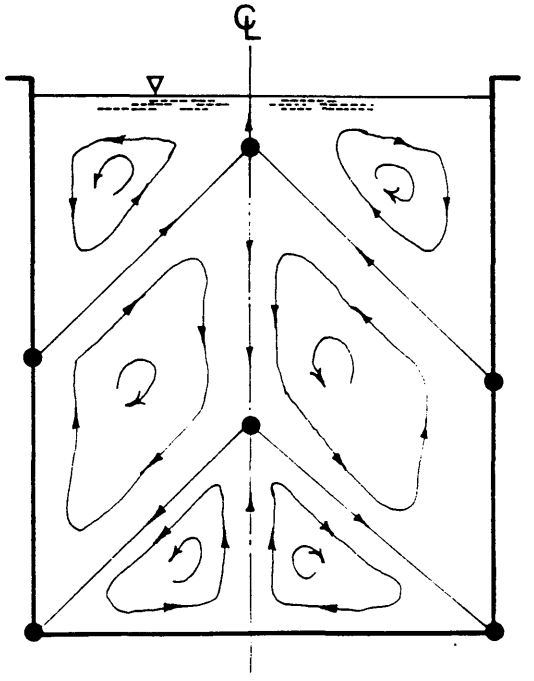

FIG.(2.4) – Secondary Flow
(after Prandtl (1952))

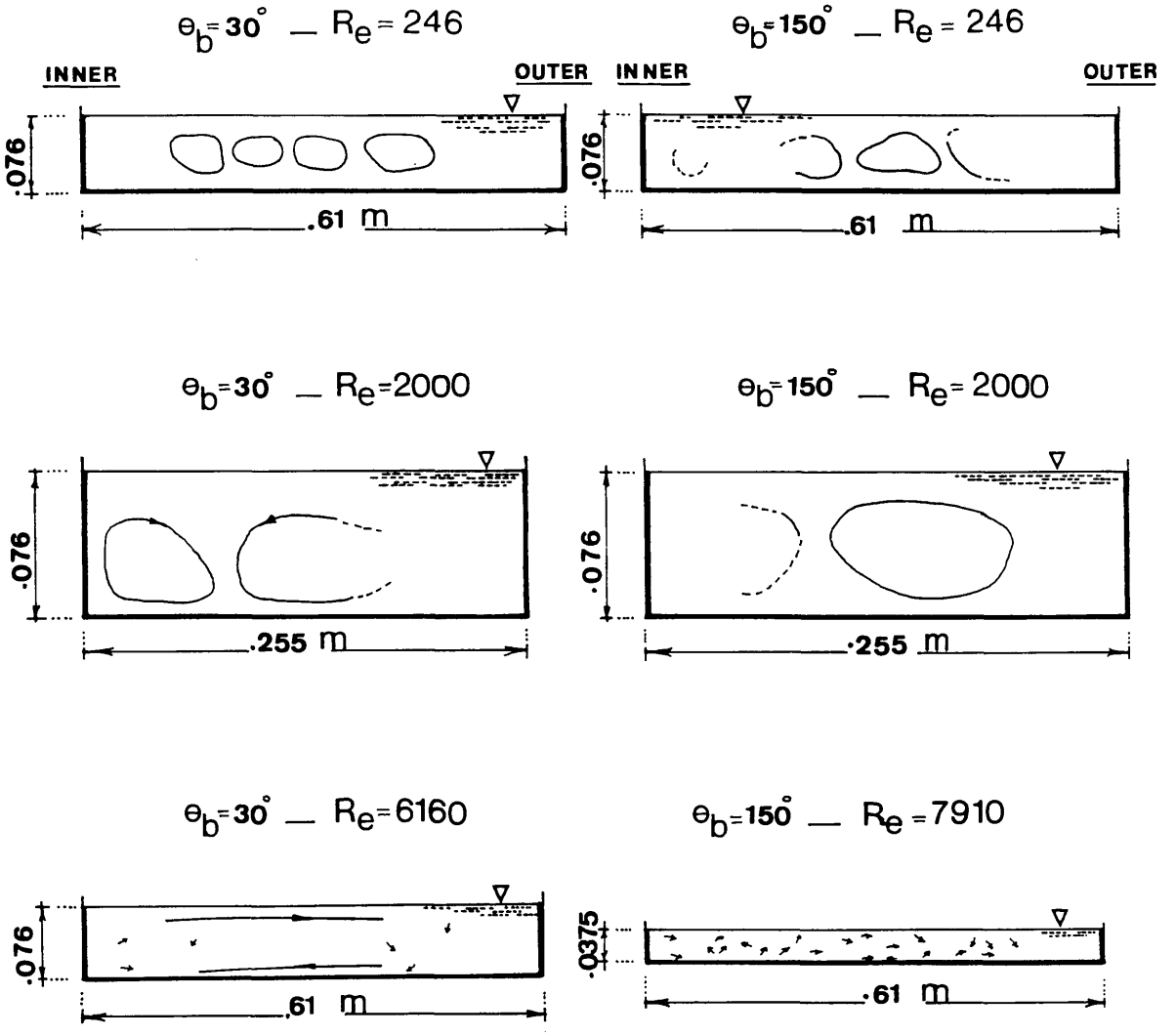

FIG.(2.5) – Patterns of Secondary Currents in a Channel Bend (after Francis et al (1970))

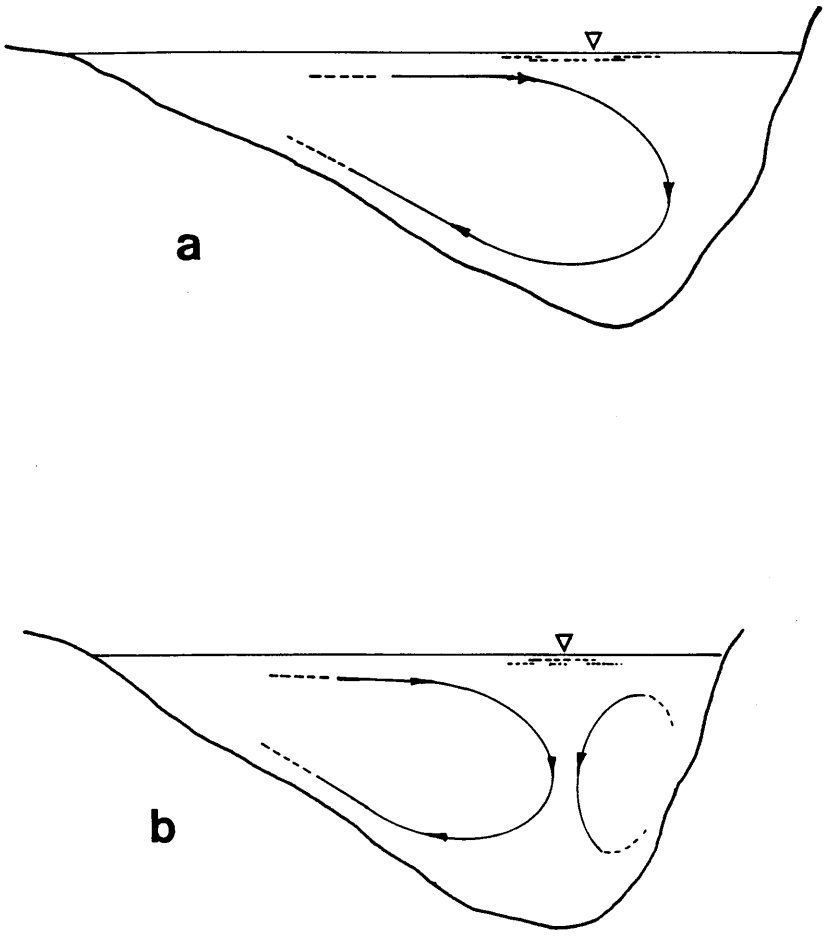

FIG.(2.6) – Secondary Flow Cells in Bends of Open Channels
(a) One– Cell Type
(b) Two– Cell Type

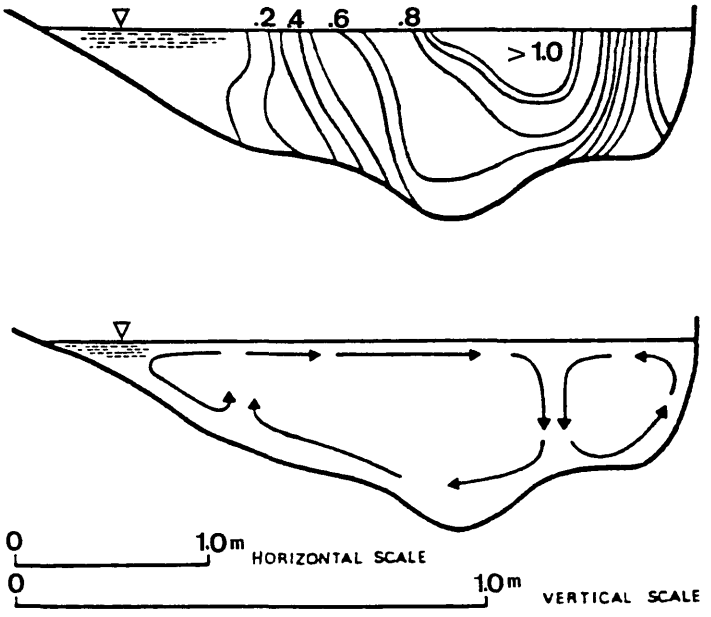

FIG.(2.7) – Velocity Distribution and Secondary Flows at Meander Apex, River DOVE. ($\theta_b = 90^\circ$, $r_m = 62.5$m , Velocities in m/s) (after Hey et al (1975))

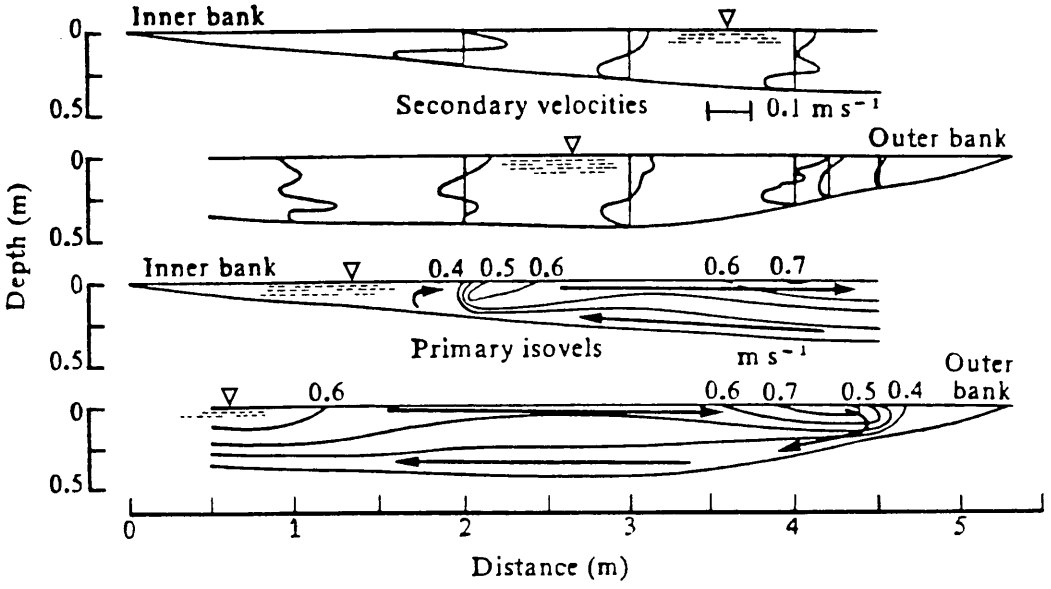

FIG.(2.8) – Primary and Secondary Velocities at Llandinam Bend, River SEVERN (B = 10m, r_m = 75m, θ_b = 62°, Q = 1.1 m^3/s) (after Bathurst et al (1977))

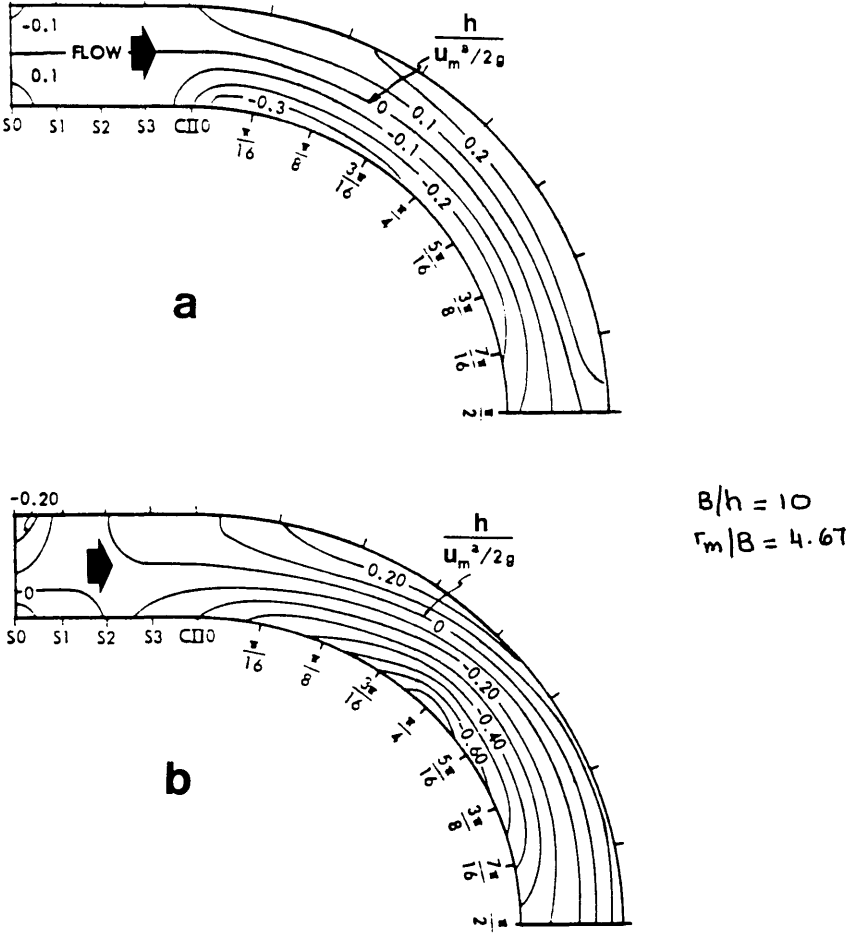

FIG.(2.9) – Water Surface Contours
(a) Trapezoidal Model
(b) Equilibrium– Bed Model
(after Yen et al (1971))

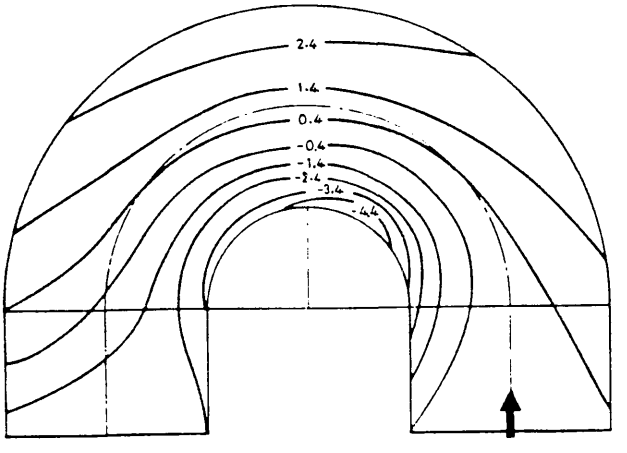

EXP. VALUES (mm)
B/h = 13.33
B/r_m = 1.0

FIG.(2.10) – Contours of Water Surface Superelevation
(after Rozovskii (1961))

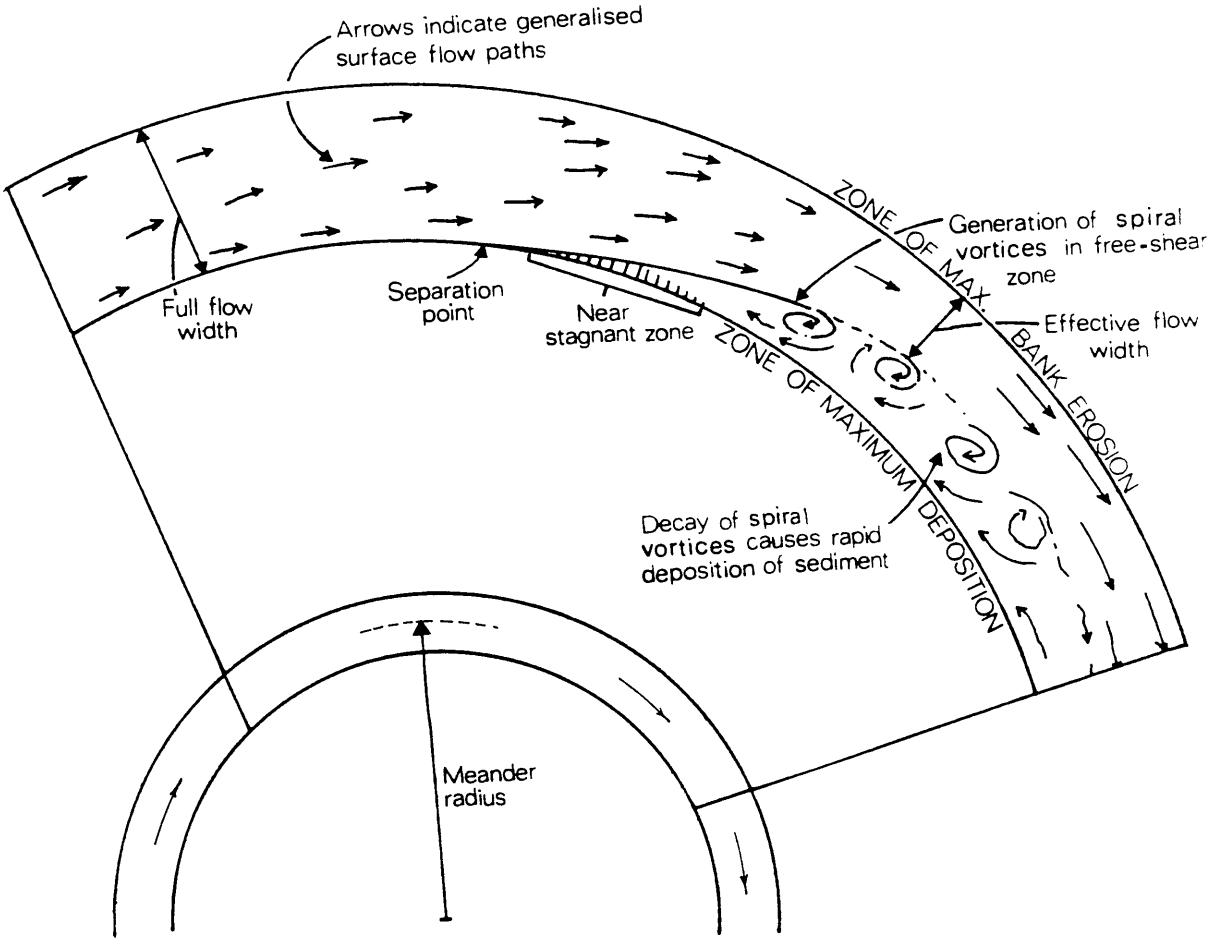

FIG.(2.11) – **Characteristics of Separated Flow in a River Meander (after Leeder et al (1975))**

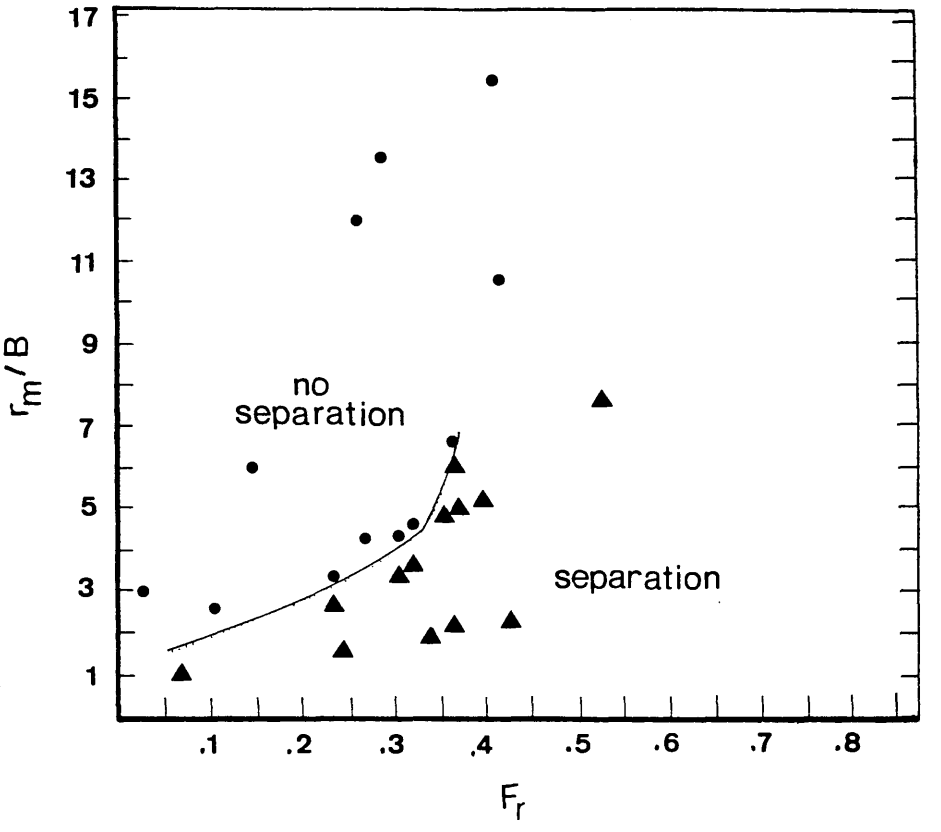

FIG.(2.12) – Occurrence of Flow Separation in River Bends
(●) No Flow Separation
(▲) Flow Separation
(after Leeder et al (1975))

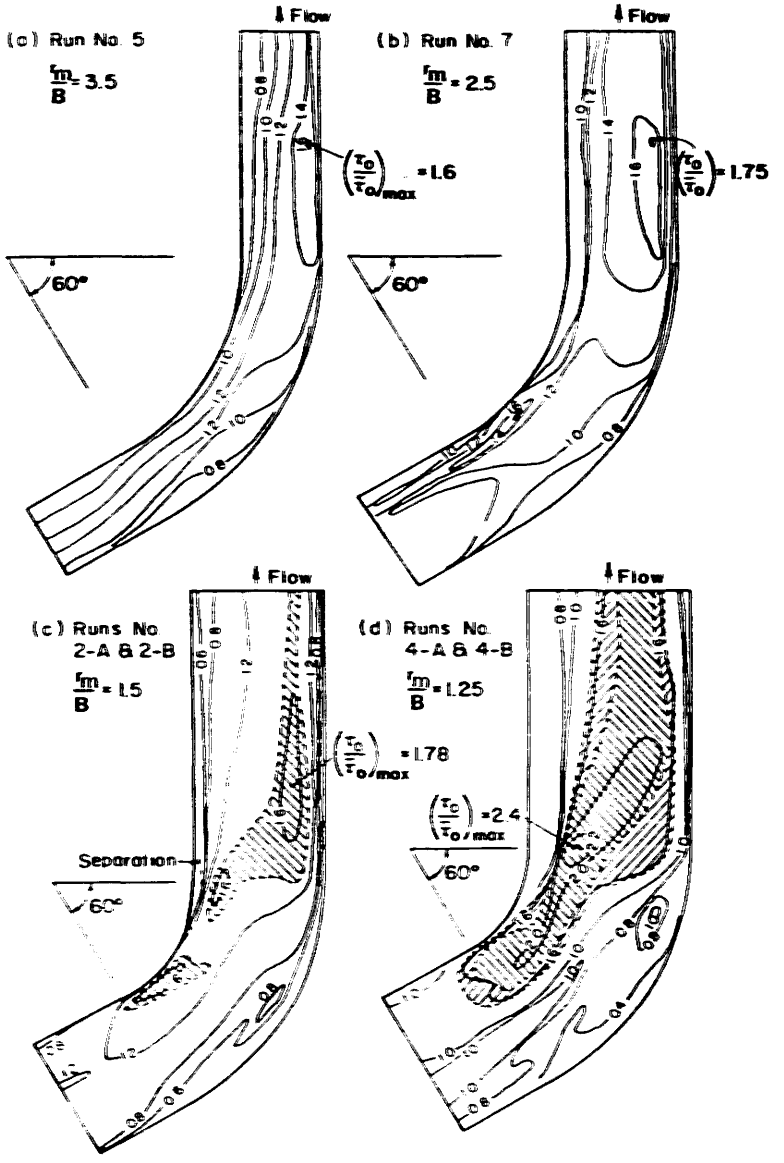

FIG.(2.13) – Different Bed Shear Stress Distributions for Different r_m/B ratios (after Ippen et al (1962))

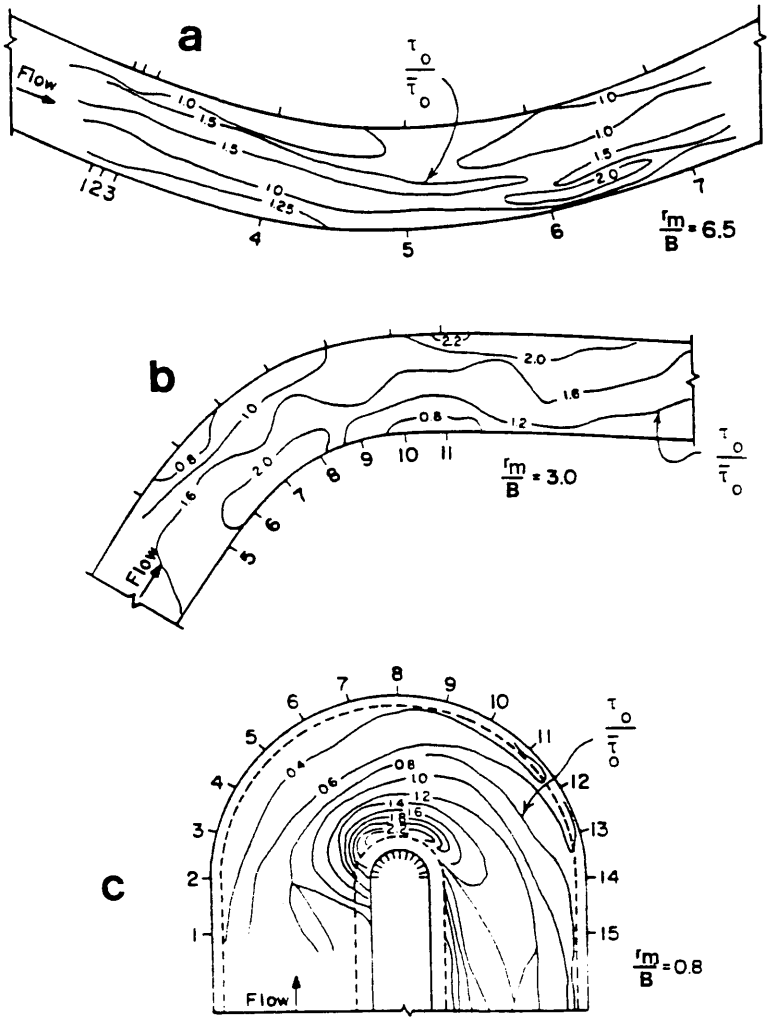

FIG.(2.14) – Shear Stress Distributions By Several Authors
(a) according to Khalid (1964)
(b) according to Varshney et al (1975)
(c) according to Choudhary et al (1977)

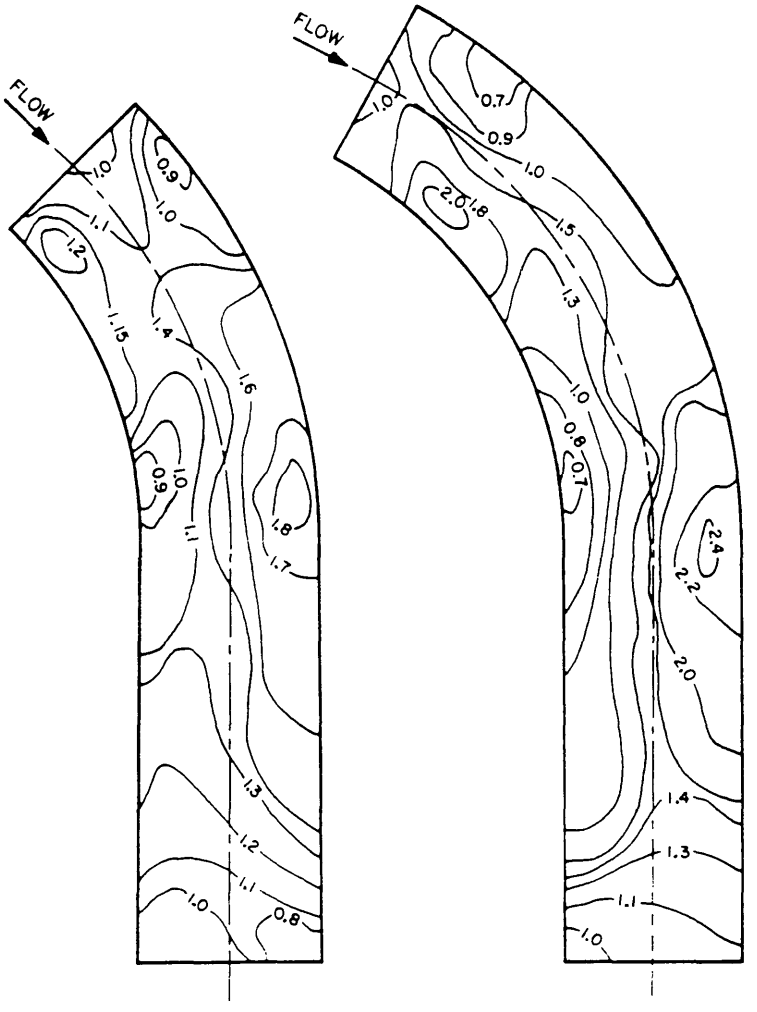

FIG.(2.15) – Observed Dimensionless Shear Stress Distributions
(a) $\theta_b = 45^\circ$
(b) $\theta_b = 60^\circ$
(after Nouh et al (1979))

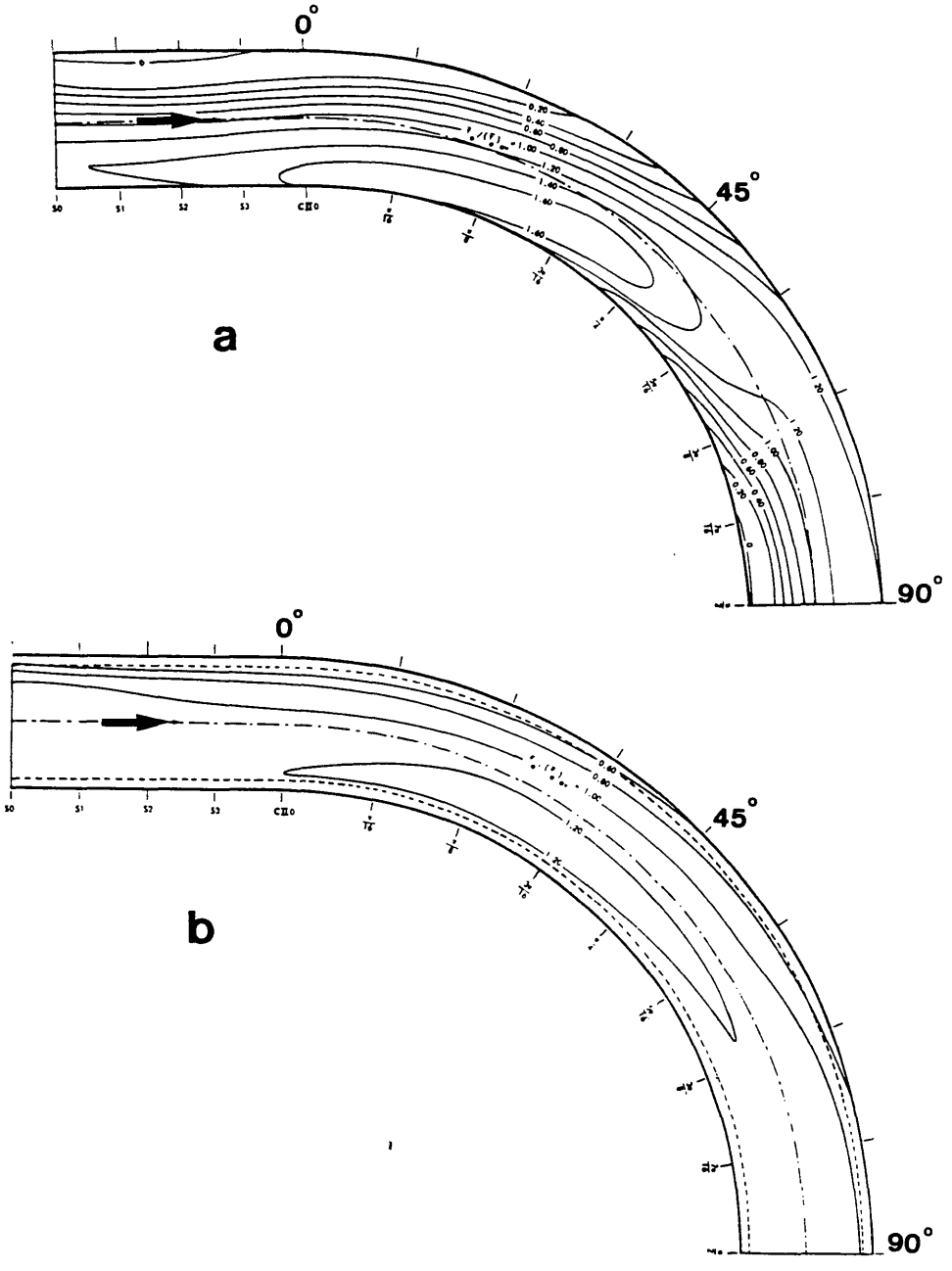

FIG.(2.16) – Bed–Shear Contours
(a) Movable Bed Model
(b) Trapezoidal Model
(after Yen (1970))

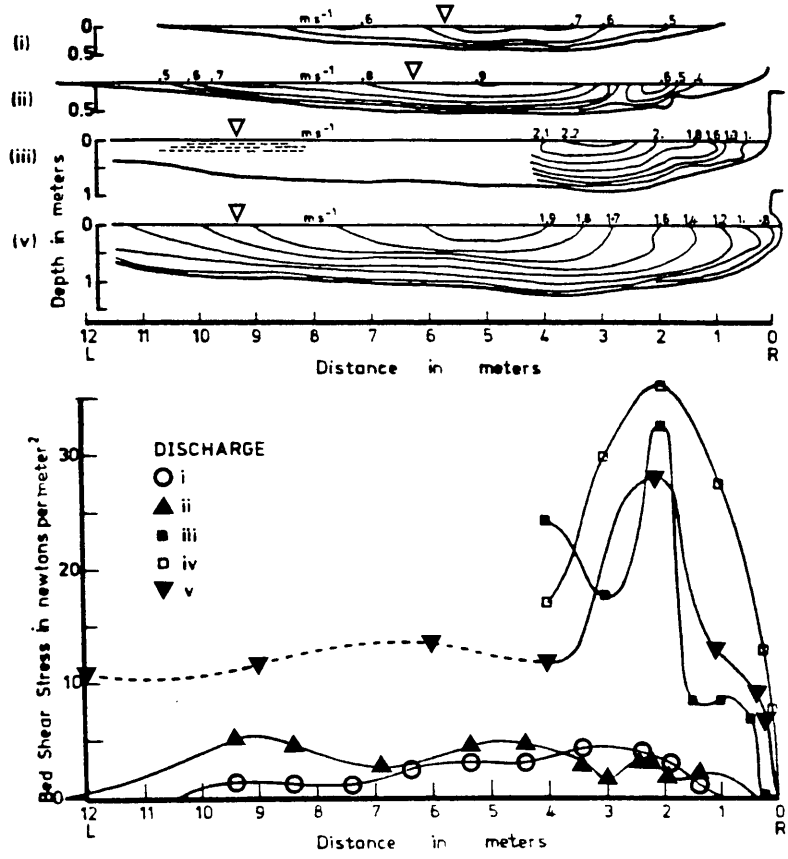

FIG.(2.17) – (a) Patterns of Longstream Isovels
(b) Distribution of Bed Shear Stress
At Llandinam Bend – River SEVERN
(i) Q = 1.12 m^3/s
(ii) Q = 2.36 m^3/s
(iii) Q = 10 m^3/s
(iv) Q = 21 m^3/s
(v) Q = 25 m^3/s

(after Bathurst et al (1979))

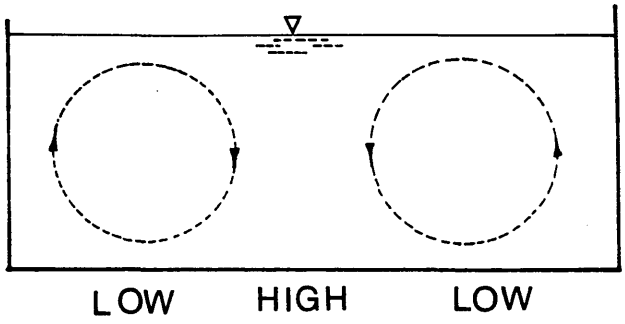

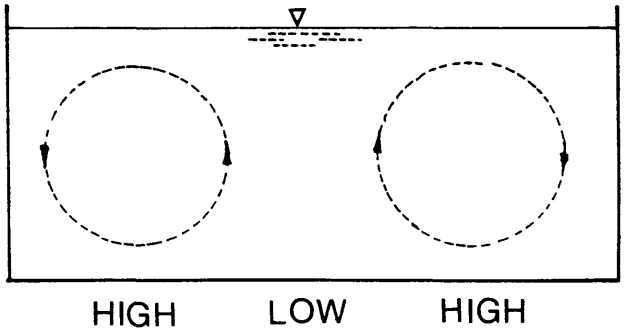

FIG.(2.18) – Effect of Converging and Diverging Secondary Flow on Boundary Shear Stress Distributions

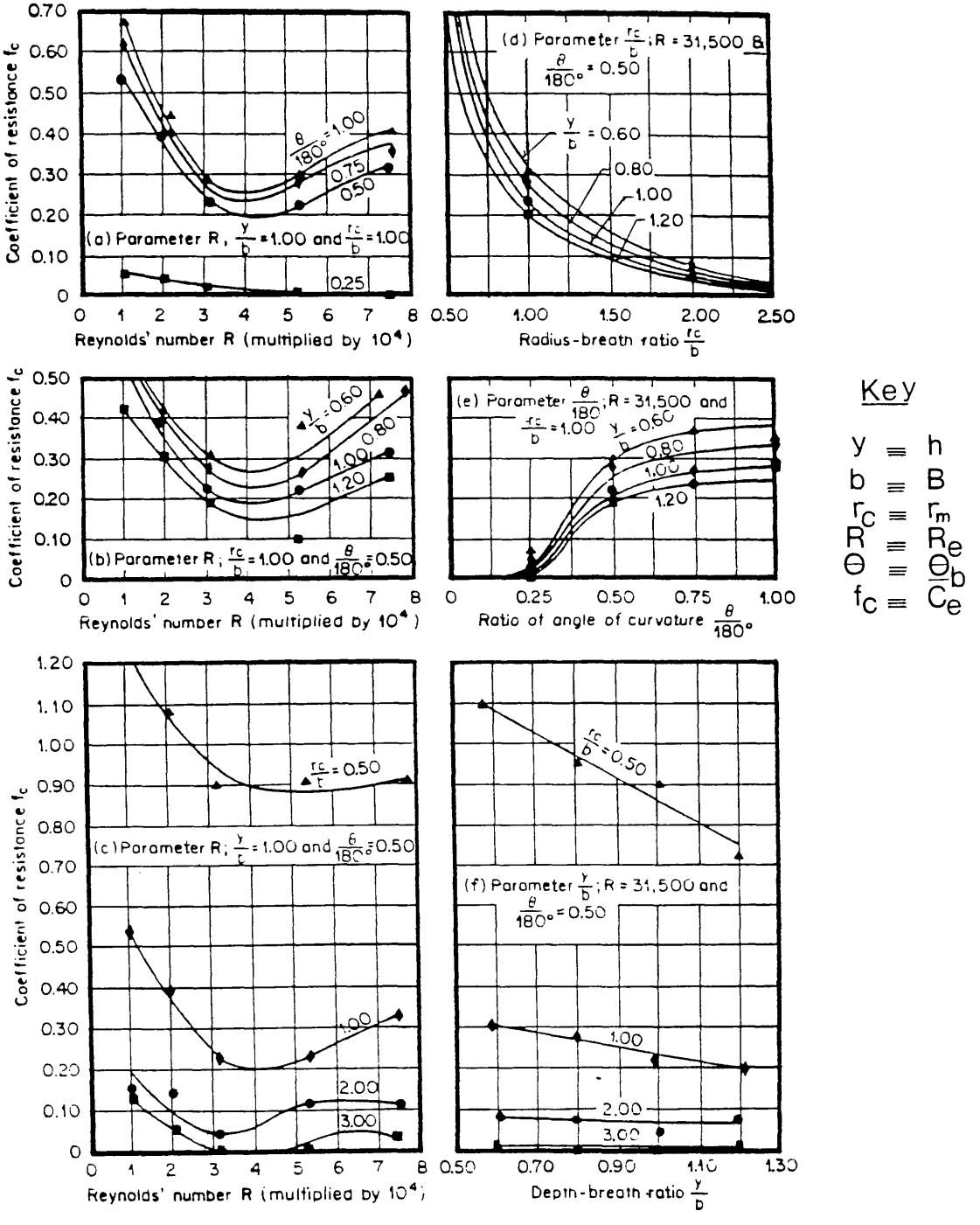

FIG.(2.19) – Experimental Parametric Functions of the Coefficient of bend resistance (after Shukry (1949))

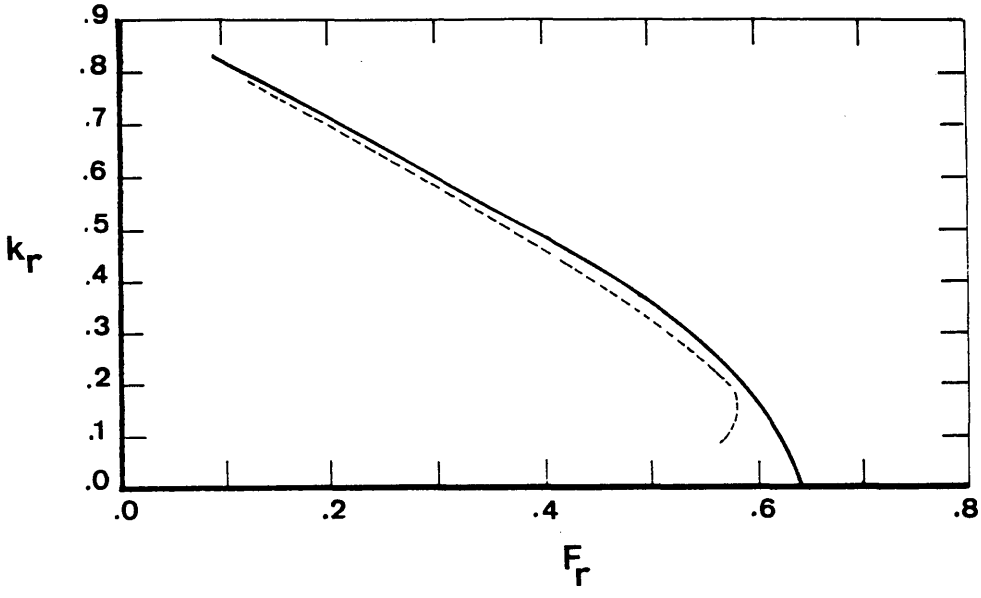

FIG.(2.20) – Relation Between Bend Geometry Coefficient k_r and Froude Number F_r for Minimum Energy Loss

—— Theoretical Solution

– – – Experimental Results

(after Soliman et al (1968))

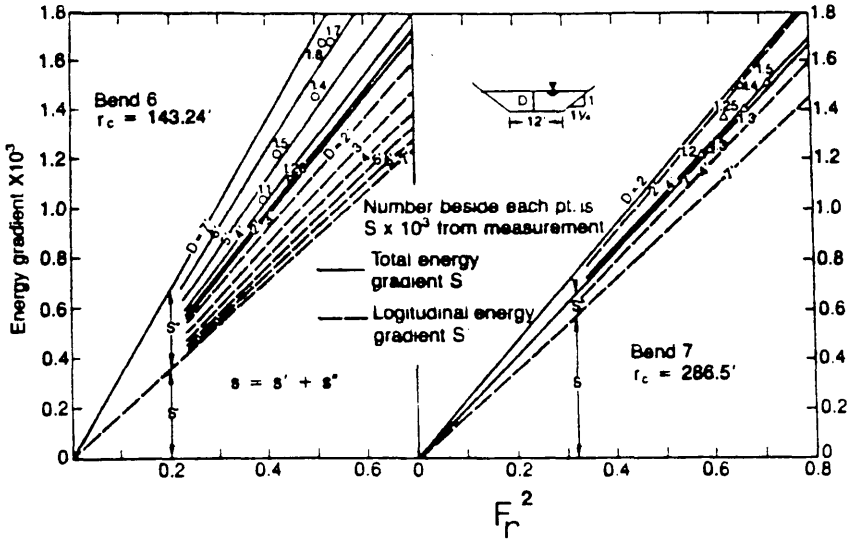

FIG.(2.21) – Energy Gradients in Relation to Froude Number F_r and Flow Depth h (after Chang (1983))

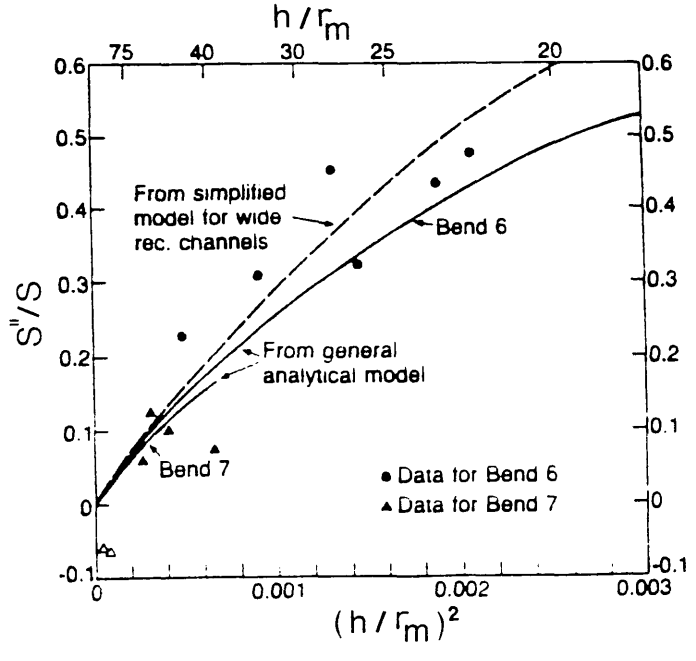

FIG.(2.22) – Ratio of Transverse to Total Energy Loss S"/S in Relation to Depth–Radius Ratio $(h/r_m)^2$ (after Chang (1983))

CHAPTER III

MATHEMATICAL FORMULATION OF FLOW IN A GENTLE WIDE CHANNEL BEND

CHAPTER III

MATHEMATICAL FORMULATION OF FLOW IN A GENTLE WIDE CHANNEL BEND

(3.1) INTRODUCTION

As has been mentioned before in the literature review (Chapter II), flow around a channel bend is very complicated. The flow structure is highly turbulent and three– dimensional. Centrifugal force produces a non– uniform velocity pattern and also causes superelevation of the water surface. The flow is further complicated by the wall friction which produces a highly non– uniform boundary shear stress distribution such that the shear stress is a maximum at the outer bank and decreases across the width to reach a minimum value at the inner bank. As a result of all these features, each producing an energy loss, the flow in the bend becomes unstable in the long term. The main features of the flow in a channel bend are as indicated below. Each of these must be incorporated into the bend model;

(1) The vertical distribution of the longitudinal and the radial components of the spatial pattern of the flow velocity.

(2) The horizontal distribution of the depth– averaged velocity across the channel width at the bend entrance and the superelevation effect as soon as it

starts to develop.

(3) The horizontal distributions (i.e. radially and longitudinally) of the depth– averaged velocity and the water surface throughout the bend. Such horizontal distributions are known as the **"horizontal problem"**.

(4) The redistribution of the vertical profile of the longitudinal component of the flow velocity along the bend. This will inherently specify the variation in the vertical component of the velocity.

(5) The growth and the decay of the radial component of the secondary circulation along and beyond the bend.

The investigation of these features will not only lead to more understanding of the complex phenomenon of flow in a channel bend, but will also essential in establishing the initial flow conditions in the bend where it intersects with the flood relief channel.

(3.2) GENERAL DYNAMIC EQUATIONS OF THE MODEL

The dynamic equations of motion for flow in a differential control volume (dx.dy.dz) are; (Hughes et al (1967))

$$\partial_t \rho + \nabla . (\rho \underline{U}) = 0 \qquad (3.1)$$

$$\rho D_t \underline{U} = -\nabla P + \underline{F} + \nabla . \tilde{\tau} \qquad (3.2)$$

where

$\rho(x,y,z,t)$	is the flow density field.
$\underline{U}(x,y,z,t)$	is the flow velocity field.
$P(x,y,z,t)$	is the flow pressure field.
$\underline{F}$	is the external body forces
$\tilde{\tau}$	is the flow shear stress tensor associated with frictional stresses.
∇	is the gradient operator ($= \partial_x \underline{i} + \partial_y \underline{j} + \partial_z \underline{k}$)
D_t	is the time total derivative.
∂_t	is the time gradient operator.

In general two more equations are required to close the system. These equations are the energy equation and the equation of state. Since the major interest is concerned with the dynamics of incompressible and homogeneous bodies of fluid, the temprature and the density fields will be uniform in space and constant with time. Therefore, the continuity and the momentum equations alone will be sufficient to describe the spatial structure of the flow (i.e. the velocity and the pressure fields).

It should be noted that since some of the parameters involved in the main model equations are non− linear (i.e. the convective and the advective terms of the inertia force $\rho\ D_t\ \underline{U}$), rigorous analytical solutions to the equations are either extremely complicated or impossible. Consequently, most of the solutions have been obtained numerically (i.e. with a small associated error) by using the finite difference technique.

(3.3) GENERAL MODEL ASSUMPTIONS

(3.3.1) The flow is steady, i.e. the order of magnitude of the local term of the time total derivative is assumed to be much smaller than the order of magnitude of the other convective terms.

(3.3.2) The density field of the flow is homogeneous, i.e. the internal gravity waves and density currents are neglected.

(3.3.3) The flow is assumed to be incompressible.

(3.3.4) The concept of eddy viscosity is introduced to model the momentum exchange between the flow layers (horizontally and vertically). Applying the **"mixing length"** theory, the shear stress tensor $\tilde{\tau}$ in a turbulent flow is assumed to be in a linear relationship with the time rate of strain tensor $\tilde{e}$ ($\tilde{e}$ defined as the tensor of the mean rates of strain of the flow).

(3.3.5) The molecular momentum flux between the fluid molecules is assumed to be much smaller than the eddy turbulent momentum flux, so it is neglected.

(3.3.6) The horizontal turbulent momentum flux is assumed to be much smaller than the vertical turbulent momentum flux, so it is neglected. This assumption is applicable for channel bends of large aspect ratios.

(3.3.7) The vertical distribution of the pressure field is assumed to follow the hydrostatic law. This assumption is always held for bends of large tightness ratios. This particular assumption will be proved mathematically in the following section of the model analysis.

(3.3.8) The water surface fluctuations are assumed to be much smaller than the average water depth in the channel. This assumption allows the application of the boundary condition at the undisturbed mean surface rather than at the actual free surface. Consequently, the boundary condition at the water surface becomes linear.

(3.3.9) There are no tangential shear stresses at the air/water interface and the spatial pattern of the wind shear stress will be neglected over the considered region of study in the channel bend.

(3.3.10) The spatial variations of the atmospheric pressure can be neglected over the studied area of the bend. Hence, the atmospheric pressure can be assumed to be uniform.

(3.3.11) The effect of the earth's rotation on the circulation pattern of the flow can be neglected. Therefore, the Coriolis force can be neglected and the only applied body forces on the flow will be gravity and centrifugal forces.

(3.3.12) The vertical distribution of the longitudinal component of the flow velocity field is assumed to follow the classical "Prandtl– Von Karman" logarithmic law. The reason for this assumption will be discussed in a following section of the analysis.

(3.3.13) Finally, no deformation or movement of the channel bed and banks will take place. The channel boundaries will be assumed rigid and the cross section will be uniform and rectangular.

(3.4) MATHEMATICAL ANALYSIS

For convenience, a polar cylindrical coordinate system (r,s,z) has been chosen to describe the flow parameters in the model equations. The coordinate axes are as shown in Fig.(3.1).

Applying the above stated assumptions to the dynamic equations of motion, equations (3.1) and (3.2), the body force $\underline{F}$ can be represented by the gravity force as:

$$\underline{F} = \rho \underline{G} \qquad (3.3)$$

where $\underline{G}$ is the gravitational acceleration vector. Also, applying the eddy viscosity concept to the shear stress term ($\nabla . \tilde{\tau}$), it can be modelled as

$$\nabla . \tilde{\tau} = \nabla . (\rho \nu \quad \nabla \underline{U}) \qquad (3.4)$$

where ν is the kinematic eddy viscosity of the flow. Substituting equations (3.3) and (3.4) into equation (3.2), and after dropping the terms that include $1/r^2$ and lower and limiting the second order gradients to r and z directions only, the model equations of the flow can be expressed in cylindrical polar coordinates as follows: (Kumar (1976))

– the continuity equation

$$1/r \; \partial_r(r \; u_r) + \partial_s u_s + \partial_z u_z = 0 \qquad (3.5)$$

– the momentum equation

$$u_r\,\partial_r u_r + u_s\,\partial_s u_r + u_z\,\partial_z u_r - u_s{}^2/r = -1/\rho\,\partial_r P + \nu[1/r\,\partial_r u_r + \partial_{rr} u_r + \partial_{zz} u_r] + 2\,\partial_r \nu\,\partial_r u_r + \partial_z \nu\,(\partial_z u_r + \partial_r u_z) \qquad (3.6.1)$$

$$u_r\,\partial_r u_s + u_s\,\partial_s u_s + u_z\,\partial_z u_s + u_r\,u_s/r = -1/\rho\,\partial_s P + \nu[1/r\,\partial_r u_s + \partial_{rr} u_s + \partial_{zz} u_s] + \partial_r \nu\,(\partial_r u_s - u_s/r) + \partial_z \nu\,\partial_z u_s \qquad (3.6.2)$$

$$u_r\,\partial_r u_z + u_s\,\partial_s u_z + u_z\,\partial_z u_z = -g - 1/\rho\,\partial_z P + \nu[1/r\,\partial_r u_z + \partial_{rr} u_z + \partial_{zz} u_z] + \partial_r \nu\,(\partial_z u_r + \partial_r u_z) + 2\,\partial_z \nu\,\partial_z u_z \qquad (3.6.3)$$

where

$\partial_r, \partial_s, \partial_z$	are the gradient operators in r,s,z directions respectively.
$\partial_{rr}, \partial_{zz}$	are the second order gradients in r and z directions respectively
u_r, u_s, u_z	are the velocity components in r,s,z directions respectively.
P	is the pressure field of the flow
ν	is the kinematic eddy viscosity of the flow
g	is the gravitational acceleration operates downwards.

Equations (3.5) to (3.6.3) are highly complicated and therefore rather inconvenient in use. These equations can be simplified considerably in the case of a gentle wide channel bend, i.e. where the order of magnitude of the average water depth **h** is much smaller than the channel width **B** and in turn to its radius of curvature **r** . In such a wide bend, the influence of bank friction and the associated shear layer along the banks is only significant in a comparatively narrow layer of thickness (i.e. boundary layer thickness) varying from h to 1.5h (see e.g. Rozovskii (1961), De Vriend (1976), (1977), Kalkwijk et al (1980), Spyratos (1981), Hussein et al (1986) and others). The remaining central part of

the channel is practically unaffected by the bank friction. Hence, considerations only will be limited to the main part of the flow where the effect of the side wall boundaries (banks) will be ignored.

If use of this simplification is to be justified, then the order of magnitude of the error associated with it must be calculated. To accomplish this, the order of magnitude of each term of the model equations must be first evaluated. Equation (3.5) can be written as;

$$\partial_z u_z = - (\partial_r u_r + u_r/r + \partial_s u_s) \qquad (3.7)$$

By the use of the **"mean value"** theorem, the vertical component of the velocity can be determined as ;

$$(u_z)_m = \int \partial_z u_z \, dz \qquad \text{for} \quad 0 \leq z/h \leq 1$$

and from equation (3.7),

$$\begin{aligned} (u_z)_m &= - \int (\partial_r u_r + u_r/r + \partial_s u_s)_m \, dz \\ &= - (\partial_r u_r + u_r/r + \partial_s u_s)_m \cdot z \end{aligned} \qquad (3.8)$$

where **"m"** represents the mean values within the limits of integration (i.e. from 0 to h).

For a wide channel bend where the ratios **h/B** and **h/r** are of small magnitude, it can be expected that the vertical component of the velocity u_z is small in comparison with the longitudinal and the radial components (i.e. u_s , u_r respectively). If the right hand side of equation (3.8) is multiplied and divided by r at the same time, it becomes;

$$(u_z)_m = - r\,(\partial_r u_r + u_r/r + \partial_s u_s)_m \,.(z/r) \qquad (3.9)$$

From equation (3.9) it can be seen that u_z is a function of **z/r** and, in turn, is a function of **h/r** which is of a small order of magnitude in a wide channel bend. Therefore, u_z will be small compared with u_s and u_r , the order of magnitude of u_z being determined by the ratio h/r . By introducing these new variables:

$$z = z'\,h/r \;,\quad u_z = u_z'\,h/r \quad \text{and} \quad \nu = \nu_o\,\nu' \qquad (3.10)$$

where ν_o and ν' are the mean and the non–dimensional eddy viscosity of the flow. With these variables the order of magnitude of z' will be of the same order of magnitude as r , s and the order of magnitude of u_z' will be the same as of u_r and u_s . Substituting the new variables z', u_z' and ν' into equations (3.6.1), (3.6.2) and (3.6.3), the following equations will be obtained after some simple transformations;

$$u_r\,\partial_r u_r + u_s\,\partial_s u_r + u_z'\,\partial_{z'} u_r - u_s^2/r = - 1/\rho\,\partial_r P + \nu_o\,[2\,\partial_r(\nu'\,\partial_r u_r) + r^2/h^2\,\partial_{z'}(\nu'\,\partial_r u_r) + \partial_{z'}(\nu'\,\partial_r u_{z'}) + 1/r\,\nu'\,\partial_r u_r] \qquad (3.11.1)$$

$$u_r\,\partial_r u_s + u_s\,\partial_s u_s + u_z'\,\partial_{z'} u_s + u_r\,u_s/r = - 1/\rho\,\partial_s P + \nu_o\,[\partial_r(\nu'\,\partial_r u_s) + r^2/h^2\,\partial_{z'}(\nu'\,\partial_{z'} u_s)] \qquad (3.11.2)$$

$$(h/r)[u_r\,\partial_r u_{z'} + u_s\,\partial_s u_{z'} + u_{z'}\,\partial_{z'} u_{z'}] = - g - 1/\rho\,\partial_z P + \nu_o\,[(h/r)\,\partial_r(\nu'\,\partial_r u_{z'}) + \nu'\,\partial_{z'} u_{z'} + (r/h)\,\partial_r(\nu'\,\partial_{z'} u_r) + \nu'/r\,\partial_r u_r] \qquad (3.11.3)$$

It can be seen that in equations (3.11.1) and (3.11.2), the third term between the square brackets on the right hand side (namely $r^2/h^2\ \partial_{z'}(\nu'\ \partial_{z'}u_r)$ and $r^2/h^2\ \partial_{z'}(\nu'\ \partial_{z'}u_s)$ respectively) are of a considerably greater order of magnitude than the other terms between the brackets. Therefore, the other terms may be dropped. The order of magnitude of the resulting error will be of the order of h^2/r^2 which is negligible.

Also in equation (3.11.3) the only other terms between the square brackets, which should be retained, are those with the order of magnitude of r/h. Dropping the other terms will resullt in an error of order of magnitude h/r. After dropping the relatively insignificant terms from equations (3.11.1) to (3.11.3), the following system of equations is obtained;

$$u_r\ \partial_r u_r + u_s\ \partial_s u_r + u_{z'}\ \partial_{z'} u_r - u_s^2/r = -\ 1/\rho\ \partial_r P + \nu_o\ r^2/h^2\ [\partial_{z'}(\nu'\ \partial_{z'} u_r)] \qquad (3.12.1)$$

$$u_r\ \partial_r u_s + u_s\ \partial_s u_s + u_{z'}\ \partial_{z'} u_s + u_r\ u_s/r = -\ 1/\rho\ \partial_s P + \nu_o\ r^2/h^2\ [\partial_{z'}(\nu'\ \partial_{z'} u_s)] \qquad (3.12.2)$$

$$(h/r)\ [u_r\ \partial_r u_{z'} + u_s\ \partial_s u_{z'} + u_{z'}\ \partial_{z'} u_{z'}] = -\ g - 1/\rho\ \partial_z P + \nu_o\ r/h\ [\partial_r(\nu'\ \partial_{z'} u_r)] \qquad (3.12.3)$$

If comparison is now made between the shear stress terms on the right hand side, that are dependent on the turbulent viscosity, with the inertia terms on the left hand side of equations (3.12.1) and (3.12.2). It will noticed that the shear stress terms have an associated factor " $\nu_o\ r^2/h^2$ ". If the viscosity parameter ν_o is not of small magnitude, all inertia terms of the left hand side may be dropped. Motion under these conditions is represented by a laminar flow with a very small Reynolds number (i.e. the inertia force $\ll$ the viscous force). If this case is

excluded from consideration, then the only other possibility of the kinematic eddy viscosity ν_o being of small magnitude whose order is equal or less than h^2/r^2, which is the proper condition to be considered. Consequently, the order of magnitude of the factor " $\nu_o\ r^2/h^2$ " is unity.

If equation (3.12.3) is considered, bearing in mind the order of magnitude of ν_o is h^2/r^2, then all the terms of the equation except the expression " $-\ 1/\rho\ \partial_z P\ -\ g$ " will be of the order of magnitude of h/r. Therefore, it can be assumed, with an accuracy of h/r, that;

$$g + 1/\rho\ \partial_z P = 0 \qquad (3.13)$$

Thus it may be assumed that, for a wide channel bend, the vertical distribution of the pressure field follows the "hydrostatic law". Similar conclusion were reported earlier by Rozovskii (1961), Yen et at (1971), Engelund (1974), Kikkawa et at (1976), De Vriend (1976), (1977), Zimmermann et al (1978), Kalkwijk et al (1980) and others. If equation (3.13) is integrated vertically using the boundary condition that the pressure is atmospheric at the water surface, i.e.

$$\text{At}\quad z/h = 1 \qquad P = P_{atm} \qquad (3.14)$$

the result will be:

$$P = P_{atm} + \rho\ g\ (h - z) \qquad (3.15)$$

i.e. The pressure field is equal to a hydrostatic part plus a dynamic part (i.e. pressure due to motion). As a result, the horizontal pressure gradients can be expressed in terms of the slopes of the water surface, i.e.

$$\partial_r P = \rho\, g\, S_r = \rho\, g\, \partial_r h \qquad (3.16)$$

and $$\partial_s P = -\rho\, g\, S_s = -\rho\, g\, \partial_s h \qquad (3.17)$$

where S_r and S_s are the radial and the longitudinal water surface slopes respectively.

Hence, if in equations (3.12.1), (3.12.2) and (3.12.3) all terms of the order of magnitude of h/r and lower are dropped, the final system of bend model equations for steady, incompressible and homogeneous flow may be obtained, after reverting to the original variables, as:

$$u_r\, \partial_r u_r + u_s\, \partial_s u_r + u_z\, \partial_z u_r - u_s{}^2/r = -g\, S_r + \partial_z(\nu\, \partial_z u_r) \qquad (3.18.1)$$

$$u_r\, \partial_r u_s + u_s\, \partial_s u_s + u_z\, \partial_z u_s + u_r u_s/r = g\, S_s + \partial_z(\nu\, \partial_z u_s) \qquad (3.18.2)$$

$$g + 1/\rho\, \partial_z P = 0 \qquad (3.18.3)$$

with the continuity equation reading:

$$\partial_r u_r + u_r/r + \partial_s u_s + \partial_z u_z = 0 \qquad (3.19)$$

In the following sections the solution of these equations, with the proper boundary conditions, will be obtained through a series of sub– models. Each sub– model will solve one particular problem of the flow. The general solution of the flow around a channel bend may be achieved by joining these sub– models together. These sub– models and their objectives are as follows :

(3.5) Width– averaged Model: from which the vertical distribution of the radial component of the flow velocity " u_r " will be obtained.

(3.6) Depth– averaged Model: from which the radial distribution of the depth– averaged velocity " u_{mb} " at the entrance to the channel bend will be modelled.

(3.7) Depth– Averaged Model: from which the horizontal distribution of the water depth " h " and the depth– averaged velocity " u_m " along the curved path of the bend will be obtained.

(3.8) Width– Averaged Model: for modelling the redistribution of the vertical profile of the longitudinal component of the velocity " u_s " along the bend course.

(3.9) Width– Averaged Model: to solve the problem of the growth and the decay of " u_r " along and beyond the bend.

As an independent calibration of the solutions to be obtained from the above mentioned sub– models, a set of comparisons with the experimental data obtained from other authors will be made throughout the mathematical analysis as appropriate. Comparisons with the writer's experimental data will be discussed in more detail in Chapter VI which is concerned with the analysis and the evaluation of the experimental results.

(3.5) Width–Averaged Model: Determination of the Radial Velocity Component

In this section, the analytical solution of the radial velocity component u_r will be obtained for a gentle wide channel bend. A **"gentle"** bend can be defined as a bend in which the ratio between the mid radius of curvature and the channel width **"r_m/B"** is of the order of 3 or more. In a gentle bend, the flow behaviour tends to a stable condition at which the velocity distribution at all sections is the same, that is independent of the local bend angle θ_b . Consequently, all derivatives of the velocities with respect to the coordinate system " s " in the dynamic model equations of motion vanish i.e.

$$\partial_s u_r \simeq \partial_s u_s \simeq 0 \qquad (3.20)$$

So, equations (3.18.1), (3.18.2) become

$$u_r\,\partial_r u_r + u_z\,\partial_z u_r - u_s^2/r = -g\,S_r + \partial_z(\nu\,\partial_z u_r) \qquad (3.21.1)$$

$$u_r\,\partial_r u_s + u_z\,\partial_z u_s + u_r u_s/r = g\,S_s + \partial_z(\nu\,\partial_z u_s) \qquad (3.21.2)$$

and the continuity equation becomes

$$\partial_r u_r + u_r/r + \partial_z u_z = 0 \qquad (3.22)$$

Equations (3.21.1) to (3.22) represent the general model equations for the flow in a gentle wide channel bend. These equations are non–linear, second order partial differential equations. In a gentle bend, the transverse velocity components u_r , u_z are relatively small with respect to the main component u_s Therefore, it is reasonable to assume, as a first approximation, that the vertical distribution of

the longitudinal velocity u_s and the turbulent momentum exchange coefficient (i.e. the turbulent eddy viscosity ν) will remain virtually the same as in the straight section upstream of the bend. These assumptions have been used before for example by Makkaveev (1933), Rozovskii (1961), Engulend (1974), De Vriend (1976), (1977), (1983), Nouh et al (1979), Hussein (1984) and others. These investigators have shown that the assumptions do not preclude solutions of relatively high accuracy.

Since the transverse velocity components u_r , u_z are small in comparison with u_s , it is possible to ignore the non-linear inertia terms involved in these variables. The momentum equation in the radial direction, equation (3.21.1), can be used to determine the vertical distribution of u_r . By neglecting the inertia terms $u_r\ \partial_r u_r$ and $u_z\ \partial_z u_r$ with magnitudes of a second order, then equation (3.21.1) will assume the form:

$$g\ S_r = u_s^2/r + \partial_z(\nu\ \partial_z u_r) \qquad (3.23)$$

This is a linear, second order, partial differential equation. The order of magnitude of the error involved in forming this equation is of "h^2/r^2" . Equation (3.23) describes the flow motion in the radial direction of the bend as a balance between the centrifugal force, the pressure gradient force (in terms of S_r) and the force due to the turbulent shear stresses. The analytical solution of this equation can be obtained by knowing the vertical distribution of the longitudinal velocity component $u_s(z)$. The vertical distribution of $u_s(z)$ can be assumed to follow the logarithmic law (Prandtl (1952)), which reads:

$$(u_{sm} - u_s)/\ u_* = \ln(z/h)\ /\ K \qquad (3.24)$$

where

u_{sm} is the maximum velocity at the water surface

u_* is the shear (or friction) velocity

K is the "Von– Karman" universal constant (= 0.4)

Use of the logarithmic law for the longitudinal velocity component u_s has the following advantages:

(1) It is valid for both smooth and rough channel boundaries where the roughness is modelled through the parameter u_* . Also, it reflects correctly the changes in the form of the velocity distribution curve in relation to boundary roughness. Since the left hand side of equation (3.24) represents the **"velocity defect"** of the flow. The shear velocity u_* can be related to the boundary shear stress τ_{0s} as:

$$u_* = \sqrt{(\tau_{0s}/\rho)} \qquad (3.25)$$

where τ_{0s} is the longitudinal component of the boundary shear stress.

(2) It introduces an equal vertical momentum exchange between the flow layers through the assumption of equal velocity fluctuation components in the longitudinal and the radial directions (i.e. u_s' and u_r'), through the Prandtl mixing length theory, resulting in a more realistic formulation of the shear stress term. Using the mixing length theory, the fluctuation components of the velocity can be expressed as:

$$u_s' = \ell\, \partial_z u_s \quad \text{and} \quad u_r' = \ell\, \partial_z u_r \qquad (3.26)$$

where ℓ is the mixing length and u_s' , u_r' are the velocity fluctuation

components in s and r directions respectively. By applying the continuity principle, the fluctuation component in the z– direction u_z' can be expressed as:

$$u_z' = \sqrt{[(u_s'^2)_m + (u_r'^2)_m]} \qquad (3.27)$$

where **"m"** represents the mean value of the fluctuation component.

Since the order of magnitude of the longitudinal velocity component u_s is greater than the order of magnitude of its radial component u_r . Hence, it can be assumed that their fluctuation components follow a similar manner, i.e.

$$\because O[u_r] \ll O[u_s] \qquad \therefore O[u_r'] \ll O[u_s'] \qquad (3.28)$$

As a result, the fluctuation component u_z' becomes:

$$u_z' \simeq u_s' = \ell\, \partial_z u_s \qquad (3.29)$$

The vertical shear stress in the longitudinal and the radial directions, i.e. τ_{sz} and τ_{rz} and their relation to the vertical momentum exchange may be expressed as;

$$\tau_{sz} = -\rho\,(u_s'u_z')_m = \rho\,\nu_{sz}\,\partial_z u_s$$
$$\tau_{rz} = -\rho\,(u_r'u_z')_m = \rho\,\nu_{rz}\,\partial_z u_r \qquad (3.30)$$

where ν_{sz} and ν_{rz} are the vertical eddy viscosities in "s" and "r" directions respectively. The associated shear stress components τ_{sz} and τ_{rz} can be expressed in terms of the mixing length ℓ as ;

$$\tau_{sz} = \rho\,\ell_{sz}^2\,(\partial_z u_s)^2 \qquad \text{and} \qquad \tau_{rz} = \rho\,\ell_{rz}^2\,\partial_z u_r\,\partial_z u_s \qquad (3.31)$$

By comparing equations (3.29), (3.30) and (3.31), it can be stated that:

$$\nu_{sz} = \nu_{rz} = \nu = \ell^2 \, \partial_z u_s$$

with $$\ell = K \, |\partial_z u_s| \, / \, |\partial_{zz} u_s| \qquad (3.32)$$

From the foregoing, it may be concluded from the above analysis that the mode of the vertical variation of the momentum exchange coefficient (i.e. ν) has the same behaviour longitudinally (i.e. along s– direction) and radially (i.e. along r– direction) for the flow in a wide channel bend.

As mentioned previously, in the above mentioned analysis, that for a two dimensional turbulent flow in a wide channel bend, the vertical distribution of u_s has the same profile as if it was applied for a uniform straight channel. Consequently, the vertical distribution of the turbulent eddy viscosity ν assumed to possess the same characteristics regardless of whether the channel was straight or curved. Such assumptions are the basis for most mathematical models that have been developed recently (e.g. see Engelund (1974), De Vriend (1976), (1977), (1983), Nouh et al (1979), Kikkawa et al (1976) and Kalkwijk et al (1980) and others).

By introducing the flow depth in a non– dimensional form λ , the logarithmic law for the longitudinal velocity component u_s in equation (3.24) will become:

$$(u_{sm} - u_s) / u_* = (\ln \lambda) / K \qquad (3.33)$$

where $$\lambda = z/h \qquad (3.34)$$

Applying the "Chezy" equation for the local depth– averaged velocity u_m and replacing the friction velocity u_* by the boundary shear stress τ_{0s} , u_m

and u_* may be expressed as:

$$u_m / u_* = C / \sqrt{g} = C' \qquad (3.35)$$

where C and C' are the dimensional and the non-dimensional Chezy coefficient of roughness. Substitution of equation (3.35) into equation (3.33) yields:

$$u_s = u_{sm} - \zeta(\ln \lambda)\, u_m \qquad (3.36)$$

where $$\zeta = 1 / K C' \qquad (3.37)$$

The maximum velocity at the water surface u_{sm} may be obtained by the integration of the u_m vertically from the bottom at $\lambda = 0$ to the surface at $\lambda = 1$ as

$$u_m = \int_0^1 u_s \, d\lambda \qquad (3.38)$$

From equation (3.36), u_m will read;

$$u_m = u_{sm} - \zeta u_m$$

or $$u_{sm} = u_m [1 + \zeta] \qquad (3.39)$$

Substituting equation (3.39) into equation (3.36), the vertical distribution of the longitudinal velocity component u_s may be obtained as:

$$u_s = u_m [\, 1 + \zeta (1 + \ln \lambda) \,] \qquad (3.40)$$

By differentiating equation (3.40) with respect to λ and substituting the result into equation (3.30), τ_{sz} will become:

$$\tau_{sz} = \rho \nu \zeta u_m / h \qquad (3.41)$$

The shear stress τ_{sz} in equation (3.41) is inversely proportional to the depth h. In the central portion of a wide channel bend, of a uniform cross section, the vertical distribution of the shear stress is linear with depth being maximum τ_{os} at the bottom and zero at the surface (in the absence of wind shear stress). So, τ_{sz} at any depth λ may be obtained as:

$$\tau_{sz} = \tau_{os} (1 - \lambda) \qquad (3.42)$$

Substituting equation (3.25) into (3.42), the vertical distribution of the shear stress τ_{sz} will be:

$$\tau_{sz} = \rho u_*^2 (1 - \lambda) \qquad (3.43)$$

Comparing equations (3.41) and (3.43), the vertical distribution of the turbulent eddy viscosity ν can be obtained as:

$$\nu = K h u_* \lambda (1 - \lambda) \qquad (3.44)$$

Which gives the familiar parabolic distribution of the eddy viscosity which has been confirmed experimentally to be realistic (see Jobson et al (1970)). The coefficient ν is zero at both the channel bottom and at the water surface i.e. where $\lambda = 0$ and 1 respectively. The maximum eddy viscosity ν_{max} exists at $\lambda = 0.5$ and has the value:

$$\nu_{max} = K h u_* /4 \qquad (3.45)$$

Returning to the momentum equation of the flow in the radial direction, i.e. equation (3.23), and by substituting the expression λ into it, then:

$$g\ S_r = u_s^2/r + (1/h^2)\ \partial_\lambda(\nu\ \partial_\lambda u_r) \qquad (3.46)$$

Introduction of the variable u_s from equation (3.40) yields;

$$g\ h^2\ S_r = (h^2\ u_m^2/r)[\ 1 + 2\zeta\ (1 + \ln\ \lambda) + \zeta^2\ (1 + \ln\ \lambda)^2\ ]$$

$$+ \partial_\lambda(\nu\ \partial_\lambda u_r) \qquad (3.47)$$

(3.5.1) Boundary Conditions

Two boundary conditions are needed for the solution of equation (3.47). These boundary conditions are:

(B.1) <u>At the water surface</u>, the assumption of the ab-sence of tangential wind shear stresses will cause the radial component of the shear stress to vanish i.e.

$$\tau_{rz}[\lambda=1] = (\nu\ /\ h)\ \partial_\lambda u_r[\lambda=1] = 0 \qquad (3.48)$$

(B.2) <u>In the plane of the channel cross section</u>, the net radial discharge Q_r , in the central portion, vanishes along any vertical column of the flow i.e.

$$Q_r = {}_0\int^1\ u_r\ d\lambda = 0 \qquad (3.49)$$

This boundary condition is applicable in the case of two–dimensional motion i.e. when the vertical velocity component u_z , that causes any redistribution of u_r

vertically in the cross section, becomes negligible. Below, this condition will be proved mathematically.

From the continuity equation, i.e. equation (3.22), the vertical velocity component u_z reads:

$$u_z = \int \partial_\lambda u_z \, d\lambda = - (1/r) \int \partial_r (r \, u_r) \, d\lambda \qquad (3.50)$$

Since ∂_r is an arbitrary differential operator for the radial direction and is independent of λ , therefore equation (3.50) may be rewritten in the form of:

$$\int \partial_\lambda u_z \, d\lambda = - (1/r) \, \partial_r [\, r \int u_r \, d\lambda \,]$$

$$= - (\, u_z[\lambda = 1] - u_z[\lambda = 0] \,) \qquad (3.51)$$

The velocity component u_z must be zero at the surface since the water surface fluctuations are assumed to be much smaller than the water depth. Furthermore at the channel bottom, where the flow direction is expected to follow the boundary, u_z must also vanish. Therefore, it is reasonable to state from equation (3.51) that:

$$u_z = u_z[\lambda = 1] = u_z[\lambda = 0] = 0 \qquad (3.52)$$

which proves the validity of the boundary condition expressed through equation (3.49).

(3.5.2) **The Analytical Solution**

Turning now to equation (3.47) and integrating with respect to λ, it will read:

$$\nu\, \partial_\lambda u_r = (h^2\, u_m{}^2/r)\, [\, \int\{(g\, S_r\, r/u_m{}^2) + 1\}\, d\lambda + 2\zeta \int(1 + \ln \lambda)\, d\lambda$$

$$+ \zeta^2 \int(1 + \ln \lambda)^2\, d\lambda\,] + I_1 \qquad (3.53)$$

where I_1 is the integration constant. Introducing the coefficient ξ which relates to the coefficient ζ by:

$$\xi = \zeta + 1 \qquad (3.54)$$

and applying the boundary condition (B.1) to equation (3.53), the integration constant I_1 may be written as:

$$I_1 = (h^2\, u_m{}^2/r)[\, \xi^2 + 2\, \zeta^2 - 2(\xi/\zeta) - (r\, S_r\, g/u_m{}^2)] \qquad (3.55)$$

By substituting I_1 into equation (3.53) and after slight rearrangement, equation (3.56) is obtained:

$$\nu\, \partial_\lambda u_r = (h^2\, u_m{}^2/r)\, [(1 - \lambda)\{\, \xi^2 - (r\, S_r\, g/u_m{}^2)\} - 2\, (\xi/\zeta)$$

$$\{\lambda(\lambda - 1) + 1\} + \zeta^2\, \{\lambda \ln \lambda\, (\ln \lambda - 2) + 2(\lambda - 1)\}] \qquad (3.56)$$

Substitution of the value of the turbulent eddy viscosity ν from equation (3.44) into equation (3.56) gives:

$$\partial_\lambda u_r = (u_m\ h/r)\ \zeta\ C'^2\ [\ \lambda^{-1}\ \{\xi^2 - (r\ S_r\ g/u_m^2)\} - 2\ (\xi/\zeta)$$

$$\{(1-\lambda)^{-1}\ (\ln\ \lambda) + \lambda^{-1}\} + \zeta^2\ \{(1-\lambda)^{-1}\ (\ln\ \lambda)\ (\ln\ \lambda - 2\lambda) - (2/\lambda)\}] \qquad (3.57)$$

Again by integrating equation (3.57) with respect to λ, the vertical distribution of the radial velocity component can be obtained as:

$$(u_r/u_m)(r/h) = \zeta\ C'^2\ [\{\xi^2 - (r\ S_r\ g/u_m^2)\}\ \int\ \lambda^{-1}\ d\lambda - 2\ (\xi/\zeta)$$

$$\int\{(1-\lambda)^{-1}\ (\ln\ \lambda) + \lambda^{-1}\}\ d\lambda + \zeta^2\ \int\{(1-\lambda)^{-1}\ (\ln\ \lambda)$$

$$(\ln\ \lambda - 2\lambda) - (2/\lambda)\}\ d\lambda\ ]\ +\ I_2 \qquad (3.58)$$

where I_2 is the constant that results from the integration process. This constant can be determined by applying the boundary condition (B.2) to equation (3.58). The solution for I_2 is:

$$I_2 = (h\ u_m/r)\ \zeta\ C'^2\ [\ \xi^2 - (r\ S_r\ g/u_m^2)] \qquad (3.59)$$

Substitution of equation (3.59) into equation (3.58) gives the general formula for the prediction of the vertical distribution of the radial velocity component as;

$$(u_r/u_m)(r/h) = \zeta\ C'^2\ [\ (\ln\ \lambda + 1)\{\ \xi^2 - (r\ S_r\ g/u_m^2)\} -$$

$$- 2(\xi/\zeta)\ \Phi_1(\lambda) + \zeta^2\ \Phi_2(\lambda)\ ] \qquad (3.60)$$

where

$$\Phi_1(\lambda) = \int[\ (1-\lambda)^{-1}\ (\ln\ \lambda) + \lambda^{-1}\ ]\ d\lambda \qquad (3.61)$$

and

$$\Phi_2(\lambda) = - \int[(1-\lambda)^{-1} (\ln \lambda)(\ln \lambda - 2\lambda) - (2/\lambda)] \, d\lambda \tag{3.62}$$

with the condition that:

$$_0\int^1 \Phi_1(\lambda) \, d\lambda = {}_0\int^1 \Phi_2(\lambda) \, d\lambda = 0 \tag{3.63}$$

The analytical solution of $\Phi_1(\lambda)$ and $\Phi_2(\lambda)$ will be given in detail in Appendix (B). Fig.(3.2) gives the vertical distribution of these functions.

(3.5.3) Determination of the Radial Surface Slope

The solution for u_r is not yet complete since the magnitude of the transverse surface slope S_r is still unknown. In order to determine this value, the main forces that influence the radial profile of the water surface have to be studied. This may be done by considering the equilibrium condition of the forces applied to a fluid column of the flow in the interior region of the plane of the cross section away from the walls as in Fig.(3.3). If the base of the fluid column has the dimensions "dr. ds" , and if it is assumed that the vertical distribution of pressure follows the hydrostatic law. Then the balance between the applied forces on the fluid column of the flow will be:

$$\underset{\text{centrifugal}}{[\ \rho(\beta\ u_m{}^2/r)ds\ dr\ h]} + \underset{\text{pressure gradient}}{[(\rho\ g\ h\ \partial_r h)ds\ dr]} + \underset{\text{friction}}{[(\tau_{0r})\ ds\ dr]} = 0 \tag{3.64}$$

where

β is the momentum flux correction factor necessary to take account of the non– uniform vertical distribution of u_s

u_m is the depth– averaged velocity along the depth of the flow

τ_{or} is the radial component of the bounary shear stress.

From equation (3.64), the condition of the transverse equilibrium may be written as;

$$S_r = \partial_r h = \beta\,(u_m^2/g\ r) + \tau_{or}/(\rho\ g\ h) \qquad (3.65)$$

Equation (3.65) can also be obtained from the integration of equation (3.23) vertically from $\lambda = 0$ to 1 , through the use of equation (3.30) and the equality " $u_s^2 = \beta\ u_m^2$ ". It may be concluded from equation (3.65) that the radial water surface slope S_r is dependent on:

(1) The centrifugal force which, in turn, is proportional to the square of the local depth– averaged velocity u_m^2 and is inversely proportional to the local radius of curvature r . So, it may be expected that the maximum depth will occur at the outer bank of the channel bend while the minimum depth will take place at the inner bank.

(2) The radial component of the bottom shear stress τ_{or} . Its order of magnitude may be evaluated approximately, for the case of a hydraulically smooth bed, as follows:

The radial velocity component u_r in the upper part of the depth is directed towards the outer bank of the bend, and in the lower part of the depth is directed towards the inner bank. Therefore, the vertical distribution of u_r may be

expected to follow the profile shown in Fig.(3.4). The value of u_r will be zero at the channel bed (including the thickness of the laminar viscous sub-layer). From Fig. (3.4) it may be seen that the vertical profile of u_r will pass through a point " T " at which $\partial_\lambda u_r = 0$ and consequently $\tau_{0r} = 0$. If the vertical distance from the channel bed to the point T is assumed to be " δ ", then the equilibrium condition for the fluid column having that height δ will read:

$$[(\rho\ g\ S_r)\ dr\ ds\ \delta] + [\rho\{{}_0\int^{\delta}\ (u_s{}^2/r)\ dz\}\ ds\ dr] + [\tau_{0r}\ dr\ ds] = 0 \qquad (3.66)$$

or

$$\tau_{0r} = \rho\ g\ S_r\ \delta - \rho\ {}_0\int^{\delta}\ (u_s{}^2/r)\ dz \qquad (3.67)$$

From equation (3.67) it may be concluded that the order of magnitude of τ_{0r} is:

$$0\ [\tau_{0r}] \ \angle\ 0\ [\rho\ g\ S_r\ \delta]$$
$$\angle\ 0\ [\rho\ g\ S_r\ h\ (\delta/h)] \qquad (3.68)$$

Thus, knowing the value of δ , the order of magnitude of τ_{0r} may be obtained. Since for channels of a smooth bed condition δ is very small, then it may be concluded that the effect of τ_{0r} on the radial water surface slope S_r can be neglected. The order of magnitude of the error associated with this approximation can be estimated from equation (3.68), but will not exceed δ/h and this can normally be considered negligible. Similar conclusion was previously reported by Rozovskii (1961) and De Vriend (1976), Hussein (1984) and Hussein et al (1986).

According to the above, the radial water surface slope S_r for a smooth channel bend will have the value:

$$S_r \cong \beta\, u_m^2/g\, r \qquad (3.69)$$

with

$$\beta = [{}_0\int^1 (u_s^2/g\, r)\, d\lambda] \,/\, [u_m^2/g\, r] \qquad (3.70)$$

The coefficient β , the momentum flux correction factor, can be calculated from equation (3.70) by substituting the value of u_s from equation (3.40) and carrying out the integration with respect to λ , it will become

$$\beta = 1 + \zeta^2 \qquad (3.71)$$

where $\zeta = 1/(K\ C')$ from equation (3.37). Fig.(3.5) gives the relation between β and the channel bottom roughness through the non-dimensional coefficients C' and ζ .

Hence, the final form of the vertical distribution of the radial velocity component u_r can be obtained by substituting the value of S_r from equation (3.69) into equation (3.60). The solution will read, after slight re-arrangement, as:

$$(u_r/u_m)(r/h) = \zeta\, C'^2[(\xi^2 - \beta)(\ln \lambda + 1) - 2(\xi/\zeta)\, \Phi_1(\lambda) + \zeta^2\, \Phi_2(\lambda)] \qquad (3.72)$$

where $\zeta = 1/(K\ C')$, $\xi = 1 + \zeta$ and $\beta = 1 + \zeta^2$ are coefficients which are dependent on the channel bottom roughness.

Equation (3.72) represents the basic equation of the width-averaged mathematical model. The influence of the model on the mathematical formulation of the following sub-models is extremely high, as will be shown later. Therefore, calibration and verification of the model is essential. To accomplish this, results

from the model equation, equation (3.72), will be compared not only with these obtained from previous analytical models and experimental data, but also with field data.

(3.5.4) Comparisons With Existing Analytical Models

Bendegom (1947) (from Jansen et al (1979)) assumed that the vertical profile of u_s follows the power law profile. This together with the assumptions of zero radial velocity at the channel bed and zero net radial discharge, allowed a formula for u_r to be predicted as:

$$(u_r/u_m)(r/h) = K^{-2}\,[(\bar{n}+2)^{-1}\,\bar{n}^2\,(\bar{n}+1)\,{}_0\!\int^1 (1-\lambda^{\bar{n}+1})/(1-\lambda^{\bar{n}})\,d\lambda$$

$$-\,\bar{n}\,(\bar{n}+1)^2\,(\bar{n}+3)^{-1}\,\lambda^{1/\bar{n}}] \qquad (3.73)$$

where $\bar{n}$ is the value of the power law (varies between 4 and 9), while the other variables are as previously defined.

Rozovskii (1961) applied the same assumptions, but used a logarithmic distribution for modelling the longitudinal velocity component u_s , and obtained:

$$(u_r/u_m)(r/h) = K^{-2}\,[\,F_1(\lambda) - \zeta\,F_4(\lambda)\,] \qquad (3.74)$$

where

$$F_1(\lambda) = {}_0\!\int^1 2\,\ln\,\lambda/(\lambda-1)\,d\lambda \qquad (3.75)$$

$$F_2(\lambda) = {}_0\!\int^1 (\ln\,\lambda)^2/(\lambda-1)\,d\lambda \qquad (3.76)$$

and

$$F_4(\lambda) = F_2(\lambda) + 0.8\ (1 + \ln \lambda) \qquad (3.77)$$

Bouwmeester (1972) modified Rozovskii's solution by making the additional assumption that the longitudinal velocity component was also zero at the channel bed, giving:

$$(u_r/u_m)(r/h) = K^{-2}\ [\ F_1(\lambda) + \zeta\ F_2(\lambda) - 2(1 - \zeta^2) - 2\zeta(1-\zeta)\ \ln \lambda\ ] \qquad (3.78)$$

Recently, Kikkawa et al (1976) developed an analytical model based upon the assumption of uniform vertical distribution of the eddy viscosity. By applying the logarithmic law for the vertical profile of the longitudinal velocity u_s , Kikkawa et al predicted the vertical distribution of u_r as:

$$(u_r/u_m)(r/h) = K^{-1}\ [\ \eta_1(\lambda) - \zeta\ \eta_2(\lambda)\ ] \qquad (3.79)$$

where

$$\eta_1(\lambda) = -15\ [\lambda^2 \ln \lambda - 0.5\ \lambda^2 + (15/54)] \qquad (3.80)$$

$$\eta_2(\lambda) = 7.5\ [\lambda^2 \ln^2 \lambda - \lambda^2 \ln \lambda + 0.5\ \lambda^2 - (19/54)] \qquad (3.81)$$

Fig.(3.6) gives comparisons of the predicted profile of the radial velocity component from equation (3.72), in a non-dimensional form "(u_r/u_m) (r/h) K^2",

with these from the Bendegom, Rozovskii, Bouwmeester and Kikkawa et al models. In applying the Bendegom model, " $\bar{n}$ " was taken as 8 ; and for the Rozovskii, Bouwmeester and Kikkawa et al models, C' was 17.56 (i.e. smooth bed with C = 55). From the Figure it can be seen that the agreement is generally very good.

(3.5.5) Comparisons With Experimental and Field Data

Comparisons with experimental and field data are more important for model verification. These comparisons will confirm the capability of the model in predicting the radial velocity component for different flow conditions, different channel bed roughness and different bend geometries. Figures (3.7) to (3.9) give a series of comparisons with the data obtained from Kondrat'ev et al (1959), Rozovskii (1961), Kikkawa et al (1976) and Odgaard (1982) repectively. In general, the agreement is very satisfactory with data from the first two sources and is good with that from the last two. In Fig.(3.9), it is encouraging to note that in the comparison with data from "Sacramento River", given by Odgaard (1982), a fairly good agreement is obtained with the theoretical prediction. It should also be noted that Figures (3.7) and (3.8), are for smooth channel boundaries (C' = 17.56), while in Fig.(3.9) the channel boundary is considered rough (C' = 9.58).

Hence, on the basis of the comparisons with both existing analytical and experimental results, the use of the present width–averaged model for the prediction of the radial component of the secondary currents u_r is considered justified. Attention will now be given to the formulation of the other sub–models listed previously.

(3.6) Depth– Averaged Model: Distribution of the Depth– Averaged Velocity at the Bend Entrance

In this model, the distribution of the depth– averaged velocity across the channel width at the bend entrance will be predicted. The general solution which models this distribution will be derived from the momentum **Bernoulli** equation. The only applicable boundary condition required for the solution is the equality of the flow discharge before and at the bend entrance. Due to the implicit introduction of this boundary condition to the general model equation, the solution will be obtained numerically through the use of the finite difference technique.

When the flow passes from a straight reach into a bend, a transverse water surface slope is generated due to centrifugal force. As a result of the developed superelevation in the water surface, the distribution of the depth– averaged velocity across the channel width becomes essentially non– uniform (i.e. existence of the Bernoulli effect in the flow). The maximum velocity occurs at the inner bank and the minimum at the outer bank.

Consider the flow motion at two sections, section (S) in the straight part before the bend, and section (B) at the bend entry (see Fig.(3.10)). Applying the Bernoulli equation of motion, per unit width of the channel, between these two sections:

$$u_{ms}^2/2 + P_s/\rho + g\, z_s = u_{mb}^2/2 + P_b/\rho + g\, z_b + h_f \qquad (3.82)$$

where

u_{ms} , u_{mb} are the depth– averaged velocities per unit width of the channel at sections (S) and (B) respectively.

P_s , P_b are the static pressure heads of the flow at sections (S) and (B) respectively.

z_s , z_b are the position heads relative to a reference datum, for sections (S) and (B) respectively.

h_f is the total head loss of the flow between sections (S) and (B) .

ρ is the flow density.

g is the gravitational acceleration.

If the distance between sections (S) and (B) is relatively small, the head loss h_f and the difference between the position heads z_s and z_b may be ignored. Furthermore, by applying the hydrostatic law for the pressure head at section (S) and (B), equation (3.82) becomes:

$$u_{ms}^2/2 + g\, h_s \cong u_{mb}^2/2 + g\, h_b$$

or

$$\Delta h = (1/2\, g)[u_{ms}^2 - u_{mb}^2] \qquad (3.83)$$

where $\Delta h = h_b - h_s$, is the difference of the water surface levels between the two sections (see also Fig.(3.10)).

The value of Δh can be calculated by considering the equilibrium condition of the forces acting upon a fluid column of the flow in the radial direction. This approach has been discussed in detail in a previous section, section (3.5.3), where Δh can be determined through the integration of the radial water surface slope S_r with respect to r , i.e.

$$\Delta h = \int S_r\, dr = \int (\beta\, u_{mb}^2/g\, r)\, dr + c \qquad (3.84)$$

where c is the integration constant. By substituting the value of Δh from

equation (3.83) into equation (3.84) and differentiating the resulting equation with respect to r, it reads:

$$d_r(u_{ms}^2/2g) = d_r(u_{mb}^2/2g) + \beta\, u_{mb}^2/gr \qquad (3.85)$$

where $d_r = d/dr$, is the gradient operator along r−direction. By assuming that the value of β at the bend entrance is the same as for the straight reach upstream i.e. $\simeq 1.0$, and by multiplying by " $2\,r^2$ ", equation (3.85) becomes:

$$d_r(u_{ms}^2/2) = d_r(u_{mb}^2) + 2\, u_{mb}^2/r \qquad (3.86)$$

Which is a non−homogeneneous, first order linear differential equation for u_{mb}^2. The general analytical solution for this equation is: (see Vygodsky (1971))

$$u_{mb}^2 = [\ \int\{d_r(u_{ms}^2)\ \exp(\int 2/r\ dr)\}\ dr + c_1\ ]\ \exp(-\int 2/r\ dr) \qquad (3.87)$$

where c_1 is the integration constant. This constant can be obtained from the condition of continuity by assuming that the flow discharge at sections (S) and (B) are equal, i.e.

$$Q_s = h_s\, B\, u_{ms} = h_s\,(r_o - r_i)\, u_{ms} = {}_{ri}\int^{ro} (u_{mb}\, h_b)\ dr \qquad (3.88)$$

where Q_s is the flow discharge at section (S), and r_i and r_o are the inner and the outer radii of the bend. The expression $(r_o - r_i)$ represents the channel width at section (B). By substituting the value of u_{mb} from equation (3.87) into equation (3.88), it will become:

$$Q_s = {}_{ri}\int^{ro} [\ (h_b/r)\ \{\int r^2\ d_r(u_{ms}{}^2)\ dr + c_1\}^{1/2}\ ]\ dr \qquad (3.89)$$

Equation (3.87) and (3.89) are the general equations for the distribution of the depth–averaged velocity u_{mb} at the bend entrance. These two equations are applicable to any distribution law for the depth–averaged velocity u_{ms} before the bend. Hence, the solution of this problem can be achieved if the distribution of u_{ms} is known.

A special case can be found where the distribution of u_{ms} is uniform. In this particular case, its derivative with respect to r in equation (3.87) will become zero. As a consequence of that, equation (3.87) will read:

$$u_{mb}\ r = \sqrt{c_1} = \text{constant} \qquad (3.90)$$

i.e. it is converted to give the law of a " **potential vortex** ", where $\sqrt{c_1}$ represents the strength of the circulation involved in this motion. With the use of the boundary condition stated in equation (3.89), the value of $\sqrt{c_1}$ can be determined as:

$$\sqrt{c_1} = (Q_s/h_b)\ /\ \ln(r_o/r_i) \qquad (3.91)$$

Substituting the values of $\sqrt{c_1}$ and Q_s into equation (3.90), the distribution of u_{mb} at the bend entrance can be obtained, it is:

$$(u_{mb}/u_{ms})(h_b/h_s) = (r_o - r_i)\ /\ [r\ \ln(r_o/r_i)] \qquad (3.92)$$

Equation (3.92) gives the distribution of the depth–averaged velocity u_{mb} across the channel width at the bend entrance. It is only applicable in the form when the distribution of the depth–averaged velocity in the approach flow is uniform. Combination of equations (3.83) and (3.92) allow the superelevation Δh to be written as:

$$\Delta h = (u_{ms}^2/2g) \left[1 - R_b^2 \right] \qquad (3.93)$$

where

$$R_b = (h_s/h_b) (r_o - r_i) / [r \ln(r_o/r_i)] \qquad \text{for} \quad r_i \leq r \leq r_o \qquad (3.94)$$

If $h_s \cong h_b$, then equation (3.93) indicates a hyperbolic variation of the water surface in the radial direction, which is in accordance with the requirement of a potential vortex flow. Thus, the radial profile of the water surface varies only with the radial distribution of momentum and the total superelevation is a function only of the mean momentum of the approach flow.

An interesting feature of the potential vortex theory is that it can provide a relation between the boundary shear stress distribution and the channel geometry (in terms of the bend tightness ratio) at the bend entrance. Below, this relation will be obtained and discussed.

According to equation (3.35), section (3.5), the relation between the friction and the depth–averaged velocities for the inner and the outer bend radii can be expressed as:

$$u_{mi} / u_{mo} = u_{*i} C' / (u_{*o} C')$$

$$= u_{*i} / u_{*o} = \sqrt{(\tau_i / \tau_o)} \qquad (3.95)$$

where

u_{*i} & u_{mi} are the friction and the depth–averaged velocities at the inner bend radius respectively.

u_{*o} & u_{mo} are the friction and the depth–averaged velocities at the outer bend radius respectively.

τ_i & τ_o are the longitudinal components of the bed shear stress at the inner and the outer bend radii.

C' is the non–dimensional Chezy coefficient.

By applying the potential vortex theory, expressed in equation (3.90), for the depth–averaged velocities u_{mi} and u_{mo} , and using equation (3.95), it will give

$$u_{mi} / u_{mo} = u_{*i} / u_{*o} = r_o / r_i$$

$$= [2 (r_m/B) + 1] / [2 (r_m/B) - 1] \qquad (3.96)$$

Equation (3.96) shows clearly the importance of the bend tightness ratio r_m/B on the distribution of the bed shear stress. Fig.(3.11) gives the relation between the velocity ratios (i.e. u_{mi}/u_{mo} and u_{*i}/u_{*o}) and the ratio r_m/B . From Fig.(3.11) it can be concluded that:

(1) The velocity ratios u_{mi}/u_{mo} and u_{*i}/u_{*o} are inversely proportional to r_m/B .

(2) For $r_m/B \geq 3.0$ (i.e. gently curved bends), the variation in the velocity ratios is almost uniform.

(3) For $r_m/B \leq 2.0$ (i.e. strongly cuved bends), the variation in the velocity ratios increases rapidly.

(4) For $r_m/B = 0.5$, the velocity ratios u_{mi}/u_{mo} and $u_{*i}/u_{*o} \rightarrow \infty$, i.e. a hypothetical case cannot occur in actual flows.

The above discussion confirms the experimental results obtained by previous investigators which indicated the important role of the bend tightness ratio on the distribution of the boundary shear stress in channel bends (see also section (2.6), Chapter II).

(3.6.1) Numerical Representation

Turning to the general model equation for u_{mb} i.e. equation (3.87), it is noticed that the boundary condition required for the determination of the integration constant, which expressed in equation (3.89), is implicitly introduced. This makes it rather difficult to solve the equation analytically. Hence, the general solution for the depth–averaged velocity u_{mb} will be obtained numerically. The following numerical solution can be applied to any distribution law for the depth–averaged velocity u_{ms} in the approach flow. It is no longer essential that the approach flow is uniform.

For the purposes of the numerical solution, the channel width at the bend entrance is divided into " i " sections of a total " N " where :

$$\text{" N i} = r_o - r_i = B = \text{the channel width "}$$

In this case, equation (3.87) can be expressed in the form ;

$$u_{mb}[i+1] = (\sum_i \{r^2[i]\ \Delta u_{ms}^2 + c_1\})^{1/2} / r[i+1] \qquad (3.97)$$

where

$$\Delta u_{ms}^2 = u_{ms}^2[i+1] - u_{ms}^2[i] \quad \text{for} \quad 1 \leq i \leq N-1 \qquad (3.98)$$

The integration constant c_1 , which can be calculated from the boundary condition as given in equation (3.89), may be expressed after slight transformation as ;

$$c_1 = Q_s^2\ (r^2[i]/h^2[i]) - \sum_i (r^2[i]\ \Delta u_{ms}^2) \qquad (3.99)$$

where Q_s is the flow discharge which can be obtained from equation (3.88). In Appendix (D), the computational procedure of this sub– model is given in the form of a flow chart called " BENENT " .

The calibration of this sub– model will be introduced together with the calibration of the following sub– model, that deals with the solution of the horizontal problem (to be described in section (3.7)).

(3.7) Depth– Averaged Model : Solution of the Horizontal Problem

In this model, the horizontal variations of the depth– averaged velocity $u_m(r,s)$ and the flow depth $h(r,s)$, radially and longitudinally along the bend course, will be determined. Such a determination is usually called the solution of the horizontal problem. The general model equations will be derived analytically from the momentum equation of motion in the longitudinal s– direction. The solution of the model equation will be carried out numerically using a finite difference scheme.

In order to study the horizontal variations of the flow field (i.e. u_m and h) along the bend, the momentum equation in s– direction for a differential control volume (dr.ds.dz) has to be considered. It will be repeated for convenience from equation (3.18.2), section (3.4), as:

$$u_r\, \partial_r u_s + u_s\, \partial_s u_s + u_z\, \partial_z u_s + u_r\, u_s/r = g\, S_s + 1/\rho\, \partial_z \tau_{sz} \qquad (3.18.2)$$

where

u_r, u_s, u_z	are the velocity components in r,s,z respectively.
$\partial_r, \partial_s, \partial_z$	are the gradient operators in r,s,z respectively.
S_s	is the longitudinal water surface slope.
τ_{sz}	is the longitudinal component of the shear stress.
ρ	is the flow density.
g	is the gravitational acceleration.

The first three terms on the left hand side of equation (3.18.2), which represent the non– linear inretia terms, have the same order of magnitude as the other terms. Ignoring these inertia terms would lead eventually to serious errors and unrealistic solutions. Therefore, the non– linear inertia terms play a major

role in the mathematical formulation of the horizontal problem and hence, will be included.

The general model equation can be obtained through the integration of equation (3.18.2) vertically. The only difficulty, that has to be first overcome, is the existence of the vertical velocity component u_z and the vertical gradient of the longitudinal velocity component $\partial_z u_s$. This can be done through the use of the continuity equation.

From the theory of differentiation of a product of two variables, it can be written that:

$$u_z \, \partial_z u_s = \partial_z(u_s u_z) - u_s \, \partial_z u_z \qquad (3.100)$$

Then the term $u_z \, \partial_z u_s$ in equation (3.18.2) can be substituted by the terms expressed on the right hand side of equation (3.100). Before doing so, the value of $\partial_z u_z$ has to be known. This can be found from the continuity equation, equation (3.7), section (3.4), as:

$$\partial_z u_z = - [\, \partial_r u_r + u_r/r + \partial_s u_s \,] \qquad (3.7)$$

Substituting the value of $\partial_z u_z$ into equation (3.100) gives:

$$u_z \, \partial_z u_s = \partial_z(u_s u_z) + u_s [\, \partial_r u_r + u_r/r + \partial_s u_s \,] \qquad (3.101)$$

Then the value of $u_z \, \partial_z u_s$, in equation (3.18.2), can be substituted by the terms expressed in equation (3.101). Equation (3.18.2) will now read, after slight modification, as:

$$\partial_r(u_r u_s) + 2\, u_r u_s/r + \partial_s u_s^2 + \partial_z(u_s u_z) = g\, S_s + 1/\rho\ \partial_z \tau_{sz} \qquad (3.102)$$

The first two terms of the left hand side of equation (3.102) can be expressed, through the theory of differentiation, as:

$$\partial_r(u_r u_s) + 2\, u_r u_s/r = (1/r^2)\ [\ \partial_r(r^2\, u_r u_s)\ ] \qquad (3.103)$$

Then, by substituting equation (3.103) into equation (3.102), it will give the form:

$$(1/r^2)[\partial_r(r^2\, u_r u_s)] + \partial_s u_s^2 + \partial_z(u_s u_z) = g\, S_s + 1/\rho\ \partial_z \tau_{sz} \qquad (3.104)$$

Equation (3.104) is a new version of the momentum equation of motion expressed in equation (3.18.2). The integration of equation (3.104) vertically will give the general model equation required for the solution of the horizontal variations of the flow, longitudinally and radially, around the channel bend.

According to the aforesaid, writing equation (3.104) in the integral form gives:

$$\int_0^h (1/r^2)\ \partial_r(r^2\, u_r u_s)\ dz + \int_0^h \partial_s u_s^2\ dz + \int_0^h \partial_z(u_s u_z)\ dz$$

$$= g\, S_s\, h + \int_0^h (1/\rho)\ \partial_z \tau_{sz}\ dz \qquad (3.105)$$

But

$$\int_0^h \partial_z(u_s u_z)\ dz = u_s u_z\ [z=h] - u_s u_z\ [z=0] = 0 \qquad (3.106)$$

Since $u_z\ [z=h] = u_z\ [z=0] = 0$ from equation (3.52), section (3.5.1).

Also,

$$ {}_0\int^h (1/\rho)\ \partial_z \tau_{sz}\ dz = (1/\rho)\ (\ \tau_{sz}\ [z=h] - \tau_{sz}\ [z=0]\ ) $$

$$ = - \tau_{0s} / \rho = - u_*^2 \qquad (3.107) $$

where $\tau_{sz}\ [z=h] = 0$ through the assumption of the absence of wind shear stress at the water surface (see boundary condition (B.1), equation (3.48), section (3.5.1)).

By substituting the values of the integrals expressed in equations (3.106) and (3.107) into equation (3.105), it becomes:

$$ \partial_s \Psi_1 + (1/r^2)\ \partial_r (r^2\ \Psi_2) = g\ S_s\ h - u_*^2 \qquad (3.108) $$

where

$$ \Psi_1 = h\ {}_0\int^1 u_s^2\ d\lambda \qquad (3.109) $$

and

$$ \Psi_2 = h\ {}_0\int^h u_r u_s\ d\lambda \qquad (3.110) $$

Equation (3.108) is the basic equation for the depth-averaged model. The determination of the integrals Ψ_1 and Ψ_2 will lead eventually to the final form of the general model equation. In order to accomplish this, the vertical distributions of u_s and u_r, from equations (3.40) and (3.72) respectively, section (3.5), have to be considered. By combining equations (3.40) and (3.109) and integrating, Ψ_1 will read:

$$ \Psi_1 = \beta\ h\ u_m^2 \qquad (3.111) $$

Similarly combining equations (3.40) and (3.72) and integrating, an equation for Ψ_2 may be obtained. Solution of this equation is more difficult however, than that for Ψ_1 , because of the involvement of the integration functions $\Phi_1(\lambda)$ and $\Phi_2(\lambda)$ that are included in the determination of u_r (see equation (3.72), section (3.5.3)). Combination of equation (3.110) with equations (3.40) and (3.72), a solution of Ψ_2 may be obtained in the form:

$$\Psi_2 = (u_m^2\, h^2/r)\, \zeta\, C'^2[\, \zeta\, (\xi^2 - \beta) - 2\, (\xi/\zeta)\, \Phi_3 + \zeta^2\, \Phi_4 - 2\, \xi\, \Phi_5 + (1/\zeta)\, \Phi_6\,] \qquad (3.112)$$

where

$$\Phi_3 = {}_0\int^1 \Phi_1(\lambda)\, d\lambda = 0 \qquad (3.113)$$

$$\Phi_4 = {}_0\int^1 \Phi_2(\lambda)\, d\lambda = 0 \qquad (3.114)$$

$$\Phi_5 = {}_0\int^1 (\ln \lambda + 1)\, \Phi_1(\lambda)\, d\lambda \qquad (3.115)$$

$$\Phi_6 = {}_0\int^1 (\ln \lambda + 1)\, \Phi_2(\lambda)\, d\lambda \qquad (3.116)$$

The values of the integrals Φ_3 and Φ_4 are essentially **zero** as their integration limits match those of the boundary condition required for the solution of the integration functions $\Phi_1(\lambda)$ and $\Phi_2(\lambda)$ (see equation (3.63), section (3.5.2)). The analytical solution of the mathematical integrals Φ_5 and Φ_6 will be discussed in detail in Appendix (C). The final form of the solution is:

$$\Psi_2 = \gamma\, h^2\, u_m^2\, /\, r \qquad (3.117)$$

where

$$\gamma = \zeta^2 C'^2[\, \xi^2 - \beta - 1.182\ (\xi/\zeta) + (0.744/\zeta^2)] \qquad (3.118)$$

with $\zeta = 1/(KC')$, $\beta = 1 + \zeta^2$ and $\xi = 1 + \zeta$.

where K is the Von– Karman constant and C' is the non– dimensional Chezy coefficient. The coefficient γ is known as the **secondary flow convection factor.** Its importance lies in the term $(1/r^2)\ \partial_r(r^2\ \Psi_2)$, equation (3.108), which simulates the transverse exchange of the main flow momentum by the secondary currents. Fig.(3.12) gives a graphical representation of the coefficient γ as a function of C' . Also included in the Figure are comparisons with different distributions of γ as suggested by Rozovskii (1961) and Kalkwijk et al (1980).

Substituting the values of Ψ_1 and Ψ_2 from equations (3.111) and (3.117) into equation (3.108), the resulting equation will read:

$$\beta\ \partial_s(h\ u_m^2) + (\gamma/r^2)\ \partial_r(h^2\ r\ u_m^2) = g\ h\ S_s - u_*^2 \qquad (3.119)$$

Which represents the general model equation for the horizontal problem (i.e. for the distribution of u_m and h) along the bend path. The first and the second terms on the left hand side of equation (3.119) are the main (longitudinal) and the secondary (radial) convection terms of the inertia terms. The other two terms on the right hand side are the pressure gradient and the friction terms.

Equation (3.119) is a non– linear partial differential equation. The exact analytical solution to it, is a rather complicated task. Hence, numerical integration in the form of the method of finite differences will be used. Before doing so, equation (3.119) has still to be arranged in a simpler form in order to make the

numerical treatment easier to deal with. To accomplish this, the main and the secondary convection terms can be simplified by the differentiation with respect to "s" and "r" as;

$$\beta\ \partial_s(h\ u_m^2) = \beta\ [\ u_m^2\ \partial_s h + 2\ h\ u_m\ \partial_s u_m\ ] \qquad (3.120)$$

and

$$(\gamma/r^2)\ \partial_r(h^2\ r\ u_m^2) = (\gamma/r^2)[u_m^2\ h^2 + r\ \partial_r(u_m^2\ h^2)] \qquad (3.121)$$

Substituting equations (3.120) and (3.121) into equation (3.119), the later after slight transformation, will give the form:

$$\partial_s u_m = -(\gamma/\beta)(1/r)\ \partial_r(h\ u_m) + 0.5\ S_s\ [\ g/(\beta\ u_m) - u_m/h\ ] - 0.5\ [\ u_m/(\beta\ h)\ ]\ [\ (1/C'^2) + \gamma\ (h/r)^2\ ] \qquad (3.122)$$

Equation (3.122) is an explicit version of equation (3.119) for the variation of the depth–averaged velocity u_m along the bend course. In order to express this model equation in a finite difference form, the bend cross section has to be divided into a concentric mesh. At each grid point [i,j] the depth–averaged velocity $u_m[i,j]$ can be computed. In Appendix (D), the finite difference scheme for all grid points in the channel bend is given (see Fig.(D.2)). The numerical computation starts at the inner bank and proceeds in radius increments Δr acoss the channel to the outer bank. Then, the computation proceeds longitudinally in steps of the bend angle $\Theta_b[j]$. It was found after many preliminary test runs that 11 sections across the channel width and 1.25° angle increments along the tested 60° bend were sufficient to obtain satisfactory results i.e., in the concentric mesh, the limits for the grid points were:

" $1 \leq i \leq N$ and $1 \leq j \leq M$ "

where $N = 11$ and $M = 49$ for the tested 60° channel bend.

So, using the finite difference grid described above, equation (3.122) can be written in the form:

$$u_m[i,j+1] = u_m[i,j] - \Delta s \{ (\gamma/\beta) \Delta(h\ u_m)/\Delta r \} + 0.5\ \Delta s\ S_s[i,j] \{(g/\beta)\ (1/u_m[i,j]) - u_m[i,j]/h[i,j]\} - 0.5\ \{1/(\beta\ C'^2)\}\ \Delta s\ (u_m[i,j]/h[i,j]) - 0.5\ (\gamma/\beta)\ \Delta s\ u_m[i,j]\ h[i,j]/r^2[i] \quad (3.123)$$

where

$$\Delta s = r[i]\ \Delta\Theta_b \quad (3.124)$$

$$\Delta\Theta_b = \Theta_b[j+1] - \Theta_b[j] \quad (3.125)$$

$$\Delta r = r[i+1] - r[i] \quad (3.126)$$

$$\Delta h = h[i,j+1] - h[i,j] \quad (3.127)$$

$$\Delta(h\ u_m) = (h\ u_m)[i+1,j] - (h\ u_m)[i,j] \quad (3.128)$$

$$S_s[i,j] = \Delta h\ /\ \Delta s \quad (3.129)$$

The initial value of $S_s[i,j]$ was obtained from the continuity equation i.e.

$$S_s[i,j] = (1/C'^2)\ (u_m[i,j]\ /\ h[i,j])^2 \quad (3.130)$$

While the value of $h[i,j+1]$ was calculated, at the different grid points, as:

$$h[i,j+1] = h[i,j] - \Delta s\ \ S_s[i,j] \quad (3.131)$$

By the use of the distribution of the depth–averaged velocity u_{mb} and the flow depth h at the bend entrance (which can be obtained previously from the

model described in section (3.6)), equation (3.123) can be used to compute the horizontal variations of u_m and h in the channel bend.

A flow chart " **HORDIS** " showing the steps of the numerical solution is given in Appendix (D).

(3.7.1) Comparisons With Existing Experimental Data

Fig.(3.13) gives comparisons between results obtained using equation (3.123) and the experimental data given by Yen et al (1971) for the transverse profile of the water surface at $\theta_b = 22°$ and $45°$. In each case, the theoretical predictions agree very well with the experimental data.

Figures (3.14) and (3.15) give further comparisons with the experimental results obtained by Tamai et al (1983a) and (1983b) for the water depth h and the depth–averaged velocity u_m , at different θ_b values, for two different test runs. The predictions of h and u_m at the bend entrance, i.e. at $\theta_b = 0°$, were obtained from the numerical solution of the previous sub–model (equation (3.97), section (3.6)). In both test runs, the theoretical predictions of h and u_m are, in general, in a satisfactory agreement with the observations.

(3.8) Width–Averaged Model: Redistribution of the Vertical Profile of the Longitudinal Velocity Component Along the Bend

The redistribution of the vertical profile of the longitudinal velocity component u_s of the flow, due to the effect of the secondary circulation, will be obtained in this model. The effect of the currents in the plane of the cross section of a channel bend is to increase the vertical exchange of momentum between the horizontal layers of the flow. As a consequence, the maximum velocity no longer occurs at the water surface (as suggested by the logarithmic profile), but at a certain depth below the surface. The depth below the surface depends on the the water depth, the aspect ratio and mainly on the order of magnitude of the secondary currents (i.e. u_r and u_z) with respect to that of the longitudinal component u_s . The process, that is to be described in this model, is only valid for a gentle wide channel bend, i.e. where the aspect ratio B/h and the bend tightness r_m/B are high. Since the exact solution of this vertical momentum exchange phenomenon is extremely difficult, the model equation will be derived analytically from the momentum equation in s–direction (as expressed in equation (3.18.2), section (3.4)), while its solution will be carried out numerically.

It will be assumed that in the central region of a wide channel bend, the frictional force due to shear stress between the horizontal layers of the flow, is in balance with the pressure gradient force as expressed is terms of longitudinal water surface gradient. In the case of a uniform flow in a straight channel, this longitudinal surface gradient models the gravity force applied to the flow. This assumption allows the application of the **"Chezy formula"** for the depth–averaged velocity u_m , where the gravity force is in balance with the tractive force (i.e. force due to shear stress). This assumption, however, has been successfully used by Rozovskii (1961), Nouh et al (1979) and Hussein et al (1986).

Using the above assumption, equation (3.18.2) becomes:

$$u_s \, \partial_s u_s = - [u_r \, \partial_r u_s + (u_r u_s / r + u_z \, \partial_z u_s] = 0 \qquad (3.132)$$

Which is a non– linear equation made up of inertia terms and the $u_r u_s / r$ which results from the use of the cylindrical polar coordinate system.

But, since:

$$u_s \, \partial_s u_s = \partial_s u_s^2 \, / \, 2 \qquad (3.133)$$

and

$$u_r \, \partial_r u_s + (u_r u_s / r) = u_r \, [\partial_r (r \, u_s)] \, / \, r \qquad (3.134)$$

Then, by substituting the variables expressed in equations (3.133) and (3.134) into equation (3.132), it becomes:

$$\partial_s u_s^2 = -2 \, [\, (u_r / r) \, \partial_r (r \, u_s) + u_z \, \partial_z u_s \,] \qquad (3.135)$$

Equation (3.135) represents the general model equation for the redistribution of the vertical profile of u_s around the channel bend. It is a first order , non– linear partial differential equation for u_s^2 . A solution of this equation may be obtained if the values of u_r and u_z are known. The value of u_r may be obtained from equation (3.72), section (3.5.2), while u_z may be obtained from the continuity equation as:

$$u_z = - \int_0^z [\, u_r / r + \partial_r u_r + \partial_s u_s \,] \, dz \qquad \text{for} \quad 0 \leq z \leq h \qquad (3.136)$$

where u_z can be obtained at any vertical coordinate z. The term $\partial_s u_s$ can be determined by matching the longitudinal gradient of the depth–averaged velocity i.e. $\partial_s u_m$ through the differentiation of equation (3.40), section (3.5), with respect to s, i.e.

$$\partial_s u_s = \partial_s u_m [1 + \zeta (1 + \ln \lambda)] \qquad (3.137)$$

where the gradient $\partial_s u_m$ can be obtained from the numerical solution of the depth–averaged model described in section (3.7).

In order to obtain the numerical solution of equation (3.135), the flow depth h will be divided into " k " sections of a total " L " where:

" L k = h = flow depth "

where L = 21 i.e. the flow depth will be divided into 20 sections

Then the model equation may be given in finite difference form as:

$$u_s{}^2[i,j,k+1] = u_s{}^2[i,j,k] - 2\,\Delta s\,\{(u_r[i,j,k]/r[i])\,\Delta(r\,u_s)/\Delta r\} - 2\,\Delta s\,u_z[i,j,k](\Delta u_s / \Delta z) \qquad (3.138)$$

where

$$\Delta z = z[k+1] - z[k] \qquad (3.139)$$

$$\Delta(r\,u_s) = \{r[i+1]\,u_s[i+1,j,k]\} - \{r[i]\,u_s[i,j,k]\} \qquad (3.140)$$

and

$$\Delta(u_s) = u_s[i,j,k+1] - u_s[i,j,k] \qquad (3.141)$$

The value of $u_z[i,j,k]$, which is expressed in equation (3.136), may also be written, with the use of equation (3.137), in finite difference form as:

$$u_z[i,j,k+1] = u_z[i,j,k] - \Delta z \{ (u_r[i,j,k]/r[i]) + (\Delta u_r/\Delta r) \} - \Delta z (\Delta u_m/\Delta s) \{1 + \zeta (1 + \ln z[k]/h)\} \qquad (3.142)$$

where

$$\Delta u_r = u_r[i+1,j,k] - u_r[i,j,k] \qquad (3.143)$$

$$\Delta u_m = u_m[i,j+1,k] - u_m[i,j,k] \qquad (3.144)$$

The model equations expressed in finite difference form (i.e. equations (3.138) to (3.144)) allow the prediction of the vertical variation of $u_s[i,j,k]$ at any grid point $[i,j]$ in the interior region of the channel bend. However, by applying the limits of the grid points, which are: "$1 \leq i \leq 11$, $1 \leq j \leq 49$, $1 \leq k \leq 21$", the three–dimensional pattern of u_s can be obtained.

Appendix (D) gives the numerical procedure described in this model through a flow chart called " **VERDIS** " .

The calibration and verification of this model will be discussed in Chapter VI along with the writer's experimental results.

(3.9) Width– Averaged Model: Growth and Decay of Radial Velocities Along and Beyond the Bend

The problem of the growth and decay of the radial velocity component u_r along the curved path of a wide bend will be discussed in this model. The model will be divided into two parts. In the first part the problem of the decay of u_r beyond the bend will be formulated analytically, while the final model equation will be solved numerically. In the second part, the development of u_r along the channel bend will be assumed to behave similarly to its decaying process. The dynamic model equation will be derived from the momentum equation in the radial direction.

It should be mentioned that the formulation of this model will follow the assumptions that have been successfully employed by previous investigators e.g. Rozovskii (1961), Nouh et al (1979), Spyratos (1981), Hussein (1984), Chang (1983), (1985) and others.

(3.9.1) Decay of Radial Velocities Beyond the Bend

In a straight reach beyond the bend there will be a gradual decay of u_r and consequently, a tendency to a rectilinear (parallelism) condition of the streamlines of the flow. This is caused by the disappearence of the centrifugal force and the associated radial pressure gradient force. This condition forms the basis of the mathematical formulation of the decaying phenomenon of u_r . The basic equation for this model is the momentum equation in r– direction, i.e. equation (3.18.1), section (3.4), which reads:

$$u_r\ \partial_r u_r + u_s\ \partial_s u_r + u_z\ \partial_z u_r - (u_s{}^2/r) = - g\ S_r + \partial_z(\nu\ \partial_z u_r) \qquad (3.18.1)$$

If the driving centrifugal force and the corresponding radial water surface slope) terms in equation (3.18.1) can be ignored, being of a secondary importance in the straight reach beyond the bend. Then the flow motion will be controlled by the balance between the inertia forces and the force due to the radial component of the shear stress as:

$$[u_r\ \partial_r u_r + u_z\ \partial_z u_r] + u_s\ \partial_s u_r = \partial_z(\nu\ \partial_z u_r) \qquad (3.145)$$

Furthermore, the first two terms on the left hand side of equation (3.145) can be ignored being of small order of magnitude relative to the shear stress term. The order of magnitude of the error involved in this process is " h^2/r^2 " (see also section (3.5)). Hence, equation (3.145) may become:

$$u_s\ \partial_s u_r = \partial_z(\nu\ \partial_z u_r) \qquad (3.146)$$

Which represents the general model equation for the decay of u_r beyond the bend. Due to the ignoring of the non-linear inertia terms, the following analysis will be only valid in a gentle wide channel bend.

If the decay starts at the bend exit i.e. at $x = 0$, equation (3.146) becomes:

$$u_x\ \partial_x u_r = \partial_\lambda(\nu\ \partial_\lambda u_r)\ /\ h^2 \qquad (3.147)$$

where $\lambda = z/h$, is the non-dimensional depth variable, u_x represents the longitudinal velocity component of the flow in the straight reach beyond the bend,

and ∂_x is the differential distance beyond the exit which is equivalent to the gradient operator ∂_s in the bend. Substituting the value of u_x and ν (from equations (3.40) and (3.44) respectively, section (3.5)) into equation (3.147), gives:

$$\partial_x u_r = (K^2 \zeta/h)\, \partial_\lambda[\lambda\,(\lambda-1)\,\partial_\lambda u_r] \,/\, [1 + \zeta\,(\ln\lambda + 1)] \qquad (3.148)$$

where $\zeta = 1/(K\,C')$, C' is the non-dimensional Chezy coefficient and K is the Von-Karman constant. Equation (3.148) is the final model equation for the decaying of the residual radial component of the secondary circulation u_r. It simply states that, in a width-averaged model, the horizontal gradient of u_r can be obtained in terms of its vertical gradient and the channel boundary roughness. This equation is a non-linear, second order, partial differential equation. Integration of which gives two integration constants and hence, two boundary conditions if it is to be solved. One of these can be found from the vertical profile of u_r , which is described in equation (3.72), section (3.5.2). While the other boundary condition can be obtained from the assumption that the net radial discharge Q_r along a vertical column of the flow is zero (see boundary condition (B.2), equation (3.49), section (3.5.1)).

Using the same procedure as described for the previous sub-models, the model equation, equation (3.148), can be expressed in the finite difference form as:

$$u_r[i,j,k+1] = u_r[i,j,k] - \Delta x\,(k^2 \zeta/h[i,j])\,\{1 + \zeta\,(1 + \ln\lambda[i,j,k])\}^{-1}$$

$$\{(1 - 2\,\lambda[i,j,k](\Delta u_r/\Delta z) + z[k]\,(1 - \lambda[i,j,k])(\Delta^2 u_r/\Delta z^2)\} \qquad (3.149)$$

where

$$\Delta x = x[j+1] - x[j] \qquad (3.150)$$

$$\Delta z = z[k+1] - z[k] \qquad (3.151)$$

$$\Delta u_r = u_r[i,j,k+1] - u_r[i,j,k] \qquad (3.152)$$

$$\lambda[i,j,k] = z[k] \; / \; h[i,j] \qquad (3.153)$$

and

$$\Delta^2 u_r/\Delta z^2 = \{u_r[i,j,k+1] - 2u_r[i,j,k] + u_r[i,j,k-1]\} \; / \; \{ z[k+1] - z[k] \}^2 \qquad (3.154)$$

Equations (3.149) to (3.154) give the solution for the decaying of $u_r[i,j,k]$ at an interior grid point [i,j]. Knowing the radial variations of the vertical profile of u_r , a three-dimensional solution may be obtained.

In Appendix (D), the numerical approach used for the prediction of the decaying of the radial velocity of the flow, in a gentle wide channel bend, will be given through a flow chart called " GRODEC " .

(3.9.1.1) Comparisons With Existing Analytical Models and Experimental Data

In the analysis described above, it has been assumed that the decaying process of u_r will start at the bend exit. If it is assumed that the length of the straight channel beyond the bend, over which the decaying process takes place, is equivalent to the length over which the residual radial velocity component u_r reduces to 10% of its initial value. Then, according to Rozovskii (1961):

$$(u_{rd} \; / \; u_r) = \exp \; (-x_d \; \zeta \; K/h) \qquad (3.155)$$

where u_{rd} is the residual radial velocity component at a distance x_d downstream of the bend exit. For a 10% residual of u_r, Rozovskii (1961) estimated the length downstream of the bend would be:

$$x_{dt} = 2.3\ C'\ h \qquad (3.156)$$

where x_{dt} is the length downstream of the bend at which the residual radial velocity u_r reduces to 10% of its initial value.

Nouh et al (1979) suggested the following formula for u_{rd} based upon the same criterion:

$$(u_{rd} / u_r) = \exp(-1.3\ x_d\ \zeta\ K/h) \qquad (3.157)$$

In this case, for a 10% residual circulation:

$$x_{dt} = 1.77\ C'\ h \qquad (3.158)$$

Recently, Spyratos (1981) suggested that:

$$(u_{rd} / u_r) = \exp(-1.53\ x_d\ \zeta\ K/h) \qquad (3.159)$$

with

$$x_{dt} = 1.5\ C'h \quad \text{(for 10\% residual circulation)} \qquad (3.160)$$

In this study, the numerical solution of equation (3.149) suggests that:

$$(u_{rd} / u_r) = \exp(-1.22\ x_d\ \zeta\ K/h) \qquad (3.161)$$

Which gives, for a 10% residual radial velocity component, a distance x_{dt} from the bend exit of:

$$x_{dt} = 1.88\ C'\ h \qquad (3.162)$$

Accordingly, it can be concluded that, in a gentle wide channel bend followed by a straight reach, the total length affected by the secondary circulation can be predicted as:

$$X_t = \underbrace{(\pi\ r_m\ \theta_b\ /\ 180)}_{\text{along bend}} + \underbrace{N_t\ C'\ h}_{\text{beyond bend}} \qquad (3.163)$$

where

X_t is the total distance measured from the bend entrance.

r_m is the mid radius of bend curvature

θ_b is the central angle of the bend (in degrees)

N_t is a coeffecient which can vary as

$$" \ 1.50 \leq N_t \leq 2.3 \ "$$

Fig.(3.16) gives comparisons of the numerical model expressed in equation (3.149) with the previous analytical models described above. It can be seen that the predicted profile follows very closely that given by the solution of Nouh et al (1979).

Fig. (3.17) gives a comparison with the experimental data taken from Rozovskii (1961) for the decay of the surface and the bottom radial velocities. The agreement is very satisfactory.

(3.9.2) Growth of Radial Velocities Along the Bend

To solve the problem of the development of u_r within the bend, an approach similar to that used to determine the decay of u_r may be used. When the flow enters the bend, the centrifugal force acts upon it producing the radial water surface slope. It may be assumed that the rate of development of the centrifugal force is the same as that of the radial gradient of the pressure force (which is modelled by the surface slope). Considering that these two forces are in balance and that terms of the small order of magnitude (i.e. the inertia terms) may be omitted. Then the momentum equation in r− direction, equation (3.18.1), section (3.4), may be developed as in section (3.9.1), equation (3.146), to give:

$$u_s \, \partial_s(u_{ro} - u_r) = \partial_z[\nu \, \partial_z(u_{ro} - u_r)] \qquad (3.164)$$

in which u_{ro} is the radial velocity component at the location where the maximum development takes place. Rozovskii (1961) defined this location as Θ_{lim} , which is defined as the bend angle (i.e. Θ_b) value at which the growth of the secondary circulation is effectively completed. The reason for replacing u_r by " $u_{ro} - u_r$ " is that, when the flow enters the channel bend, a gradual increase in the radial velocity component occurs on approaching the location Θ_{lim}. In doing so, the expression " $u_{ro} - u_r$ " decreases till it becomes zero (i.e. $u_r = u_{ro}$) at the same location according to the same procedure used for the problem of the decaying of the radial velocity u_r beyond the bend.

Introducing the values of u_s and ν to equation (3.164), in the same manner as in section (3.9.1), it will read:

$$\partial_s(u_{ro} - u_r) = (K^2\ \zeta/h)\ \partial_\lambda[\lambda\ (1 - \lambda)\ \partial_\lambda(u_{ro} - u_r)]$$
$$[\ 1 + \zeta(\ln\ \lambda + 1)] \qquad (3.165)$$

Applying the same boundary conditions as in section (3.9.1), equation (3.165) may be written in the finite difference form as:

$$u_r[i,j,k+1] = u_r[i,j,k] - (K^2\ \zeta/h)\ \Delta s\ \{(1 - 2\lambda[i,j,k])\ \Delta(u_{ro} - u_r)/\Delta z$$
$$+ z[k]\ (1 - \lambda[i,j,k])\ \Delta^2(u_{ro} - u_r)/(\Delta z)^2\}$$
$$/\ \{1 + \zeta(\ln\ \lambda[i,j,k] + 1)\} \qquad (3.166)$$

where

$$\Delta(u_{ro} - u_r) = (u_{ro} - u_r)[i,j,k+1] - (u_{ro} - u_r)[i,j,k] \qquad (3.167)$$

and

$$\Delta^2(u_{ro} - u_r) = (u_{ro} - u_r)[i,j,k+1] - 2(u_{ro} - u_r)[i,j,k]$$
$$+ (u_{ro} - u_r)[i,j,k-1] \qquad (3.168)$$

The position of the maximum development of u_r , i.e. Θ_{lim} , in the channel bend can be predicted in the same manner to that of the distance " x_{dt} " required for the decaying of u_r beyond the bend. The numerical solution suggests a value of Θ_{lim} as:

$$\Theta_{lim} = 1.88\ \ C'\ \ (h/r) \qquad (3.169)$$

However, Rozovskii (1961) suggested:

$$\Theta_{lim} = 2.30\ C'\ \ (h/r) \qquad (3.170)$$

and Nouh et al (1979) predicted:

$$\theta_{lim} = 1.77\ C' \quad (h/r) \qquad (3.171)$$

While Spyratos (1981) suggested:

$$\theta_{lim} = 1.5\ C' \quad (h/r) \qquad (3.172)$$

It seems from these comparisons that value θ_{lim} as predicted herein lies between these given by the other formulae. Similarly to the predicted distance x_{dt} , for the decay of u_r , θ_{lim} can be predicted as:

$$\theta_{lim} = N_t\ C' \ (h/r) \qquad (3.173)$$

with

" $1.5 \leq N_t \leq 2.3$ "

Flow chart " GRODEC " will give also the computational procedure used for the prediction of the growth of the radial component of the cesondary currents, to be shown in Appendix (D).

(3.10) SUMMARY

From the mathematical formulation expressed in this Chapter, the following conclusions can be drawn:

(3.10.1) A mathematical model for the flow in a gentle wide channel bend is suggested. This model is divided into a series of sub– models from which the following may be obtained:

- Vertical distribution of the radial velocity component u_r (through section (3.5)).
- Distribution of the depth–averaged velocity u_{mb} at the bend entrance (through section (3.6)).
- Horizontal variations of the water depth h and the depth–averaged velocity u_m (through section (3.7)).
- Redistribution of the vertical profile of the longitudinal velocity component u_s (through section (3.8)).
- Growth and decay of the radial velocity component u_r along and beyond the channel bend (through secton (3.9)).

(3.10.2) Equation (3.72) allows the vertical profile of the radial velocity component u_r to be calculated. The equation is based on the assumption that the vertical profile of the longitudinal velocity component u_s follows the logarithmic law.

(3.10.3) A general numerical solution is suggested for the radial distribution of the depth–averaged velocity u_{mb} at the entrance of the bend. It has been shown that the prediction of the potential free vortex law of the transverse water surface profile is only applicable in the special case where the depth–averaged velocity in the approach channel is uniform.

(3.10.4) By use of the potential vortex theory for the flow at the bend entrance, a relation between the bend tightness ratio r_m/B and the velocity ratios u_{mi}/u_{mo} & u_{*i}/u_{*o} of the flow (which model the boundary shear stresses at the inner and the outer bend radii) is derived. For a channel bend with a bend tightness ratio $r_m/B \geq 3$, the radial distribution of the boundary shear stress is found to be nearly uniform.

(3.10.5) A general first order, non–linear partial differential equation for the solution of the horizontal problem (i.e. horizontal variations of h and u_m) around a gentle wide channel bend is suggested (equation (3.119)) and solved numerically with the aid of the continuity equation.

(3.10.6) The effect of the secondary currents on the horizontal distribution of the depth–averaged velocity was modelled through the secondary flow convection factor " γ " (expressed in equation (3.118)) in the general model equation of the depth–averaged velocity. The influence of the factor " γ " on the radial gradient of u_m and on the boundary roughness (through the coefficients C' , ζ and ξ) was also given.

(3.10.7) An approximate numerical solution for the redistribution of the vertical profile of the longitudinal velocity component u_s , based upon matching the depth–averaged velocity gradient $\partial_s u_m$ with the point velocity gradient $\partial_s u_s$, is given. This assumption allows the determination of the vertical component of the velocity field u_z as a part of the solution.

(3.10.8) Based upon the numerical solution, a formula is suggested for the decay of the radial velocity component u_r . From this, it was found possible to estimate the total length of the flow affected by the secondary circulation both in and beyond the bend (in equation (3.163)).

(3.10.9) For most of the sub–models, it was found possible to compare the results predicted with these of existing analytical models and with experimental data reported in the literature. In general, the agreement was very satisfactory.

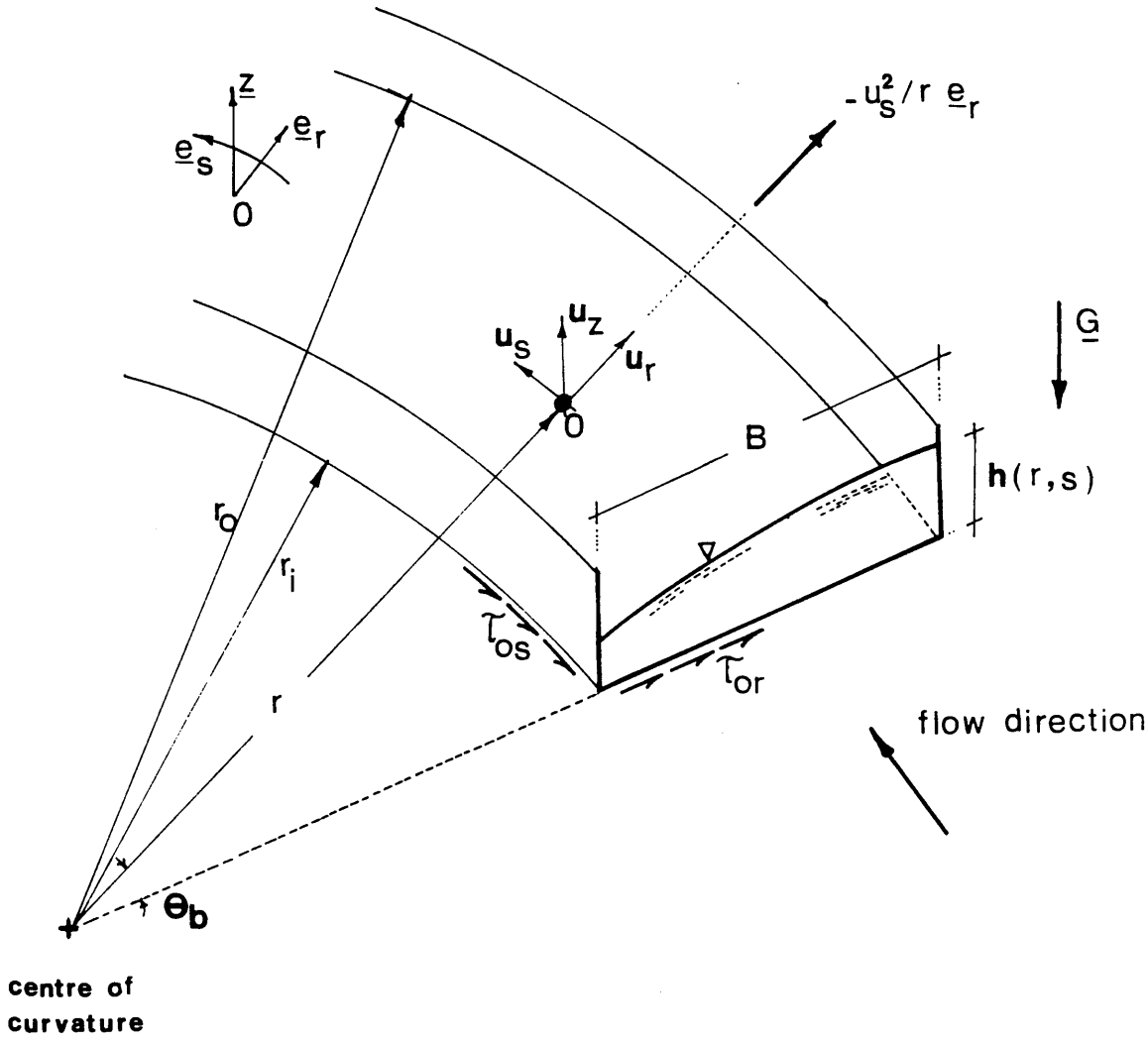

FIG.(3.1) – Coordinate System and Forces

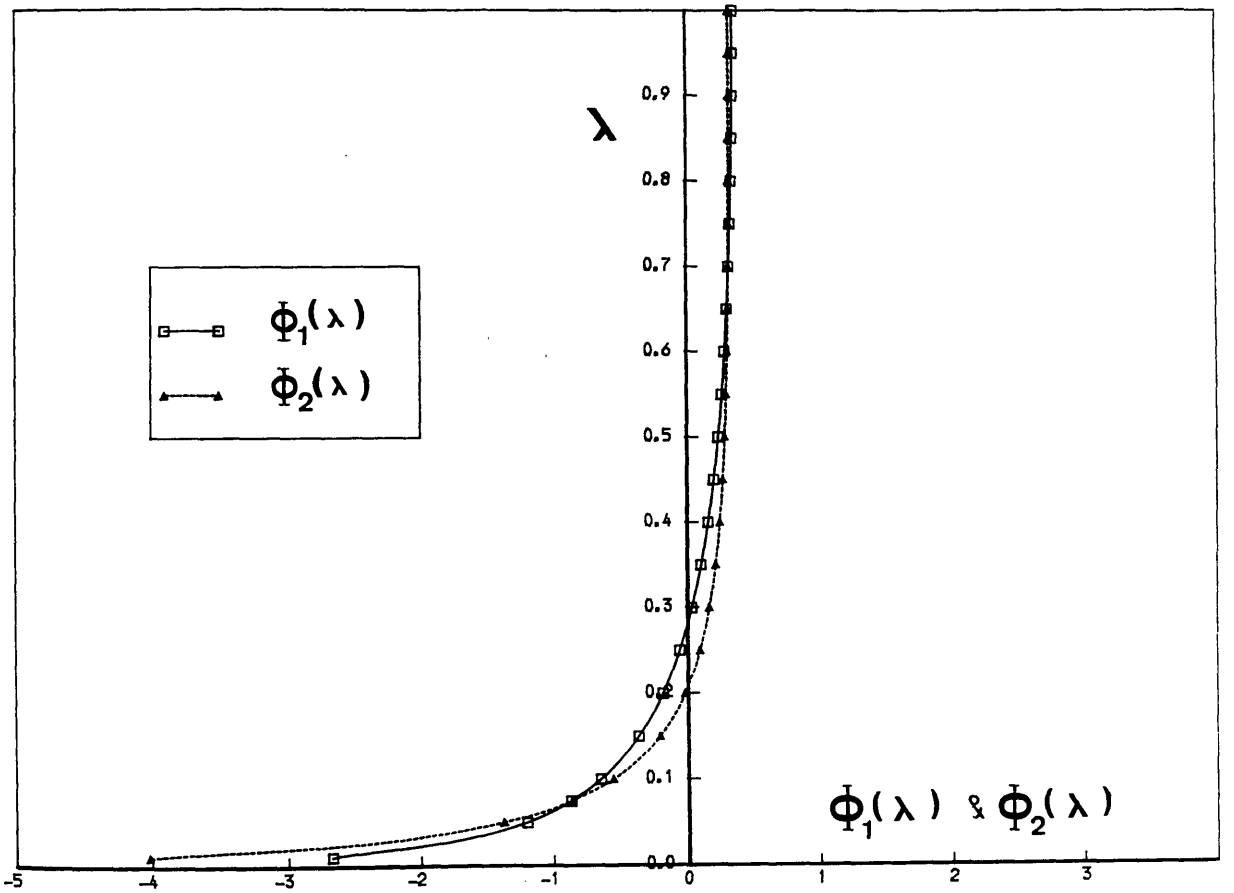

FIG.(3.2) – Vertical Distribution of the Mathematical Integration Functions $\Phi_1(\lambda)$ & $\Phi_2(\lambda)$

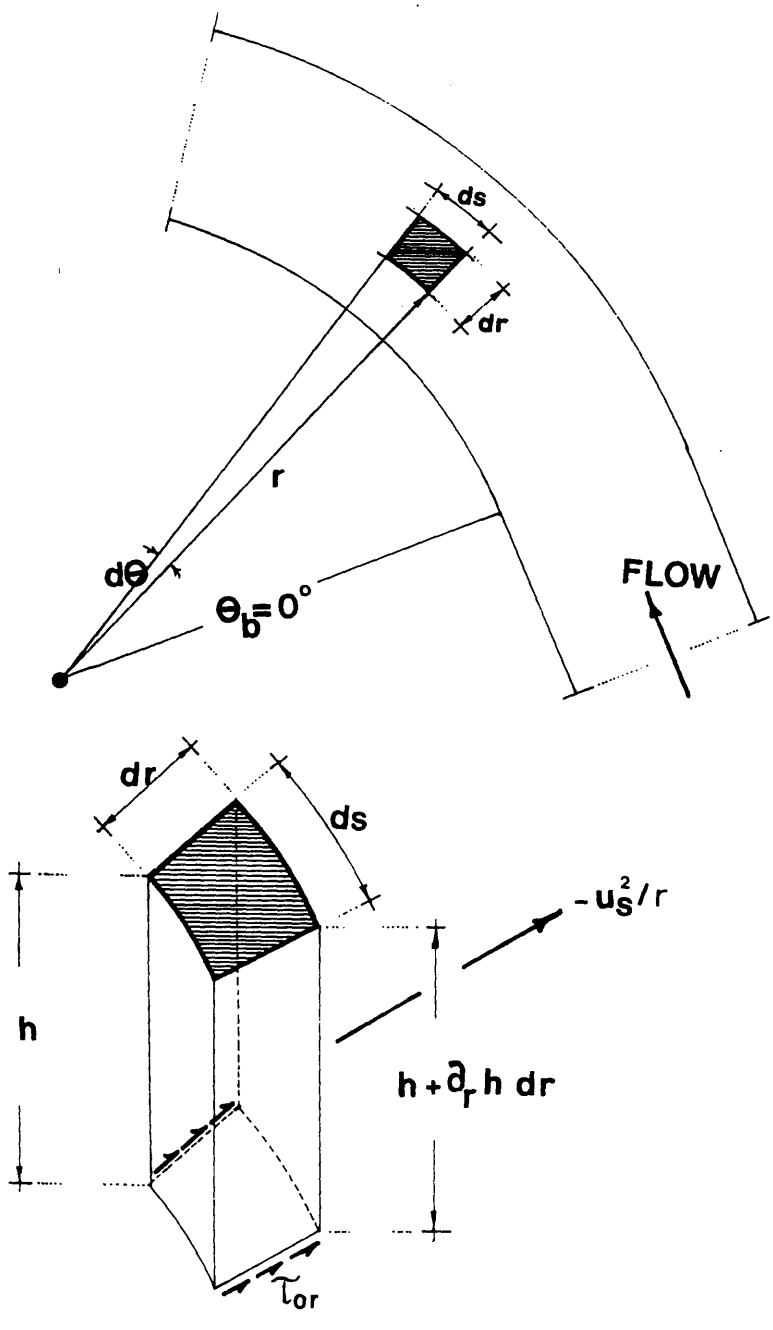

FIG.(3.3) — Main Forces Acting on a Vertical Column (ds . dr . h) of the Flow in the Radial Direction

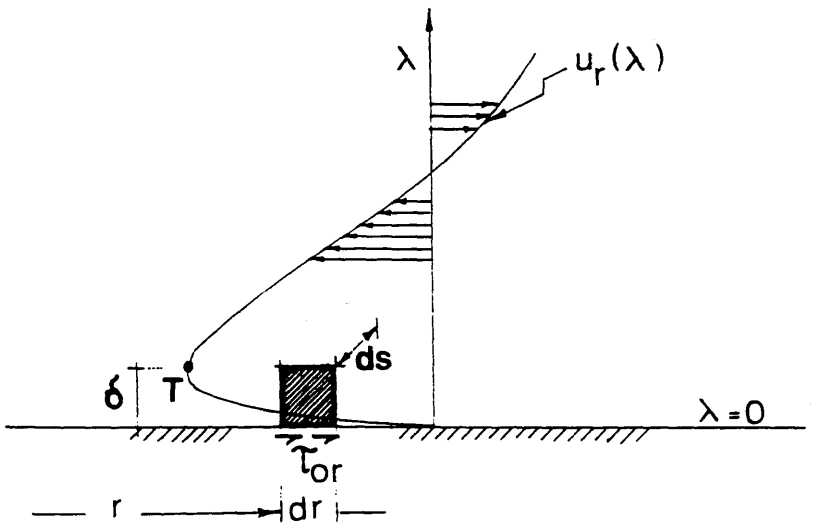

FIG.(3.4) – Distribution of the $u_r(\lambda)$ near the Channel Bed

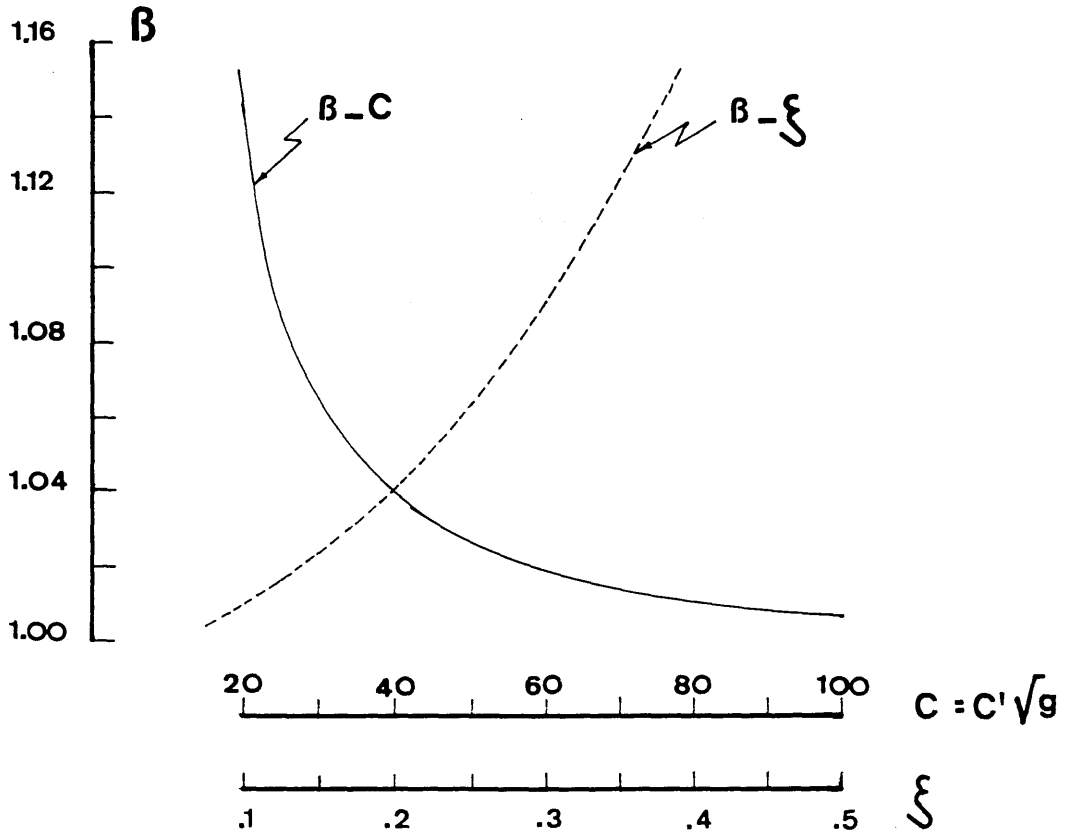

FIG.(3.5) – Relation Between the Momentum Flux Correction Factor ß and the Coefficients C' and ξ of Bed Roughness

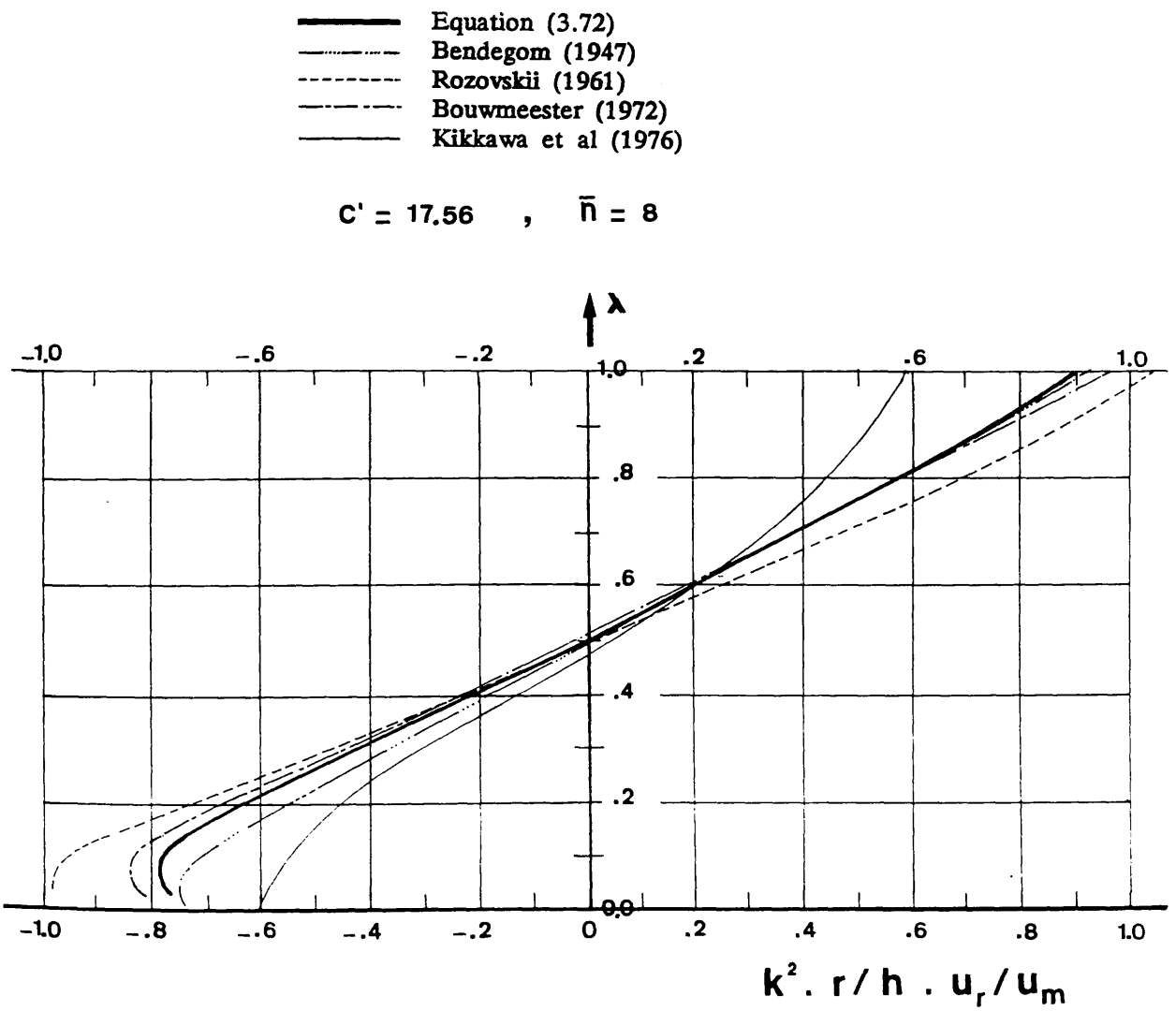

FIG.(3.6) – Comparisons of the Predicted Profile of $u_r(\lambda)$ with Previous Analytical Models

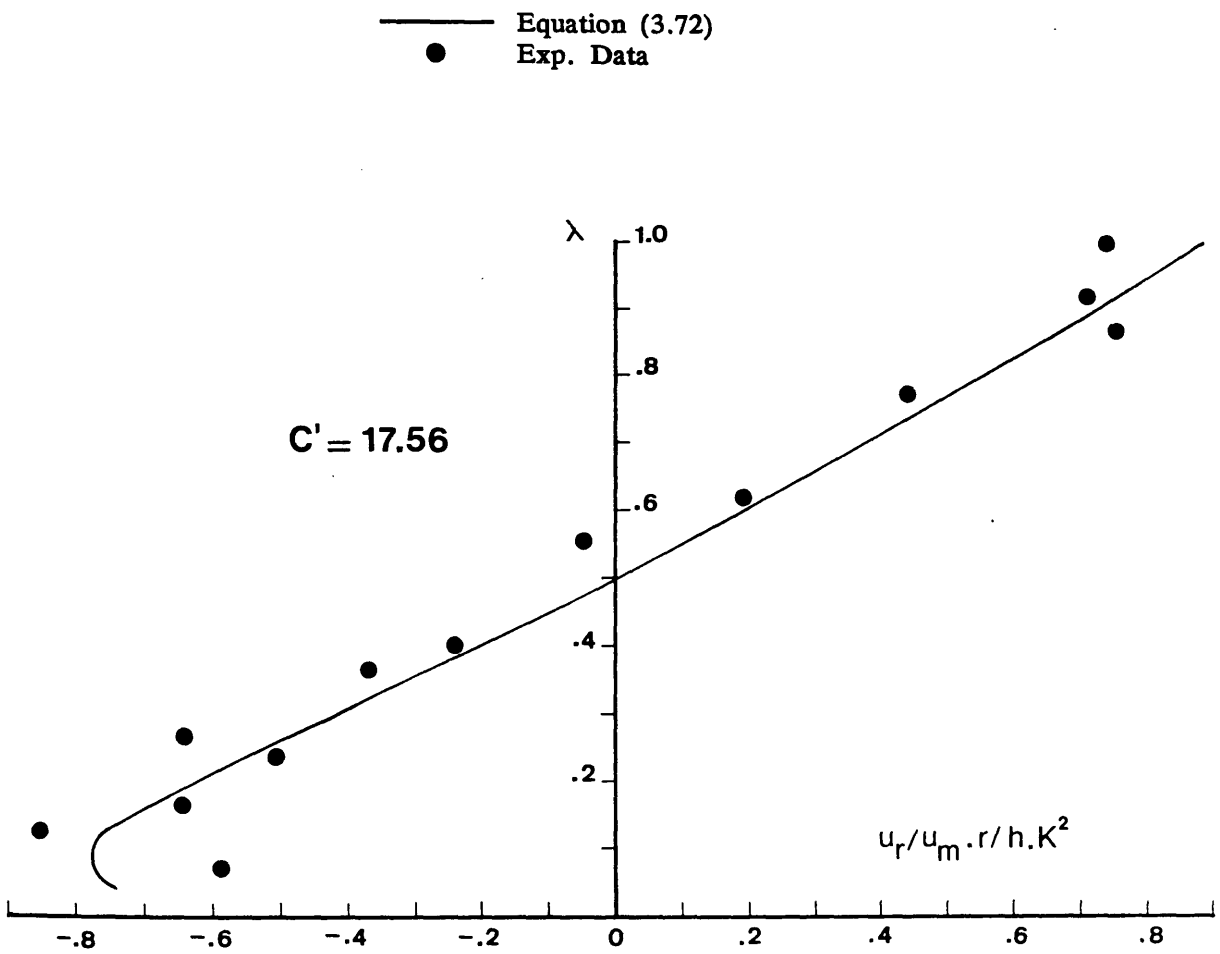

FIG.(3.7) – Comparison of the Predicted Profile of $u_r(\lambda)$ with the Experimental Data obtained from Kondrat'ev et al (1959)

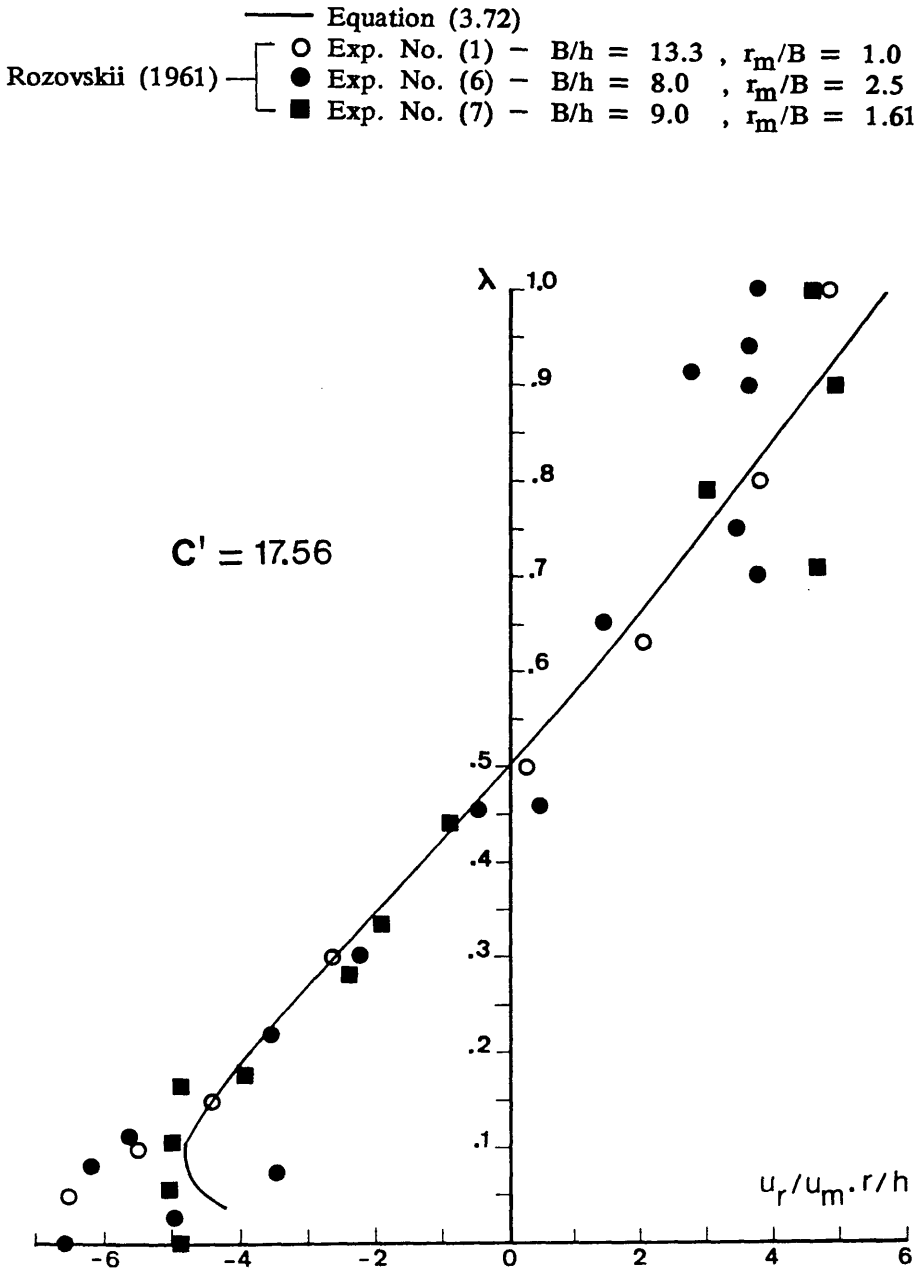

FIG.(3.8) – Comparisons of the Predicted Profile of $u_r(\lambda)$ with the Data given by Rozovskii (1961)

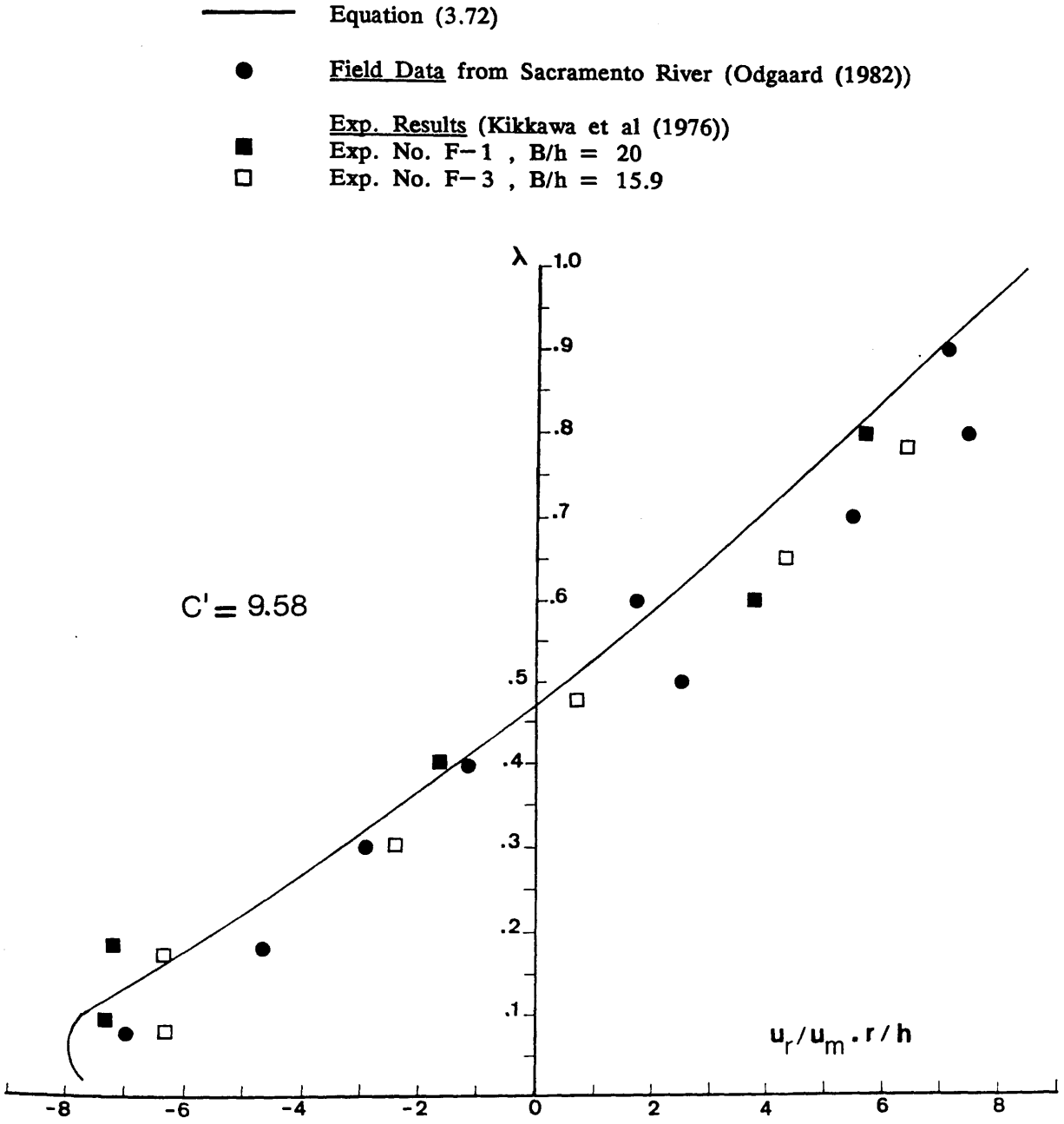

FIG.(3.9) – Comparisons of the Predicted Profile of $u_r(\lambda)$ with:

- Field Data from Sacramento River (Odgaard (1982))
- Experimental Results (Kikkawa et al (1976))

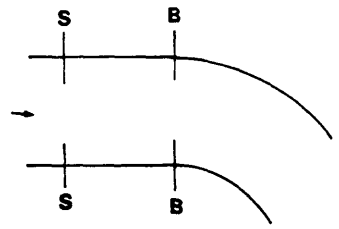

Plan

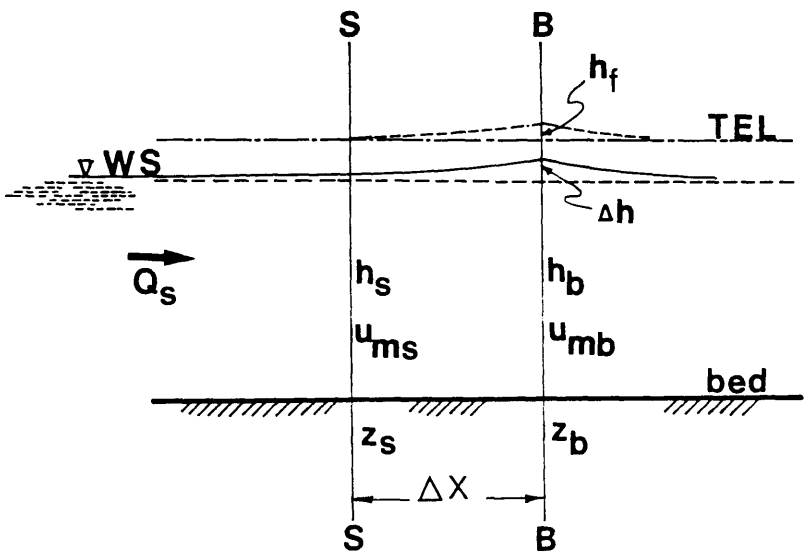

Long. Sec.

FIG.(3.10) – Profiles of Flow Surface and Energy at the Bend Entrance

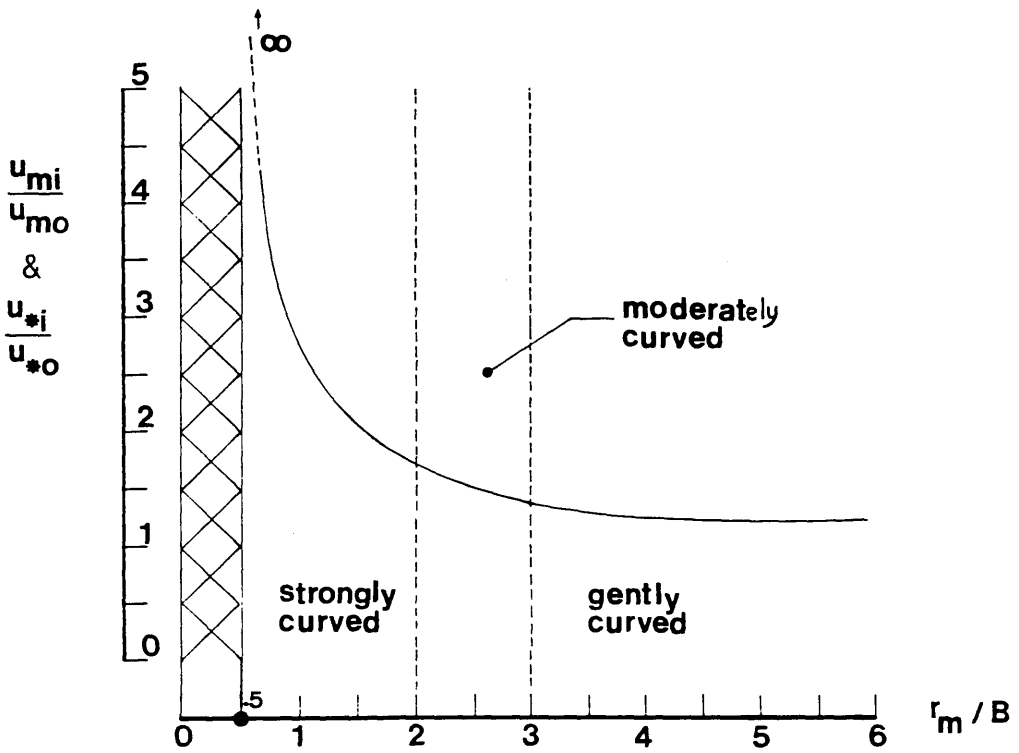

FIG.(3.11) – Relation Between the Velocity Ratios u_{mi}/u_{mo} & u_{*i}/u_{*o} and the Bend Tightness Ratio r_m/B

——— Equation (3.118)

—·—·— Rozovskii (1961) : $\gamma = 0.75\ \zeta\ /\ K$

- - - - - - - Kalkwijk et al (1980) : $\gamma = 5\ \zeta - 15.6\ \zeta^2 + 37.5\ \zeta^3$

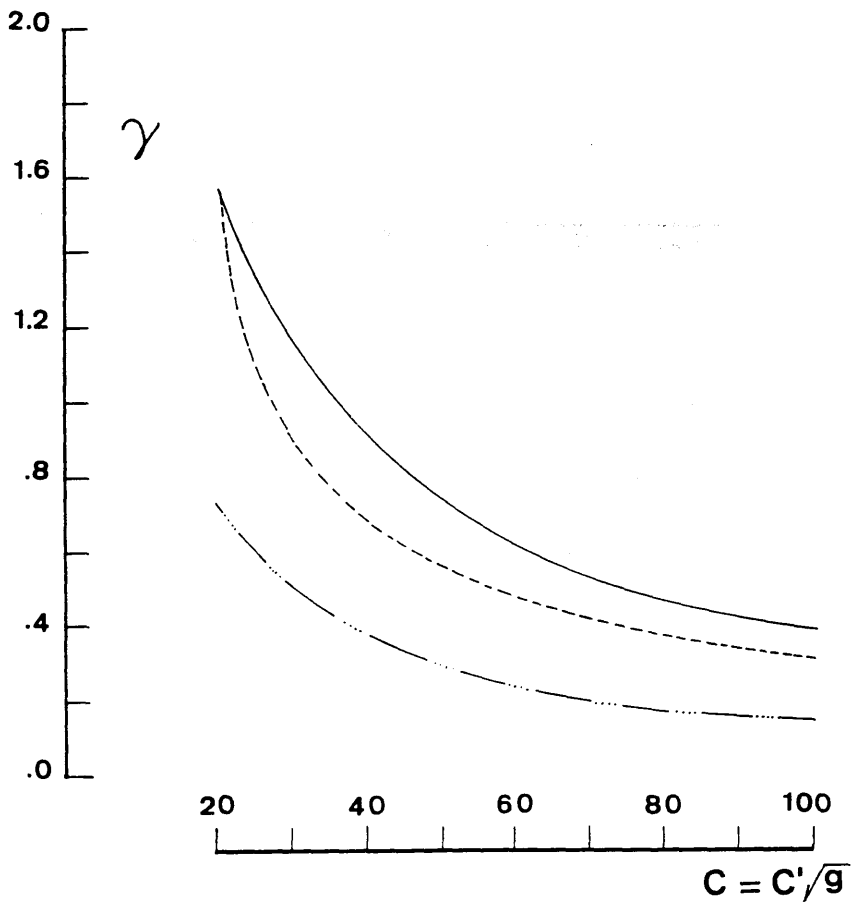

FIG.(3.12) – Graphical Representation of the Secondary Flow Convection Factor " γ " as a Function of C', Comparisons with Previous Analytical Models

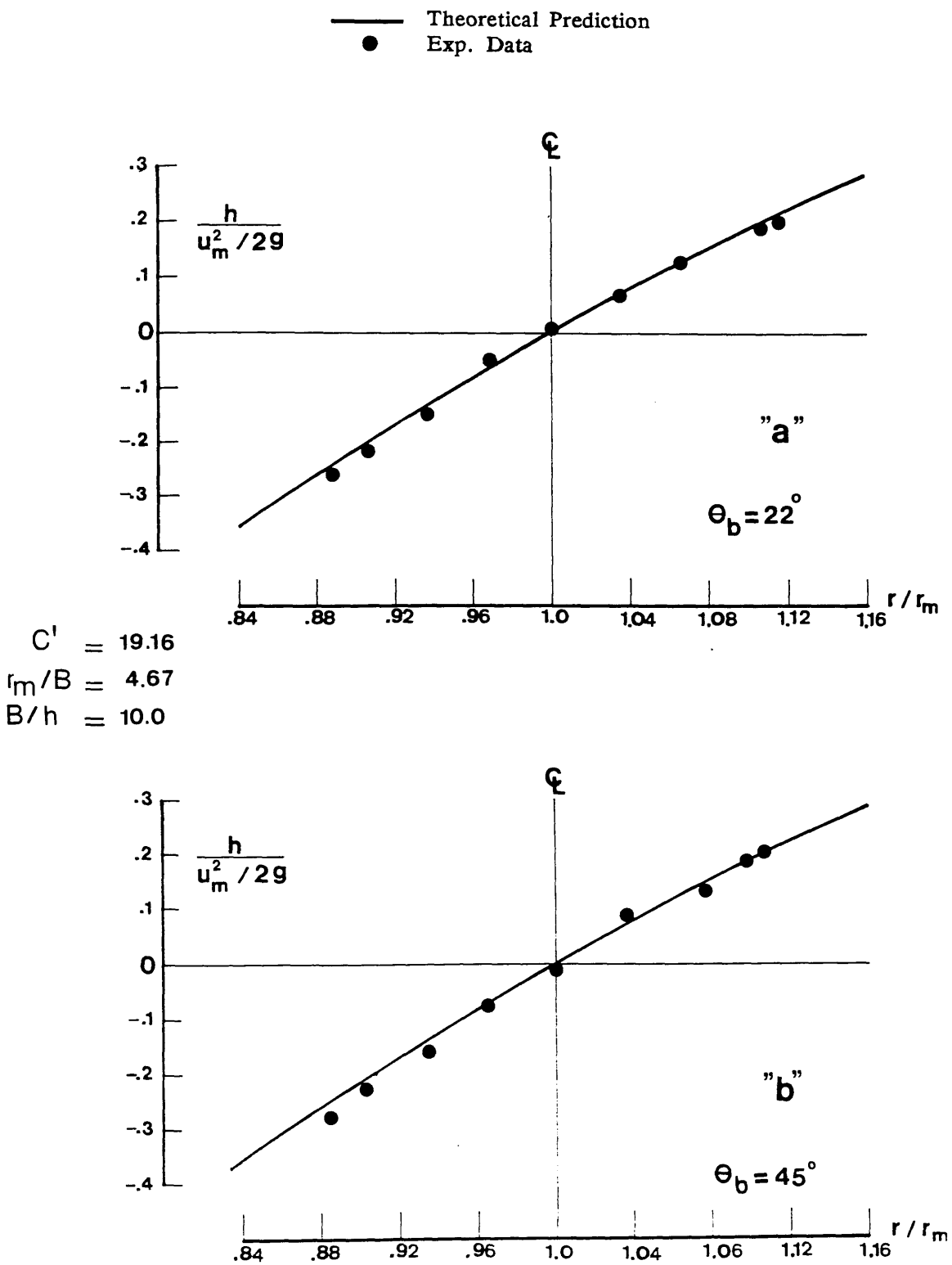

FIG.(3.13) – Comparisons of the Predicted Radial Surface Profiles with the Experimental Data given by Yen et al (1971)
(a) at $\theta_b = 22^\circ$
(b) at $\theta_b = 45^\circ$

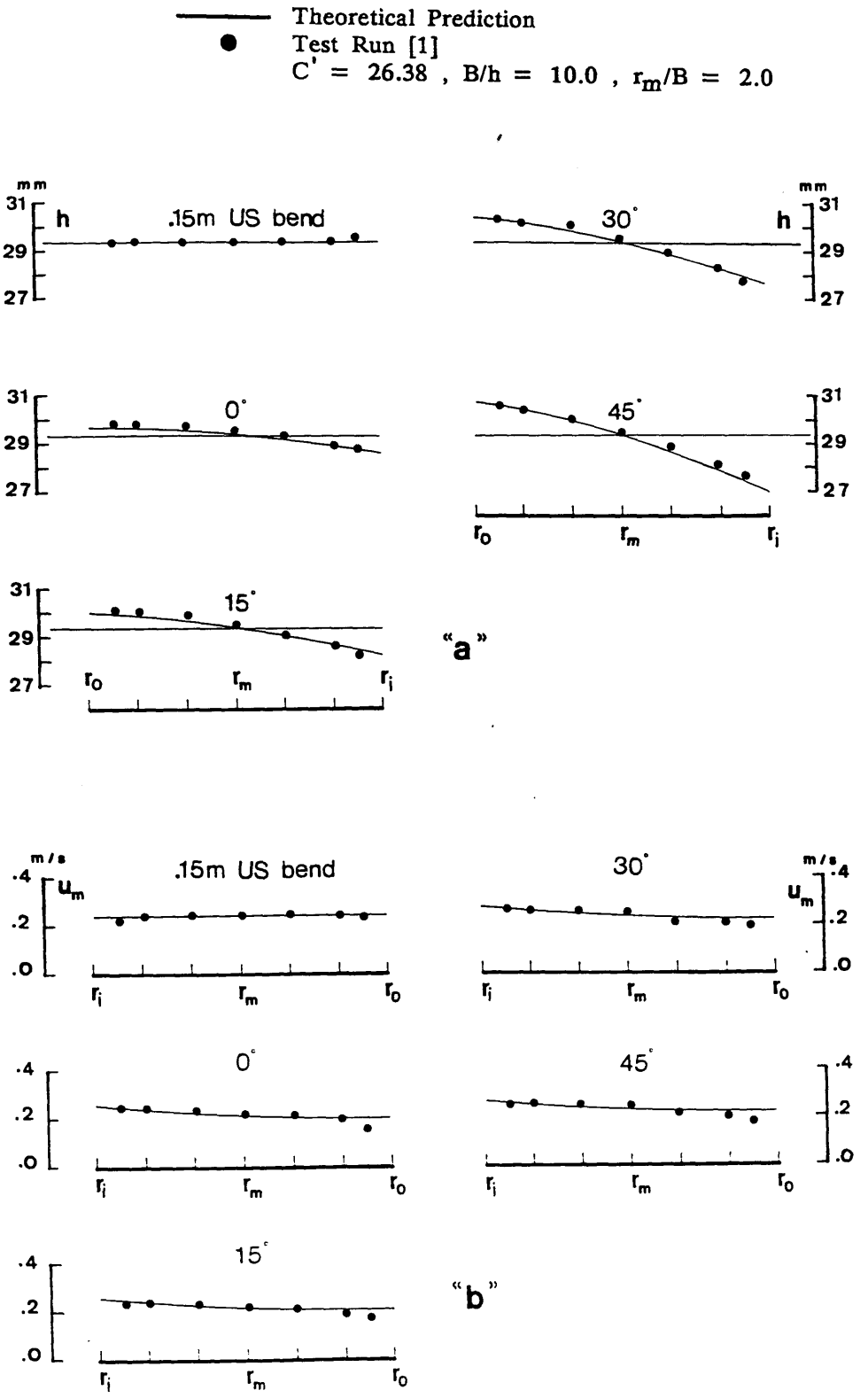

FIG.(3.14) – Comparisons of the Predicted Surface Profiles and Depth–Averaged Velocities with the Experimental Results obtained by Tamai et al (1983a)
(a) Water Surface Profiles
(b) Depth–Averaged Velocities

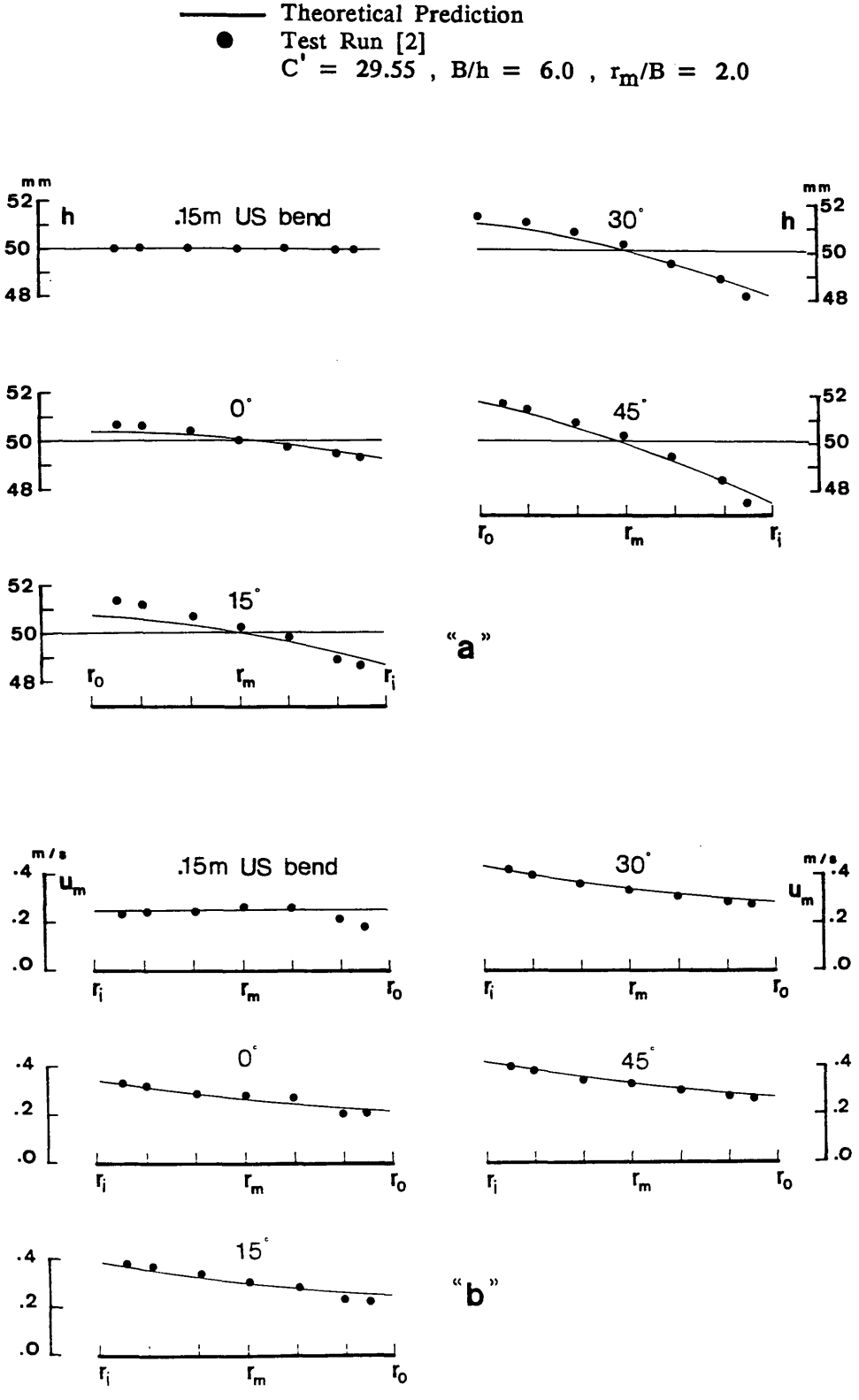

FIG.(3.15) – Comparisons of the Predicted Surface Profiles and Depth–Averaged Velocities with the Experimental Results obtained by Tamai et al (1983b)
(a) Water Surface Profiles
(b) Depth–Averaged Velocities

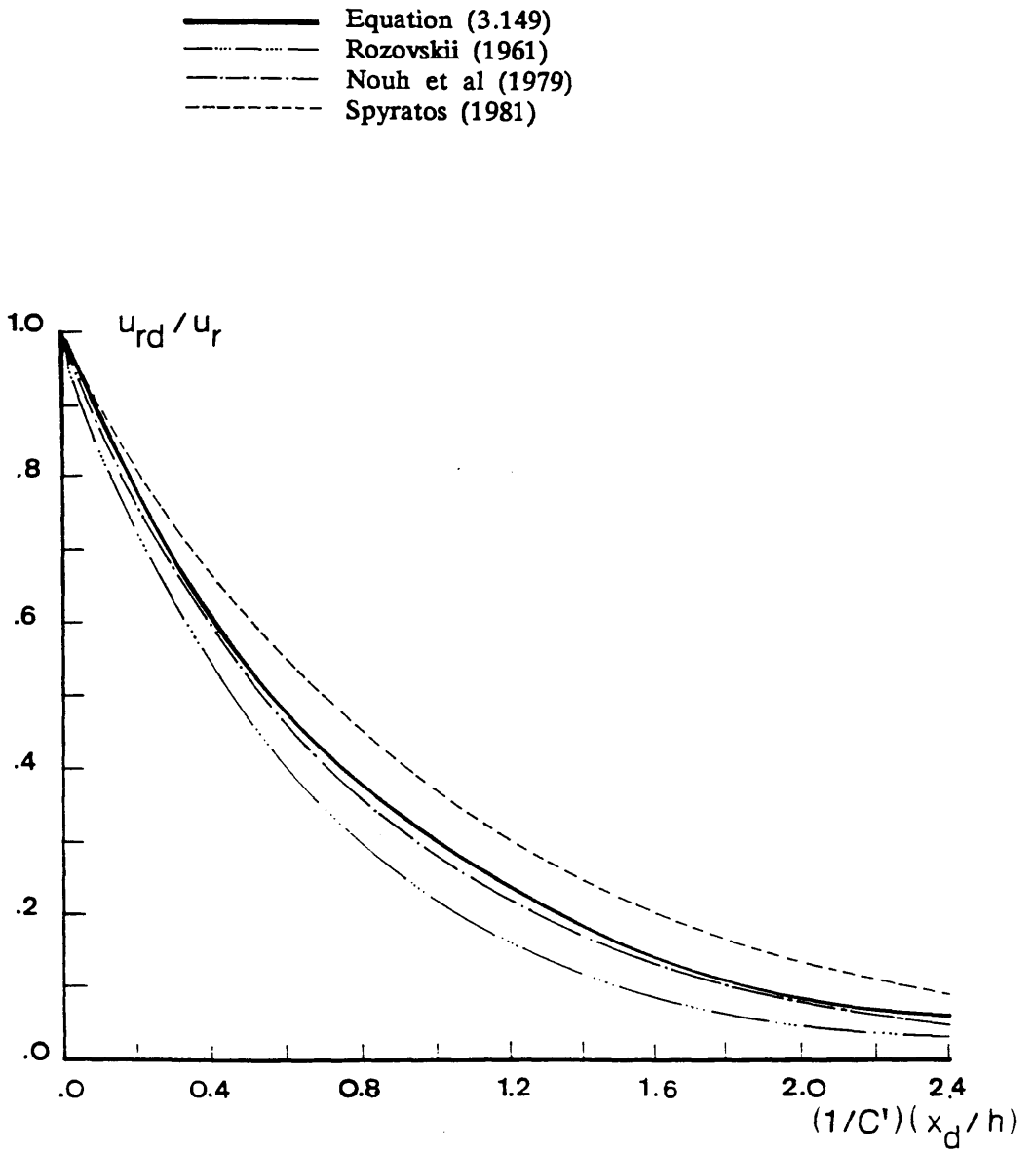

FIG.(3.16) – Decay of the Radial Velocities Beyond the Bend – Comparisons with Previous Analytical Models

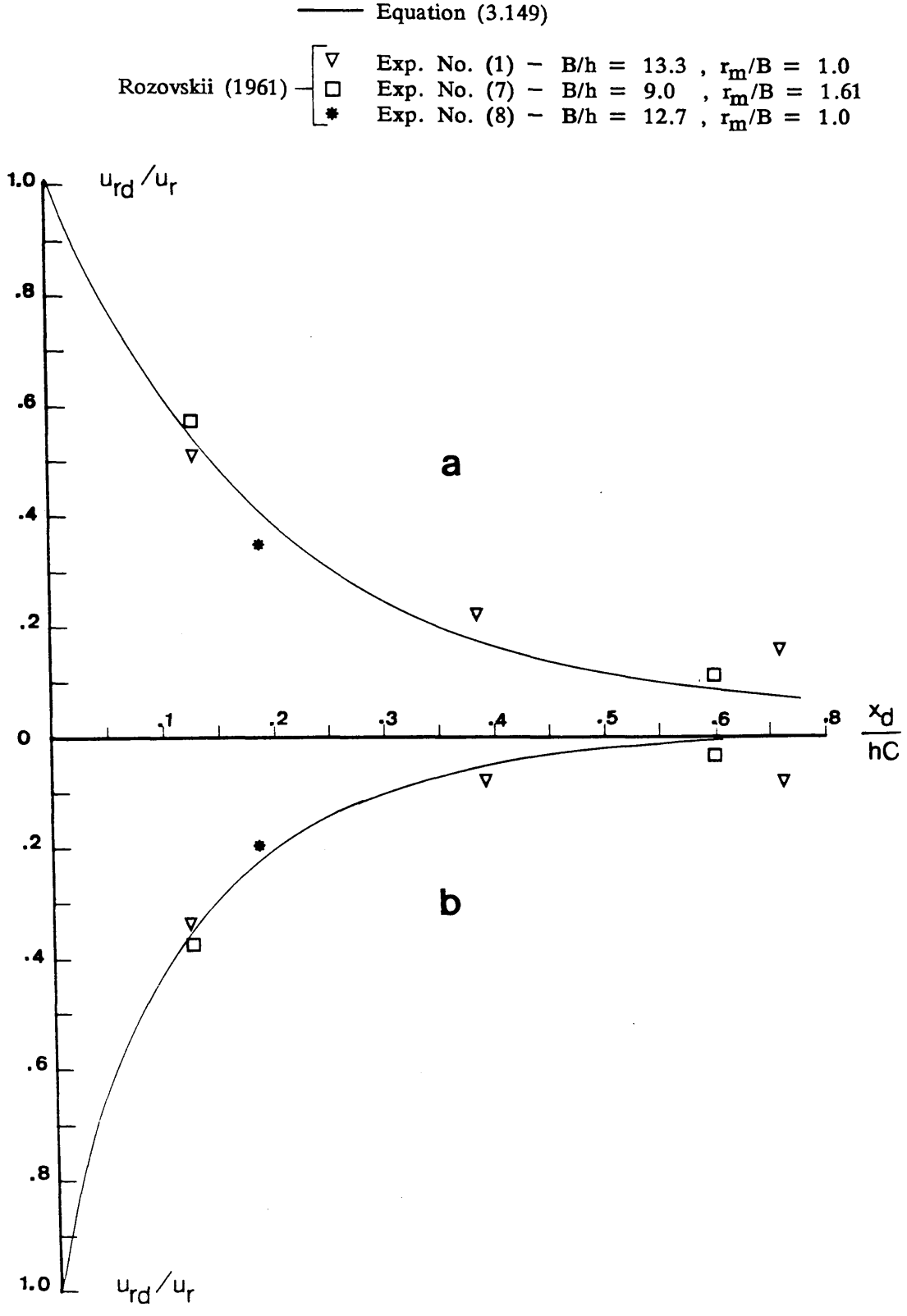

FIG.(3.17) – Decay of the Radial Velocities Beyond the Bend – Comparisons with the Experimental Data given by Rozovskii (1961)
(a) at λ = 0.9
(b) at λ = 0.1

CHAPTER IV

FORMULATION OF BEND FLOW AT THE FLOOD RELIEF CHANNEL INTERSECTION

CHAPTER IV

FORMULATION OF BEND FLOW AT THE FLOOD RELIEF CHANNEL INTERSECTION

(4.1) INTRODUCTION

In this Chapter, the effect of a flood relief channel on the horizontal variations of water depth and depth–averaged velocity in a gentle wide channel bend will be considered. Such hydraulic behaviour can be treated as a spatially varied flow with a non–uniform (decreasing) discharge resulting from the spilling of excess water into the flood channel. The dynamic equation for this type of flow can be formulated by considering the momentum in the main direction of the flow. The analysis will be carried out in two parts. The first part will deal with the dynamics of the flow at the intersection where the main channel is straight and of a uniform cross section. The second part will deal with the effects of replacing the straight main channel with a curved channel (i.e. the effects of the superelevation of the water surface and the radial distortion of the depth–averaged velocities). In the latter case, the initial flow conditions will be taken from the depth–averaged model described in Chapter III , section (3.7).

Using the boundary layer theory, the flow entering the flood relief channel will be modelled as the flow over a side weir with a long base or broad crest. Despite the flow diversity and the formation of local vortices at the upstream junction of the intersection, the conventional weir equation will be used. The

influence of these vortices will be simulated by the use of empirical coefficients in the weir equation. The effect of the flood relief channel dimensions (i.e. the weir crest height C_h and the weir crest width C_w) on the flow behaviour in the bend channel will also be included. As well, the effect of the drowning of the flow at the downstream end of the flood channel.

The dynamic spatially varied flow equation and the weir equation will be solved simultaneously to give the solution of the horizontal flow problem at the intersection. In order to reduce the number of simplifications and approximations, the equations concerned will be solved numerically using the finite difference technique.

(4.2) MAIN MODEL ASSUMPTIONS

The following assumptions are required for the mathematical formulation of the model:

(4.2.1) The flow in the main channel is assumed to be approximately unidirectional. In reality, there are strong cross currents present in the form of a spiral flow particular-ly in the flood relief channel. The effect of these currents is to produce a highly momentum exchange between the flow layers and to produce a shear layer above the weir crest. Both of which are extremely difficult to model. The justification for ignoring these effects comes from experimental measurements made by El– khashab (1975) and El– khashab et al (1976) which show that the magnitudes of these secondary currents produce only a small energy loss compared with the loss due to friction.

(4.2.2) The flow entering the flood relief channel may be modelled as a flow over a side weir with a broad crest. Despite the fact that the flow over the weir crest makes a considerable angle with the direction normal to the crest, it has been assumed that a conventional weir equation for the flow discharge per step length along the weir crest may be used. Hence, the weir equation given by the British Standard BS:3680 will be used.

(4.2.3) Despite the fact that the flow, especially at the upstream junction, may have some curvature and irregularities in the water surface, the vertical distribution of the pressure field is assumed to be hydrostatic, i.e. the assumption of a parallel flow is made.

(4.2.4) The slope of the main channel is taken to be relatively small. So, its effect on the pressure and shear forces in the channel cross section can be neglected.

(4.2.5) The momentum flux correction factor β and the kinetic energy coefficient α are assumed to be constant in the main channel along the whole length of the intersection. Their values are taken to be that usually accepted for open channel flows. Justification for this assumption is given in the experimental results of Subramanya et al (1972), Balmforth et al (1977), (1978), (1983), Ranja Raju et al (1979), Hager (1983), (1986), Uyumaz et al (1985) and others.

(4.3) MATHEMATICAL TREATMENT

As previously stated, the model will deal first with the dynamics of the flow at the intersection where the main channel is straight and of a uniform cross section. Then, the analysis will be extended and modified to cope with the

implications of the bend curvature on the flow characteristics.

Previous analytical models either emloyed the energy principle (e.g. De–Marchi (1934), Frazer (1954), (1957), Chow (1959), and Hager (1983), (1984), (1986)) or the momentum principle (e.g. Nimmo (1927), Cramp (1939), Taylor (1942), Tults (1956), Smith (1973), Balmforth et al (1977), (1978), (1983)). In applying the energy principle, a constant value of the total energy of the flow along the intersection is always assumed. The validity of this assumption has been confirmed experimentally by many investigators. Nevertheless, El–khashab et al (1976) showed that, for an intersection with a considerable large crest width, the assumption of a constant total energy has not sustained. Therefore, it has been decided to use the momentum principle in the mathematical formulation of the model.

(4.3.1) Dynamic Momentum Equation for Spatially Varied Flow in a Straight Channel

(4.3.1.1) Derivation of the Model Equation

Consider a flow in a straight open channel, with water depth h and mean velocity u, entering the intersection with the flood relief channel (Fig.(4.1)). In this case, some of the flow momentum in the main stream will be lost by the spilling of the water across the side weir crest (see Tults (1956) and Smith (1973), (1974)). By considering section (1) and section (2) in the main channel spaced a distance Δx apart, with discharges Q and $Q - \Delta Q$ respectively. Then, the momentum principle can be applied by equating the sum of the total forces acting on the considered control volume in the main stream direcrion with the rate of change of momentum between the two sections. The main forces applied to the

channel in the direction of the flow are :

(a) The pressure force which is assumed to be hydrostatic.

(b) The gravity force due to the inclination of the channel invert.

(c) The friction (tractive) force due to the bed shear stress.

So, the sum of all applied forces is:

$$\sum F = \Delta P + F_g - F_\tau \qquad (4.1)$$

where

$\sum F$ is the sum of the total forces acting on the control volume.

ΔP is the difference in the hydrostatic pressure force between sections (1) and (2) ($= - \rho\ g\ A\ \Delta h$).

F_g is the gravity force ($= \rho\ g\ A\ S_0\ \Delta x$).

F_τ is the friction force ($= - \rho\ g\ A\ S_f\ \Delta x$).

A is the channel cross sectional area.

Δh is the difference in the water depth between sections (1) and (2) respectively.

ρ is the flow density.

g is the gravitational acceleration.

S_0 is the channel bed slope.

S_f is the total energy (friction) slope which can be obtained from either Manning or Chezy equation of motion.

The total rate of change of momentum between the two sections is:

$$\partial_t M = \rho\ \beta(Q - \Delta Q)(u + \Delta u) - \rho\ \beta\ Q\ u + \rho\ \Delta Q\ [u + (\Delta u/2)]$$

$$= \rho\ \beta\ Q\ \Delta u \qquad (\text{for } \Delta Q\ \Delta u \ll 1) \qquad (4.2)$$

where β is the momentum coefficient which models the non-uniformty of the mean velocity in the channel cross section, due to the effect of the boundary friction.

Equating equations (4.1) and (4.2) will give after some simplifications:

$$\Delta x\ (S_0 - S_f) - \Delta h = \beta\ Q\ \Delta u\ /\ (g\ A) \qquad (4.3)$$

Dividing by Δx and taking the limit of Δx to zero, equation (4.3) will read:

$$d_x h = S_0 - S_f - \beta\ (1/g)\ d_x(Q\ du/A) \qquad (4.4)$$

where $d_x = d/dx$, is the gradient operator along x-direction. The last term on the right hand side of equation (4.4) can be differentiated as:

$$\beta\ (1/g)\ d_x(Q\ du/A) = \beta[d_x u\ Q/(g\ A)] + \beta\ du\ [(A\ d_x Q - Q\ d_x A)/(g\ A^2)] \qquad (4.5)$$

But since,

$$d_x A = d_h A\ .\ d_x h = B\ d_x h \qquad (4.6)$$

where $d_h A = B$, i.e. the water surface width. Substitution of equation (4.6) into equation (4.5), will give:

$$\beta\ (1/g)\ d_x(Q\ du) = \beta\ (u\ du/g) + \beta\ (du\ d_x Q/A) - \beta\ (Q\ B\ d_x h\ du/A^2) \qquad (4.7)$$

The mean velocity gradient $d_x u$ between sections (1) and (2) can be expressed as:

$$d_x u = d_x[\{(Q + \Delta Q)/(A + \Delta A)\} - (Q/A)] \qquad (4.8)$$

Which gives after dropping the second order terms;

$$d_x u = \beta\ Q\ B\ d_x h\ /\ A^2 \qquad (4.9)$$

Substituting the value of the mean velocity gradient from equation (4.9) into equation (4.7) and refering to equation (4.4), the resulting equation will become after slight transformations;

$$d_x h = [S_0 - S_f - (1/g)\ (2\beta - 1)\ d_x Q\ (u + dQ/A)]\ /\ [1 - \beta\ (F_r^2 + \Delta F_r^2)] \qquad (4.10)$$

where

$$F_r^2 = Q\ [\ u\ B\ /\ (g\ A^2)] \qquad (4.11)$$

and

$$\Delta F_r^2 = |dQ|\ [\ u\ B\ /\ (g\ A^2)] \qquad (4.12)$$

where F_r^2 and ΔF_r^2 are expressions for the flow Froude number such that:

$$\Delta F_r^2\ /\ F_r^2 = |dQ|\ /\ Q \qquad (4.13)$$

Equation (4.10) represents the general model equation of motion for spatially varied flow with a decreasing discharge. The values d_xQ and dQ represent the discharge components (i.e. gradient and value) which are resulted from the spilling across the side weir.

However, equation (4.10) cannot be solved since h is a variable as well as Q . So, another equation is still needed to obtain the solution. This equation is the conventional weir equation which can be written per step length Δx as:

$$d_xQ_w = C_f \; h_w^{1.5} \qquad (4.14)$$

where

Q_w is the flow discharge over the side weir crest.

d_x is the gradient operator along the crest width (= d/dx).

C_f is the weir coefficient which includes, in general, the discharge and the velocity coefficients.

h_w is the water head above the crest level (= $h - C_h$).

h is the water depth upstream of the weir.

C_h is the weir crest height.

Hence, by considering the proper value of the weir coefficient C_f (which differs according to the type of the weir and its dimensions), the solution of the spatially varied flow equation (4.10) can be acheived, with the aid of the weir equation i.e. equation (4.14), using a suitable numerical technique.

The direction of the computations, however, depend mainly on (see Chow (1959), Balmforth et al (1978) and Hager (1983)):

(1) The state of the approach flow.

(2) The downstream condition in the main channel.

(3) The crest height C_h of the side weir.

If the approach flow is subcritical and a flow control device (e.g. a weir or sluice gate) is placed downstream of the intersection, the computations should start from the downstream end and work towards the upstream end. This is because the surface profile , in this case, is governed by the effect of the backwater curve produced by the control device. In contrast if the approach flow is supercritical and no flow control device is placed, the computations should start from the upstream end and work downstream.

With respect to the third factor, the influence on the computations direction can be stated as:

– For weirs of low crest levels, the supercritical condition in the flow prevails and hence, the computations should start from the upstream end of the intersection and work downstream.

– For weirs of high crest levels, the subcritical behaviour in the flow dominates and hence, the computations should start from the downstream end of the intersection and work upstream.

Before proceeding towards adopting this approach to modelling the flow characteristics in the channel bend at the intersection with the flood relief channel, the model equation has to be first calibrated and verified. To accomplish this, the model will be checked against other mathematical models as well as experimental results obtained from the literature. It should be mentioned, before carrying out the calibration, that the only data available for comparisons were from tests using

sharp crested weirs (i.e. thin plate weirs). Probably the only exception, to the writer's knowledge, is the work published by Ranga Raju et al (1979). Unfortunately, it does not give sufficient information for suitable quantitative comparisons. The following set of comparisons will include cases of subcritical as well as supercritical flows.

(4.3.1.2) Comparisons With Previous Analytical Models and Experimental Results

Chow (1957), (1959) developed a step computational method based on the assumption of constant energy head of flow along the side weir. Chow predicted the variations in the water surface elevation in the main channel as:

$$\Delta h = \alpha [(Q_1/g) (u_1 + u_2)/(Q_1 + Q_2)] \Delta u [1 - (\Delta Q/2Q_1)] - S_f \Delta x \quad (4.15)$$

where

α is the kinetic energy coefficient.

Δh is the variation in the water surface elevation between the upstream and the downstream ends of element Δx .

u_1 & Q_1 are the velocity and the discharge at upstream end of element Δx .

u_2 & Q_2 are the velocity and the discharge at downstream end of element Δx .

$\Delta Q = Q_1 - Q_2$ (to be obtained from the weir equation).

S_f is the friction slope (assumed to be constant).

More recently, Balmforth et al (1977), (1978) suggested a method (known as

B&S method) based on numerical integration of a combination of the spatially varied equation and the weir equation. For this, the surface gradient could be expressed as:

$$d_x h = [S_0 - S_f + (u/g\ A)\ d_x Q\ (2\beta - 1)] / [1 - F_r^2] \qquad (4.16)$$

The similarity between equation (4.16) and the writer's equation (i.e. equation (4.10)) should be noted. The difference between the two equations is the additional terms dQ/A in the numerator and ΔF_r^2 in the denominator right hand side of equation (4.10).

The flow discharge Q_w over a sharp crested weir (which is required for the comparison requirements) can be expressed as:

$$d_x Q_w = (2/3)\ \sqrt{(2\ g)}\ C_d\ [h - C_h]^{1.5} \qquad (4.17)$$

where C_d is the discharge coefficient which can be calculated with a satisfactory accuracy from standard equations (e.g. Rehbock equation, see Ackers et al (1978)). By combining equation (4.17) with both the Chow method (equation (4.15)) and the B&S method (equation (4.16)), comparisons with the writer's suggested equation, equation (4.10), can be made for the case of a subcritical flow. Fig.(4.2) shows the comparison of predicted longitudinal water surface profiles in the main channel when the flow is via a double sharp crested weir. While Fig.(4.3) gives the corresponding predicted profiles of the discharge in the main channel. Both Figures show a reasonable agreement among the methods. In Table (4.1), the % difference in the water depth h and in the flow discharge Q, along the intersection, calculated by these methods is shown. It can be seen that the differences in predicting the water depth are smaller than those for the flow discharge.

Comparisons can also be made with previous experimental results for both subcritical and supercritical flow conditions. For subcritical flows, Fig.(4.4) shows the comparisons of water depths predicted by equation (4.10) with experimental observations obtained by El– khashab et al (1976).

For the case of supercritical flows, comparisons with the experimental data obtained from Frazer (1954) and El– khashab et al (1976) were made. Fig.(4.5) gives comparisons with Fraser's data for the discharge variations along the weir crest plotted as a ratio of the channel flow Q to the initial flow value Q_0 at the side weir entrance (i.e. as Q/Q_0 ratio), for two different test runs. The comparisons with El– khashab's results for the water surface profile and the variation of the side weir discharge Q_w along the weir crest width are given in Fig.(4.6).

The comparisons shown in Figures (4.2) to (4.6) are considered to adequately justify the use of the proposed dynamic model equation (i.e. equation (4.10)), in the case of a straight channel with sharp edged side weirs. In the lack of any other information, it is considered both necessary and justifiable to proceed to apply equation (4.10) (if necessary in a slightly modified form) to the case of a channel bend with a single broad crested side weir.

(4.3.2) Modelling of the Bend Effect on the Flow at the Intersection With the Flood Relief Channel

As mentioned in section (4.3.1.1), equation (4.10) is considered to be the basic equation for the modelling of the flood relief effect on the horizontal variations of the flow in the channel bend. However, because of variations in

depth–averaged velocity u_m and water depth h across the width of a curved channel, direct application of equation (4.10) would lead to considerable errors. The equation, or rather the approach in which it is applied, must be modified to cope with the radial variation of u_m and h. In order to do this, the channel bend cross section is divided into a series of concentric strips of equal width. Each strip can be treated as a separate channel with a certain depth–averaged (mean) velocity u_m and a certain (mean) water depth h. The validity of this procedure depends on the degree of curvature (i.e. the bend tightness ratio r_m/B) of the channel bend and the the aspect ratio of the flow B/h. The shallower and less curved the bend, the more realistic the results obtained. Thus, consideration will be limited to gentle wide channel bends (i.e. with $r_m/B \geq 3$ and $B/h \geq 10$, where r_m is the bend mid radius and B is the bend width).

As stated previously in the model assumptions, the flow entering the flood relief channel will be treated as a flow over a side weir with a long base or broad crest. Previous experimental investigations for the flow over side weirs of sharp crests (see e.g. Chow (1957), (1959), Balmforth et al (1977), (1978) and Uyumaz et al (1985)) have shown that the coefficient of the weir discharge C_d is sensibly independent of the orientation of the weir, i.e. whether the weir is placed normal to or along the direction of the flow in the main channel. It has been assumed that this will also be true for the case of broad crested weirs and extended to cover the case for flow in curved channels.

The main difference between flow in straight and curved channels is the effects of the superelevation and the secondary circulation. These effects have been taken into account by assuming that each of the concentric sub–channels (i.e. strips), into which the bend is divided, contributes to the overflow according to its mean water depth. The contribution increases as water depth increases and hence,

the sub—channels closest to the side weir contribute most to the overflow.

Based on the appropriate British Standard (namely, BS3680 : Part 4E :1980 and Part 4B : 1986) and the above assumptions, the discharge dQ_{fR} over the side weir per step length dC_w , along the crest width, may be written as:

$$(dQ_{fR} / dC_w) = (2/3)^{1.5} \sqrt{g}\ C_d\ C_v\ (h - C_h)^{1.5} \qquad (4.18)$$

where

C_d is the coefficient of weir discharge.

C_v is the velocity coefficient which allows for the effect of the approach velocity.

h is the total water depth.

C_h is the weir crest height.

f is the drowned flow reduction factor.

Values of C_d , C_v and f may be obtained from the British Standard. Inclusion of the drowned flow reduction factor allows conditions at the downstream end of the flood relief channel to be modelled.

By combining the weir equation, i.e. equation (4.18), and the spatially varied flow equation, i.e. equation (4.10), the final model equations of the horizontal problem (i.e. the horizontal variations of u_m and h) in the channel bend can be obtained at the intersection with the flood relief channel. The finite difference scheme for all grid points in the channel bend at the intersection is given in Appendix (D). The corresponding side weir flow equation in a typical bend strip $[i,\ell]$ is:

$$Q_{fR}[i,\ell] = A_c \quad \Delta S_{fR} \; (\; h[i,\ell] - C_h \;)^{1.5} \qquad (4.19)$$

The side weir discharge taken by the neighbouring strip $[i+1,\ell]$ can be expressed as:

$$Q_{fR}[i+1,\ell] = Q_{fR}[i,\ell] \; (r_f[i+1] \; / \; r_f[i]) \; \{ \; (h[i+1,\ell] - C_h) \; / \; (h[i,\ell] - C_h)\}^{1.5} \qquad (4.20)$$

with

$$r_f[i] = (\; r[i+1] + r[i] \;) \; / \; 2 \qquad (4.21)$$

$$\Delta S_{fR} = \Theta_{fR}[\ell+1] \; r_f[i] - \Theta_{fR}[\ell] \; r_f[i] \qquad (4.22)$$

$$A_c = (2/3)^{1.5} \; \sqrt{g} \; C_v \; C_d \; f \; / \; (N-1) \qquad (4.23)$$

where

A_c is the weir coefficient.

$h[i,\ell]$ is the water depth in strip $[i,\ell]$.

$r_f[i]$ is the mid radius of strip $[i,\ell]$.

N is the number of radial sections across the bend width.

$N-1$ is the number of strips across the bend width.

$Q_{fR}[i,\ell]$ is the flow spilled across the side weir from strip $[i,\ell]$.

$\Theta_{fR}[\ell]$ is the local bend angle at the intersection.

ΔS_{fR} is the curved step length along the crest width for strip $[i,\ell]$.

The corresponding spatially varied flow equation in the typical strip $[i,\ell]$, expressed in finite difference scheme, is:

$$\Delta h / \Delta S_{fR} = \{ S_0 - S_f[i,\ell] - (1/g)\ (2\ \beta - 1)\ (Q_{fR}[i,\ell]/A[i,\ell])\ (u_m[i,\ell] + Q_{fR}[i,\ell]/A[i,\ell])\ (1/\Delta S_{fR}) \} / \{ 1 - (F_r^2[i,\ell] + \Delta F_r^2[i,\ell]) \} \quad (4.24)$$

with

$$\Delta h = h[i,\ell+1] - h[i,\ell] \quad (4.25)$$

$$F_r^2[i,\ell] = \beta\ Q[i,\ell]\ \{u_m[i,\ell]\ \Delta r/(g\ A[i,\ell])\} \quad (4.26)$$

$$\Delta F_r^2[i,\ell] = F_r^2[i,\ell]\ Q_{fR}[i,\ell]/\ Q[i,\ell] \quad (4.27)$$

$$Q[i,\ell] = u_m[i,\ell]\ A[i,\ell] \quad (4.28)$$

$$S_f[i,\ell] = (1/C^2)\ u_m^2[i,\ell]/\ H_r[i,\ell] \quad (4.29)$$

and

$$H_r[i,\ell] = A[i,\ell]/(\Delta r + h_a[i,\ell]) \quad (4.30)$$

$$h_a[i,\ell] = h[i+1,\ell] + h[i,\ell] \quad (4.31)$$

$$A[i,\ell] = h[i,\ell]\ \Delta r \quad (4.32)$$

$$\Delta r = r[i+1] - r[i] \quad (4.33)$$

where

$H_r[i,\ell]$ is the hydraulic radius of strip $[i,\ell]$.

$h_a[i,\ell]$ is the sum of the water depths at the sides of strip $[i,\ell]$.

$S_f[i,\ell]$ is the slope of the total energy line of flow in strip $[i,\ell]$.

$u_m[i,\ell]$ is the mean velocity in strip $[i,\ell]$.

$Q[i,\ell]$ is the discharge in strip $[i,\ell]$.

$A[i,\ell]$ is the flow area in strip $[i,\ell]$.

S_0 is the average bed slope of the invert.

Δr is the width of the strip $[i,\ell]$.

β is the momentum flux correction factor.

C is the Chezy coefficient of bed roughness.

g is the gravitational acceleration.

The simultaneous solution of equation (4.24) and the weir equation (4.19) can be obtained by any numerical standard method of integration (see e.g. Price (1977) and Chapra et al (1985)). The initial conditions of the flow at the upstream section of the intersection are obtained from the depth–averaged bend model developed in section (3.7) , Chapter III .

In the present investigation, only cases of subcritical conditions are considered in the formulation of the bend flow at the intersection. Since the parameters of the flow, downstream of the intersection, were not initially known, the assumption of constant specific energy was essential. The individual application of this assumption to each bed strip allows the variables u_m and h to be determined at the downstream end of the intersection. This, in turn, allows the computations to proceed along the intersection towards the upstream end (i.e. from $\Theta_b = 35^\circ$ to $\Theta_b = 25^\circ$).

It was found after many preliminary test runs that 0.25° angle increments along the intersection was sufficient to obtain satisfactory results, i.e. the limits for the grid points, in the concentric mech, were:

$$" 1 \leq i \leq N-1 " \quad \text{and} \quad " 1 \leq \ell \leq MM "$$

where " $N-1 = 10$ " and " $MM = 41$ " for the tested 10° angle intersection.

Using the above limits, the assumption of constant specific energy along the intersection can be expressed, in finite difference form, as:

$$E[i,\ell=1] = E[i,\ell=MM] \tag{4.34}$$

where

$$E[i,\ell=1] = h[i,\ell=1] + (1/2g)(u_m[i,\ell=1])^2 \tag{4.35}$$

$$E[i,\ell=MM] = h[i,\ell=MM] + (1/2g)\,(Q_F/A)^2 \tag{4.36}$$

$$A = \Delta r\ h[i,\ell=MM] \tag{4.37}$$

$$Q_F = Q[i,\ell=1] - Q_{fR}[i,\ell=1 \rightarrow MM] \tag{4.38}$$

with

$$Q_{fR}[i,\ell=1 \rightarrow MM] = \Sigma_\ell\ Q_{fR}[i,\ell] \qquad \text{for } 1 \leq \ell \leq MM \tag{4.39}$$

In Appendix (D), the computational procedure of this model is explained in detail through a flow chart called " **FLOREL** " .

(4.4) SUMMARY

The steps taken in the development of a 2– D (depth– averaged) model for simulating the effects of a flood relief channel on the horizontal variation of the flow components in a channel bend may be summarised as follows:

(4.4.1) Using the momentum principle, a dynamic equation for the flow in a straight channel at the intersection with a side overflow was developed. This equation was combined with the weir equation so that variations in depth and discharge within the channel could be predicted. The predictions were checked against previous numerical models and experimental results, for cases of sub– and supercritical flows, and found to be satisfactory.

(4.4.2) The influence of the bend curvature on the flow in the main channel was introduced through the division of the bend cross section into a series of concentric strips each with different water depth h and depth–averaged velocity u_m . Each bend strip was considered to behave as a separate channel and the model equations were applied individually to each sub–channel.

(4.4.3) For cases of subcritical conditions, the assumption of constant specific energy for the flow at the intersection was applied individually to each concentric bend strip. Use of this assumption was essential to obtain both the local water depth h and the local depth–averaged velocity u_m , in each bend strip, at the downstream end from which the computations start.

(4.5) CONCLUSIONS

The combination of the bend model, developed in Chapter III , with the spatially varied equation, formulated in this Chapter, has produced a model which allows the simulation of the effects of a flood relief channel (modelled as a side weir) on the flow in a channel bend. The model is capable of coping with variations in the flood relief channel dimensions and with conditions imposed at the downstream end of the flood channel.

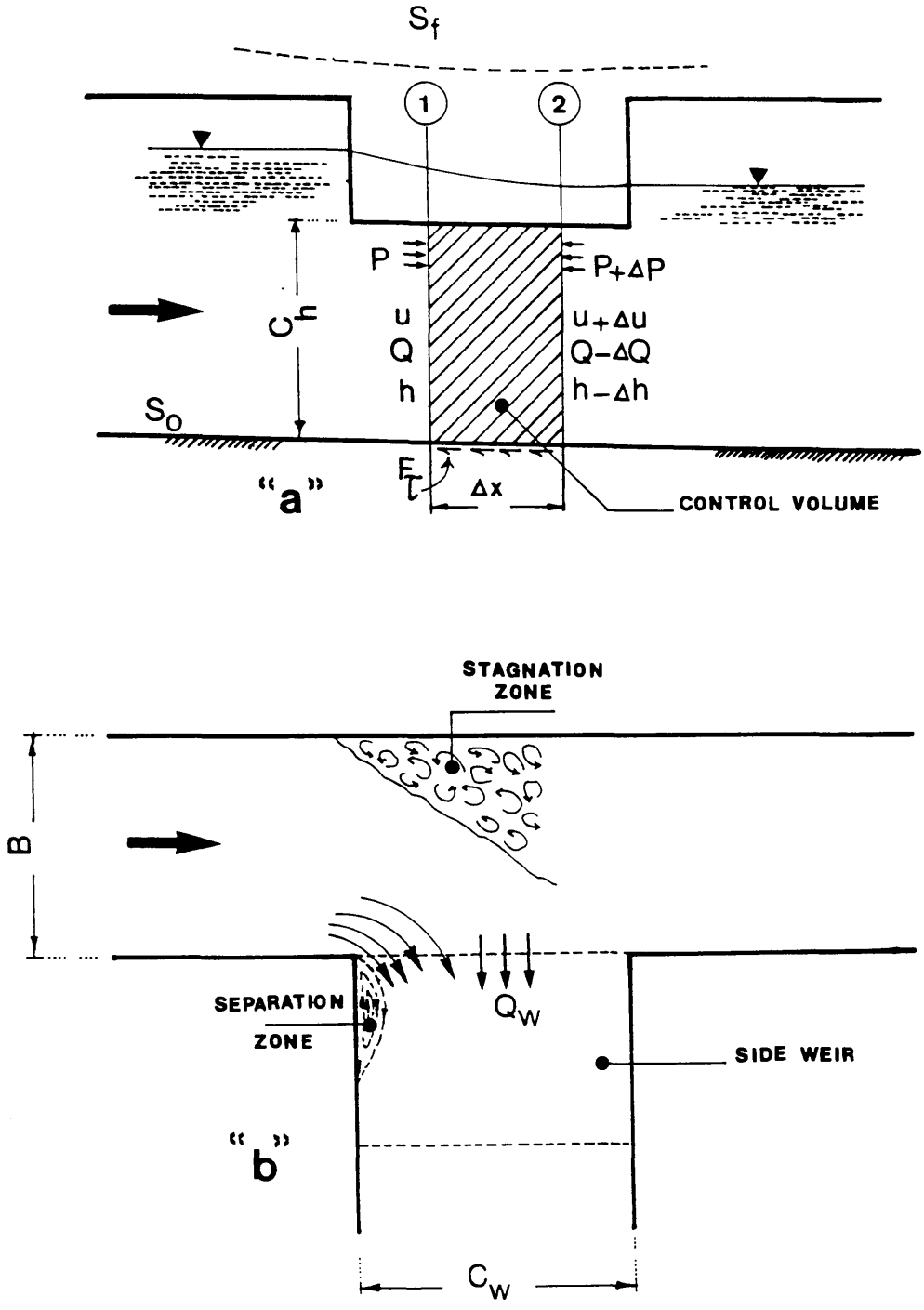

FIG.(4.1) – Characteristics of Flow in a Channel with Discharge over a Broad Crested Side Weir

(a) Elevation

(b) Plan

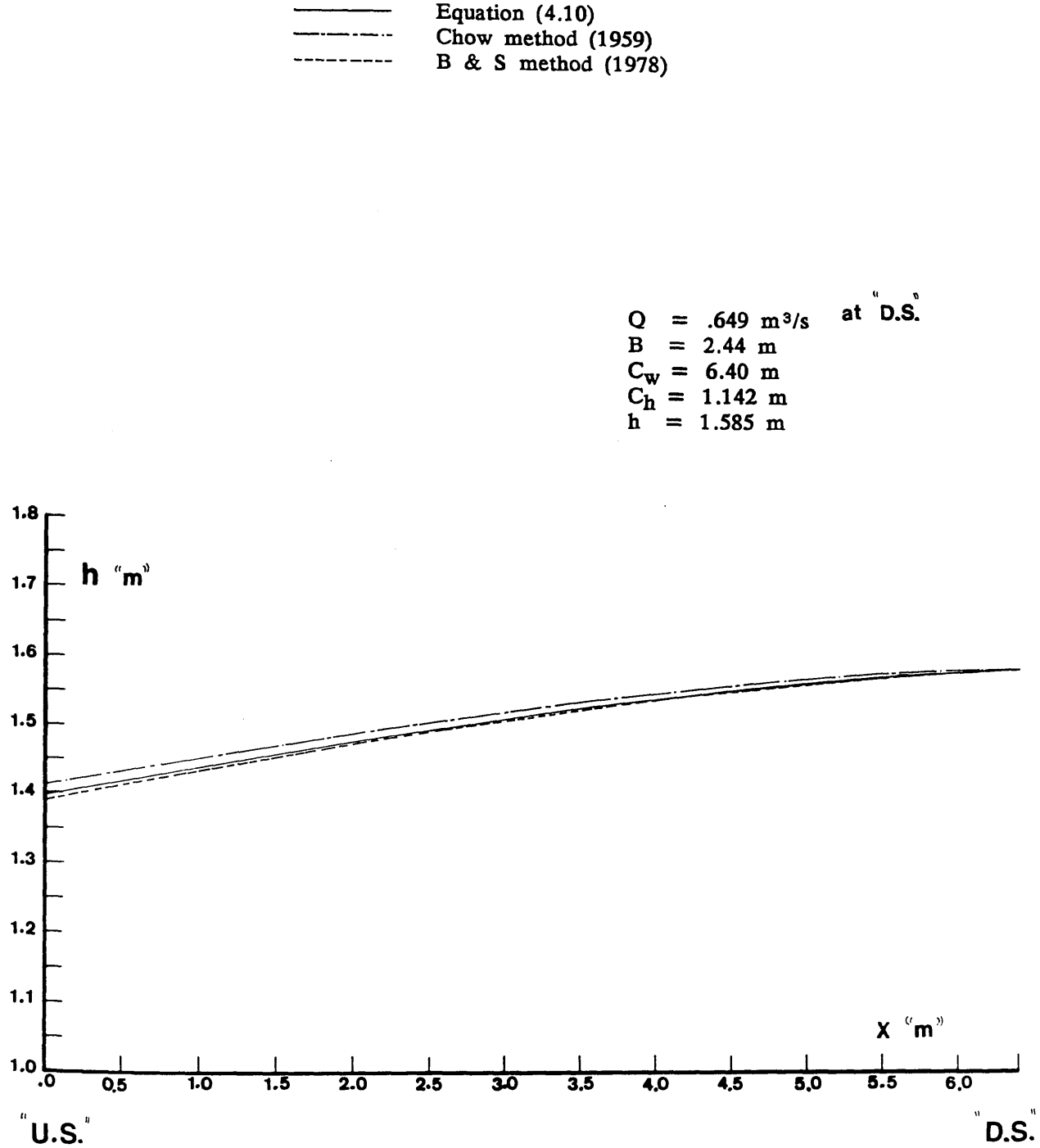

Fig.(4.2) — Predicted Water Surface Profile in the Main Channel along the Intersection for Subcritical Flow Condition, Comparisons with Previous Numerical Models

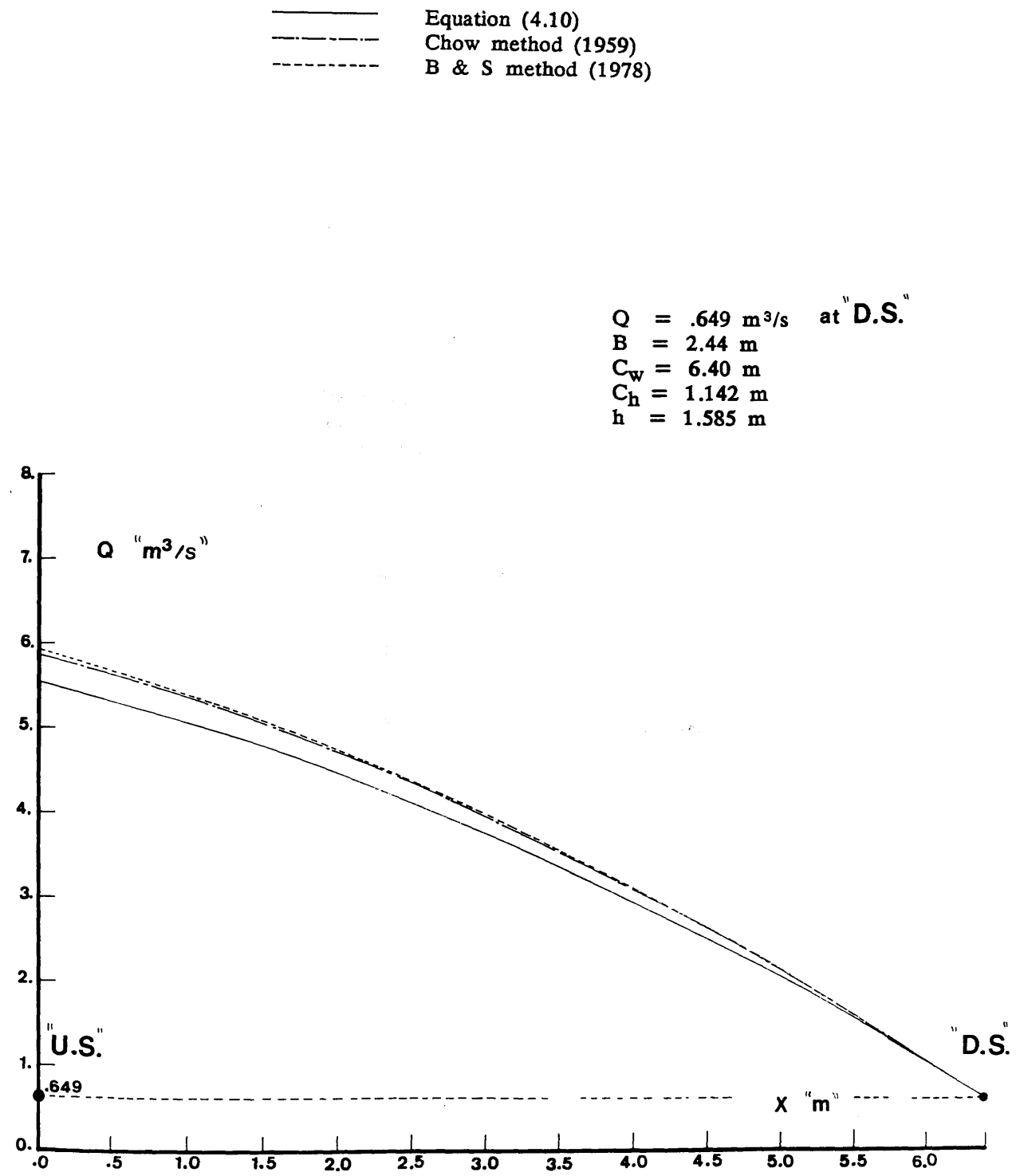

Fig.(4.3) — Predicted Flow Discharge Profile in the Main Channel along the Intersection for Subcritical Flow Condition, Comparisons with Previous Numerical Models

TABLE (4.1) – % Difference of the Predicted Water Depth and Flow Discharge along the Intersection for Subcritical Flow Condition, Comparisons with Previous Numerical Models

Method	Depth at upstream end of weir h (m)	%Diff. h	Flow at upstream end of weir Q (m^3/s)	%Diff. Q
Chow (1959)	1.4130	+1.04	5.8537	+5.32
B&S (1978)	1.3941	−0.32	5.9417	+6.54
Eqn (4.10)	1.3985	–	5.5706	–

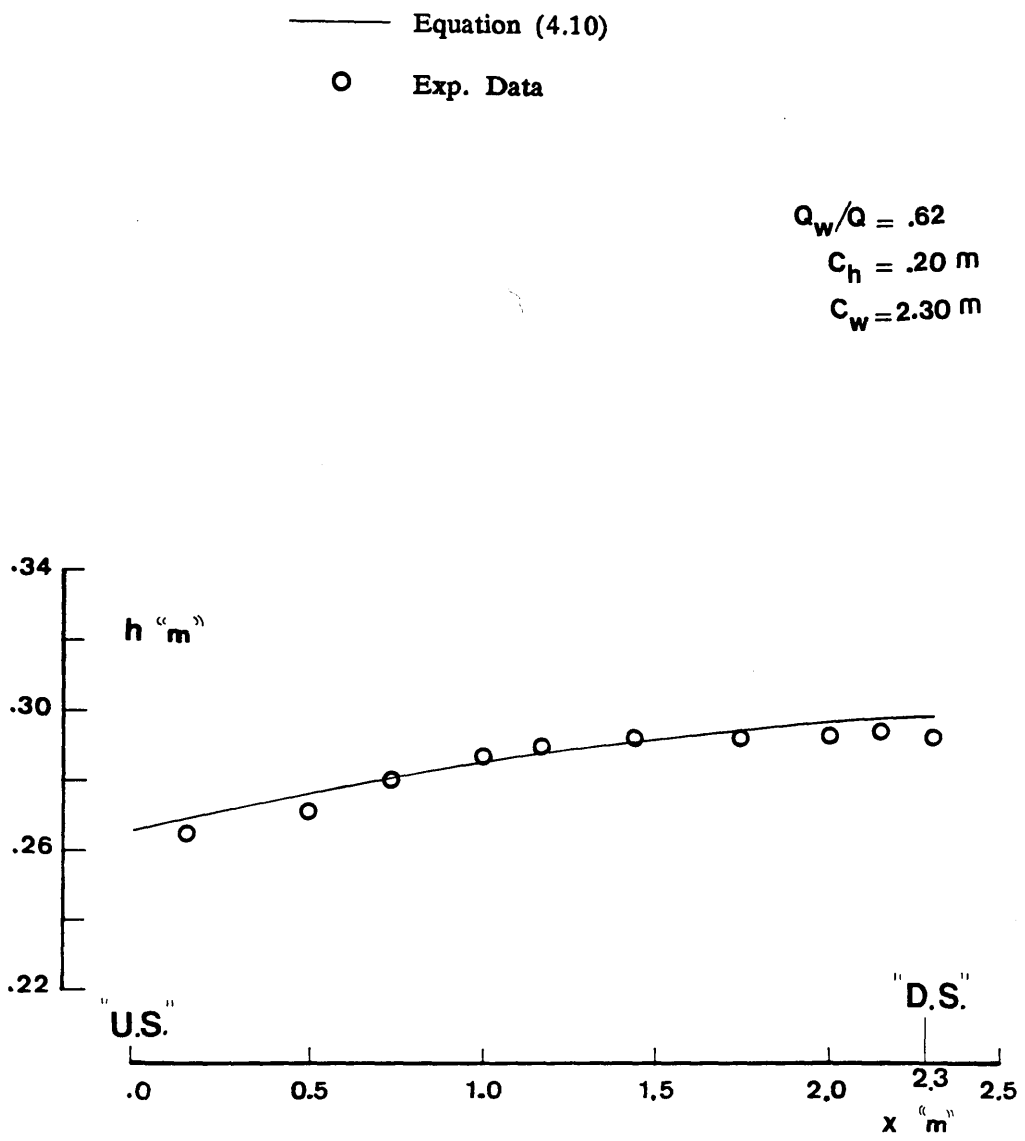

FIG.(4.4) – Comparison of the Predicted Water Surface Profile along the Intersection with the Experimental Data given by El–khashab et al (1976) for Subcritical Flow Condition

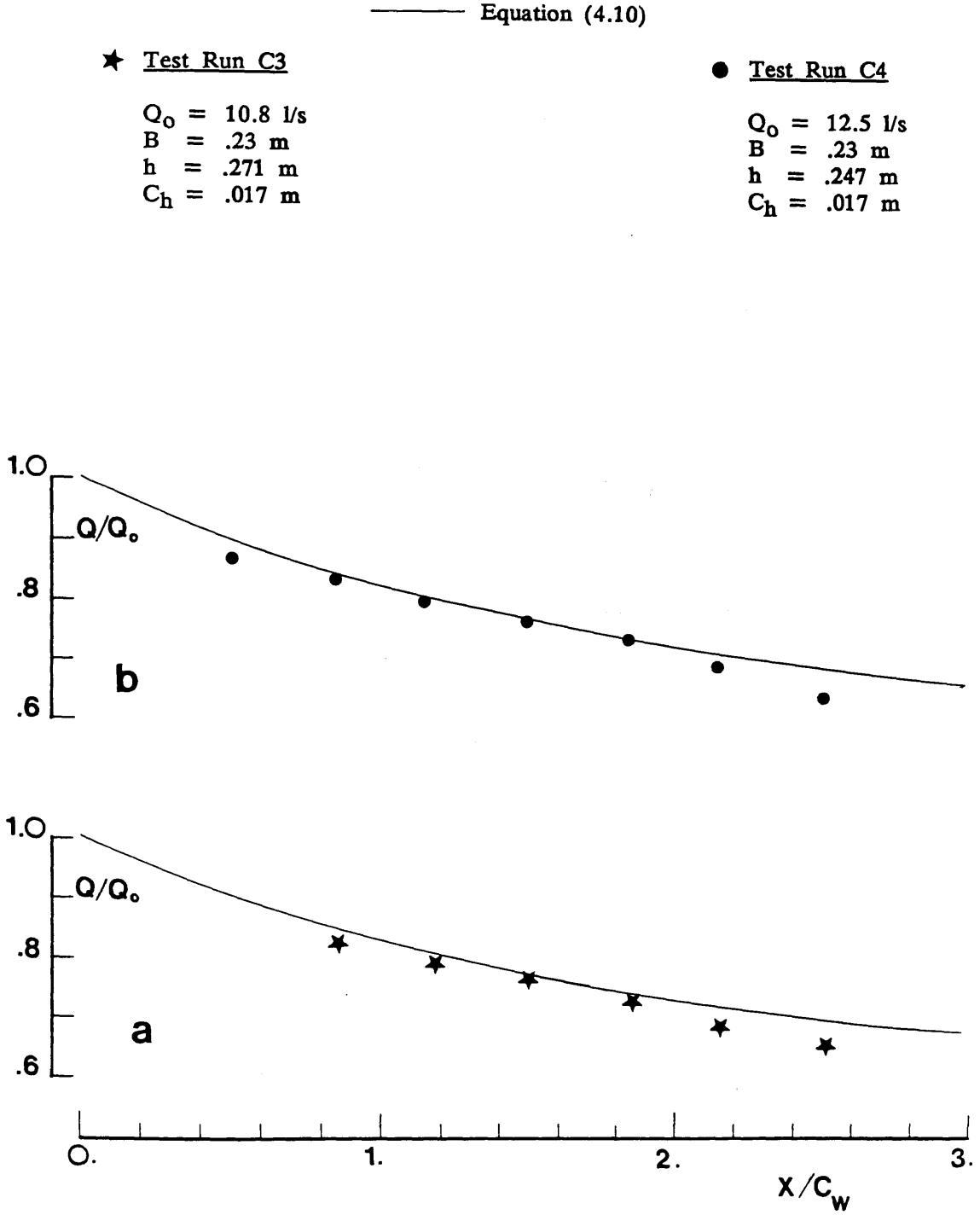

FIG.(4.5) – Comparisons of the Predicted Flow Discharge along the Intersection with the Experimental Data given by Frazer (1954) for Supercritical Flow Condition
(a) Test Run C3
(b) Test Run C4

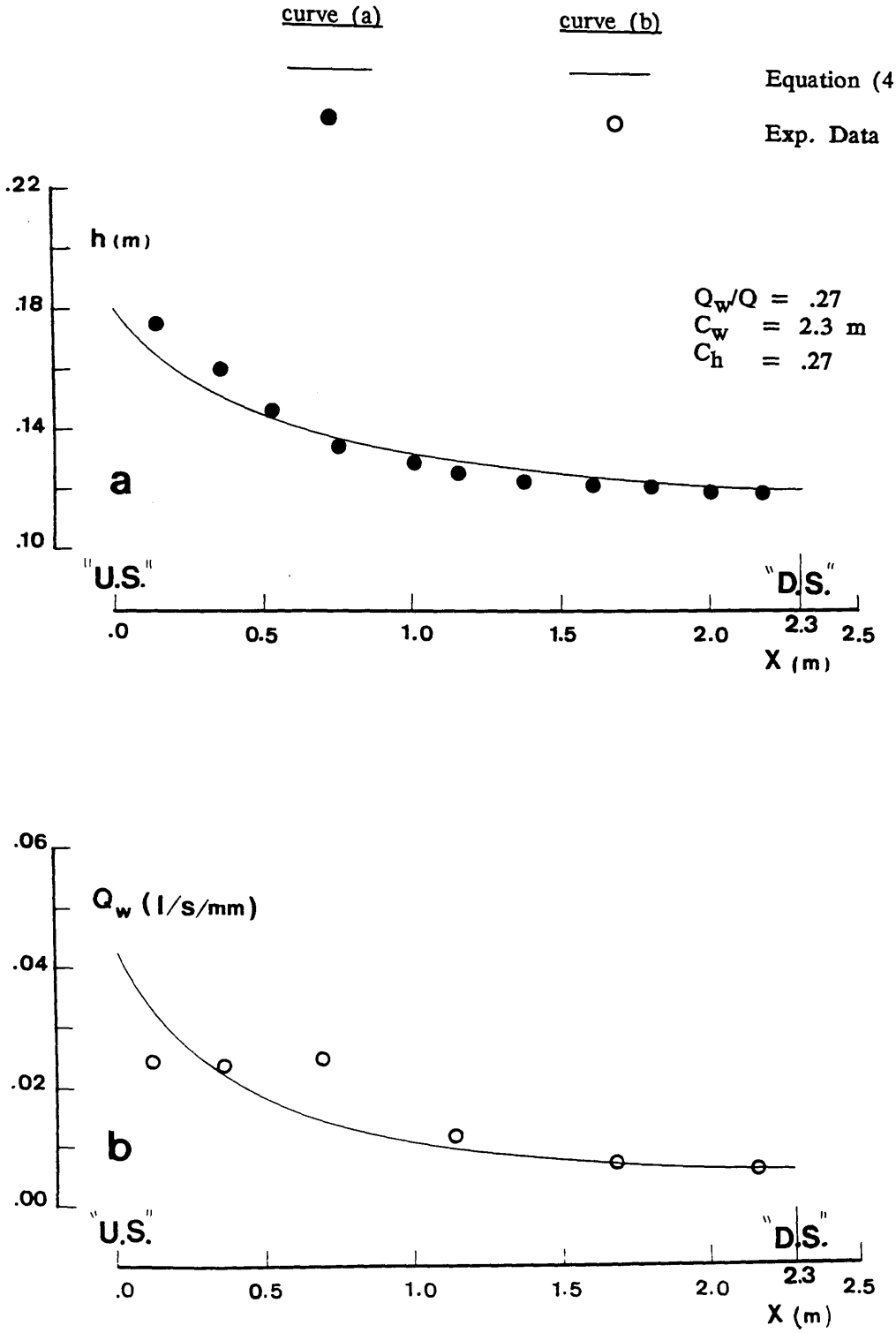

FIG.(4.6) – Comparisons of the Predicted Flow Profiles with the Experimental Data given by El–khashab et al (1976) for Supercritical Flow Condition

(a) Water Surface Profile
(b) Side Weir Discharge

CHAPTER V

EXPERIMENTAL INVESTIGATION OF THE PROBLEM

CHAPTER V

EXPERIMENTAL INVESTIGATION OF THE PROBLEM

(5.1) INTRODUCTION

The physical model, which will be described in this Chapter, was designed and built specifically to provide data for the verification of the mathematical models described in Chapters III and IV . Also included in this Chapter will be the description of the instrumentation used in collecting the data and details of the relevant calibration procedures. The procedure adopted for the different experimental test runs will also be indicated.

It was decided at the design stage that the physical model should be available for use by the Department of Civil Engineering after the current research programme was completed. The model, therefore, required some features which were not necessary for the present study. These features will be mentioned whenever appropriate.

A recirculating system was chosen for the model as no facility existed in the laboratory for storing large quantities of water. Hence, water flowing out of the channel was collected in sump tanks and then pumped back to the channel inlet tank and hence, back along the flume. Fig(5.1) and Plate (5.1) show the general lay– out of the model.

(5.2) THE FLUME

(5.2.1) Design Considerations

The flume consists of a 60° bend lying between two straight reaches. Careful consideration was given to the lengths of the two straight reaches so that a uniform and fully developed flow was established at the entrance to the bend.

In order to establish uniform flow in the channel, an adjustable sluice gate was placed at the end of the flume. Since the uniform flow condition was to be obtained artifically, the stations at which readings were taken had to be sufficiently far away from the sluice gate. This would prevent the measured flow behaviour from being significantly affected by the sluice gate. A distance of 0.80m was considered satisfactory for this purpose in view of the relatively small rates of flow used.

In order to ensure a fully developed flow (i.e. one in which the boundary layer thickness reaches the water surface) at the bend entrance, the length of the upstream straight part of the flume was determined by means of the Blasius equation for the growth of the boundary layer. This equation has been successfully used by previous investigators (e.g. see Ippen et al (1962) and Baird (1984)). This equation reads;

$$h / x_{fd} = 0.38 / R_e^{-0.2} \qquad (5.1)$$

with

$$R_e = u\, x_{fd} / \nu \qquad (5.2)$$

where

x_{fd}	is the required length of the channel to achieve a fully developed flow condition assuming turbulent flow at the channel entrance.
h	is the corresponding boundary layer thickness.
Re	is the Reynolds number of the flow.
u	is the mean velocity of the flow.
ν	is the flow kinematic viscosity.

After applying the equation to the anticipated range of flow conditions, the length of the upstream straight reach of the flume was chosen to be 4.0m.

The condition adopted in the design of the 60° bend part of the flume was that the bend should be gentle, i.e. the relative bend curvature (or the bend tightness ratio r_m/B) should be ≥ 3 . For this ratio, many investigators (see e.g. Shukry (1949), Bagnold (1960), Leopold et al (1960), (1966), and Soliman et al (1968) and others) have concluded that the flow resistance and energy loss due to bend curvature is minimum. On this basis, a mean bend radius of 1.50m and a channel width of 0.50m was chosen.

The flood relief channel was chosen to lie between 25° and 35° bend angles. This was to allow a considerable bend effect on the flow behaviour at the intersection. The flood channel is 0.30m wide i.e. 60% of the width of the main channel. As mentioned previously, it had been decided to simulate the action of the flood relief channel by means of a broad crested weir. The weir was placed at the upstream end of the flood channel. The characteristic of the weir was that its length was the same as its width. Details of the lay-out and sizes of the various parts of the flume system are shown in Fig.(5.2).

(5.2.2) Construction of the Flume

The 4.0m long, 0.5m wide and 0.12m high upstream straight part of the flume was constructed from 18mm thick varnished plywood. It was made in two sections, each of 2m long, and joined by means of splice plates. Once joined, the flume was attached to two 8" x 4" longitudinal battens and the whole assembly supported on two tables with adjustable legs.

The bend section of the flume was constructed with a plywood base as before but with walls of 2mm thick aluminium. A gap was left in the outer wall between bend angles of 25° and 35° to accomodate the flood relief channel. The flood relief channel was constructed in much the same way as the upstream channel but with channel dimensions of 0.8m long, 0.3m wide and 0.12m high. Entry to the flood channel was controlled by a broad crested weir made up of 0.3 x 0.3m , 5mm thick perspex sheets. The perspex weir could be built up from 5mm to the full channel wall height in 5mm steps as required.

Downstream of the bend section was a further 0.8m long straight section again made from plywood and terminating in the controlling sluice gate. The sluice gate was made from 3mm thick brass plate and had dimensions of 490 x 80mm.

The bend, flood relief and downstream channels are supported on an 18mm thick plywood base plate which was, in turn, supported on six jacks fixed to the sump tanks.

The flume was provided with two instrument carriages, one for use in the straight sections and one for use in the bend section.

(5.2.3) Determination of Bed Slope Profile

After a survey of the literature, it was decided that a fairly typical river slope was in the order of 1/1000 to 1/2000 and so, a figure in this range was adopted for the model. As indicated previously, there were a number of jacking and leveling points built into the model supports. Unfortunately, it was found that not all of these operated independently and some difficulty was encountered in obtaining a uniform slope throughout the model. The slope was determined from a series of levels taken by means of a surveyors level and graduated scale. Levels were taken at 0.25m intervals along the upstream straight channel and at 5° intervals around the bend section. A best fitted slope line was obtained by using the method of least squares and is shown realtive to the measured bed levels in Fig.(5.3). Table (5.1) gives the difference between the measured bed levels and those calculated using the best fit slope line.

The slope was measured according to the above procedure before and after the test runs and values of 4.77×10^{-4} and 5.1×10^{-4} were obtained respectively. A value of 5.1×10^{-4} was adopted for comparisons with the mathematical model results.

(5.2.4) Coefficient of Roughness

The coefficient of roughness (Manning's " n ") for the material (i.e. plywood sheets) of the flume was taken from another investigation carried out in the Department. The results of this investigation are shown in Fig.(5.4) (after

Ervine et al (1989)) from which a value of 0.01 was adopted as the Manning roughness coefficient.

(5.3) WATER SUPPLY SYSTEM

As mentioned previously, a recirculating water system was designed for the operation of the model. The syatem consisted of two sump tanks, a pump, a control valve and an inlet tank as shown in Fig.(5.5). The system also incorporated an orifice plate for flow measurement purposes.

Since water is discharged from the flume at two points (namely, by way of the sluice gate at the end of the flume and by way of the flood relief channel), two sump tanks were required. Each of these was a galvinised steel tank of dimensions (1.83 x 1.22 x .91)m. The tanks were connected by a 0.30m length steel pipe of internal diameter Φ = 0.3m.

A MYSON MSK 150–4210 electrically driven centifugal pump of 40 l/sec capacity was connected directly to the sump tanks. The pump capacity was much in excess that required for the present experiments but was chosen with a view to future use of the apparatus. A 6" gate valve was placed on the discharge side of the pump to control the discharge passing to the inlet tank. The actual discharge passing upstream was measured by means of an orifice plate inserted in the 6" pipeline linking the sump and the inlet tanks at a distance of 2.36m from the gate valve. Details of the design and calibration of the orifice plate will be given later in section (5.4.2).

After passing through the orifice plate, the flow was directed into a

galvinised steel inlet tank (1.22 x 1.22 x 1.22)m from which it passed into the flume.

(5.4) INSTRUMENTATION

Experimental measurements were divided into three groups:

- **Measurements of water surface profiles.**
- **Measurements of deviation angles of horizontal resultant velocities.**
- **Measurements of local longitudinal velocities.**

In each group, measurements were carried out firstly, for the channel bend alone and then after the introduction of the flood relief channel. The discharge in the main channel and, where appropriate, in the flood relief channel were also recorded.

The instrumentation used for these measurements is listed in Table (5.2). The details of any necessary calibrations are given in the following sections.

(5.4.1) Pitot Static Tube

A Pitot static tube was used both to measure the local longitudinal velocities throughout the channel cross section and to calibrate the orifice plate which was used to measure the total flow in the system. An inclined manometer was used to obtain the output from the Pitot static tube.

(5.4.2) Orifice Plate

One of the most effective devices for measuring the discharge in a closed conduit is the Orifice Plate as outlined in the British Standard BS1042: Section 1.1 : 1981 and Section 1.4 : 1984. When inserted into a pipeline, an orifice plate causes a contraction of the flow and hence, produces an energy head loss. The head loss can be related to the rate of fluid flow and be recorded by a manometer through measuring the pressure head difference between two tapping points, one upstream and the other downstream of the orifice place. As specified in the British Standard, the tapping points should be at D and D/2 upstream and downstream the orifice plate (where D is the inner diameter of the upstream pipe).

According to BS1042: Section 1.4 : 1984, the flow discharge through the orifice plate is given by:

$$Q_{op} = C_{op}\, E_v\, \epsilon\, (\pi\, d^2/4)\, \surd\, (2\, g\, \Delta h_{op}) \qquad (5.3)$$

where

Q_{op} is the discharge through the orifice.

d is the diameter (or throat) of the orifice.

C_{op} is the discharge coefficient.

ϵ is the expansibility factor (= 1.0 for incompressible flow).

Δh_{op} is the pressure head difference between the upstream and the downstream side of the orifice plate.

g is the acceleration of gravity.

E_v is the velocity approach factor which can be obtained from the relation ;

$$E_v = 1 \,/\, \surd\, (1 - \mu^4) \qquad (5.4)$$

where

μ is the diameter ratio (= d/D).

D is the inner diameter of the upstream pipe.

On the basis of the range of the expected maximum rate of flow, the diameter coefficient μ was chosen 0.55, i.e. the orifice diameter was 84mm. Based upon the method specified in BS1042 : Section 1.1 : 1981 and Section 1.4 : 1984 , the values for each parameter in the flow equation (5.3) were calculated. These values are:

$$E_v = 1.05$$

$$\epsilon = 1.00$$

$$d = 84\text{mm} \ (\mu = 0.55)$$

$$g = 9.8066 \text{ m/s}$$

The coefficient of discharge C_{op} depends on the Reynolds number (and hence the flow discharge in the upstream pipe Q_o). Again according to the British Standard, after applying the above given values:

$$C_{op} = .6041 + .000658 \ (10^{-6} / R_{eo})^{.75} \qquad (5.5)$$

with

$$R_{eo} = u_o \, D/\nu = 4 \, Q_o/(\pi \, D \, \nu) \qquad (5.6)$$

where

Q_o is the discharge of the upstream flow.

R_{eo} is the Reynolds number of the upstream flow.

u_o is the mean flow velocity in the upstream pipe.

ν is the kinematic water viscosity (1.141×10^{-6} m^2/s).

The design details of the orifice plate are shown in Fig.(5.6) and the arrangement of the orifice plate is given in Plate (5.2).

In order to conform to the British Standard, the orifice plate should be positioned such that the distance from the plate to the next disturbance in the flow should be a minimum of 7 pipe diameters on the downstream side and 60 pipe diameters on the upstream side. In the present situation, this means that the orifice plate should be at least 1.06m from the inlet tank and at 9.10m from the gate valve even with the valve 1/4 open. The configuration of the model was such that only some 3m of straight pipe was available between the gate valve and the inlet tank. It was decided to satisfy the downstream requirement of 1.06m and hence, not to satisfy the upstream condition. This problem had been encountered previously by Baird (1984) who also found that space restrictions prevented placing of an orifice plate according to the British Standard requirements. He found that if account were taken of this in the calibration stage, satisfactory and reliable results could still be obtained.

(5.4.2.1) Calibration of the Orifice Plate

The orifice plate calibration was carried out using two different methods. Results from these methods were checked against the theoretical predic-tion given by equation (5.3) from BS1042. These two methods were:

(a) Use of Pitot static tube:

The mean flow velocity at a section 0.25m upstream of the bend was obtained by integrating point values of velocity over the channel cross

section. Multiplication of the mean velocity by the cross sectional area gave the discharge.

(b) Volumetric basis:

The control valve was opened for a short period of time allowing water to enter the inlet tank. The rise in water level in the tank was measured and since the plan area of the tank was known, the volume entering the tank in a given time could be obtained and hence the discharge rate.

In both methods (a) and (b), the corresponding water head difference from the vertical manometer was measured and the theoretical values of discharge were calculated. The results of a number of applications of each method and the corresponding best fitted lines for each method are shown in Fig. (5.7). The results show that for a wide range of flow rates, the agreement with the theoretical prediction is good. However, there were some reservations about using the equation as given in the British Standard because, as indicated previously, not all the conditions given by the British Standard were satisfied particularly in respect of the placing of the orifice plate in relation to the control valve. Similarly, the accuracy of the volumetric method was a little suspect because of the very short times which had to be used for the collection of water in the inlet tank. Thus, it was decided to use the calibration equation obtained by use of the Pitot static tube. This equation was:

$$Q_{op} = 15.47\ (\Delta h_{op})^{.48} \qquad (5.7)$$

where Q_{op} is in l/s and Δh_{op} is in meters.

(5.4.3) "V– notch" Tank

The flow spilled into the flood relief channel was collected in a small tank with a "V– notch" weir outlet. The weir was designed according to the recommendations contained in the British Standard BS3680:Part 4A:1981. The main dimensions and details of the tank and "V– notch" are shown in Fig.(5.8).

Use of a "V– notch" weir for discharge measurement is dependent on measuring the water level above the apex of the "V– notch". According to BS3680, the water level should be measured at a distance upstream of the notch equal to 4 → 5 times the maximum anticipated head over the notch. In the present case, this was estimated to be about 100mm and hence, the measuring section was chosen to be 400mm upstream of the notch. At this section, a tapping point at the base of the tank was connected to a stilling well by means of a small bore plastic tube. The water level in the stilling well was measured using a pointer gauge. According to BS3680:Part 4A:1981 , the flow discharge over a "V– notch" can be obtained from Kindsvater– Shen formula as:

$$Q_v = (8/15)\ C_{vn} \tan(\alpha_v/2)\ \sqrt{2g}\ h_e^{5/2} \qquad (5.8)$$

with

$$h_e = h_v + K_h \qquad (5.9)$$

where

Q_v is the flow discharge over the "V– notch" , i.e the flow in the flood relief channel.

C_{vn} is the discharge coefficient.

h_e is the effective flow head over the notch.

h_v is the measured head over the notch.

K_h is an experimentally determined quantity.

α_v is the central angle of the notch (= 90°).

For $\alpha_v = 90^\circ$, K_h has a constant value of 0.00085m.

(5.4.3.1) **Calibration of the "V– notch"**

The calibration of the "V– notch" was achieved by blocking the main channel just downstream of the intersection with the flood relief channel (i.e. at bend angle $\theta_b = 35^\circ$). Thus, all the flow was diverted into the flood relief channel and hence, into the "V– notch" tank. Simultaneous readings were taken of the water head above the "V– notch" and of the pressure head difference given by the orifice plate. The latter reading gives the discharge from the orifice plate calibration equation. Several tests runs were made for different flow rates. Fig.(5.9) gives the comparison between the orifice plate discharge and the discharge as predicted by the "V– notch" equation (equation (6.8)). Also shown in the Figure, the best fitted lines for both sets of data. It was decided that it would be better to use the equation given by the orifice plate results, since the "V– notch" equation could be influenced by yet another set of coefficients in the evaluation of discharge. Hence, the flow over the "V– notch" was determined from:

$$Q_v = 1450.25\ (h_v)^{2.47} \qquad (5.10)$$

where Q_v is in l/s and h_v is in meters.

(5.4.4) Angle Probe – Angle Measurement Transducer

The angle probe was used to measure the deviation angles of the horizontal resultant velocities. Knowing the local deviation angle and the longitudinal velocity component (by measurement with the Pitot static tube), the radial velocity component of the flow could be calculated.

The angle probe consists of a brass fin 40mm x 4mm x 1mm (thick) connected at one end to a metal rod 3mm in diameter and 200mm long forming an " L " shape. The rod of the probe is connected to an angle measurement transducer which, in turn, was connected by shielded cable to an IBM– PCXT computer that converts the deviations of the probe into the form of angles.

Fig.(5.10) gives a schematic diagram for the arrangement of the system and the probe is shown in Plate (5.3). The conversion takes place in a series of steps. Firstly, a carrier card installed in the computer converts the analogue voltages produced by the angle measurement transducer into a digital form. Secondly, the digital signals are converted into angles by means of a specially written computer program.

Readings from the angle measurement transducer were obtained at a rate of 100 readings/second. These were sampled over a period of 30 seconds giving a total of 3000 readings/sample. Some difficulties were experienced in measuring the deviation angles due to the high sensitivity of the probe to turbulent fluctuations in the flow. This difficulty was overcome by instructing the computer to operate more than one sample during the program execution, i.e. in the form of a "Do– loop" system. In each Do– loop, the mean, maximum, minimum and standard deviation values were obtained for each sample. The standard deviation value was considered as important as the mean, since it indicates the reliability of

the measurement. While the maximum and the minimum values give the range of measurements in each sample. However, with experience, it was found that 2 → 3 Do– loops were sufficient to obtain an accurate measurement of the mean deviation angle.

(5.4.4.1) Calibration of the Angle Probe

Calibration of the angle probe was carried out between 30° and 150° deviation angles from the longitudinal direction of the flow (which was initially set at 90°). As this range of angles was thought to cover the range likely to be obtained in the experimental runs. Plate (5.4) shows the arrangement of the angle probe calibration. As already mentioned, a computer program was developed to convert voltage readings from the transducer into the form of measured angles. In the calibration programme both the voltage readings and the corresponding angles were obtained.

The procedure for the initial setting and the calibration of the angle probe and the angle measurement transducer was as follows:

1 A protractor was used to mark the limits of the deviation angles (i.e. between 30° and 150°) on a sheet of paper. Then the paper was positioned in the bend part of the flume at a certain bend angle. This bend angle was chosen to be 10° .

2 At the chosen section, the angle probe was positioned such that the junction of the "L"

shaped probe coincided with the centre of the angles marked on the paper.

3 The fin of the probe was positioned at an angle 30° as marked on the paper.

4 The power supply box was switched on, and the voltage reading from the transducer was measured using a voltmeter.

5 The computer program for the calibration was set to run.

6 The voltage readings obtained from the computer were checked against the readings from the voltmeter. This step was essential in order to ensure that the computer was picking up the correct voltage readings. It was found that the difference between the two readings was almost negligible (i.e. $\pm$ .005 volts).

7 The procedure was repeated for deviation angles at 5° angle increments up to 150° .

8 Having measured the voltage corresponding to each angle, a graph of the relation between the deviation angles and the voltages was plotted. Using the least squares method, the best fitted line between the points was obtained. This is shown in Fig.(5.11).

The equation of the best fitted line was:

$$V = .0754\ \theta_d - 1.7859 \qquad (5.11)$$

where V represents the voltage reading and θ_d represents the corresponding deviation angle (in degrees).

The equation of the angle probe calibration, i.e. equation (5.11), was fed into the computer program which was used to measure the deviation angles of the resultant velocities in the flow. The computer programs developed for the probe calibration and for obtaining the deviation angles of the horizontal resultant velocities are given in Appendix (E).

The calibration of the probe was checked twice. Firstly, mid way through the experimental program and secondly, at the end of the experiments. It was found that a slight change had occurred and this required the measured angle values to be multiplied by 0.954.

(5.4.5) Pointer Gauge

A standard pointer gauge was used to obtain the water surface profiles and the water depths. The accuracy of the water surface measurements by the use of the pointer gauge was estimated to be ± 0.2mm.

(5.5) EXPERIMENTAL PROCEDURE

As mentioned earlier in section (5.4), three individual groups of test runs were carried out during the present investigation. In each of these groups, the bed level of the flood relief channel (i.e. the crest height of the side weir) was varied. Four bed levels were considered. These levels were 25mm, 45mm, 65mm and 120mm above the bed of the channel bend. In the latter case, no flow passed into the flood channel and so, a bend only situation could be tested.

The experimental procedure used for each group of test runs was as described in the following sections.

(5.5.1) Measurements of Water Surface Profiles

In measuring the water surface profiles, a total of 20 test runs were carried out; 7 test runs for the case of a channel bend alone and 13 test runs for the case of a bend with the flood relief channel. Measurements were taken in the flood channel as well as in the channel bend. The measuring stations for the water surface profiles are given in Fig.(5.12). For the case of the channel bend alone, the measuring stations were located at every 5° bend angle. In the case where the flood relief channel was introduced, 5 more stations were considered, two stations along the intersection at 27.5° and 32.5° bend angles, and three stations across the flood channel width. Furthermore, in all test runs two more stations were considered. The first station was located at 0.15m upstream of the bend and the other was similarly located downstream of the bend. Each station was divided into 7 sections at which the water surface and the bed levels were recorded by using the pointer gauge. The difference between the two levels would

give the corresponding water depth at the section. Having determined previously the bed slope of the flume (see section (5.2.3)), the actual water surface profiles were able to be obtained. Fig.(5.13) gives a flow chart for the experimental procedure of measuring the water surface profiles.

(5.5.2) Measurements of Deviation Angles and Longitudinal Velocities

Although listed as separate groups of test runs, the procedure for the measurements of the longitudinal velocities and deviation angles was sufficiently similar for them to be considered together for the discussion of procedure. Measurements of the local deviation angles and local longitudinal velocity components were carried out in the channel bend between 10° and 50° bend angles. A total of 14 test runs were performed for both deviation angles and longitudinal velocities; 7 test runs for each group at the same flow rate. In each group, 2 test runs were carried out for the case of a channel bend alone and 5 test runs for the case of a bend with the flood relief channel intersection. Fig.(5.14) shows the positions of the measuring stations. As in the case of water surface measurements, the measuring stations were located at every 5° bend angle and in addition at 27.5° and 32.5° bend angles in the test runs that involved the introduction of the flood relief channel.

Each measurement station (i.e. bend angle) was divided into 7 sections across the channel width. Each section was divided, in turn, into 6 measuring points in the vertical direction (see Fig.(5.15)). The total number of measurements of the deviation angles and the longitudinal velocities at each station (i.e. in the bend cross section) was 42. The only exception was for test run BA1−BV1 where only 5 measuring points in the vertical direction were considered, giving a total number of 36 measurements at each bend cross section. The experimental procedure for

measuring the deviation angles and the longitudinal velocities is given in Fig.(5.16) in the form of a flow chart.

Due to the large number of the measuring points, it was necessary to spread measurements over a period of more than one day. In order to ensure that the same conditions were maintained throughout the course of each set of measurements, the procedure listed below is observed:

1 The flow control valve was set at the beginning of the set of measurements and remained unchanged until the end. Flow was stopped and started by switching off and on the pump alone.

2 The setting of the sluice gate at the end of the flume was checked each time flow was started or stopped.

3 The reading on the vertical manometer connected to the orifice plate was checked at frequent intervals.

4 The water depth was measured at 1m intervals along the flume again each time flow was restarted.

5 Where appropriate, the water head above the "V– notch" was checked each time flow was restarted.

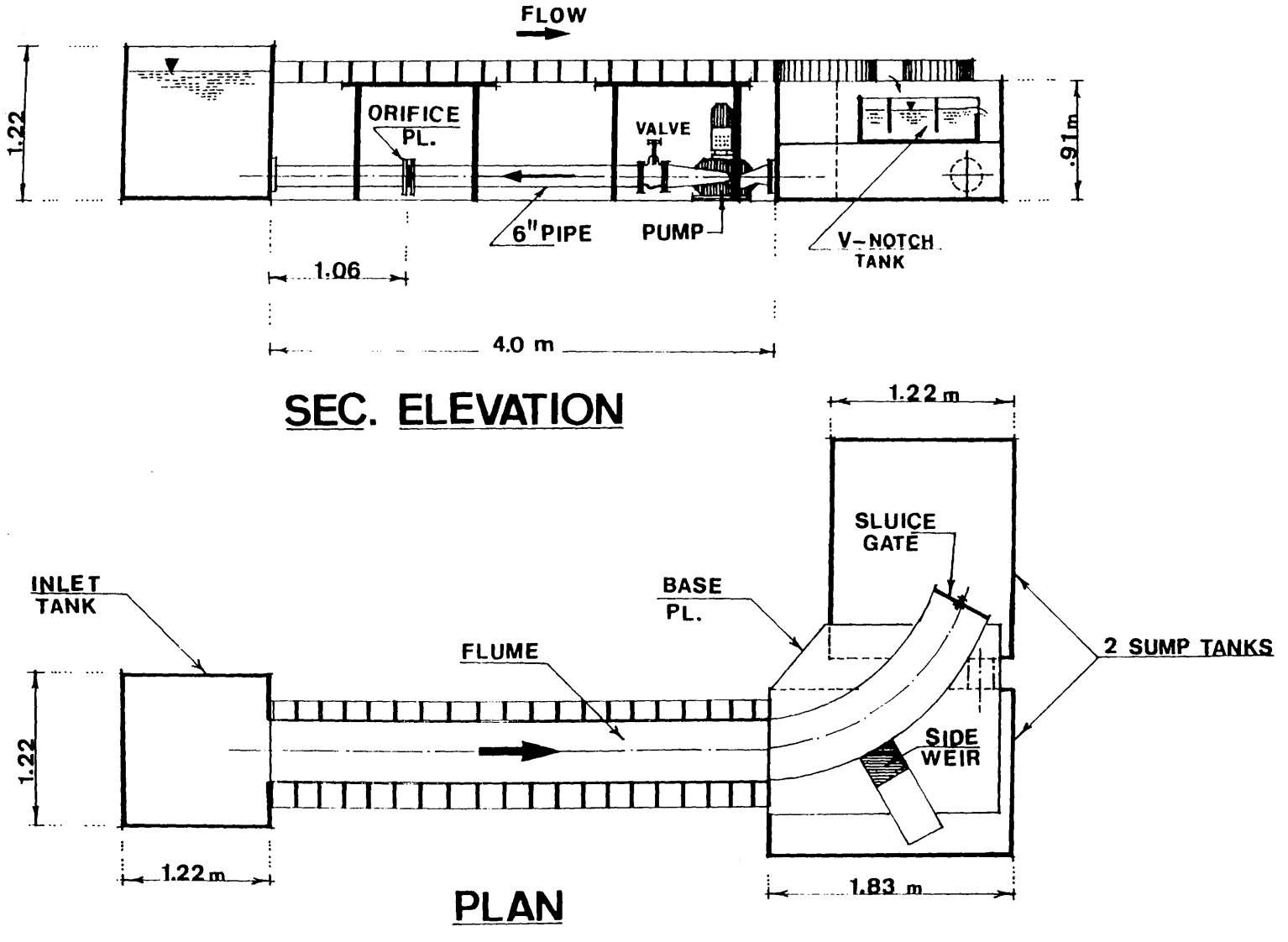

FIG.(5.1) – General Lay–out of the Model

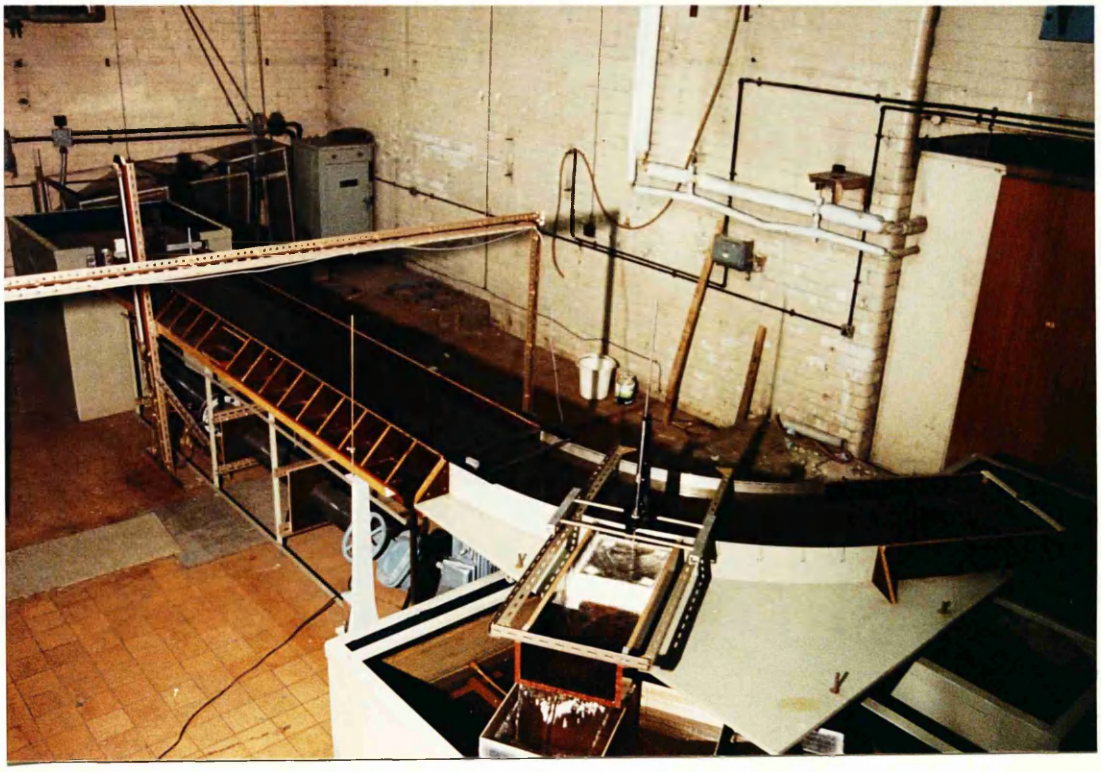

PLATE (5.1) – The Physical Model

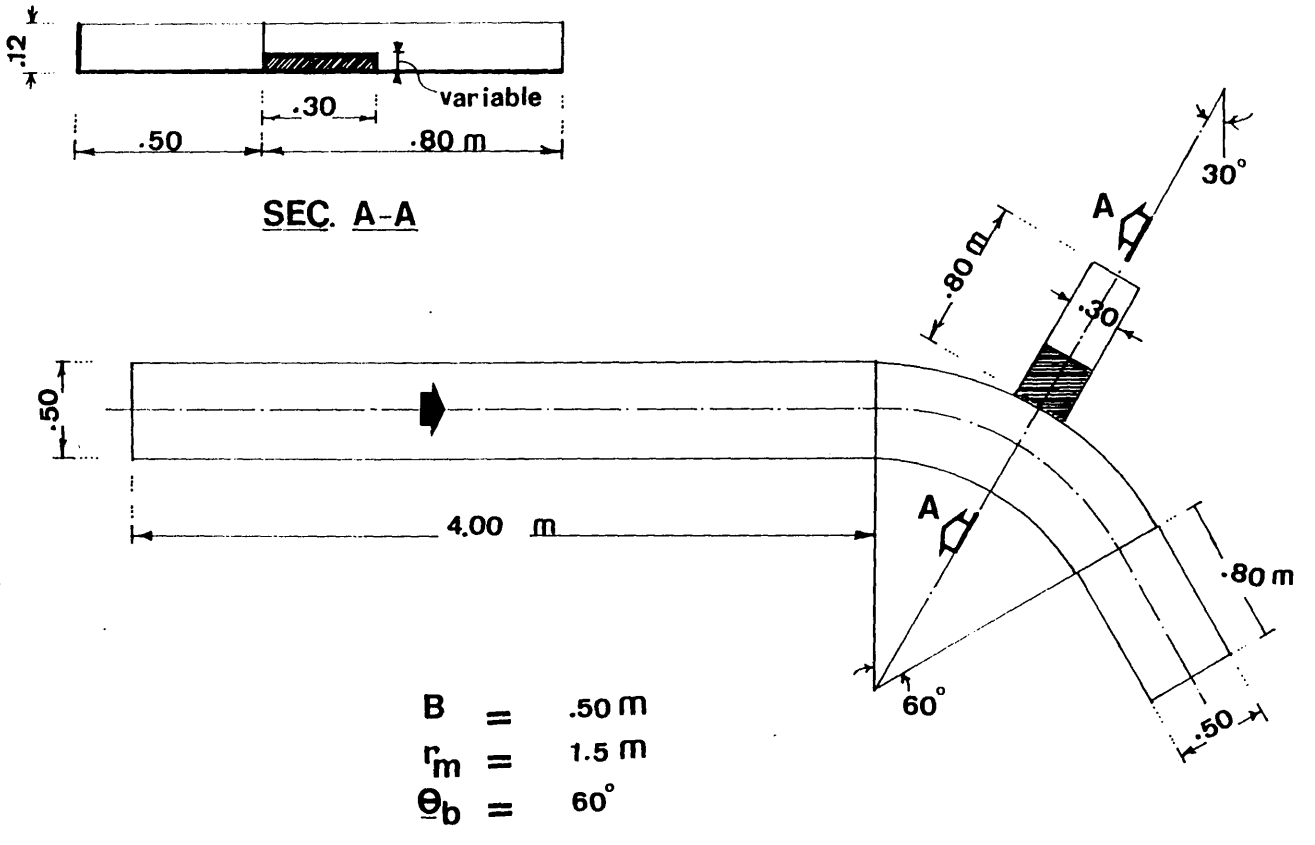

FIG.(5.2) – Main Dimensions of the Flume

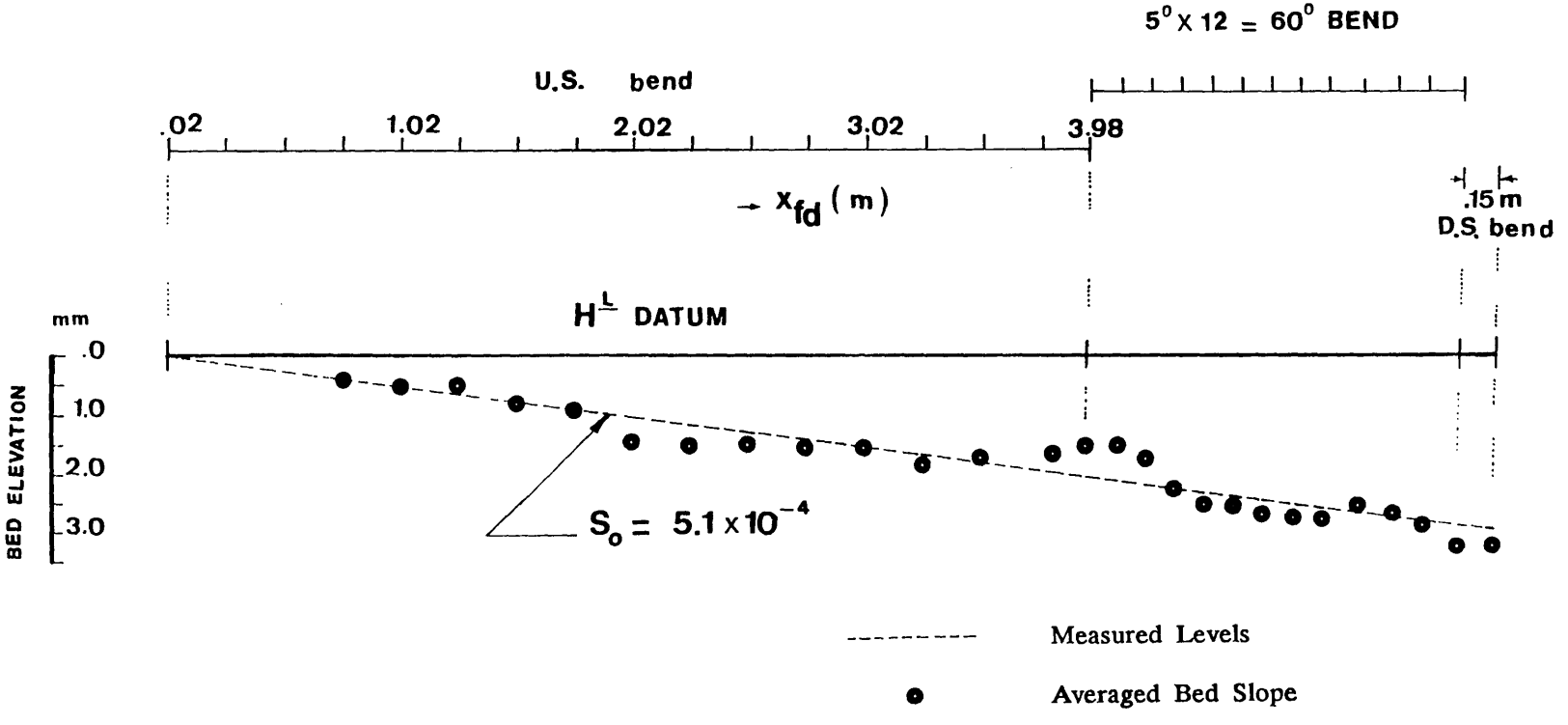

FIG.(5.3) – Longitudinal Bed Slope Profile of the Flume

TABLE (5.1) – Diffrences Between the Measured and Calculated Values of the Flume Bed Slope

x_{fd} (m)	Calculated Level (mm)	Measured Level (mm)	Difference (mm)
Upstream of the Bend			
.00	– .909	– .900	+ .009
.25	– 1.036	– 1.00	+ .036
.50	– 1.163	– 1.00	+ .163
.75	– 1.290	– 1.30	– .010
1.00	– 1.417	– 1.40	+ .017
1.25	– 1.544	– 2.00	– .456
1.50	– 1.671	– 2.00	– .329
1.75	– 1.798	– 2.00	– .202
2.00	– 1.925	– 2.00	– .075
2.25	– 2.052	– 2.00	+ .052
2.50	– 2.179	– 2.30	– .121
2.75	– 2.306	– 2.20	+ .106
3.06	– 2.465	– 2.10	+ .365
The Bend Part			
0°	– 2.542	– 2.00	+ .542
5°	– 2.611	– 2.00	+ .611
10°	– 2.675	– 2.20	– .475
15°	– 2.741	– 2.70	+ .041
20°	– 2.808	– 3.00	+ .192
25°	– 2.874	– 3.00	– .126
30°	– 2.941	– 3.10	– .159
35°	– 3.003	– 3.20	– .193
40°	– 3.074	– 3.20	– .126
45°	– 3.140	– 3.00	+ .140
50°	– 3.207	– 3.10	+ .107
55°	– 3.273	– 3.30	– .027
60°	– 3.340	– 3.70	– .360
Downstream of the Bend			
4.94	– 3.416	– 3.70	– .284

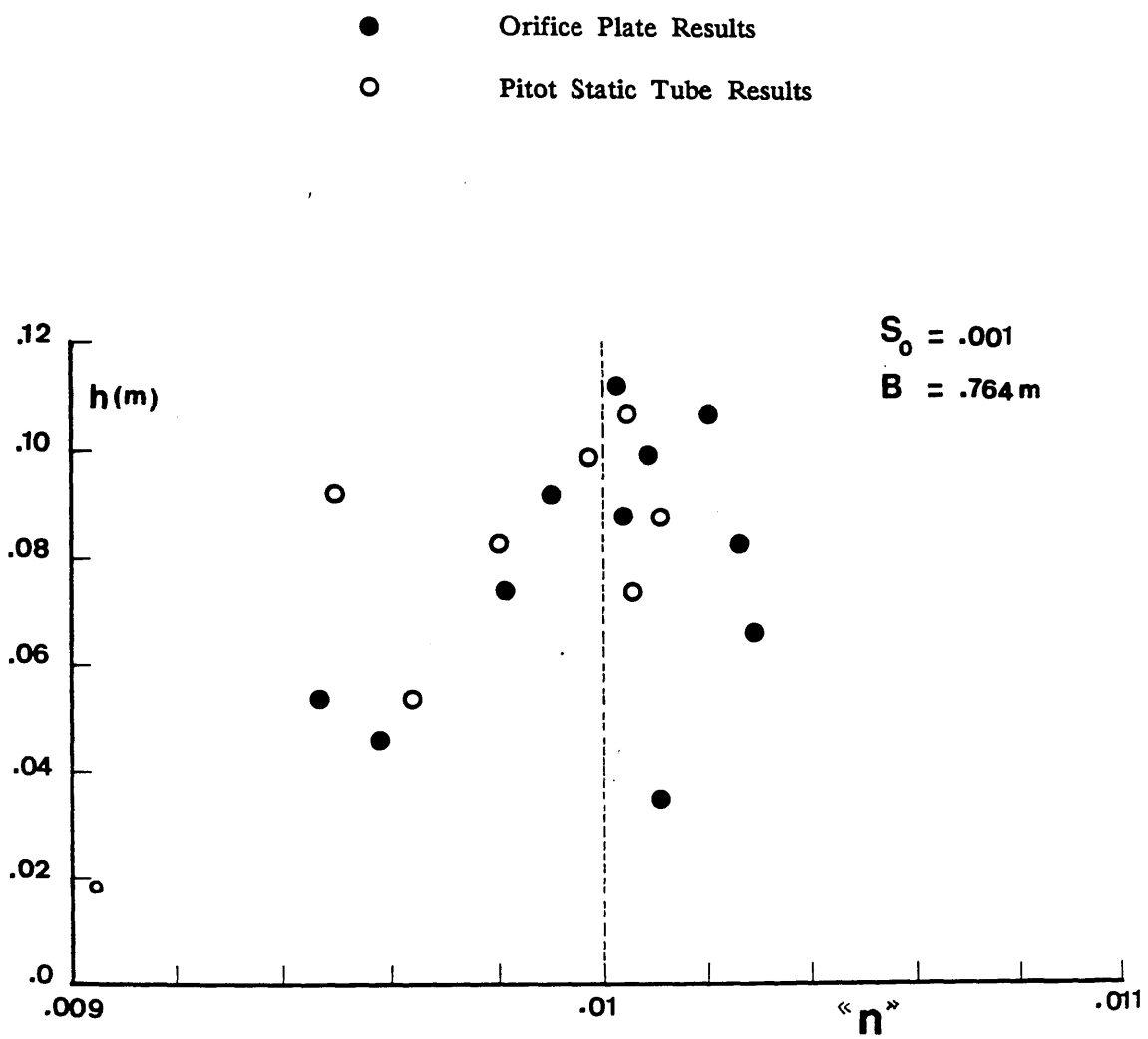

FIG.(5.4) – Coefficient of Roughness (Manning's " n ") for the Material of the Flume (after Ervine et al (1989))

CV ≡ Control Valve
IT ≡ Inlet Tank
OP ≡ Orifice Plate
P ≡ Pump
ST ≡ Sump Tank

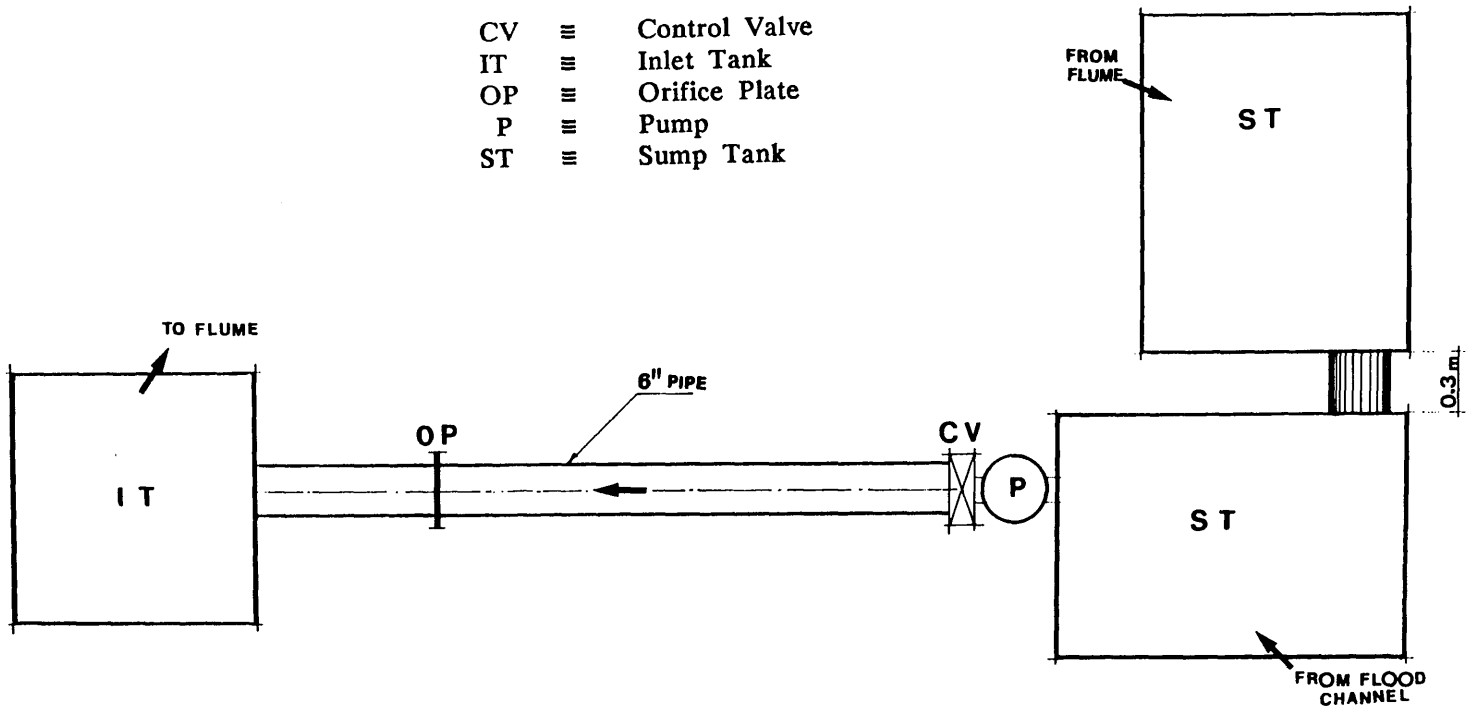

FIG.(5.5) – Water Supply System

TABLE (5.2) – Instrumentation

	Instrument	Use
–	Pitot Static Tube	(1) Measurement of the longitudinal flow velocities throughout the bend longitudinally and transversally. (2) Calibration of the Orifice Plate.
–	Orifice Plate	Measurement of the flow discharge in the flume.
–	" V– notch " Tank	Measurement of the flow taken by the flood relief channel.
–	Angle Probe & Angle Measurement Transceducer	Measurement of the deviation angles of the horizontal resultant velocities.
–	Pointer Gauge	Measurement of the water depth and the bed level of the flume.

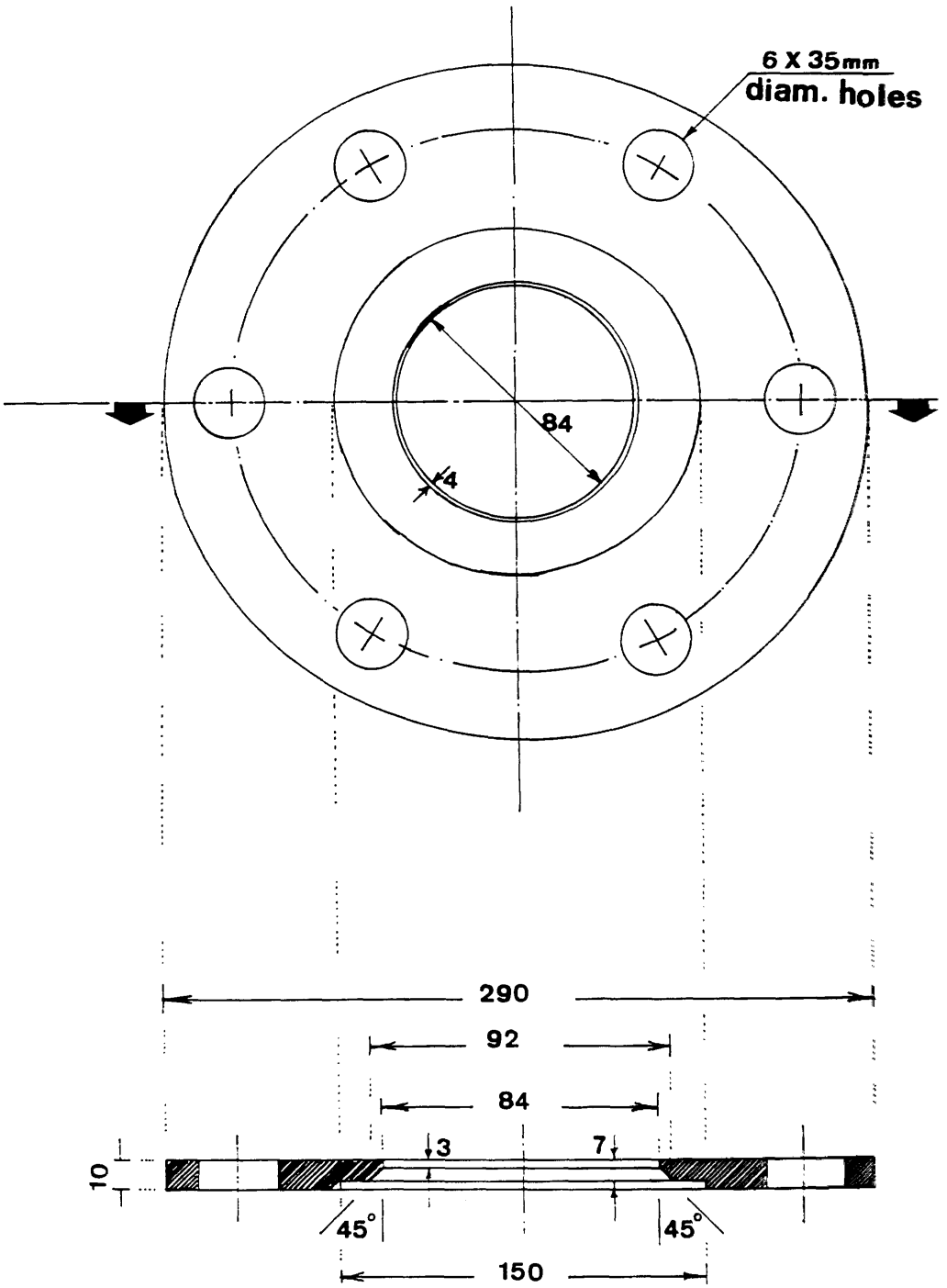

FIG.(5.6) – Details of the Orifice Plate
(dimensions are in " mm ")

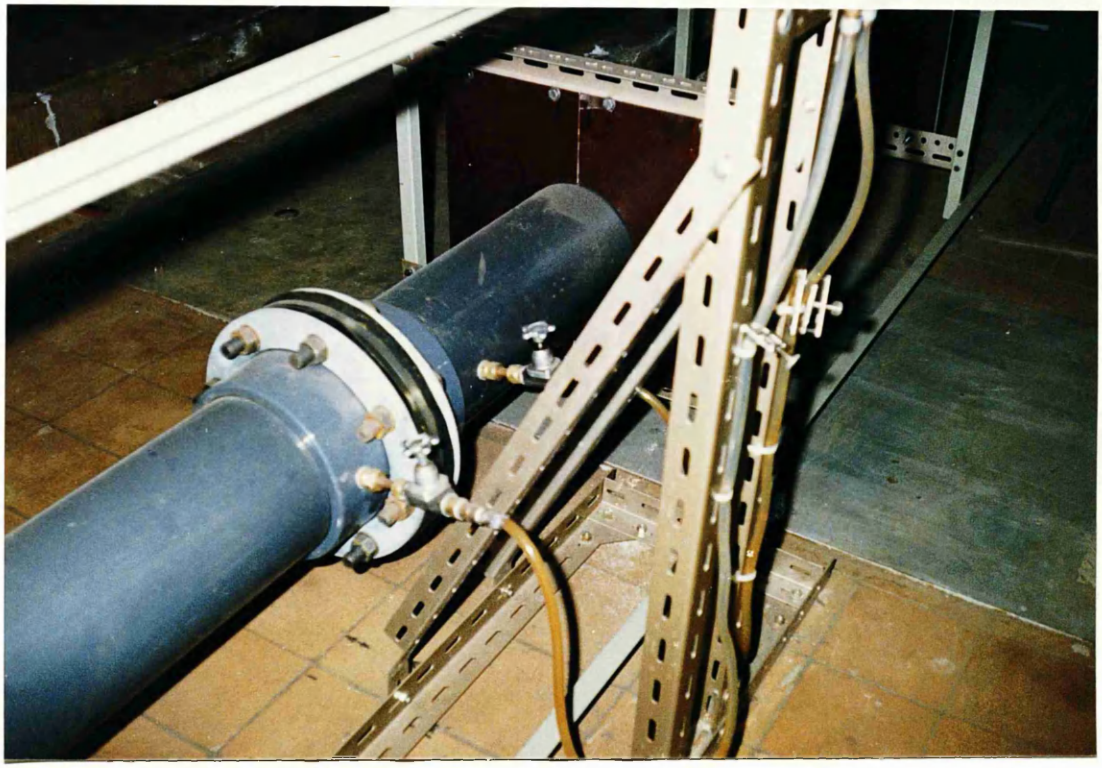

PLATE (5.2) – Arrangement of the Orifice Plate with D and D/2 Tappings

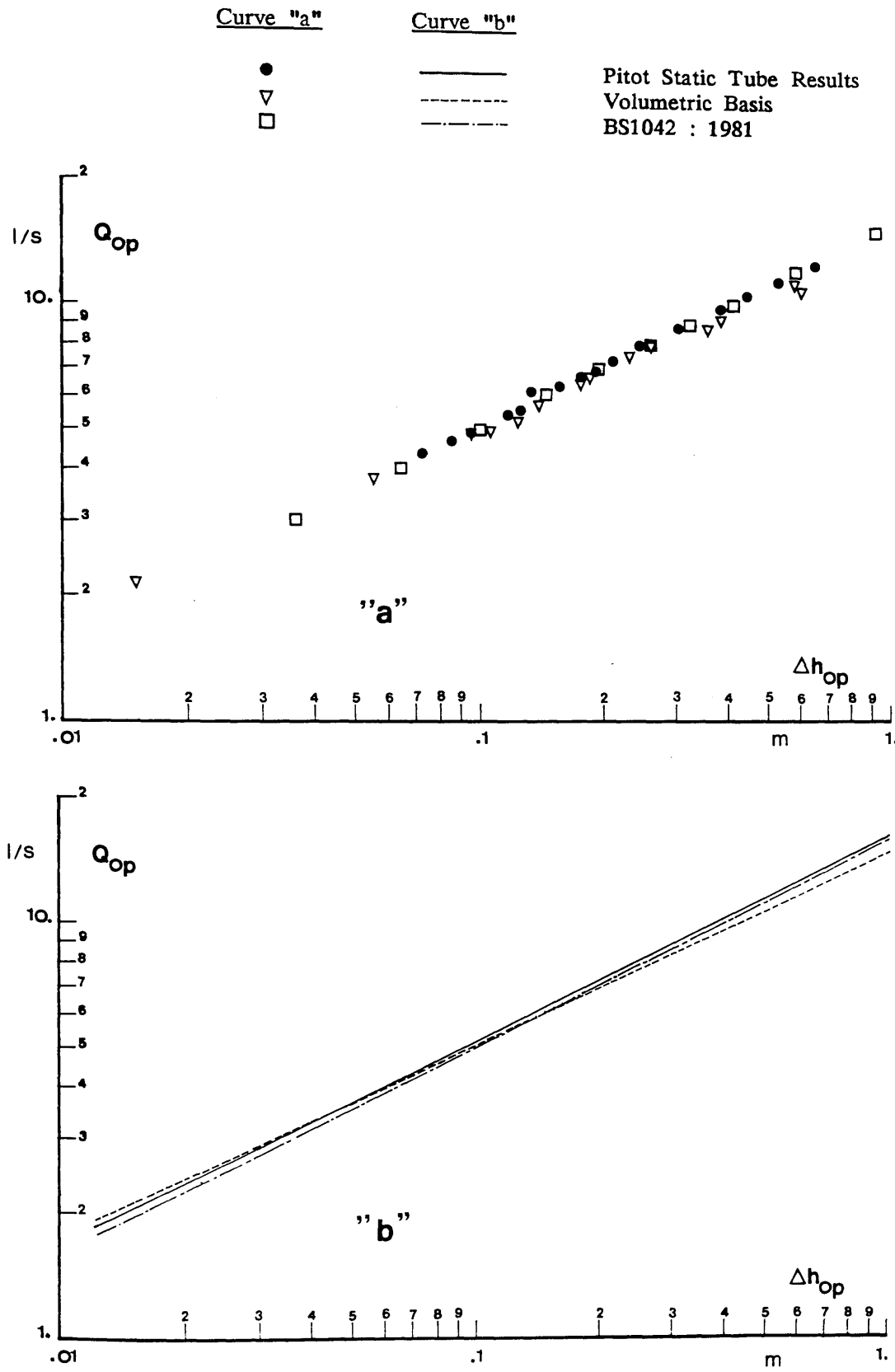

FIG.(5.7) – Calibration of the Orifice Plate
(a) Experimental and Theoretical Values
(b) Best Fitted Lines

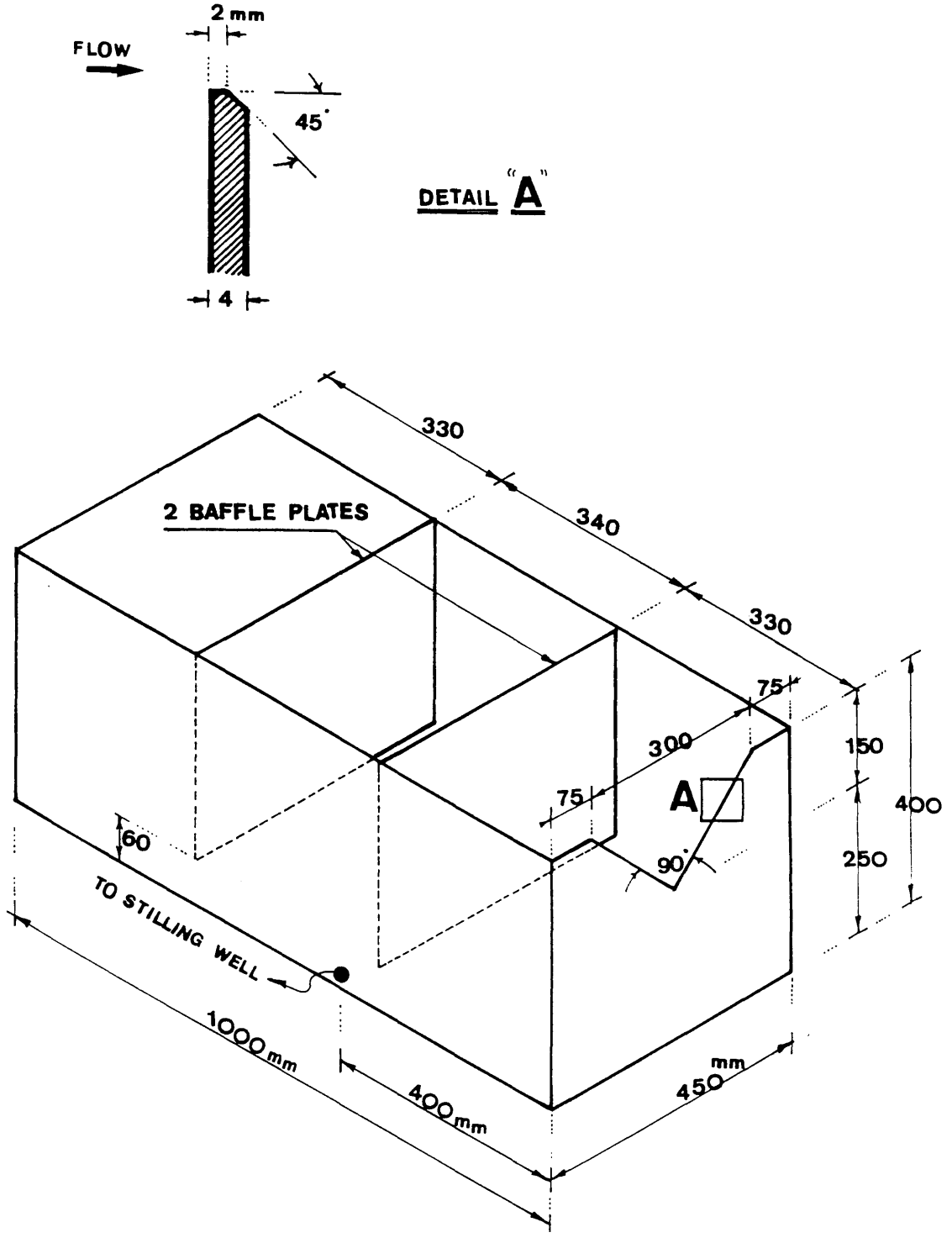

FIG.(5.8) – Details of the " V– notch " Tank

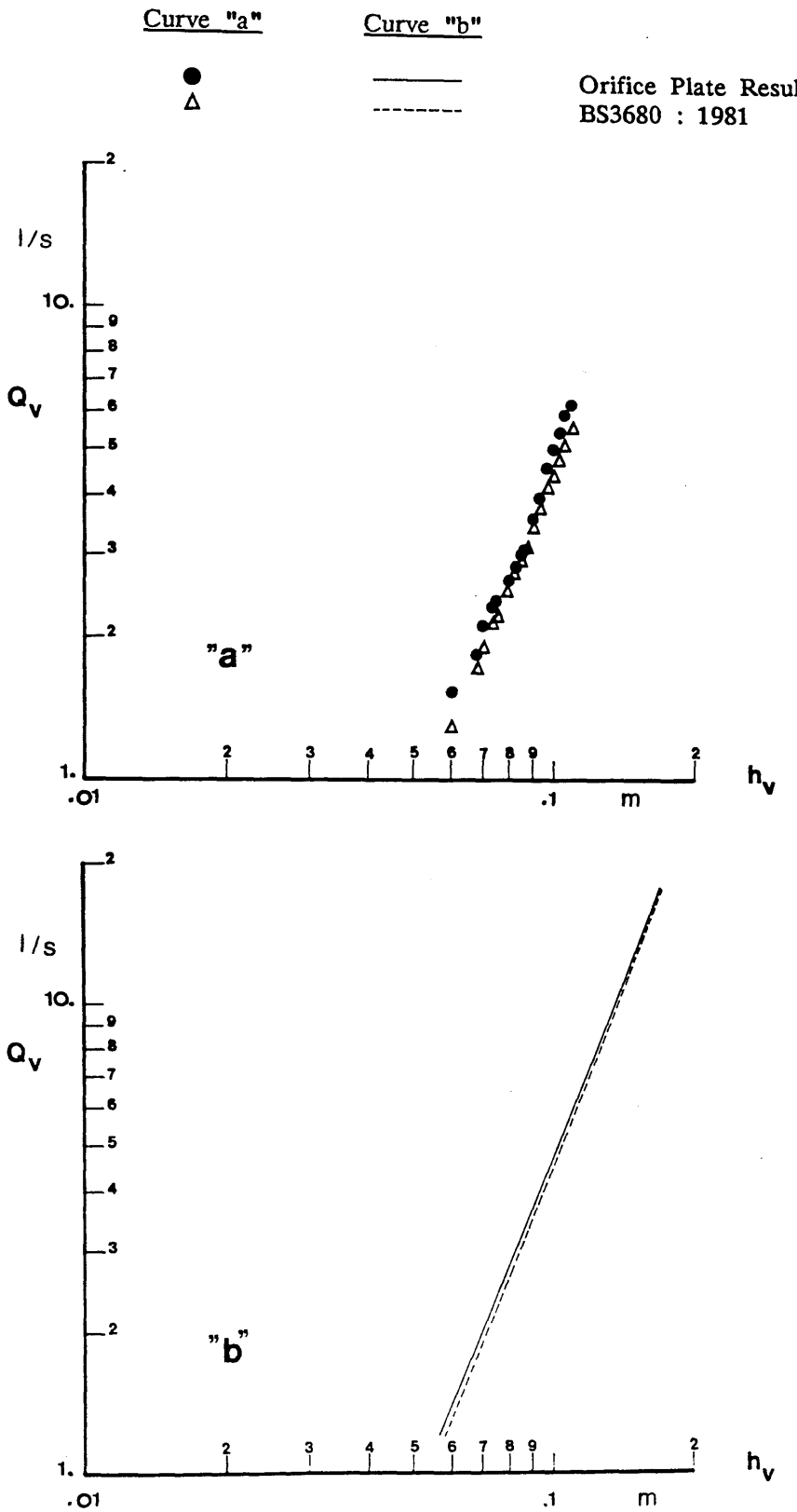

FIG.(5.9) – Calibration of the " V– notch "
(a) Experimental and Theoretical Values
(b) Best Fitted Lines

AMT	≡	Angle Measurement Transceducer
AP	≡	Angle Probe
CC	≡	Carrier Card
O/P	≡	Output
PS	≡	Power Supply
SC	≡	Shielded Cable
SW	≡	Software
TP	≡	Termination Panel

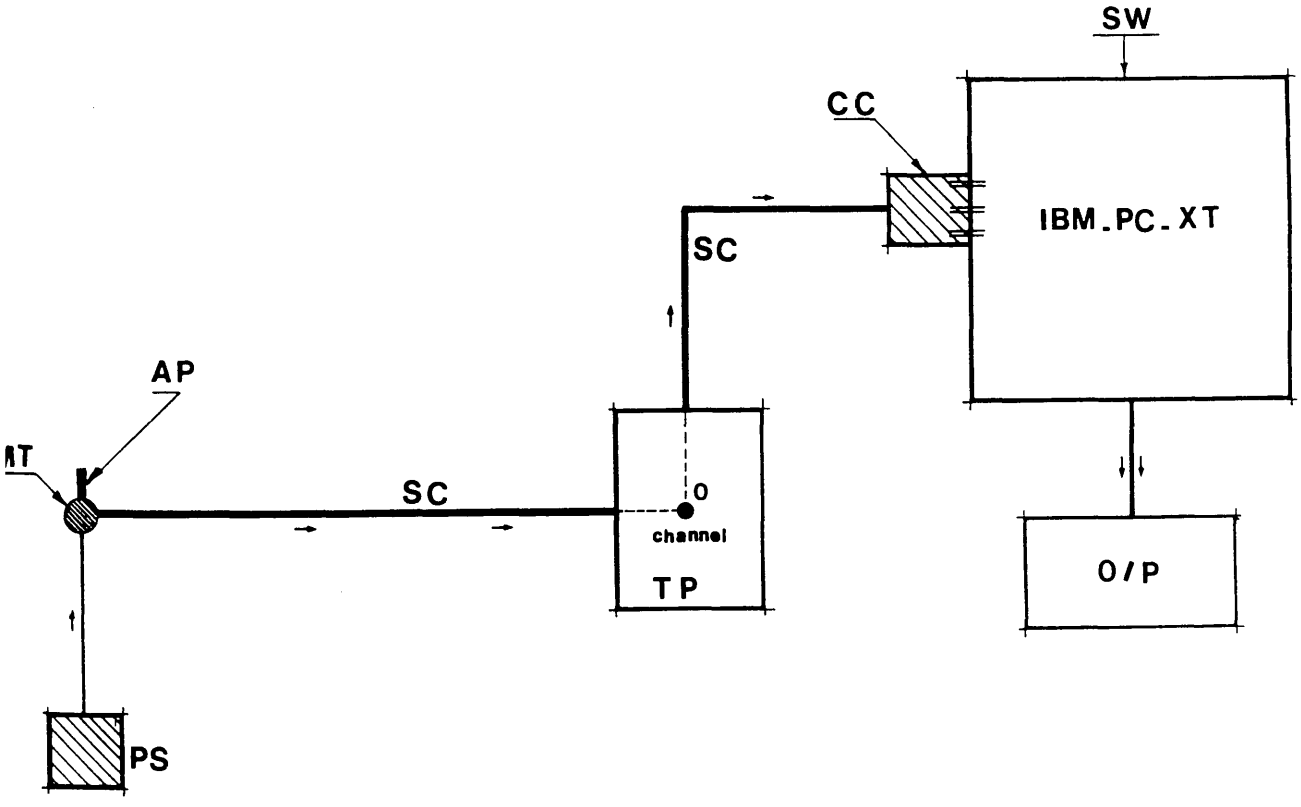

FIG.(5.10) – Schematic Diagram for the Arrangement of the Deviation Angles Measurements

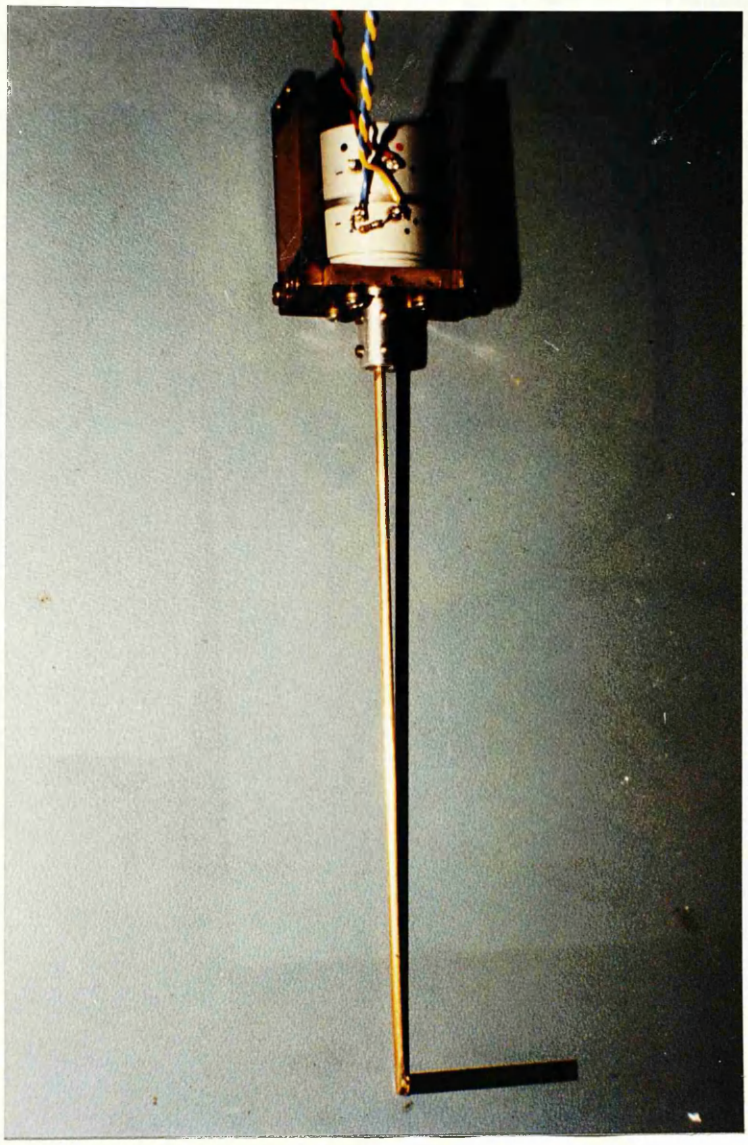

PLATE (5.3) – Angle Probe

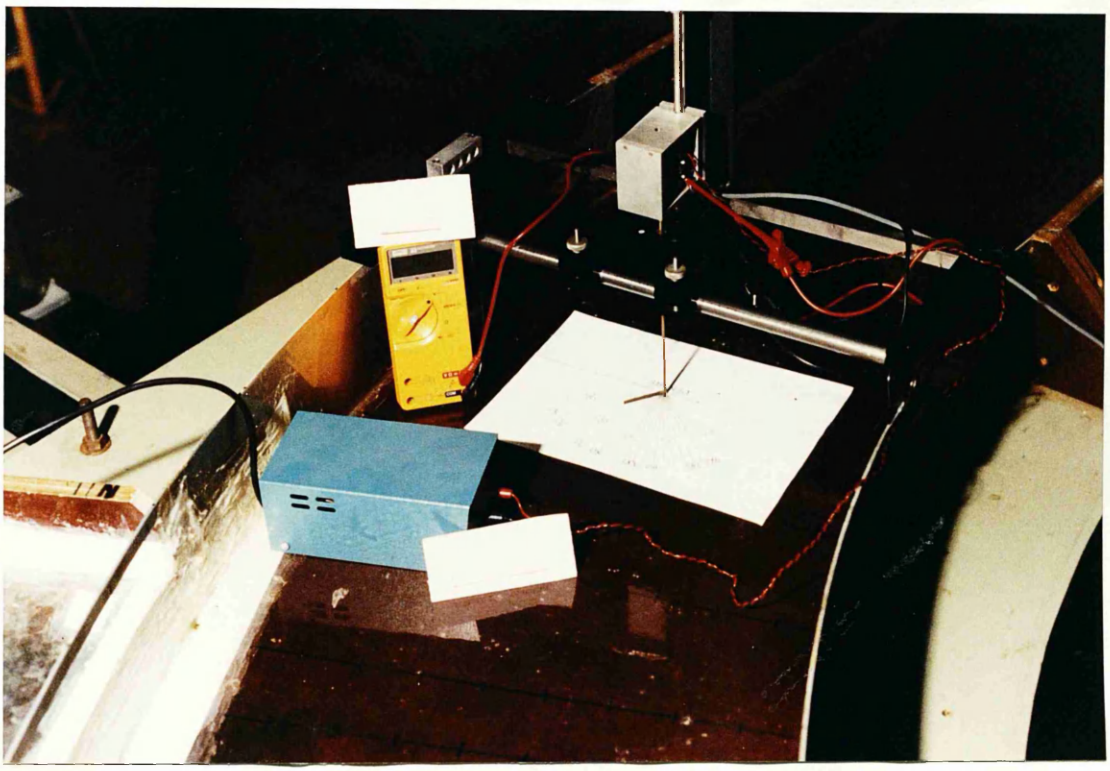

PLATE (5.4) – Arrangement of the Angle Probe Calibration

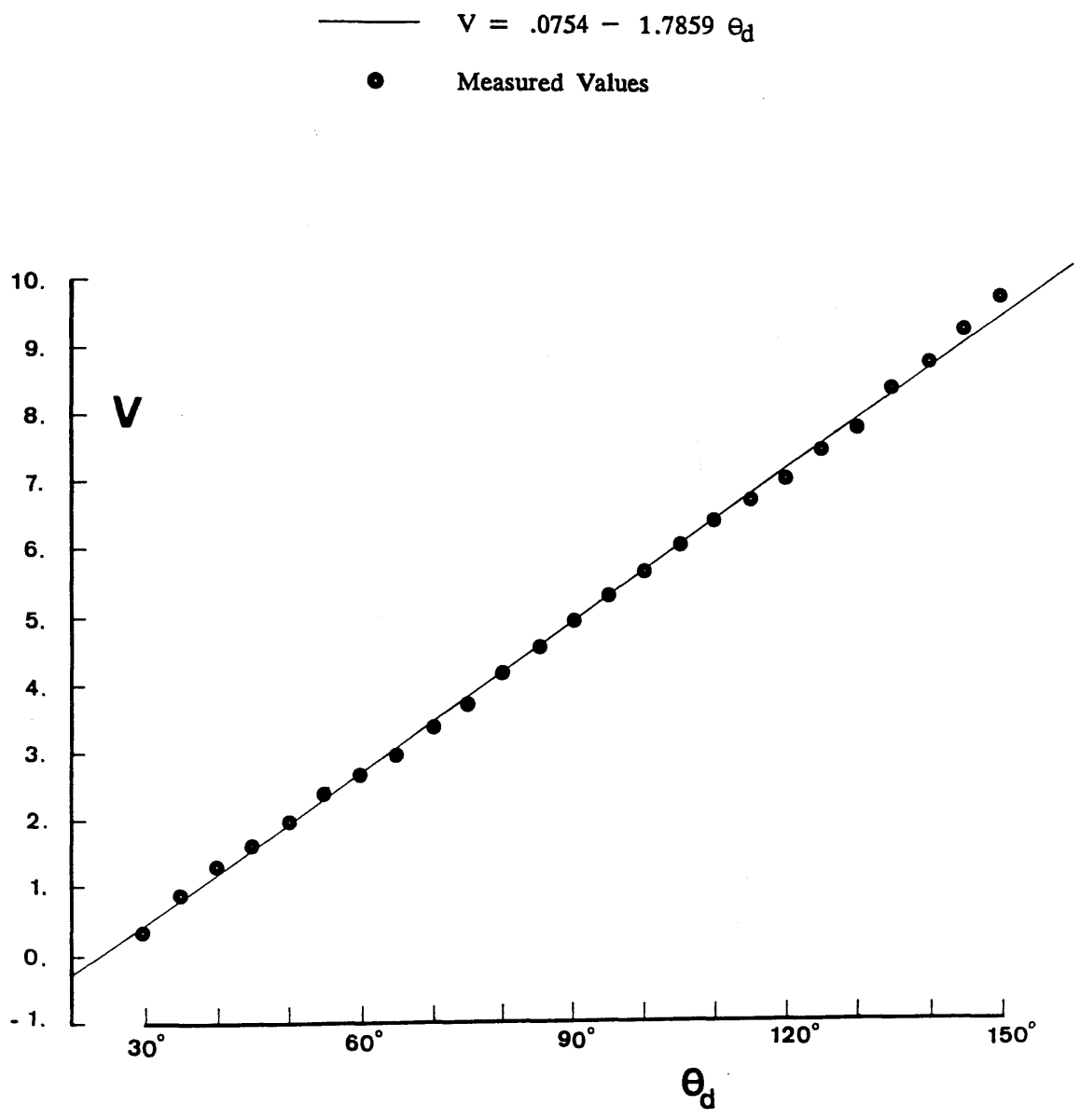

FIG.(5.11) – Calibration Curve of the Angle Probe

+ Measuring Location

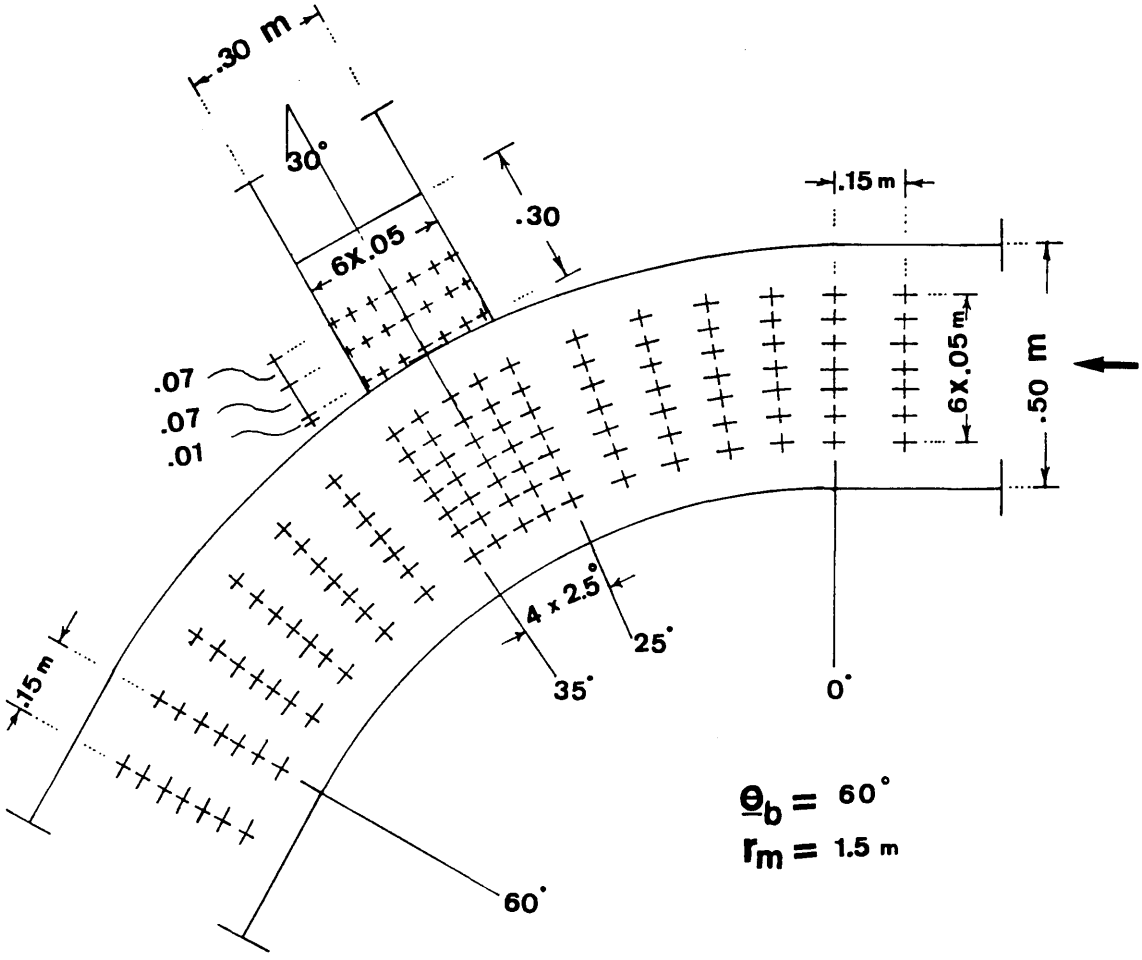

FIG.(5.12) – Measuring Locations for the Water Surface Profiles

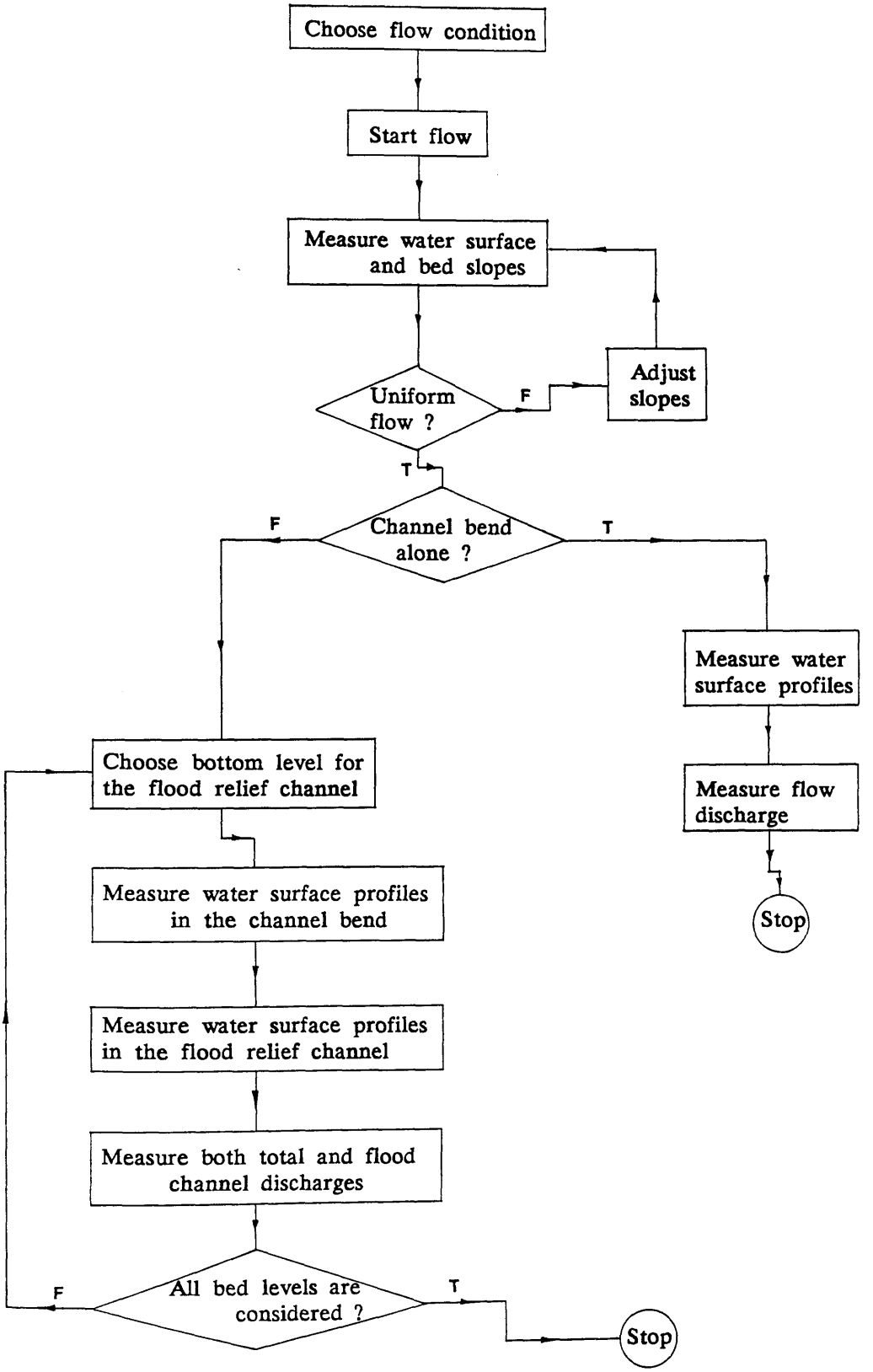

FIG.(5.13) – Experimental Procedure for Measurements of Water Surface Profiles

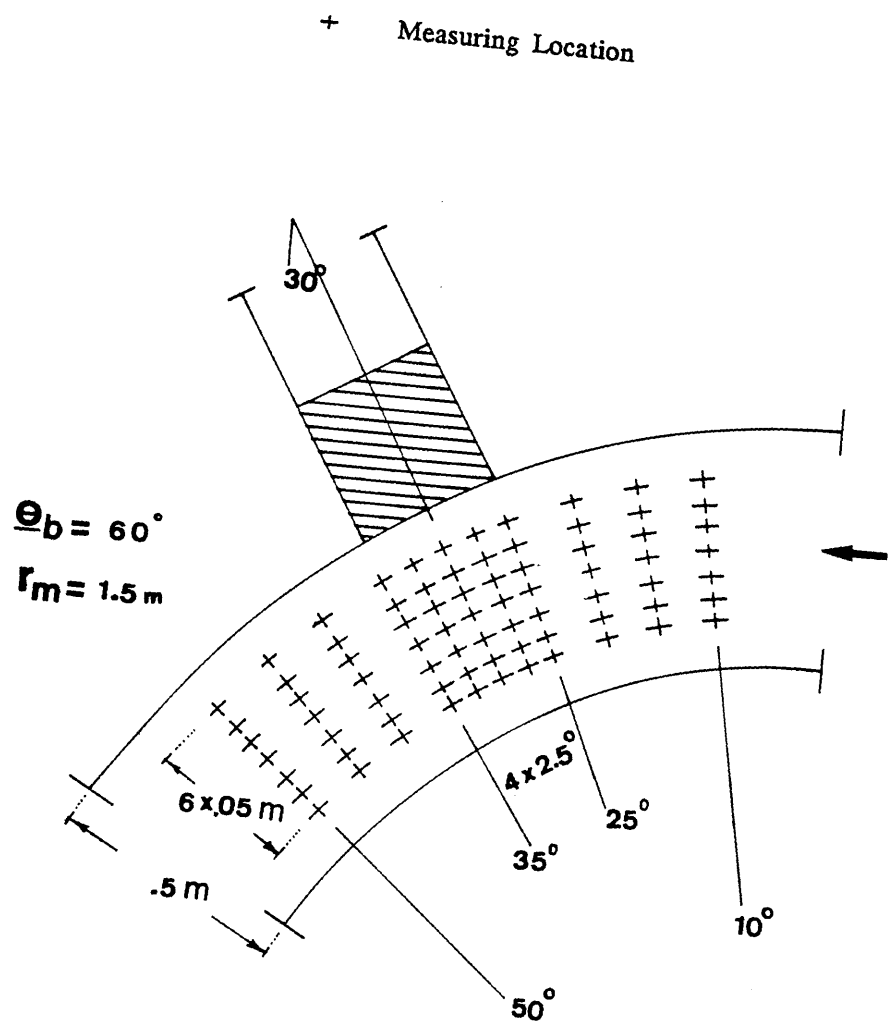

FIG.(5.14) – Measuring Locations for the Deviation Angles and Longitudinal Velocities

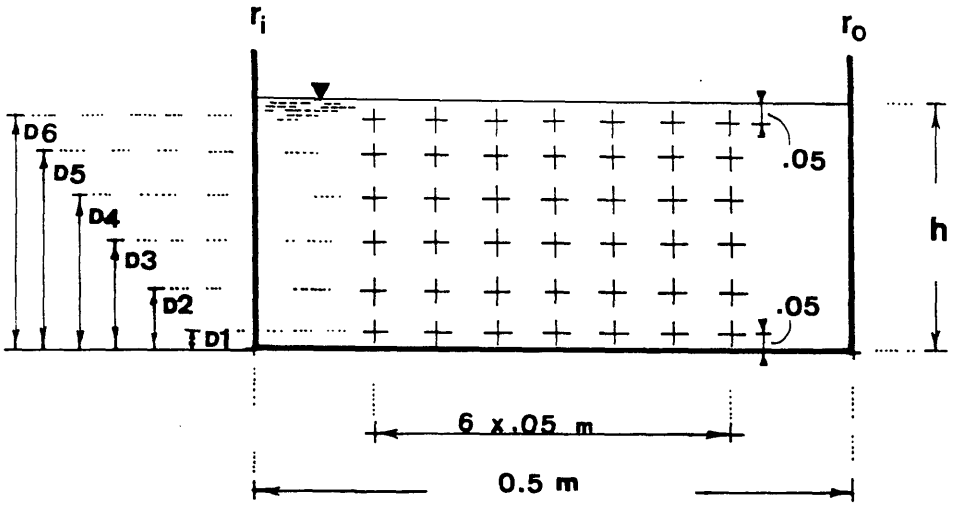

Test Run	h mm	D1 mm	D2 mm	D3 mm	D4 mm	D5 mm	D6 mm
BA1 – BV1**	50	5	15	25	35	45	—
BA2 – BV2**	60	5	15	25	35	45	55
A1 – V1	55.5	5	10	20	30	40	50
A2 – V2	70	5	15	30	40	55	65
A3 – V3	60	5	15	25	35	45	55
A4 – V4	70	5	15	30	45	55	65
A5 – V5	80	5	20	35	45	60	75

** – test run for the case of a channel bend without the intersection

FIG.(5.15) – Measuring Positions in the Bend Channel Cross Section

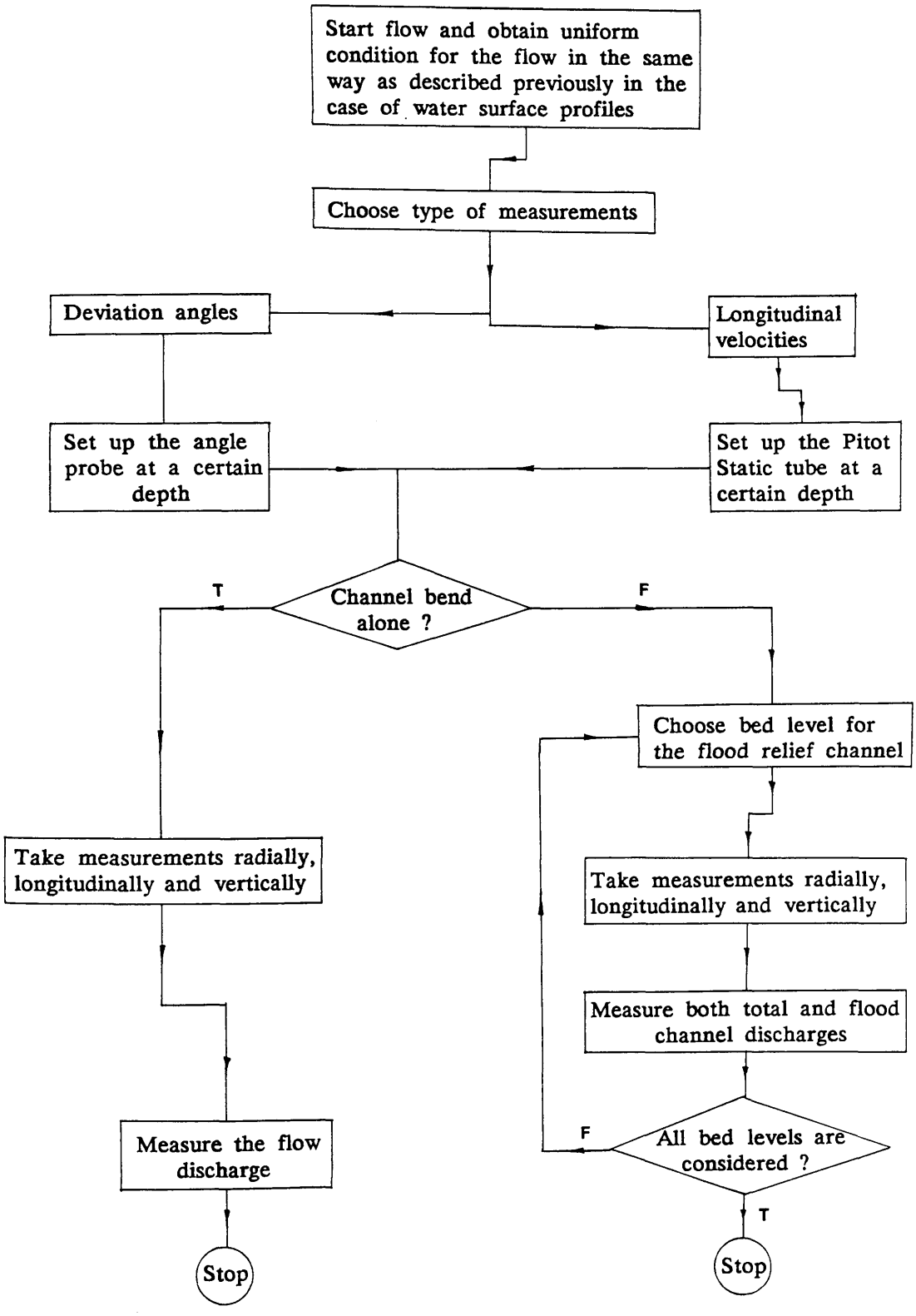

FIG.(5.16) – Experimental Procedure for Measurements of Deviation Angles and Longitudinal Velocities

CHAPTER VI

FLOW BEHAVIOUR IN A GENTLE WIDE CHANNEL BEND

CHAPTER VI

FLOW BEHAVIOUR IN A GENTLE WIDE CHANNEL BEND

(6.1) INTRODUCTION

In this Chapter, the analysis of the flow around a gentle wide channel bend will be given. In general, the analysis follows essentially the main conclusions as reported in previous investigations of curved channel flows. Under the following headings, the characteristics of the flow in a channel bend will be discussed:

- Water surface profiles.
- Distribution of depth– averaged velocities.
- Vertical distribution of longitudinal velocities.
- Secondary currents.

The flow conditions and the physical parameters of the seven test runs used for water surface profiles measurements are shown in Table (6.1). These test runs were chosen carefully to cover different flow conditions (i.e. different discharges) and different flow geometries (i.e. different B/h and h/r_m ratios).

Based on the satisfactory independent calibration of the mathematical model by data available in the literature, as given in Chapter III, two test runs for flow

velocities were considered to be sufficient for the study of their behaviour. In these test runs, both the longitudinal velocity component and local deviation angle were measured at the same flow condition and the same flow geometry. Table (6.2) gives the two test runs used for flow velocities measurements.

A feature of all nine test runs was that no distinct separation zone formed along the inner bank of the bend. This can be explained in terms of the combined effect of the bend tightness ratio r_m/B and the Froude number F_r . As previously found by Rozovskii (1961) and Leeder et al (1975) in both laboratory and in the field, the smaller the values of r_m/B and F_r , the less likely is the formation of a separation zone. In the present series of experiments " $r_m/B = 3.0$ " and " $F_r \leq 0.288$ " .

Under each of the headings, detailed comparisons will be made between the experimental results and those predicted by use of the mathematical model described in Chapter III .

(6.2) WATER SURFACE PROFILES

In all seven test runs, the observed longitudinal and radial water surface profiles along the channel bend were in close agreement with those predicted by the mathematical model, thus, confirming the validity of the assumptions of the depth–averaged model described in section (3.7), Chapter III. Typical results of the comparisons for radial water profiles are shown in Figures (6.1), (6.2), (6.3), and (6.4) for test runs WB1, WB3, WB5 and WB7 respectively. While given in Figures (6.5) and (6.6) are comparisons for the longitudinal water surface profiles for test

runs WB1 and WB7 respectively.

Examination of the Figures leads to the following conclusions :

(1) In all experiments, the water surface upstream of the bend was almost uniform , implying that the bend had no significant effect on the water surface in the straight reach upstream of the bend. This is in agreement with the results obtained by Yen et al (1971), Kalkwijk et al (1980) and Tamai et al (1983a), (1983b).

(2) As soon as the flow enters the bend, a superelevation effect in the water surface becomes noticable resulting in lower depths at the inner bank compared with those at the outer bank. This ,in turn, will result in a depth–averaged velocity profile with maximum values at the inner bank and a gradual decrease in velocity towards the outer bank (which is known as the Bernoulli effect on the velocity field).

(3) From $\Theta_b = 0° \rightarrow 20°$ (the first third of the bend), the transverse water surface gradient gradually increases due to the increase of the centrifugal effect.

(4) From $\Theta_b = 20° \rightarrow 35°$ (i.e. approximately the middle third of the bend), the superelevation effect in the water surface remains almost constant. Beyond this region, the superelevation starts to decrease. Similar observations were recorded by Yen et al (1971), Sarmah (1977) and Tamai et al (1983a) and (1983b).

(5) In the last third of the bend (i.e. from $\Theta_b = 45° \rightarrow 60°$), the radial water surface slope reduces rapidly passing through zero with a tend ncy to a reverse gradient at the bend exit.

(6) Beyond the bend, the reverse superelevation continues. It can be seen that the greatest discrepancies between the experimental and predicted results occur in this region. The probable reason for this is the backwater effect produced by the controlling sluice gate at the end of the experimental channel.

(6.3) DISTRIBUTION OF DEPTH– AVERAGED VELOCITIES

Figures (6.7) and (6.8) show the comparisons between the predicted and measured values of depth– averaged velocities for test runs BA1– BV1 and BA2– BV2 respectively. These have been plotted in the form of velocity profiles. Study of the profiles leads to the following discussion:

(1) In general, the Figures show very good agreement between the predicted and the experimental values.

(2) In order to demonstrate the effect of the secondary currents on the depth – averaged velocities, the theoretical profiles were plotted in two forms. One profile for $\gamma \neq 0$ as shown by the solid lines and the other for $\gamma = 0$ as shown by the dashed lines. The factor γ represents the secondary flow convection factor which simulates the effect of the radial exchange of the flow momentum (see equation (3.119), section (3.7), Chapter III). In the theoretical profiles, disregarding the influence of the secondary flow leads to the prediction of higher velocities near the inner bank and to lower velocities at the outer bank. Similar conclusions have been reported by De Vriend (1977) and Kalkwijk et al (1980).

Several investigators (see e.g. Einstein et al (1954), Ippen et al (1962), Fox et al (1968), De Vriend (1981) and Odgaard (1984)) have shown that the development of secondary currents influence the distribution of the depth–averaged velocities causing an outward momentum transport of flow and a gradual outward shifting of the velocity maxima towards the outer bank. The interaction between the main (longitudinal) and secondary flows becomes appreciable as soon as the secondary currents are at or near the fully developed stage. Consequently, the secondary flow convection term $(\gamma/r^2)\ \partial_r(h^2\ r\ u_m^2)$ (in equation (3.119), section (3.7), Chapter III) becomes comparable to the order of magnitude of the other terms (namely, the main flow convection, longitudinal surface slope and bed friction terms). This condition becomes more pronounced as the channel bend becomes more strongly curved. In such cases the outward shifting of the maximum velocity is the dominant feature (see Rozovskii (1961) and Leschziner et al (1979)).

In the present study both the theoretical and the experimental results show no tendency for the maximum velocity to shift towards the outer bank. The main reason for this is the short length of the bend relative to the water depths tested. It has been shown, in the mathematical formulation, that a characteristic bend length of "1.88 C' h" is required for the secondary currents to develop their full strength (see equation (3.169), section (3.9.2), Chapter III). This characteristic length corresponded to bend angles of $\simeq 95^\circ$ for test run BA1–BV1 and $\simeq 115^\circ$ for test run BA2–BV2. It is therefore obvious that the 60° channel bend tested is insufficient for the secondary currents to have a considerable effect on the distribution of the depth–averaged velocities. Nevertheless, a small loss of inward skewness can be observed in the profiles in the second half of the bend.

(3) Previous studies by, for example, Mockmore (1944), Shukry (1949) Ippen

et al (1962), Rozovskii (1961) and Hager (1984) have concluded that the flow in a channel bend can be described by means of an irrotational potential vortex theory. These irrotional flows result from the balance between the main flow inertia and the longitudinal water surface slope that arises from the growth of the superelevation of the water surface along the bend. Hence, it was considered worthwhile to try to compare the results obtained from this study (theoretically and experimentally) with the theory of potential vortex flows.

Fig.(6.9) illustrates the comparison of the depth–averaged velocities along the channel with the corresponding distribution calculated on the basis of the potential vortex formula "$u_m \cdot r = C_p$", where C_p is the value of the circulation constant. The constant C_p can be obtained from the expression "$C_p = u_{mt} \cdot r_t$", where u_{mt} is the mean velocity in the channel cross section (calculated on the basis of the rate of flow and mean flow depth) and r_t is the radius of curvature where $u_m = u_{mt}$.

The comparisons show that the results obtained from the potential vortex theory are in a good agreement with the computed and the observed results in the first half of the bend but follows a totally different trend in the second half of the bend as the secondary currents becomes effective. Therefore, any estimates based on the simpler potential vortex theory may only be used as a rough guide to the depth–averaged velocity distribution in the initial section of a gentle wide channel bend.

(4) Finally, it is interesting to calculate the eccentricity of the flow volume flux from the channel centreline based on the depth–averaged velocity distributions shown in Figures (6.7) and (6.8). The theoretical and experimental values of flow volume flux were obtained by calculating the first moment of area of the volume flux $(\bar{U}.\bar{dA}). \bar{R}$ (where $\bar{U}$ is the point velocity vector of the flow, $\bar{dA}$ is the flow area vector and $\bar{R}$ is the bend radius vector) around the inner bank. The values obtained

are shown in Fig.(6.10) in which the line of the flow volume flux may be interpreted as the **optimum flow path** around the channel bend. It can be seen that the eccentricity of the centre of the volume flux is relatively uniform along the bend path with the optimum flow path being positioned 0.1 → 0.12 times the channel width on the outer side of the channel centreline. Although the departure of the centre of volume flux is relatively small in the present study, as could be expected for a gentle wide channel bend, much more significant depatures could be anticipated in cases of strongly curved channel bends and river meanders, where the radial variations of the flow are more pronounced.

(6.4) VERTICAL DISTRIBUTION OF LONGITUDINAL VELOCITIES

The vertical profiles of the longitudinal velocities for the two test runs are shown in Figures (6.11) and (6.12). The theoretical profiles shown are based on the logarithmic distribution and it can be seen that the observed profiles are in reasonable agreement with this distribution.

The following points arise from detailed study of the Figures :

(1) In the first half of the bend (i.e. from $\Theta_b = 0^\circ \rightarrow 30^\circ$), the maximum velocity occurs at the water surface but as the effect of the secondary convection terms grow and accumulate, the velocity maxima tend to be suppressed below the water surface. This becomes noticable in the second half of the bend. Similar findings have been reported previously by several authors e.g. Rozovskii (1961), De Vriend (1977), (1981), (1983), Tamai et al (1983a), (1983b) and Damaskinidou–

Georgiadou et al (1986).

(2) In general, the comparisons between the theoretical and experimental values are good. However, it seems that the theoretical profiles are slightly overpredicted. As may be seen from the Figures, the comparisons are fairly good in central region of the channel cross section but become less accurate near the inner and the outer banks. It is thought that this difference can be attributed to the wall effect, where the vertical velocity component dominates. These findings tend to confirm those of Rozovskii (1961) and De Vriend (1977) who found the wall effect was very small for shallow bends (i.e. these with a ratio of mean depth to mean radius $h/r_m \leq .05$). The h/r_m ratio in the present series of tests was in the range of $0.033 \rightarrow 0.04$.

(3) It may also be seen that the assumption of the logarithmic distribution of the longitudinal velocity component is more valid in the remaining 80−90% of the flow depth than in the lower 10−20%. This is in agreement with results reported by Engelund (1974) and Hussein et al (1986). Despite this and the fact that it gives infinite velocity at the channel bed, assumption of the logarithmic velocity distribution has been extensivly used by previous investigators (see e.g. Rozovskii (1961), Bouwmeester (1972), Nouh et al (1979), Kikkawa at al (1980), Chang (1983), (1985) and Hussein et al (1986)). Other distributions have been proposed, e.g. Engelund (1974) suggested that the parabolic law in the lower 10−20% of the flow depth was more satisfactory and Bendegom (1947), Zimmermann et al (1978) and Ascania et al (1983) employed the power law in modelling the vertical distribution of the longitudinal velocity component. However, Anwar (1983) and Salleh (1985) indicated that none of these distributions was realistic for modelling the distribution of the velocity along a vertical because of the secondary circulation which tends to produce instability in the vertical profile of the longitudinal velocities.

The results obtained in the present study are thought to support the use of the logarithmic distribution in describing the vertical profiles of the longitudinal velocities. Although it has to be accepted that in the lower 10–20% of the flow depth, the velocities are slightly overpredicted.

(6.5) SECONDARY CURRENTS

The principal features of the transverse flow observed in the present study are essentially the same as observed in previous studies of curved channel flows by e.g. Rozovskii (1961), Fox et al (1968), Engulend (1974), Kikkawa et al (1976), De Vriend (1977), (1981), (1983), Zimmermann et al (1978), Kalkwijk et al (1980), Bathurst et al (1977), (1979), Odgaard (1982), (1984), Thorne et al (1983) and others. The analysis of the secondary currents will be addressed under the following headings :

6.5.1 Deviation angles of horizontal resultant velocities.

6.5.2 Vertical distribution of radial velocities.

6.5.3 Growth of secondary currents.

(6.5.1) Deviation Angles of Horizontal Resultant Velocities

Figures (6.13) and (6.14) illustrate comparisons between the experimental and theoretical values of the horizontal deviation angles for test runs BA1– BV1 and BA2– BV2 respectively.

From these comparisons, the following points of discussion arise:

(1) For the portion of the bend considered (i.e. from $\theta_b = 10^\circ \rightarrow 50^\circ$), the values of the deviation angles increased continually. This indicates that the secondary currents were continuing to develop throughout the bend, i.e. the decaying process of the secondary currents had not become established. If this were required, a channel bend with a larger central angle would be necessary.

(2) Deviation angles near the channel bed were found to increase more rapidly than those near the water surface. This may be attributed to the effect of the bed shear stress which tends to reduce the longitudinal velocity component u_s near the bed, while the radial velocity component u_r keeps virtually the same magnitude. So, the relative magnitude of the velocities "u_r / u_s" is greater near the channel bed than near the water surface. Consequently, deviation angles (where $\theta_d = \tan^{-1} u_r/u_s$) near the channel bed are greater than those near the water surface.

This observation justifies the assumption made in equation (3.69), section (3.5.3), Chapter (III) for wide channel bends with smooth beds. The effect of the radial component of the boundary shear stress "τ_{0r}" on the behaviour of the radial velocity component u_r can be neglected. It also validates the use of the

assumption by previous investigators such as Rozovskii (1961), De Vriend (1976), (1977), Kalkwijk et al (1980) and Damaskinidou– Georgiadou et al (1986).

(3) The horizontal deviation angles may be used to calculate the strength of the secondary currents $\%S_{rs}$. As defined by Shukry (1949), the strength of the secondary currents, within the channel cross section, is the ratio between the secondary and the main flow kinetic energies. This definition can be extended to describe the local strength of the radial velocities in the flow as:

$$\%S_{rs} = [(u_r^2/2g) / (u_s^2/2g)] \times 100 = (\tan \theta_d)^2 \times 100$$

Using the experimental values of the radial velocity component, the average strength of the secondary currents $\%S_{rs}$ along the bend path for both test runs at z/h = 0.1 and 0.9 were calculated. These are shown in Table (6.3). It can be seen that the strength of surface currents (i.e. at z/h = 0.9) is always smaller than that of the bottom currents (i.e. at z/h = 0.1) due to the effect of the bottom shear stress (as described previously in item (2)). With values of $\%S_{rs} \leq 1.84\%$ for test run BA1– BV1 and $\%S_{rs} \leq 2.32\%$ for test run BA2– BV2, the effect of additional energy losses due to bend resistance can be considered minor in gentle wide channel bends. Consequently, the main and effective energy losses are the friction losses.

(4) In general, the comparisons between the computed and the measured values of the horizontal deviation angles are satisfactory. However, the comparisons for test run BA1– BV1 are less satisfactory than those for test run BA2– BV2 especially in the region near the channel bed, where the theoretical values are underpredicted. This discrepancy arises because the bed shear stress (and hence, the

horizontal resultant velocity near bed) vector deviates less from the longitudinal direction in the case of shallower depths (test run BA1 – BV1). Similar findings are reported by De Vriend (1977) and Damaskinidou– Georgiadou et al (1986).

(6.5.2) Vertical Distribution of Radial Velocities

Figures (6.15) and (6.16) show the comparisons between the theoretical predictions and the experimental results of the radial velocity component for test runs BA1 – BV1 and BA2 – BV2 respectively. The following points of discussion arise from examination of these Figures and the data from which they are produced :

(1) In both test runs, in the central region of the channel cross section, one main cell of the secondary circulation was observed. This feature was observed in many previous experimental studies e.g. those of Mockmore (1944), Shukry (1949), Rozovskii (1961), Kikkawa et al (1976), Leschziner et al (1979) and Damaskinidou– Georgiadou et al (1986).

(2) The centre of rotation of the cell can be seen to slowly shift towards the inner bank and downwards until the bend apex is reached (i.e. at $\Theta_b = 30^\circ$). Thereafter, the centre of rotation starts to move gradually towards the outer bank.

(3) In previous laboratory studies involving both turbulent and laminar flows by Einstein et at (1954), Rozovskii (1961), De Vriend (1981) and in field studies by Bathurst et al (1977), (1979), Thorne et al (1979), (1983), a second small counter cell has been observed in the upper part of the flow near the outer bank. This cell was seen to develop shortly after entry to the bend and to persist throughout the bend. The cell which is caused mainly by bank roughness influences the distributions

of both the radial and longitudinal velocity components near the outer bank. In the present study, no evidence of this cell was found either in the mathematical or physical model results. This is not unexpected in the case of the mathematical model, since wall effects were not included in the formulation. Furthermore, in the case of the physical model, despite the fact that measurements could not be taken very close to the channel sides, it is thought that if secondary cells were present these would have become apparent in the results. As can be clearly seen no such cells appear indicating that, for a gentle wide channel bend with " $h/r_m \leq .04$ ", wall effects on the vertical distribution of the radial velocity component are negligible over the **60%** of the cross section tested. It is thought that this is sufficient to validate the assumption of negligible wall effect made in the formulation of the mathematical model, see also Rozovskii (1961), De Vriend (1977) and Kalkwijk et al (1980)).

(4) In general, computed and measured profiles are considered to be in reasonable agreement for both test runs, except at $\theta_b = 10^\circ$. At this section, the development of the secondary currents is just beginning and the bend effect is more to produce a bulk movement of water towards the inner bank (see also Fox et al (1968), Salleh (1985) and Damaskinidou– Georgiadou et al (1986)).

Percentage differences between predicted and measured velocity values have been abstracted from Figures (6.15) and (6.16) and plotted in Figures (6.17) and (6.18) in order to show these differences at different values of z/h and r/r_m ratios. Despite there being no definite trend in the absolute order of magnitude of the errors, careful study of these Figures may lead to the following points:

(1) There is considerable local variation in the secondary currents along the channel bend course.

(2) Although the absolute local order of magnitude of the errors is high, the overall order of magnitude of the error is relatively small.

(6.5.3) Growth of Secondary Currents

Figures (6.19) and (6.20) show the comparison between the predicted and the measured growth of the non–dimensional radial velocity component u_r/u_m along the bend for different values of **z/h** and $\mathbf{r/r_m}$. Examination of these Figures yields the following results:

(1) The agreement between the predicted and measured values is such that the use of the exponential profile in the mathematical model is considered justified. This conforms to conclusions previously reached by Rozovskii (1961), Nouh et al (1979), De Vriend (1976) and Chang (1985), (1986). However, it can be seen that predicted and measured results agree more closely in the first half of the bend.

(2) In the first third of the bend (i.e. from $\Theta_b = 0^\circ \rightarrow 20^\circ$), the predicted growth of the currents across the bend width is almost uniform. Beyond this angle, the growth of the currents located in the outer half of the bend is faster than that of the currents located in the inner half. This can be attributed to the increase of the outward momentum transport in the flow (and hence, the increase of the outward shifting of the velocities) towards the outer bank as the secondary currents become more effective.

(3) The predicted growth of the surface currents is slower than the growth of the bottom currents due to the local increase of the strength of the bottom currents than that of the surface ones.

(4) The rate of growth of the secondary currents is directly proportional to the rate of flow.

(6.6) GENERAL REMARKS ON THE ANALYSIS OF BEND FLOW

The foregoing analysis of the different features of the flow in a gentle wide channel bend leads to the following conclusions :

(6.6.1) In general, the comparisons between the predicted profiles and the experimental values show satisfactory agreements, thus, justifying the suggested mathematical model.

(6.6.2) The development of the superelevation at the water surface starts at the bend entrance. Along the bend, the superelevation continues to develop until $\Theta_b = 20^\circ$ is reached. From $\Theta_b = 20^\circ \rightarrow \simeq 35^\circ$, the superelevation remains effectively constant. Beyond $\Theta_b \simeq 35^\circ$, a rapid decrease in the superelevation occurs with a tendency to a reverse effect at the exit from and beyond the bend.

(6.6.3) In the first half of the bend, the effect of the secondary circulation (expressed by the secondary flow convection term) on the horizontal distribution of

the depth–averaged velocity is small compared to the main flow convection, longitudinal water surface gradient and friction terms. While in the second half of the bend, the influence of the secondary currents on the velocity distribution is significant.

(6.6.4) The use of potential vortex theory for describing the flow pattern in a gentle wide channel bend, as previously suggested by many authors, is shown to be inaccurate and should only be used to make quick qualitative estimates.

(6.6.5) The departure of the centre of the flow volume flux from the centreline of the bend is found to be in the range of 10–12% of the channel width towards the outer bank.

(6.6.6) The vertical profiles of the longitudinal velocities are found to be in close agreement with the assumption of logarithmic distribution, confirming its validity as a universal distribution for use in both straight channels and bends.

(6.6.7) Over the central 60% of the channel width, only one cell of the secondary flow is observed throughout the whole length of channel considered (i.e. from 10° to 50° bend angles). Thus, over this width of channel, wall effects can be considered negligible.

(6.6.8) The strength of the secondary currents within the tested flow conditions is found to be $\%S_{rs} \leq 2.32\ \%$. This indicates that, in a gentle wide bend, the additional energy losses due to bend resistance can be considered minor.

(6.6.9) The growth of the secondary currents have been shown to be simulated reasonably well by use of the exponential distribution. It has been shown that the growth of the bottom currents is faster than that of the surface ones. Also, the growth of the currents in the outer half of the bend is higher than the growth of those in the inner half of the bend. In addition, the rate of growth of the secondary currents increases as the flow rate increases.

TABLE (6.1) – Experimental Programme for Measurements of Water Surface Profiles

Test Run	h^* mm	Q l/s	u^{**} m/s	h/r_m	B/h	F_r	R_e
WB1	42	3.89	.185	.028	11.91	.288	6048
WB2	50.5	4.80	.190	.034	9.90	.270	7257
WB3	57	5.56	.195	.038	8.77	.261	8229
WB4	64.5	7.10	.220	.043	7.75	.277	10255
WB5	70	7.00	.200	.047	7.14	.241	9944
WB6	78	7.80	.200	.052	6.41	.229	10810
WB7	79.5	8.35	.210	.053	6.29	.238	11516

* – mean water depth upstream of the channel bend.

** – mean velocity of the flow upstream of the channel bend.

TABLE (6.2) – Experimental Programme for Measurements of LongitudinaL Velocities and Deviation Angles

Test Run	h^* mm	Q l/s	u^{**} m/s	h/r_m	B/h	F_r	R_e
BA1– BV1	50	4.38	.175	.033	10.0	.250	6629
BA2– BV2	60	5.10	.170	.040	8.33	.222	7479

* – mean water depth upstream of the channel bend.

** – mean velocity of the flow upstream of the channel bend.

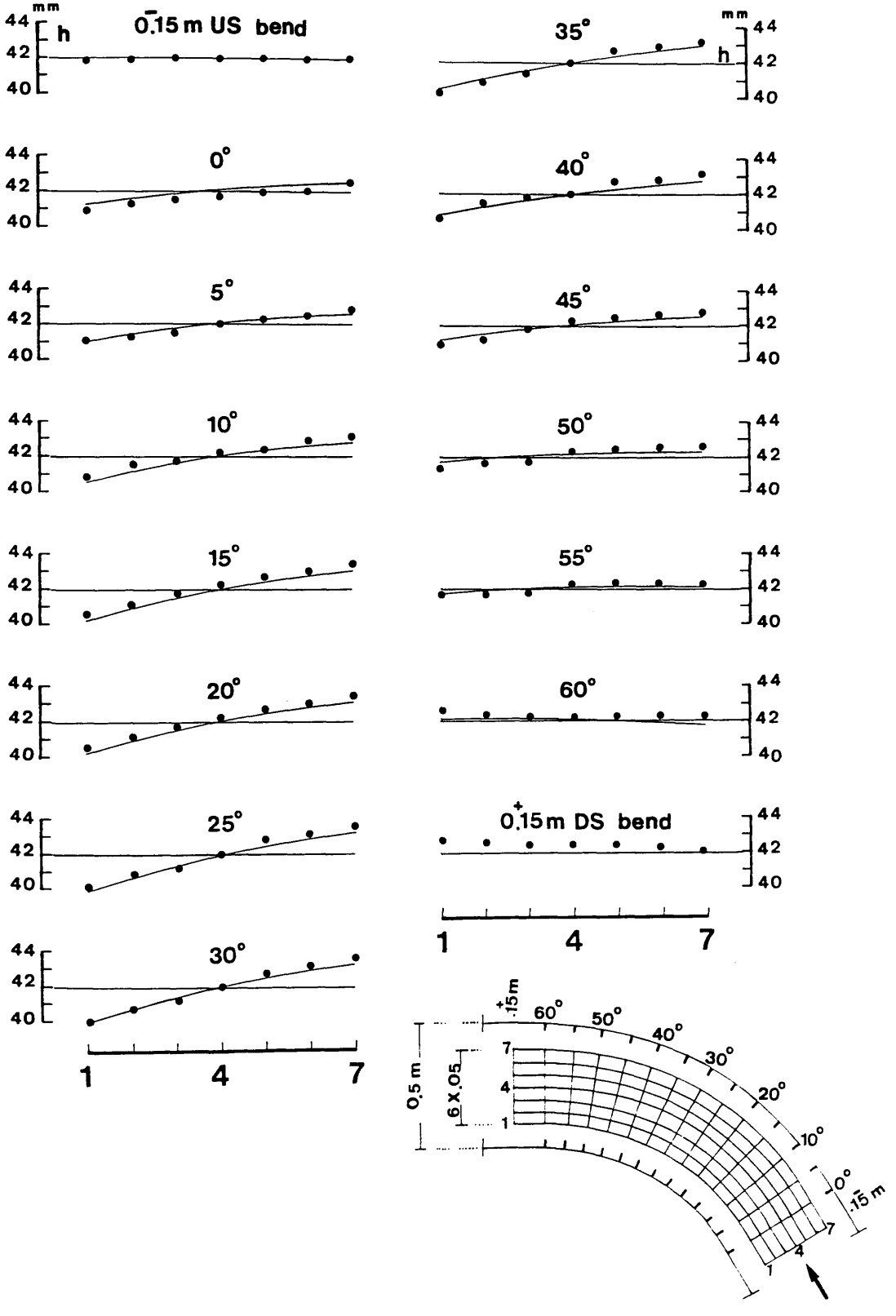

FIG.(6.1) – Comparison between the Predicted and Measured Radial Surface Profiles for Test Run WB1

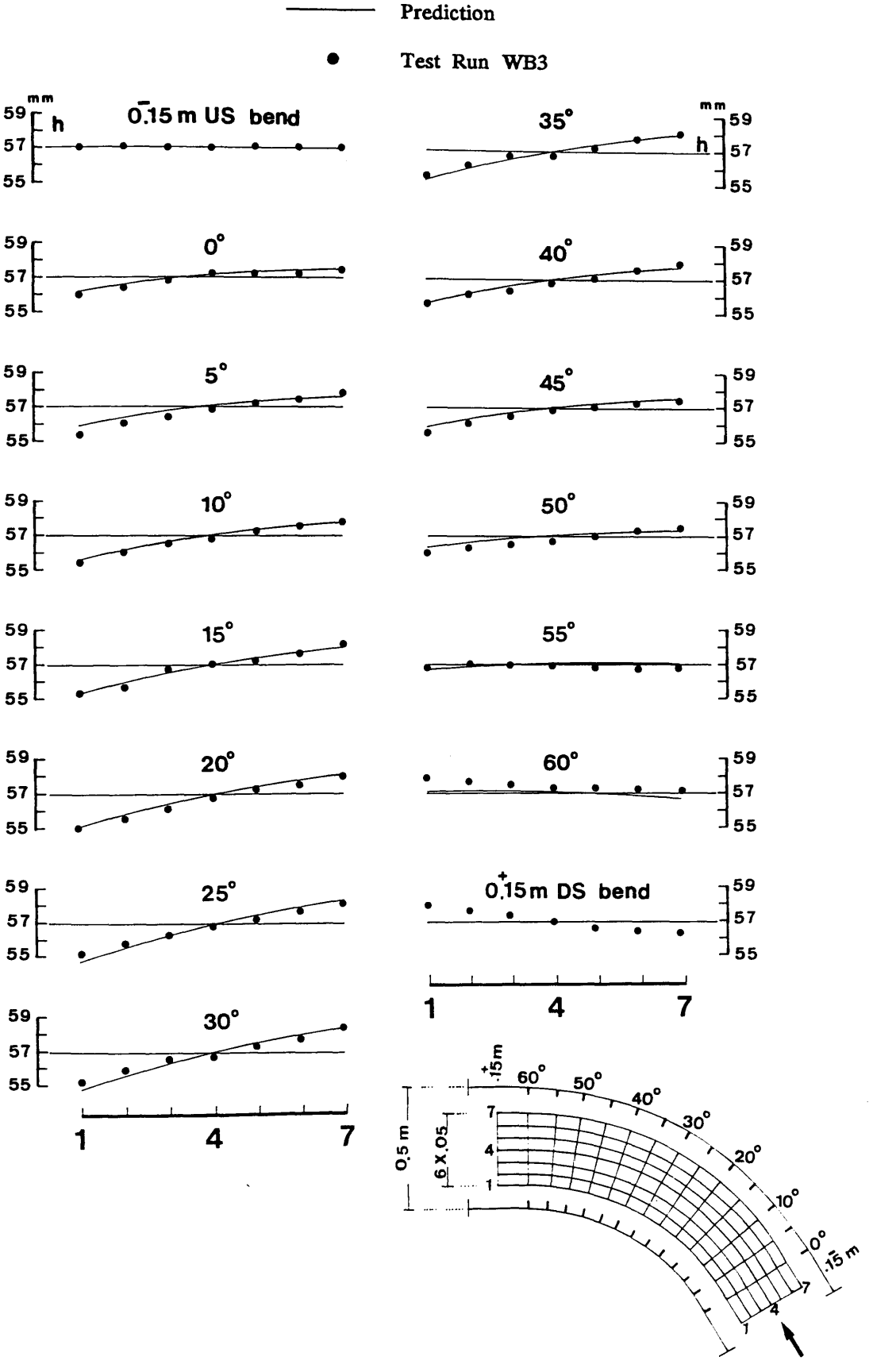

FIG.(6.2) – Comparison between the Predicted and Measured Radial Surface Profiles for Test Run WB3

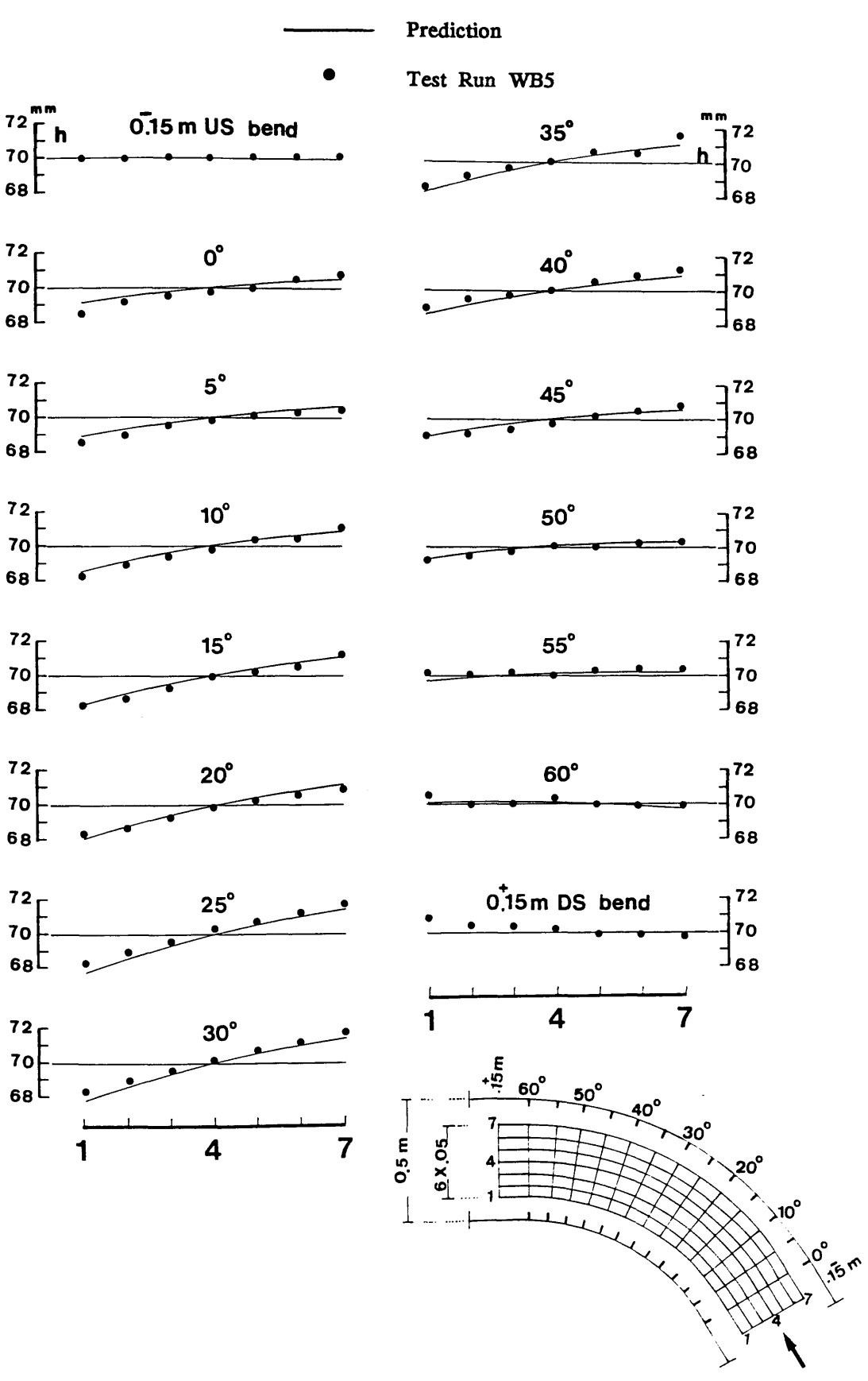

FIG.(6.3) – Comparison between the Predicted and Measured Radial Surface Profiles for Test Run WB5

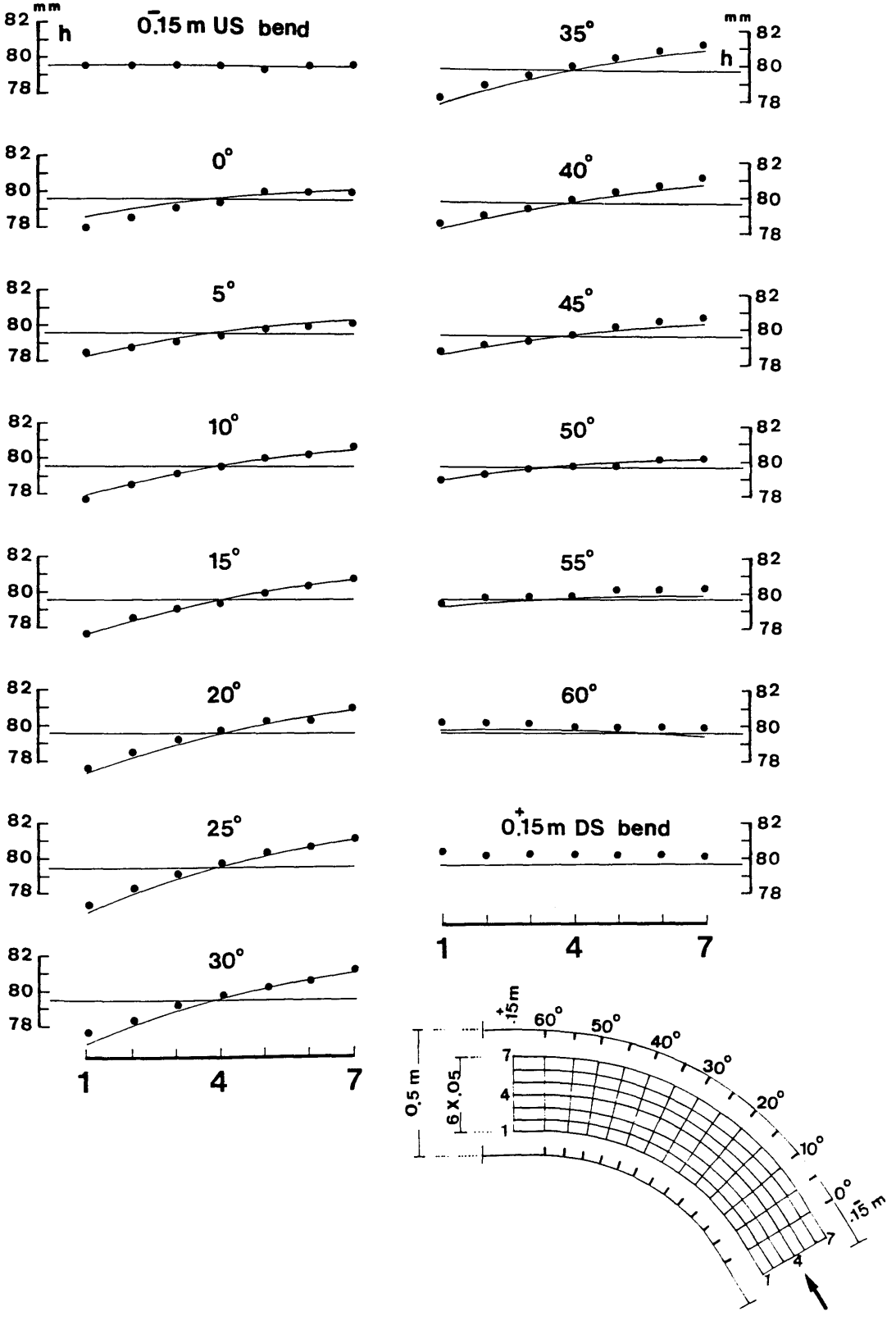

FIG.(6.4) – Comparison between the Predicted and Measured Radial Surface Profiles for Test Run WB7

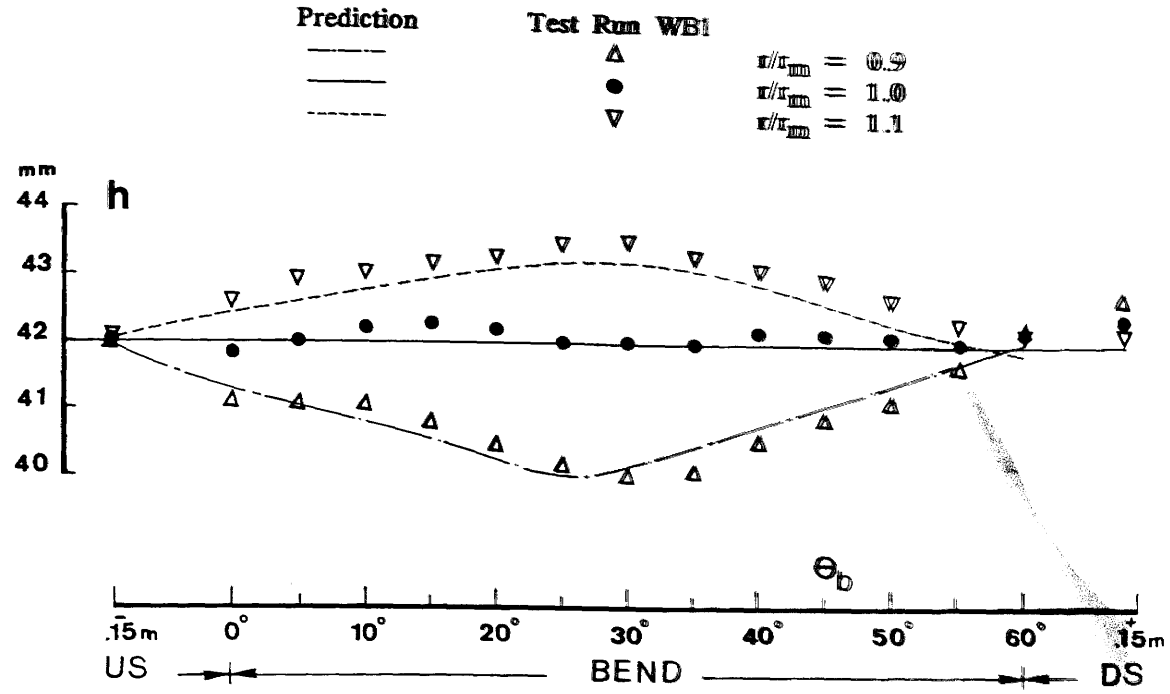

FIG.(6.5) – Comparison between the Predicted and Measured Longitudinal Surface Profiles for Test Run WB1

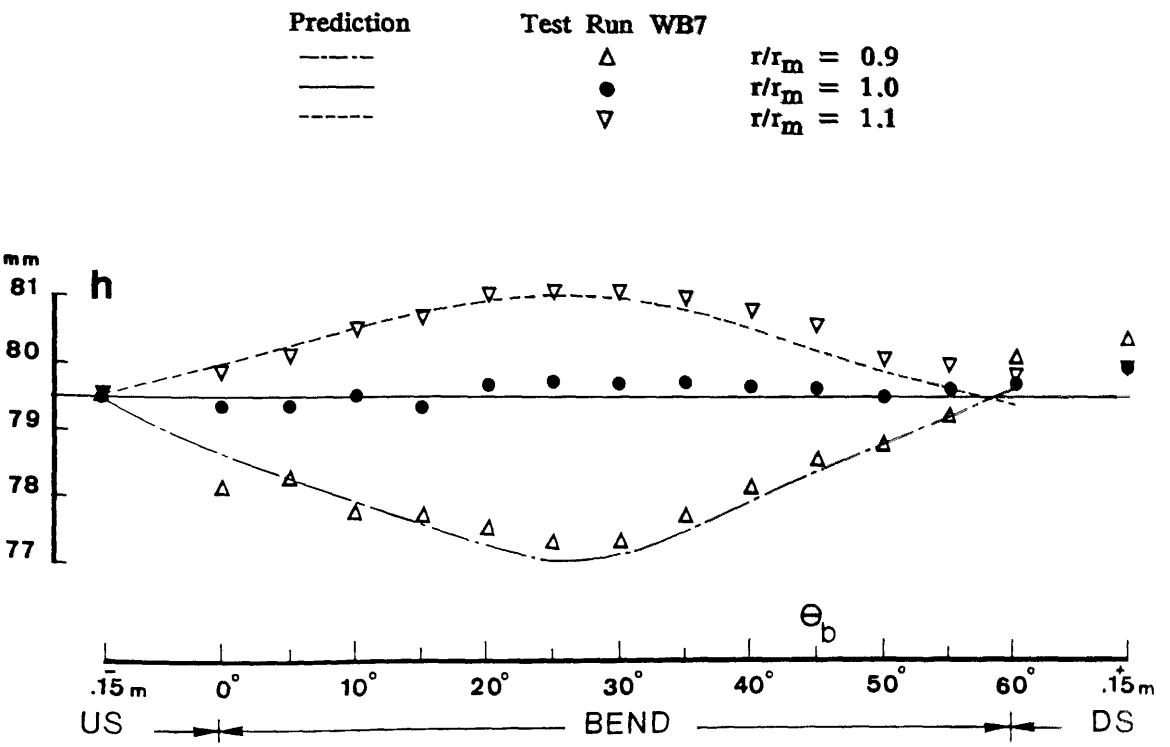

FIG.(6.6) – Comparison between the Predicted and Measured Longitudinal Surface Profiles for Test Run WB7

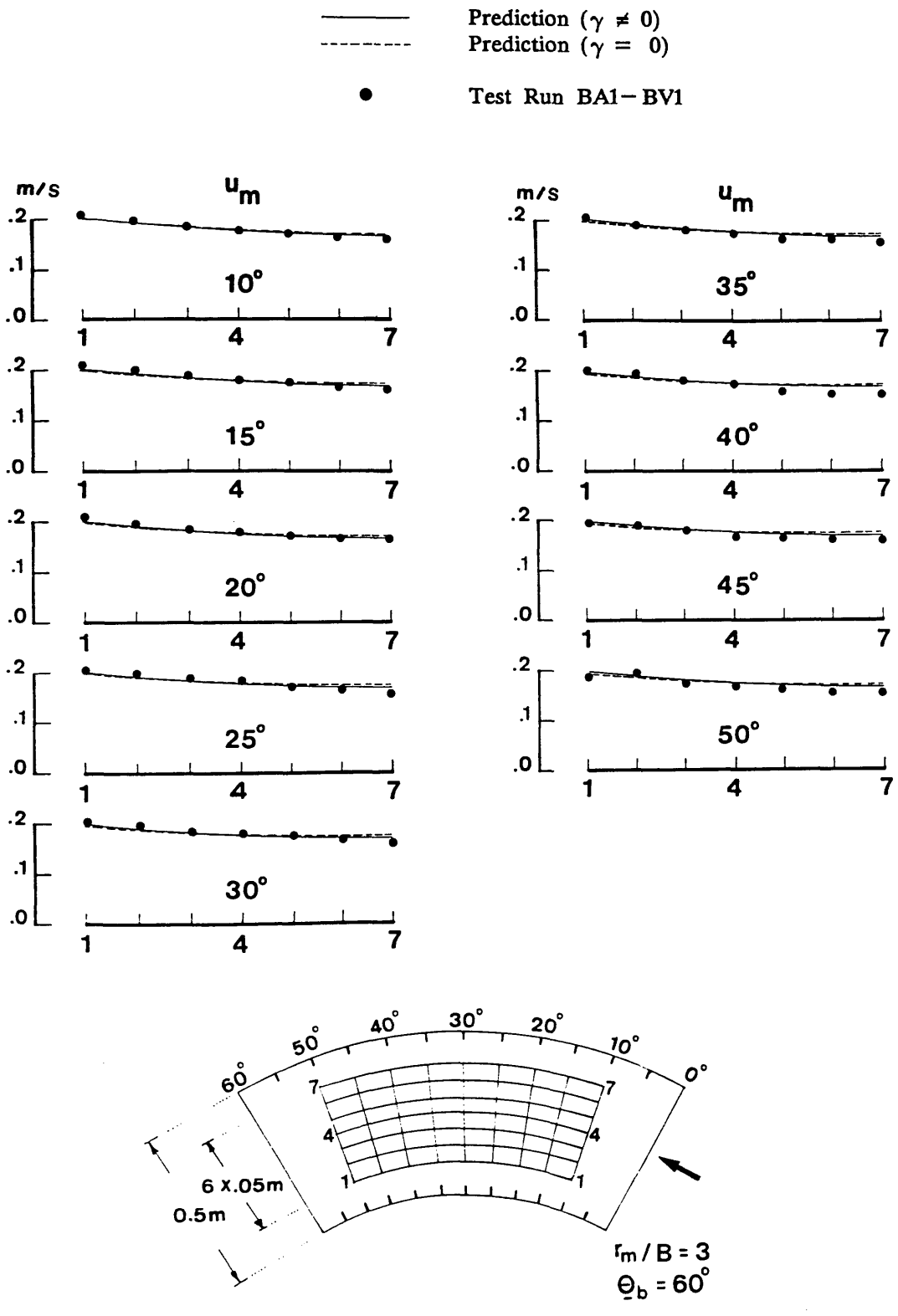

FIG.(6.7) – Comparison between the Predicted and Measured Distributions of Depth–averaged Velocities for Test Run BA1–BV1

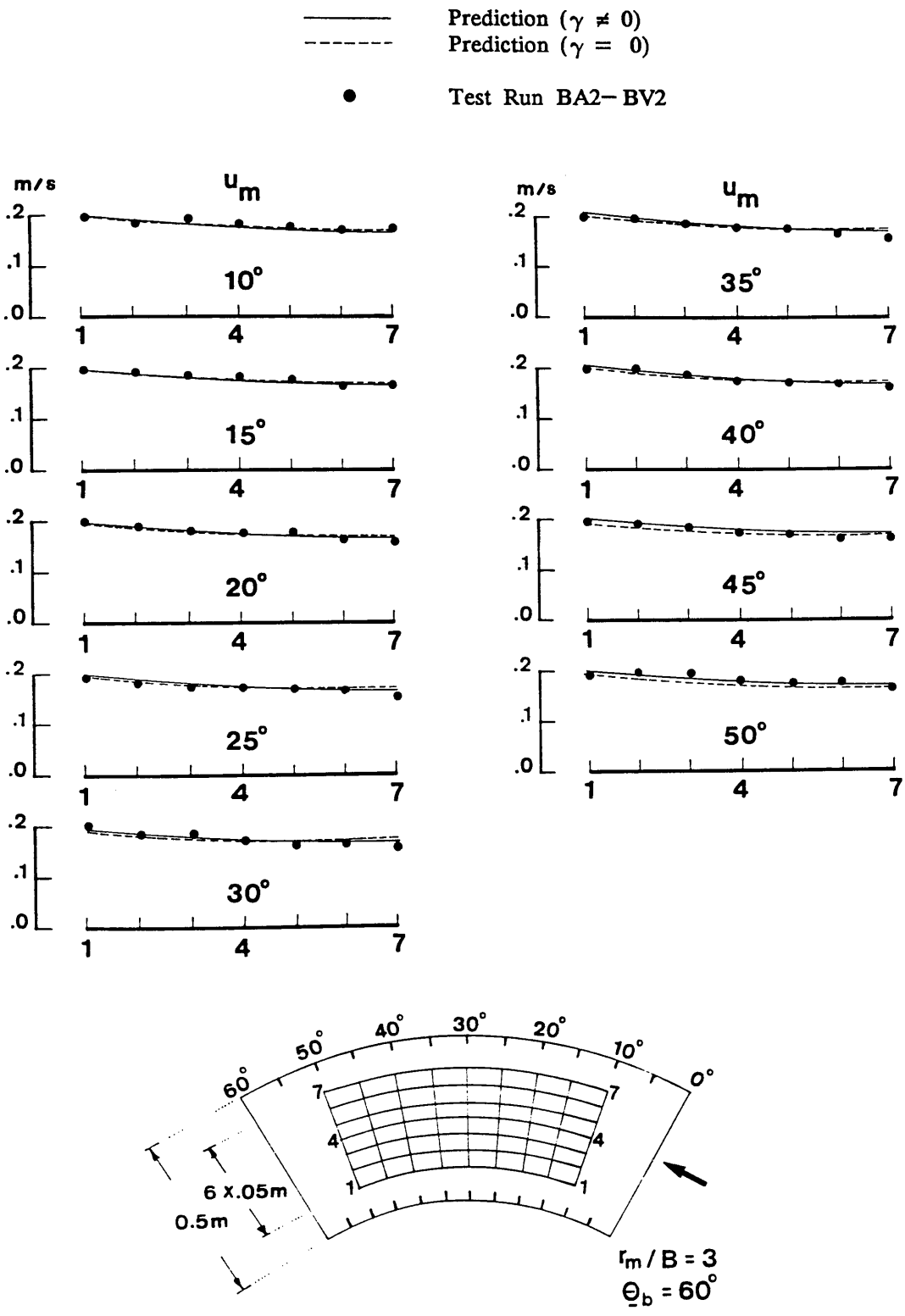

FIG.(6.8) – Comparison between the Predicted and Measured Distributions of Depth–averaged Velocities for Test Run BA2– BV2

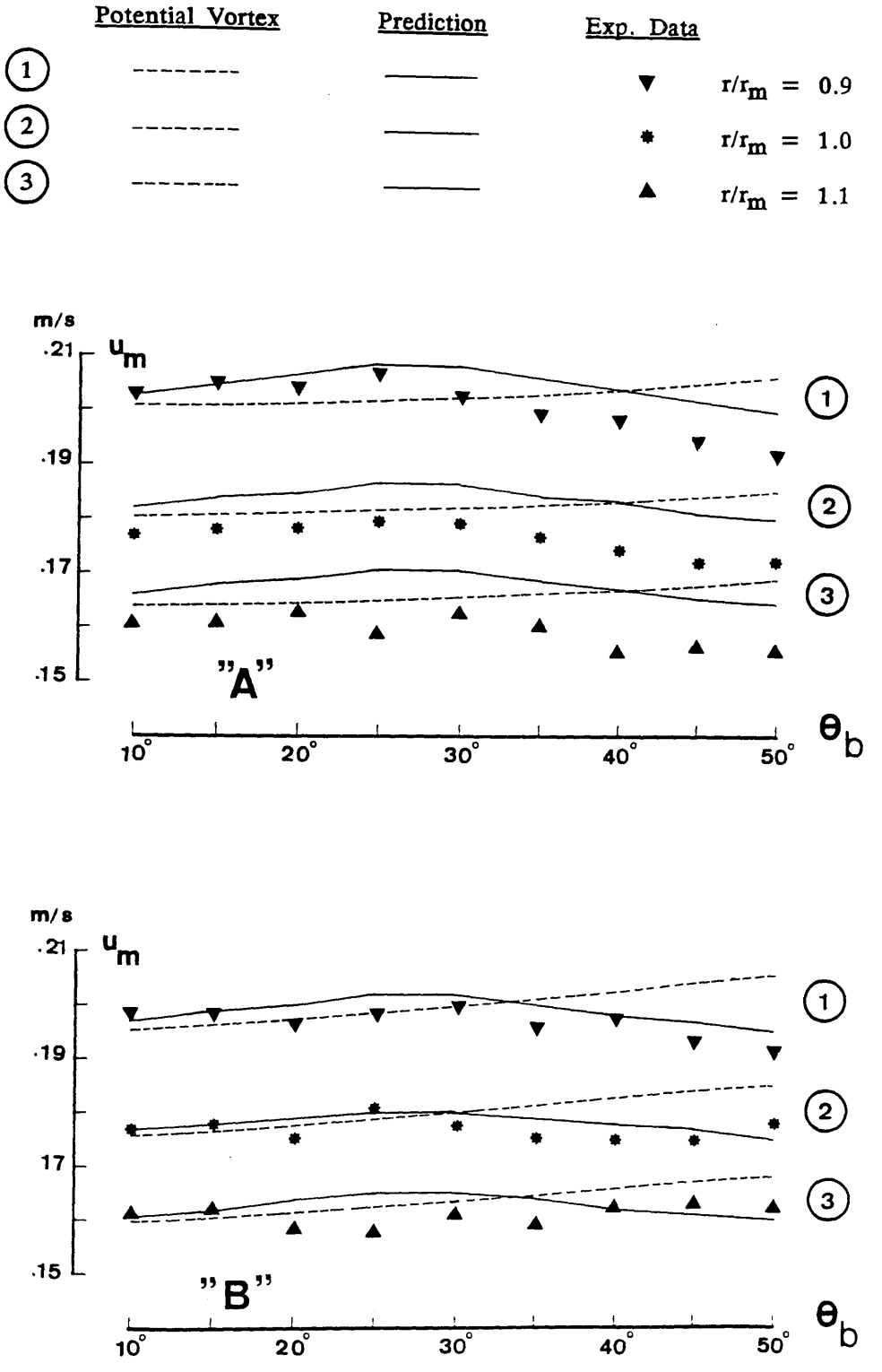

FIG.(6.9) – Comparisons of both the Predicted and Measured Profiles of the Depth–averaged Velocities With the Solution Obtained by Using the Potential Vortex Theory

(A) Test Run BA1–BV1

(B) Test Run BA2–BV2

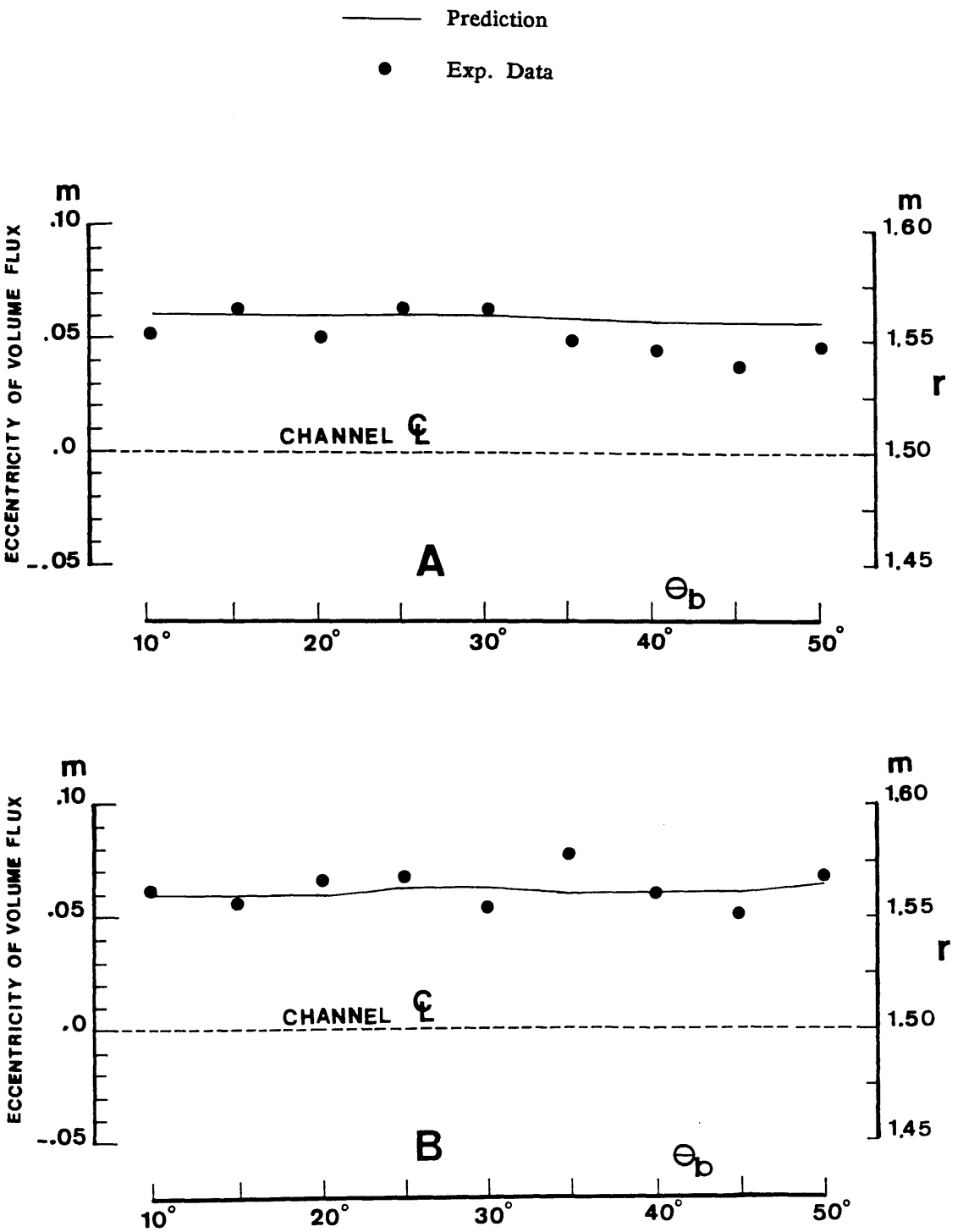

FIG.(6.10) – Comparisons between the Predicted and Measured Eccentricity of the Centre of Flow Volume Flux Along the Channel Bend
(A) Test Run BA1–BV1
(B) Test Run BA2–BV2

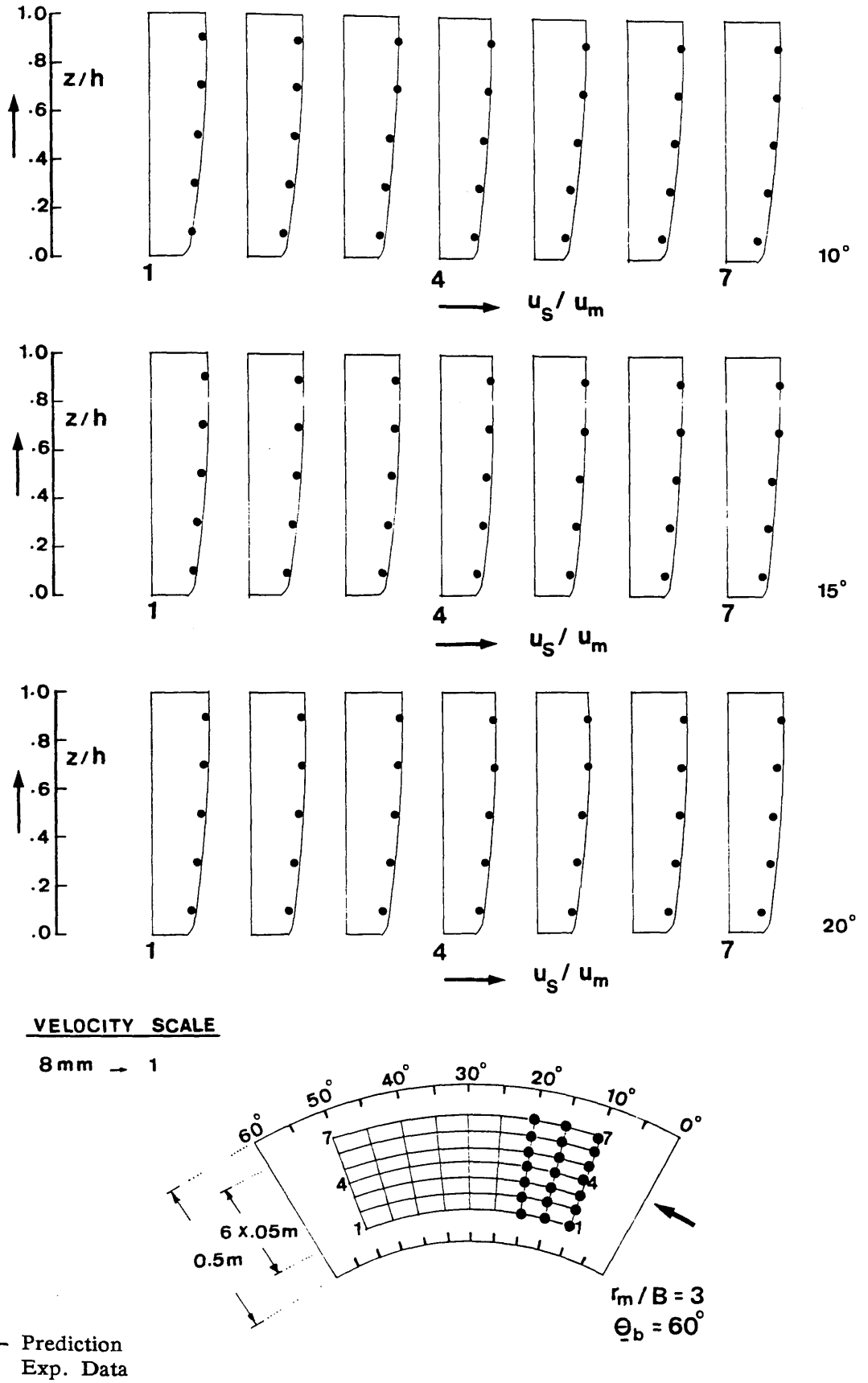

FIG.(6.11) – Comparison between Predicted and Measured Vertical Distribution of Flow longitudinal Velocities for Test Run BA1 – BV1

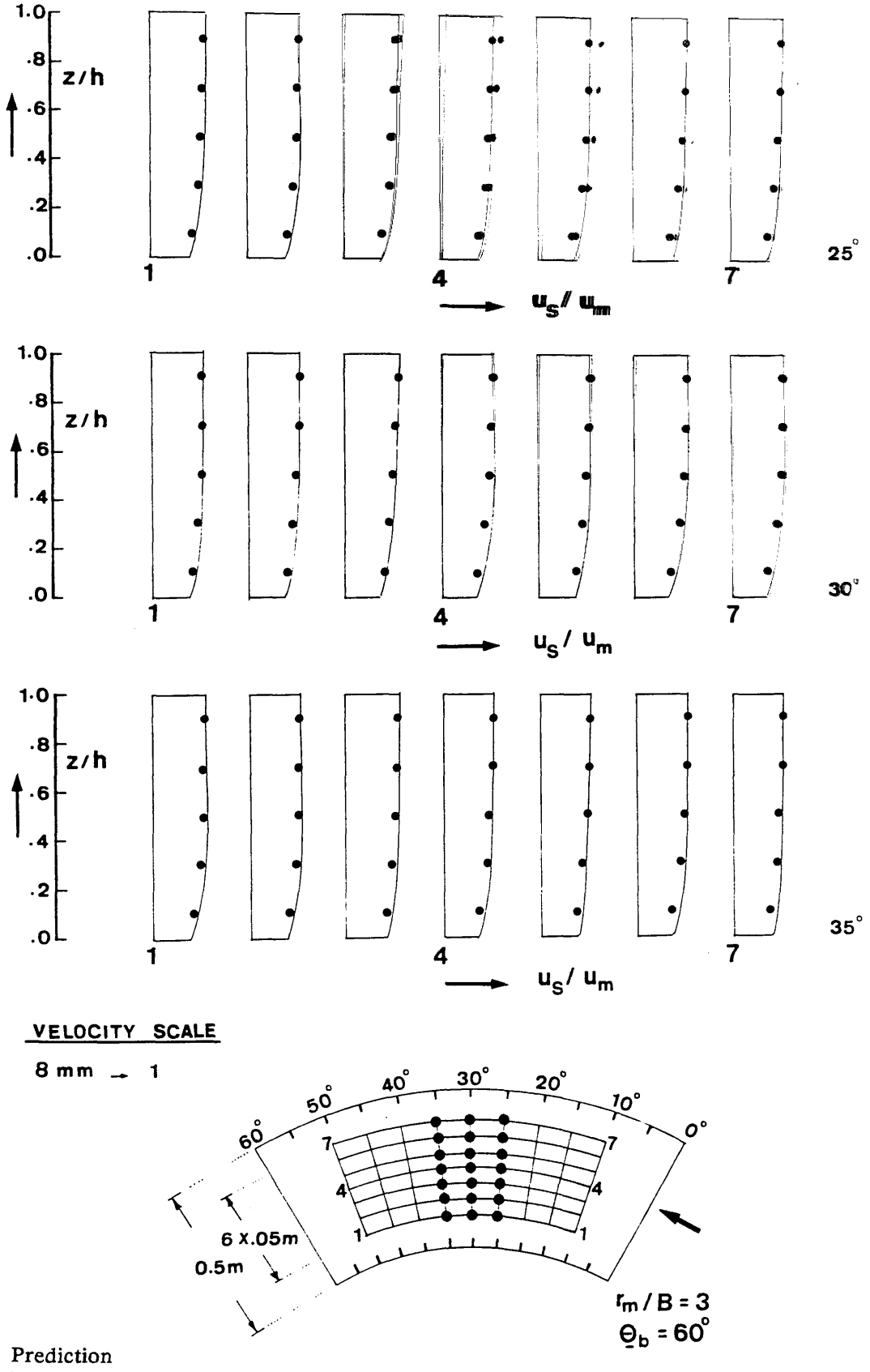

FIG.(6.11) – (Continued)

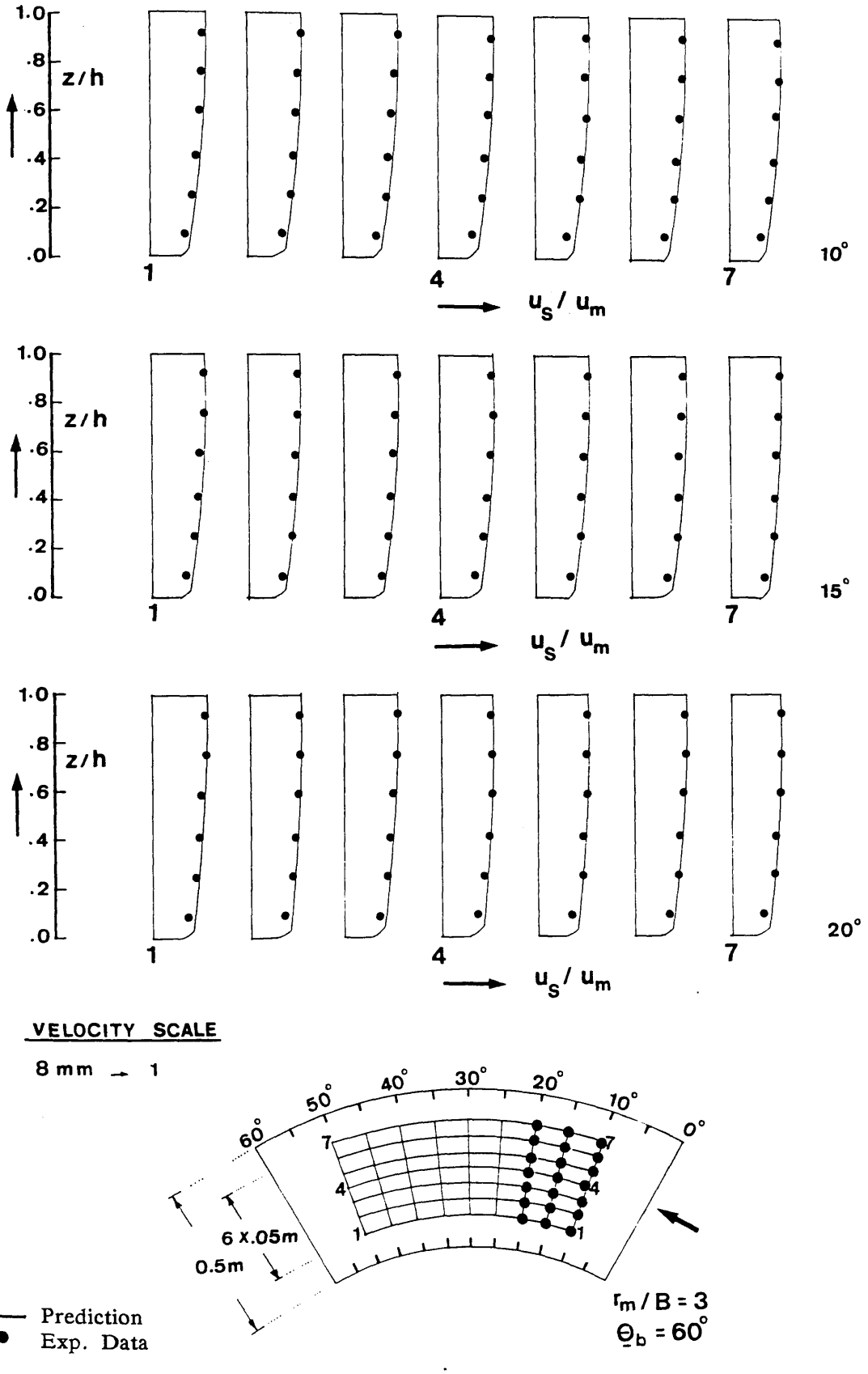

FIG.(6.12) – Comparison between Predicted and Measured Vertical Distribution of Flow longitudinal Velocities for Test Run BA2– BV2

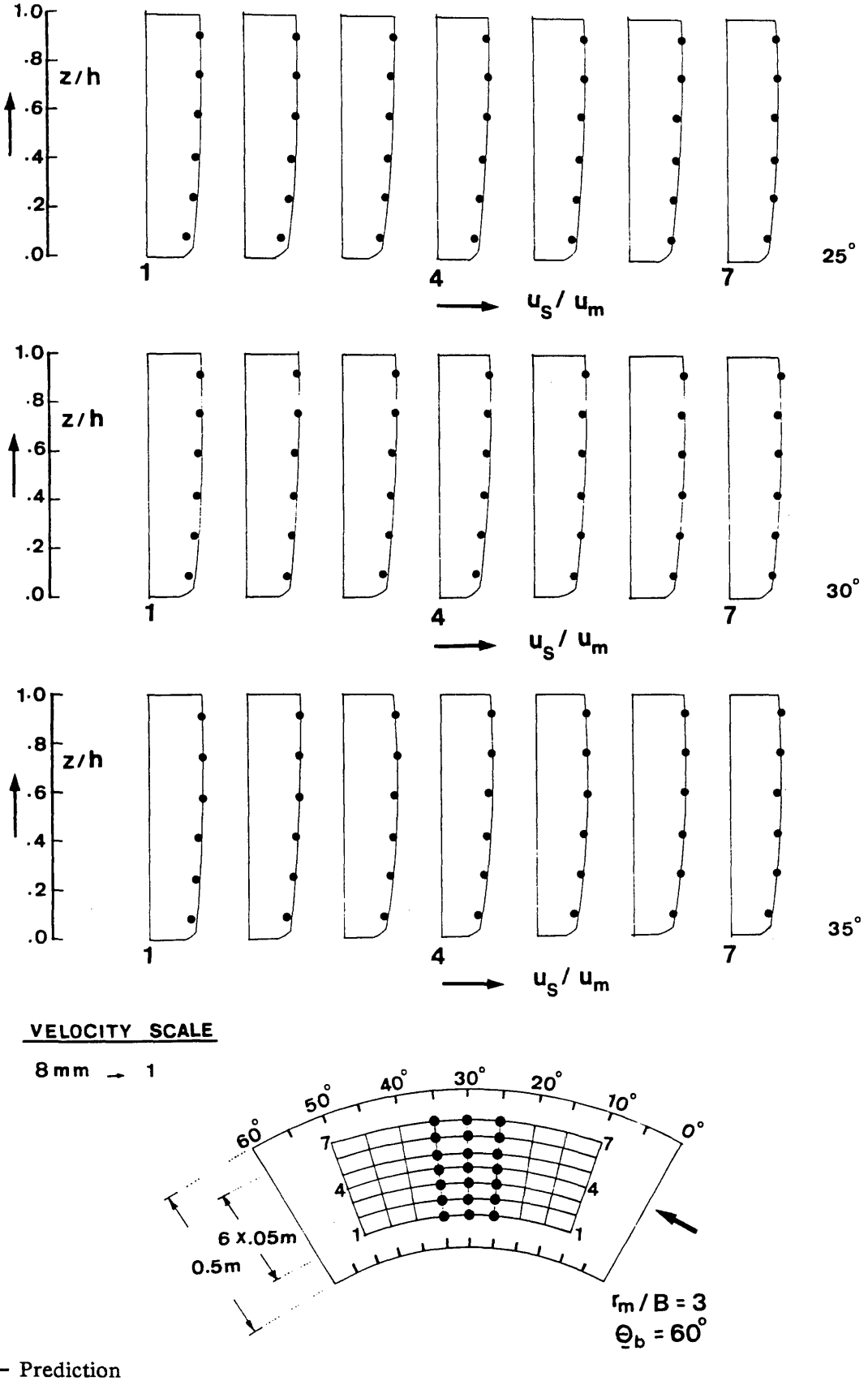

FIG.(6.12) – (Continued)

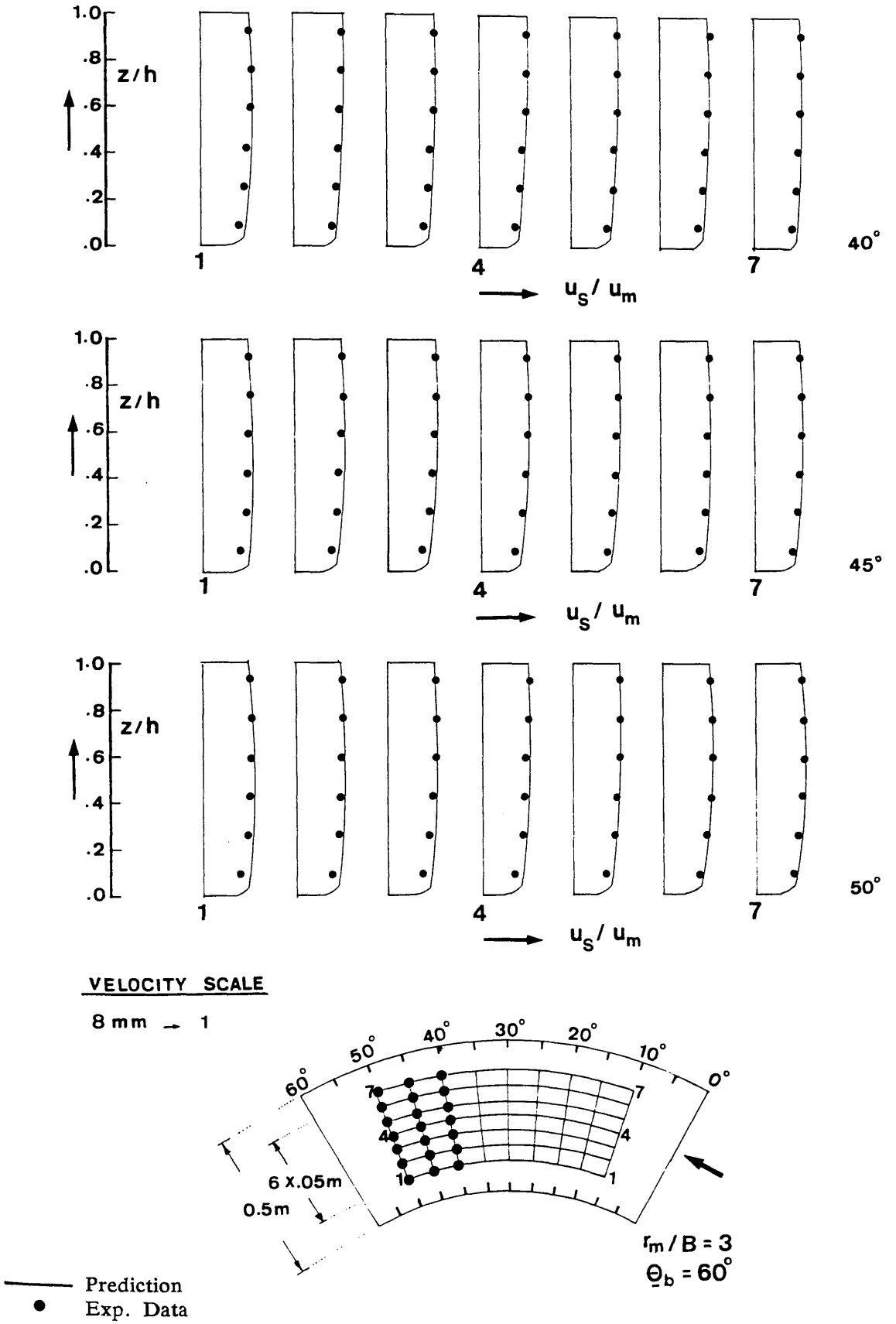

FIG.(6.12) – (Continued)

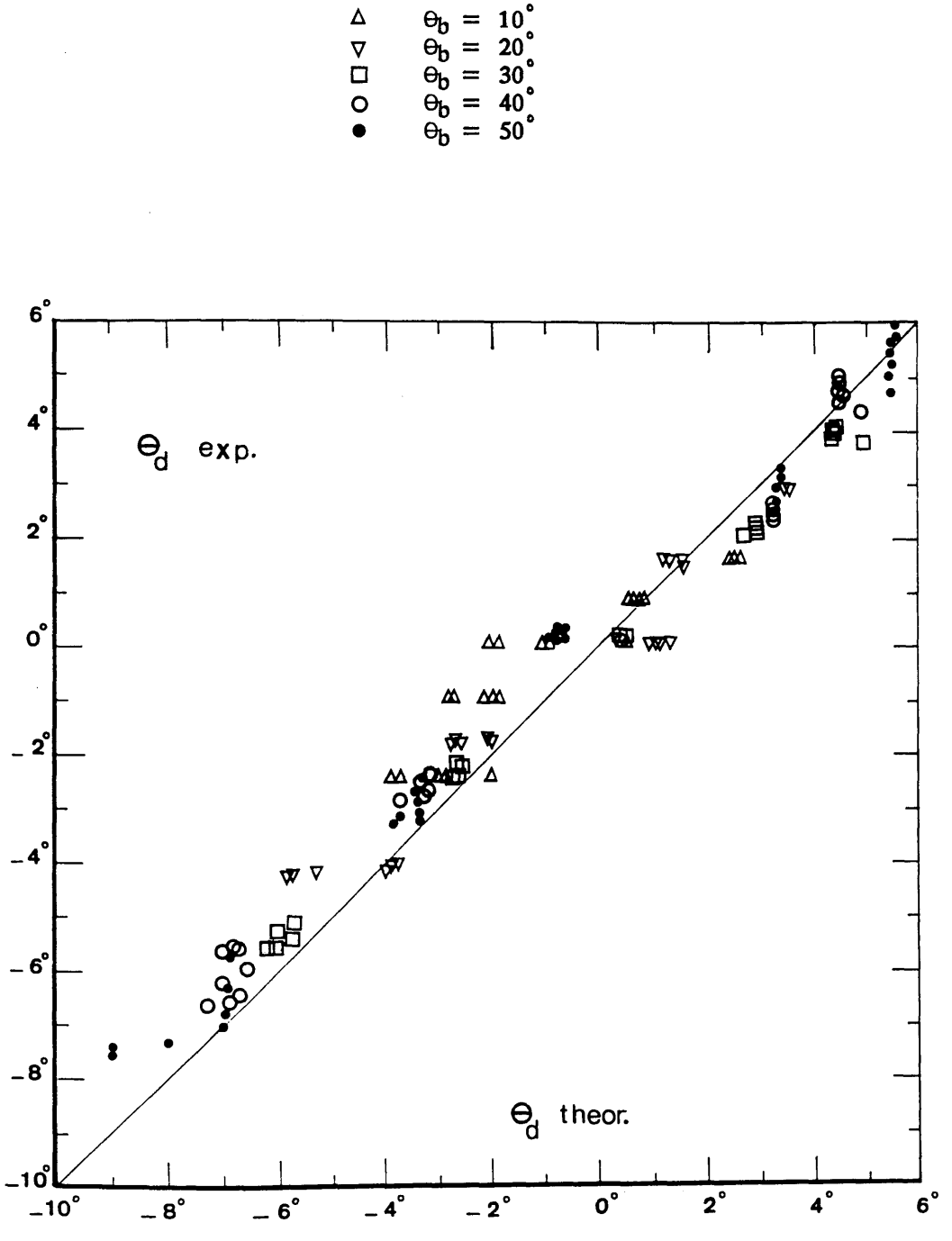

FIG.(6.13) – Comparisons between Predicted and Measured Values of Deviation Angles for Test Run BA1–BV1

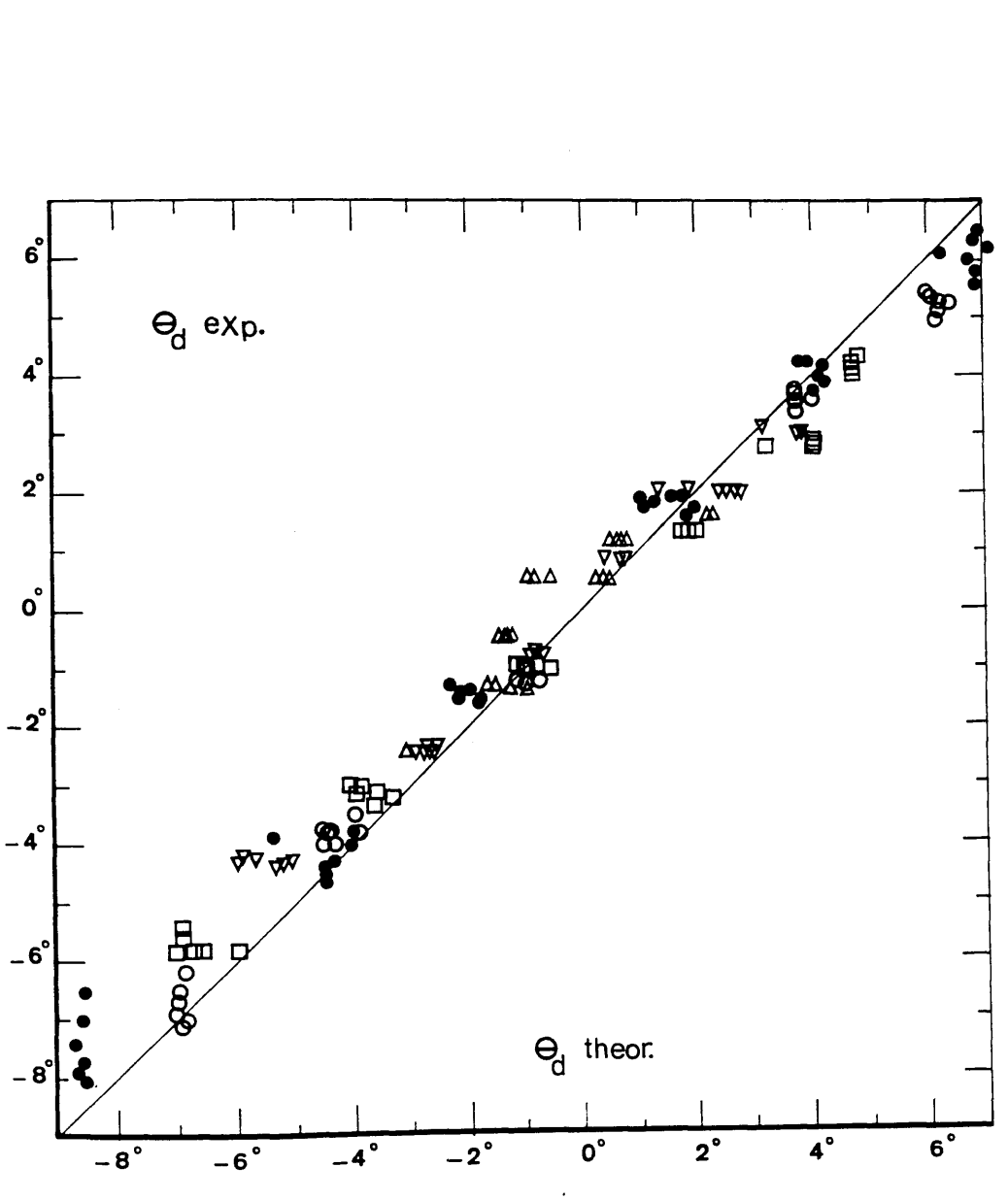

FIG.(6.14) – Comparisons between Predicted and Measured Values of Deviation Angles for Test Run BA2– BV2

TABLE (6.3) – % Variation of the Strength of the Secondary Currents $\%S_{rs}$ for Test Runs BA1–BV1 and BA2– BV2 at z/h= 0.1 and 0.9

Bend Angle	Test Run: BA1–BV1 $\%S_{rs}$		Test Run: BA2–BV2 %Srs	
	z/h= 0.1	z/h= 0.9	z/h= 0.1	z/h= 0.9
10°	.34	.19	.28	.14
20°	.74	.37	.92	.41
30°	1.20	.61	1.38	.68
40°	1.40	.64	1.49	1.16
50°	1.84	.93	2.32	1.41

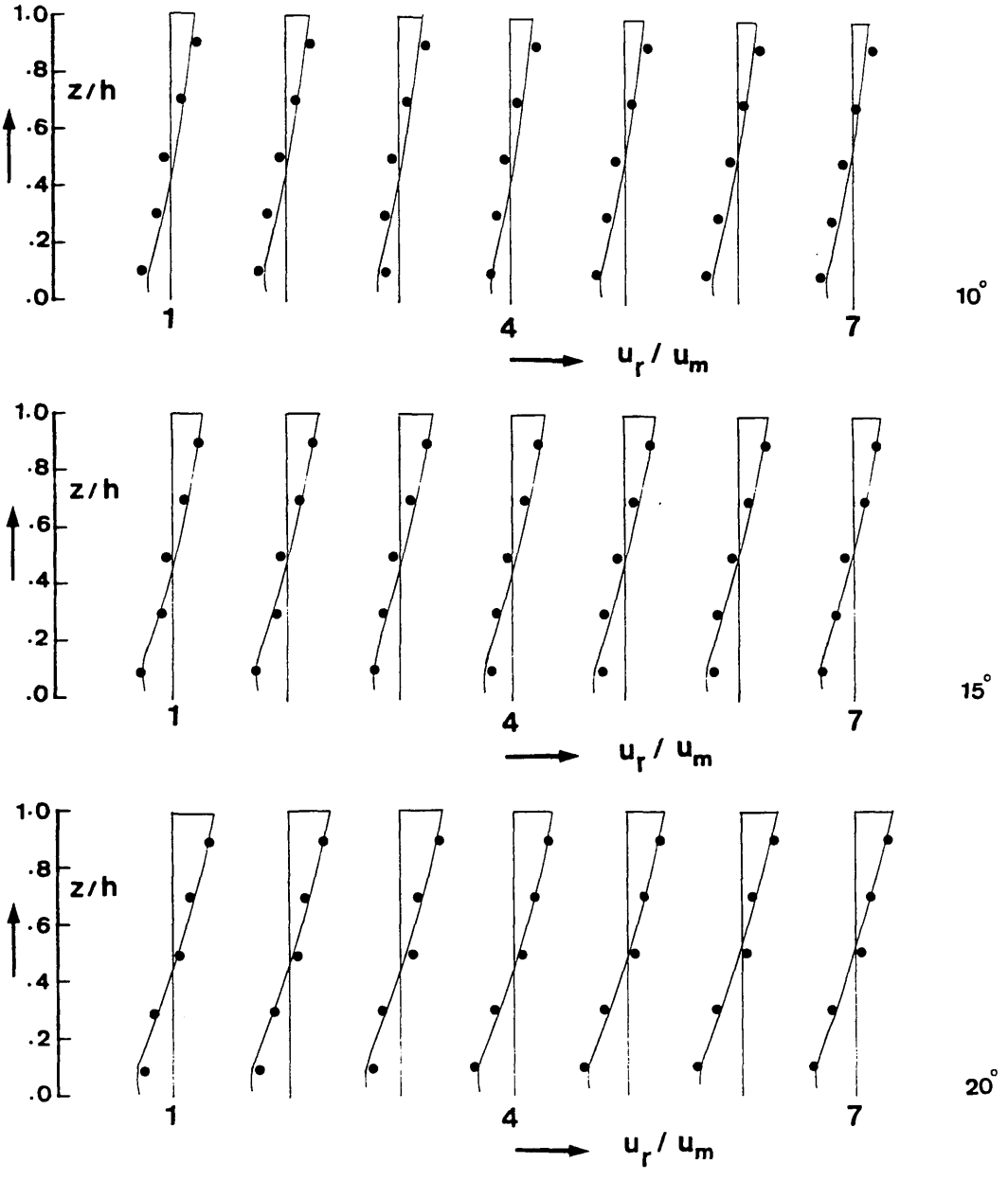

FIG.(6.15) – Comparison between Predicted and Measured Vertical Distribution of Flow Radial Velocities for Test Run BA1–BV1

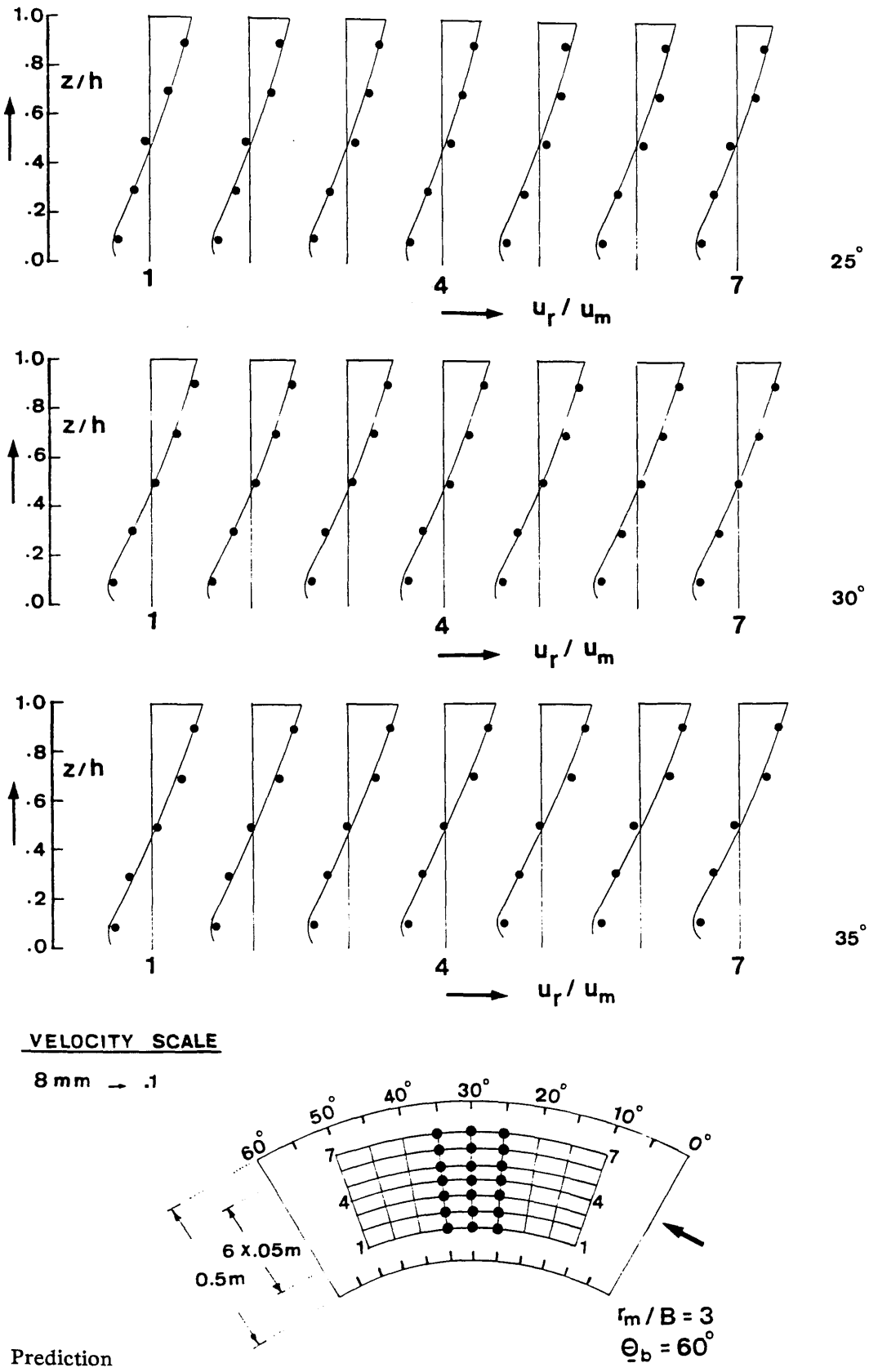

FIG.(6.15) – (Continued)

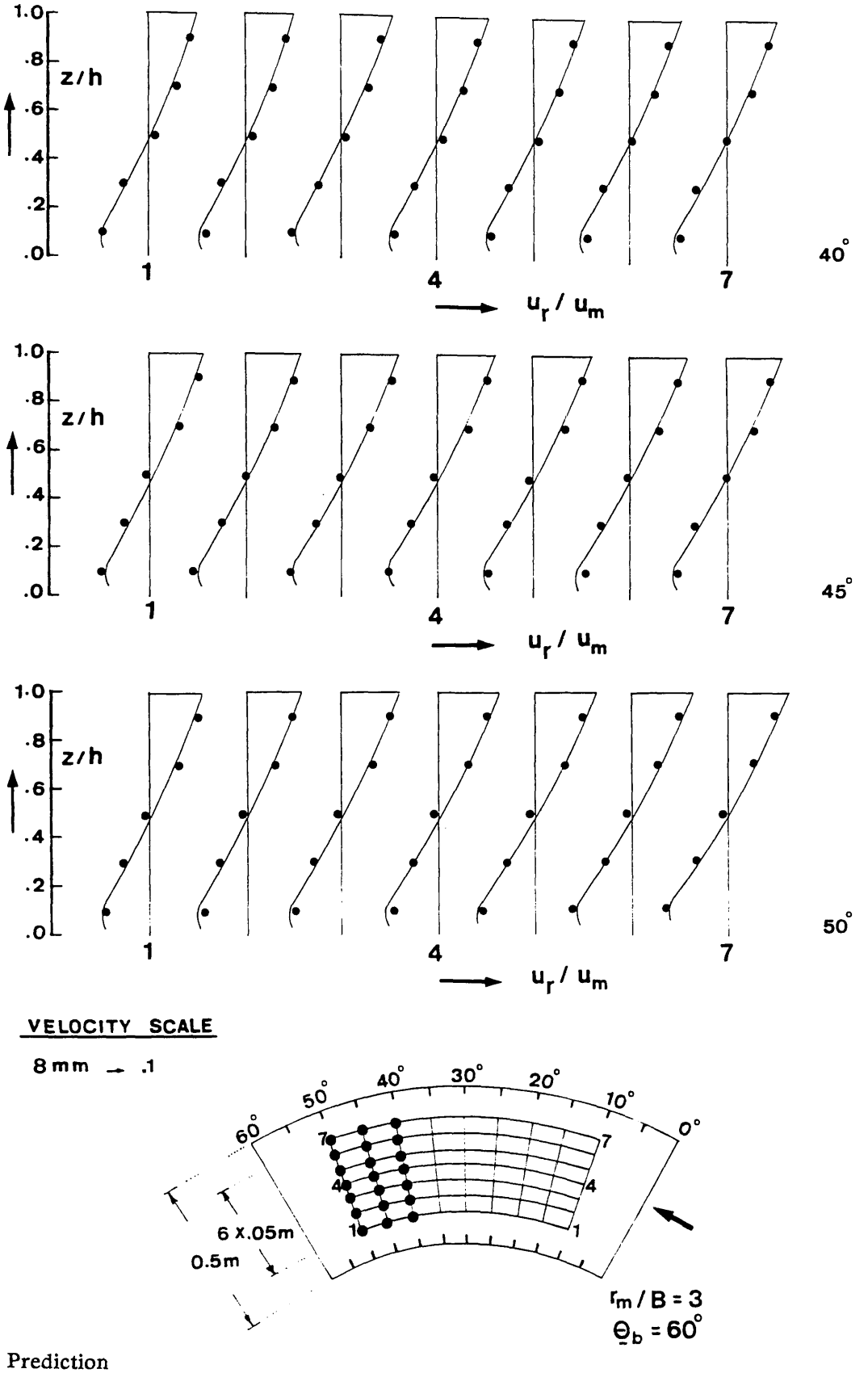

FIG.(6.15) – (Continued)

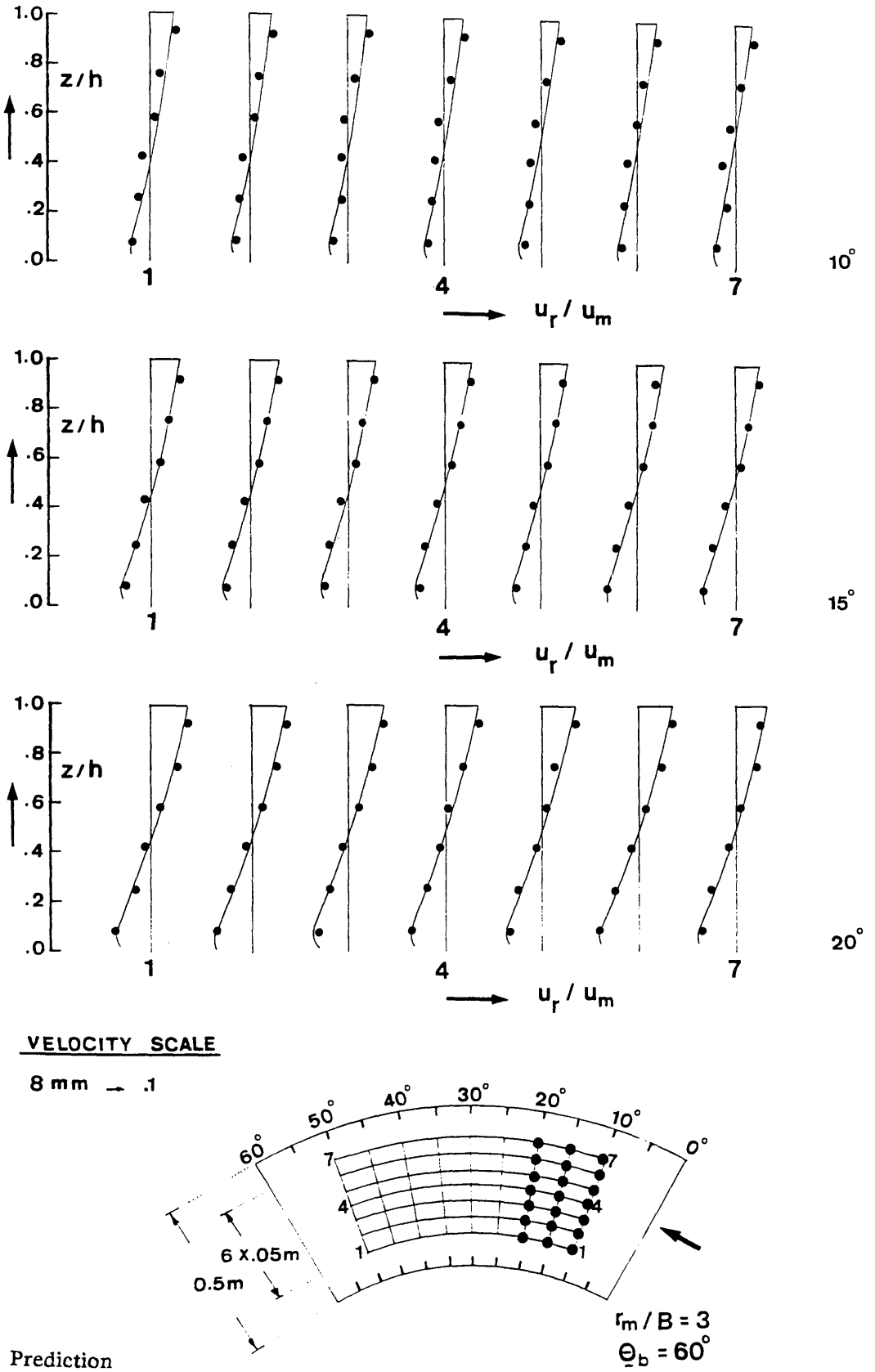

FIG.(6.16) – Comparison between Predicted and Measured Vertical Distribution of Flow Radial Velocities for Test Run BA2– BV2

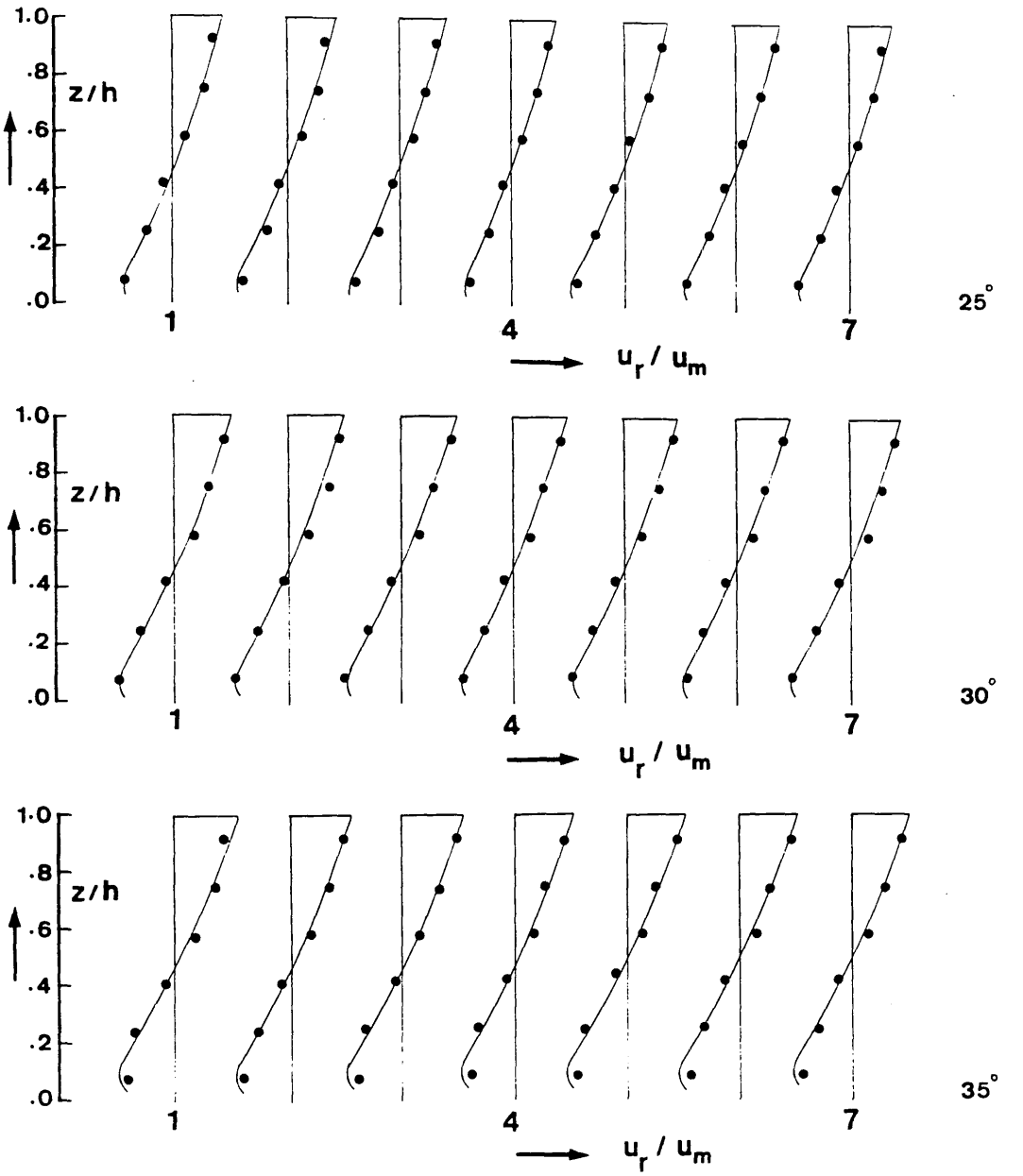

FIG.(6.16) – (Continued)

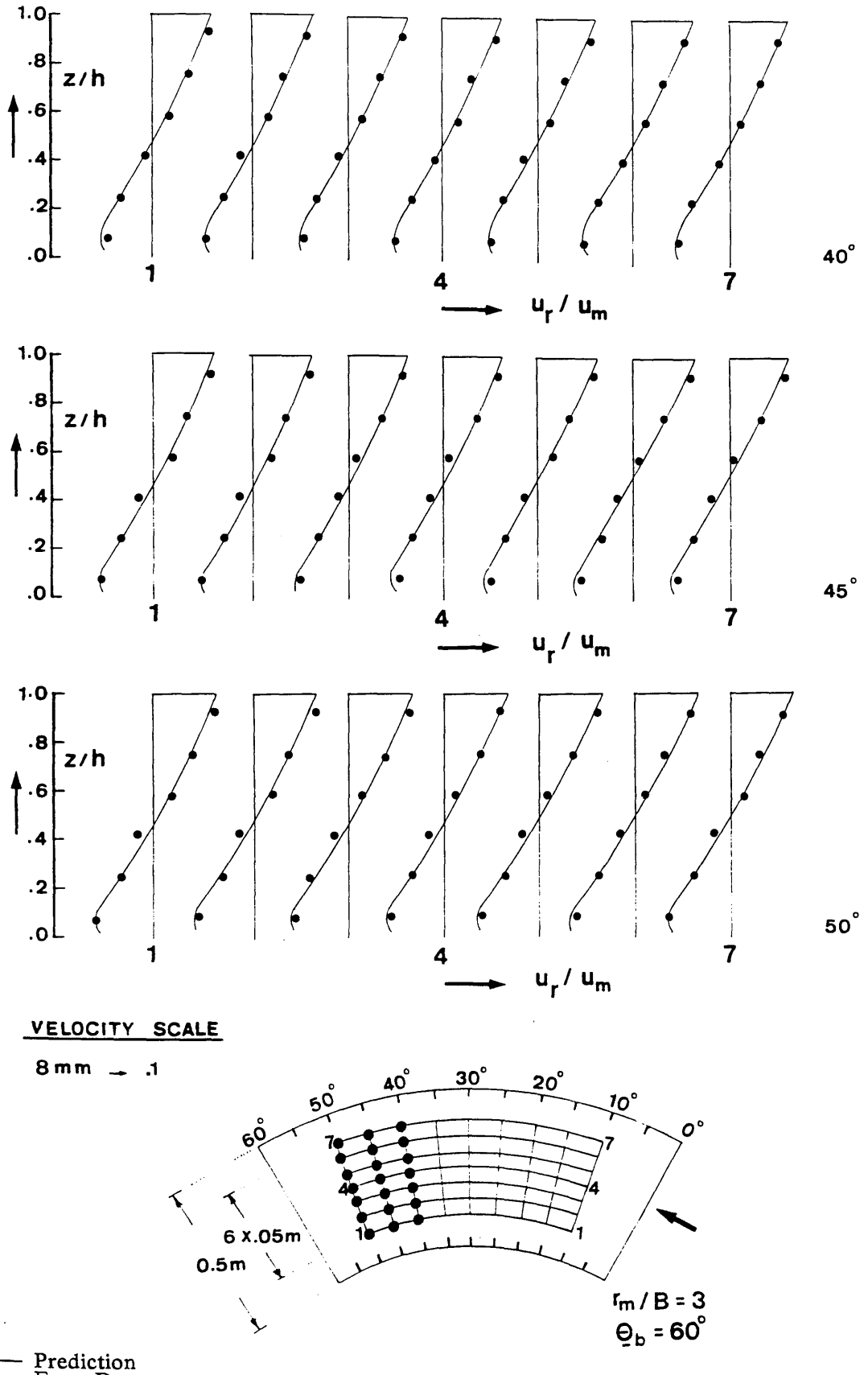

FIG.(6.16) – (Continued)

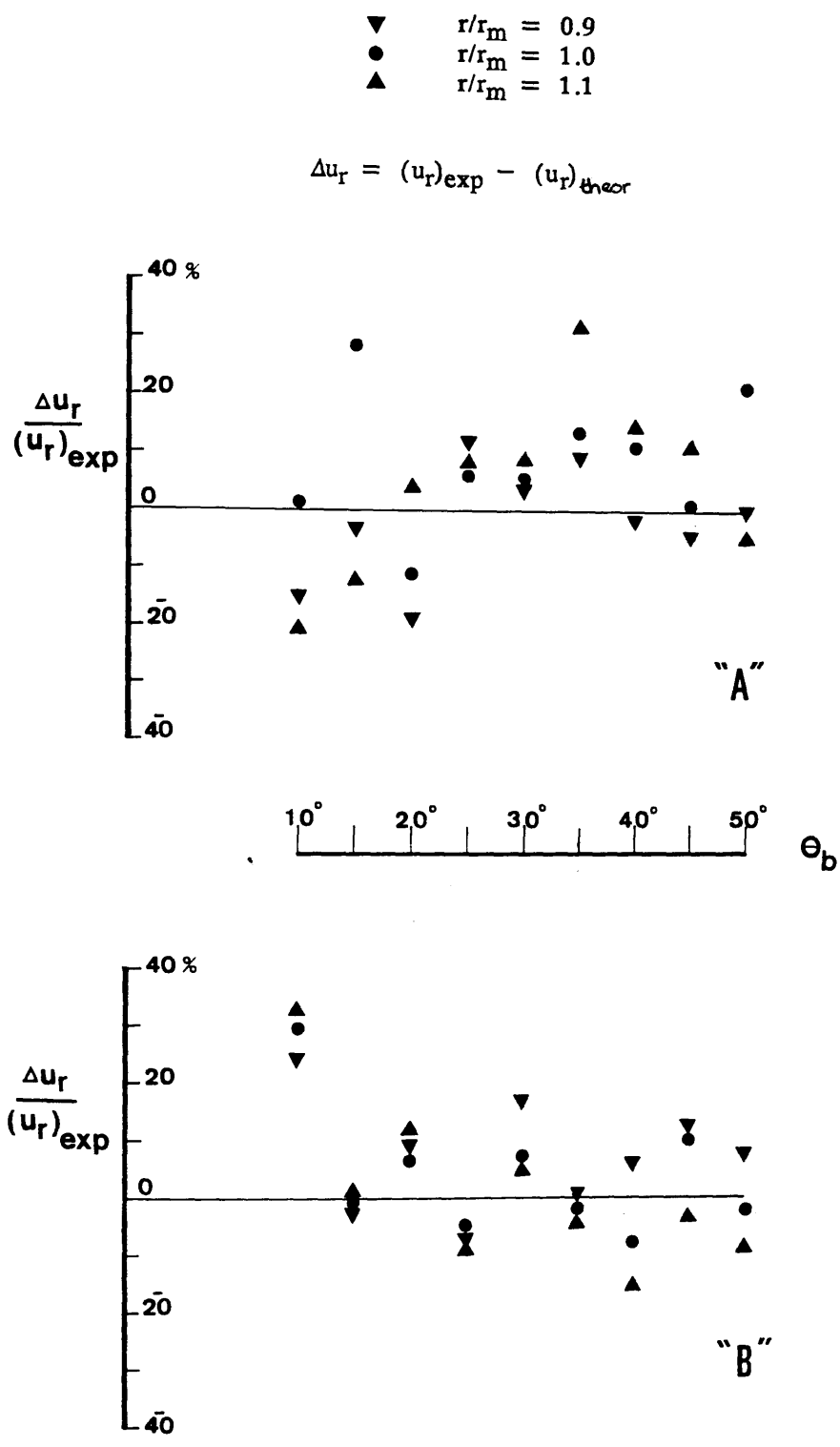

FIG.(6.17) − % Difference between the Predicted and Measured Radial Velocities Along the Channel Bend for Test Run BA1−BV1

(A) at z/h = 0.1

(B) at z/h = 0.9

▼ $r/r_m = 0.9$
● $r/r_m = 1.0$
▲ $r/r_m = 1.1$

$$\Delta u_r = (u_r)_{exp} - (u_r)_{theor}$$

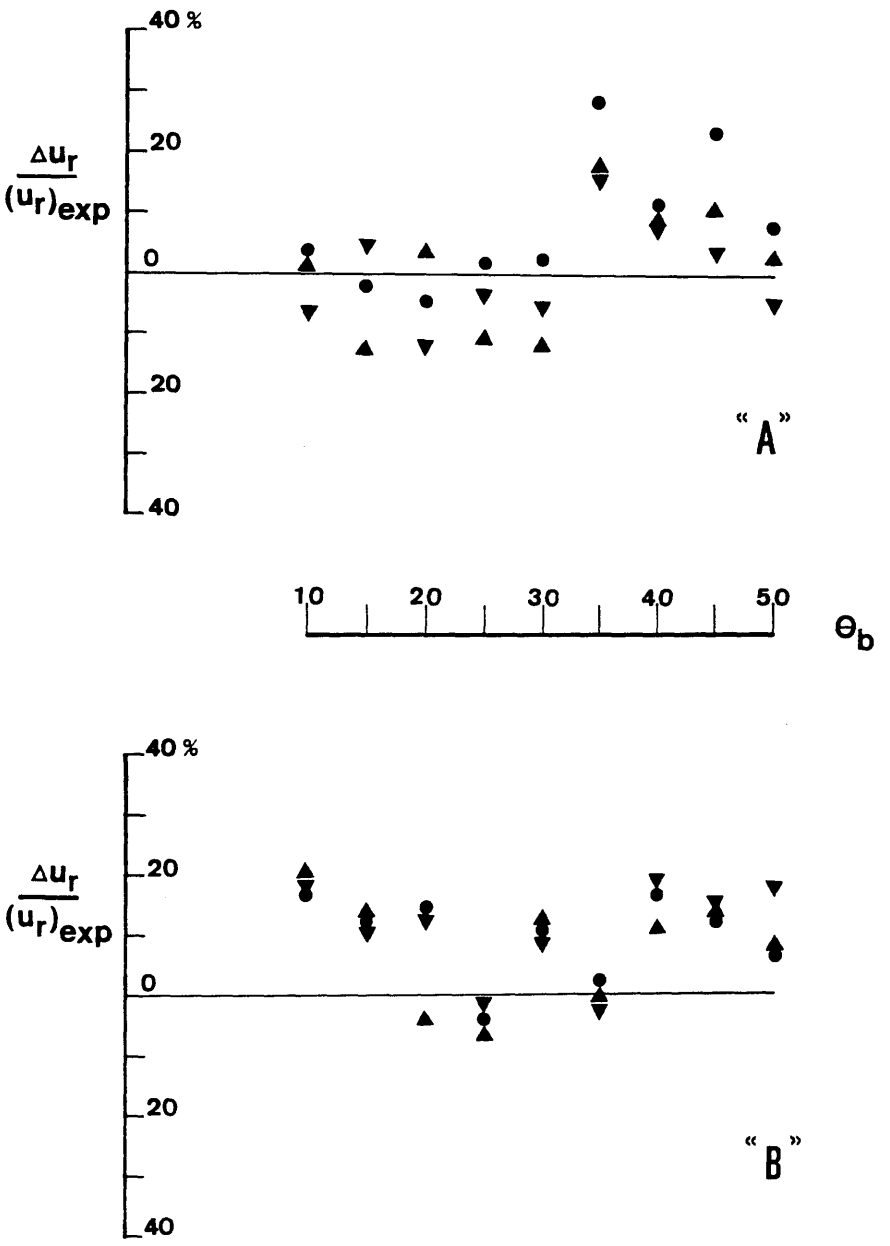

FIG.(6.18) – % Difference between the Predicted and Measured Radial Velocities Along the Channel Bend for Test Run BA2– BV2

(A) at z/h = 0.1
(B) at z/h = 0.9

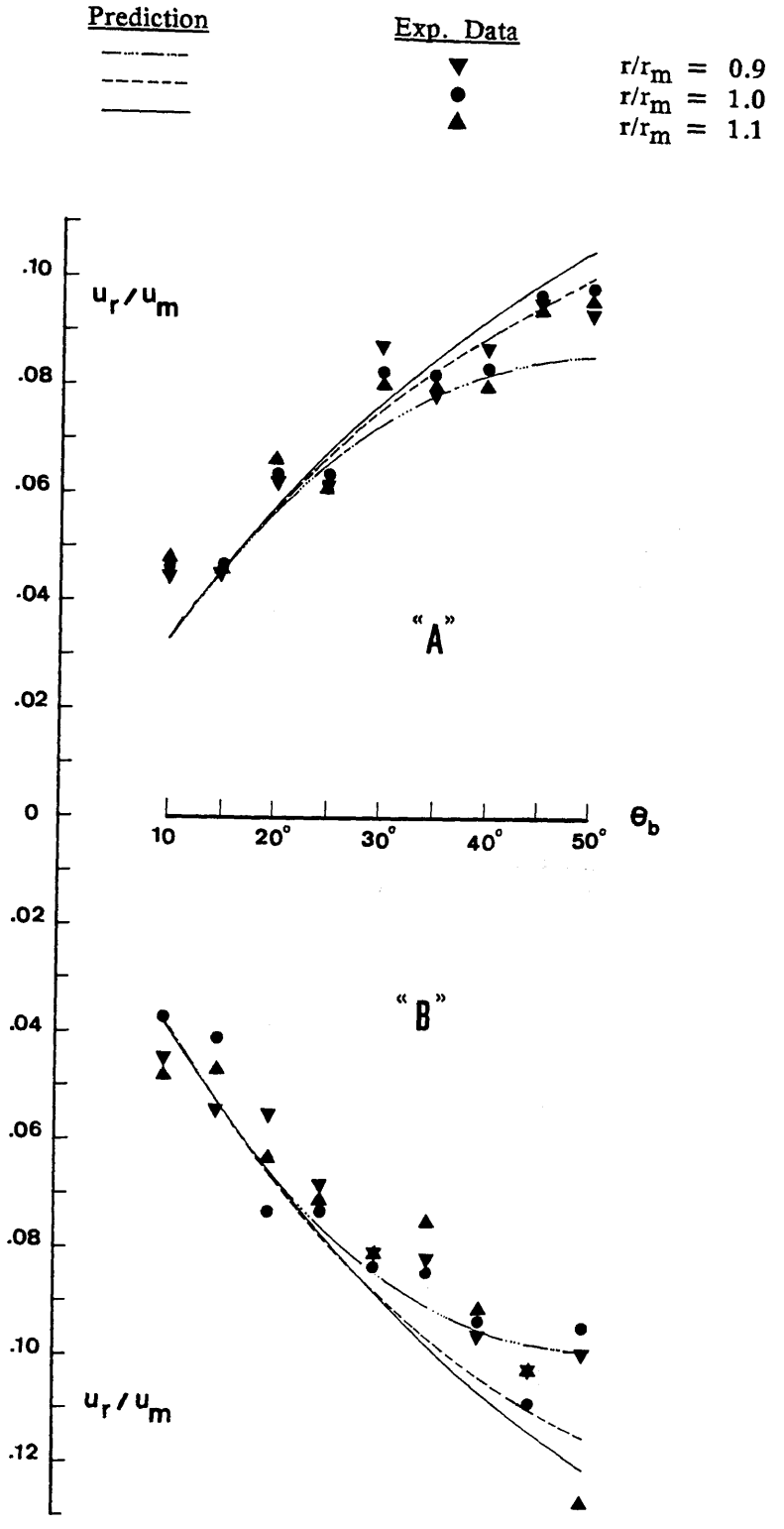

FIG.(6.19) – Comparisons between the Predicted and Measured Profiles of the Growth of the Radial Velocities Along the Channel Bend for Test Run BA1–BV1
(A) at z/h = 0.9
(B) at z/h = 0.1

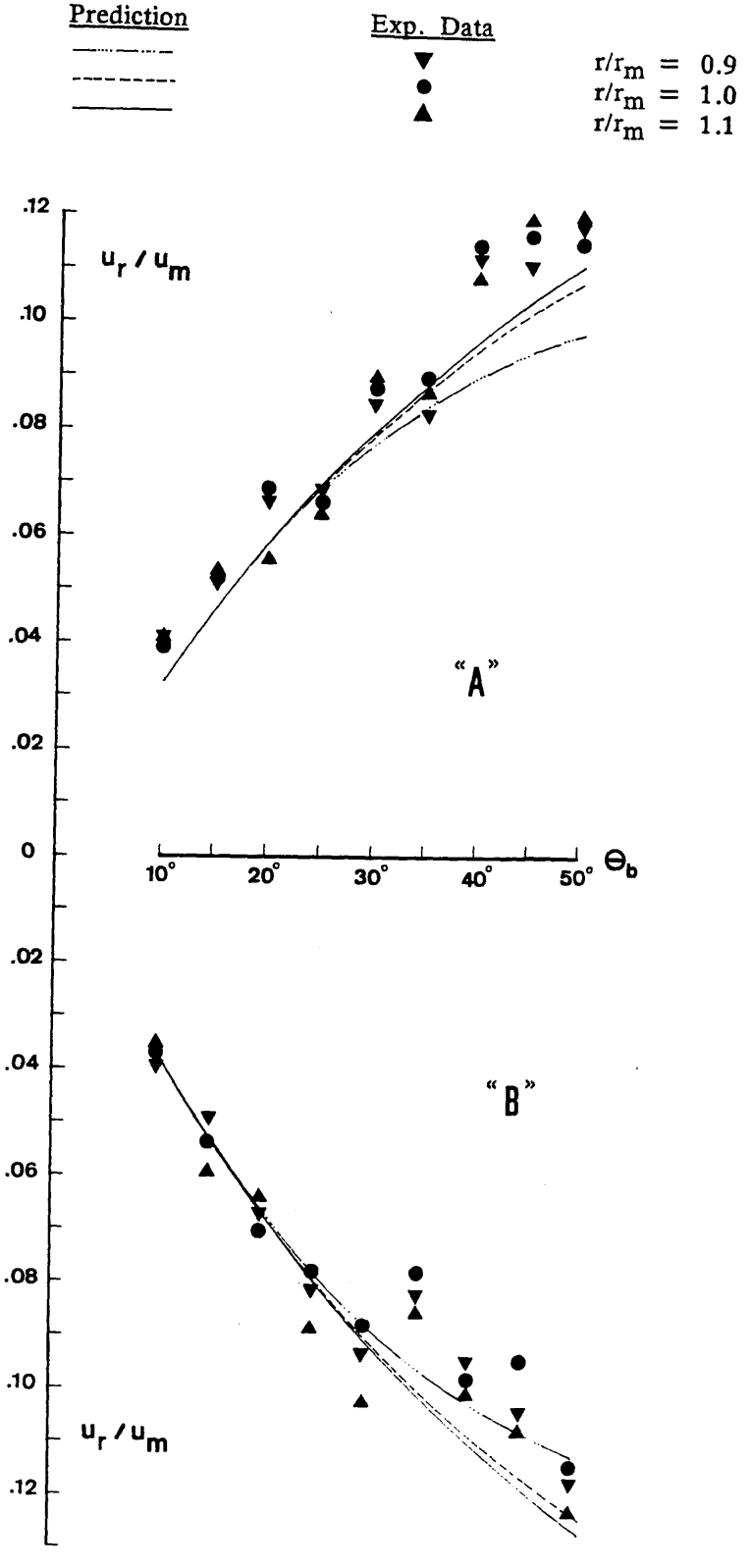

FIG.(6.20) – Comparisons between the Predicted and Measured Profiles of the Growth of the Radial Velocities Along the Channel Bend for Test Run BA2– BV2
(A) at z/h = 0.9
(B) at z/h = 0.1

CHAPTER VII

FLOW AT BEND/FLOOD RELIEF CHANNEL INTERSECTION

CHAPTER VII

FLOW AT BEND/FLOOD RELIEF CHANNEL INTERSECTION

(7.1) INTRODUCTION

Contained in this Chapter is the analysis of the flow in the channel bend at the intersection with the flood relief channel. The flow characteristics at the intersection will be analysed in a similar manner to those for the gentle wide bend, as in Chapter VI, i.e. under the following headings:

- **Water surface profiles (in both bend and flood relief channel).**
- **Distribution of depth– averaged velocities.**
- **Vertical distribution of longitudinal velocities.**
- **Deviation angles of horizontal resultant velocities.**

The experimental programmes for the measurements of water surface profiles (thirteen test runs) and flow velocites (five test runs) are given in Tables (7.1) and (7.2) respectively. In the five test runs used for the flow velocities measurements, the local longitudinal velocity component and local deviation angle were both measured at the same discharge and the same flow geometry at the intersection (i.e. same r_m/B , B/h , h_w/h ratios , where h_w is the water head above the weir crest level).

In all cases, the analysis will follow two distinct lines; quantitative analysis and qualitative analysis.

++ Quantitative Analysis

Wherever possible, quantitative comparisons will be made between the experimental results and the theoretical predictions obtained from the numerical solutions of the depth– averaged model (described previously in Chapter IV). The discussion of results will cover both the characteristics at sections upstream, along and downstream of the intersection and the effects of different bed levels of the flood channel (i.e. different h_w/h ratios).

Downstream of the intersection only experimental values will be analysed, since this section of bend channel is outwith the scope of the numerical model. Similarly in the case of deviation angles, only experimental results will be discussed.

++ Qualitative Analysis

Where appropriate, qua-litative comparisons will be made of the flow characteristics in the cases of a channel bend with and without the introduction of the flood relief channel intersection in order to show influence of the intersection on the characteristics of the bend flow.

For the purposes of the analysis, the experimental results were divided into bands of " h_w/h " ratio as follows:

Water Surface Profiles	Velocities and Deviation Angles Profiles
$h_w/h \leq .36$	$h_w/h \leq .19$
$.36 < h_w/h \leq .47$	$.19 < h_w/h \leq .36$
$h_w/h > .47$	$h_w/h > .36$

The bands were chosen to suit the way in which the test runs were carried out and correspond to conditions of high, medium and low weirs.

(7.2) WATER SURFACE PROFILES

The analysis of the water surface profiles will be divided into two parts. The first part will deal with the analysis of the profiles in the channel bend and the second will discuss the profiles across the width of the flood relief channel.

(7.2.1) In the Channel Bend

In most cases, reasonably good agreement was obtained between the observed and predicted radial and longitudinal surface profiles. In all the test runs, the water depth across the channel width in the reach upstream of the bend entrance was found to be almost constant (i.e. verifying that uniform flow existed in the approach to the bend). Typical results of the comparisons are shown in Figures

(7.1), (7.2), (7.3), (7.4), (7.5), (7.6) and (7.7) for test runs WF13, WF7, WF1, WF8, WF2, WF11 and WF5 respectively. The first three test runs are for $h_w/h \leq .36$, while the last two runs are for $h_w/h \succ .47$. The remaining two test runs are for $.36 \prec h_w/h \leq .47$.

Comparison of the radial and longitudinal surface profiles for the case of the bend with the flood relief channel with those obtained from the bend alone (i.e. Figures (6.1) to (6.6), Chapter III) leads to the following discussion:

(7.2.1.1) **Upstream of the Intersection** – ($\theta_b = 0^\circ \rightarrow 20^\circ$)

(1) For $h_w/h \leq .36$ (i.e. for test runs WF1, WF7 and WF13), the superelevation in the water surface is virtually the same in both cases.

(2) For $.36 \prec h_w/h \leq .47$ (i.e. for test runs WF2 and WF8), the superelevation has been slightly affected. A slight decrease in the superelevation was observed at $\theta_b = 20^\circ$. This reduction may be attributed to the flow diversity which causes some of the potential energy of the flow in the vicinity of the outer bank to be transformed into a kinetic energy.

(3) For $h_w/h \succ .47$ (i.e. for test runs WF5 and WF11), the water surface profiles are highly influenced by the intersection. The superelevation in the water surface is diminished considerably due to the increase in the kinetic energy of the flow near the outer bank which enhances the diversity of the flow upstream of the intersection. This feature also explains the poor comparisons between the measurements and the predictions as no account was taken in the derivation of the mathematical model of effects propagating upstream from the intersection.

(7.2.1.2) **Along the Intersection** – ($\theta_b = 25^\circ \rightarrow 35^\circ$)

(1) For $h_w/h \leq .36$ (i.e. for test runs WF1, WF7 and WF13), the superelevation remains almost the same as in the section upstream of the intersection, i.e. the longitudinal gradient of the water surface profiles is almost linear. The effect of the separation zone which develops at the upstream edge of the intersection is negligible.

(2) For $.36 < h_w/h \leq .47$ (i.e. for test runs WF2 and WF8), the separation zone draws down the water surface but the effect is restricted to the immediate vicinity of the upstream edge of the intersection. Both the predicted and measured longitudinal surface profiles tend to show a slight curvature.

(3) For $h_w/h > .47$ (i.e. for test runs WF5 and WF11), the separation zone developed at the upstream edge of the intersection expands to occupy almost 1/2 the width of the bend and about 1/2 the width of the flood channel. This produces a substantial increase in the drawdown of the water surface and as a result, the superelevation in the water surface decreases considerably. The predicted longitudinal surface profiles have now a considerable curvature and show increased deviation from the measured profiles particularly within the separation zone. In the second half of the intersection (i.e. beyond the separation zone), there is a tendency for the superelevation in the water surface to be re– developed.

(7.2.1.3) **Downstream of the Intersection** – (Θ_b= 40° → 0.15m D.S. bend)

Experimental Values Only

In all test runs (i.e. for all h_w/h ratios), the superelevation phenomenon in the water surface can be observed. However, the rate of development of the superelevation is dependent on the h_w/h ratio. The lower the h_w/h ratio, the quicker the rate of development of superelevation.

(7.2.2) Across the Flood Relief Channel

Experimental Values Only

Figures (7.8), (7.9), (7.10), (7.11), (7.12), (7.13) and (7.14) show typical water surface profiles obtained at different sections across the flood relief channel for test runs WF13, WF7, WF1, WF8, WF2, WF11 and WF5 respectively. Studying of these profiles leads to the following observations:

(1) The profiles illustrate the influence of the h_w/h on the separation zone and consequently, on the surface profiles. The higher the bed level of the flood channel, i.e. the smaller the value of h_w/h, the less the size of the separation zone becomes. The small values of flow depths measured in this zone indicate that part of the flood channel width is practically ineffective. As a result, the flow becomes more concentrated on the downstream side of the channel resulting in higher depths in this region.

(2) As the flow proceeds along the flood relief channel, the influence of the separation zone decreases. The rate at which a normal type of flow surface profile is re–established depends on the h_w/h ratio.

(3) In the absence of any flow control at the downstream end of the flood relief channel, the water surface levels decrease continuously as the flow proceeds along the channel.

(7.3) DISTRIBUTION OF DEPTH–AVERAGED VELOCITIES

In this section, the effect of the flood relief channel on the radial and longitudinal distributions of the depth–averaged velocities, in the bend, will be discussed and, where appropriate, comparisons will be made between the measured and predicted values. Figures (7.15), (7.16) and (7.17) illustrate comparisons between the measured and the predicted distributions of the depth–averaged velocities for test runs A1–V1, A3–V3 and A5–V5 respectively. The agreement is very satisfactory for the test runs A3–V3 and A5–V5 (i.e. for $h_w/h \leq .36$) but less satisfactory in case of test run A1–V1 for reasons which will be given later.

Since no attempt was made to formulate the flow mathematically in the channel bend downstream of the intersection, only experimental profiles are available in this region (i.e. from $\theta_b = 40^\circ \rightarrow 50^\circ$).

As in the case of the water surface profiles, the discussion of the depth–averaged velocities will be split into regions upstream of, along and downstream of the intersection.

Comparison of the profiles of the depth–averaged velocities for the test runs where the flood relief channel is introduced with those for the case of the bend

alone (see Figures (6.7) and (6.8), Chapter VI) leads to the following discussion:

(7.3.1) Upstream of the Intersection – ($\theta_b = 10^\circ \rightarrow 20^\circ$)

For all test runs, the maximum values of the depth–averaged velocities lie along the inner bank of the channel bend. However in the case of $h_w/h \geq .36$ (i.e. for test run A1–V1), there is a noticable flattening of the velocity profile just as the flow approaches the beginning of the intersection (i.e. from $\theta_b = 20^\circ \rightarrow 25^\circ$). This, as explained previously, is attributed to the rapid acceleration of the flow in the vicinity of the intersection which increases the rate of transforming the potential energy into the kinetic energy. This transformation, as a consequence, leads to a substantial decrease in the superelevation of the water surface and hence, to a more uniform distribution in velocities across the width of the channel bend.

(7.3.2) Along the intersection – ($\theta_b = 25^\circ \rightarrow 35^\circ$)

(1) For $h_w/h \leq .36$ (i.e. for test runs A3–V3 and A5–V5), the velocity profiles maintain virtually the same shape all along the intersection but with a gradual decrease in the magnitude of the velocities. The maximum velocities remain at the inner bank. This finding indicates that, within the above–stated h_w/h range, the effect of the cross currents on the depth–averaged flow chracteristics around a gentle wide channel bend may be considered minor.

(2) For $h_w/h > .36$ (i.e. for test run A1–V1), the measured velocity profiles are initially flatter than those for the $h_w/h \leq .36$ case, but as the flow moves along the intersection, a curved profile develops with the maximum velocity moving out

slightly from the inner bank as a stagnation zone develops. Similarly, at the outer bank, because of the marked separation zone which develops at the upstream end of the junction, the velocities of the flow entering the flood channel increase rapidly along the intersection with a corresponding decrease in the bend velocities. The formation of both the stagnation and separation zone account for the difference between the measured and predicted velocity values. The extent of the stagnation zone is dependent on the h_w/h ratio and the degree of submergence of the flow at the downstream end of the intersection. The higher the h_w/h ratio and the greater the degree of submergence, the greater is the upstream penetration of the stagnation zone.

Using flow visualisation techniques, the formation of both the stagnation and the separation zones can be seen. In the present study, it was found that the most suitable way of highlighting the two zones was to inject a weak solution of white emulsion point onto the water surface. Plates (7.1) and (7.2) show the formation of the stagnation and separation zones for test runs A1−V1 and A3−V3 respectively.

(7.3.3) Downstream of the Intersection − ($\theta_b = 40^\circ \rightarrow 50^\circ$)

Experimental Values Only

(1) In general, the behaviour of the depth−averaged velocities can be considered as a "carry over" effect of that from along the intersection.

(2) For $h_w/h \leq .19$ (i.e. for test run A5−V5), the maximum velocity along the inner bank gradually decreases while the velocity at the outer bank remains virtually constant. This process continues steadily until a uniform distribution of velocities across the bend width is eventually formed.

(3) For $.19 \prec h_w/h \leq .36$ (i.e. for test run A3– V3), the transverse distribution of the depth–averaged velocities follows very closely the same behaviour as in the previous case (i.e. for $h_w/h \leq .19$).

(4) For $h_w/h \succ .36$ (i.e. for test run A1– V1), the depth–averaged velocities along the inner bank continue to follow the decreasing trend established along the intersection but now with an increase in the central region of the bend and along the outer bank. This is a result of the increasing extent of the stagnation zone.

From the above description of the radial and longitudinal distributions of the depth–averaged velocities, it can be concluded that the suggested numerical depth–averaged model (described previously in Chapter IV) is justified for the case of $h_w/h \leq .36$. Within this range, the assumption of constant specific energy head along the intersection, which has been employed in the mathemetical formulation, is found to be realistic. Previous investigators found that the assumption of constant specific energy could be confirmed experimentally when the flow was subcritical and the main channel is straight and of a uniform cross section (e.g. see Allen (1957), Chow (1959), Subramanya et al (1972), Ranga Raju et al (1979), Uyumaz et al (1985) and others). Thus the present investigation, extends the validity of the assumption to the case where the main channel is a gentle wide bend (for $h_w/h \leq .36$ and $C_w/B = 0.6$).

For the case of $h_w/h \succ .36$, the diversity of the flow streamlines and the formation of separation/stagnation zones at the intersection tend to reduce the flow velocities substantially along the outer/inner banks of the bend. As a result, the theoretical predictions (in which the simulation of these zones is neglected) deviate considerably from the experimental values. The order of magnitude of the error

involved in ignoring the influence of these zones in the mathematical formulation may be estimated as a function of the relative water head ratio h_w/h and the relative width ratio C_w/B of the bend and the flood relief channels. The lower the h_w/h and C_w/B ratios, the less the error encountered.

Despite the variable degree of agreement between the measured and predicted channel velocities, there is remarkably consistent agreement between the measured and predicted discharge spilling into the flood relief channel (see Figures (7.18) and (7.19)). Because of this and of the degree of justification of the numerical depth–averaged model, it was thought worthwhile looking more closely at the radial and longitudinal variations of the discharge in the channel bend. Figures (7.20), (7.21) and (7.22) illustrate the theoretical predictions of these variations, in each bend strip, along the intersection for test runs A1–V1, A3–V3 and A5–V5 respectively. From the study of these predictions, the following conclusions may be drawn:

(1) The radial gradient of the bend strip discharge is increasing gradually towards the centre of curvature. As might be expected, the outer strips contribute more to the flow spilling into the flood relief channel thus reducing the discharge in the bend itself. The radial flow gradient is independent of both h_w/h ratio and strip location along the intersection (i.e. gradient of the radial flow is virtually constant).

(2) In contrast, the longitudinal discharge gradient depends on h_w/h ratio and, to a lesser extent, on the location of the bend strip. The higher the h_w/h ratio and the closer the strip position to the downstream end of the intersection, the higher the longitudinal flow gradient. For $h_w/h \leq .19$ (i.e. for test run A5–V5), the flow gradient is almost linear but for $h_w/h > .19$ (i.e for test runs A3–V3 and

A1− V1), the longitudinal gradient becomes increasingly non− linear indicating that the longitudinal flow is decreasing more rapidly.

(7.4) VERTICAL DISTRIBUTION OF LONGITUDINAL VELOCITIES

On the basis of the satisfactory results obtained from the comparisons of the depth− averaged velocities, it was considered worthwhile to try to apply the bend model for the vertical distribution of the longitudinal velocities (section (3.8), Chapter III) to the case where the intersection is introduced. The main purpose of this application is to answer the question of " **what is the influence of the flow diversity on the vertical distribution of the longitudinal velocities ?** ". Despite the fact that the mathematical formulation, for the vertical distribution of the longitudinal velocities, was based upon the assumptions of:

(1) vanishing of the net radial flow discharge along any vertical section of the flow, and

(2) matching of the longitudinal gradient of the longitudinal velocities with that of the depth− averaged velocities.

Yet, the quantitative comparisons between the theoretical predictions with the experimental measurements (where the intersection is introduced) may still be possible. That was accomplished by developing a subroutine specifically for this objective called **VEDIFL** (see Appendix (D) for its function and computational procedure). This subroutine is fed by the output of the bend model, which concerned with the vertical profiles of the longitudinal velocities (i.e. subroutine **VERDIS**, Appendix (D)), with the numerical results that obtained initially from the depth− averaged model for bend flow at the intersection (i.e. from subroutine **BENFLO**, Appendix (D)).

Figures (7.23), (7.24) and (7.25) show the comparisons between the predicted profiles with the data collected from test runs A1– V1, A3– V3 and A5– V5 respectively. As in the previous sub– sections of the Chapter, consideration of the results will be split into three parts, namely; upstream of, along and downstream of the intersection.

The corresponding Figures for the bend only situation are given in Figures (6.11) and (6.12) (Chapter VI). Comparison will be made where these are appropriate.

(7.4.1) Upstream of the Intersection – ($\theta_b = 10^\circ \rightarrow 20^\circ$)

(1) For $h_w/h \leq .36$ (i.e. for test runs A3– V3 and A5– V5), the comparisons are, in general, very satisfactory. This indicates clearly that the effect of the flood relief channel on the vertical profiles of the longitudinal velocities, upstream of the intersection, is negligible. Previous experimental investigations (e.g. see Subramanya et al (1972) and Ranga Raju et al (1979)) have reported the same conclusion for the case where the main channel is straight and of a uniform cross section.

(2) For $h_w/h > .36$ (i.e. for test run A1– V1), it can be seen that the comparisons are not as good as those for the previous cases, particularly, near the outer bank of the bend where the theoretical profiles are underpredicted. As explained previously when analysing the profiles of the water surface and depth– averaged velocities, the reason for this is the rapid acceleration of the flow which causes an increase in its kinetic energy and more deviation in its direction towards the outflow plane (i.e. the plane of the interface).

(7.4.2) **Along the Intersection** – ($\theta_b = 25^\circ \rightarrow 35^\circ$)

(1) For $h_w/h \leq .19$ (i.e. for test run A5– V5), the comparisons between the experimental and the theoretical profiles are fairly satisfactory. Nevertheless, the predictions tend to become slightly overestimated as the vertical sections of the flow become closer to the inner bank of the bend. This may be attributed to the development of the stagnation zone (even if it is in a weak state) along inner bank opposite to the interface of the intersection. In this case, the cross currents in the flow are rather weak and their effect on the vertical profiles of the longitudinal velocities may be ignored.

(2) For $.19 < h_w/h \leq .36$ (i.e. for test run A3– V3), the development of the cross currents is relatively strong and as a consequence, the decrease in the bend velocities becomes more substantial. This can clearly be seen from the discrepancies between the predicted and the measured profiles. The closer the vertical section to the outer bank, the less the measured velocities become and hence, the poorer the agreement with the predicted velocities become. The main reason for these discrepancies is that the condition, assumed in the mathematical model, of zero net radial discharge along the vertical sections of the flow is no longer valid. Along the inner bank, the formation of the stagnation zone plays a role in slowing the reduction process of the flow velocity in this zone. This results in better agreement with the predictions (refer also to Plate (7.2)).

(3) For $h_w/h > .36$ (i.e. for test run A1– V1), the cross currents in the flow become the dominant feature and as a result, the longitudinal velocities in the bend decrease dramatically. In this case, the stagnation zone is well established along the intersection and extends even further downstream of it. The measured velocity values no longer follow the same behaviour (i.e. in magnitude and in

direction) as the theoretical profiles. As in the previous case (i.e. for .19 $\lessdot$ h_w/h $\leq$ .36), the closer the section to the outer bank, the more overestimated the predictions become. Also, in the second half of the intersection (i.e. θ_b = 32.5° $\rightarrow$ 35°), a small reverse flow in the velocity profiles is observed near the channel bed at sections close to the outer bank.

(7.4.3) Downstream of the Intersection – (θ_b = 40° $\rightarrow$ 50°)

Experimental Values Only

(1) In general, as in the case of depth–averaged velocities, the behaviour of the longitudinal velocities profiles, beyond the intersection, can be described as a **"carry over"** effect of those along the intersection.

(2) For h_w/h $\leq$ .19 (i.e. for test run A5–V5), the longitudinal velocities continue to decrease gradually near the inner bank. While near the outer bank, the velocities increase at about the same rate. This process continues gradually until a nearly uniform condition across the bend width is obtained.

(3) For .19 $\lessdot$ h_w/h $\leq$ .36 (i.e. for test run A3–V3), the velocity profiles behave in a similar way to those for h_w/h $\leq$ .19 , but at a slower rate. However, the higher velocities continue to occupy the inner half of the channel. This indicates that the normal bend features of the flow are not drowned out completely by the effects of the intersection.

(4) For h_w/h $\gtrdot$ .36 (i.e. for test run A1–V1), the decrease/increase in the longitudinal velocities near the inner/outer banks occur at a faster rate than that in the previous two cases. Due to the persistence of the stagnation zone, velocities within the inner half of the channel are small. In contrast, the maximum

velocities are found to occupy almost all of the outer half of the bend cross section. This indicates that, in a natural river channel, severe scour of the bank and the bed in this region of the channel bend is likely to occur.

In addition to the features mentioned in the above discussion, the following features were observed:

(1) For $h_w/h \leq .36$ (i.e. for test runs A3– V3 and A5– V5), the maximum point velocity is always found at or near the water surface. Also, the application of the logarithmic law for the vertical distribution of the longitudinal velocities holds reasonably well with the experimental results upstream of and along the intersection.

(2) For $h_w/h > .36$ (i.e. for test run A1– V1), due to the stong development of the cross currents and the combined effect of the stagnation and separation zones, the vertical distributions of the longitudinal velocities show considerable variations in shape. This applies to all sections of the flow along and downstream of the intersection.

(7.5) DEVIATION ANGLES OF HORIZONTAL RESULTANT VELOCITIES

Experimental Values Only

In this section, consideration is given to the analysis of the deviations of the horizontal currents from the tangential direction at 11 cross sections in the bend channel. Tables (7.3), (7.4) and (7.5) give the measured values of the deviation angles for test runs A1– V1, A3– V3 and A5– V5 respectively. These values were plotted and are shown in Figures (7.26), (7.27) and (7.28) respectively.

Once again, the analysis is split into three parts; upstream of, along and downstream of the intersection and, again, comparison is made where appropriate with the corresponding Figures, i.e. Figures (6.13) and (6.14) (Chapter VI), for the case of the bend alone.

(7.5.1) Upstream of the Intersection – ($\theta_b = 10^\circ \rightarrow 20^\circ$)

(1) For $h_w/h \leq .36$ (i.e. for test runs A3– V3 and A5– V5), as could be expected from the previous examination of the velocity profiles, little effect of the intersection is propagated upstream. The bend characteristics predominate the flow. A one– cell type of the secondary circulation (as indicated by the trend of the values) is observed and there is little difference in the deviation angles across the width of the channel. This indicates that, for a bend cross section, the average value of the deviation angle is adequate for estimating the flow diversity upstream of the intersection.

(2) For $h_w/h \gtrsim .36$ (i.e. for test run A1– V1), the influence of the intersection is significant. Contrary to the case of $h_w/h \leq .36$, the flow diversity no longer remains almost constant but varies across the channel with greatest deviations being observed towards the outer bank.

(7.5.2) Along the Intersection – ($\theta_b = 25^\circ \rightarrow 35^\circ$)

(1) For $h_w/h \leq .19$ (i.e. for test run A5– V5), the behaviour of the flow located in the outer region of the bend cross section is different than that located in the inner region. In the outer region (i.e. close to the flood channel), the flow diversity increases locally. Whereas, in the inner region of the bend, the bend

characteristics continue to dominate the flow as can be seen by the relatively small deviation angles measured in this region.

(2) For $.19 < h_w/h \leq .36$ (i.e. for test run A3– V3), the diversity of the horizontal currents increases substantially and in a fairly equal increments across the bend width.

(3) For $h_w/h > .36$ (i.e. for test run A1– V1), since the flow structure is governed by the combined effect of the separation and the stagnation zones, the deviation angles increase dramatically along the intersection. The closer the location to the outer bank, the greater the deviation angle becomes.

(7.5.3) Downstream of the Intersection – ($\theta_b = 40^\circ \rightarrow 50^\circ$)

(1) For $h_w/h \leq .36$ (i.e. for test runs A3– V3 and A5– V5), the structure of the flow adjusts itself rapidly to behave in a similar manner to that upstream of the intersection. A one– cell type of the secondary currents is re– established despite the increase in the order of magnitude of the deviation angles compared with those upstream of the intersection. It can be also seen that spread of the points in case of test run A5– V5 is greater than that in case of test run A3– V3. This can be attributed to the sudden change of the flow structure near the outer bank (i.e. re– establishment of deviations towards the inner bank for the bottom currents) compared with that near the inner bank which tends to be unaffected by the intersection.

(2) For $h_w > .36$ (i.e. for test run A1– V1), the adjustment of the flow to the bend type of behaviour is at a slower rate. High values of the angles are seen

near the outer bank which indicates that, in a natural river, severe bank attack and bed scour is likely to occur just downstream of the intersection. This reinforces the similar conclusion already reached from consideration of the longitudinal velocity distributions.

(7.6) GENERAL REMARKS ON THE ANALYSIS OF BEND FLOW AT THE INTERSECTION

The foregoing analysis of the flow characteristics in the channel bend at the intersection of the flood relief channel leads to the following conclusions:

(7.6.1) For the case of $h_w/h \leq .36$, the comparisons between the predicted and the experimental values show reasonably good agreement thus, justifying the suggested mathematical depth–averaged model. However, for the case of $h_w/h > .36$, the comparisons are not as good. This can be attributed to the combined effect of both the stagnation and the separation zones that develop along the inner and the outer banks of the bend at the intersection.

(7.6.2) The assumption of constant specific energy for the flow, in all radial bend strips, along the intersection is found to be acceptable for predicting water surface and depth–averaged velocity profiles when $h_w/h \leq .36$. However when $h_w/h > .36$, the predictions are not as accurate because of the complex structure of the flow at the intersection.

(7.6.3) For the case of $h_w/h \leq .36$, the superelevation of the water surface remains almost constant along the intersection and the profiles are approximately linear.

(7.6.4) For $.36 \prec h_w/h \leq .47$, the predicted surface profiles behave non– linearly and the superelevation tends to decrease as the flow passes along the intersection.

(7.6.5) For $h_w/h \succ .47$, stagnation/separation zones along the inner/outer banks of the bend are the features which govern the shape of the surface profiles at the intersection, i.e. the centrifugal effects are of minor significance.

(7.6.6) Using the mathematical model, the longitudinal and the radial gradients of the bend discharge along the intersection can be predicted. The theoretical predictions have shown that the radial gradient of the discharge is uniform i.e. independent of the h_w/h ratio and the bend angle. In contrast, the longitudinal discharge gradient is very dependent on the h_w/h ratio.

(7.6.7) For all h_w/h ratios, the bend characteristics in the flow are re– established downstream of the intersection. However, the rate of this re– establishment depends on the h_w/h ratio. The higher the h_w/h ratio, the slower the rate of re– adjustment to the bend characteristics.

(7.6.8) By superimposing the depth– averaged model for the bend flow at the intersection on the bend model that deals with the vertical profiles of the longitudinal velocities, it was possibile to predict the vertical profiles of the velocities at the intersection. For the case of $h_w/h \leq .36$, the comparisons with the experimental values were good. But as the h_w/h ratio increases, the error that results from the assumption of a zero net radial discharge along the vertical sections of the flow becomes high and the predictions, as a consequence, become unrealistic.

(7.6.9) The distributions of the deviation angles of the horizontal resultant velocities follow very closely the behaviour of the water surface and the velocity distributions.

(7.6.10) On the basis of the overall analysis, it can be concluded that the order of magnitude of the error resulting from ignoring the radial momentum exchange in the formulation of the mathematical model can be considered minor when $h_w/h \leq .36$. While for the case of $h_w/h \succ .36$, the inclusion of the radial momentum exchange in the formulation is essential.

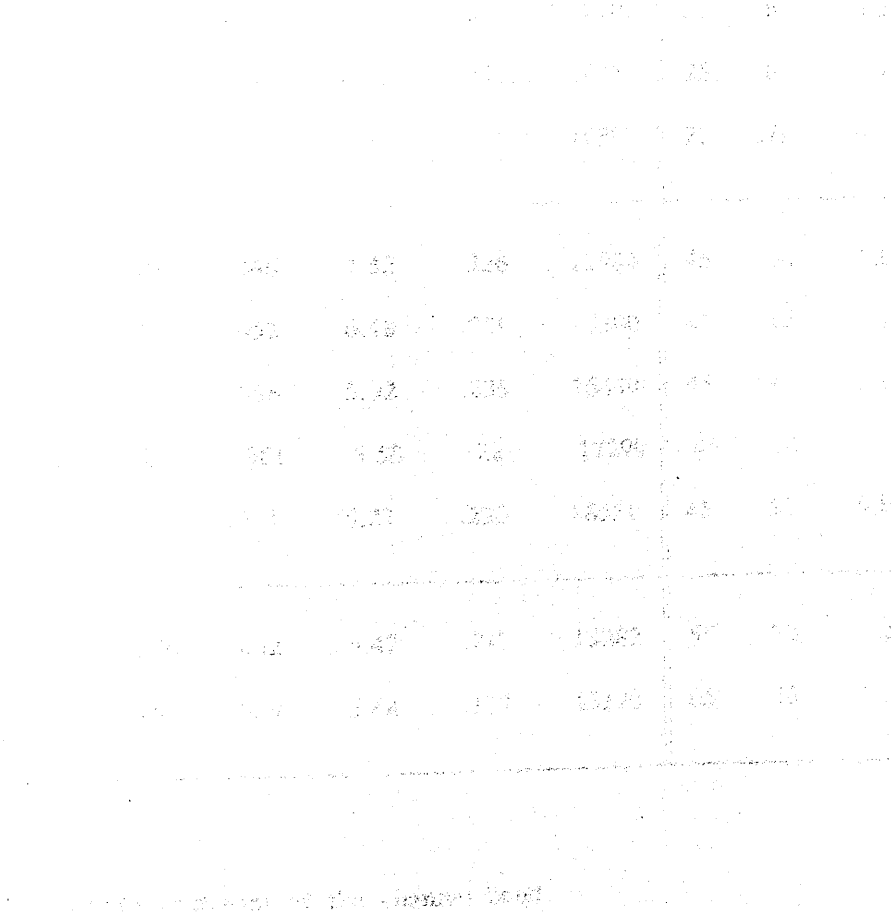

TABLE (7.1) – Experimental Programme for Measurements of Water Surface Profiles

	← CHANNEL BEND DATA							← FLOOD CHANNEL DATA →			
Test Run	h^* mm	Q l/s	u^{**} m/s	h/r_m	B/h	F_r	R_e	C_h mm	h_w/h	Q_{fR} l/s	Q_{fR}/Q
WF1	39	2.91	.149	.026	12.82	.241	5283	25	.36	.66	.23
WF2	45.8	3.94	.172	.031	10.92	.257	7162	25	.45	1.35	.34
WF3	53	5.42	.205	.035	9.43	.284	9878	25	.53	2.17	.40
WF4	67.2	7.00	.208	.045	7.44	.256	12707	25	.63	4.25	.61
WF5	76.8	7.94	.207	.051	6.51	.239	14453	25	.68	5.71	.72
WF6	87.5	8.98	.205	.058	5.71	.221	16307	25	.71	6.75	.75
WF7	68.3	6.60	.193	.046	7.32	.236	11984	45	.34	1.68	.26
WF8	77.2	8.43	.218	.052	6.48	.251	15300	45	.42	2.44	.29
WF9	84.5	9.06	.214	.056	5.92	.235	16440	45	.47	3.76	.42
WF10	91	9.53	.209	.061	5.50	.221	17290	45	.51	3.97	.42
WF11	95.8	10.21	.213	.064	5.22	.220	18551	45	.53	5.01	.49
WF12	77.3	7.30	.189	.052	6.47	.217	13282	65	.16	.57	.08
WF13	88.0	7.22	.164	.059	5.68	.177	13120	65	.26	1.33	.18

* – mean water depth upstream of the channel bend.
** – mean velocity of the flow upstream of the channel bend.

TABLE (7.2) – Experimental Programme for Measurements of Longitudinal Velocities and Deviation Angles

	← CHANNEL BEND DATA →							← FLOOD CHANNEL DATA →			
Test Run	h^* mm	Q l/s	u^{**} m/s	h/r_m	B/h	F_r	R_e	C_h mm	h_w/h	Q_{fR} l/s	Q_{fR}/Q
A1–V1	55.5	5.38	.196	.037	9.010	.266	9889	25	.55	2.24	.42
A2–V2	70	7.70	.220	.047	7.143	.266	14000	25	.64	4.08	.53
A3–V3	60	6.00	.200	.040	8.333	.261	10909	45	.25	.76	.13
A4–V4	70	7.39	.211	.047	7.143	.255	13427	45	.36	1.68	.23
A5–V5	80	6.40	.160	.053	6.250	.181	11636	65	.19	.64	.10

* – mean water depth upstream of the channel bend.
** – mean velocity of the flow upstream of the channel bend.

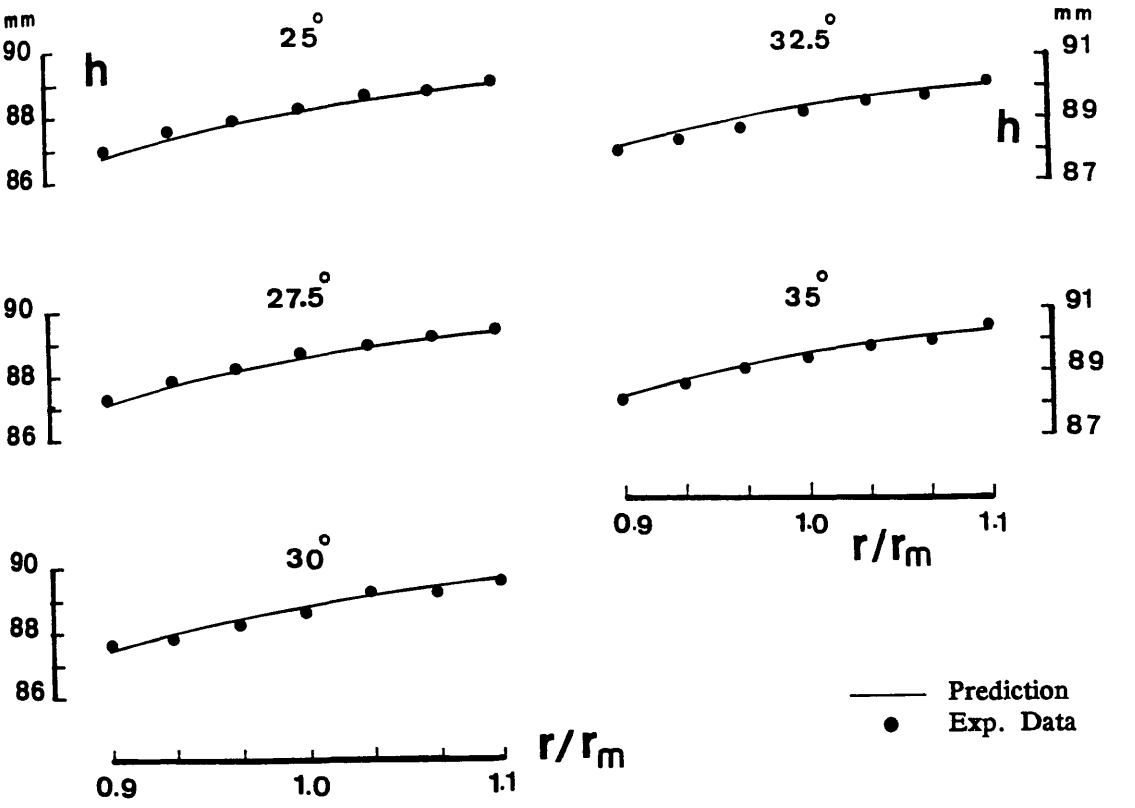

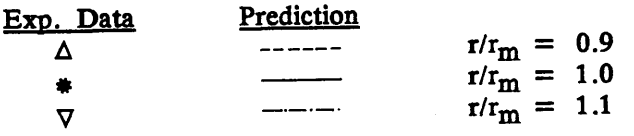

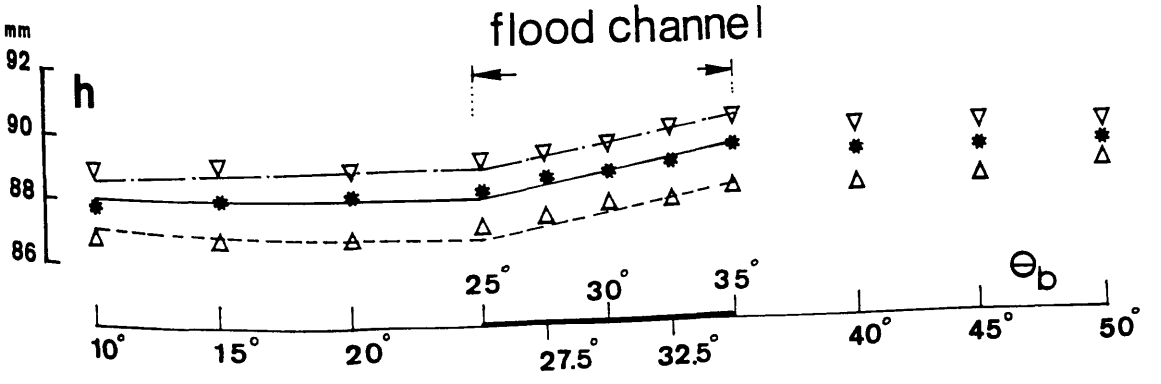

$h_w/h = .26$

Fig.(7.1) — Comparison between the Predicted and Measured Radial and Longitudinal Water Surface Profiles for Test Run WF13

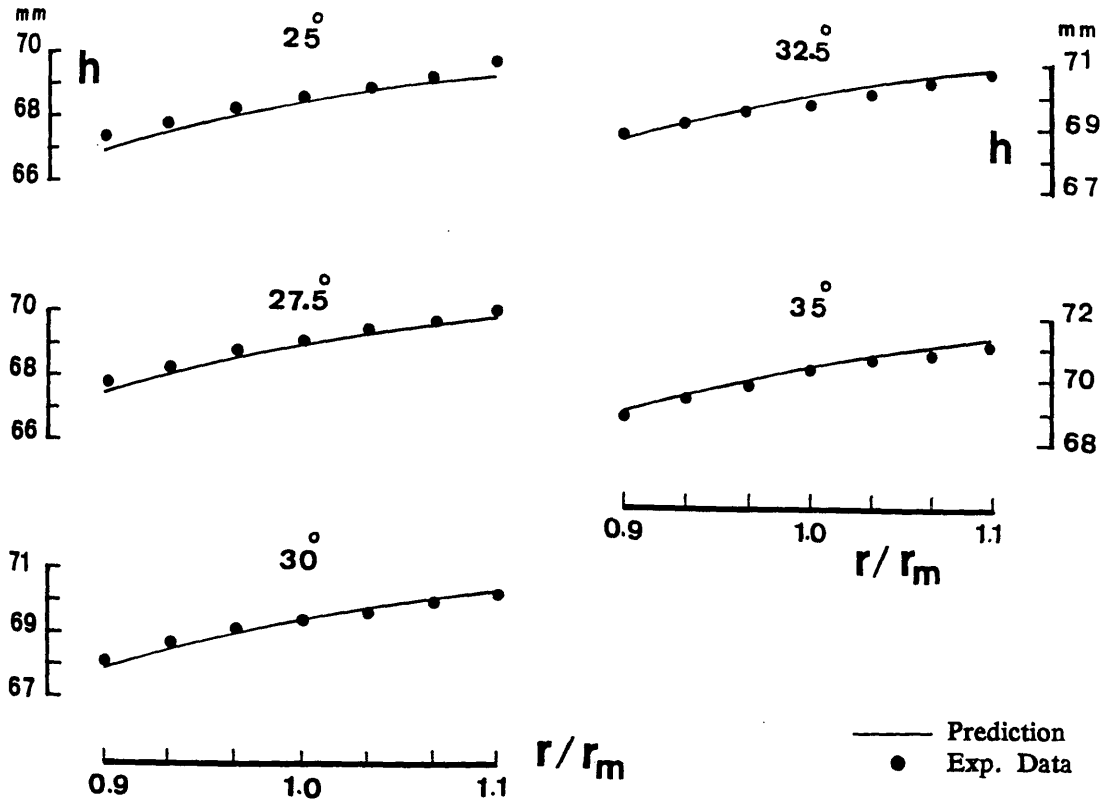

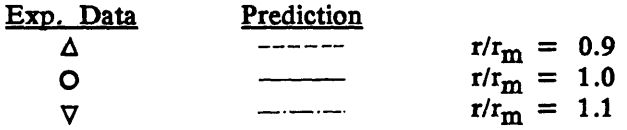

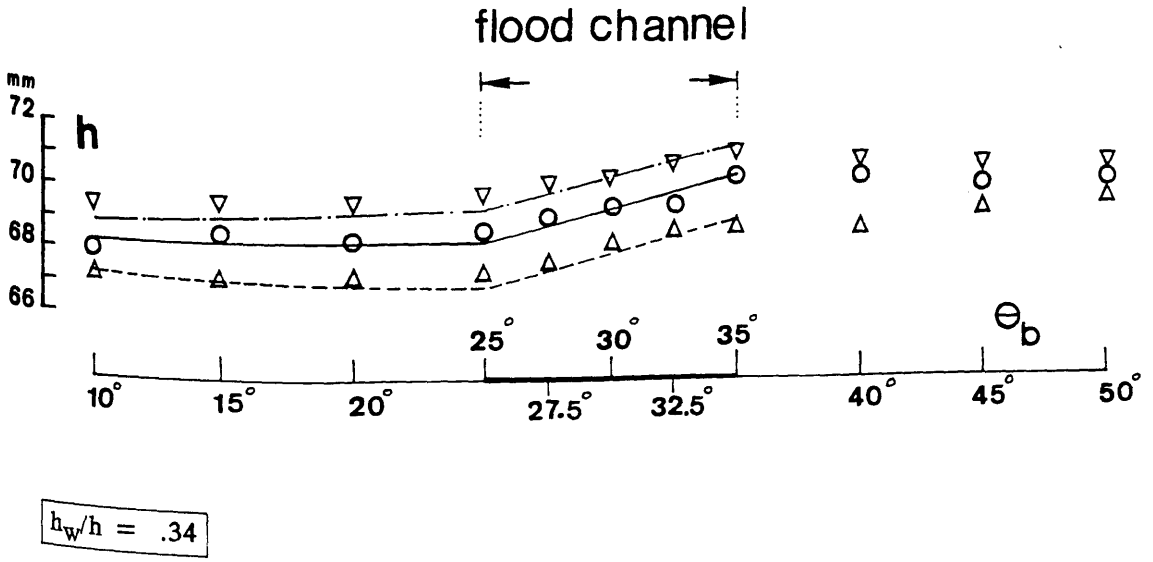

$h_w/h = .34$

Fig.(7.2) — Comparison between the Predicted and Measured Radial and Longitudinal Water Surface Profiles for Test Run WF7

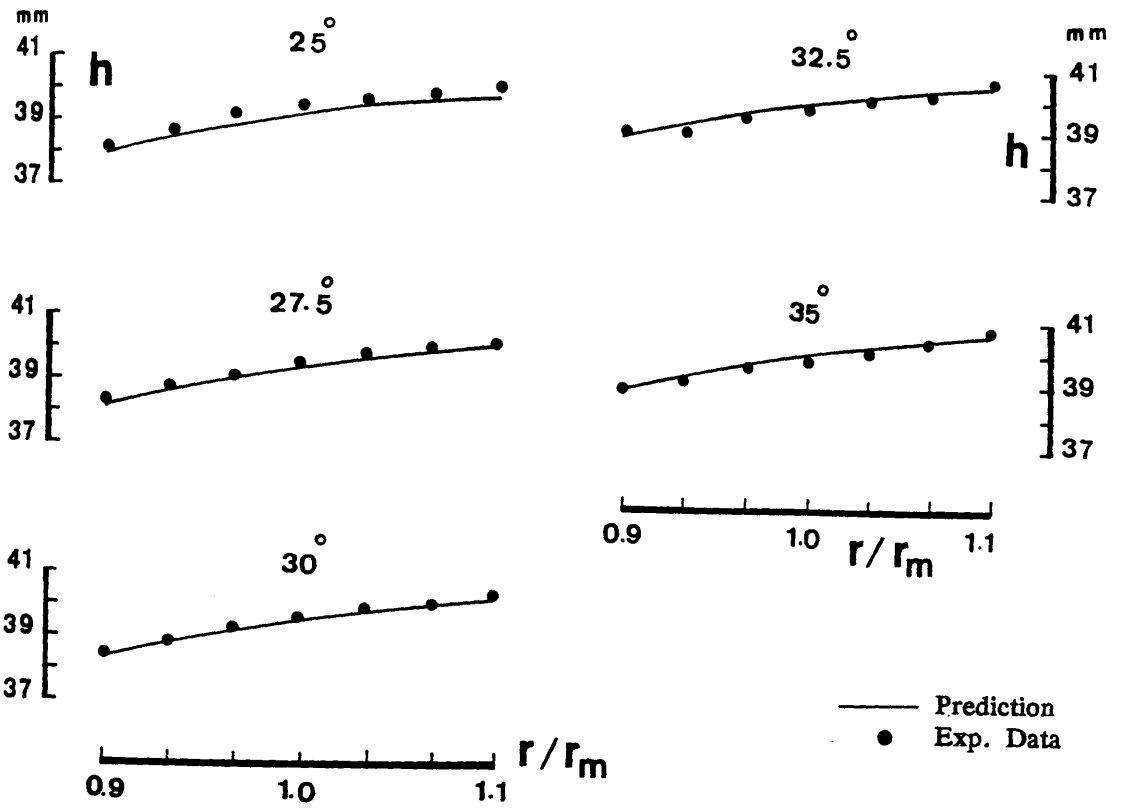

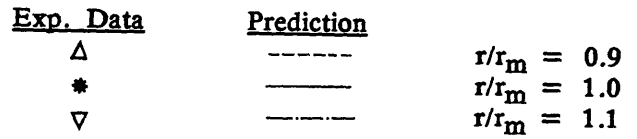

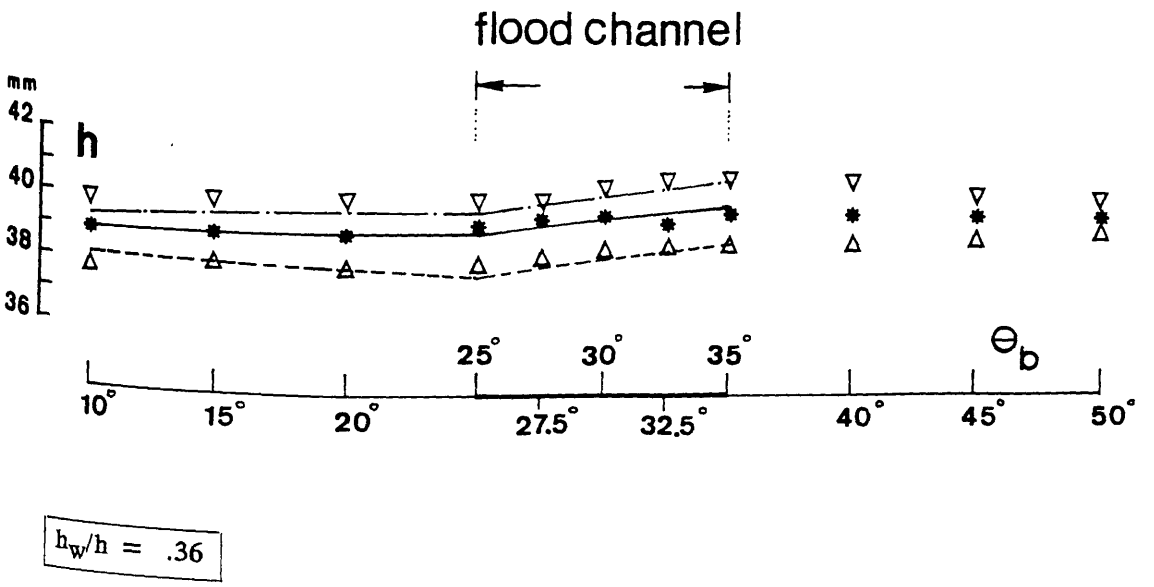

$h_w/h = .36$

Fig.(7.3) — Comparison between the Predicted and Measured Radial and Longitudinal Water Surface Profiles for Test Run WF1

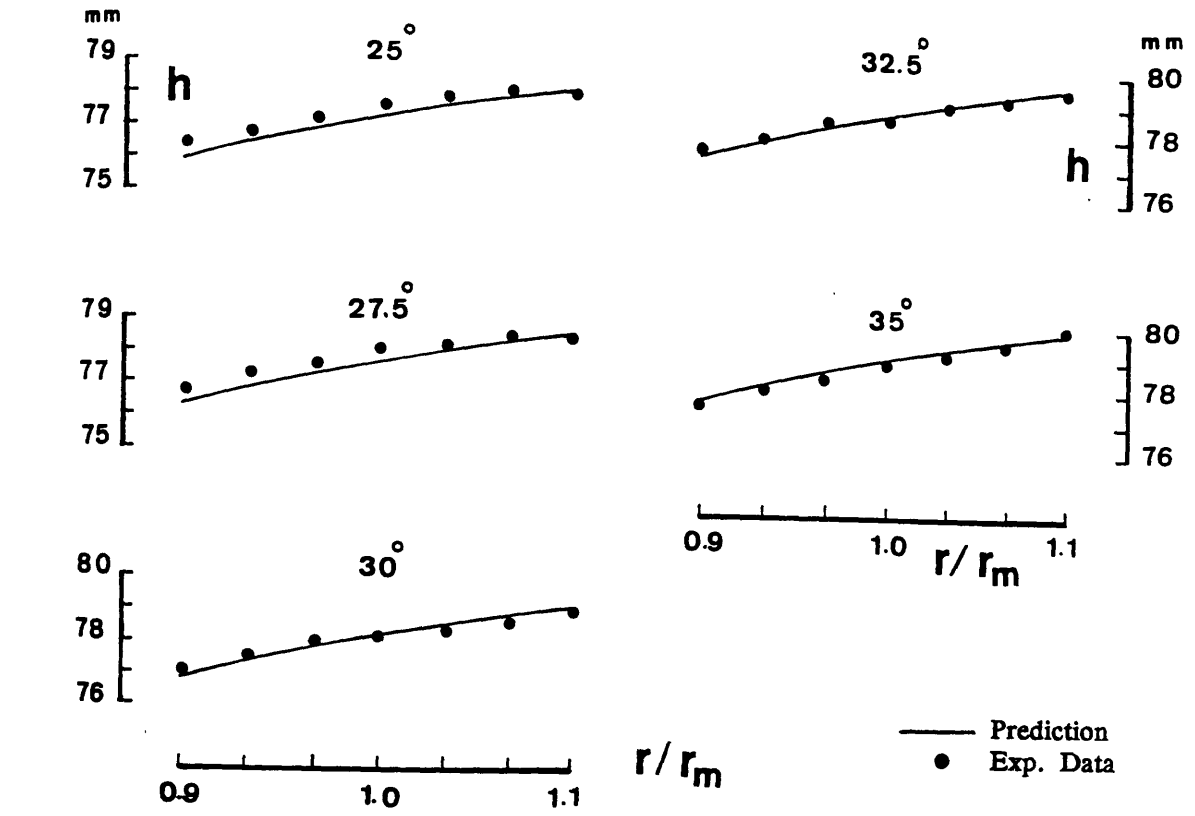

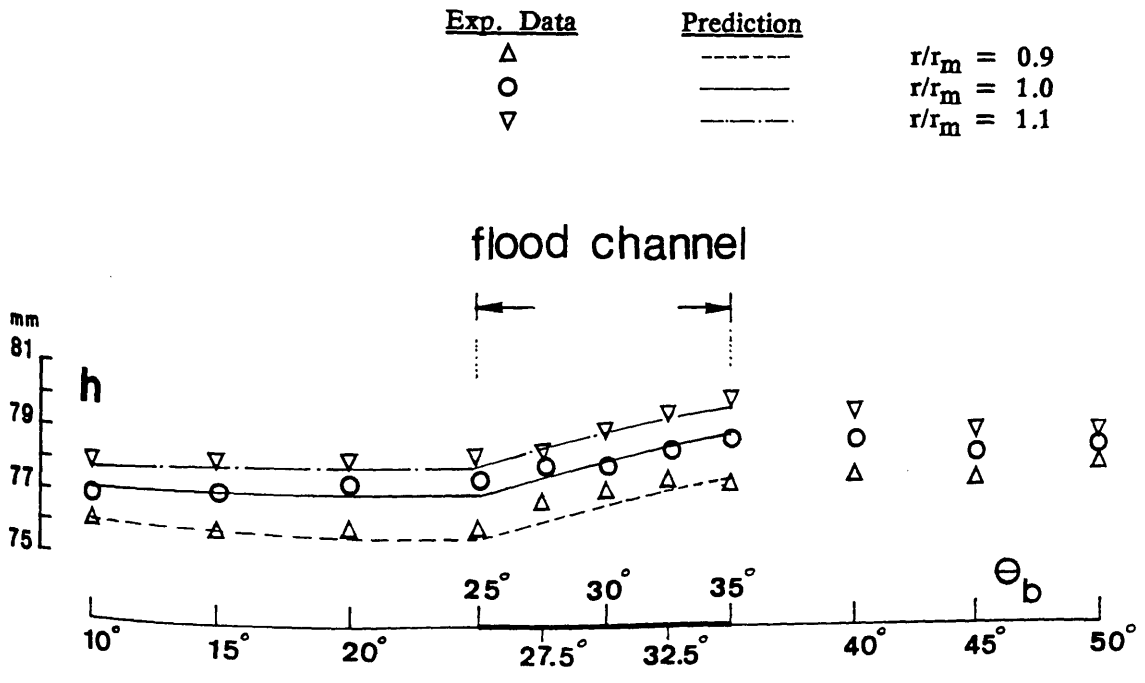

Fig.(7.4) — Comparison between the Predicted and Measured Radial and Longitudinal Water Surface Profiles for Test Run WF8

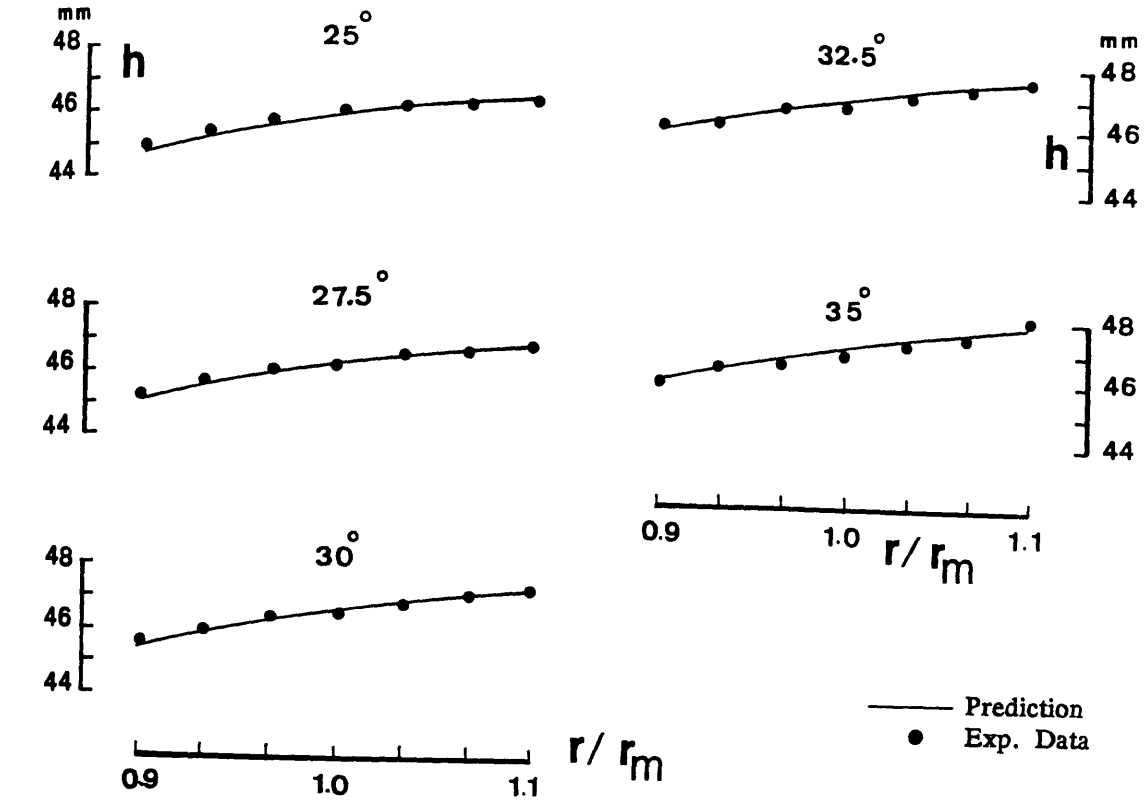

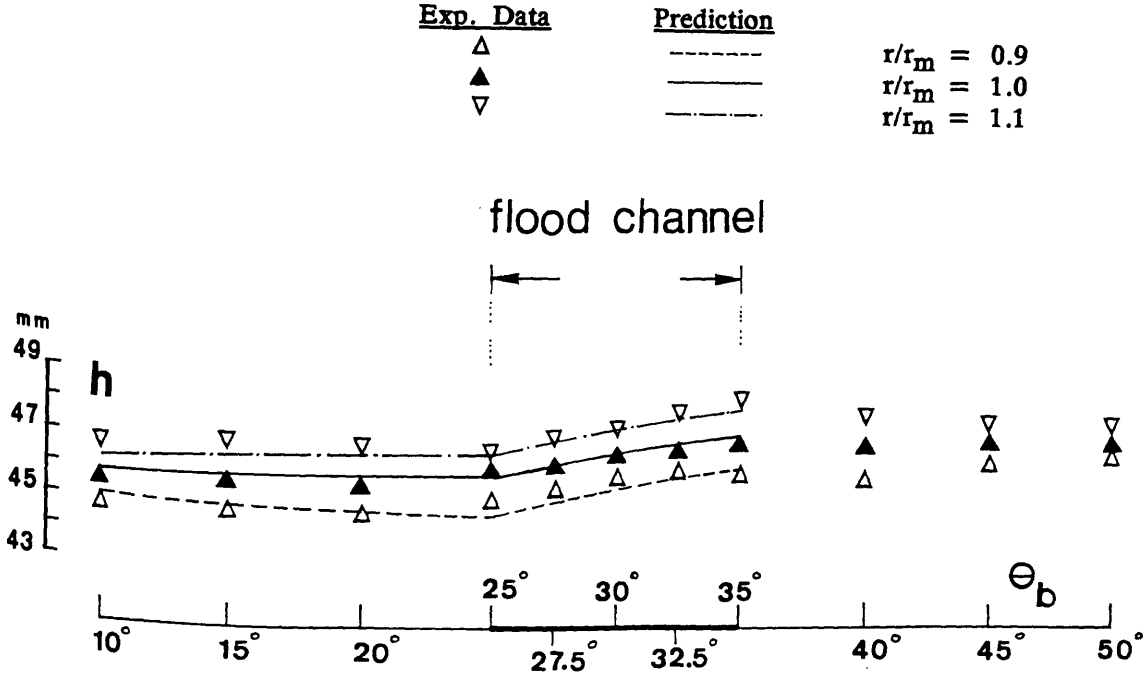

Fig.(7.5) – Comparison between the Predicted and Measured Radial and Longitudinal Water Surface Profiles for Test Run WF2

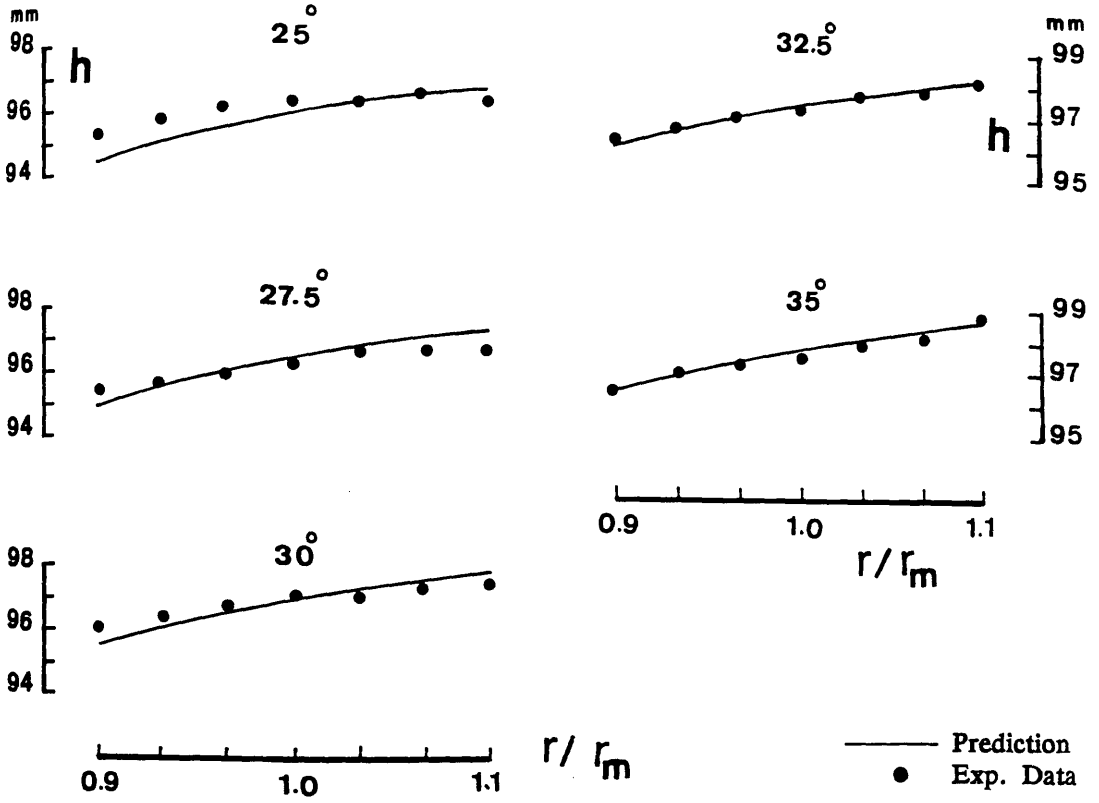

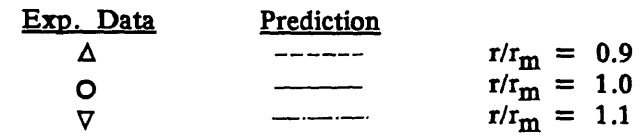

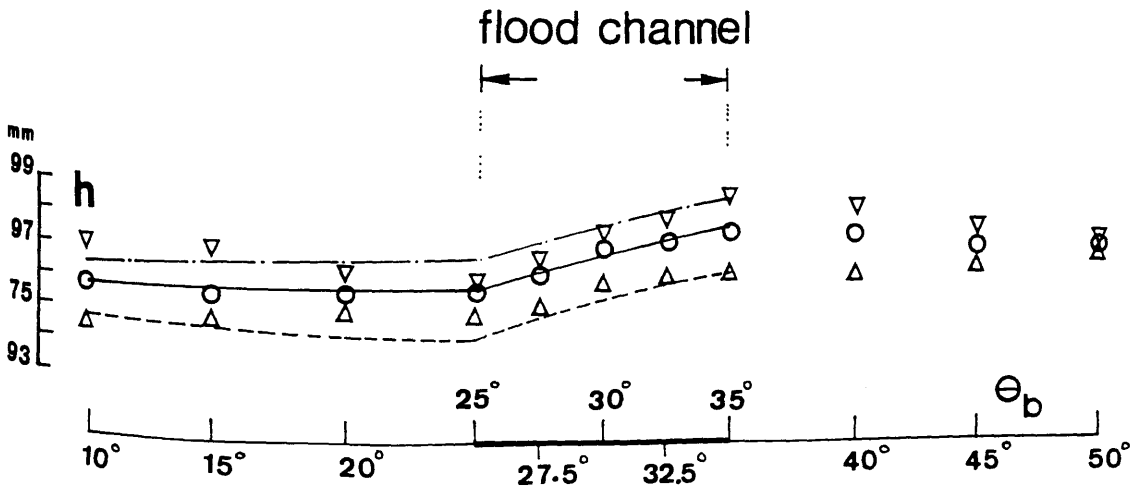

$h_w/h = .53$

Fig.(7.6) – Comparison between the Predicted and Measured Radial and Longitudinal Water Surface Profiles for Test Run WF11

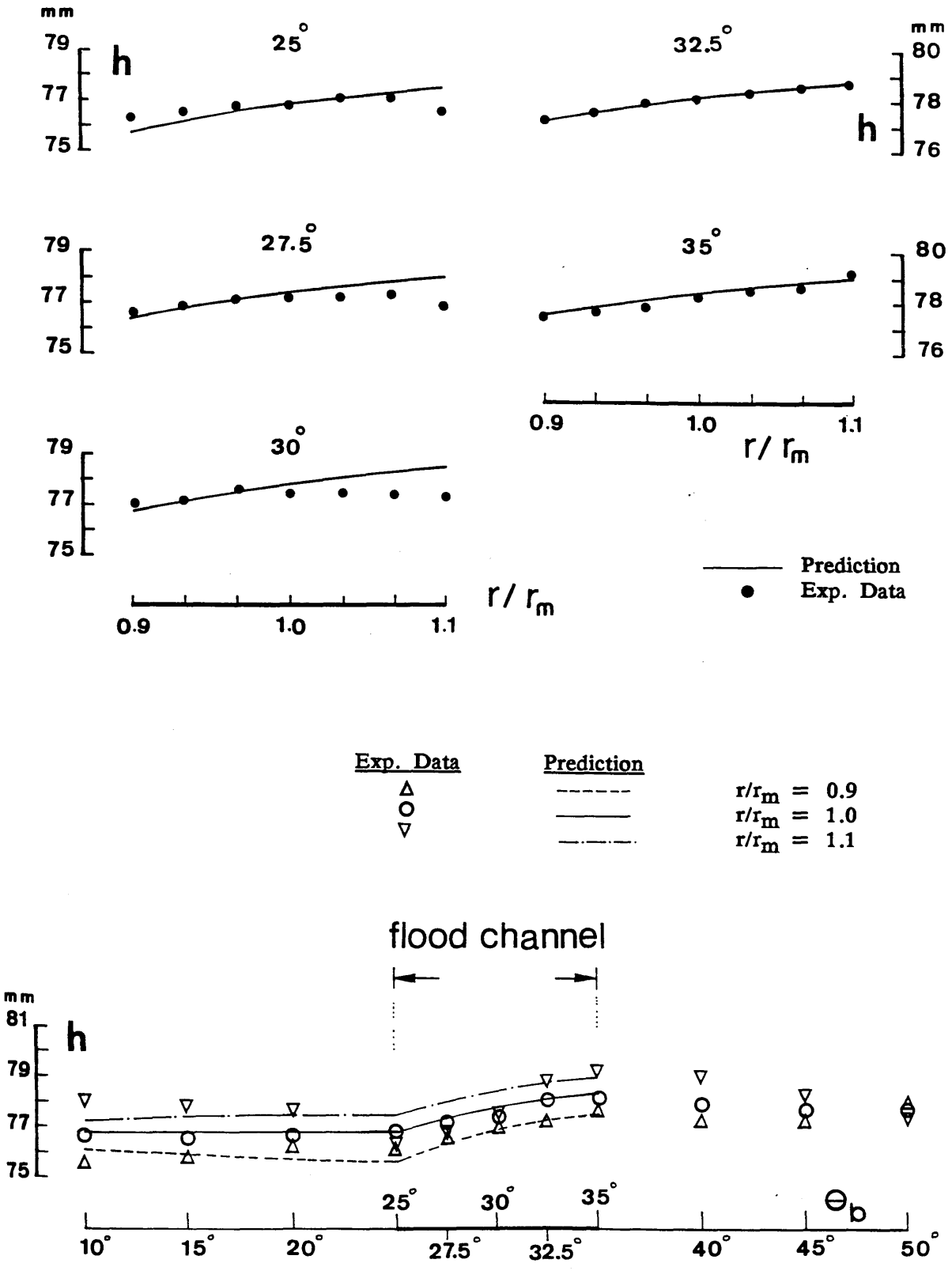

Fig.(7.7) – Comparison between the Predicted and Measured Radial and Longitudinal Water Surface Profiles for Test Run WF5

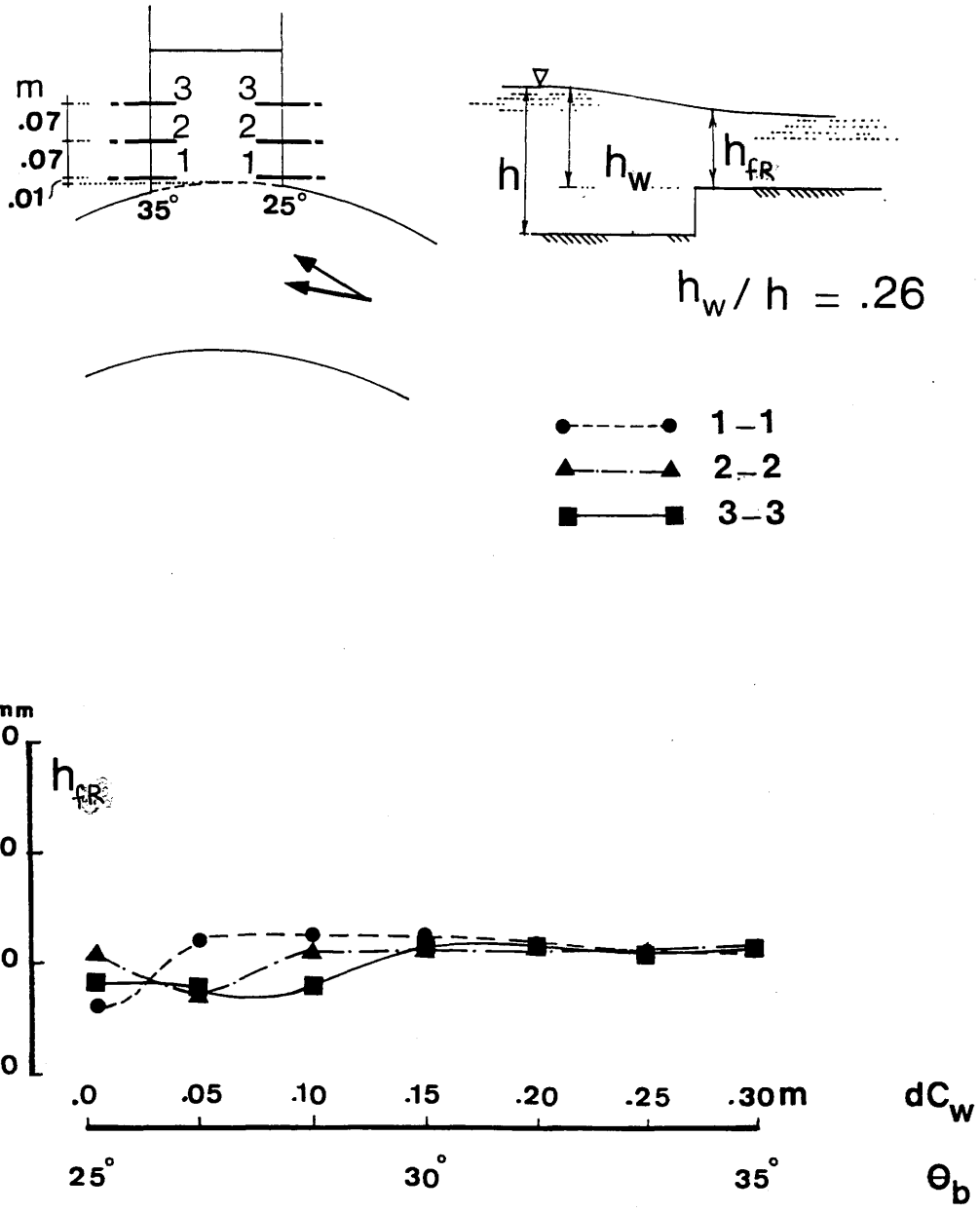

Fig.(7.8) – Measured Water Surface Profiles Across the Flood Relief Channel for Test Run WF13

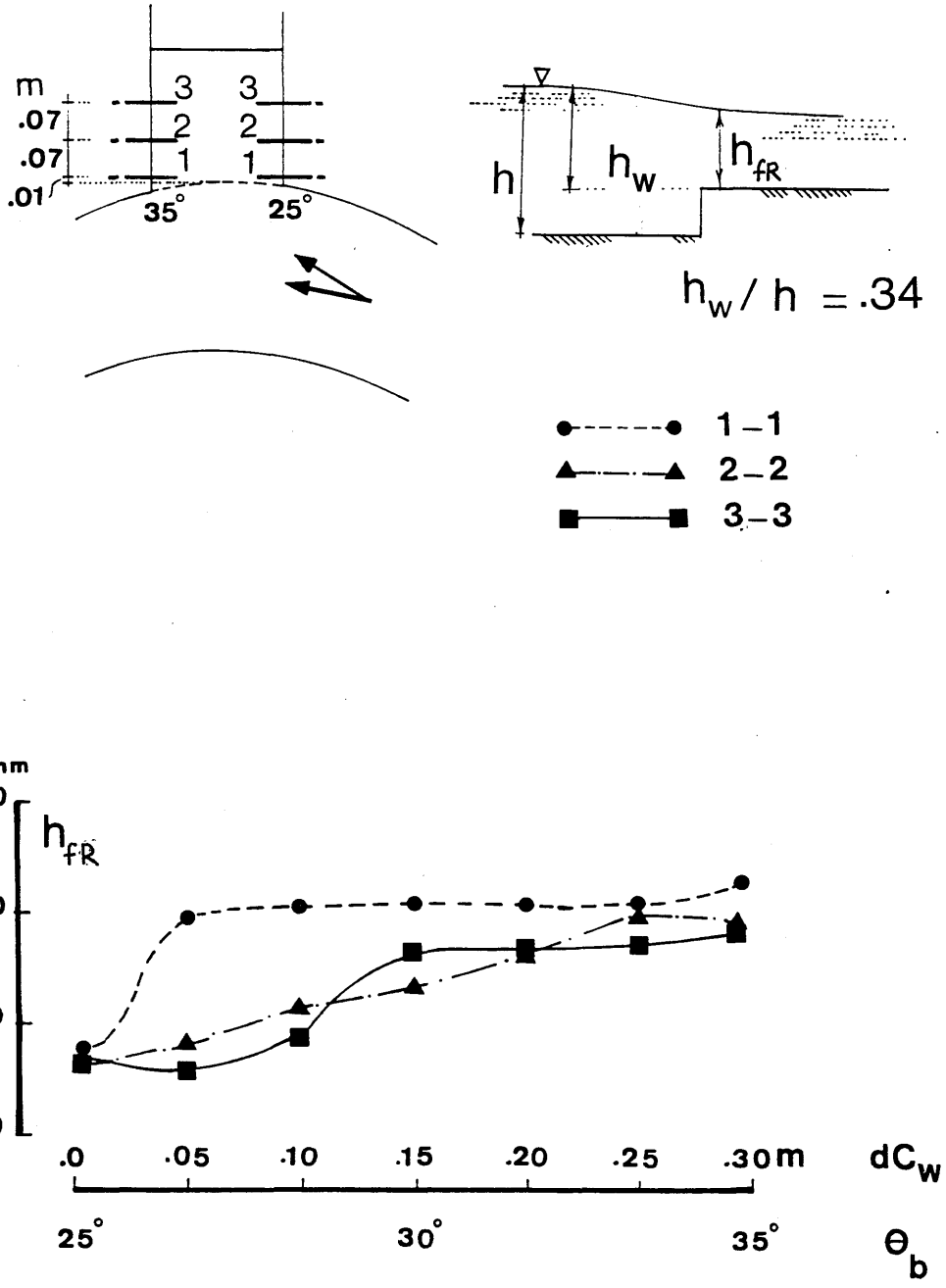

Fig.(7.9) – Measured Water Surface Profiles Across the Flood Relief Channel for Test Run WF7

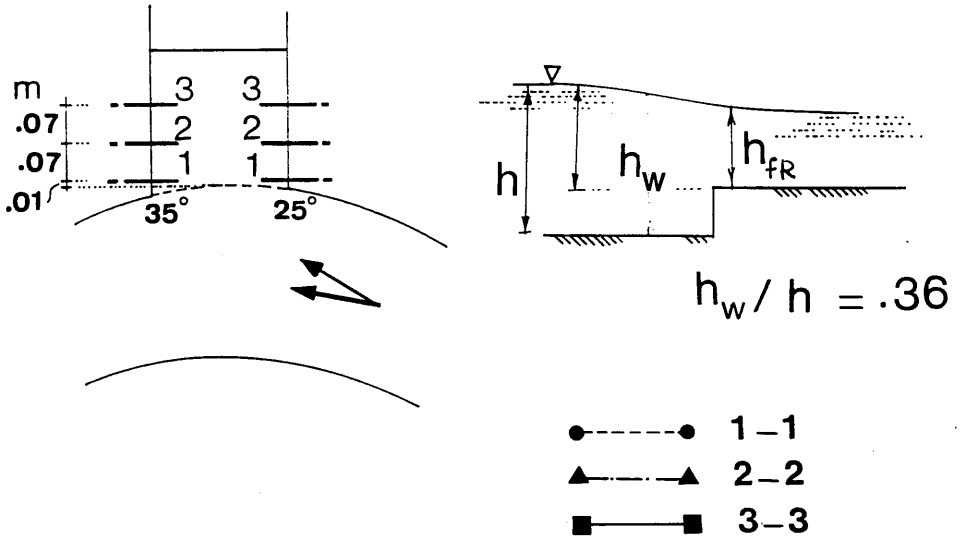

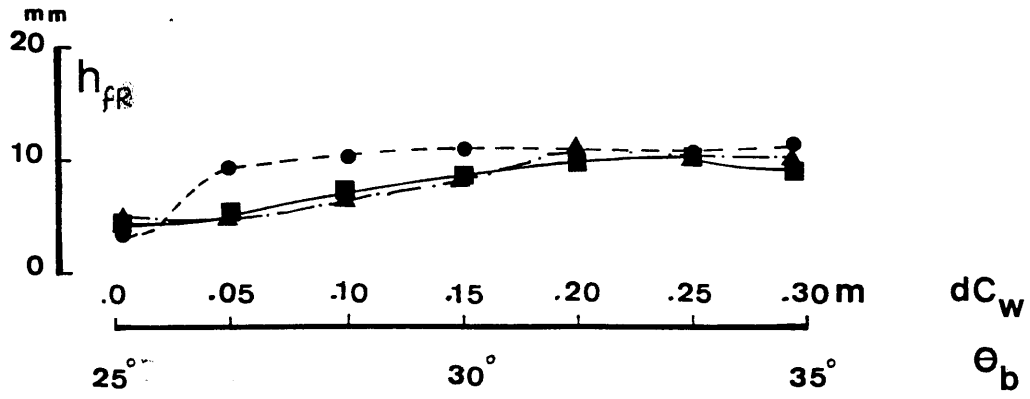

Fig.(7.10) – Measured Water Surface Profiles Across the Flood Relief Channel for Test Run WF1

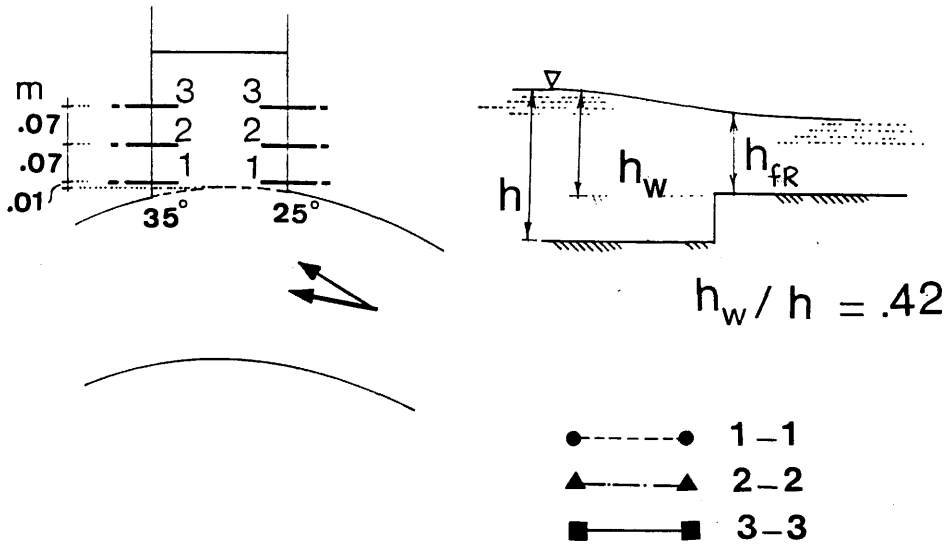

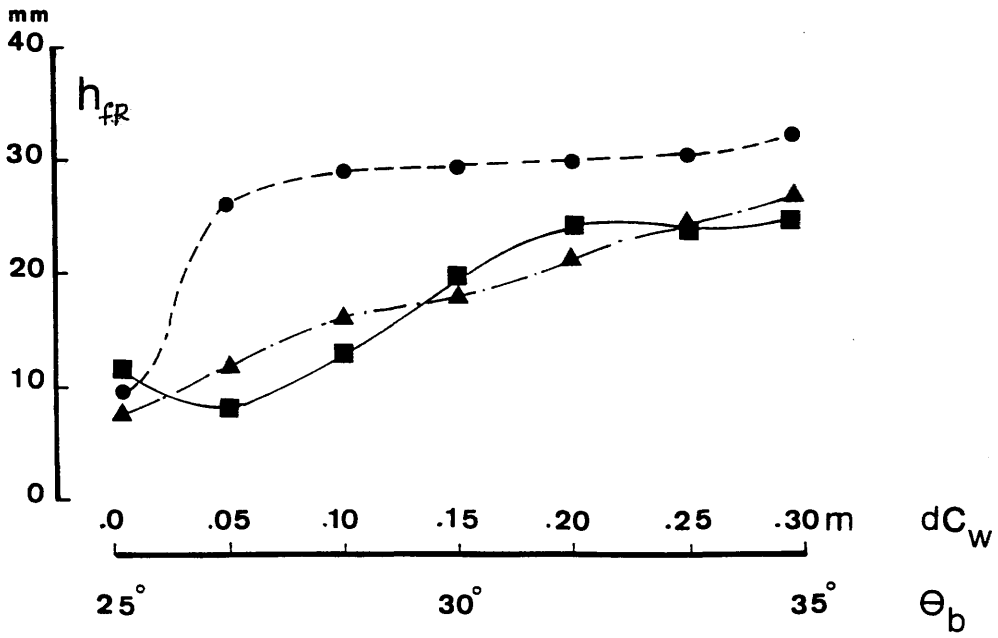

Fig.(7.11) – Measured Water Surface Profiles Across the Flood Relief Channel for Test Run WF8

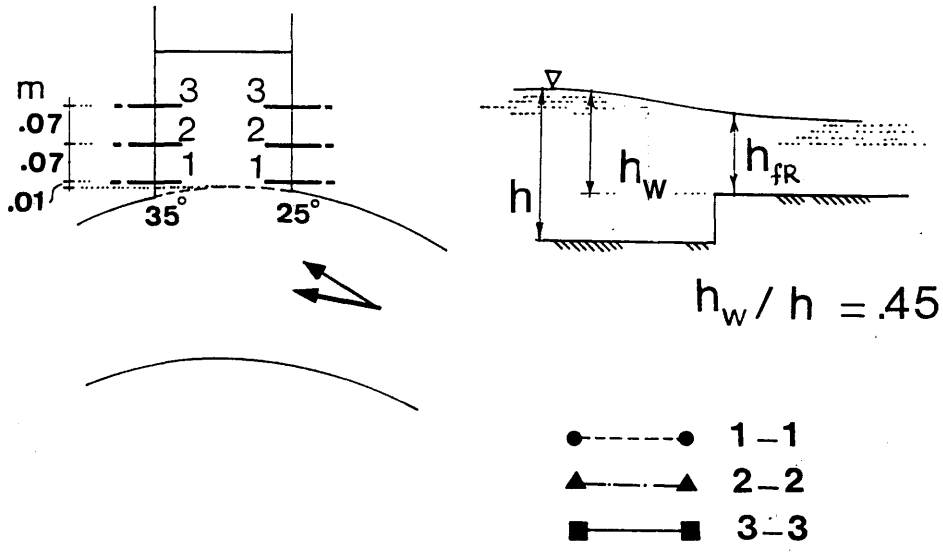

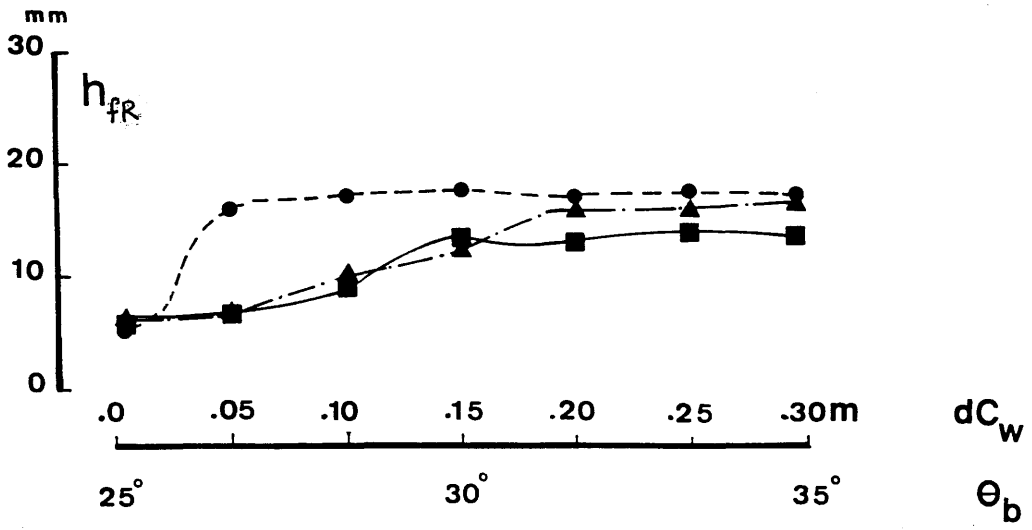

Fig.(7.12) – Measured Water Surface Profiles Across the Flood Relief Channel for Test Run WF2

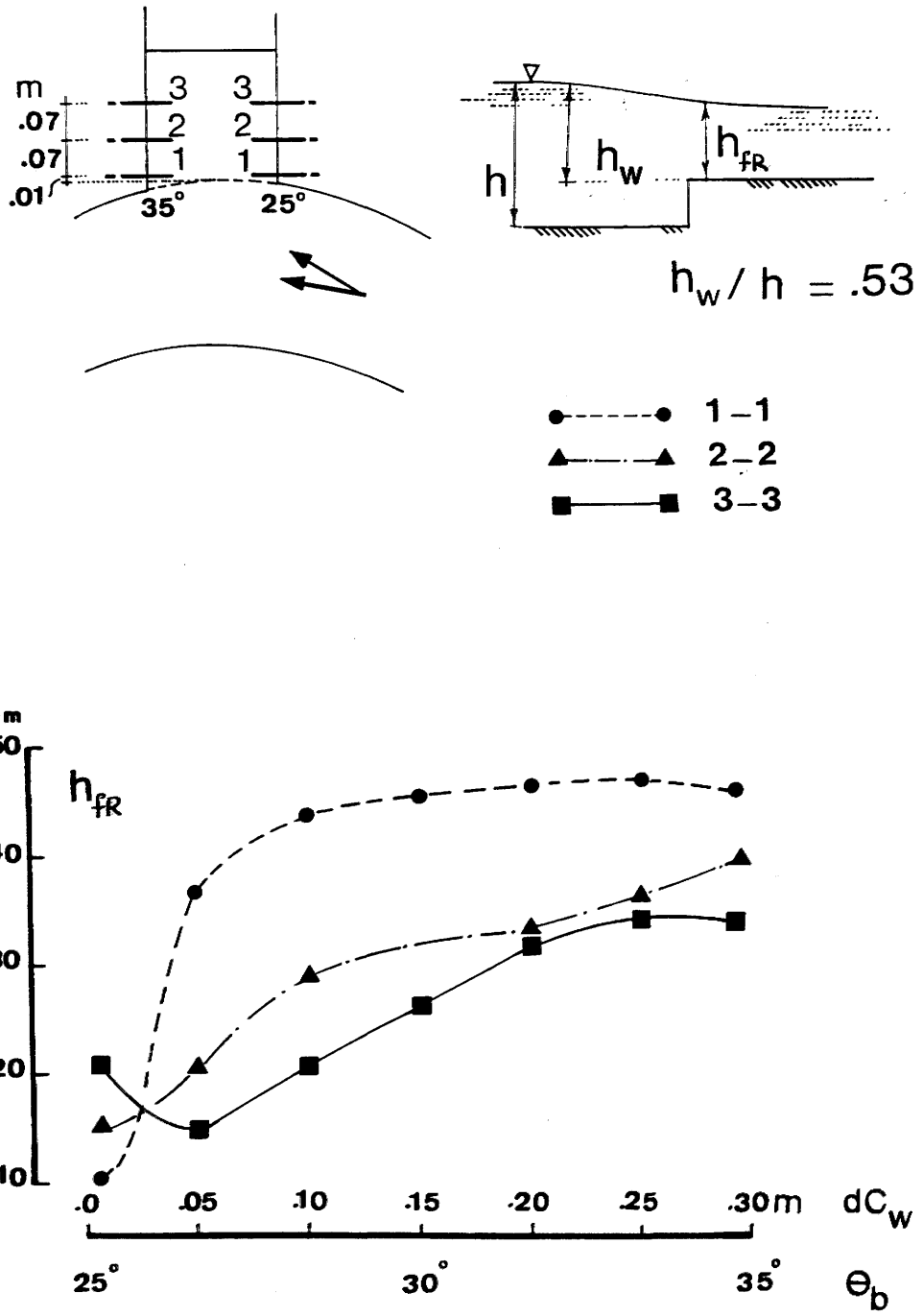

Fig.(7.13) – Measured Water Surface Profiles Across the Flood Relief Channel for Test Run WF11

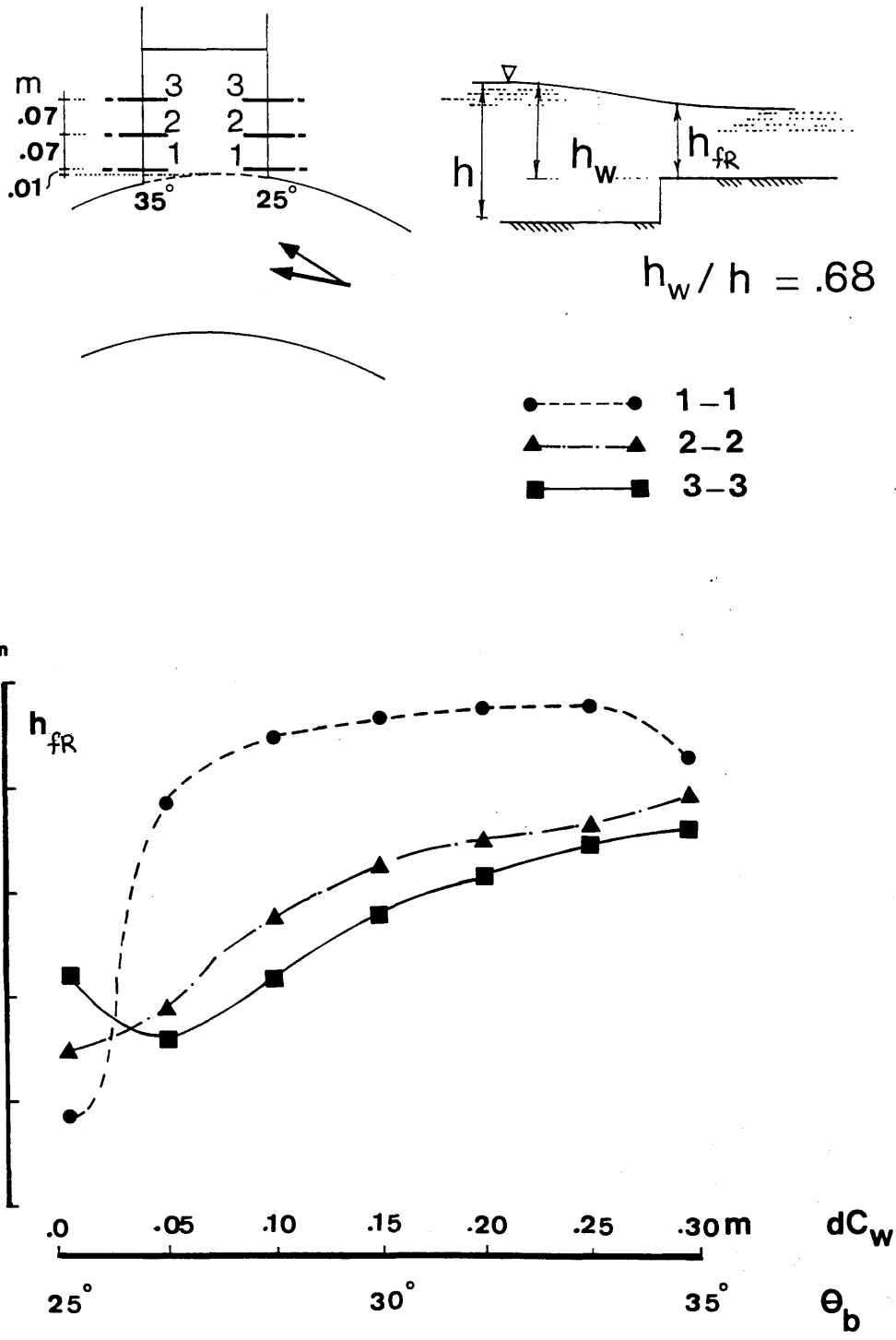

Fig.(7.14) – Measured Water Surface Profiles Across the Flood Relief Channel for Test Run WF5

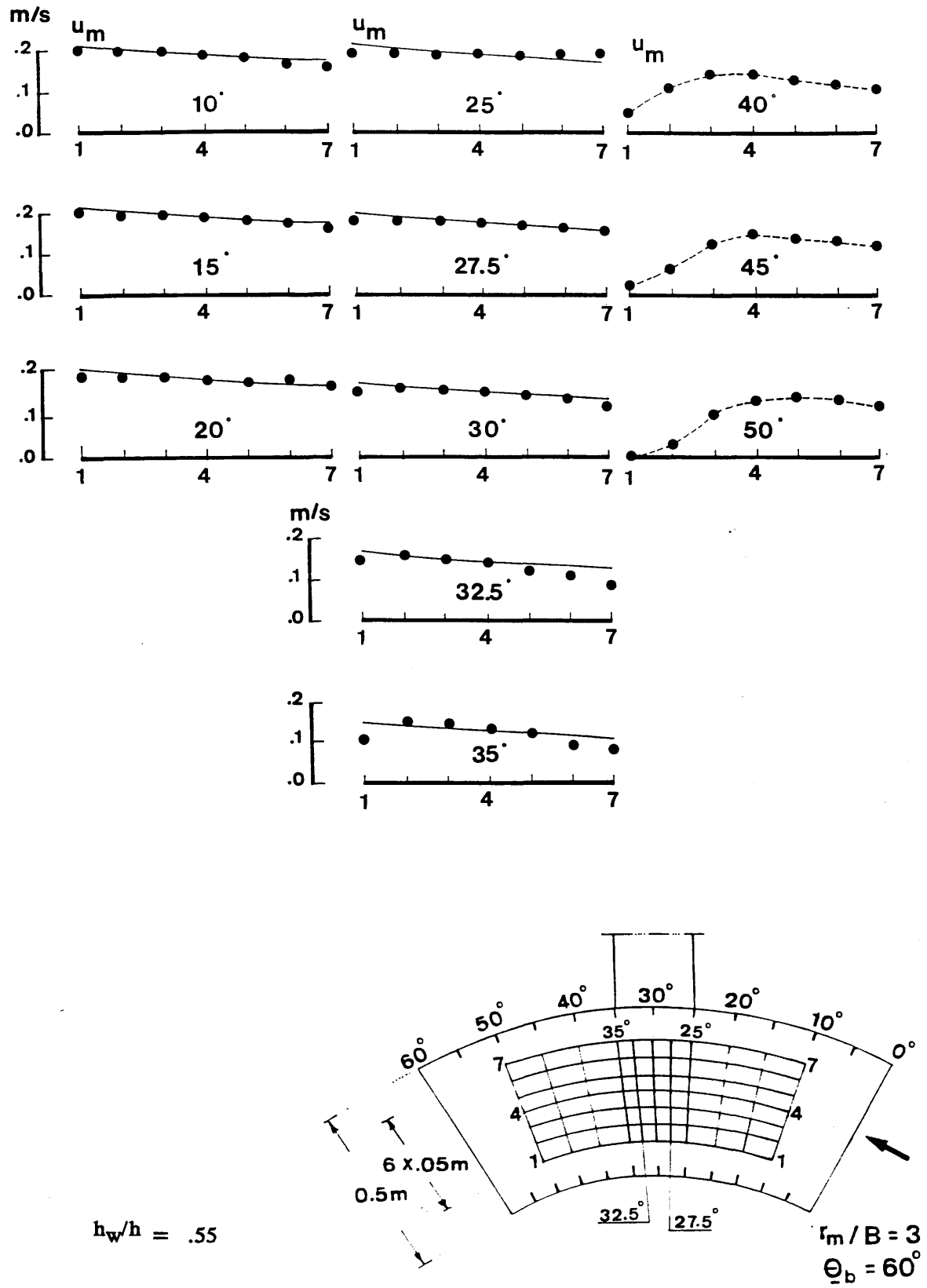

Prediction
Exp. Data ($\Theta_b = 10° \rightarrow 35°$)
Exp. Data ($\Theta_b = 40° \rightarrow 50°$)

FIG.(7.15) – Comparisons between the Predicted and Measured Depth–averaged Velocities for Test Run A1–V1

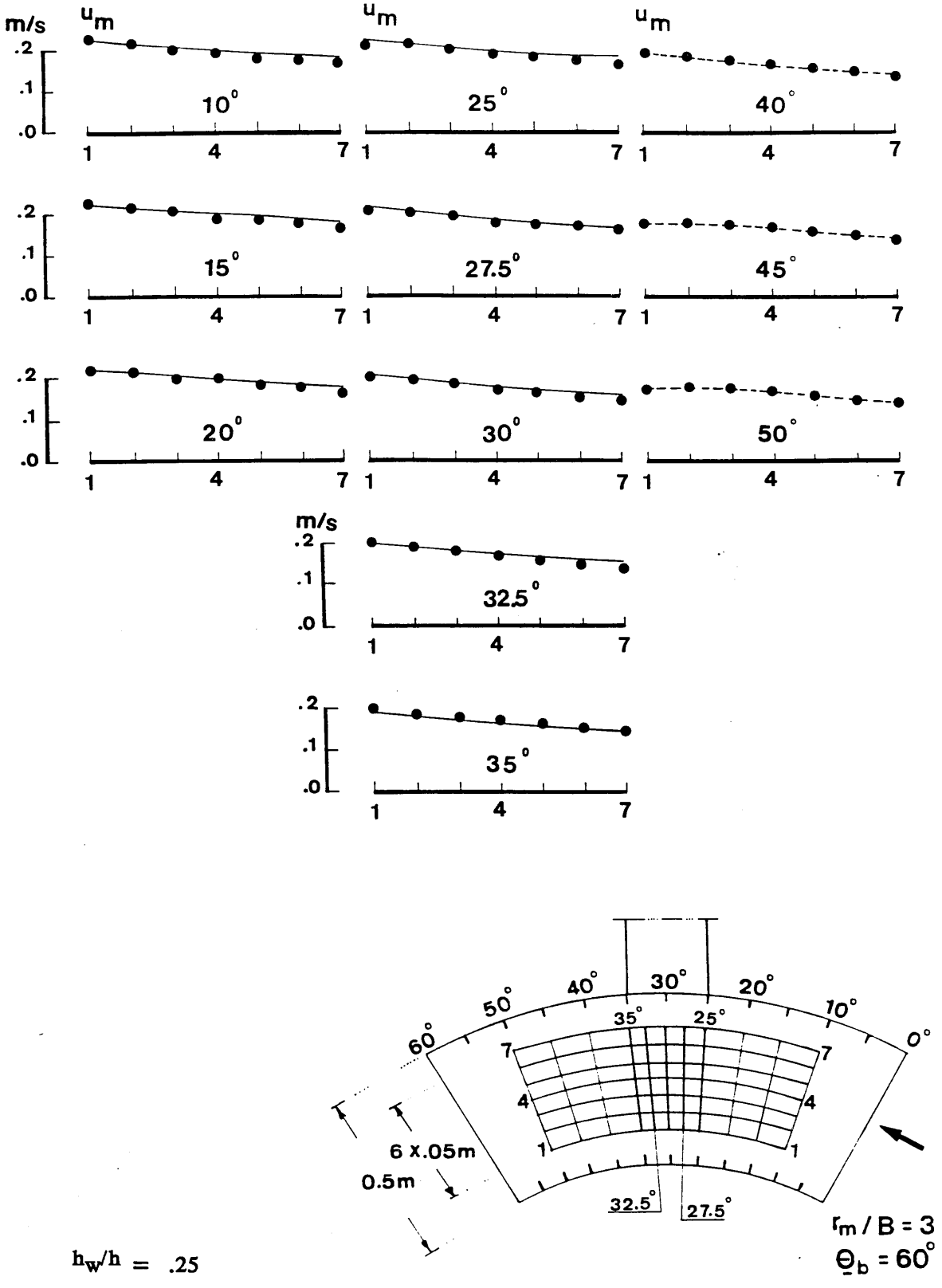

$h_w/h = .25$

Prediction
Exp. Data ($\Theta_b = 10° \rightarrow 35°$)
Exp. Data ($\Theta_b = 40° \rightarrow 50°$)

FIG.(7.16) – Comparisons between the Predicted and Measured Depth–averaged Velocities for Test Run A3–V3

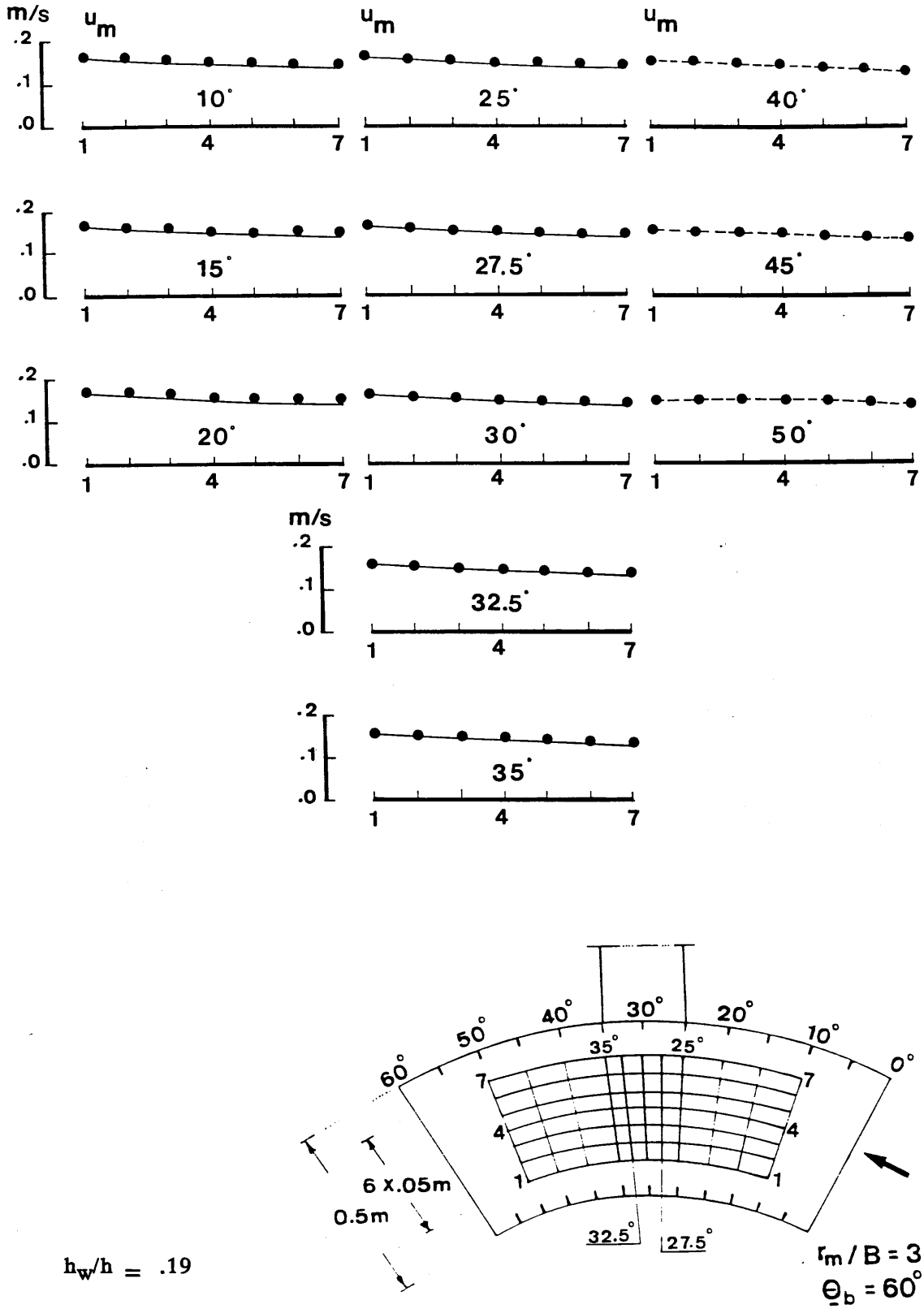

$h_w/h = .19$

——— Prediction
● Exp. Data ($\Theta_b = 10° \rightarrow 35°$)
●----● Exp. Data ($\Theta_b = 40° \rightarrow 50°$)

FIG.(7.17) – Comparisons between the Predicted and Measured Depth–averaged Velocities for Test Run A5–V5

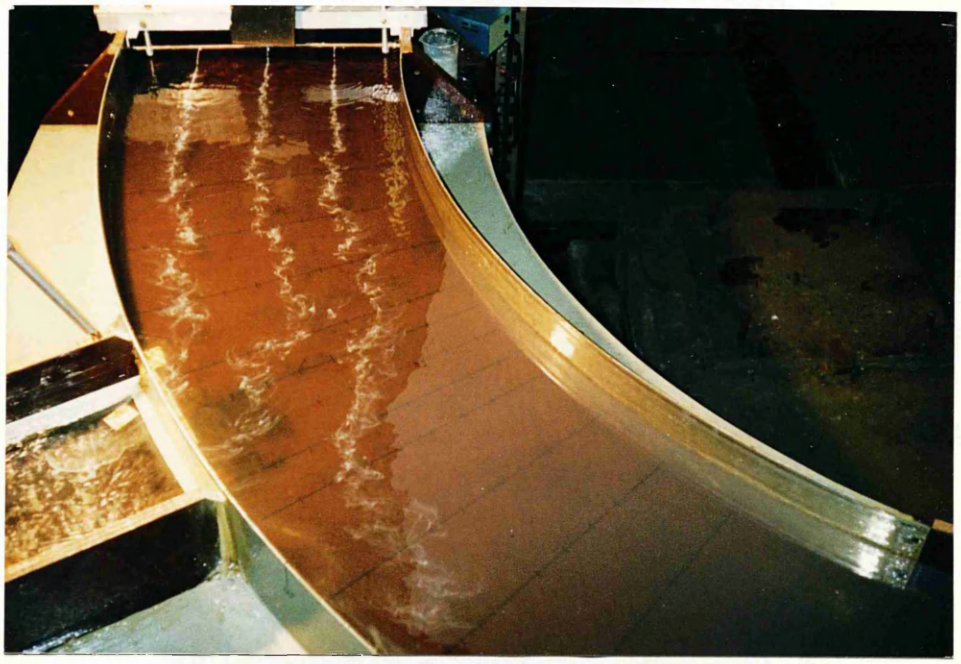

PLATE (7.1) – Stagnation and Separation Zones Developed at the Intersection for Test Run A1– V1

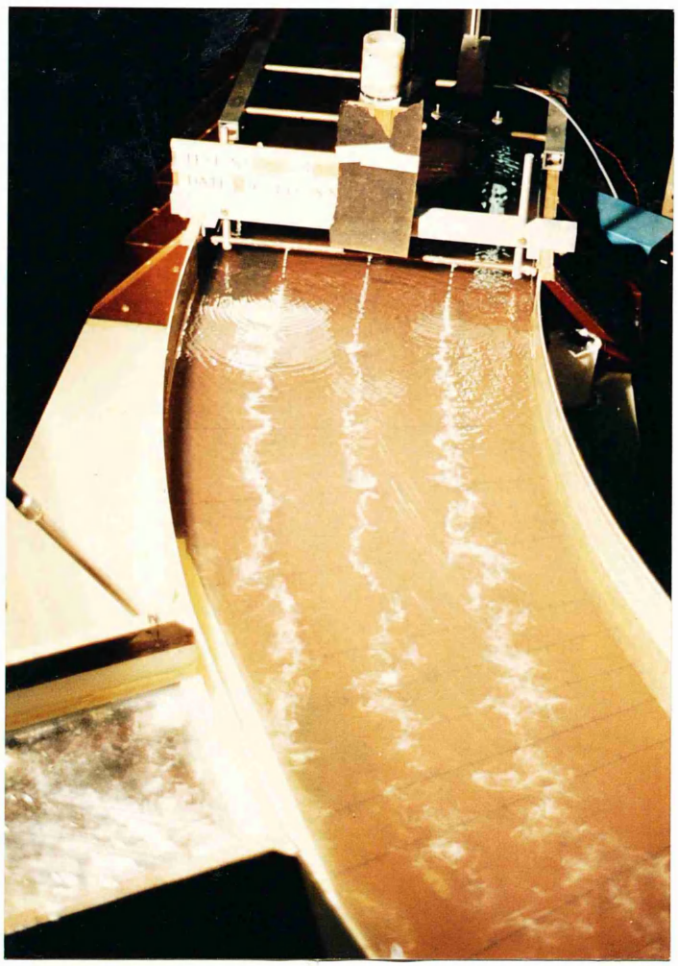

PLATE (7.2) – Stagnation and Separation Zones Developed at the Intersection for Test Run A3– V3

Test Run	symbol	Test Run	symbol
WF1	▽	WF8	◒
WF2	✱	WF9	×
WF3	▼	WF10	◐
WF4	+	WF11	★
WF5	○	WF12	△
WF6	■	WF13	●
WF7	▲		

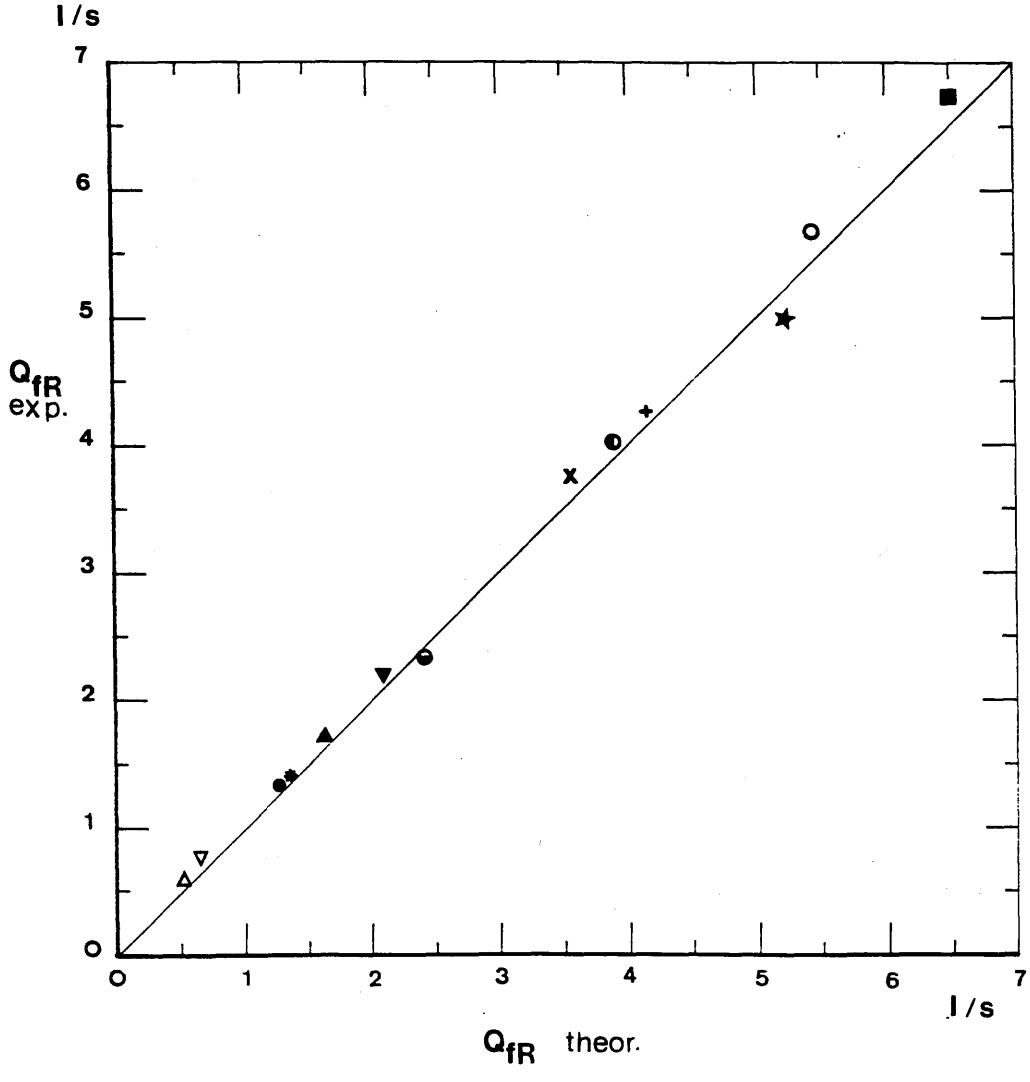

FIG.(7.18) – Comparisons between Predicted and Measured Flood Relief Channel Discharge for Measurements of Water Surface Profiles

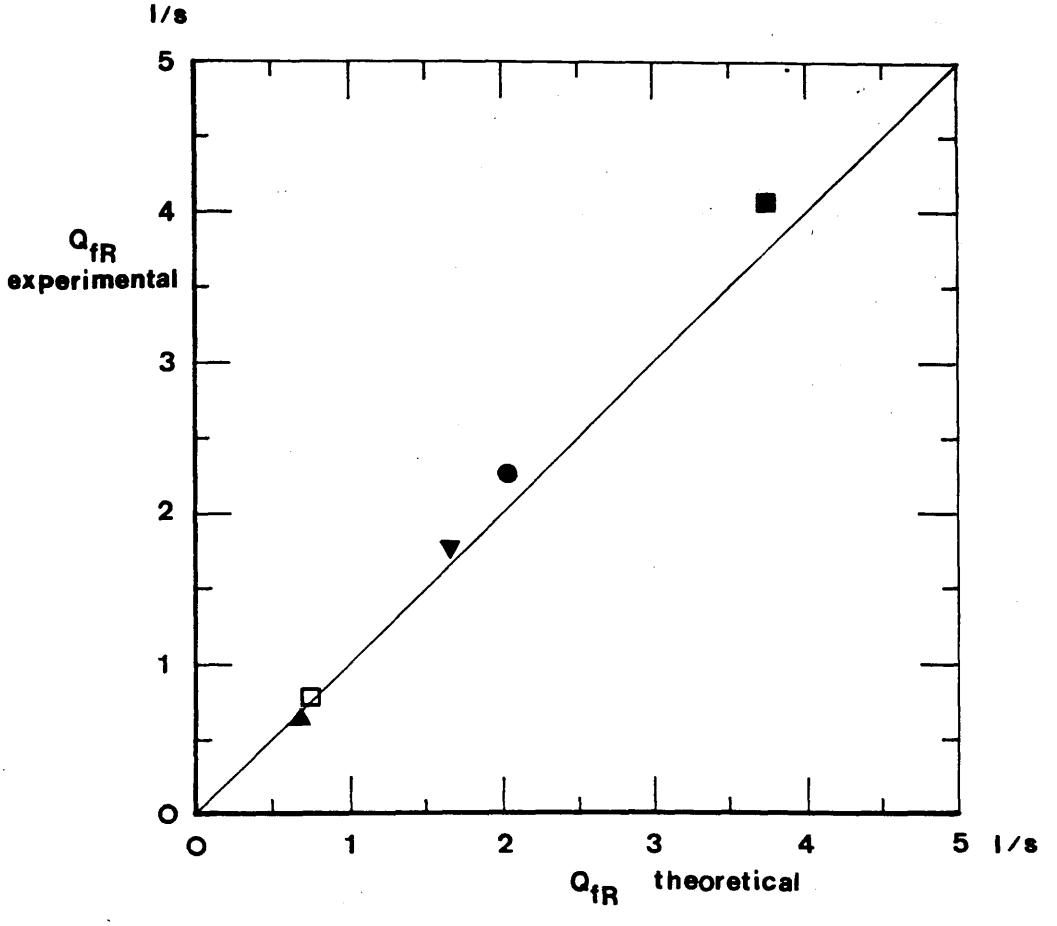

FIG.(7.19) – Comparisons between Predicted and Measured Flood Relief Channel Discharge for Measurements of Velocities and Deviation Angles

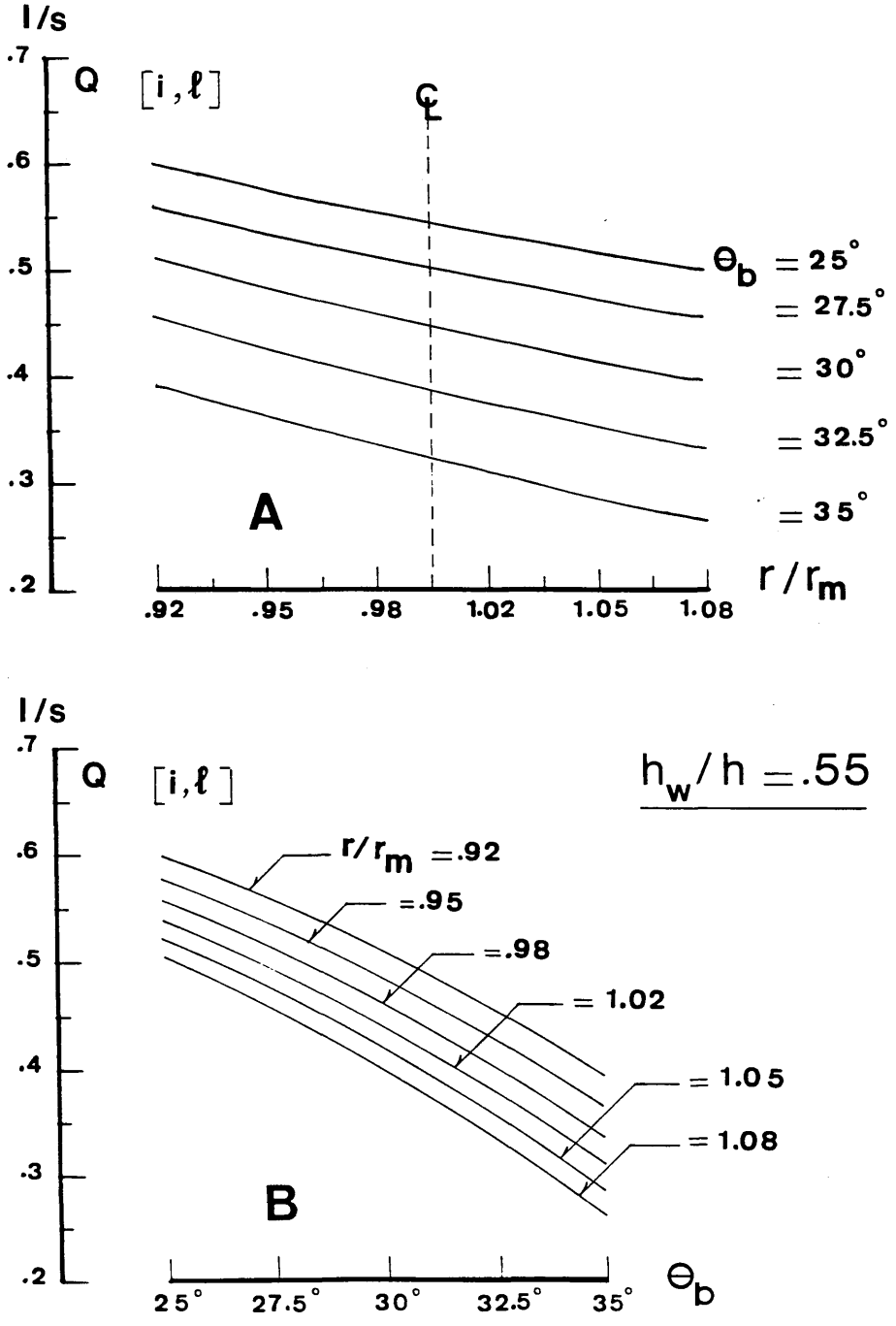

FIG.(7.20) – Predicted Radial and Longitudinal Flow Gradients in the Channel Bend at the Intersection for Test Run A1–V1

(A) Radial Gradient

(B) Longitudinal Gradient

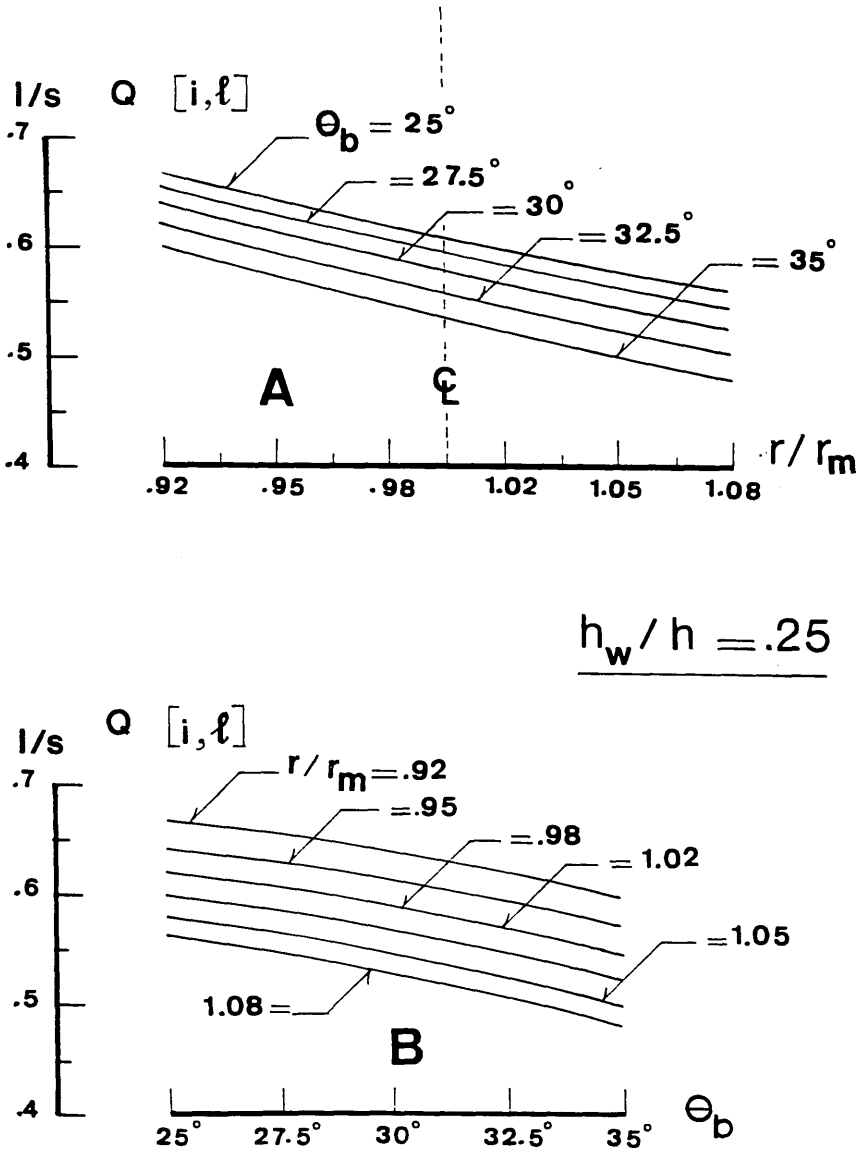

FIG.(7.21) – Predicted Radial and Longitudinal Flow Gradients in the Channel Bend at the Intersection for Test Run A3– V3

(A) Radial Gradient

(B) Longitudinal Gradient

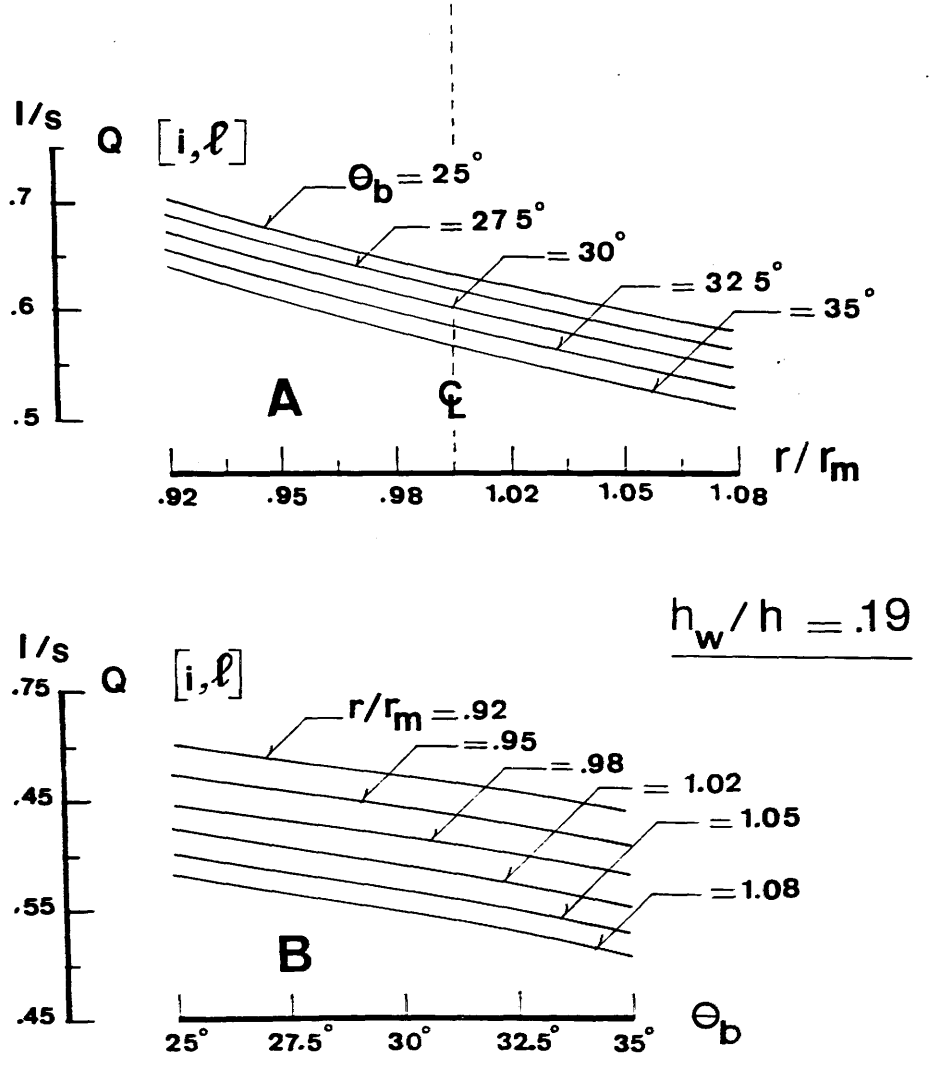

FIG.(7.22) – Predicted Radial and Longitudinal Flow Gradients in the Channel Bend at the Intersection for Test Run A5– V5

(A) Radial Gradient

(B) Longitudinal Gradient

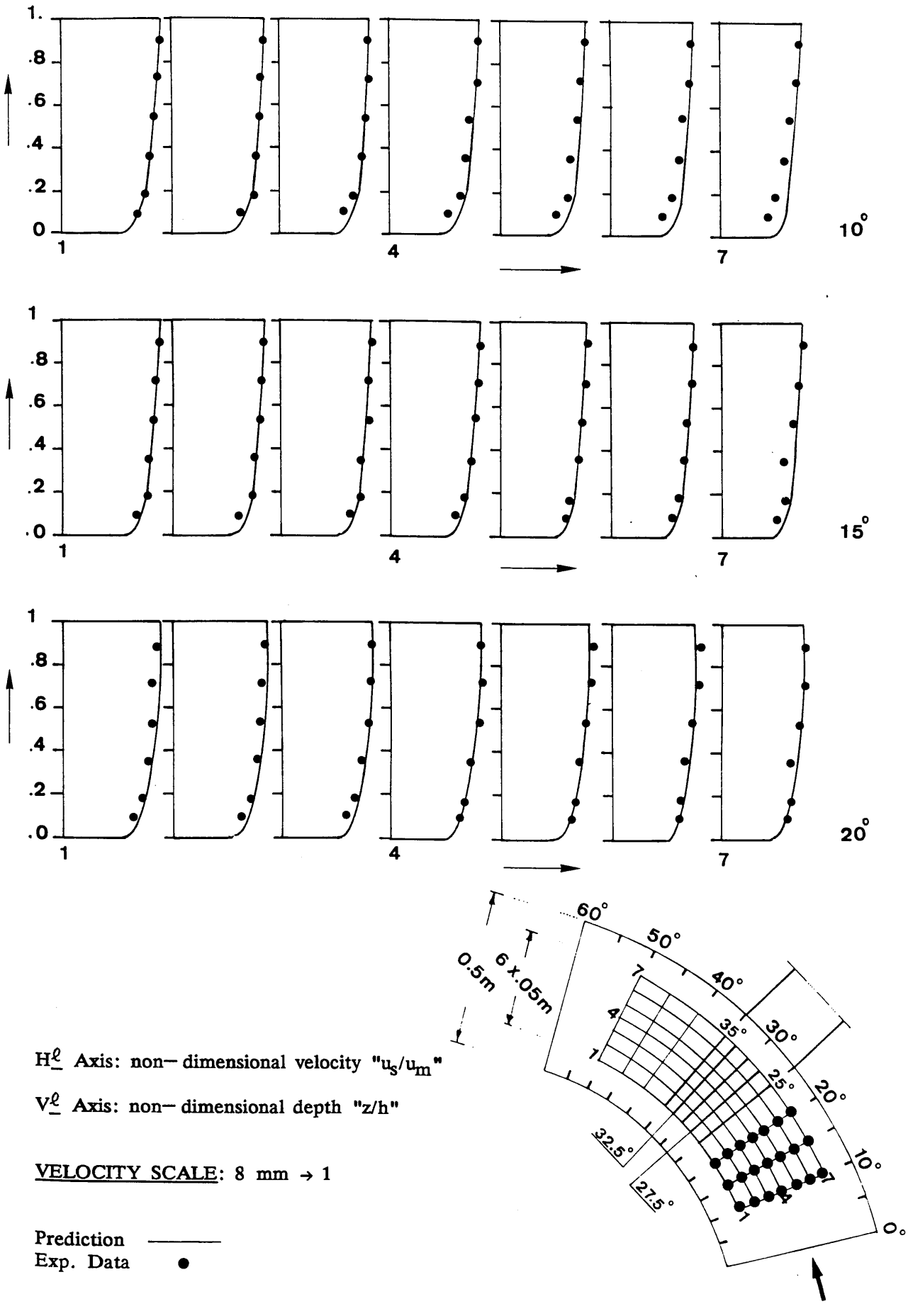

H^{ℓ} Axis: non– dimensional velocity "u_s/u_m"

V^{ℓ} Axis: non– dimensional depth "z/h"

VELOCITY SCALE: 8 mm → 1

Prediction ———

Exp. Data ●

FIG.(7.23) – Comparisons between Predicted and Measured Vertical Profiles of the Longitudinal Velocities in the Channel Bend for Test Run A1– V1

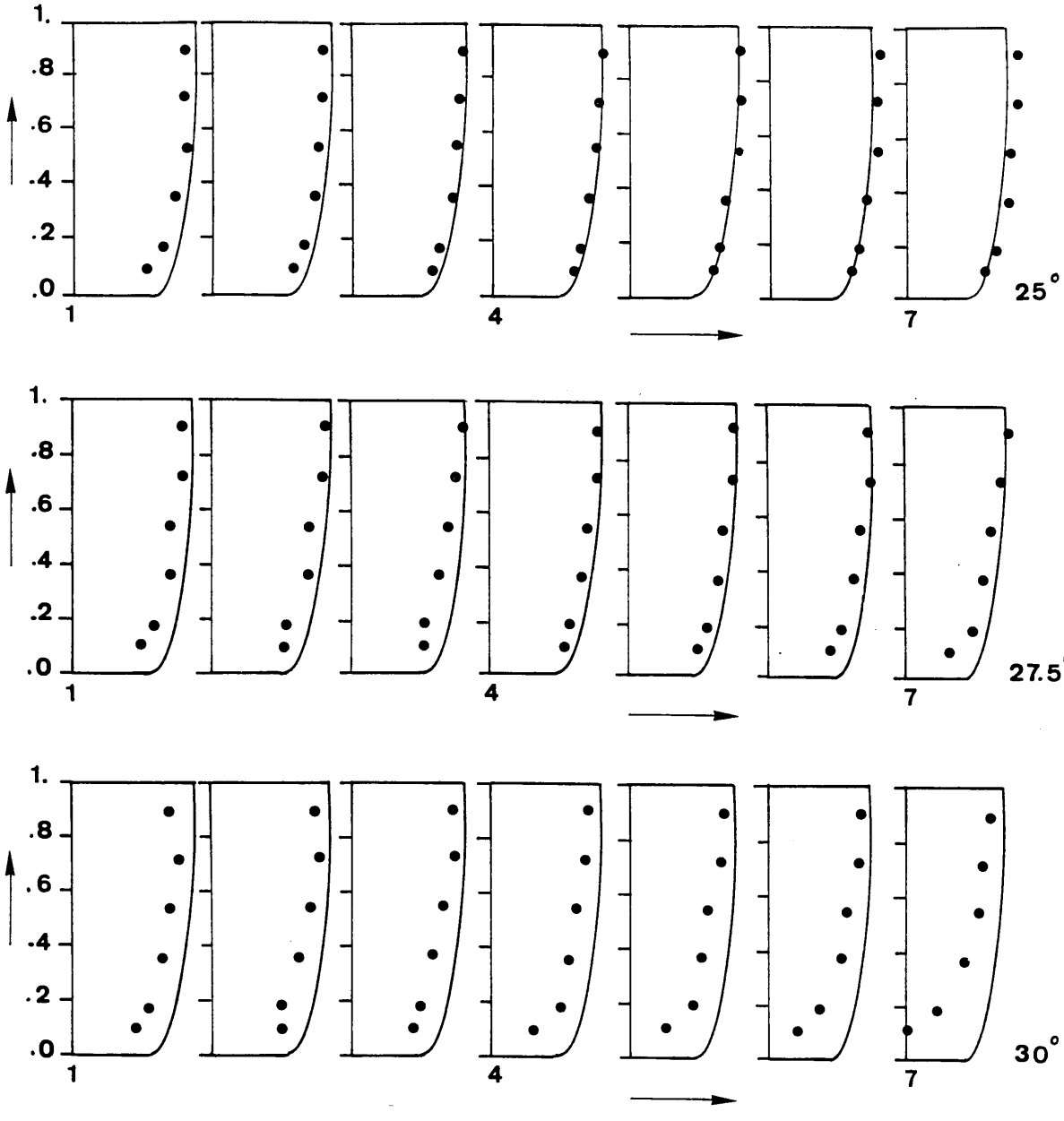

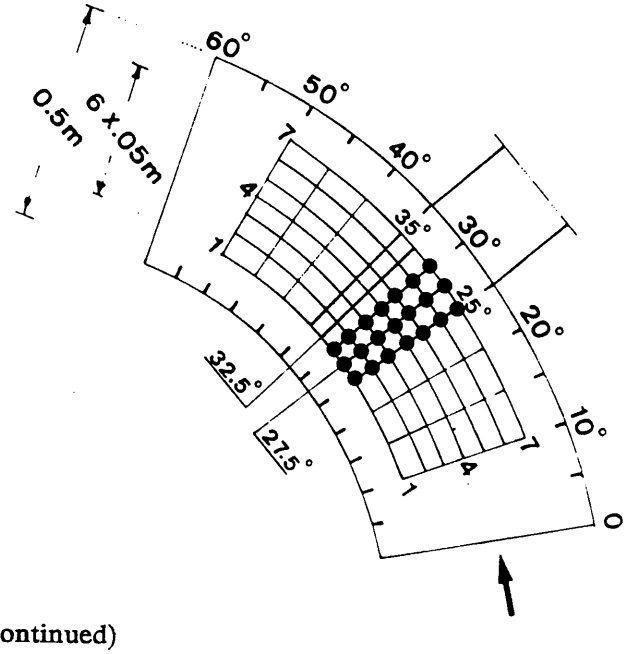

H^{ℓ} Axis: non– dimensional velocity "u_s/u_m"

V^{ℓ} Axis: non– dimensional depth "z/h"

VELOCITY SCALE: 8 mm → 1

Prediction ———

Exp. Data ●

FIG.(7.23) – (Continued)

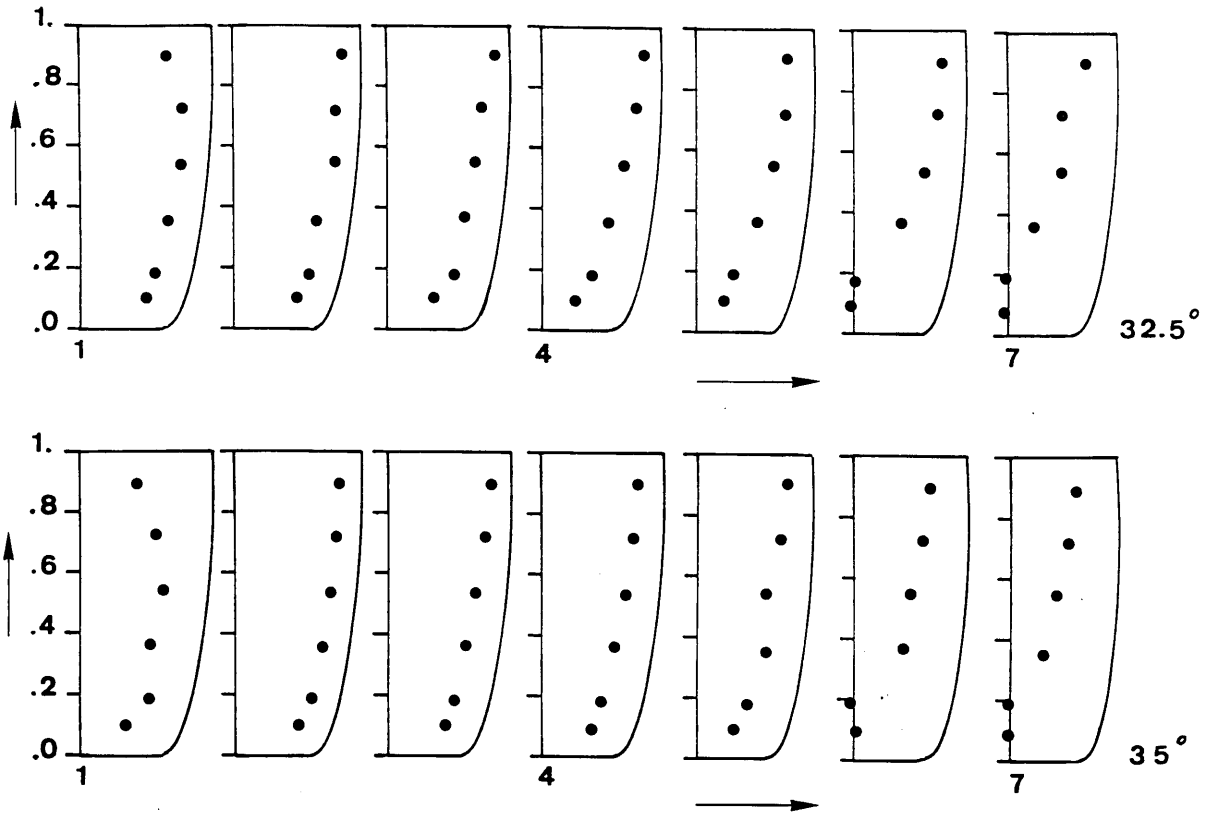

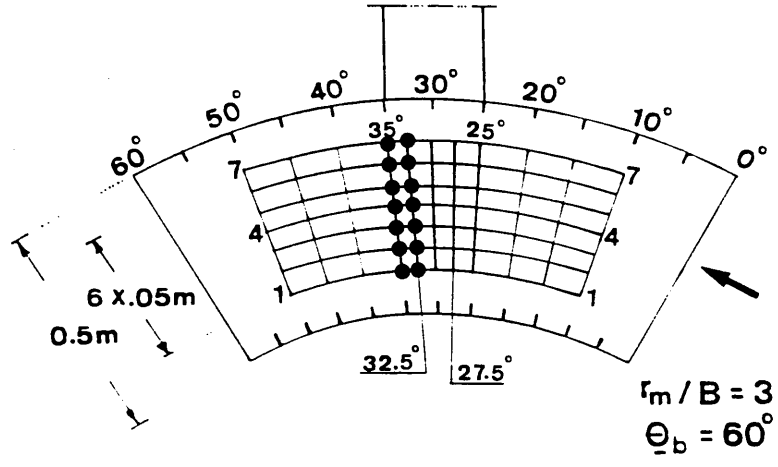

H^{ℓ} Axis: non– dimensional velocity "u_s/u_m"

V^{ℓ} Axis: non– dimensional depth "z/h"

VELOCITY SCALE: 8 mm → 1

Prediction ———
Exp. Data ●

(7.23) – (Continued)

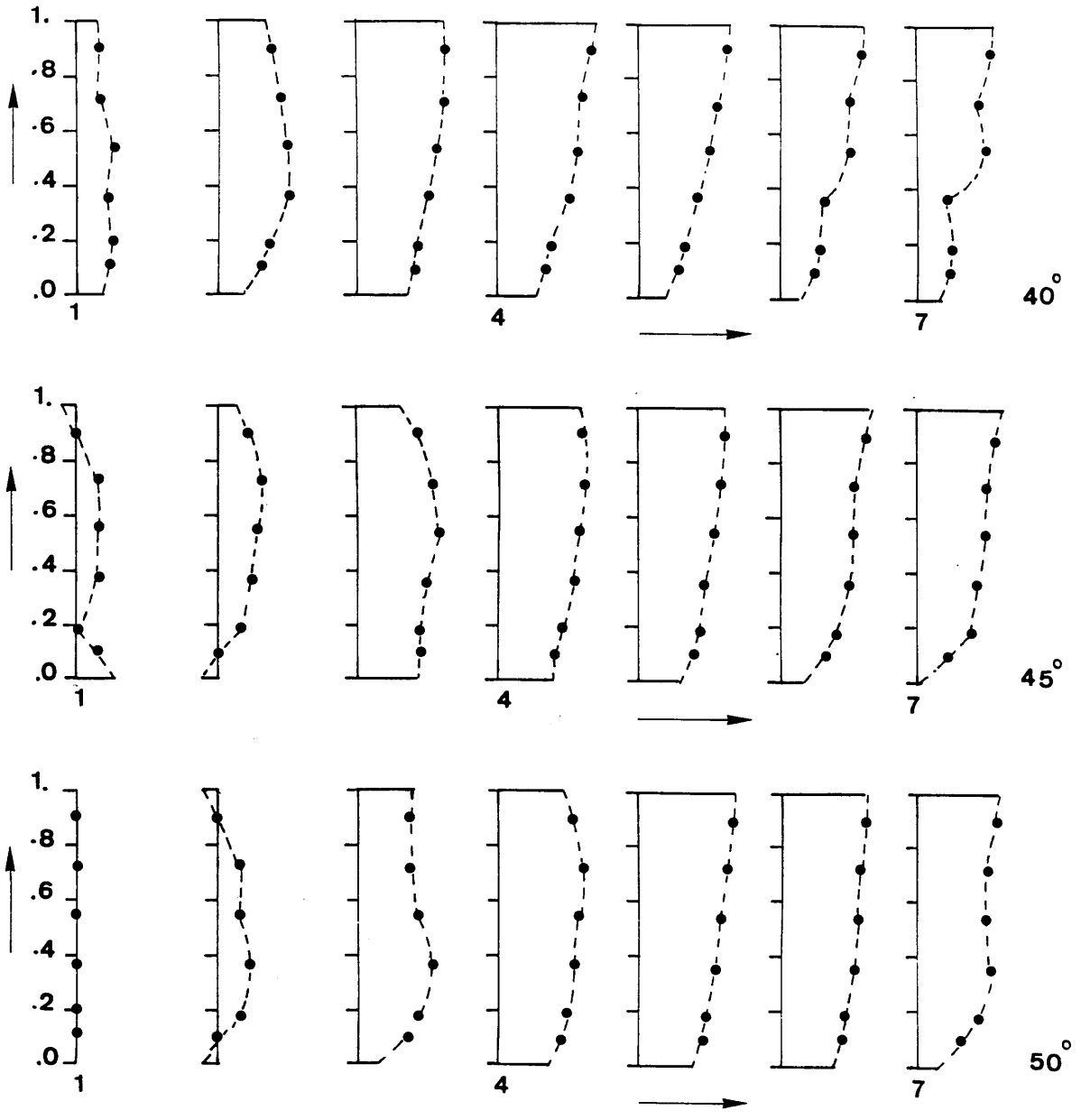

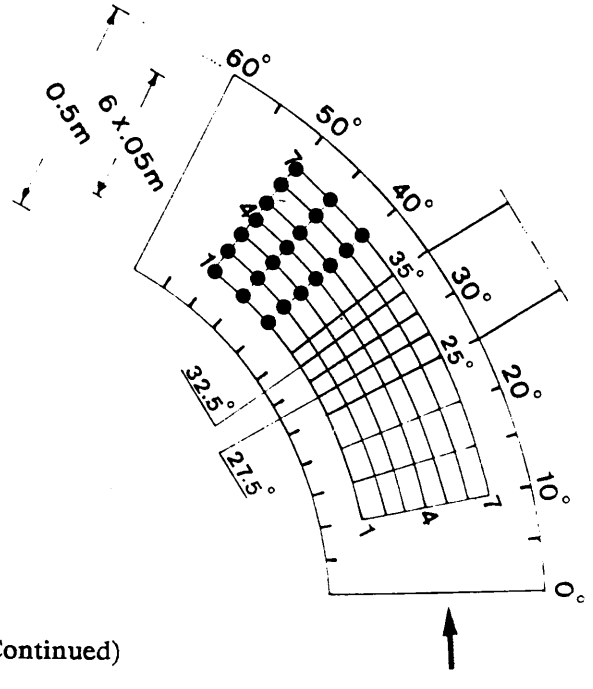

$H\underline{\ell}$ Axis: non– dimensional velocity "u_s/u_m"

$V\underline{\ell}$ Axis: non– dimensional depth "z/h"

VELOCITY SCALE: 8 mm → 1

Exp. Data ●– – – –●

FIG.(7.23) – (Continued)

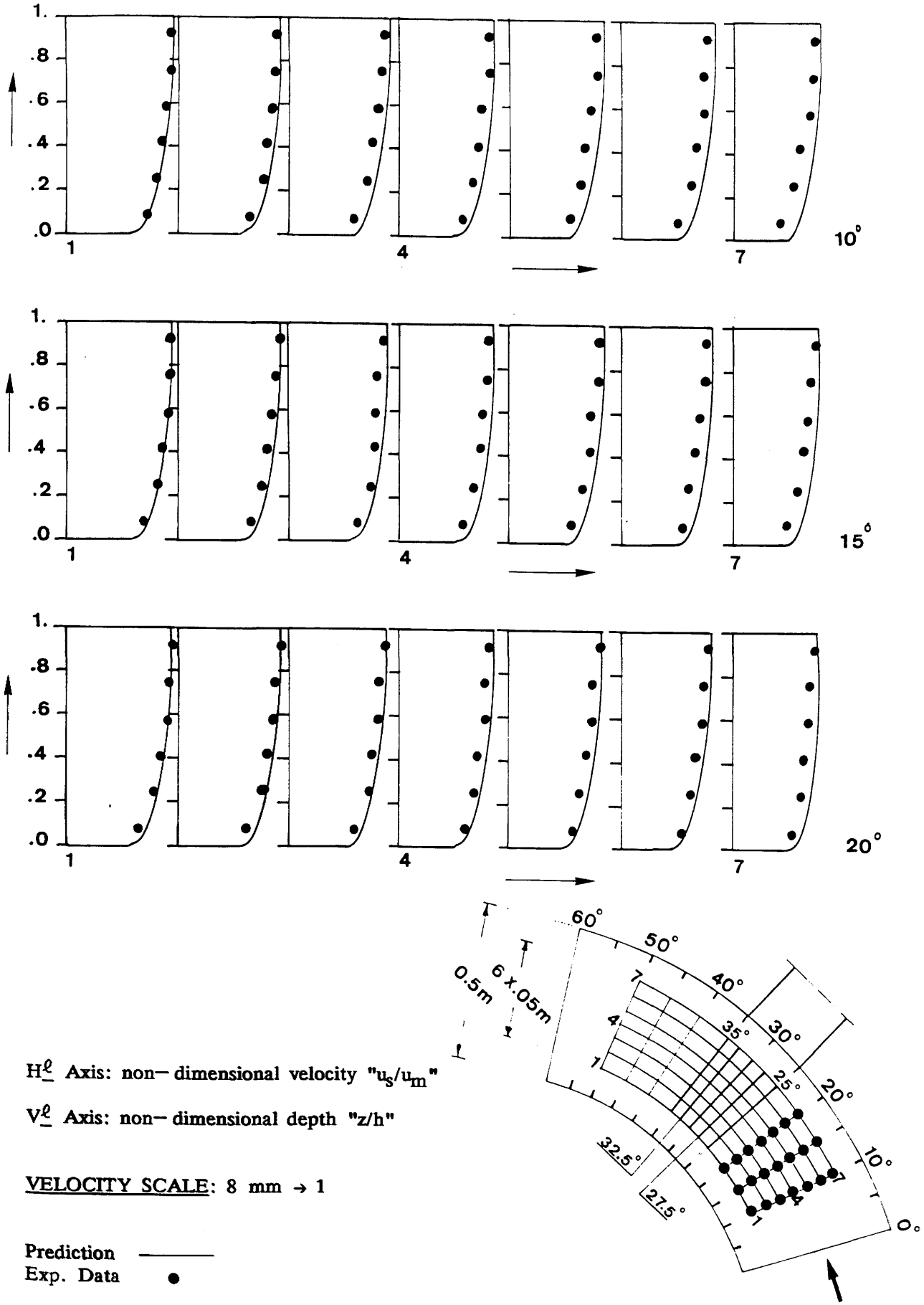

$H_{\underline{\ell}}$ Axis: non− dimensional velocity "u_s/u_m"

$V_{\underline{\ell}}$ Axis: non− dimensional depth "z/h"

VELOCITY SCALE: 8 mm → 1

Prediction ———

Exp. Data ●

FIG.(7.24) − Comparisons between Predicted and Measured Vertical Profiles of the Longitudinal Velocities in the Channel Bend for Test Run A3− V3

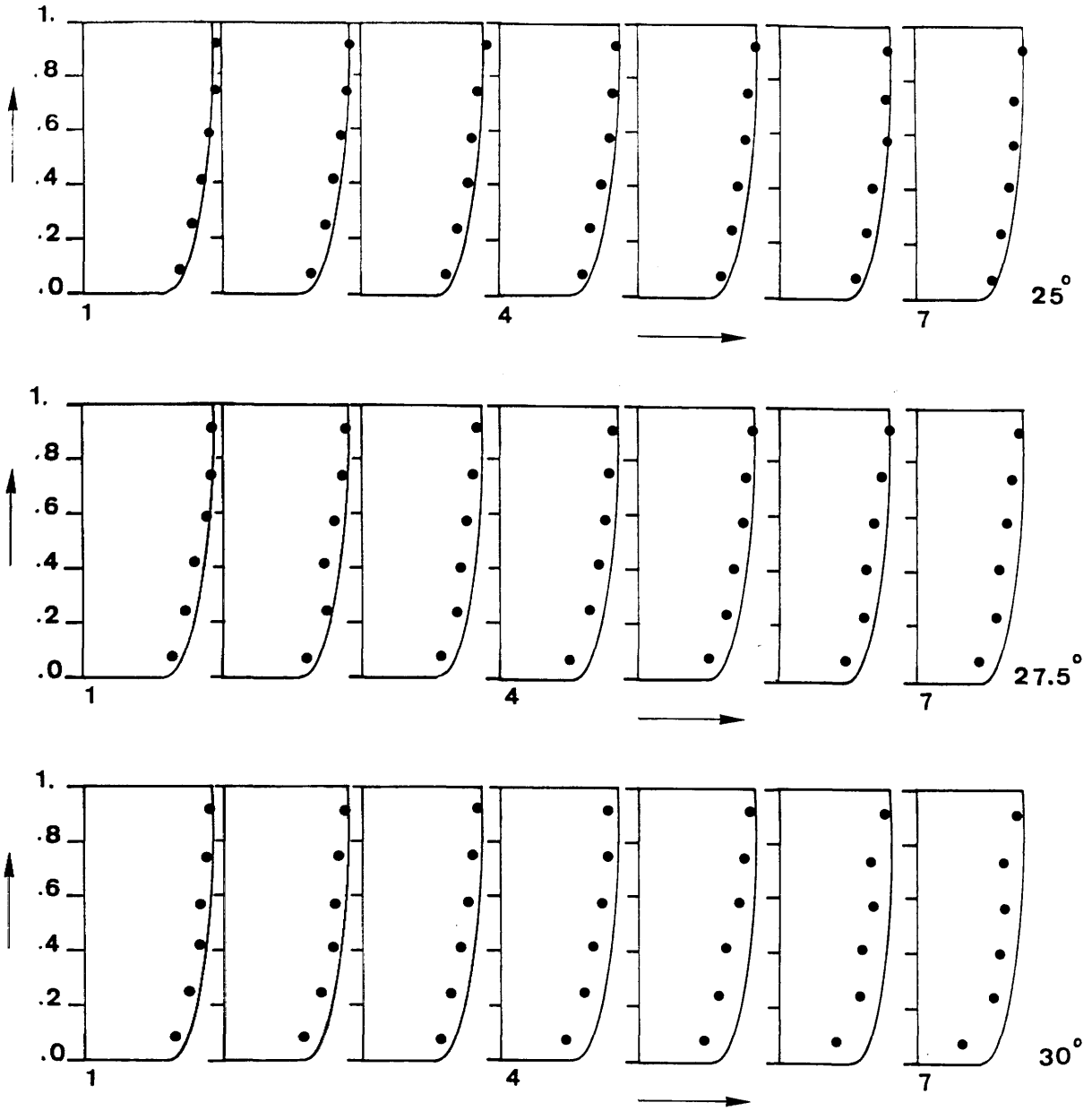

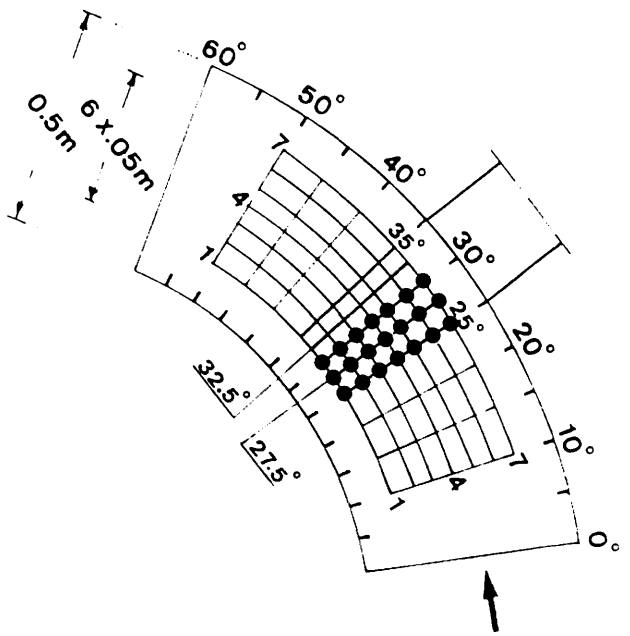

$H_{\underline{\ell}}$ Axis: non–dimensional velocity "u_s/u_m"

$V_{\underline{\ell}}$ Axis: non–dimensional depth "z/h"

VELOCITY SCALE: 8 mm → 1

Prediction ——

Exp. Data ●

FIG.(7.24) – (Continued)

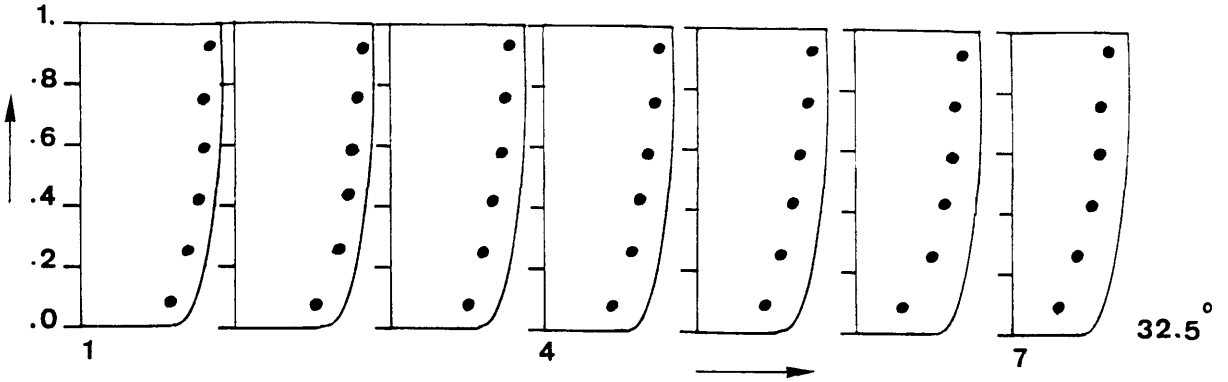

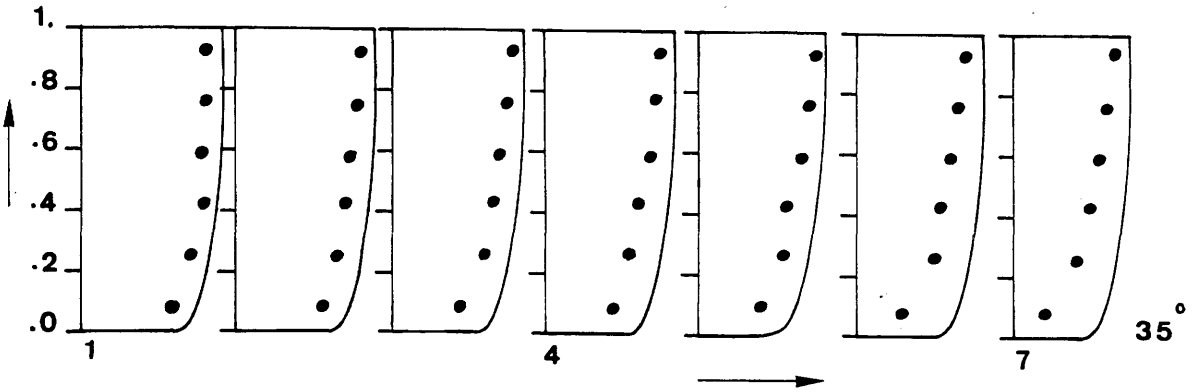

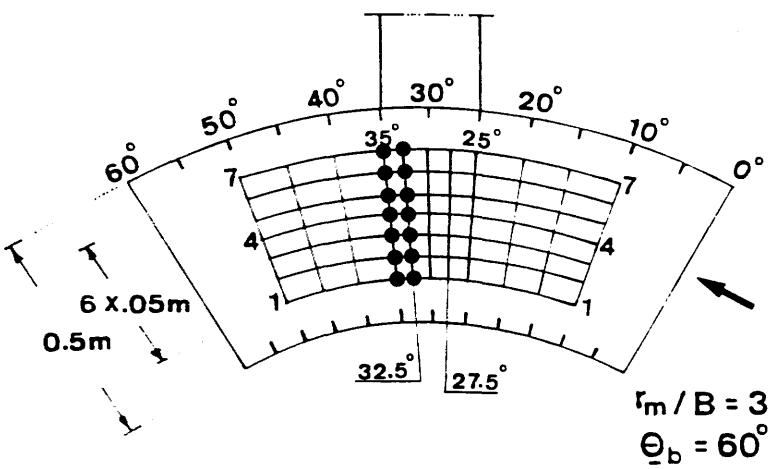

H^{ℓ} Axis: non– dimensional velocity "u_s/u_m"

V^{ℓ} Axis: non– dimensional depth "z/h"

VELOCITY SCALE: 8 mm → 1

Prediction ————
Exp. Data ●

(7.24) – (Continued)

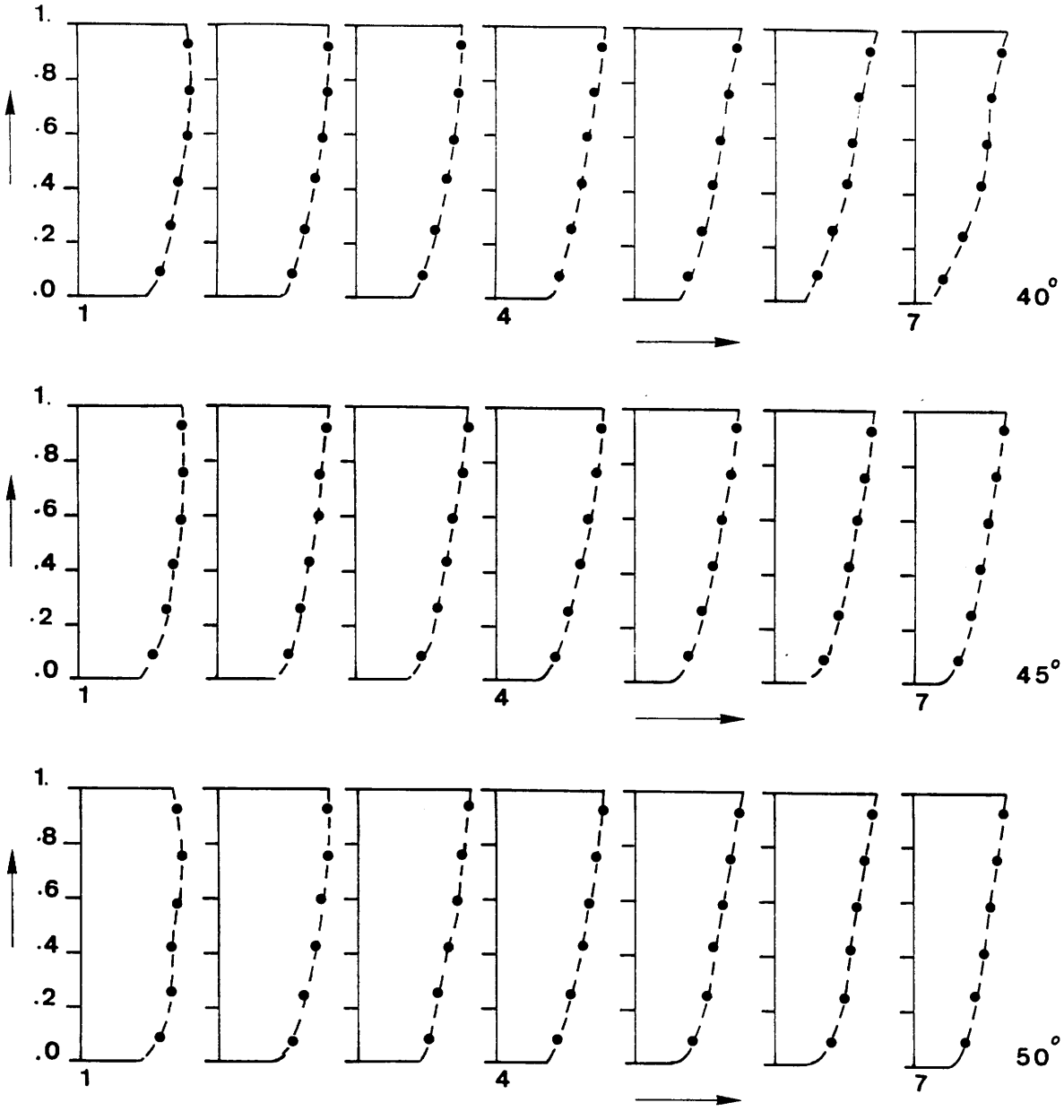

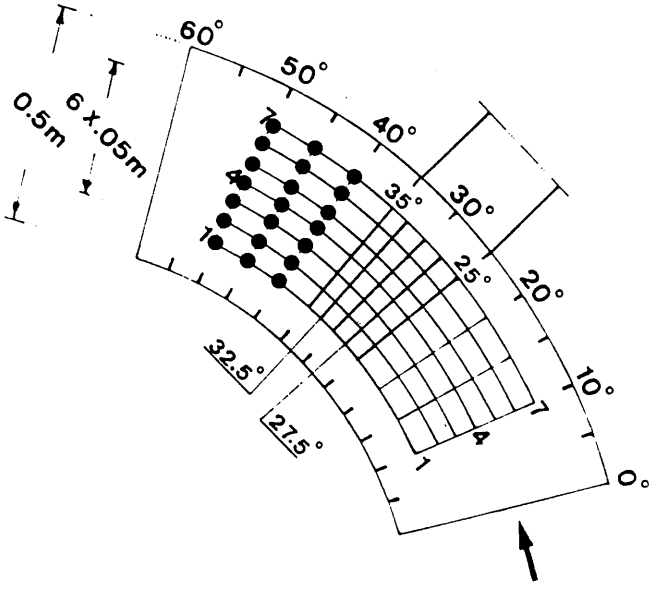

$H_{\underline{\ell}}$ Axis: non– dimensional velocity "u_s/u_m"

$V_{\underline{\ell}}$ Axis: non– dimensional depth "z/h"

VELOCITY SCALE: 8 mm → 1

Exp. Data ●– – – –●

FIG.(7.24) – (Continued)

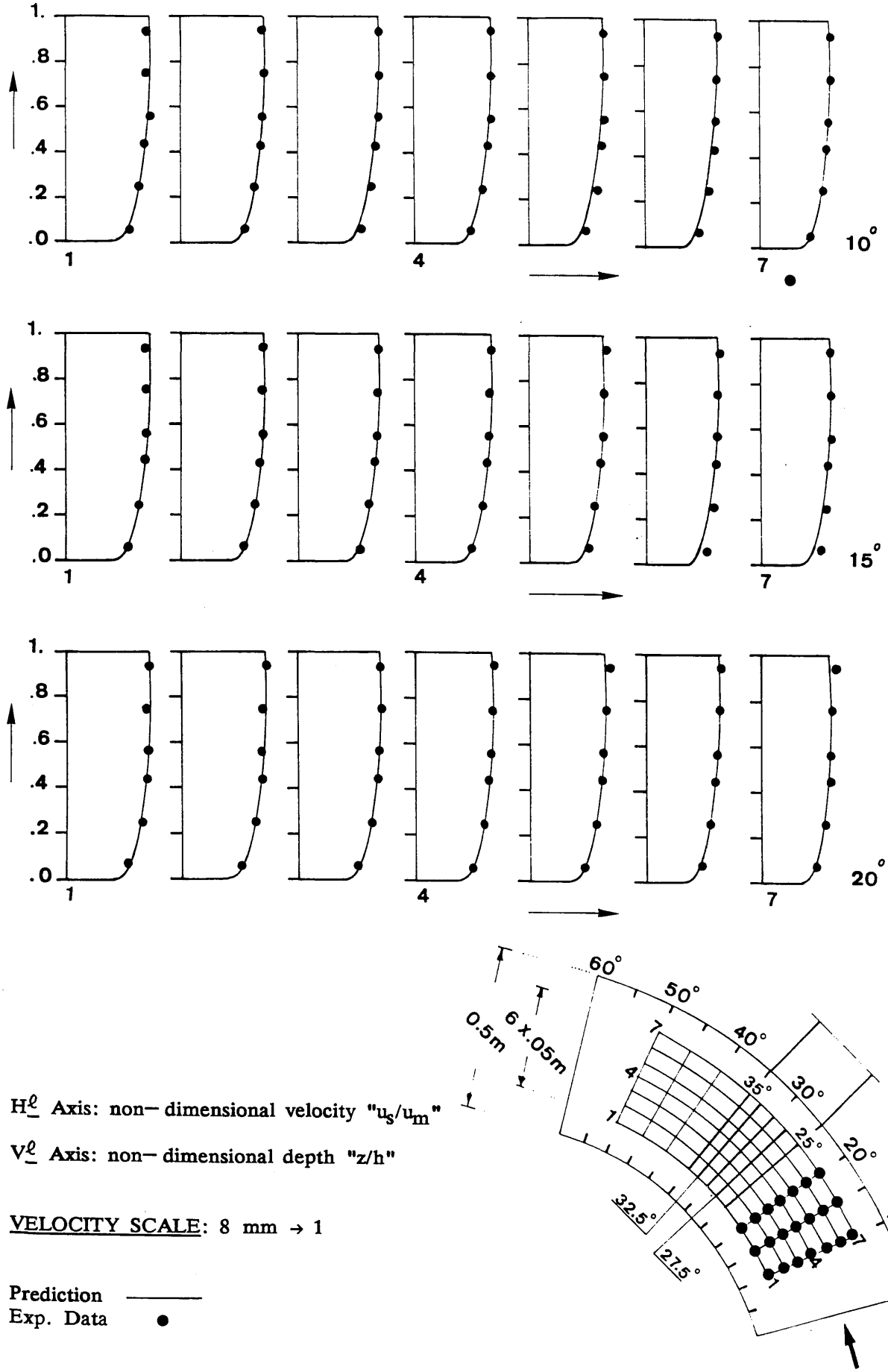

H^{ℓ} Axis: non– dimensional velocity "u_s/u_m"

V^{ℓ} Axis: non– dimensional depth "z/h"

VELOCITY SCALE: 8 mm → 1

Prediction ———

Exp. Data ●

FIG.(7.25) – Comparisons between Predicted and Measured Vertical Profiles of the Longitudinal Velocities in the Channel Bend for Test Run A5– V5

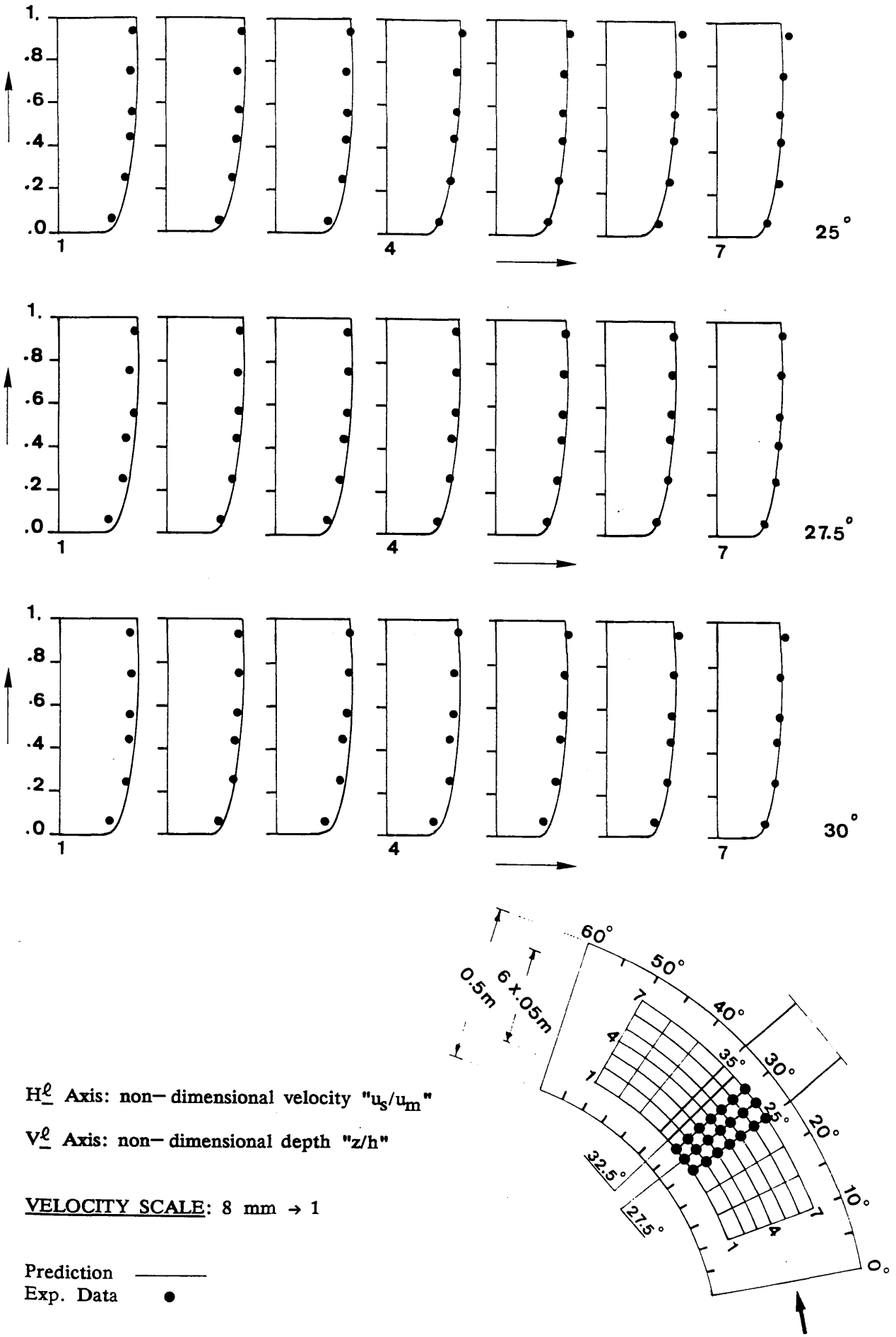

H^{ℓ} Axis: non– dimensional velocity "u_s/u_m"

V^{ℓ} Axis: non– dimensional depth "z/h"

VELOCITY SCALE: 8 mm → 1

Prediction ———

Exp. Data ●

FIG.(7.25) – (Continued)

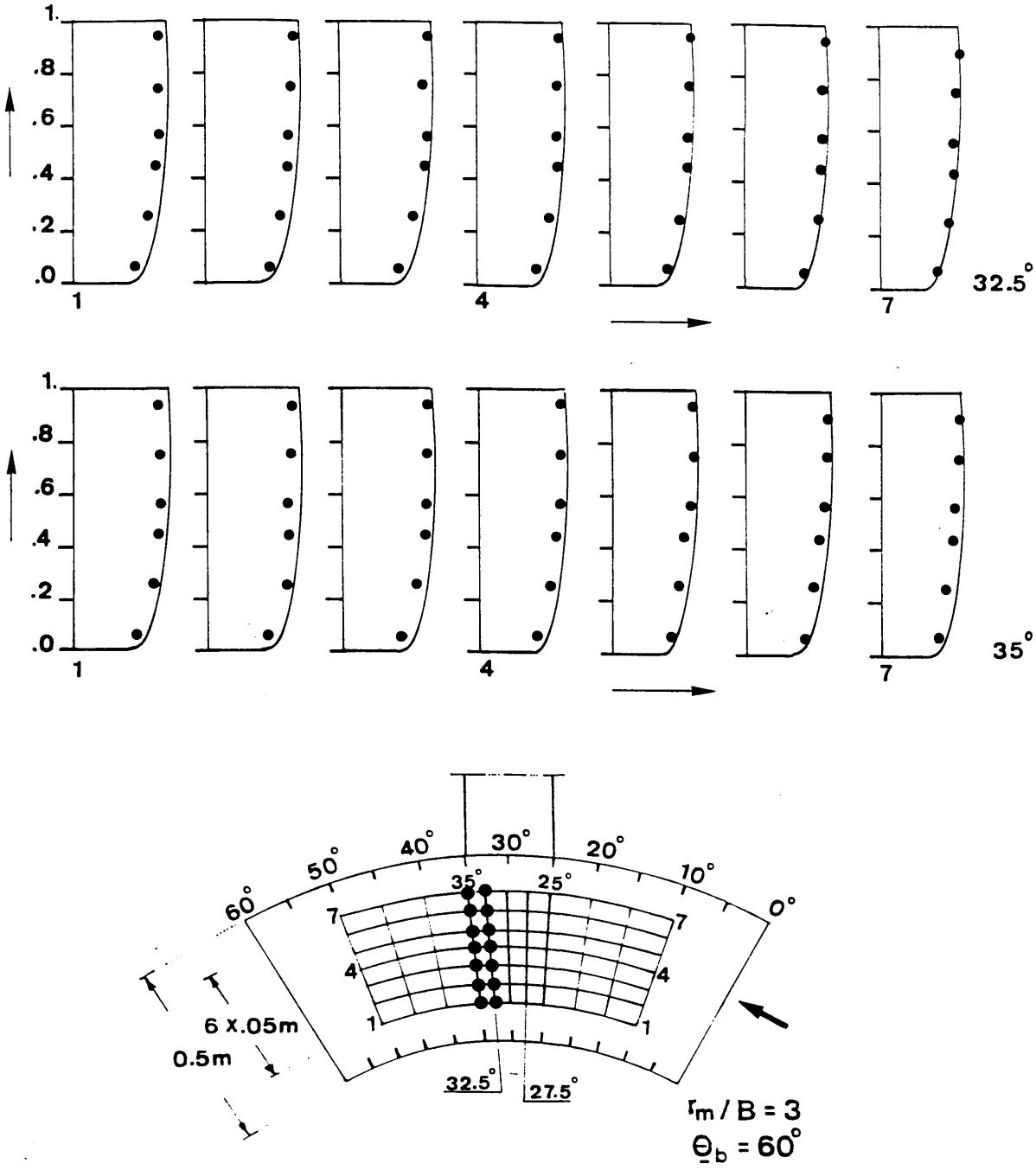

H^{ℓ} Axis: non– dimensional velocity "u_s/u_m"

V^{ℓ} Axis: non– dimensional depth "z/h"

VELOCITY SCALE: 8 mm → 1

Prediction ———
Exp. Data ●

(7.25) – (Continued)

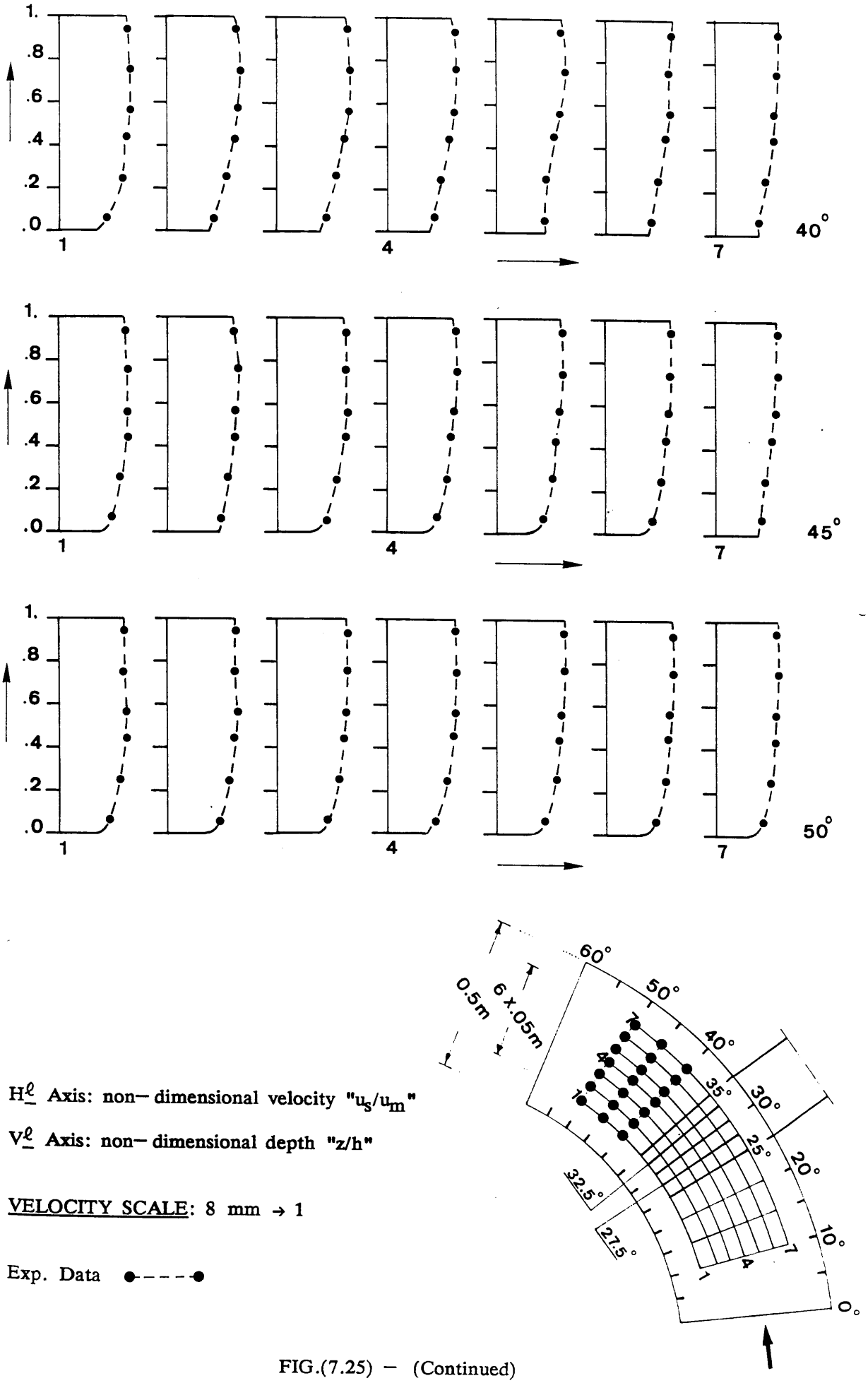

$H_{\underline{\ell}}$ Axis: non– dimensional velocity "u_s/u_m"

$V_{\underline{\ell}}$ Axis: non– dimensional depth "z/h"

VELOCITY SCALE: 8 mm → 1

Exp. Data ●– – – –●

FIG.(7.25) – (Continued)

TABLE (7.3) – Measured Values of Deviation Angles of the Horizontal Resultant Velocities for Test Run A1 – V1

Key for Tables

** + ve value indicates deviation towards the outer bank

** – ve value indicates deviation towards the inner bank

D1 = 5 mm

D2 = 10 mm

D3 = 20 mm

D4 = 30 mm

D5 = 40 mm

D6 = 50 mm

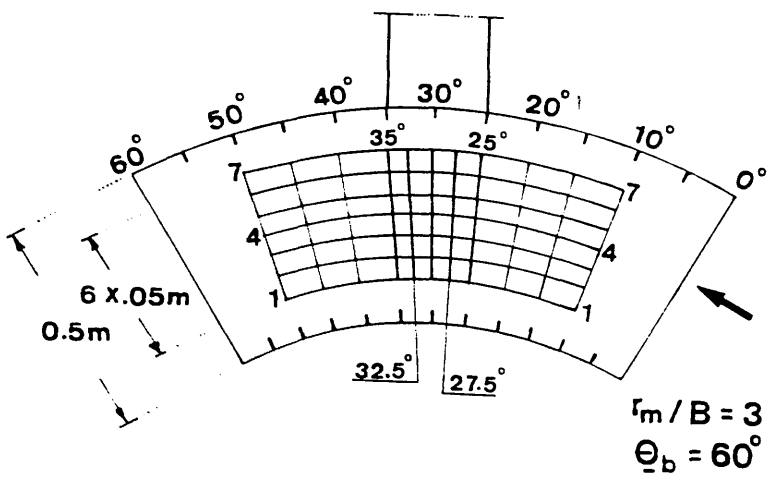

TABLE (7.3) – (Continued)

$\theta_b = 10^\circ$

Depth	1	2	3	4	5	6	7
D1	−3.02	−2.65	−2.00	−2.20	−2.85	−3.34	−2.20
D2	−1.01	−1.00	−1.00	−1.00	−1.05	−1.08	−1.19
D3	−0.00	+1.20	+1.40	−0.95	−0.80	−0.71	−0.20
D4	+1.08	+1.82	+1.95	+1.72	+0.72	+1.30	+0.51
D5	+2.08	+2.23	+2.60	+2.27	+1.86	+1.25	+0.83
D6	+3.74	+3.58	+2.57	+2.57	+2.26	+2.49	+2.51

$\theta_b = 15^\circ$

Depth	1	2	3	4	5	6	7
D1	−0.44	+0.46	+0.65	+0.43	+1.28	+0.12	−0.69
D2	+2.42	+2.33	+1.76	+2.56	+1.88	+1.74	+1.82
D3	+2.31	+2.30	+2.97	+1.49	+1.43	+1.55	+1.95
D4	+1.58	+2.23	+2.32	+2.54	+2.62	+2.37	+2.98
D5	+3.42	+3.83	+3.85	+3.85	+3.82	+3.81	+3.41
D6	+3.48	+3.67	+3.56	+3.37	+3.74	+3.79	+3.95

TABLE (7.3) – (Continued)

$\theta_b = 20^\circ$

Depth	1	2	3	4	5	6	7
D1	+3.17	+1.00	+3.19	+3.28	+3.27	+1.18	+0.19
D2	+2.88	+2.40	+3.68	+2.97	+2.07	+1.97	+2.45
D3	+4.41	+3.62	+4.34	+4.43	+3.81	+4.08	+4.80
D4	+6.56	+6.79	+6.87	+7.92	+8.11	+7.12	+7.76
D5	+8.69	+8.70	+7.10	+8.13	+8.10	+8.00	+9.16
D6	+8.28	+9.50	+9.29	+9.63	+8.34	+9.93	+9.14

$\theta_b = 25^\circ$

Depth	1	2	3	4	5	6	7
D1	+13.75	+14.70	+14.70	+14.71	+14.73	+12.66	+14.69
D2	+13.94	+16.80	+16.88	+16.82	+17.04	+17.11	+16.15
D3	+14.50	+14.94	+15.37	+15.35	+18.42	+16.75	+16.41
D4	+14.97	+16.56	+15.74	+16.56	+18.21	+16.66	+17.74
D5	+16.14	+16.51	+16.87	+17.84	+17.07	+17.59	+19.49
D6	+16.07	+16.07	+17.67	+17.78	+18.33	+19.34	+21.70

TABLE (7.3) – (Continued)

$\theta_b = 27.5^\circ$

Depth	1	2	3	4	5	6	7
D1	+14.95	+14.22	+18.35	+18.58	+18.99	+20.45	+21.43
D2	+14.90	+14.87	+18.88	+20.27	+20.31	+22.31	+24.96
D3	+18.67	+18.36	+19.32	+20.17	+20.49	+22.69	+24.96
D4	+16.91	+16.82	+19.24	+20.24	+20.45	+22.92	+25.34
D5	+14.84	+14.80	+18.61	+20.42	+20.57	+23.63	+25.70
D6	+14.54	+18.71	+19.09	+19.16	+22.14	+23.70	+26.09

$\theta_b = 30^\circ$

Depth	1	2	3	4	5	6	7
D1	+19.07	+19.08	+21.61	+25.53	+25.74	+26.29	+27.74
D2	+18.90	+20.23	+21.77	+22.46	+24.90	+28.33	+30.65
D3	+19.81	+19.88	+20.27	+22.64	+27.03	+27.81	+28.64
D4	+18.93	+20.45	+20.50	+21.87	+28.14	+28.27	+28.73
D5	+18.76	+20.33	+22.25	+22.28	+23.61	+29.39	+30.03
D6	+20.02	+19.91	+21.86	+24.80	+25.09	+28.52	+32.81

TABLE (7.3) – (Continued)

$\theta_b = 32.5^\circ$

Depth	1	2	3	4	5	6	7
D1	+19.00	+25.51	+25.53	+29.20	+29.51	+31.83	+32.15
D2	+18.50	+18.77	+22.25	+24.00	+29.70	+31.28	+32.88
D3	+21.31	+21.92	+22.13	+26.84	+26.98	+33.68	+35.39
D4	+20.05	+20.43	+21.86	+23.01	+28.27	+28.66	+35.08
D5	+20.36	+20.34	+20.42	+23.60	+25.05	+33.09	+35.58
D6	+20.25	+20.23	+20.41	+22.52	+30.13	+33.67	+33.82

$\theta_b = 35^\circ$

Depth	1	2	3	4	5	6	7
D1	+19.07	+21.92	+21.96	+30.84	+30.97	+31.32	+33.14
D2	+20.14	+20.93	+23.35	+23.39	+28.63	+29.24	+33.50
D3	+19.93	+20.20	+22.65	+23.70	+28.46	+33.60	+34.13
D4	+21.32	+21.29	+22.57	+25.56	+28.02	+30.84	+34.68
D5	+20.37	+20.73	+22.19	+22.27	+23.61	+27.81	+34.32
D6	+26.41	+22.49	+22.52	+22.50	+26.44	+33.58	+34.50

TABLE (7.3) – (Continued)

$\theta_b = 40^\circ$

Depth	1	2	3	4	5	6	7
D1	+21.19	+13.42	+11.36	+7.91	+7.18	+0.80	−4.23
D2	+21.54	+15.47	+13.42	+11.28	+9.82	+2.61	−2.33
D3	+21.69	+21.52	+19.46	+16.52	+16.46	+11.62	−0.93
D4	+21.29	+20.93	+21.11	+21.11	+21.07	+21.25	+14.94
D5	+20.33	+18.85	+18.78	+20.56	+20.56	+22.18	+21.85
D6	+22.97	+22.72	+22.65	+23.31	+23.37	+23.30	+25.75

$\theta_b = 45^\circ$

Depth	1	2	3	4	5	6	7
D1	+11.48	+4.10	−0.25	−3.20	−3.20	−3.61	−6.89
D2	+17.80	+10.02	+2.50	+0.27	−1.65	−2.48	−4.25
D3	+21.68	+14.24	+10.86	+10.52	+8.10	−1.44	−3.61
D4	+24.29	+17.14	+13.85	+13.75	+13.96	+5.74	+4.18
D5	+24.74	+18.92	+18.92	+15.66	+14.67	+14.46	+13.07
D6	+25.24	+22.13	+21.98	+20.40	+20.83	+21.35	+20.19

TABLE (7.3) – (Continued)

$\theta_b = 50^\circ$

Depth	1	2	3	4	5	6	7
D1	*****	−7.74	−8.40	−8.43	−10.18	−8.56	−8.56
D2	*****	+2.69	+0.93	−3.31	−3.21	−3.52	−5.40
D3	*****	+9.00	+6.10	+0.90	+0.57	−0.80	−0.86
D4	*****	+8.92	+7.00	+7.11	+5.21	+3.79	+4.41
D5	*****	+9.95	+9.96	+9.05	+9.07	+9.73	+10.23
D6	*****	+17.24	+17.86	+17.51	+17.81	+16.99	+17.61

***** – measurements are not reliable

TABLE (7.4) – Measured Values of Deviation Angles of the Horizontal Resultant Velocities for Test Run A3– V3

Key for Tables

** + ve value indicates deviation towards the outer bank

** – ve value indicates deviation towards the inner bank

D1 = 5 mm

D2 = 15 mm

D3 = 25 mm

D4 = 35 mm

D5 = 45 mm

D6 = 55 mm

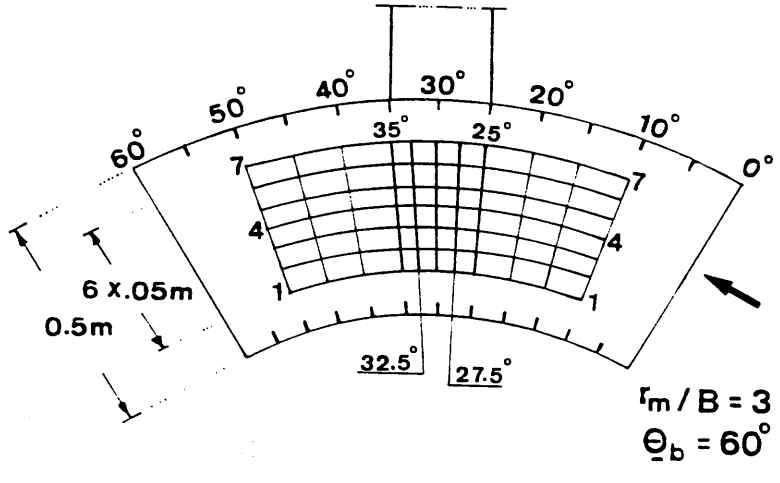

TABLE (7.4) – (Continued)

$\theta_b = 10^\circ$

Depth	1	2	3	4	5	6	7
D1	−3.02	−3.64	−3.05	−3.99	−3.99	−3.04	−3.05
D2	−2.72	−2.31	−2.36	−2.33	−2.73	−2.30	−2.77
D3	−0.79	−0.85	−0.81	−0.81	−0.79	−0.80	−0.82
D4	+0.38	+0.35	+0.47	+0.45	+0.65	+0.29	+0.45
D5	+2.78	+2.86	+2.55	+2.61	+2.74	+2.75	+2.61
D6	+3.93	+3.94	+3.97	+3.95	+3.10	+3.10	+3.18

$\theta_b = 15^\circ$

Depth	1	2	3	4	5	6	7
D1	−4.05	−3.56	−3.78	−3.46	−3.49	−3.53	−3.27
D2	−2.28	−2.22	−2.17	−2.13	−2.11	−2.14	−2.64
D3	−1.98	−1.74	−1.69	−1.78	−1.68	−1.62	−1.14
D4	+0.88	+0.50	+0.79	+0.94	+0.90	+0.88	+0.89
D5	+2.45	+2.93	+2.32	+2.70	+2.34	+2.25	+2.25
D6	+3.70	+3.70	+3.67	+3.75	+3.69	+3.77	+3.79

TABLE (7.4) – (Continued)

$\theta_b = 20^\circ$

Depth	1	2	3	4	5	6	7
D1	−3.51	−3.49	−3.91	−4.25	−3.96	−4.40	−4.43
D2	−2.35	−2.96	−2.24	−2.27	−2.17	−2.30	−2.63
D3	−1.20	−1.69	−1.58	−1.55	−1.53	−1.58	−1.16
D4	+1.15	+1.07	+1.05	+1.10	+1.09	+1.10	+1.10
D5	+3.20	+3.81	+3.86	+3.46	+3.15	+3.24	+3.11
D6	+4.62	+4.63	+4.62	+4.52	+4.65	+4.60	+4.63

$\theta_b = 25^\circ$

Depth	1	2	3	4	5	6	7
D1	−0.45	−0.50	−0.48	−0.72	−0.27	−0.28	−0.03
D2	+0.23	+0.82	+0.32	+0.84	+0.76	+0.83	+1.41
D3	+3.33	+3.52	+3.74	+3.75	+4.16	+4.42	+4.50
D4	+4.04	+4.97	+4.85	+5.96	+5.56	+5.95	+5.91
D5	+6.44	+6.60	+6.34	+6.73	+7.35	+7.42	+7.36
D6	+7.37	+7.37	+7.84	+7.90	+8.24	+8.30	+8.33

TABLE (7.4) – (Continued)

$\theta_b = 27.5^\circ$

Depth	1	2	3	4	5	6	7
D1	+1.74	+1.91	+2.39	+2.52	+2.52	+2.66	+2.78
D2	+5.16	+5.29	+5.82	+5.83	+5.63	+6.77	+6.52
D3	+6.63	+6.63	+6.68	+6.78	+7.69	+7.71	+7.57
D4	+7.49	+7.47	+7.63	+8.40	+8.45	+8.66	+8.81
D5	+9.48	+9.41	+9.27	+9.40	+9.37	+10.06	+10.89
D6	+10.39	+10.40	+10.90	+11.59	+11.68	+11.67	+12.54

$\theta_b = 30^\circ$

Depth	1	2	3	4	5	6	7
D1	+3.23	+3.29	+3.71	+3.45	+3.26	+3.94	+4.19
D2	+6.82	+6.87	+6.82	+6.83	+6.74	+7.54	+7.96
D3	+9.76	+9.76	+9.76	+9.71	+9.69	+9.72	+10.58
D4	+11.52	+11.45	+11.48	+11.47	+11.44	+11.80	+12.13
D5	+13.32	+13.27	+13.91	+13.93	+13.88	+14.00	+14.87
D6	+16.24	+16.24	+16.36	+16.15	+16.06	+16.95	+17.70

TABLE (7.4) – (Continued)

$\theta_b = 32.5^\circ$

Depth	1	2	3	4	5	6	7
D1	+3.56	+3.44	+3.55	+4.17	+4.86	+5.49	+5.72
D2	+6.95	+6.95	+7.89	+7.87	+7.63	+7.34	+7.55
D3	+10.67	+10.68	+10.57	+11.61	+11.69	+11.69	+11.69
D4	+11.87	+12.77	+12.56	+13.41	+13.47	+13.74	+13.84
D5	+14.47	+14.43	+14.44	+15.26	+15.26	+15.82	+15.77
D6	+16.23	+16.26	+16.10	+16.29	+16.59	+17.27	+18.19

$\theta_b = 35^\circ$

Depth	1	2	3	4	5	6	7
D1	+0.58	+0.02	+0.46	+0.97	+0.89	+1.05	+1.87
D2	+4.82	+4.80	+4.85	+4.59	+4.56	+5.30	+5.36
D3	+10.60	+10.63	+10.52	+10.87	+10.83	+11.30	+10.73
D4	+11.72	+12.25	+12.54	+12.49	+12.52	+13.51	+13.70
D5	+13.47	+13.43	+13.39	+13.34	+14.40	+14.78	+14.98
D6	+16.20	+16.65	+16.23	+16.63	+16.61	+18.24	+18.22

TABLE (7.4) – (Continued)

$\theta_b = 40^\circ$

Depth	1	2	3	4	5	6	7
D1	−7.60	−7.59	−7.75	−7.30	−7.73	−8.34	−8.32
D2	−3.79	−4.32	−4.49	−4.78	−4.44	−4.08	−4.50
D3	−1.86	−1.83	−1.73	−2.85	−2.82	−2.86	−2.09
D4	+3.07	+3.51	+3.56	+3.74	+3.78	+3.76	+3.80
D5	+8.41	+8.45	+8.75	+8.41	+8.42	+10.41	+10.93
D6	+10.07	+10.70	+10.92	+10.94	+10.01	+12.99	+12.21

$\theta_b = 45^\circ$

Depth	1	2	3	4	5	6	7
D1	−6.70	−7.46	−7.70	−8.66	−8.68	−8.69	−8.17
D2	−3.56	−3.89	−3.92	−4.16	−3.22	−4.46	−4.19
D3	−1.00	−1.04	−1.18	−1.23	−1.60	−1.73	−1.16
D4	+2.83	+2.45	+2.40	+2.64	+2.27	+2.10	+2.44
D5	+5.07	+5.89	+5.49	+6.38	+6.78	+6.78	+6.28
D6	+8.08	+8.86	+9.97	+9.95	+10.02	+10.08	+10.36

TABLE (7.4) – (Continued)

$\theta_b = 50^\circ$

Depth	1	2	3	4	5	6	7
D1	−8.85	−8.07	−8.79	−8.17	−8.02	−8.36	−8.03
D2	−2.51	−2.51	−3.42	−2.82	−3.25	−3.02	−3.26
D3	+0.14	−0.79	−0.06	−0.96	−0.10	−0.88	−0.08
D4	+2.52	+3.63	+2.93	+2.53	+2.57	+2.58	+2.80
D5	+5.49	+5.46	+5.47	+5.52	+6.73	+6.70	+6.66
D6	+7.07	+7.93	+7.98	+9.03	+9.10	+9.09	+9.07

TABLE (7.5) – Measured Values of Deviation Angles of the Horizontal Resultant Velocities for Test Run A5– V5

Key for Tables

** + ve value indicates deviation towards the outer bank

** – ve value indicates deviation towards the inner bank

D1 = 5 mm

D2 = 20 mm

D3 = 35 mm

D4 = 45 mm

D5 = 60 mm

D6 = 75 mm

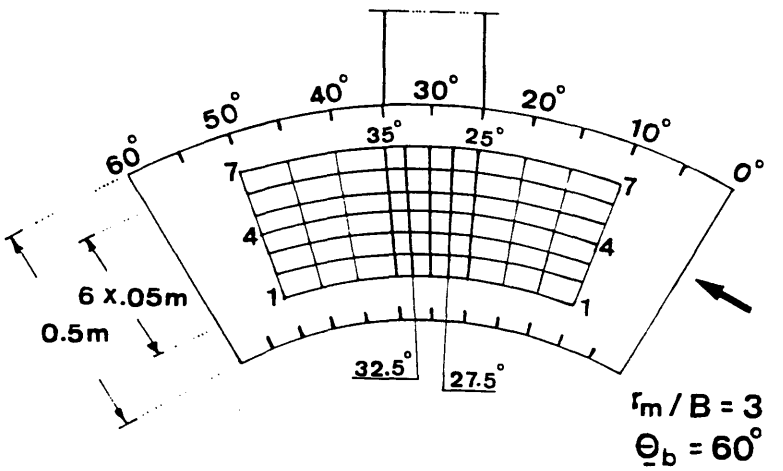

TABLE (7.5) – (Continued)

$\theta_b = 10^\circ$

Depth	1	2	3	4	5	6	7
D1	−3.53	−3.54	−3.82	−3.16	−3.63	−3.50	−4.28
D2	−1.93	−1.94	−1.96	−2.04	−2.65	−2.04	−2.01
D3	−0.42	−0.57	−0.42	−0.52	−0.21	−0.47	−0.56
D4	+0.38	+0.42	+0.84	+0.42	+0.46	+0.36	+0.43
D5	+2.18	+2.19	+2.54	+2.38	+2.19	+2.17	+2.11
D6	+3.19	+3.58	+3.02	+3.88	+3.15	+3.26	+3.08

$\theta_b = 15^\circ$

Depth	1	2	3	4	5	6	7
D1	−3.60	−3.56	−3.63	−4.22	−4.82	−4.87	−4.30
D2	−1.00	−1.87	−1.97	−2.07	−2.21	−2.08	−2.01
D3	−0.40	−0.55	−0.42	−0.35	−0.53	−0.56	−0.52
D4	+0.93	+0.31	+0.35	+0.26	+0.29	+0.39	+0.54
D5	+1.90	+1.79	+1.16	+1.15	+1.81	+1.82	+1.86
D6	+3.43	+3.46	+3.49	+3.13	+3.52	+3.04	+3.20

TABLE (7.5) – (Continued)

$\theta_b = 20^\circ$

Depth	1	2	3	4	5	6	7
D1	−3.60	−3.78	−3.24	−3.75	−3.66	−3.85	−3.26
D2	−1.43	−1.12	−1.00	−1.95	−1.75	−1.99	−2.01
D3	+0.86	+0.62	+0.98	+0.54	+0.15	+0.66	+0.66
D4	+2.32	+2.24	+2.24	+1.79	+1.85	+1.30	+1.15
D5	+3.33	+3.23	+3.23	+3.14	+2.75	+2.76	+2.94
D6	+3.93	+4.38	+4.00	+4.46	+3.47	+4.04	+4.34

$\theta_b = 25^\circ$

Depth	1	2	3	4	5	6	7
D1	−3.52	−3.56	−3.55	−3.52	−1.82	−1.91	−0.92
D2	−0.40	−0.43	−0.46	−0.57	−0.42	−0.46	+0.92
D3	+2.08	+2.10	+2.14	+2.17	+2.92	+3.03	+3.07
D4	+2.30	+2.50	+3.31	+3.32	+3.34	+3.33	+3.32
D5	+3.68	+3.45	+3.67	+4.62	+4.45	+4.46	+4.43
D6	+4.88	+4.84	+4.83	+5.86	+5.86	+5.07	+5.09

TABLE (7.5) – (Continued)

$\theta_b = 27.5^\circ$

Depth	1	2	3	4	5	6	7
D1	−3.47	−3.48	−3.50	−0.12	−0.43	+1.92	+1.05
D2	+0.26	+0.28	+0.21	+0.74	+0.66	+0.71	+0.68
D3	+0.52	+0.63	+0.69	+3.60	+3.33	+7.86	+7.89
D4	+3.31	+3.40	+3.37	+3.37	+3.45	+7.44	+7.50
D5	+7.37	+7.36	+7.67	+7.98	+8.08	+8.44	+8.24
D6	+5.05	+8.92	+8.89	+8.88	+8.88	+13.10	+9.05

$\theta_b = 30^\circ$

Depth	1	2	3	4	5	6	7
D1	−3.55	+3.50	+3.46	+1.91	+1.94	+1.99	+2.00
D2	+2.26	+2.26	+2.60	+3.78	+3.74	+3.76	+3.01
D3	+3.52	+3.38	+4.85	+4.61	+4.65	+7.80	+8.57
D4	+5.66	+5.54	+6.75	+7.34	+7.68	+7.43	+8.75
D5	+7.03	+7.21	+7.20	+7.85	+8.23	+8.47	+10.20
D6	+8.98	+8.08	+8.99	+8.24	+8.94	+14.54	+13.09

TABLE (7.5) – (Continued)

$\theta_b = 32.5^\circ$

Depth	1	2	3	4	5	6	7
D1	−3.51	−3.57	−3.49	−3.47	−0.47	+1.94	+2.01
D2	+0.23	+0.25	+0.22	+0.22	+0.21	+1.96	+1.73
D3	+2.65	+2.86	+2.94	+2.94	+8.11	+8.49	+8.53
D4	+3.57	+3.54	+3.54	+3.54	+7.38	+8.65	+8.79
D5	+7.23	+7.26	+7.43	+7.45	+8.56	+10.33	+10.49
D6	+13.15	+13.25	+8.92	+8.91	+11.57	+13.17	+13.18

$\theta_b = 35^\circ$

Depth	1	2	3	4	5	6	7
D1	−6.00	−6.04	−3.42	−1.85	−1.54	−3.49	−3.46
D2	+0.28	+0.34	+0.46	+0.71	+0.93	+0.99	+0.99
D3	+3.47	+3.53	+3.52	+3.53	+7.33	+7.25	+7.17
D4	+7.34	+7.34	+7.38	+7.40	+7.33	+7.32	+7.42
D5	+7.86	+7.76	+7.68	+7.60	+7.99	+10.40	+10.28
D6	+8.94	+8.94	+8.97	+8.97	+8.98	+9.00	+9.01

TABLE (7.5) – (Continued)

$\theta_b = 40^\circ$

Depth	1	2	3	4	5	6	7
D1	−6.19	−6.19	−6.26	−6.12	−6.14	−6.17	−6.06
D2	+0.22	+0.19	+0.47	+0.19	+0.38	+0.23	−3.49
D3	+2.89	+2.95	+3.01	+2.94	+2.92	+2.11	+2.11
D4	+3.52	+3.55	+3.55	+3.54	+3.55	+3.53	+3.47
D5	+7.35	+7.36	+7.36	+7.63	+3.59	+3.54	+3.48
D6	+11.59	+11.61	+11.62	+11.59	+8.81	+8.87	+8.92

$\theta_b = 45^\circ$

Depth	1	2	3	4	5	6	7
D1	−6.11	−6.11	−6.13	−6.15	−6.15	−6.12	−7.21
D2	+0.10	−0.32	−0.44	−6.05	−5.83	−6.07	−8.10
D3	+2.17	+2.95	+2.90	−3.43	−3.33	−3.52	−3.58
D4	+3.57	+3.58	+3.55	+3.55	+3.39	+3.36	+3.51
D5	+8.83	+6.65	+5.65	+4.61	+4.59	+4.56	+4.19
D6	+14.53	+13.17	+13.14	+13.15	+13.15	+9.12	+9.08

TABLE (7.5) – (Continued)

$\theta_b = 50^\circ$

Depth	1	2	3	4	5	6	7
D1	−6.16	−7.63	−7.79	−6.91	−6.51	−7.41	−7.43
D2	−3.44	−3.47	−5.95	−5.99	−6.00	−6.04	−7.11
D3	−3.73	−3.48	−3.52	−3.54	−3.57	−3.62	−3.62
D4	+3.42	+3.26	+3.47	+3.21	+3.39	+3.55	+3.08
D5	+4.91	+4.89	+4.88	+4.90	+4.89	+4.49	+4.83
D6	+13.17	+13.14	+13.11	+10.41	+13.07	+13.08	+10.07

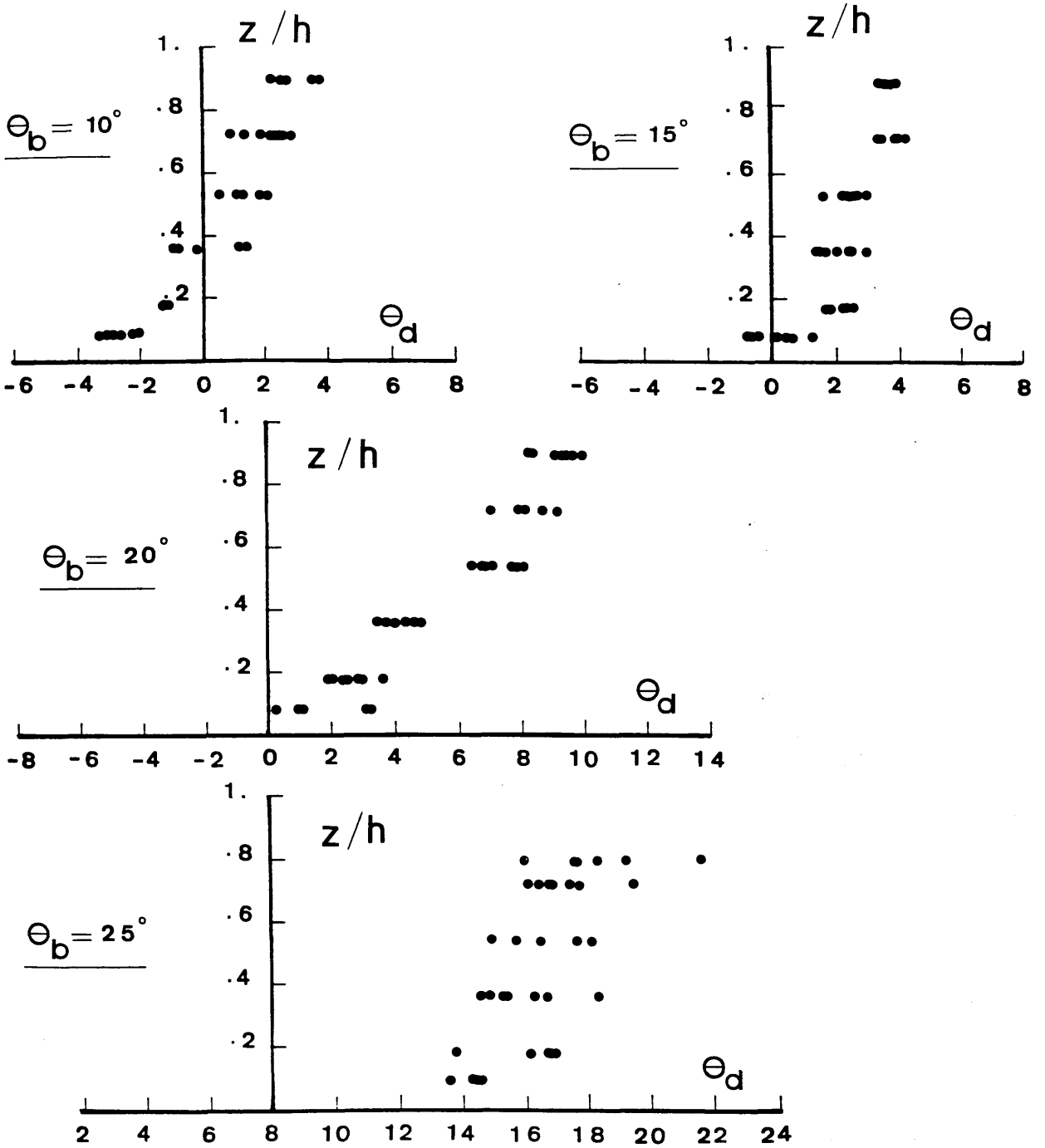

Θ_b ≡ local bend angle
Θ_d ≡ local deviation angle (in degrees)
z/h ≡ non–dimensional water depth

FIG.(7.26) – Distributions of Measured Deviation Angles of the Horizontal Resultant Currents Along the Bend Channel for Test Run A1–V1

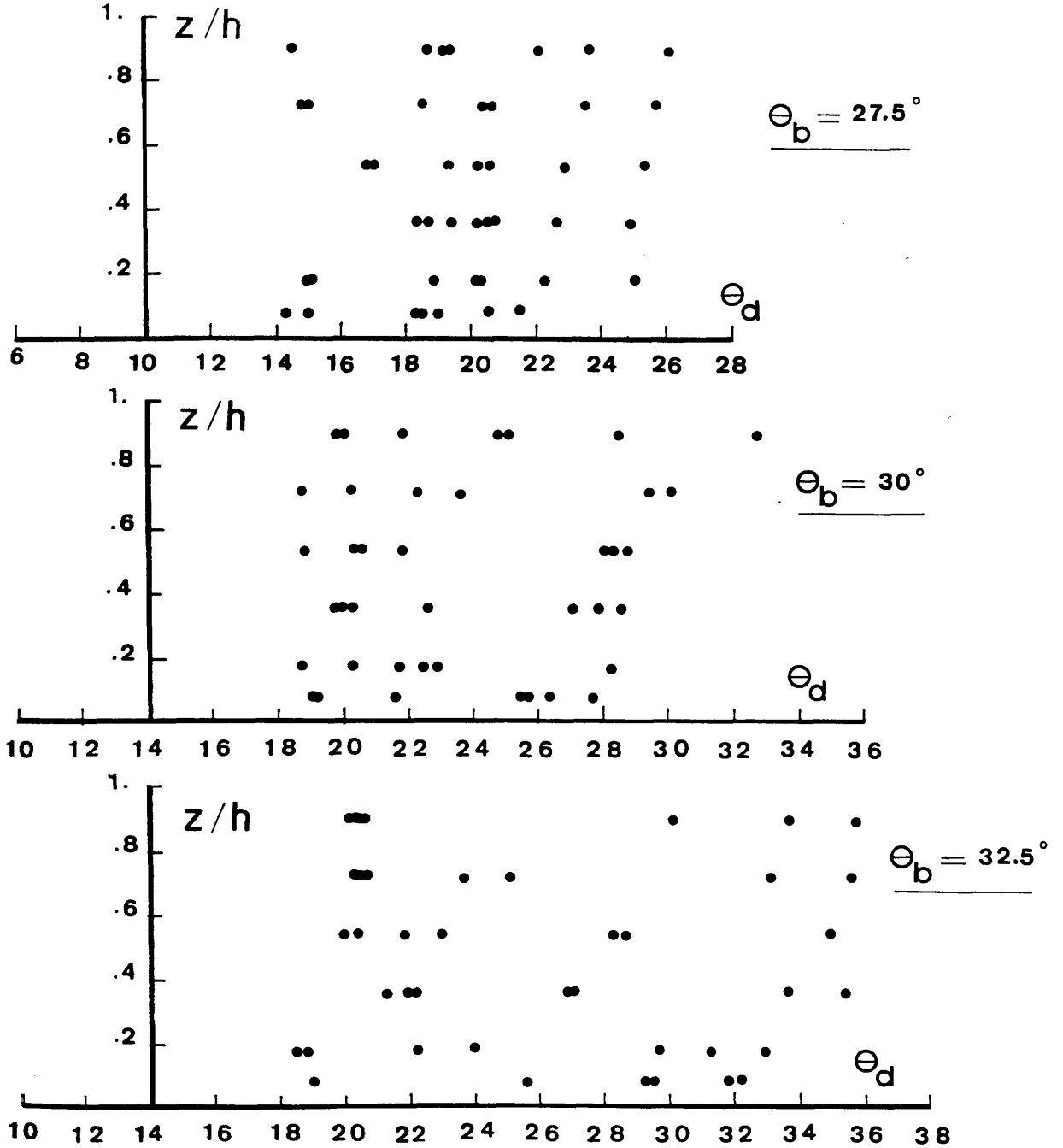

Θ_b ≡ local bend angle
Θ_d ≡ local deviation angle (in degrees)
z/h ≡ non−dimensional water depth

FIG.(7.26) − (Continued)

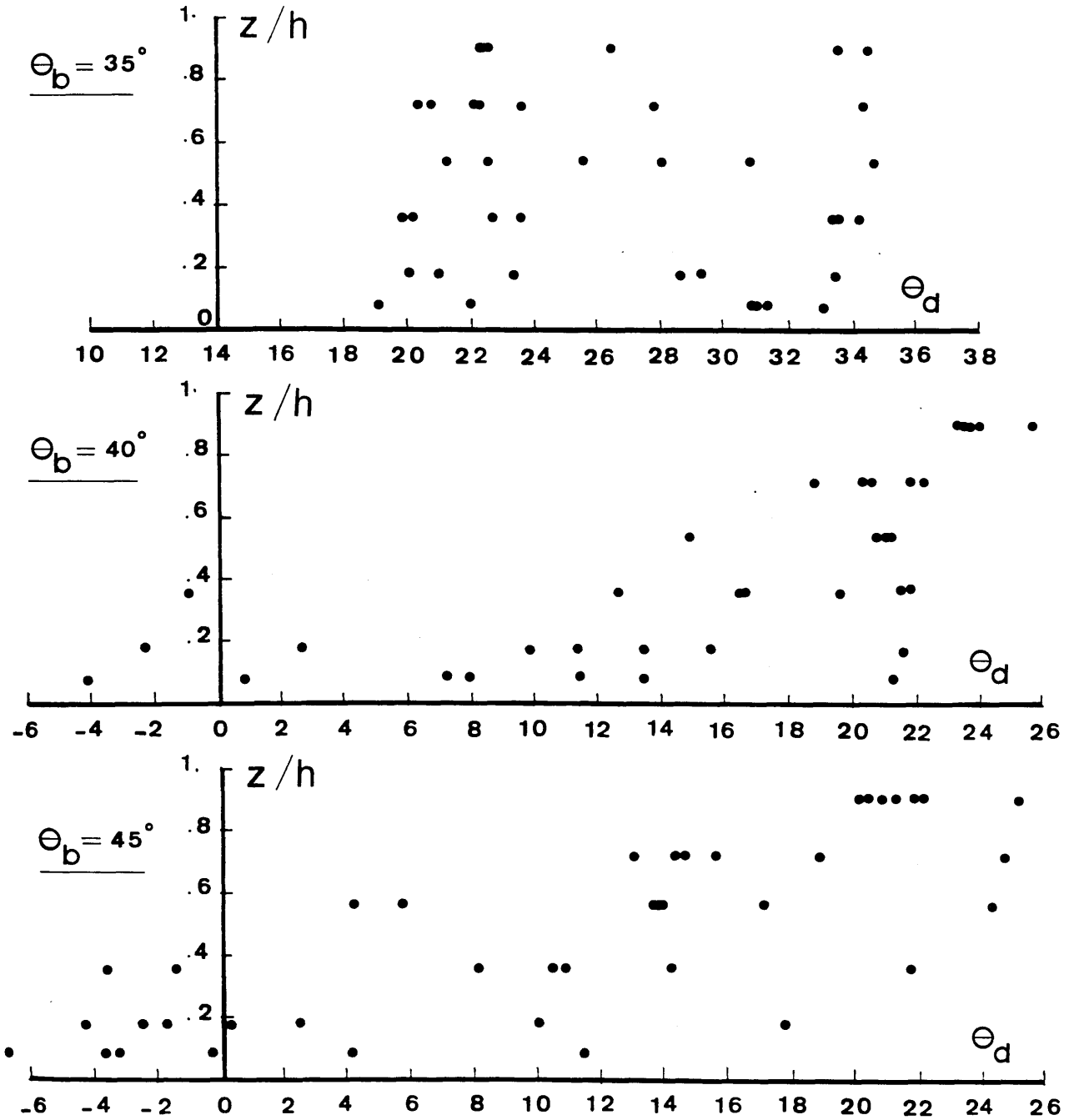

Θ_b ≡ local bend angle
Θ_d ≡ local deviation angle (in degrees)
z/h ≡ non−dimensional water depth

FIG.(7.26) − (Continued)

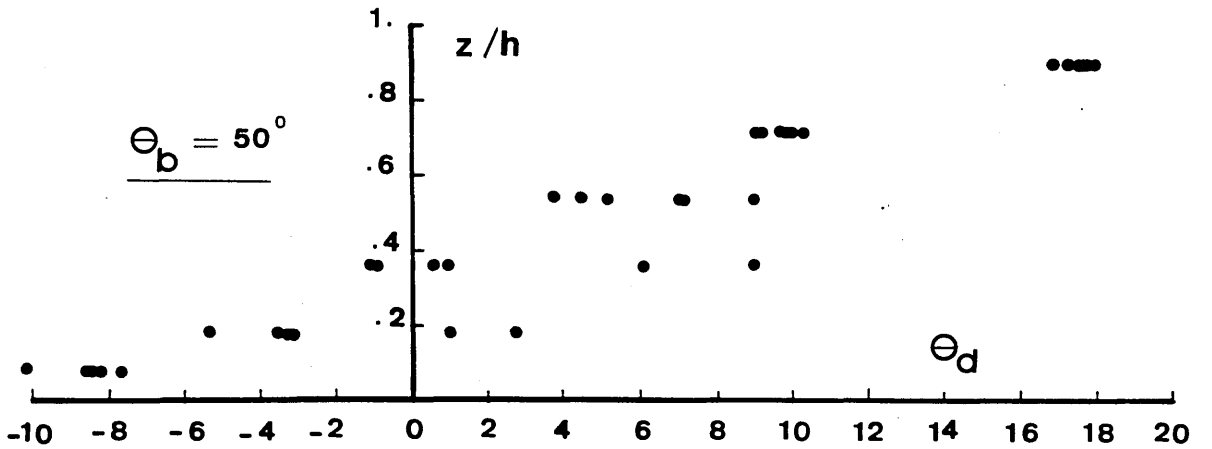

Θ_b ≡ local bend angle
Θ_d ≡ local deviation angle (in degrees)
z/h ≡ non– dimensional water depth

FIG.(7.26) – (Continued)

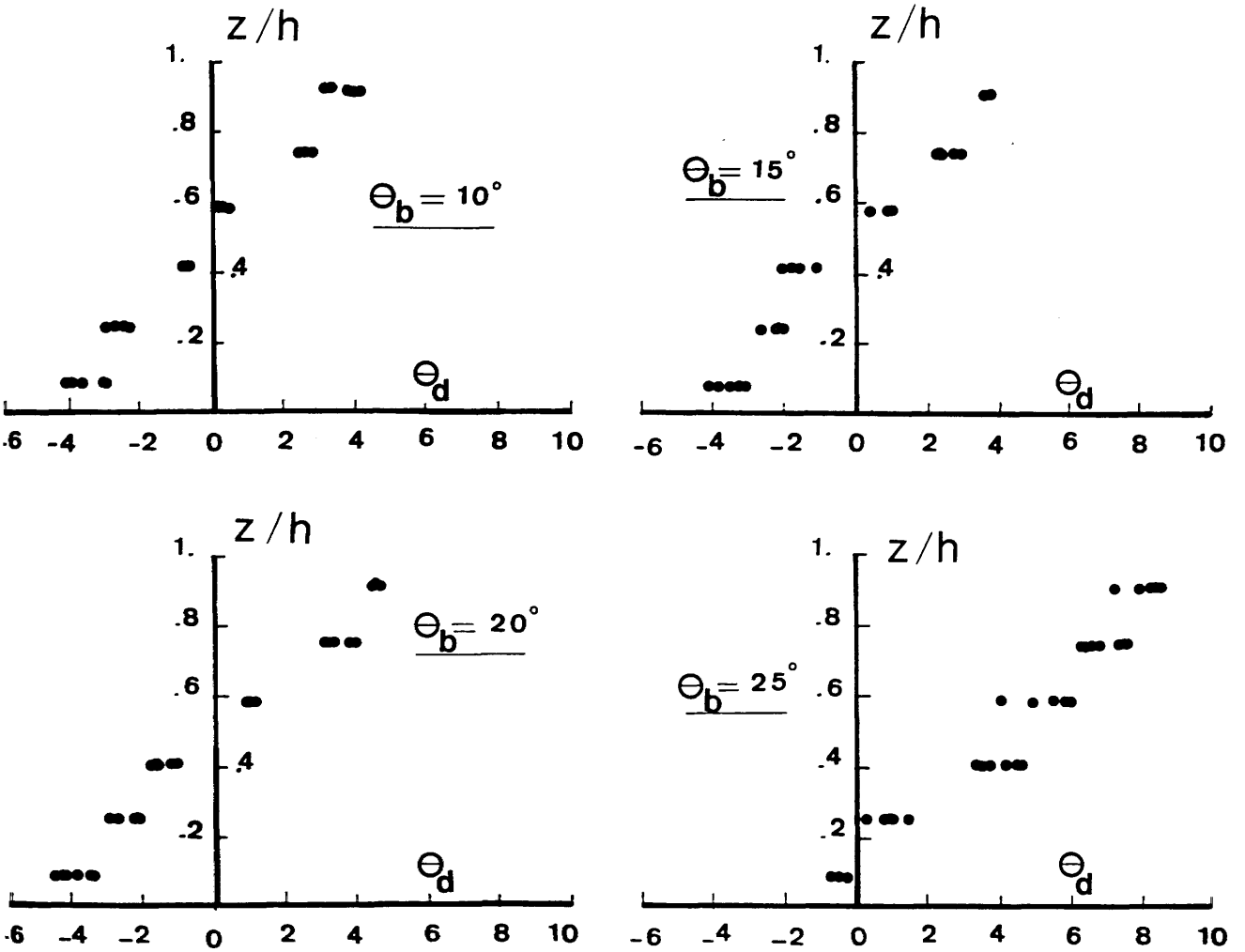

Θ_b ≡ local bend angle
Θ_d ≡ local deviation angle (in degrees)
z/h ≡ non−dimensional water depth

FIG.(7.27) − Distributions of Measured Deviation Angles of the Horizontal Resultant Currents Along the Bend Channel for Test Run A3− V3

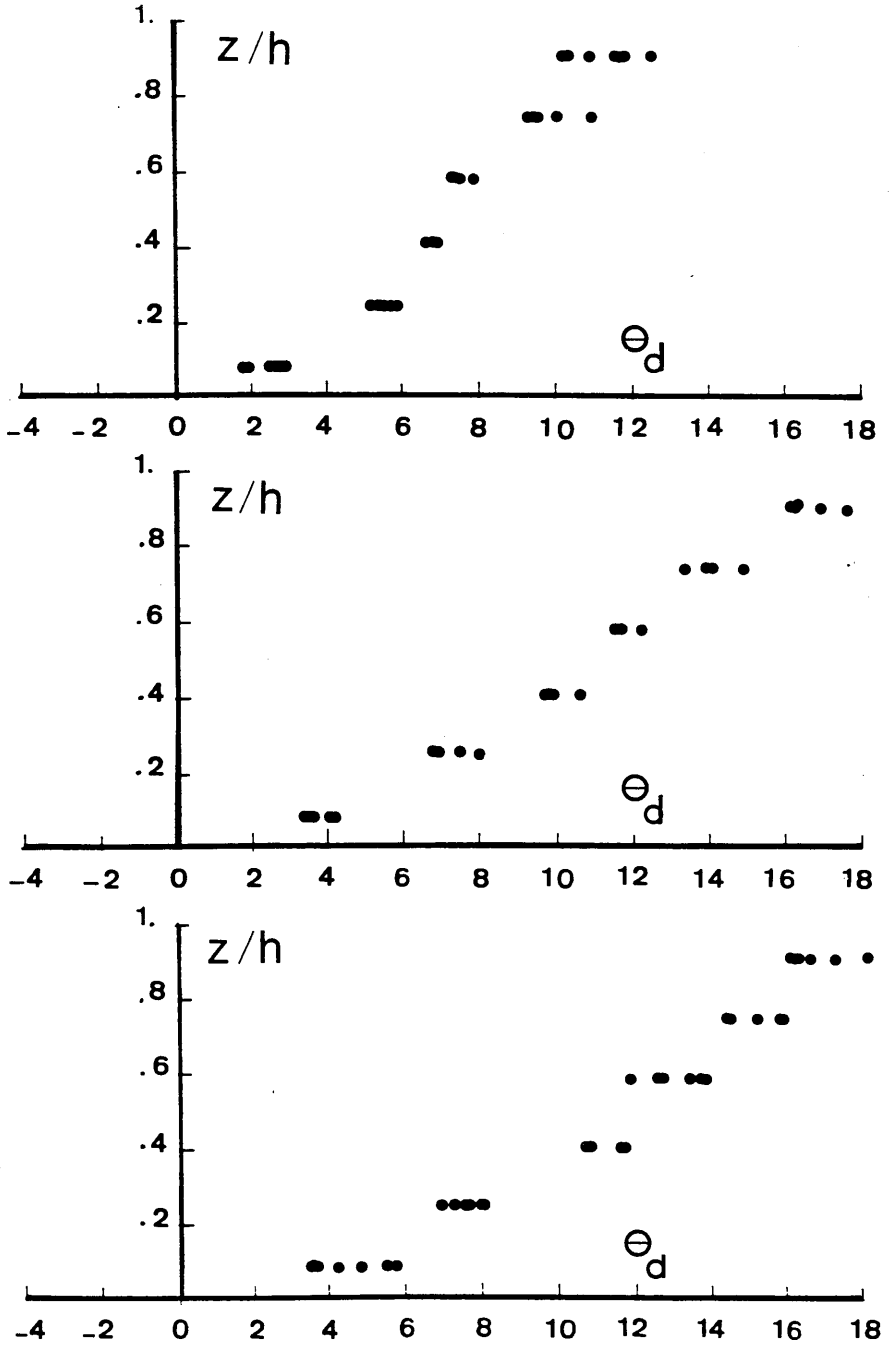

Θ_b ≡ local bend angle
Θ_d ≡ local deviation angle (in degrees)
z/h ≡ non−dimensional water depth

FIG.(7.27) − (Continued)

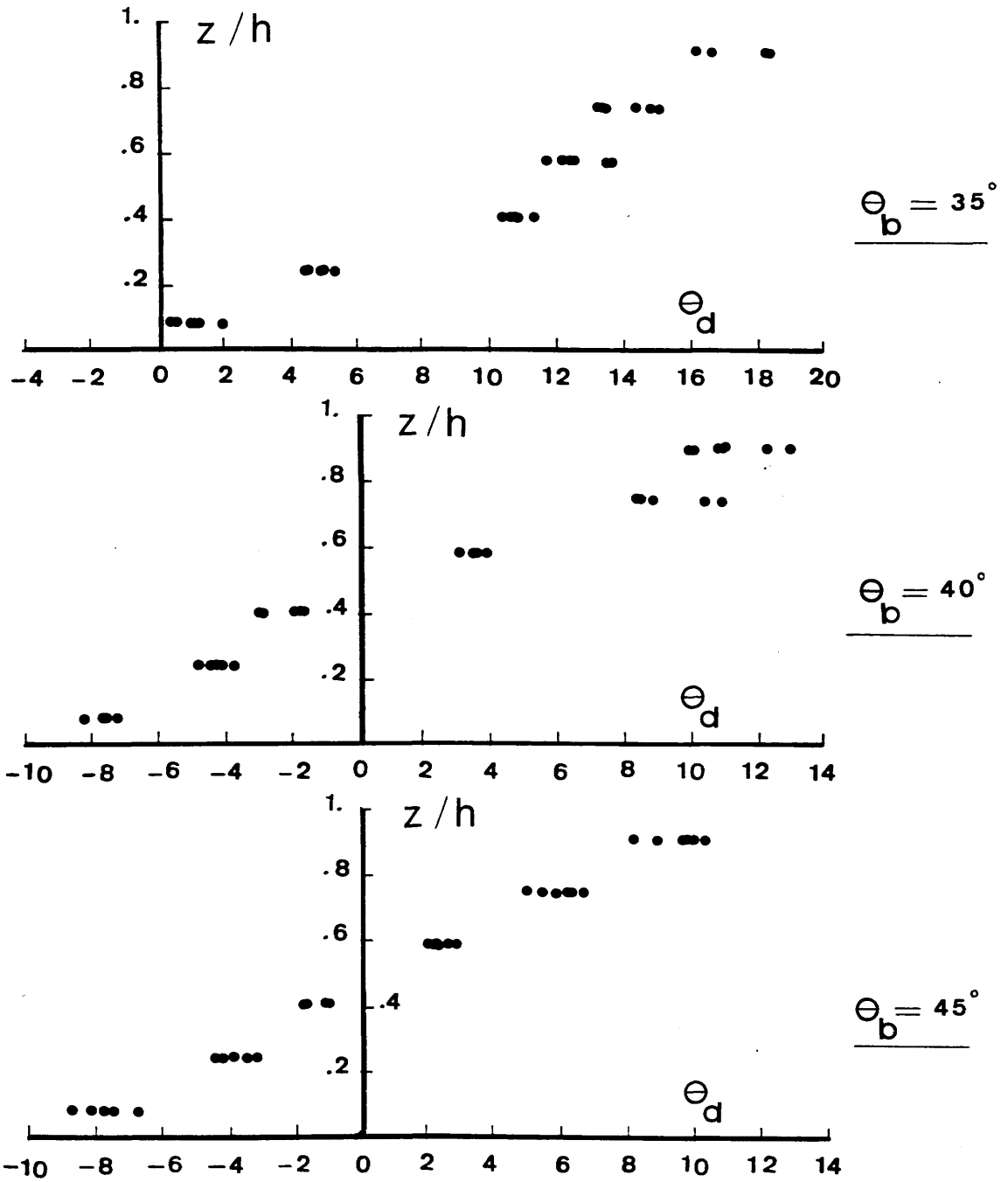

Θ_b ≡ local bend angle
Θ_d ≡ local deviation angle (in degrees)
z/h ≡ non− dimensional water depth

FIG.(7.27) − (Continued)

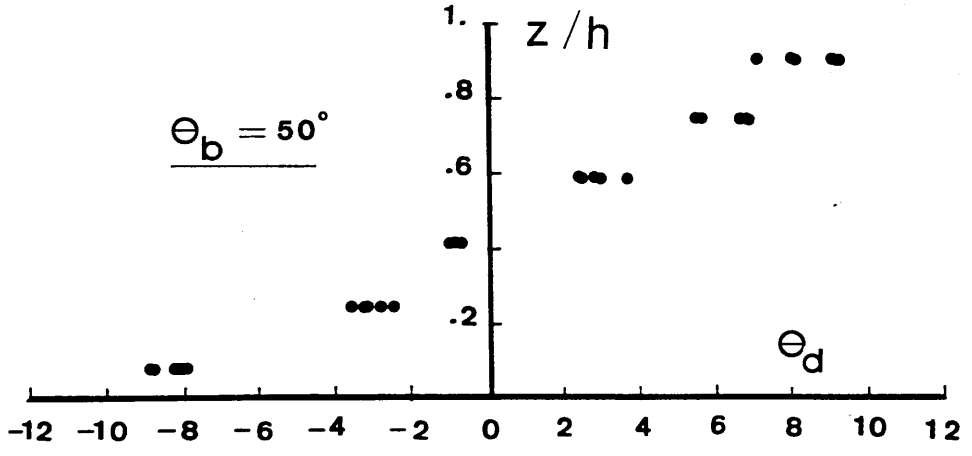

Θ_b ≡ local bend angle
Θ_d ≡ local deviation angle (in degrees)
z/h ≡ non– dimensional water depth

FIG.(7.27) – (Continued)

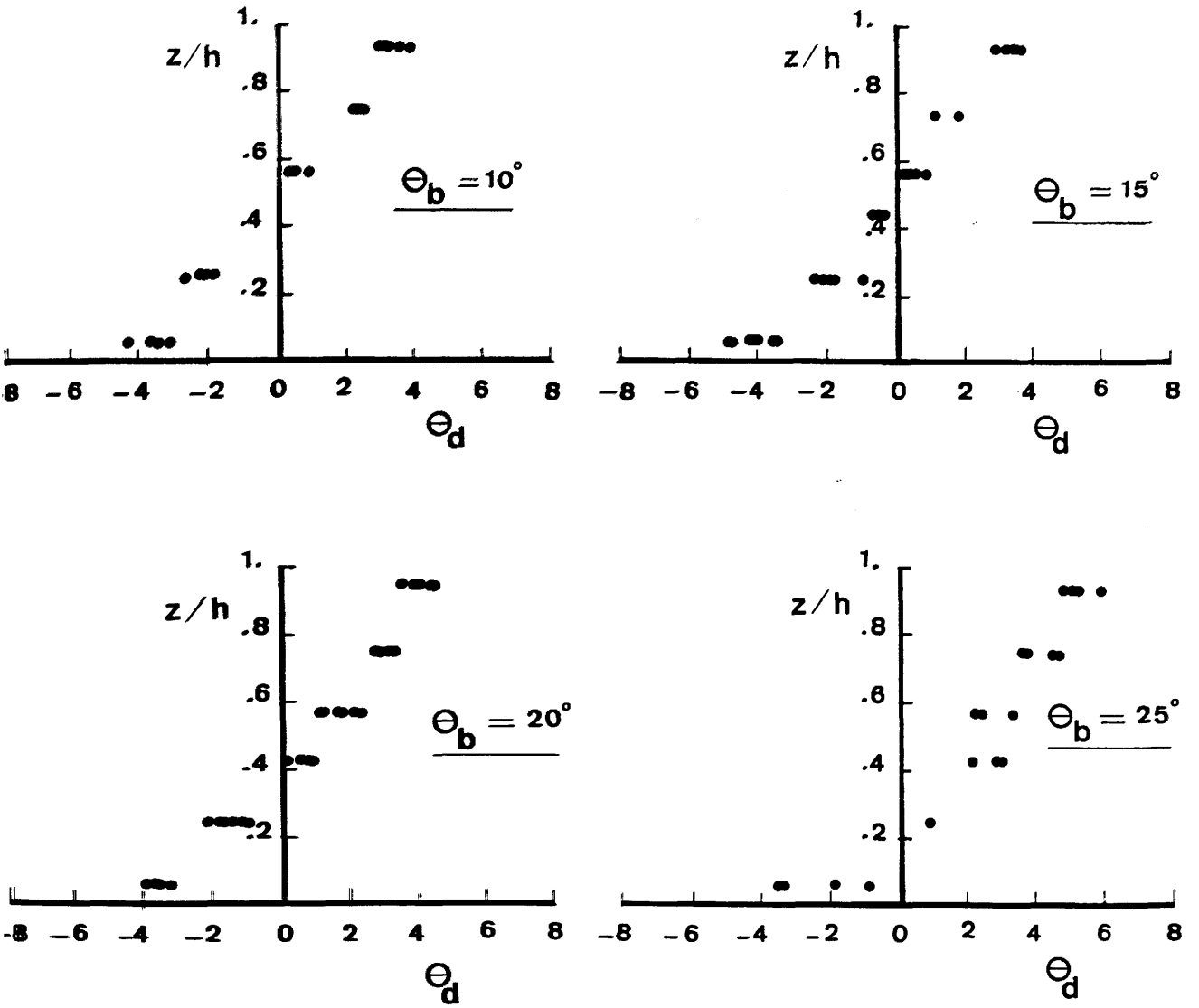

Θ_b ≡ local bend angle
Θ_d ≡ local deviation angle (in degrees)
z/h ≡ non-dimensional water depth

FIG.(7.28) – Distributions of Measured Deviation Angles of the Horizontal Resultant Currents Along the Bend Channel for Test Run A5–V5

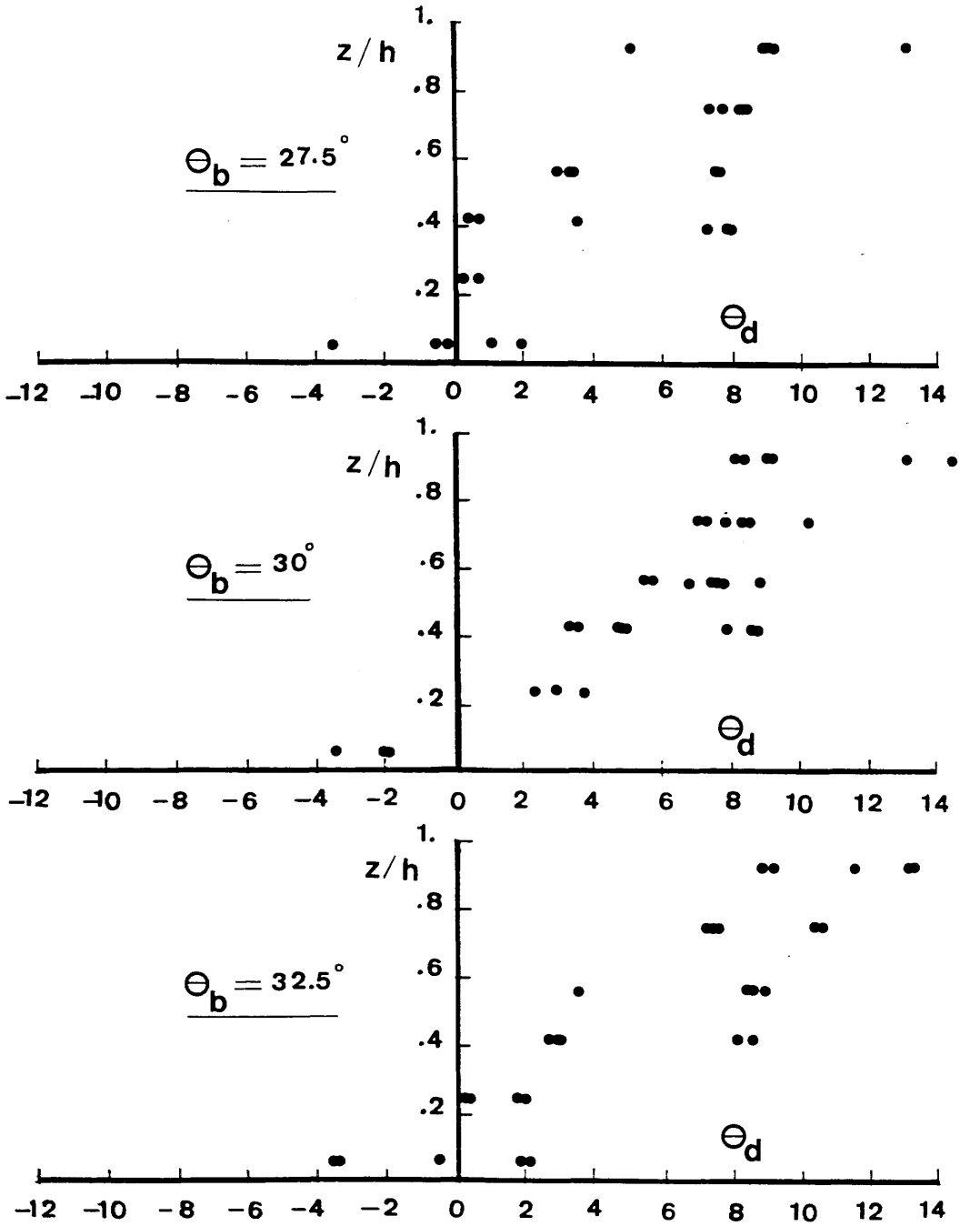

Θ_b ≡ local bend angle
Θ_d ≡ local deviation angle (in degrees)
z/h ≡ non−dimensional water depth

FIG.(7.28) − (Continued)

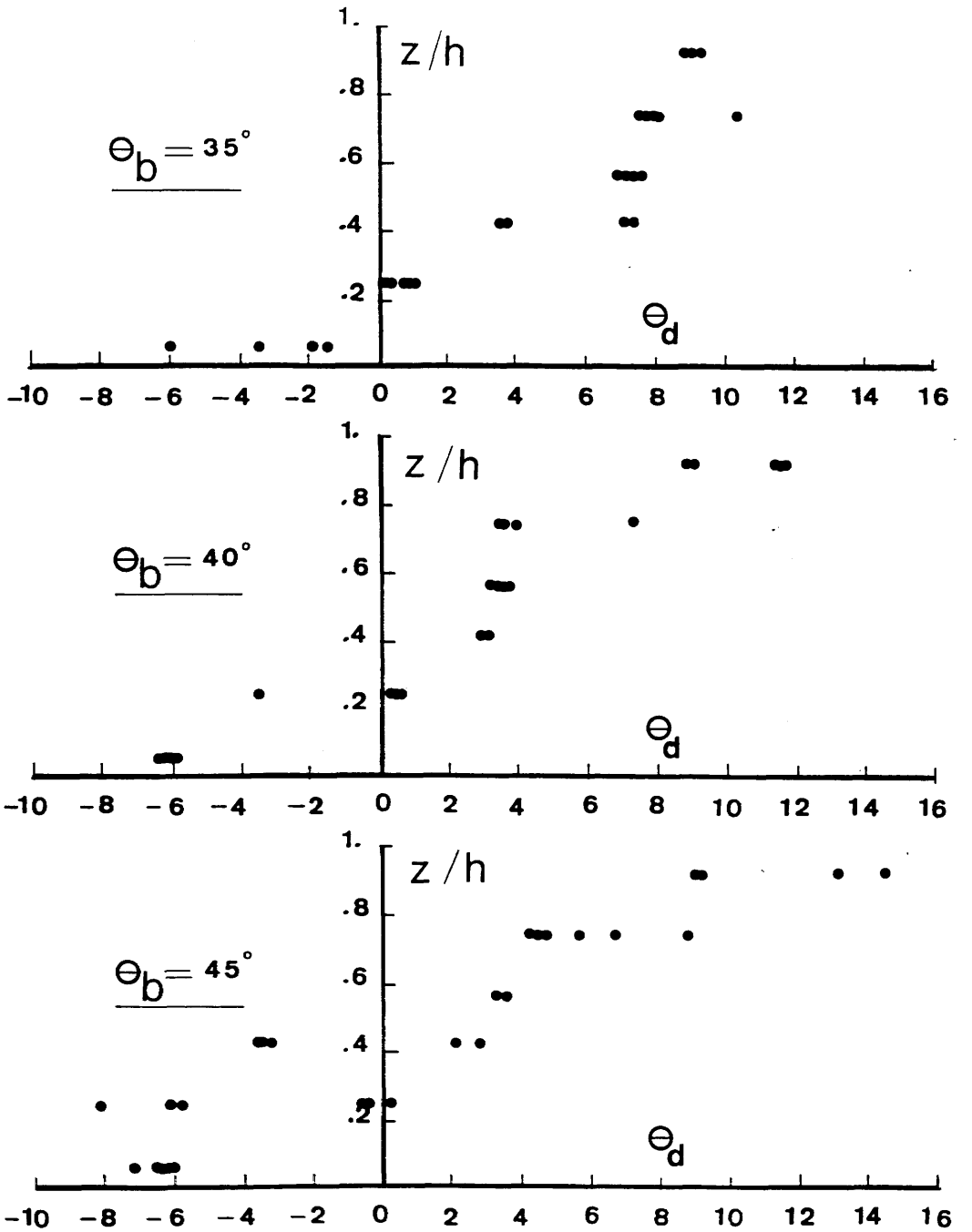

Θ_b ≡ local bend angle
Θ_d ≡ local deviation angle (in degrees)
z/h ≡ non−dimensional water depth

FIG.(7.28) − (Continued)

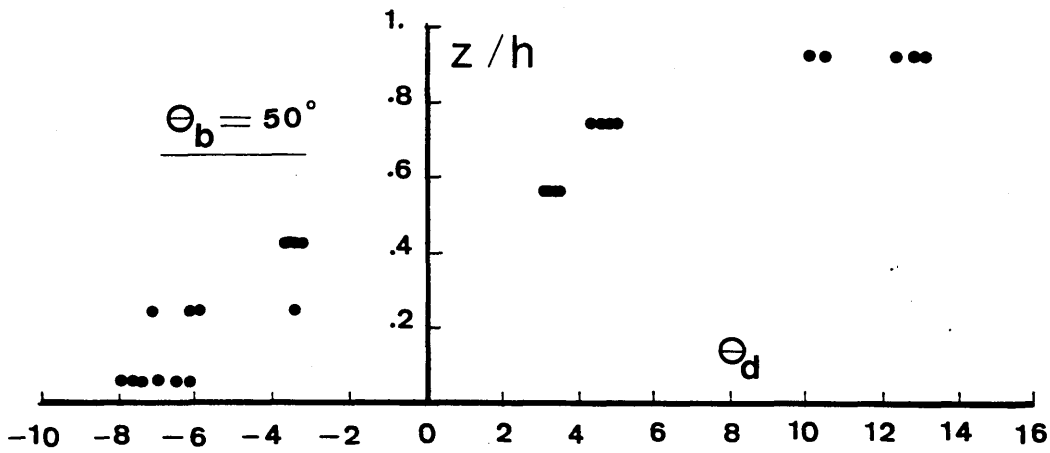

Θ_b ≡ local bend angle
Θ_d ≡ local deviation angle (in degrees)
z/h ≡ non− dimensional water depth

FIG.(7.28) − (Continued)

CHAPTER VIII

SUMMARY, CONCLUSIONS AND RECOMMENDATIONS

CHAPTER VIII

SUMMARY , CONCLUSIONS AND RECOMMENDATIONS

(8.1) SUMMARY

The characteristics of flow in a gentle wide channel bend at the intersection with a flood relief channel were studied. The study was restricted to the case of subcritical flows in a bend with rigid boundaries and a uniform rectangular cross section. The effect of the intersection on the water surface profiles and on the velocity distributions was shown. Two approaches were employed in the investigation, namely:

- **The Mathematical Approach**
- **The Experimental Approach**

(8.1.1) The Mathematical Approach

The mathematical formulation of the problem was divided into two main stages. In the first stage, the formulation of flow around a channel bend was undertaken. This is given in Chapter III. The bend model was divided into a series of sub– models. Each sub– model simulated one particular aspect of the bend flow. These sub– models and their objectives were:

- Width– Averaged Model 1: from which the vertical distribution of the radial velocities is obtained.

- Depth– Averaged Model 1: from which the radial distribution of the depth– averaged velocities at the entrance to the bend is modelled.

- Depth– Averaged Model 2: from which the horizontal distribution of the water depth and the depth– averaged velocities in the channel bend is determined.

- Width– Averaged Model 2: for modelling of the re– distribution of the vertical profile of the longitudinal velocities along the bend course.

- Width– Averaged Model 3: in order to formulate the problem of the growth and decay of the radial velocities along and beyond the bend.

The general solution of the flow around the channel bend was achieved by joining these sub– models together (as described in detail in Appendix (D)). In most cases, the solutions for the different models were obtained numerically using a finite difference technique. The sub– models were verified using quantitative comparisons with existing mathematical models, experimental results and some field data from the literature. In general, the comparisons showed very good agreement.

In the second stage of the formulation, the effects of the flood relief channel intersection on the bend flow characteristics were simulated. This stage was also divided into two steps. Firstly, before proceeding to a curved channel situation, a dynamic equation for the flow in a straight channel at the intersection with a side overflow was developed using the momentum principle. This equation was combined with the conventional weir equation to predict the variations in depth and velocities along the intersection. The predictions obtained from the combined equations were checked against existing numerical models and experimental results, for cases of sub- and supercritical flows. These were found to be satisfactory. Secondly, having verified the form of the dynamic equation necessary for dealing with combined channel flows and overflows, consideration was given to the curved channel situation. In this case, the flow entering the flood relief channel was modelled as a flow over a side weir with a broad crest. The influence of the bend curvature (i.e. the superelevation effect at the water surface and the distortion of depth-averaged velocities) on the flow was introduced by dividing the bend cross section into a series of concentric strips each with a different water depth and a different depth-averaged velocity. Each bend strip was treated as a separate sub-channel and the model equations were applied to each of the sub-channels. The assumption of constant specific energy for the flow along the intersection was employed in the formulation and was found to be justified. The solutions were obtained numerically by using a standard computational method.

Finally, the width-averaged bend model was applied without modification in order to study the influence of the diversity and cross currents of the flow, produced by the intersection, on the vertical profiles of the longitudinal velocities. Quantitative comparisons with experimental profiles (obtained from the present study) were made and the effect of the intersection on the profiles was discussed in detail.

(8.1.2) The Experimental Approach

A physical laboratory model was designed and built (as described in Chapter V) in order to provide data suitable for the verification of the mathematical model. Experimental measurements were divided into three groups:

- Measurements of water surface profiles.
- Measurements of deviation angles of horizontal resultant velocities.
- Measurements of longitudinal velocities.

In each group, measurements were carried out for both the channel bend alone and after the introduction of the flood relief channel. Water surface profiles were measured in both bend and flood relief channels while measurements of both deviation angles and longitudinal velocities were restricted to the channel bend. Surface profiles were measured using a standard pointer gauge. Deviation angles were measured by connecting an " L-shaped " probe to an IBM computer via a voltage measuring transducer. The longitudinal velocities were obtained by using a Pitot static tube. The radial velocities were calculated using the deviation angles and the longitudinal velocities.

The geometrical dimensions of the laboratory model were:

- total bend angle $\theta_b = 60^\circ$
- mid bend radius $r_m = 1.5$ m
- bend tightness ratio $r_m/B = 3$
- longitudinal bed slope $S_o = 5.1 \times 10^{-4}$
- Coefficient of bed roughness $n = .01$ (smooth bed)

- width of the flood channel C_w = .30 m
- bed level height of the flood channel (weir crest height) C_h = .025 , .045 , .065 m
- length of the flood channel = .30 m

Tests were run under the following range of flow conditions:

- In the case of the channel bend alone:
  - flow discharge in the bend Q = 3.89 → 8.35 l/s
  - flow aspect ratio B/h = 6.29 → 11.91
  - Froude number of the flow F_r = .222 → .288
  - Reynolds number of the flow R_e = 6048 → 11516
- In the case of the bend with the flood relief channel:
  - flow discharge in the bend Q = 2.91 → 10.21 l/s
  - flow discharge ratio Q_{fR}/Q = .08 → .75
  - water head ratio h_w/h = .16 → .71
  - flow aspect ratio B/h = 5.22 → 12.82
  - Froude number of the flow F_r = .177 → .284
  - Reynolds number of the flow R_e = 5283 → 18551

(8.2) USE LIMITATION OF THE MATHEMATICAL MODEL

The satisfactory justification of the mathematical models confirms their validity in simulating the different flow features in a channel bend with and without the introduction of a flood relief channel intersection. However, due to the nature of

their formulation, there are restrictions to the application of the models. These restrictions are as follows:

(8.2.1) Bend Flow

(1) The influence of wall friction was neglected, i.e. the vertical component of the secondary currents (which dominates the cell structure of the currents at or near the channels walls) was ignored. Therefore, the application of the models is restricted to the central region of the channel cross section and to gentle wide channel bends. Within the central 60% of the channel width, the comparisons between the theoretical predictions and the experimental results proved to be very satisfactory.

(2) The use of the logarithmic distribution for the vertical profiles of the longitudinal velocities prevents the direct application of the models at or near the channel bed, i.e. in the lower 10 → 20% of the flow depth. However, the validity of this distribution over the remaining 80 → 90% of the flow depth was found to be justified in this study.

(3) The formulation dealt only with channels with rigid boundaries and a uniform rectangular cross section. This coupled with the use of the logarithmic velocity distribution means that only very limited predictions of bed scour and deposition can be made. However, it would be relatively straight forward to introduce another type of velocity distribution (e.g. parabolic or power distribution), so that a finite value of velocity can be found at the bed of the channel. From this, the distribution of the longitudinal and radial boundary shear stresses in the bend could be determined. Hence, changes in bed topography could be predicted through the simulation of the driving forces of the sediment motion.

(8.2.2) Bend Flow at the Intersection

(1) In modelling the horizontal problem of the flow (i.e. the horizontal variations of water depth and depth–averaged velocity), the transverse momentum exchange between the vertical sections of the flow was not considered. This resulted from the division of the bend cross section into concentric separately–behaved strips. Despite this, satisfactory agreement was obtained between the theoretical and the experimental profiles for cases of $h_w/h \leq .36$ (i.e. for the case of high and medium weirs). In the case of medium to low and low weirs (i.e. for $h_w/h \succ .36$), the radial momentum exchange can no longer be considered negligible as may be seen from the much poorer agreement between the theoretical and experimental profiles for these situations.

(2) The effect of the flow diversity and vortices produced by the intersection on the upstream approaching flow in the channel bend was not included in the formulation. The experimental results show that these factors only become important for cases of $h_w/h \succ .36$.

(3) No attempt was made in the formulation to simulate the stagnation and separation zones which form at the intersection. Again, it is only the higher water head ratios, i.e. $h_w/h \succ .36$, that these zones have a significant effect on the flow profiles.

Since the model equations were mainly solved by using numerical techniques, the results obtained were, to a certain extent, dependent on the size of the finite difference grid and the number of iterations used. Again these could be varied

depending on the particular circumstances prevailing at the time. However, it is thought that the limits chosen and the resulting relatively short execution time make the models suitable for practical use.

(8.3) CONCLUSIONS

The analysis of the different features of the flow in a gentle wide channel bend with and without the introduction of the flood relief channel allows a number of conclusions to be drawn. However, the main general conclusion from this study is that:

" The characteristics of the horizontal flow in a channel bend at the intersection with a flood relief channel can be predicted successfully by combining a 2D bend model and a spatially varied flow equation. The analysis shows that the suggested mathematical model can be used satisfactorily for high to medium flood channel bed levels . It is further shown that the bend characteristics continue to dominate the flow again for high to medium (weir) flood channel bed levels but that at medium to low (weir) channel bed levels, the local effects produced by the intersection predominate. "

Detailed conclusions can also be obtained and these will be presented separately for the case of flow in the wide bend alone and for the case where the

flood relief channel is introduced.

(8.3.1) For Flow in a Gentle Wide Channel Bend

(8.3.1.1) Flow in a gentle bend can be simulated adequately by means of a quasi 3D model, i.e. a model based on the interaction of 1D width–averaged models and a 2D depth–averaged model.

(8.3.1.2) The development of the superelevation at the water surface starts at the bend entrance. In the first third of the bend, the superelevation continues to develop. In the middle third of the bend path, the superelevation remains effectively constant. In the last third of the bend, a rapid decrease in the superelevation occurs with a tendency to a reverse effect at the exit from and beyond the channel bend.

(8.3.1.3) The effect of the secondary circulation on the horizontal distribution of depth–averaged velocities is small in the first half of the bend but becomes larger in the second half.

(8.3.1.4) Over the central 60% of the channel width, only one cell of the secondary flow was observed throughout the whole length of channel considered.

(8.3.1.5) Growth and decay of the secondary currents, along and beyond the bend, can be predicted reasonably well by means of the exponential distribution. This allows the length of the channel affected by the secondary circulation to be estimated. It has also been shown that the growth of the bottom

currents and those located in the outer half of the bend is faster than that of the surface currents and those located in the inner half of the bend.

(8.3.1.6) Within the tested flow conditions, the strength of the currents is found to be $\leq$ 2.32% of the main currents. From this, it was concluded that the additional energy losses due to bend resistance can be considered minor.

(8.3.1.7) By applying potential vortex theory to the flow at the bend entrance, the relationship between the degree of bend curvature (in terms of r_m/B) and the ratio between the inner and outer boundary shear stresses (in terms of u_{*i}/u_{*o}) was derived. The radial distribution of the boundary shear stresses was found to have an approximately uniform distribution for gently curved bends (i.e. for bends with $r_m/B \geq 3$).

(8.3.1.8) Several authors go further than this and recommended that potential vortex theory can be used for describing the flow pattern within a channel bend. It has been demonstrated in this study that the use of this theory is inaccurate and should be only used to make quick qualitative estimates.

(8.3.1.9) The departure of the centre of the flow volume flux from the centreline of the bend was found to be small, in the range of 10 $\rightarrow$ 12% of the channel width. The departure was towards the outer bank.

(8.3.1.10) The vertical profiles of the longitudinal velocities were found to be in close agreement with the logarithmic distribution (i.e. the familiar "Prandtl– Von Karman" equation) in the upper 80 $\rightarrow$ 90% of the flow depth. In the lower 10 $\rightarrow$ 20% of depth, the logarithmic distribution tends to overestimate the velocities.

(8.3.1.11) By matching the longitudinal gradient of both the point and depth–averaged velocities, an approximate numerical solution was obtained for the redistribution of the vertical profiles of the longitudinal velocities due to the effect of the secondary currents. This allows the vertical velocity component to be determined as a part of the solution.

(8.3.2) For Combined Bend and Flood Channel Flow

(8.3.2.1) The influence of the bend curvature on the flow in the main channel (i.e. the superelevation and the secondary circulation effects) was modelled throught the division of the bend cross section into a series of concentric strips. Each strip, with different mean depth and mean velocity, was considered to behave as a separate sub–channel. The model equations (i.e. the spatially varied flow equation, which was developed initially by using the momentum principle, and the conventional weir equation) were applied individually to each sub–channel. The analysis shows that this procedure can satisfactorily simulate the combined bend and flood channel effects.

(8.3.2.2) The assumption of constant specific energy for the bend flow at the intersection employed in this study was found satisfactory for the case of $h_w/h \leq .36$ (i.e. for high and medium weirs).

(8.3.2.3) The bend flow profiles (i.e. water surface, velocities and deviation angles profiles), in the reach upstream of the intersection, depends on the h_w/h ratio as:

+ For $h_w/h \leq .36$ (i.e. for high and medium weirs), the flow profiles are governed by the bend characteristics, i.e. the intersection effects are not propagated upstream.

+ For $h_w/h > .36$ (i.e. for medium to low and low weirs), the intersection characteristics (i.e. the cross currents and the formation of both stagnation and separation zones) control the flow.

(8.3.2.4) The behaviour of the surface profiles of the bend flow, along the intersection, again depends on the h_w/h ratio as:

+ For $h_w/h \leq .36$ (i.e. for high and medium weirs), the superelevation of the water surface remains almost the same as for the bend alone situation.

+ For $.36 < h_w/h \leq .47$ (i.e. for medium to low weirs), the superelevation tends to show a decrease.

+ For $h_w/h > .47$ (i.e. for low weirs), the stagnation/separation zones at the inner/outer banks of the bend are the features which govern the shape of the surface profiles. In this case, the centrifugal effects on the profiles are of minor significance.

(8.3.2.5) The influence of the h_w/h ratio on the distributions of velocities and deviation angles along the intersection is:

+ For $h_w/h \leq .36$ (i.e. for high and medium weirs), the effect of the bend characteristics on the profiles prevails.

+ For $h_w/h > .36$ (i.e. for medium to low and low weirs), the flow

profiles are mainly affected by the intersection characteristics rather than the bend characteristics.

(8.3.2.6) Downstream of the intersection, the bend characteristics in the flow are re–established for all h_w/h ratios. The rate of this re–establishment depends on the h_w/h ratio. The higher the h_w/h ratio, the slower the rate of re–adjustment to the bend characteristics.

(8.3.2.7) Using the numerical results obtained from the depth–averaged model for the flow along the intersection, the longitudinal and radial gradients of the bend discharge were predicted. The theoretical predictions show that the radial gradient of the discharge is independent of the h_w/h ratio, while the longitudinal gradient is very much dependent on the ratio.

(8.4) RECOMMENDATIONS

In the practical case of full or partial neck cut–off of a meander loop, there are two intersections between the bend and the cut–off channel flow; an upstream intersection and downstream intersection. This investigation has dealt only with the characteristics of the flow at the upstream intersection. It would now be logical to move to the study and simulation of the characteristics of the flow at the downstream intersection. This would be the main recommendation for further study. But in the course of the present investigation, some interesting questions have risen and study of these would lead to more understanding of both the bend and intersection problem. These questions are:

1 Since only channels with rigid boundaries were considered, what will be the behaviour of the flow when loose boundaries are introduced ? . Clearly this would be a very complicated situation to study both mathematically and experimentally. As an intermediate step, it would be worthwhile modifying the physical model bed such that it takes the form of a typical bend bed topography.

2 With the introduction of loose boundaries, what is the time variation effect on the bed form characteristics in the channel bend at the intersection ? . This effect is crucial on the long term regime of the flow in the bend and on the local variation of the channel bed topography at the intersection.

3 Since only a gentle wide channel bend is considered, what is the effect of increasing the degree of bend curvature on the flow behaviour in both bend and flood channel ? In this case, the inclusion of the wall effects and the radial exchange of the flow momentum in the mathematical formulation becomes essential.

4 What is the effect of placing a flow control at the downstream end of the flood relief channel on the bend flow profiles and allowing the weir effect to be drowned ?

5 For applications other than to rivers, what would be the effect, on the flow profiles, of replacing the broad crested weir by a sharp crested weir ?

In addition, study should also be made of the flow pattern within the meander loop itself both with and without the introduction the cut–off channel. This is essential for determining the parameters that affect the migration rate of meanders in natural rivers and for a greater understanding of one of the most complex problems of river morphology.

BIBLIOGRAPHY

BIBLIOGRAPHY

- ABDULLA, M.A. - 1976
"A laboratory study of the effect of bend geometry on deposition and scour", M.Sc. Thesis, Univ. of Strathclyde, Glasgow

- ACKERS, P. - 1957
"A theoretical consideration of side weir as storm-water overflows", J. Inst. of Civ. Eng., Vol. 6, proc. paper 11, p. 250

- ACKERS,P.,WHITE,W.R.,PERKINS,J.A. and HARRISON,J.M. - 1978
"Weirs and flumes for flow measurements", John Wiley & Sons Ltd., New York N.Y.

- ALLEN, J.R.L. - 1965
"A review of the origin and characteristics of recent alluvial sediments", Sedimentology, Vol. 5, No. 2, p. 89

- ANWER, H.O. - 1986
"Turbulent structure in a river bend", J. Hydr. Eng., ASCE, Vol. 112, No. 8, proc. paper 20811, p. 657

- BAIRD, J.I. - 1984
"The hydraulic characteristics of channels with overbank flood plain flow", Ph.D. Thesis, Univ. of Glasgow, Glasgow

- BAGNOLD, A.R. - 1960
"Some aspects of the shape of river meanders", U.S. Geological Survey, Prof. paper No. 282-E

- BALMFORTH, D.J. and SARGINSON, E.J. - 1977
"Discussion of, Experimental investigation of flow over side weirs, by El-khashab, A.M.M. and Smith, K.V.H., proc. paper 12402, 1976", J. Hydr. Div., ASCE, No. HY8, p. 941

- BALMFORTH, D.J. and SARGINSON, E.J. - 1978
"A comparison of methods of analysis of side weir flow", J. Inst. of Municipal Eng., Vol. 105, No. 10, p. 273

– BALMFORTH, D.J. and SARGINSON, E.J. – 1983
"The effects of curvature in supercritical side weir flow", J. Hydr. Res., Vol. 21, No. 5, p. 333

– BATHURST, J.C., THORNE, C.R. and HEY, R.D. – 1977
"Direct measurements of secondary currents in river bends", Nature, Vol. 269, p.504

– BATHURST, J.C., THORNE, C.R. and HEY, R.D. – 1979
"Secondary flow and shear stress at river bends", J. Hydr. Div., ASCE, Vol. 105, No. HY10, proc. paper 14906, p.1277

– BECK, S. – 1983
"Mathematical modelling of meander interaction", proc. of Inter. Conf. of River Meandering, ASCE, New Orleans, Louisiana, p. 932

– BHOWMIK, N.G. and STALL, J.B. – 1978
"Hydraulics of flow in the Kaskaskia river", proc. Hydr. Div. Speciality Conf. on Verification of mathematical and Physical models in hydraulics enginnering, ASCE, p. 79

– BOUWMEESTER, J. – 1972
"Basic principles for the movement of water in natural and artificial water courses", Internal note, Delft Univ. of Techn., Delft

– BRADSHAW, P. – 1971
"An introduction to turbulence and its measurement", Pergamon Press Ltd., Library of Congress, Cat. card No. 75–152527, Oxford

– BRICE, J.C. – 1983
"Planform properties of meandering rivers", proc. of Inter. Conf. of River Meandering, ASCE, New Orleans, Louisiana, p. 1

– BRITISH STANDARD INSTITUTION BS:1042, BSI – 1981
"Measurements of fluid flow in closed conduits", Section 1.1, "Specification for square– edged orifice plates, nozzles and venturi tubes inserted in circular cross section conduits running full"

– BRITISH STANDARD INSTITUTION BS:1042, BSI – 1984
"Measurements of fluid flow in closed conduits", Section 1.4, "Guide to use of devices specified in sections 1.1 and 1.2"

– BRITISH STANDARD INSTITUTION BS:3680, BSI – 1980
"Methods of measurements of liquid flow in open channels", part 4E, "Free over–fall weirs of finite width (rectangular broad–crested weirs)"

- BRITISH STANDARD INSTITUTION BS:3680, BSI - 1981
"Methods of measurements of liquid flow in open channels", Part 4A, "Weirs and flumes - Thin plate weirs"

- BRITISH STANDARD INSTITUTION BS:3680, BSI - 1986
"Methods of measurements of liquid flow in open channels", part 4B, "Triangular profile weirs"

- CALLANDER, R.C. - 1978
"River meandering", Ann. Rev. of Fluid Mech., Vol. 10, proc. paper 8119, p. 129

- CHACINSKI, T.M. and FRANCIS, J.R.D. - 1952
"Discussion of,on the origin of river meanders, by Werner, P.W.", Trans., Amer. Geophys. Union, Vol. 33, No. 5, p. 771

- CHADWICK, A.J. and MORFETT, J.C. - 1986
"Hydraulics in civil engineering", Allen & Unwin (Publishers) Ltd., London

- CHANG, H.H. - 1983
"Energy expenditure in curved open channels", J. Hydr. Div., ASCE, Vol. 109, No. 7, proc. paper 18096, p. 1012

- CHANG, H.H. - 1984a
"Analysis of river meanders", J. Hydr. Eng., ASCE, Vol. 110, No. 1, proc. paper 18501, p. 37

- CHANG, H.H. - 1984b
"Variation of flow resistance through curved channels", J. Hydr. Eng., ASCE, Vol. 110, No. 12, proc. paper 19348, p. 1772

- CHANG, H.H. - 1985a
"River morphology and thresholds", J. Hydr. Eng., ASCE, Vol. 111, No. 3, proc. paper 19561, p. 503

- CHANG, H.H. - 1985b
"Water and sediment routing through curved channels", J. Hydr. Eng., ASCE, Vol. 111, No. 4, proc. paper 19656, p. 644

- CHAPRA, S.C. and CANALE, R.R. - 1985
"Numerical methods for engineers with personal computer applications", McGraw-Hill Book Co., Inc., New York N.Y.

- CHEN, G. and SHEN, H.W. - 1983
"River curvature-width ratio effect on shear stress", proc. of Inter. Conf. on River Meandering, ASCE, New Orleans, Louisiana, p. 687

– CHIU, C.L. and HSIUNG, D.E. – 1981
"Secondary flow,shear stress and sediment transport", J. Hydr. Div., ASCE, Vol. 107, No. HY7, proc. paper 16365, p. 879

– CHIU, C.L. and LIN, G.F. – 1983
"Computation of 3–D flow and shear in open channels", J. Hydraulic Eng., ASCE, Vol. 109, No. 11, proc. paper 18351, p. 1424

– CHOUDHARY, U.K. and NARASINHAM, S. – 1977
"Flow in 180° open channel rigid boundary bends", J. Hydr. Div., ASCE, Vol. 103, No. HY6, proc. paper 12966, p. 651

– CHOW, V.T. – 1957
"Discussion of, Flood protection of canal by lateral spillways, by Tults (1956), proc. paper 1077", J. Hydr. Div., ASCE, Vol. 83, No. HY2, p. 47

– CHOW, V.T. – 1959
"Open channel hydraulics", McGraw–Hill Book Company, Inc., New York N. Y.

– CRAMP, T.R. – 1939
"Lateral spillway channels", Trans., ASCE, proc. paper 2069, p. 606

– DAMASKINIDOU–GEORGIADOU, A. – 1980
"Investigation of flow in a curved converging channel", Ph.D. Thesis, Univ. of Southampton, England.

– DAMASKINIDOU–GEORGIADOU, A. and SMITH, K.V.H. – 1986
"Flow in curved converging channel", J. Hydr. Eng., ASCE, Vol. 112, No. 6, proc. paper 20671, p. 476

– DE–MARCHI, G. – 1934
"Essay on the performance of lateral weirs", L'Energia Elettrica, Milano, Italy, Vol. 11, No. 11, p. 849

– DE VRIEND, H.J. – 1976
"A mathematical model of steady flow in curved shallow channels", Report No. 76–1, Dept. of Civil Eng., Delft Univ. Techn., Delft

– DE VRIEND, H.J. – 1977
"A mathematical model of steady flow in curved shallow channels", J. Hydr. Res., Vol. 15, No. 1, p. 37

– DE VRIEND, H.J. – 1981
"Velocity distribution in a curved rectangular channels", J. Fluid Mech., Vol. 107, p. 423

- DE VRIEND, H.J. and STRUIKSMA, N. - 1983a
"Flow and bed deformation in river bends", proc. of Inter. Conf. on River Meandering, ASCE, New Orleans, Louisiana, p. 810

- DE VRIEND, H.J. and GELDOF, H.J. - 1983b
"Main flow velocity in short river bends", J. Hydr. Eng., ASCE, Vol. 109, No. 7, proc. paper 18097, p. 991

- DIETRICH, W.E., SMITH, J.D. and DUNNE, T. - 1979
"Flow and sediment transport in a sand bedded meander", J. of Geology, Vol. 87, p. 305

- DOERINGSFELD, H.A. and BARKER, C.L. - 1939
"Pressure-momentum theory applied to the broad-crested weir", Trans., ASCE, proc. paper 2117, p. 934

- EINSTEIN, H.A. and HARDER, J.A. - 1954
"Velocity distribution and the boundary layer at channel bends", Trans., Amer. Geophys. Union, Vol. 35, No. 1, p. 114

- EINSTEIN, H.A. and LI, H. - 1958
"Secondary currents in straight channels", Trans., Amer. Geophys. Union, Vol. 39, No. 6, p. 1085

- EINSTEIN, H.A. and SHEN, H.W. - 1964
"A study on meandering in straight alluvial channels", J. of Geophys. Res., Vol. 69, No. 24, p. 5239

- EL-KHASHAB, A.M.M. - 1975
"Hydraulica of flow over side weirs", Ph.D. Thesis, Univ. of Southampton, England

- EL-KHASHAB, A.M.M. and SMITH, K.V.H. - 1976
"Experimental investigation of flow over side weirs", J. Hydr. Div., ASCE, Vol. 102, No. HY9, proc. paper 12402, p. 1255

- ENGELUND, F. - 1974
"Flow and bed topography in channel bends", J. Hydr. Div., ASCE, Vol. 100, No. HY11, proc. paper 10963, p. 1631

- ERVINE, D.A. and JASEM, H. - 1989
"Flood mechanisms in meandering channels with flood plain flow", Proc. of 23rd Congress of IAHR, ottawa, Canada

- FALCON ASCANIO, M. and KENNEDY, J.F. - 1983
"Flow in alluvial-river curves", J. Fluid Mech., Vol. 133, p. 1

– FARES, Y.R. – 1984
"Three–dimensional wind–driven currents in large closed basins", M.Sc. Thesis, Cairo Univ., Egypt

– FARES, Y.R. – 1989
"Computer program for flow at bend/flood relief channel intersection", Internal Report, Dept. of Civil Eng., Univ. of Glasgow, Scotland

– FARES, Y.R. and HERBERTSON, J.G. – 1990
"Partial cut–off of meander loops – a comparison of mathematical and physical model results", Inter. Conf. on River Flood Hydraulics, Wallingford, England – [under review]

– FISK, H.N. – 1944
"Geological investigation of the alluvial valley of the lower Mississippi river", Mississippi River Commission, Vicksburg, Missi., 78 pp.

– FOX, J.A. and BALL, D.J. – 1968
"The analysis of secondary flow in bends in open channels", J. Inst. of Civ. Eng., Vol. 39, proc. paper 7087, p. 467

– FRANCIS, J.R.D. and ASFARI, A.F. – 1970
"Visualization of spiral motion in curved open channels of large width", Nature, Vol. 225, p. 725

– FRASER, W. – 1954
"The behaviour of side weirs in prismatic rectangular channels", Ph.D. Thesis, Univ. of Glasgow, Glasgow

– FRASER, W. – 1957
"The behaviour of side weirs in prismatic rectangular channels", J. Inst. of Civ. Eng., Vol. 6, proc. paper 14, p. 305

– GAGLIANO, S.M. and HOWARD, P.C. – 1983
"The neck cutoff oxbow lake cycle along the lower mississippi river", proc. of Inter. Conf. of River Meandering, ASCE, New Orleans, Louisiana, p. 147

– HAGER, W.H. – 1983
"Open channel hydraulics of flows with increasing discharge", J. Hydr. Res., Vol. 21, No. 3, p. 177

– HAGER, W.H. – 1984
"An approximate treatment of flow in branches and bends", J. Inst. of Mech. Eng., Vol. 198 C, No. 4, p. 63

- HAGER, W.H. and VOLKART, P.U. - 1986
"Distribution channels", J. Hydr. Eng., ASCE, Vol. 112, No. 10, proc. paper 20966, p. 935

- HAGER, W.H. - 1986
"Lateral outflow over side weirs", J. Hydr. Eng., ASCE, Vol. 113, No. 4, proc. paper 21385, p. 491

- HALL, G.W. - 1962
"Analytical determination of the discharge characteristics of broad crested weirs using boundary layer theory", J. Inst. of Civ. Eng., Vol. 22, proc. paper 6607, p. 177

- HERBERTSON, J.G. and FARES, Y.R. - 1988a
"Characteristics of flow at the intersection of river meanders and flood relief (cut-off) channels", proc. of Inter. Conf. on River Regime, paper E2, Wallingford, Oxfordshire, England, p. 191

- HERBERTSON, J.G. and FARES, Y.R. - 1988b
"The effect of flood relief channels on the flow pattern at channel bends", proc. of Inter. Conf. on Fluvial Hydraulics, Budapest, Hungary, p. 280

- HEY, R.D. and THORNE, C.R. - 1975
"Secondary flows in river channels", Area, Vol. 7, p. 191

- HEY, R.D. and THORNE, C.R. - 1976
"Discussion of, Secondary flows in river channels", Area, Vol. 8, p. 234

- HUGHES, W.F. and BRIGHTON, J.A. - 1967
"Theory and problems of fluid dynamics", Schaum's Outline Series, McGraw - Hill Book Co., New York N.Y.

- HUSSEIN, A.S.A. - 1984
"Curved guide wall sediment excluder", Ph.D. Thesis, Univ. of Southampton , England

- HUSSEIN, A.S.A. and SMITH, K.V.H. - 1986
"Flow and bed deviation angle in curved open channels", J. Hydr. Res., Vol. 24, No. 2, p. 93

- IKEDA, S. and NISHIMURA, T. - 1985
"Bed topography in bends of sand-silt rivers", J. Hydr. Eng., ASCE, Vol. 111, No. 11, proc. paper 20133, p. 1397

- IKEDA, S. and NISHIMURA, T. - 1986
"Flow and bed profile in meandering sand-silt rivers", J. Hydr. Eng., ASCE, Vol. 112, No. 7, proc. paper 20716, p. 562

– IPPEN, A.T. and DRINKER, P.A. – 1962
"Boundary shear stresses in curved trapizoidal channels", J. Hydr. Div., ASCE, Vol. 88, No. HY5, proc. paper 3273, p. 143

– JOBSON, H.E. and SAYRE, W.W. – 1970
"Vertical transfer in open channel flow", J. Hydr. Div., ASCE, Vol. 96, No. HY3, proc. paper 7148, p. 703

– JANSEN, P.Ph., BENDEGOM, L.V., BERG, J.V.D., VRIES ,M.D. and ZANEN, A. – 1979
"Principles of river engineering, the non–tidal alluvial river", Pitman Publishing Ltd., london

– JULIEN, P.Y. and THORNE, C.R. – 1984
"Discussion of, Flow and bed topography in alluvial channel bend", J. Hydr. Eng., ASCE, Vol. 110, p. 1031

– KALKWIJK, J.P.TH. and DE VRIEND, H.J. – 1980
"Computation of the flow in shallow river bends", J. Hydr. Res., Vol. 18, No. 4, p. 327

– KENNEDY, J.F., NAKATO, T. and ODGAARD, A.J. – 1983
"Analysis, numerical modelling and experimental investigation of flow in river bends", proc. of Inter. Conf. on River Meandering, ASCE, New Orleans, Louisiana, p. 843

– KHALID, S.A. – 1964
"Flow dynamics in trapezoidal open channel bends", Ph.D. Thesis, Colorado State Univ., Colorado, USA

– KIKKAWA, H., IKEDA, S. and KITAGAWA, A. – 1976
"Flow and bed topography in curved open channels", J. Hydr. Div., ASCE, Vol. 102, No. HY9, proc. paper 12416, p. 1327

– KLAASSEN, J.G. and VAN ZANTEN, B.H.J. – 1989
"On cut–off ratios of curved channels", proc. of 23rd Congress of IAHR, Ottawa, Canada

– KONDRAT'EV, N.E., LYAPIN, A.N., POPOV, I.V., PIN'KOVSKII, S.I., FEDOROV, N.N. and YAKUNIN, I.N. – 1959
"River flow and river channel formation", National Scientific Foundation, Washington DC, USA

– KUMAR, K.L. – 1976
"Engineering fluid mechanics", Eurasia Publishing Ltd., Ram Nagar, New Delhi – 110055

- LEEDER, M.R. and BRIDGES, P.H. - 1975
"Flow separation in meander bends", Nature, Vol. 253, p. 338

- LEOPOLD, L.B. and WOLMAN, M.G. - 1960
"River meanders", Bull. of Geolog. Soc. of Amer., Vol. 71, p. 769

- LEOPOLD, L.B. and LANGBEIN, W.B. - 1966
"River meanders", Scientific American, Vol. 214, No. 6, p. 60

- LESCHZINER, M.A. and RODI, W. - 1979
"Calculation of strongly curved open channel flow", J. Hydr. Div., ASCE, Vol. 105, No. HY10, proc. paper 14927, p. 1297

- MAKKAVEEV, V.M. - 1933
"Concerning stream flows in channels and general equations of turbulent flow of fluids", Proc. of 4th Hydrological Conf. of Baltic States, Report No. 91

- MOCKMORE, C.A. - 1943
"Flow around bends in stable channels", Trans., ASCE, proc. paper 2217, p. 593

- NIMMO, W.H.R. - 1927
"Side spillways for regulating diversion canals", Trans., ASCE, proc. paper 1694, p. 1561

- NOUH, M.A. and TOWNSEND, R.D. - 1979
"Shear-stress distribution in stable channel bends", J. Hydr. Div., ASCE, Vol. 105, No. HY10, proc. paper 14898, p. 1233

- ODGAARD, A.J. - 1981
"Transverse bed slope in alluvial channel bends", J. Hydr. Div., ASCE, Vol. 107, No. HY12, proc. paper 16750, p. 1677

- ODGAARD, A.J. - 1982
"Bed characteristics in alluvial channel bends", J. Hydr. Div., ASCE, Vol. 108, No. HY11, proc. paper 17452, p. 1268

- ODGAARD, A.J. - 1984
"Flow and bed topography in alluvial channel bend", J. Hydr. Eng., ASCE, Vol. 110, No. 4, proc. paper 18748, p. 512

- ONISHI, Y., JAIN, S.C. and KENNEDY, J.F. - 1976
"Effects of meandering in alluvial streams", J. Hydr. Div., ASCE, Vol. 102, No. HY7, proc. paper 12248, p. 899

– PACHECO– CEBALLOS, R. – 1983
"Energy losses and shear stresses in channel bends", J. Hydr. Eng., ASCE, Vol. 109, No. 6, proc. paper 18051, p. 881

– PRANDTL, L. – 1952
"Essentials of fluid dynamics", First Edition, Blackie, London, England

– PRASAD, R. – 1970
"Numerical method of computing flow profiles", J. Hydr. Div., ASCE, Vol. 96, No. HY1, proc. paper 7005, p. 75

– PRICE, R.K. – 1977
"A mathematical model for river flow – Theoretical development", Report No. INT 127, Hydraulic Research Station, Wallingford, England

– RAMAMURTHY, A.S. and SATISH, M.G. – 1988
"Division of flow in short open channel branches", J. Hydr. Eng., ASCE, Vol. 114, No. 4, proc. paper 22384, p. 428

– RANGA RAJU, K.G., PRASAD, B. and GUPTA, S.K. – 1979
"Side weirs in rectangular channel", J. Hydr. Div., ASCE, Vol. 105, No. HY5, proc. paper 14596, p. 547

– ROZOVSKII, I.L. – 1961
"Flow of water in bends of open channels", Acad. of Science of Ukra. USSR , Keiv , 1957, available from the office of techn. services, US Dept. of Commerce, PST Cat.No. 363

– SALLEH, M.N.B. – 1985
"Numerical and experimental investigations of flow around bend in open channels", Ph.D. Thesis, Univ. of Strathclyde, Glasgow

– SARMAH, S.B. – 1977
"Studies of bed topography in a 45° bend channel", M.Sc. Thesis, Univ. of Strathclyde, Glasgow

– SHEN, H.W. – 1971
"River mechanics", printed in U.S.A. by the editor, P.O. Box 606, Fort Collins, USA 80521

– SHUKRY, A. – 1949
"Flow around bends in an open channel flume", Trans., ASCE, Vol. 115, proc. paper 2411, p. 751

- SHUKRY, A. - 1963
"Discussion of, Boundary shear stresses in curved trapezoidal channel, by Ippen, A.T. and Drinker, P.A., 1962, proc. paper 3273", J. Hydr. Div., ASCE, No. HY3, p.333

- SIEGENTHALER, M.C. and SHEN, H.W. - 1983
"Shear stress uncertainties in bends from equations", proc. of Inter. Conf. on River Meandering, ASCE, New Orleans, Louisiana, p. 662

- SIMONS, D.B. - 1971
"River and canal morphology", From SHEN, H.W., "River mechanics", Chapter 20, Published by the editor, Colorado, USA, 60 pp.

- SMITH, K.V.H. - 1973
"Computer programming for flow over side weirs", J. Hydr. Div., ASCE, Vol. 99, No. HY3, proc. paper 9626, p. 495

- SMITH, K.V.H. - 1974
"Closure of discussion of, Computer programming for flow over side weirs", J. Hydr. Div., ASCE, No. HY1, p. 1722

- SOLIMAN, M.M. and TINNEY, E.R. - 1968
"Flow around 180° bends in open rectangular channels", J. Hydr. Div., ASCE, Vol. 94, No. HY4, proc. paper 6027, p. 893

- SPYRATOS, G. - 1981
"A numerical model for flow velocities in a 90° channel bend", M.Sc. Thesis, Univ. of Strathclyde , Glasgow

- STEFFLER, P.M., RAJARATNAM,N. and PETERSON, A.W. - 1985
"Water surface at change of channel curvature", J. Hydr. Eng., ASCE, Vol. 111, No. 5, proc. paper 19697 , p. 866

- SUBRAMANYA, K. and AWASTHY, S.C. - 1972
"Spatially varied flow over side-weirs", J. Hydr. Div., ASCE, Vol. 98, No. HY1, proc. paper 8627, p. 1

- TAMAI, N. and MOHAMED, A.A. - 1983a
"Experimental study on the development of depth-averaged flow in rectangular continuous bends", proc. of the 27th meeting of Japaneese Hydr. Eng., JSCE, p. 85

- TAMAI, N. , IKEUCHI, K. and MOHAMED, A.A. - 1983b
"Evolution of depth-averaged flow fields in meandering channels", proc. of Inter. Conf. on River Meandering, ASCE, New Orleans, Louisiana, p. 964

- TAMAI,N.,IKEUCHI,K.,YAMAZAKI,A. and MOHAMED,A.A. - 1983c
"Experimental analysis on the open channel flow in rectangular continuous bends", J. of Hydroscience and Hydraulic Eng., Vol. 1, No. 2, p. 17

- TAYLOR, E.H. - 1942
"Flow charateristics at rectangular open-channel junctions", Trans., ASCE, proc. paper 2223, p. 893

- THOMSON, J. - 1876
"On the origin of winding of rivers in alluvial plains with remarks on the flow of water around bends in pipes", Proc. Royal Soc., london, Series A, Vol. 25, p. 5

- THORN, R.B. - 1966
"River engineering and water conservation works", Butterworths & Co. (Publishers) Ltd., London

- THORNE, C.R. and HEY, R.D. - 1979
"Direct measurements of secondary currents at river inflexion point", Nature, Vol. 280, p. 226

- THORNE,C.R. and RAIS,S. - 1983
"Secondary current measurements in a meander river", proc. of Inter. Conf. on River Meandering , ASCE, New Orleans, Louisiana, p. 675

- TULTS, H. - 1956
"Flood protection of canals by lateral spillways", J. Hydr. Div., ASCE, Vol. 82, No. HY5, proc. paper 1077, p. 1077-1

- UYUMAZ, A. and MUSLU, Y. - 1985
"Flow over side weirs in circular channels", J. Hydr. Eng., ASCE, Vol. 111, No. 1, proc. paper 19414, p. 144

- VARSHNEY, D.V. and GRADE, R.J. - 1975
"Shear distribution in bends in rectangular channels", J. Hydr. Div., ASCE, Vol. 101, No. HY8, proc. paper 11513, p. 1053

- VYGODSKY, M. - 1971
"Mathematical handbook, higher mathematics", MIR Publishers, Moscow

- WEBBER, N.B. and GREATED, C.A. - 1966
"An investigation of flow behaviour at the junction of rectangular channels", J. Inst. of Civ. Eng., proc. paper 6901, p. 321

- WILSON, I.G. - 1973
"Equilibrium cross-section of meandering and braided rivers", Nature , Vol. 241 , p. 393

– WINKLEY, B.R. – 1971
"Practical aspects of river regulation and control", From SHEN, H.W., "River mechanics", Chapter 19, Published by the editor, Colorado, USA, 78 pp

– YEN, B.C. – 1971
"Spatially varied open–channel flow equations", Techn. Report, Dept. of Interior, Washington D.C.

– YEN, B.C. – 1975
"Further study on open–channel flow equations", Report No. SFB 80/T/49, Univ. of Illinois, Illinois, USA

– YEN, B.C. and WENZEL, H.G. – 1970
"Dynamic equation for steady spatially varied flow", J. Hydr. Div., ASCE, Vol. 96, No. HY3, proc. paper 7179, p. 801

– YEN, C.L. – 1970
"Bed topography effect on flow in a meander", J. Hydr. Div., ASCE, Vol. 96, No. HY1, proc. paper 7003, p. 57

– YEN, C.L. and YEN, B.C. – 1971
"Water surface configuration in channel bends", J. Hydr. Div., ASCE, Vol. 97, No. HY2, proc. paper 7928, p. 303

– ZIMMERMANN, C. and KENNEDY, J.F. – 1978
"Transverse bed slopes in curved alluvial streams", J. Hydr. Div., ASCE, Vol. 104, No. HY1, proc. paper 13482, p. 33

APPENDICES

APPENDIX (A)

PUBLICATIONS

– HERBERTSON, J.G. and FARES, Y.R. – 1988a

" Characteristics of Flow at the Intersection of River Meanders and Flood Relief (Cut–Off) Channels ", Proceedings of the International Conference on **RIVER REGIME**, paper E2 , IAHR, Wallingford, Oxfordshire, England, UK, p. 191

– HERBERTSON, J.G. and FARES, Y.R. – 1988b

" The Effect of Flood Relief Channels on the Flow Pattern at Channel Bends ", Proceeding of the International Conference on **FLUVIAL HYDRAULICS**, IAHR, Budapest, Hungary, p. 280

– FARES, Y.R. – 1989

" Computer Program for Flow at Bend / Flood Relief Channel Intersection ", Internal Report, Department of Civil Engineering, University of Glasgow, Glasgow, Scotland, UK

– FARES, Y.R. and HERBERTSON, J.G. – 1990

" Partial Cut–off of Meander Loops – A Comparison of Mathematical and Physical Model Results ", International Conference on **RIVER FLOOD HYDRAULICS**, IAHR, Wallingford, England [under review]

APPENDIX (B)

DETERMINATION OF THE INTEGRATION FUNCTIONS FOR THE RADIAL VELOCITIES

In this Appendix, the analytical solution of the mathematical integration functions $\Phi_1(\lambda)$ and $\Phi_2(\lambda)$ that are involved in determining the vertical profile of the radial component of the current $u_r(\lambda)$ is given. The solution is obtained by the use of the theory of power series (see Vygodsky (1971)). The absolute order of magnitude of the error that results from neglecting the higher order terms in the analysis of both functions is found to be $\leq 10^{-5}$.

Refering to equations (3.61) and (3.62), section (3.5.2), Chapter III, the integration functions $\Phi_1(\lambda)$ and $\Phi_2(\lambda)$ read:

$$\Phi_1(\lambda) = \int \lambda^{-1} + (1-\lambda)^{-1} \ln \lambda \quad d\lambda \qquad (3.61)$$

and

$$\Phi_2(\lambda) = - \int[\ln \lambda (1-\lambda)^{-1} (\ln \lambda - 2\lambda) - (2/\lambda)] \, d\lambda \qquad (3.62)$$

The boundary condition which applies to these functions is

$$_0\int^1 \Phi_1(\lambda) \quad d\lambda = {}_0\int^1 \Phi_2(\lambda) \quad d\lambda = 0 \qquad (3.63)$$

(B.1) Solution of Integration Function $\Phi_1(\lambda)$

The function $\Phi_1(\lambda)$ can be divided into two sub-functions $\Phi_{1\,1}(\lambda)$ and $\Phi_{1\,2}(\lambda)$

as follows:

$$\Phi_{11}(\lambda) = \int \lambda^{-1} \, d\lambda \qquad \text{(B-1)}$$

and $$\Phi_{12}(\lambda) = \int (1-\lambda)^{-1} \ln \lambda \, d\lambda \qquad \text{(B-2)}$$

with the boundary condition of:

$$_0\int^1 \Phi_{11}(\lambda) \, d\lambda = {}_0\int^1 \Phi_{12}(\lambda) \, d\lambda = 0 \qquad \text{(B-3)}$$

The first sub-function $\Phi_{11}(\lambda)$ may be expressed as:

$$\Phi_{11}(\lambda) = \ln \lambda + \hbar_1 \qquad \text{(B-4)}$$

where $\hbar_1$ is the integration constant which can be obtained by applying the boundary condition, expressed in equation (B-3), as:

$$_0\int^1 \Phi_{11}(\lambda) \, d\lambda = \lambda (\ln \lambda - 1 + \hbar_1) = 0 \qquad \text{(B-5)}$$

which gives

$$\hbar_1 = 1 \qquad \text{(B-6)}$$

Then the solution of $\Phi_{11}(\lambda)$ becomes:

$$\Phi_{11}(\lambda) = \ln \lambda + 1 \qquad \text{(B-7)}$$

The solution of the second sub-function $\Phi_{12}(\lambda)$ can be obtained through the integration process of an alternative variable λ which is related to the original variable λ by:

$$\lambda = 1 - \lambda \qquad \text{and} \qquad d\lambda = -d\lambda \qquad \text{(B-8)}$$

By introducing the variable λ to equation (B−2), it will read:

$$\Phi_{1\,2}(\lambda) = - \int \lambda^{-1} \ln (1-\lambda) \; d\lambda \qquad \text{(B−9)}$$

Applying power series theory to the logarithmic expression in equation (B−9), it will read:

$$\ln (1-\lambda) = - \lambda - \lambda^2/2 - \lambda^3/3 - \lambda^4/4 - \ldots\ldots \quad \text{for} \quad 0 < |\lambda| \leq 1$$

$$= - \sum_i \lambda^i/i \qquad \text{for} \quad 0 < |\lambda| \leq 1 \qquad \text{(B−10)}$$

Substitution of the expansion expressed in equation (B−10) into equation (B−9) will give after integration:

$$\Phi_{1\,2}(\lambda) = \sum_i \lambda^i/i^2 + \hbar_2 \qquad \text{for} \quad 0 < |\lambda| \leq 1 \qquad \text{(B−11)}$$

where $\hbar_2$ is the constant that results form the integration process. This constant can be obtained from the boundary condition stated in equation (B−3) as:

$$_0\int^1 \Phi_{1\,2}(\lambda) \; d\lambda = [\, \sum_i \lambda^{i+1}/\{i^2 \, (i+1)\} \,] + \hbar_2 = 0 \qquad \text{(B−12)}$$

The value of the integration constant $\hbar_2$, according to equation (B−12) is found to be:

$$\hbar_2 \simeq - .645 \qquad \text{(B−13)}$$

Substituting the value of $\hbar_2$ into equation (B−11) and introducing the original variable λ to the equation, the solution of the sub−function $\Phi_{1\,2}(\lambda)$ can be written

in the form:

$$\Phi_{12}(\lambda) = \sum_i (1-\lambda)^i/i^2 \quad - .645 \qquad \text{(B-14)}$$

By combining the solutions of $\Phi_{11}(\lambda)$ and $\Phi_{12}(\lambda)$, obtained from equations (B-7) and (B-14) respectively, the general solution of the integration function $\Phi_1(\lambda)$ can be determined; it is:

$$\Phi_1(\lambda) = .355 + \ln \lambda + \sum_i (1-\lambda)^i/i^2 \qquad \text{for } 0 < |\lambda| \leq 1 \qquad \text{(B-15)}$$

(B.2) Solution of Integration Function $\Phi_2(\lambda)$

The integration function $\Phi_2(\lambda)$ can be divided into sub-functions in a similar manner to that described in the foregoing section:

$$\Phi_2(\lambda) = 2\,\Phi_1(\lambda) + \Phi_{21}(\lambda) \qquad \text{(B-16)}$$

where

$$\Phi_{21}(\lambda) = - \int (1-\lambda)^{-1} \ln^2 \lambda \; d\lambda \qquad \text{(B-17)}$$

The sub-function $\Phi_{21}(\lambda)$ can be treated in the same way as described previously in the case of $\Phi_{12}(\lambda)$. After introducing the variable λ to equation (B-17), it will read:

$$\Phi_{21}(\lambda) = \int \lambda^{-1} \ln (1-\lambda) \; d\lambda \qquad \text{(B-18)}$$

Using the logarithmic expansion for the expression $\ln (1-\lambda)$, as given in equation (B-10), the integrad $\lambda^{-1} \ln (1-\lambda)$, after some re-arrangement will give the form:

$$\lambda^{-1} \ln (1-\lambda) = \lambda (1 + \lambda) + A_\lambda + B_\lambda \qquad \text{(B-19)}$$

where

$$A_\lambda = \sum_i \lambda^{i-1} [(1/I_i) + 2 E_i] \qquad \text{for } i = 4,6,8,10,..... \qquad \text{(B-20)}$$

$$B_\lambda = 2 \sum_i \lambda^{i-1} [(1/J_i) + F_i] \qquad \text{for } i = 5,7,9,11..... \qquad \text{(B-21)}$$

with

$$\begin{aligned} I_i &= i && \text{for } i = 4 \\ &= 1.5\ i && \text{for } i = 6 \\ &= 2\ i && \text{for } i = 8 \\ &= 2.5\ i && \text{for } i = 10 \quad .....\text{etc} \end{aligned} \qquad \text{(B-22)}$$

$$\begin{aligned} E_i &= [1/(I_i-1)] && \text{for } i = 4 \\ &= [1/(I_i-1) + 1/(I_i-4)] && \text{for } i = 6 \\ &= [1/(I_i-1) + 1/(I_i-4) + 1/(I_i-9)] && \text{for } i = 8 \\ &= [1/(I_i-1) + 1/(I_i-4) + 1/(I_i-9) + 1/(I_i-16)] && \text{for } i = 10 \\ & && .....\text{etc} \end{aligned} \qquad \text{(B-23)}$$

$$J_i = (i^2 - 1)/4 \qquad \text{for } i = 5,7,9,11,.....\text{etc} \qquad \text{(B-24)}$$

$$\begin{aligned} F_i &= 1/(J_i-2) && \text{for } i = 5 \\ &= [1/(J_i-2) + 1/(J_i-6)] && \text{for } i = 7 \\ &= [1/(J_i-2) + 1/(J_i-6) + 1/(J_i-12)] && \text{for } i = 9 \\ &= [1/(J_i-2) + 1/(J_i-6) + 1/(J_i-12) + 1/(J_i-20)] && \text{for } i = 11 \\ & && .....\text{etc} \end{aligned} \qquad \text{(B-25)}$$

Then, the integration of $\Phi_{21}(\lambda)$ from equation (B−18), with the use of equation (B−19), will give

$$\Phi_{21}(\lambda) = \lambda^2/2 + \lambda^3/3 + \sum_i (\lambda^i/i)\,[(1/I_i) + 2\,E_i]$$

$$+ 2\sum_i (\lambda^i/i)\,[(1/J_i) + F_i] + \hbar_3 \qquad \text{(B−26)}$$

The integration constant $\hbar_3$ can be determined from the boundary condition:

$$\int_0^1 \Phi_{21}(\lambda)\,d\lambda = 0$$

$$= \lambda^3/6 + \lambda^4/12 + \sum_i [\lambda^{i+1}/\{i(i+1)\}]\,[(1/I_i) + 2\,E_i]$$

$$+ 2\sum_i [\lambda^{i+1}/\{i(i+1)\}]\,[(1/J_i) + F_i] + \hbar_3 \qquad \text{(B−27)}$$

The solution is:

$$\hbar_3 \simeq -.384 \qquad \text{(B−28)}$$

By substituting the value of $\hbar_3$ into equation (B−26) and returning to equation (B−16), the general solution of the function $\Phi_2(\lambda)$ can be obtained. After reverting to the original variable λ , the solution reads:

$$\Phi_2(\lambda) = -.384 + 2\,\Phi_1(\lambda) + (1-\lambda)^2/2 + (1-\lambda)^3/3$$

$$+ A_\lambda + B_\lambda \qquad \text{for } 0 < |\lambda| \leq 1 \qquad \text{(B−29)}$$

where

$$A_\lambda = \sum_i [(1-\lambda)^i/i] [(1/I_i) + 2 E_i] \qquad \text{for } i = 4,6,8,10,.....$$

(B-30)

and

$$B_\lambda = 2 \sum_i [(1-\lambda)^i/i)] [(1/J_i) + F_i] \qquad \text{for } i = 5,7,9,11,....$$

(B-31)

APPENDIX (C)

DETERMINATION OF THE SECONDARY FLOW CONVECTION FACTOR

In this Appendix, an expression for the secondary flow convection factor γ , which simulates the radial momentum exchange in the formulation of the horizontal problem, section (3.7), Chapter III, is given. The determination of γ depends essentially on the vertical distributions of the integration functions $\Phi_1(\lambda)$ and $\Phi_2(\lambda)$ (refer to Appendix (B) for the analytical solutions of these functions).

By considering the basic equation of the depth–averaged model, equation (3.108), section (3.7), namely:

$$\partial_s \Psi_1 + (1/r^2)\ \partial_r(r^2\ \Psi_2) = g\ S_s\ h - u_*^2 \qquad (3.108)$$

This equation gives the equilibrium condition between the main and secondary convection terms of the inertia force (on the left hand side of the equation), and the pressure gradient and friction forces (on the right hand side). Apart from the secondary convection term " $(1/r^2)\ \partial_r(r^2\ \Psi_2)$ " , all other terms are already determined. The variable Ψ_2 is a function of h , u_m , r and γ . It is expressed in equation (3.117), section (3.7), as:

$$\Psi_2 = (u_m^2\ h^2/r)\ \gamma \qquad (3.117)$$

The secondary convection factor γ which was expressed implicitly through equation (3.112), section (3.7), can be written in an explicit form as:

$$\gamma = \zeta^2 C'^2 [\xi^2 - \beta - (\xi/\zeta^2) \Phi_3 + \zeta \Phi_4 - 2 (\xi/\zeta) \Phi_5 + (1/\zeta^2) \Phi_6] \qquad (C-1)$$

where

$$\Phi_3 = {}_0\int^1 \Phi_1(\lambda) \, d\lambda = 0 \qquad (3.113)$$

$$\Phi_4 = {}_0\int^1 \Phi_2(\lambda) \, d\lambda = 0 \qquad (3.114)$$

$$\Phi_5 = {}_0\int^1 (\ln \lambda + 1) \Phi_1(\lambda) \, d\lambda \qquad (3.115)$$

$$\Phi_6 = {}_0\int^1 (\ln \lambda + 1) \Phi_2(\lambda) \, d\lambda \qquad (3.116)$$

with $\zeta = 1/(KC')$, $\beta = 1 + \zeta^2$, $\xi = 1 + \zeta$

where K is the Von–Karman constant, C' is the non–dimensional Chezy coefficient and β is the momentum flux correction factor. The solution of the integrals Φ_3 and Φ_4 is essentially zero as their integration limits match those of the boundary condition required for the solution of the integration functions $\Phi_1(\lambda)$ and $\Phi_2(\lambda)$ (see equation (3.63), section (3.5.2), Chapter III and also Appendix (B)). Hence, equation (C–1) will reduce to:

$$\gamma = \zeta^2 C'^2 [\xi^2 - \beta - 2 (\xi/\zeta) \Phi_5 + (1/\zeta^2) \Phi_6] \qquad (C-2)$$

The solution of Φ_5 and Φ_6 will then lead to the determination of the factor γ as well as the variable Ψ_2 .

(C.1) Determination of Integral Φ_5

By introducing the solution of the function $\Phi_1(\lambda)$ from equation (B−15), Appendix (B), to equation (3.115), the integral Φ_5 becomes:

$$\Phi_5 = \Phi_{51} + \Phi_{52} + \Phi_{53} \qquad (C-3)$$

where

$$\Phi_{51} = .355 \; {}_0\int^1 (\ln \lambda + 1) \; d\lambda \qquad (C-4)$$

$$\Phi_{52} = {}_0\int^1 (\ln \lambda + 1) \ln \lambda \; d\lambda \qquad (C-5)$$

$$\Phi_{53} = {}_0\int^1 (\ln \lambda + 1) \left[\sum_i (1-\lambda)^i / i^2 \right] d\lambda \qquad (C-6)$$

Solution of the integral Φ_{51} may be obtained as:

$$\Phi_{51} = .355 \; \lambda \ln \lambda$$

$$= 0 \quad \text{by applying the integration limits} \qquad (C-7)$$

Similarly, solution of Φ_{53} can be written as:

$$\Phi_{52} = \lambda (\ln^2 \lambda + 1)$$

$$= 1 \quad \text{by applying the integration limits} \qquad (C-8)$$

With respect to the last sub−integral Φ_{53} , it can be divided into:

$$\Phi_{53} = {}_0\int^1 \sum_i (1-\lambda)^i / i^2 \; d\lambda + {}_0\int^1 \ln \lambda \left[\sum_i (1-\lambda)^i / i^2 \right] d\lambda \qquad (C-9)$$

But since (from Vygodsky (1971)):

$$\int \lambda^i \ln \lambda \, d\lambda = \lambda^{i+1} [\{\ln \lambda/(i+1)\} - \{1/(i+1)^2\}] \qquad \text{for } |i| \geq 1 \qquad (C-10)$$

Then, by the use of equation (C−10), a solution for Φ_{53} may be obtained. After slight re−arrangement, the integration of equation (C−9) reads:

$$\Phi_{53} = \sum_i [(1-\lambda)^{i+1}/\{i^2 (i+1)\}][\ln (1-\lambda) - \{1/(i+1)\}] + \sum_i [(1-\lambda)^{i+1}/\{i^2 (i+1)\}] \qquad \text{for } |i| \geq 1 \qquad (C-11)$$

After applying the integration limits, the value of Φ_{53} becomes:

$$\Phi_{53} \simeq - .409 \qquad (C-12)$$

The absolute order of magnitude of the error involved in the integration process, that results from ignoring the higher order terms of the expansions, is found to be $\leq 10^{-4}$.

Combination of equations (C−7), (C−8) and (C−12) can bring about the final solution of the integral Φ_5 ; it is:

$$\Phi_5 \simeq .591 \qquad (C-13)$$

(C.2) Determination of Integral Φ_6

Refering to equation (3.116), with the aid of the distribution of $\Phi_2(\lambda)$ from equation (B−29), Appendix (B), the integral Φ_6 can also be solved through the division to sub−integrals as:

$$\Phi_6 = \Phi_{61} + \Phi_{62} + \Phi_{63} + \Phi_{64} \qquad (C-14)$$

where

$$\Phi_{61} = 2\ \Phi_5 \qquad (C-15)$$

$$\Phi_{62} = -\ .384\ {}_0\int^1 (\ln \lambda + 1)\ d\lambda \qquad (C-16)$$

$$\Phi_{63} = {}_0\int^1 (\ln \lambda + 1)\ [(1-\lambda)^2/2 + (1-\lambda)^3/3]\ d\lambda \qquad (C-17)$$

$$\Phi_{64} = {}_0\int^1 (\ln \lambda + 1)\ [\ A_\lambda + B_\lambda\ ]\ d\lambda \qquad (C-18)$$

where A_λ and B_λ are power expansions for the integration function $\Phi_2(\lambda)$ and defined in equations (B−30) and (B−31) respectively, Appendix (B).

The solution of the first two sub−integrals can be determined at once; their solution is:

$$\Phi_{61} = 1.182 \quad \text{and} \quad \Phi_{62} = 0 \qquad (C-19)$$

With respect to the sub−integral Φ_{63} , a solution can be obtained by employing the integration law expressed in equation (C–10), as:

$$\Phi_{63} = {}_0\int^1 [\ 5/6 - 2\ \lambda + 3/2\ \lambda^2 - \lambda^3/3\ ]\ (\ln \lambda + 1)\ d\lambda$$

$$= -\ .229 \qquad (C-20)$$

Finally, the determination of the last sub−integral Φ_{64} can be obtained by substituting the distributions of the power expansions A_λ and B_λ as given in Appendix (B). Then by using the integration law expressed in equation (C−10), a solution for Φ_{64} may be obtained. Refering to equation (C−18), it may be

re— written as:

$$\Phi_{64} = {}_0\int^1 (A_\lambda + B_\lambda) + \ln \lambda \, (A_\lambda + B_\lambda)$$

$$= \sum_i [(1-\lambda)^{i+1}/\{i(i+1)\}] \, [(1/I_i) + 2\, E_i] +$$

$$2 \sum_i [(1-\lambda)^{i+1}/\{i(i+1)\}] \, [(1/J_i) + F_i] +$$

$${}_0\int^1 \ln \lambda \sum_i [(1-\lambda)^i/i] \, [(1/I_i) + 2\, E_i] \, d\lambda +$$

$$2 \, {}_0\int^1 \ln \lambda \sum_i [(1-\lambda)^i/i] \, [(1/J_i) + F_i] \, d\lambda \qquad (C-21)$$

where the power expansions I_i , J_i , E_i and F_i are defined previously in Appendix (B). By the use of equation (C— 10), the solution of equation (C— 21) can be obtained; it reads:

$$\Phi_{64} \simeq - \ .209 \qquad (C-22)$$

The absolute order of magnitude of the error involved in the integration process is again found to be $\leq 10^{-4}$. By combining the solutions of the different sub— integrals Φ_{61} , Φ_{62} , Φ_{63} and Φ_{64} , the value of the integral Φ_6 can finally be given, it is:

$$\Phi_6 = .744 \qquad (C-23)$$

Based upon the above— described analytical solutions for the integrals Φ_5 and Φ_6 , the expression for the secondary flow convection factor can be determined. This expression reads:

$$\gamma = \zeta^2 \, C'^2 \, [\, \xi^2 - \beta - 1.182 \, (\xi/\zeta) + .744/\zeta^2] \qquad (C-24)$$

APPENDIX (D)

COMPUTER PROGRAM

Given in this Appendix are the computational procedures developed for the study of the flow characteristics in a gentle wide channel bend with (as formulated in Chapter IV) and without the introduction of the flood relief channel (as formulated in Chapter III). The computer program consists of 11 subroutines. These subroutines are:

- DATA
- MASO1
- MASO2
- SECCRT
- GRODEC
- BENENT
- HORDIS
- VERDIS
- FLOREL
- BENFLO
- VEDIFL

Subroutine DATA is required for preparing the flow and physical channel parameters for use in subsequent computations.

Subroutines **MASO1** and **MASO2** are used for solving the integration functions $\Phi_1(\lambda)$ and $\Phi_2(\lambda)$ in cases of rough and smooth channel beds respectively.

Subroutines **SECCRT, GRODEC, BENENT, HORDIS** and **VERDIS** are used for simulating the spatial structure of the flow in the case of a channel bend alone.

Subroutines **FLOREL, BENFLO** and **VEDIFL** are used for modelling the intersection effect on the characteristics of the flow in the channel bend. While **FLOREL** and **BENFLO** simulates the effect on the horizontal problem, **VEDIFL** gives the effect on the vertical distribution of the longitudinal velocities.

Table (D.1) gives the classification and detailed objectives of the different subroutines, while Fig.(D.1) shows a schematic representation of the computational procedure involving the subroutines.

Figures (D.2) and (D.3) show the finite difference schemes, grid systems and zones of validity for the computational procedures of the different subroutines. Fig.(D.2) is for the case of a channel bend alone and Fig.(D.3) is for the case of a bend with the introduction of a flood relief channel.

Fig.(D.4) gives the computational procedure within each subroutine in the form of flow charts. A listing of the FORTRAN program is reported elsewhere (see Fares (1989)).

TABLE (D.1) – Classification of the Different Program Subroutines

Subroutine	Function
– DATA	for preparation of the required data for the computational procedure i.e. channel bend geometry and flow conditions.
– MASO1	for solving the integration functions $\Phi_1(\lambda)$ and $\Phi_2(\lambda)$ that are involved in predicting the distribution of the radial velocity component $u_r(\lambda)$ for the case of a channel bend with a rough bed.
– MASO2	same function as for MASO1 but for the case of a channel bend with a smooth bed.
– SECCRT	for predicting the vertical distribution of the radial velocity component $u_r(\lambda)$.
– GRODEC	separate subroutine for determining the decay and the growth of $u_r(\lambda)$. The limit angle Θ_{lim} at which $u_r(\lambda)$ is fully developed is determined. The profile of the growth and decay of $u_r(\lambda)$ is also obtained.

- BENENT — for predicting the redistribution of the depth–averaged velocity u_m at the bend entrance.

- HORDIS — for solving the horizontal problem of the flow along the channel bend i.e. for determining the horizontal variation of u_m and h .

- VERDIS — for determining the redistribution of the longitudinal velocities $u_s(\lambda)$ along the bend. This is obtained by the determination of the vertical velocities $u_z(\lambda)$. The spatial structure of the current is then obtained as are the local horizontal resultant velocities and local deviation angles.

- FLOREL — for predicting the effect of the flood relief channel on the horizontal variations of the flow i.e. effect on u_m and h. The procedure is based on dividing the bend cross section into a series of concentric strips and calculating the flow taken by the flood channel from each strip. The assumption of constant energy for each bend strip is employed along the intersection for cases of subcritical flows.

- BENFLO — for calculating the magnitude of the flow components at the node points of the finite difference scheme from the components for each radial strip calculated using FLOREL. The calculations are made using the mean value theorem for each node between two successive radial strips in the channel bend.

- VEDIFL — for simulating the intersection effect on the vertical distribution of the longitudinal velocities in the channel bend

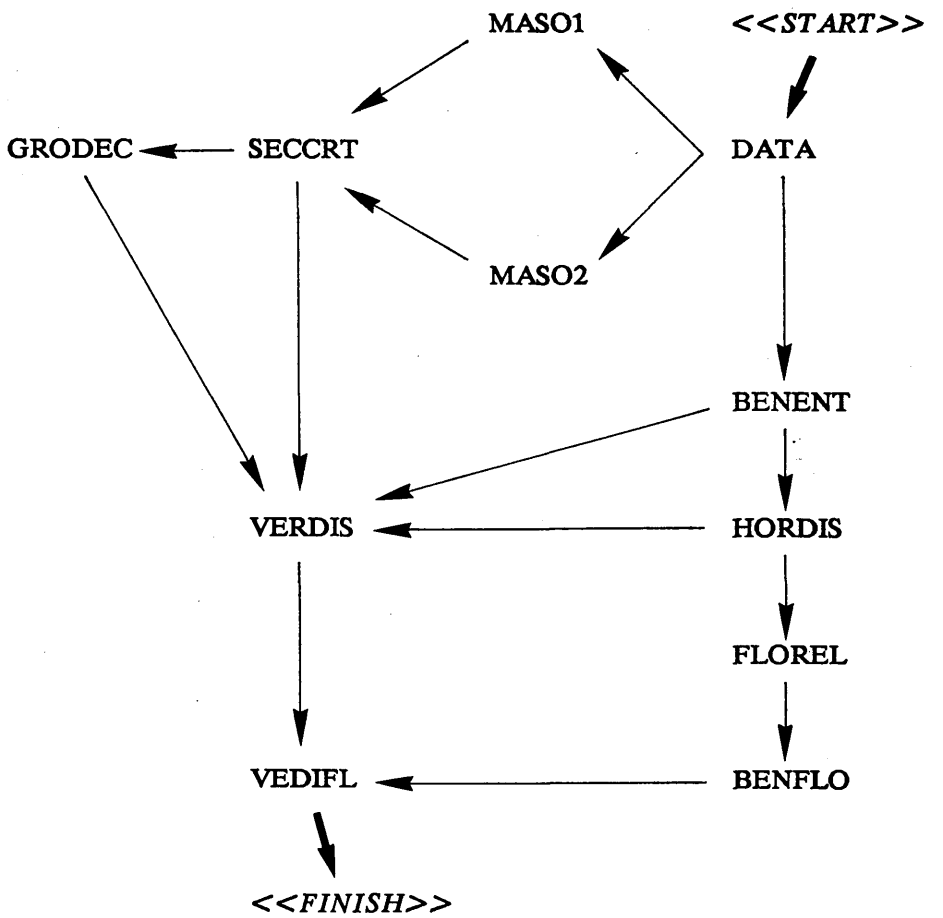

FIG.(D.1) – Schematic representation of the Computational Procedure Involving the Different Subroutines in the Program

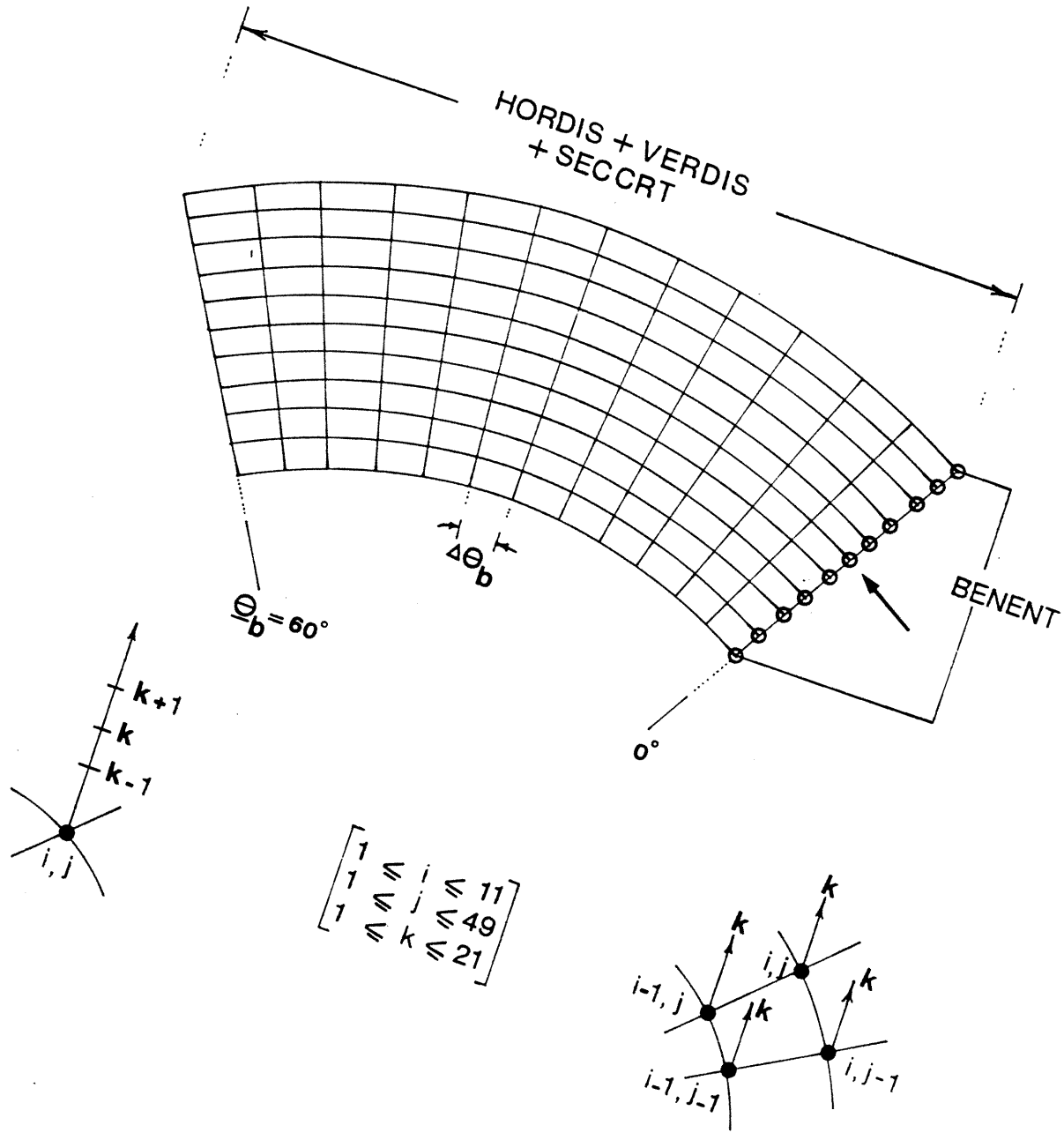

FIG.(D.2) – Grid System for the Computational Procedure of Subroutines SECCRT, BENENT, HORDIS and VERDIS

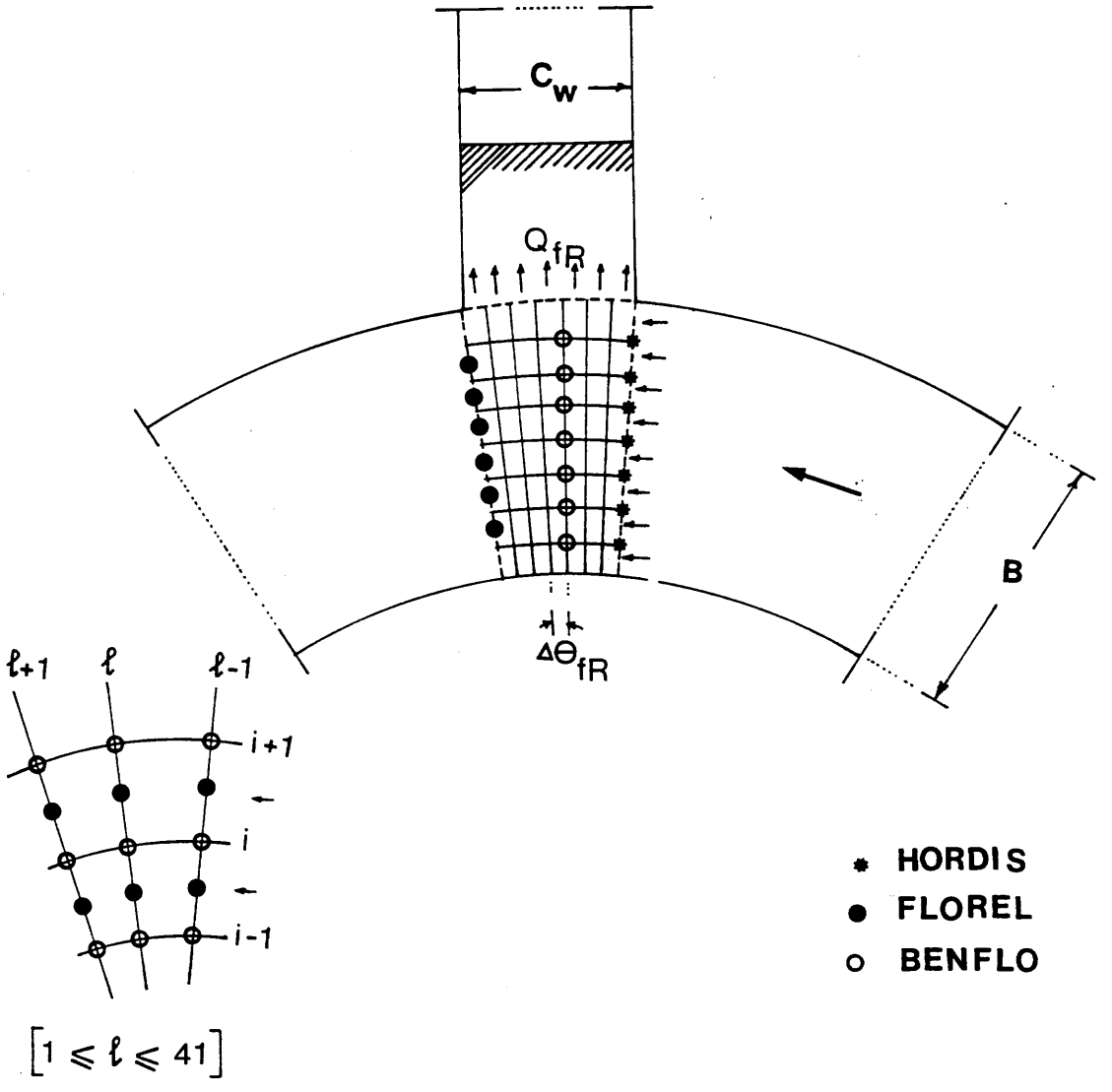

FIG.(D.3) – Grid System for the Computational Procedure of Subroutines FLOREL and BENFLO

FIG.(D.4) – Flow Charts of the Computational Procedures Used in the Subroutines

Key for Flow Charts

Flow Chart		Mathematical Model
C1	≡	integration constant c_1
E(I,W)	≡	$E[i,\ell]$
DA(I,J,K)	≡	$\Theta_d[i,j,k]$
DHF(I,W)	≡	$h[i,\ell]$
DHT(I,J)	≡	$h[i,j]$
DHTF(I,W)	≡	$(h[i+1,\ell] + h[i,\ell])/2$ for $1 \leq i \leq N-1$
DUMLT(I,J)	≡	$\Delta u_m[i,j]/\Delta s$
FRF(I,W)	≡	$F_r[i,\ell]$
I,J,K	≡	i,j,k
I,W	≡	i,ℓ
N,M,L	≡	N,M,L
MM	≡	MM
QBF(I,W)	≡	$Q[i,\ell]$
QQ, QQ1	≡	+ ve and − ve area of the radial discharge Q_r
QWF(I,W)	≡	$Q_{fR}[i,\ell]$
SFF(I,W)	≡	$S_f[i,\ell]$
SLT(I,J)	≡	$S_s[i,j]$
SRT(I,J)	≡	$S_r[i,j]$
THL(I,J)	≡	$\Theta_{lim}[i,j]$
THET(J)	≡	$\Theta_b[j]$
THET(F)	≡	$\Theta_b(j)$ at $\ell = 1$
THW(W)	≡	$\Theta_b[\ell]$
TV(I,J,K)	≡	$\{(u_s[i,j,k])^2 + (u_r[i,j,k])^2\}^{1/2}$
UB(I,1)	≡	$u_{mb}[i,1]$
UBF(I,W)	≡	$u_m[i,\ell]$
UBT(I,J)	≡	$u_m[i,j]$
UBTF(I,W)	≡	$(u_m[i+1,\ell] + u_m[i+\ell])/2$ for $1 \leq i \leq N-1$
ULB(I,J,K)	≡	$u_s[i,j,k]$
ULBF(I,W,K)	≡	um[i,ℓ,k]
UR(K)	≡	$u_r(\lambda)$ for the case of a smooth bed
URD(K)	≡	$u_{rd}(\lambda)$ for the case of a smooth bed
URB(I,J,K)	≡	$u_r[i,j,k]$
URR(K)	≡	$u_r(\lambda)$ for the case of a rough bed
URRD(K)	≡	$u_{rd}(\lambda)$ for the case of a rough bed
ΔURD	≡	±ve correction for URD(K)
ΔURRD	≡	±ve correction for URRD(K)
UZB(I,J,K)	≡	$u_z[i,j,k]$
X	≡	x_d
XI1(K), XI2(K)	≡	$\Phi_1(\lambda)$, $\Phi_2(\lambda)$
XL	≡	x_{dt}
ΔX	≡	step length downstream of the bend

– Subroutine SECCRT

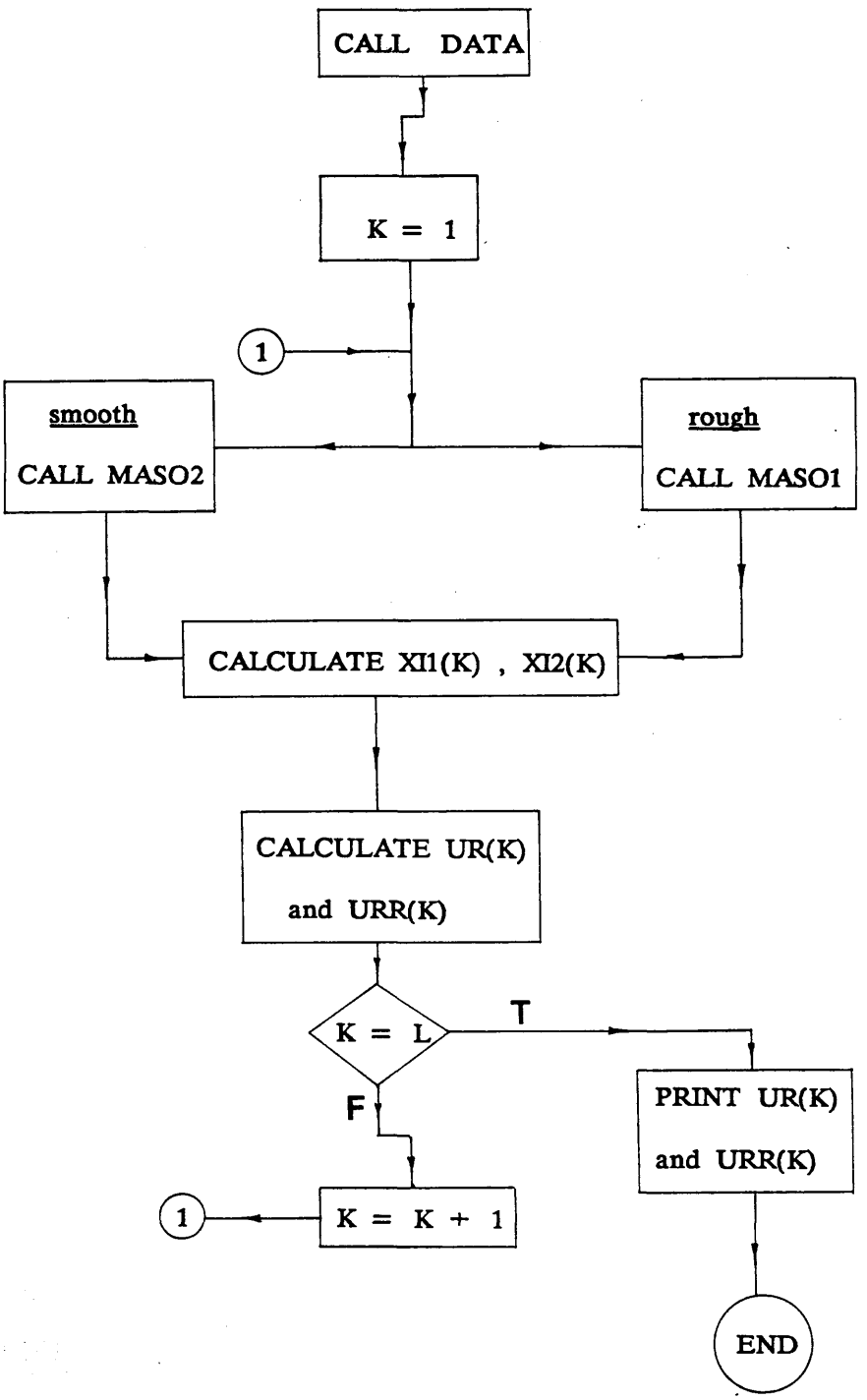

– Subroutine GRODEC

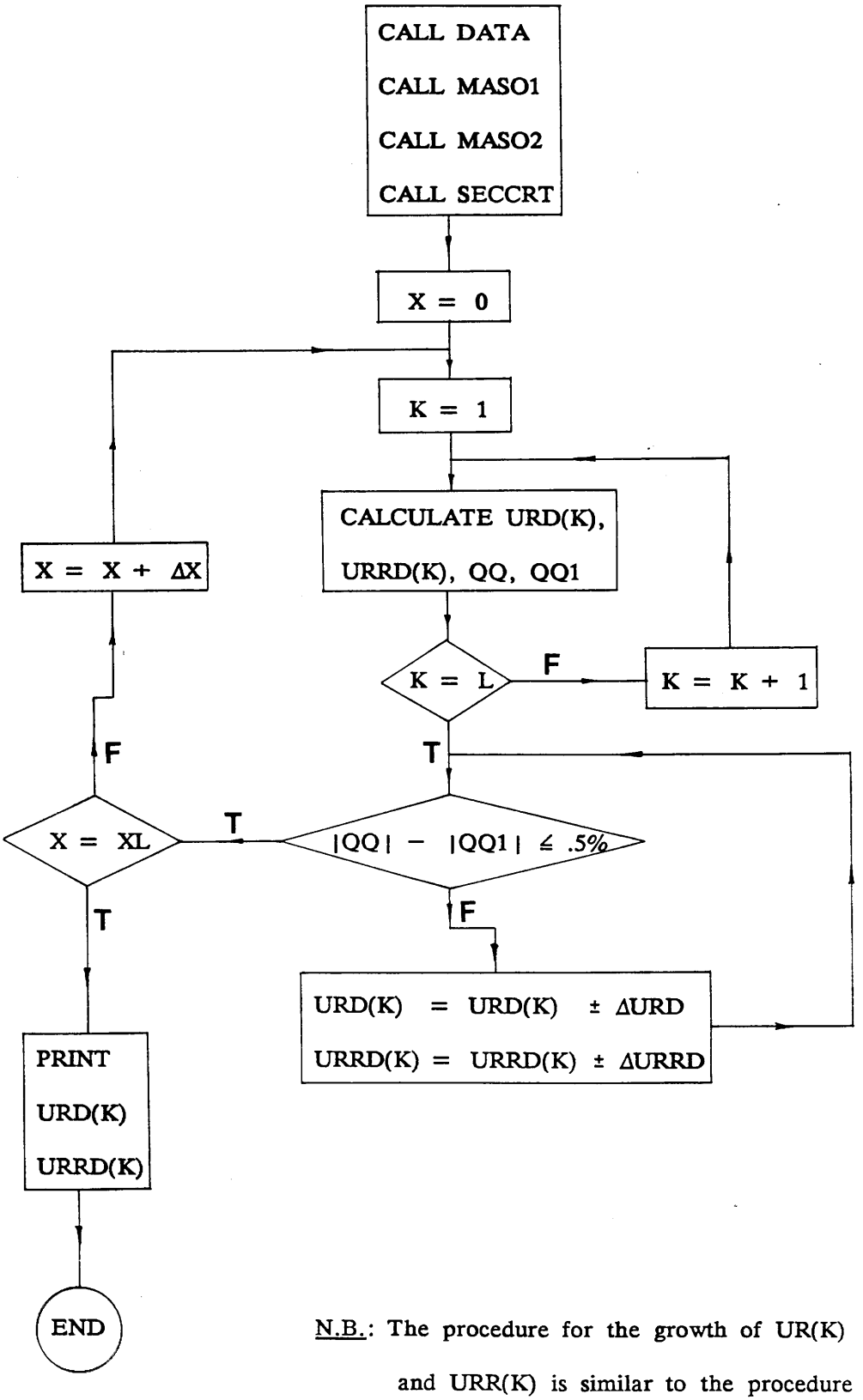

N.B.: The procedure for the growth of UR(K) and URR(K) is similar to the procedure described in this subroutine

– Subroutine BENENT

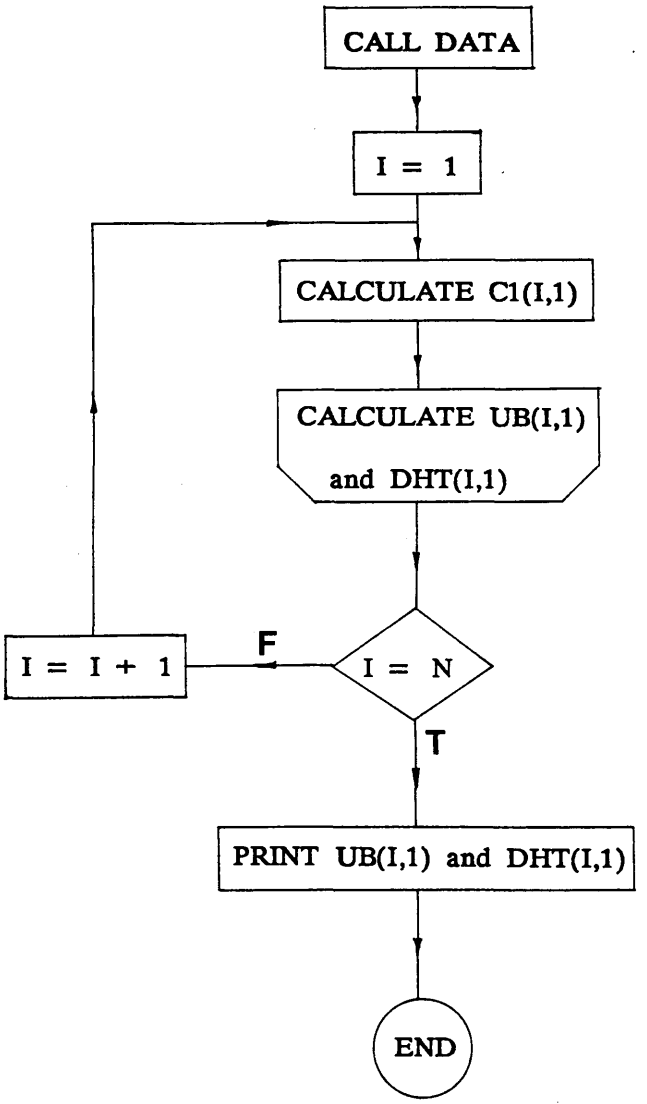

– Subroutine HORDIS

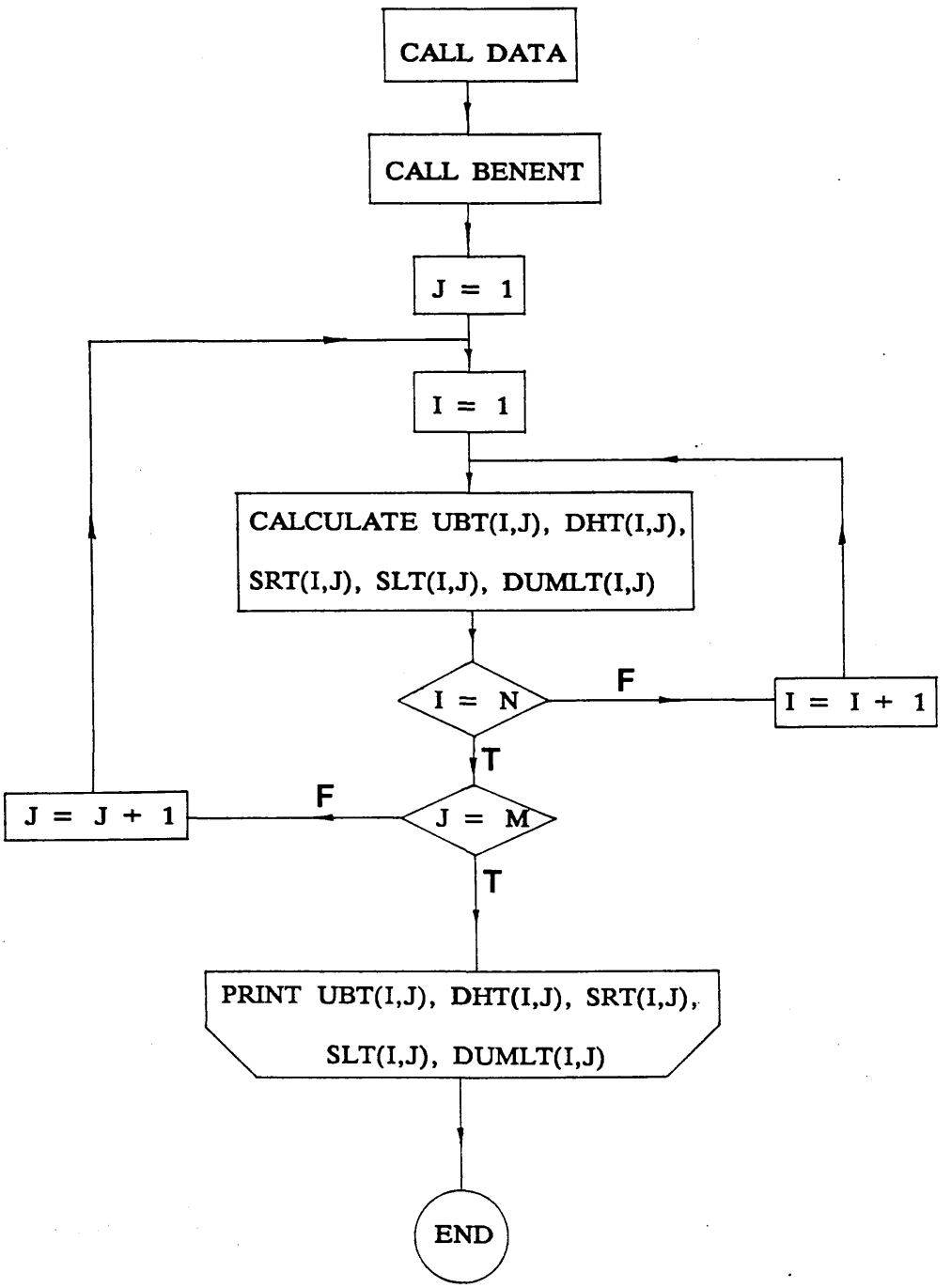

– Subroutine VERDIS

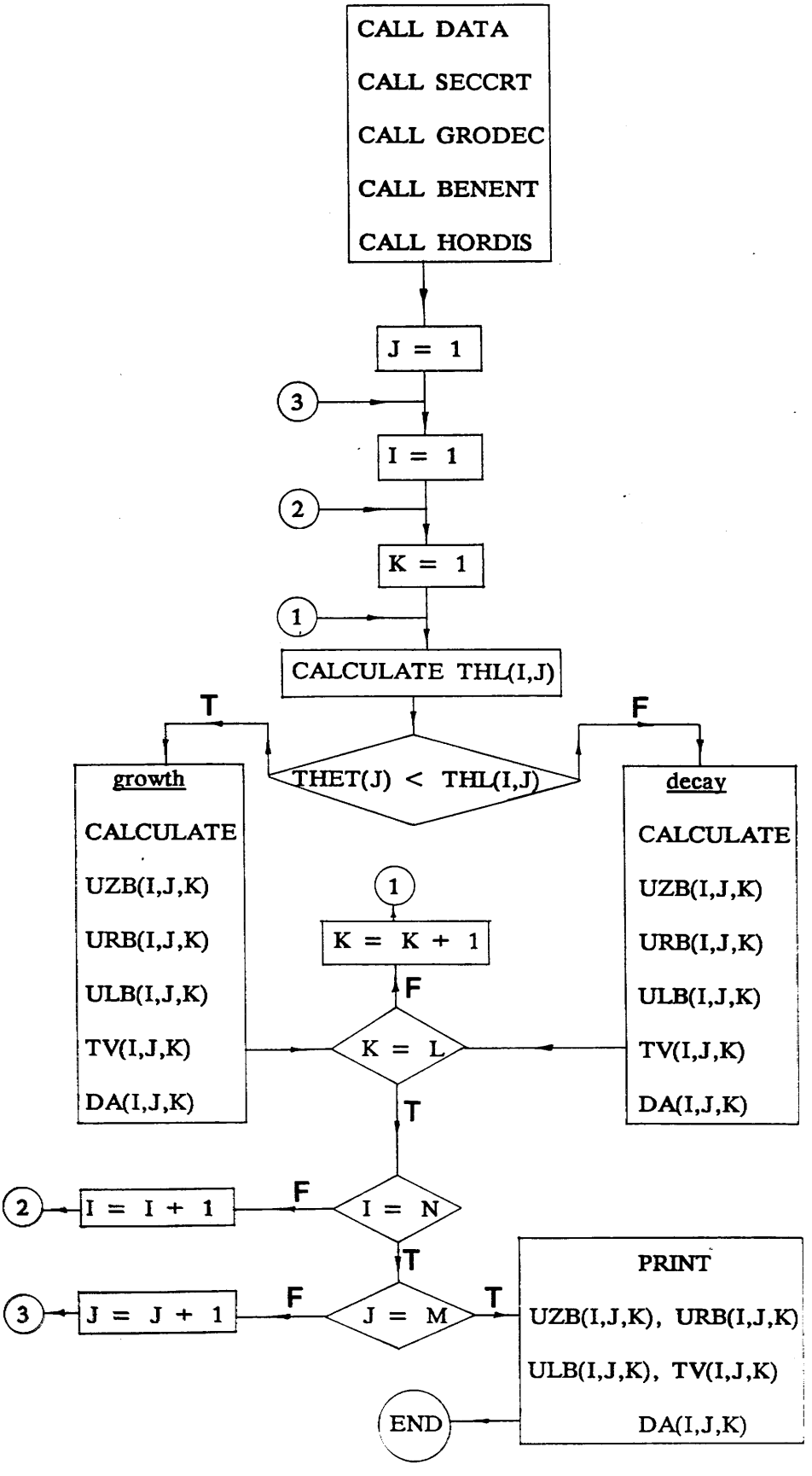

- Subroutine FLOREL

N.B. W is an integer index

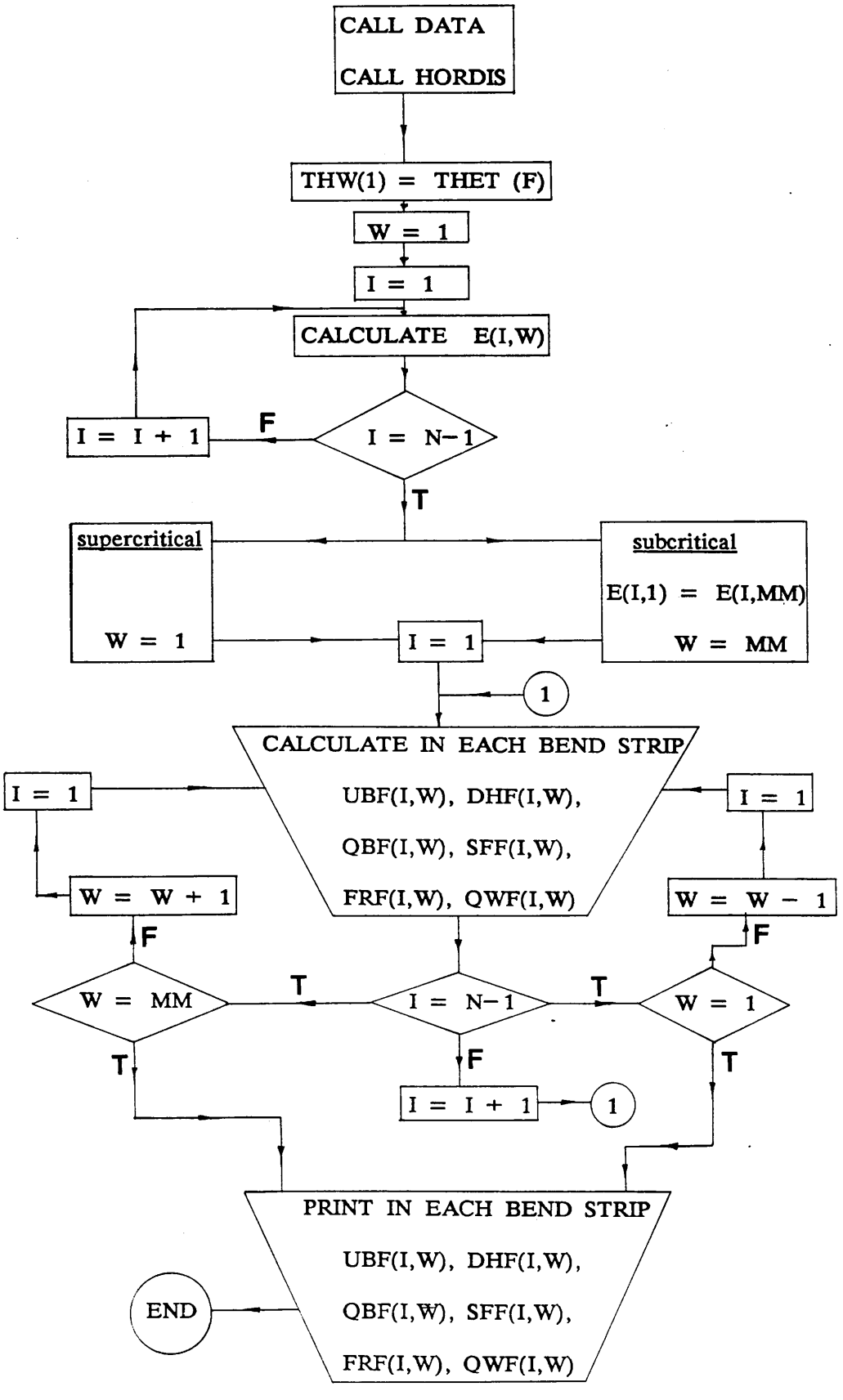

– Subroutine BENFLO

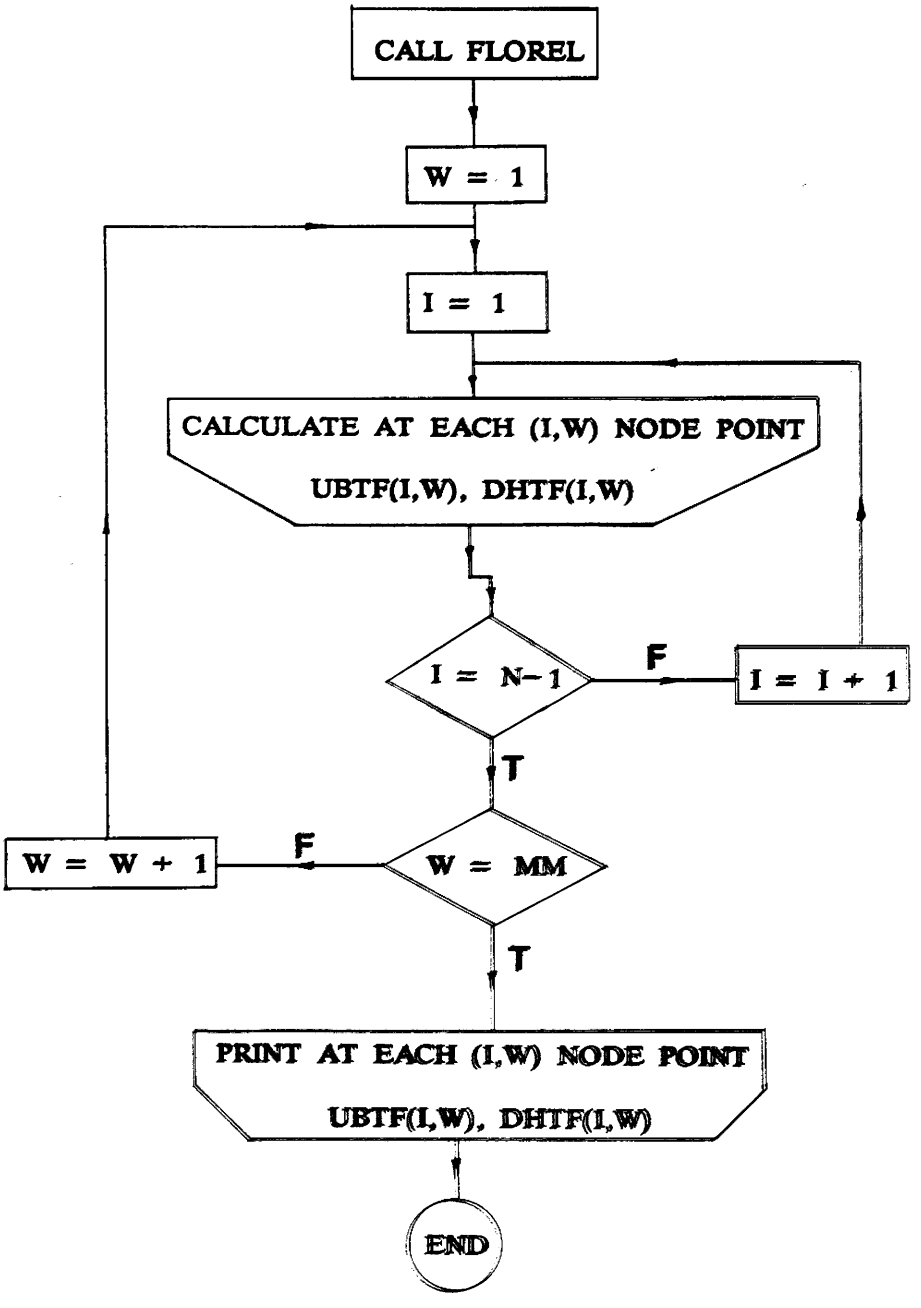

– Subroutine VEDIFL

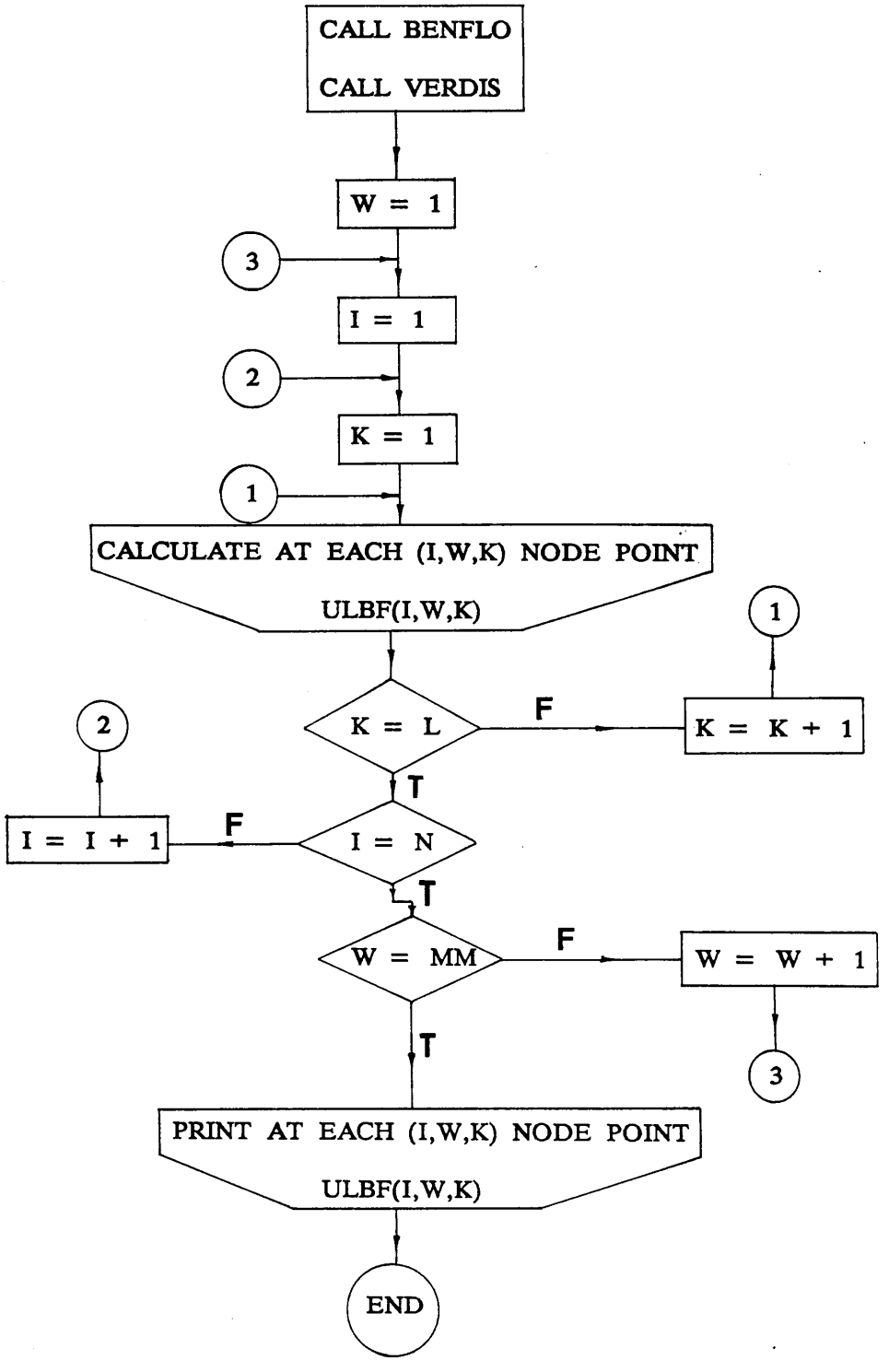

APPENDIX (E)

CALIBRATION AND EXECUTION PROGRAMS FOR THE ANGLE PROBE

In this Appendix, listings of the computer programs used for calibrating the angle probe and for obtaining the deviation angles of the horizontal resultant velocities in the flow are given. The two programs are namely:

(E.1) Calibration Pragram

(E.2) Execution Program

(E.1) Calibration Program

```
\    SAMPLE PROGRAM X
\    THIS PROGRAM USED IN STATIC
\    CALIBRATION OF ANGLE MEASUREMENT DEVICE
\    FREQUENCY SET AT 100 Hz ( ie 100 SAMPLE.X )


INTEGER SCALAR ERROR.CODE
INTEGER SCALAR SEGMT
INTEGER SCALAR CHN
INTEGER SCALAR GAIN
INTEGER SCALAR Z.CHN
INTEGER SCALAR RANGE
INTEGER SCALAR W
INTEGER SCALAR ADATA
REAL DIM[ 3000 ] ARRAY POSITIONX
: ERROR?
   CALL[ PCI46S , ERR.SYS , ERROR.CODE ]
   ERROR.CODE 0 <> IF
      "TYPE ERROR.CODE . CR
   ELSE
      "DROP
   THEN
;
: SAMPLE.X
CR ." SETTING ARRAYS TO ZERO"
0 POSITIONX :=
CR
" 61"H SET.VECT
CALL[ PCI46S , SYSINIT ]
" C000"H SEGMT :=
CALL[ PCI46S , INIT , SEGMT ]
" ERROR FOUND DURING INIT" ERROR?
CR ." PROGRAM SAMPLE.X"
CR
CR ." SETTING GAIN AND RANGE"
0 CHN :=
1 GAIN :=
-1 Z.CHN :=
1 RANGE :=
3001 W :=
CR
CR ." CONFIGURING CHANNEL 0"
CALL[ PCI46S , CNF.AI , CHN , GAIN , Z.CHN , RANGE ]
" ERROR FOUND DURING CNF.AI" ERROR?
CR
CR ." READING CHANNEL"
\ SET FREQUENCY OF SAMPLING
INV 1000. *
SYNC.PERIOD
CR ." DATA AQUISITION LOOP"
W 1 DO
SYNCHRONIZE
CALL[ PCI46S , READ.CH , AI.T , CHN , ADATA ]
ADATA POSITIONX [ I ] :=
LOOP
CR ." DATA CONVERSION"


POSITIONX 20.0 * 4096.0 / 10.0 - GAIN / POSITIONX :=


CR ." NUMBER OF READINGS ON CHANNEL 0 WAS" W 1 - .
;
```

```
\ DETERMINE STATISTICAL PROPERTIES
REAL SCALAR ANGLE
: RESULTSX

CR ." ANGLE (DEGREES) =" ANGLE .
CR ." ANGLE MEASUREMENTS (VOLTS)"
CR ." MEAN VOLTAGE =" POSITIONX MEAN .
CR
CR
;
```

(E.2) Execution Program

```
\  SAMPLE PROGRAM 2 -- ANALOG INPUT WITH PCI-20002M

\    THIS PROGRAM READS AN ANALOG INPUT WITH A PCI-20002M-1
\    USING THE FOLLOWING PCI-20046S-1 INSTRUCTIONS :
\
\        SYSINIT      INIT      ERR.SYS      CNF.AI
\        READ.CH
\
INTEGER SCALAR ERROR.CODE
INTEGER SCALAR SEGMT
INTEGER SCALAR CHN
INTEGER SCALAR GAIN
INTEGER SCALAR Z.CHN
INTEGER SCALAR RANGE
INTEGER SCALAR W
INTEGER SCALAR ADATA
REAL DIM[ 3000 ] ARRAY POSITION0
\
\
\  DEFINE A GENERAL PURPOSE ERROR PROCESSING ROUTINE.
\
: ERROR?              \ ( String --- )
   CALL[ PCI46S , ERR.SYS , ERROR.CODE ]
   ERROR.CODE 0 <> IF
      "TYPE ERROR.CODE . CR
   ELSE
      "DROP
   THEN
;
: SAMPLE.2
CR ." SETTING ARRAYS TO ZERO"
0 POSITION0 :=
\
\  INITIALIZE THE PCI-20046S-4 SYSTEM.  THIS SEQUENCE MUST BE
\  GIVEN PRIOR TO CALLING ANY OTHER PCI-20046S-4 INSTRUCTION.
\
   CR
   " 61"H SET.VECT
   CALL[ PCI46S , SYSINIT ]
\
\  SEGMT, DEFINED BELOW, CONTAINS THE BASE ADDRESS OF THE CARRIER.
\  WE USE " C000"H, BUT YOU CAN SET IT ANYWHERE. REFER TO THE
\  CARRIER MANUAL FOR MORE INFORMATION.
\  [ PCI46S , INIT , SEGMT ] MUST BE CALLED ONCE FOR EACH CARRIER
\  IN THE SYSTEM, EACH WITH ITS OWN ADDRESS.
\
   " C000"H SEGMT :=
    CALL[ PCI46S , INIT , SEGMT ]
\
\  CHECK FOR A SYSTEM ERROR.  DURING DEBUG, CALL ERR.SYS OFTEN,
\  POSSIBLY AFTER EVERY CALL TO THE PCI-20046S-4.  IT IS A GOOD
\  IDEA TO LEAVE A FEW ERR.SYS CALLS IN A FINISHED PROGRAM TO
\  MONITOR THE STATUS OF THE SYSTEM.
\
   " ERROR FOUND DURING INIT" ERROR?
\
\
   CR ." PROGRAM SAMPLE.2"
   CR
   CR ." SETTING GAIN AND RANGE"

   0 CHN :=
   1 GAIN :=
   -1 Z.CHN :=
```

```
   1 RANGE :=
\ W IS THE NUMBER OF READINGS +1 ON CHANNEL
   3001 W :=
   CR
   CR ." CONFIGURING CHANNEL 0"
CALL[ PCI46S , CNF.AI , CHN , GAIN , Z.CHN , RANGE ]
   " ERROR FOUND DURING CNF.AI" ERROR?
\
\  READ THE ANALOG INPUT CHANNEL.
\
   CR
   CR ." READING CHANNEL"
\
\  SCAN CHANNEL 0 AT 100 Hz
   SYNC.ERROR.ON
   INV 1000. *
   SYNC.PERIOD
   W 1 DO
   SYNCHRONIZE
   CALL[ PCI46S , READ.CH , AI.T , CHN , ADATA ]
\
\
\  GIVE THE ADC READING, ADATA, TO ARRAY AND CONVERT
\
\  THE ASSUMPTION IS THAT THE PCI-20002M-1 MODULE IS SET
\  UP FOR +/- 10 VOLTS.
\
\
\
\
\
\
   ADATA POSITION0 [ I ] :=
\
\
   LOOP
   CR ." END OF AQUISITION LOOP"
\
\ CONVERT ARRAY FROM ANALOGUE VOLTAGE
\ TO DIGITAL VOLTAGE TO ANGLE

  POSITION0 20.0 * 4096.0 / 10.0 - GAIN / 1.9020 + 0.0764 / POSITION0 :=

\ PRINT OUT NUMBER OF READINGS FROM CHANNEL

  CR ." NUMBER OF READINGS ON CHANNEL 0 WAS" W 1 - .
  CR
;

\ DETERMINE STATISTICAL PROPERTIES
\ AND PRINT OUT
12 STRING TEST
: RESULTS
  CR ." ANGLE PROBE RESULT"
  CR
  CR ." TEST No" 4 SPACES TEST "TYPE
  CR ." MEAN ANGLE =" POSITION0 MEAN . ." DEGREES"
  CR ." STANDARD DEVIATION =" POSITION0 VARIANCE SQRT .
  CR ." MAXIMUM ANGLE =" POSITION0 []MAX . ." DEGREES"
  CR ." MINIMUM ANGLE =" POSITION0 []MIN . ." DEGREES"
  CR
  CR
;
```

```
: PROC
  4 1 DO
  100 SAMPLE.2
  OUT>PRINTER
  CR ." LOOP NUMBER =" I .
  RESULTS

  CONSOLE
  LOOP
;
```